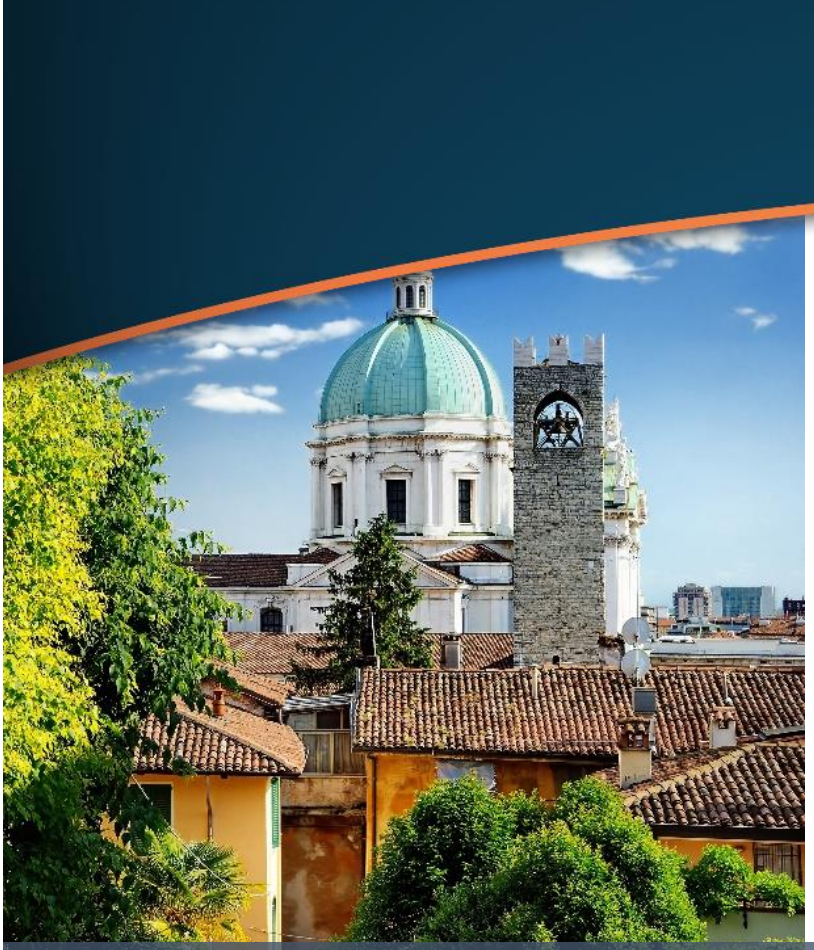

25th IMEKO TC-4 INTERNATIONAL SYMPOSIUM ON

MEASUREMENT OF ELECTRICAL QUANTITIES

SEPTEMBER 12-14, 2022

BRESCIA, ITALY

PROCEEDINGS

ISBN: 978-92-990090-1-7

25th IMEKO TC-4 International Symposium

IMEKO TC-4 2022

PROCEEDINGS

September 12 - 14, 2022 | Brescia, Italy

ISBN: 978-92-990090-1-7

Welcome Message from the General Chairs

On behalf of the Organizing Committee, we cordially welcome you to the 25th IMEKO TC4 Symposium.

The Symposium is held in the thirty-eighth year of the establishment of the IMEKO Technical Committee n.4 "Measurement of Electrical Quantities", and, in Italy, for the sixth time starting from the first edition in 1986 (Como), followed by the 10th edition in 1998 (Naples), 16th edition in 2008 (Florence), 20th edition in 2014 (Benevento), and 24th edition in 2020 (Palermo). The last IMEKO TC4 Symposium has been held online. This year, the IMEKO TC4 Symposium takes place in Brescia, in Northern Italy, specifically in the Lombardy Region. Brescia is an industrial town with a significant historical heritage.

Sites and heritage protected by UNESCO range from the precious **rock engravings in Camonica Valley** to the **archaeological area in the heart of old Brescia**. The **monastery of San Salvatore – Santa Giulia** and **Roman Brescia Archaeological Park** have been listed as a UNESCO Heritage Site on 25th June 2011 as part of the serial site "*Lombards in Italy. Places of Power (568-774 A.D.)*". The monastery complex was modified over the centuries and is a combination of different styles. This valuable monument includes the **Santa Giulia Museum** with its permanent collections and temporary exhibitions, the **Lombard basilica of San Salvatore** with the crypt, the Nun's Choir, and the 16th century church of S. Maria in Solario. Inside the Santa Giulia Museum there are remains of old Roman villas (called domus).In the nearby **Roman Brescia Archaeological Park**, located along Via Musei near Piazza del Foro, one of the oldest squares in Brescia, you can admire the **Capitoline Temple** (73 A.D.) with the new display of the **Winged Victory** and the **Roman Theatre**.

The province of Brescia offers an extraordinary variety of landscapes. Every area has a rich, unique history. Brescia's three lakes, Lake Garda, Lake Idro, and Lake Iseo have their own individual character: Mediterranean. Franciacorta is characterized by gentle rolling hills covered by vineyards. If you are a, you can't miss the green forests and mountains of Camonica Valley, Trompia Valley, and Sabbia Valley are the ideal area for sports and nature enthusiast.

Brescia is a perfect frame for these prestigious events. It is, in fact, a further occasion to meet old friends and new people from all over the world, as well as to engage with them a continuous comparison directed to achieve wider views on the scientific and technological progress of instrumentation and measurement.

We wish to take this opportunity to thank all the Technical Program Committee members, the Special Session Organizers, and the anonymous Reviewers who contributed to make this outstanding program possible, as well as the Authors for submitting their papers and sharing their scientific findings with the IMEKO TC-4 community. The technical program was particularly difficult to arrange, because we received a significant number of abstract from all over the world. Conference time limits allowed us to select only 69 papers. We thank all the local Organizing Committee members that devoted significant efforts to the organization of the two events.

Emilio Sardini, University of Brescia, Italy
Luca De Vito, University of Sannio, Italy

IMEKO TC-4 2022 **General Chairs**

Technical Program Overview

The technical program of the 25th International Symposium IMEKO TC-4 evolves over three days and includes three keynote speeches, thirteen oral sessions and a poster session.
The keynote speeches are

- *How to evolve chemical sensors from a university laboratory to the industrial world for Electronic Nose applications* by Giorgio Sberveglieri, University of Brescia and Nano Sensor Systems;
- *Quantum Electronics in Metrology: Cornerstones and Topical Developments*, by Hansjörg Scherer, Physikalisch-Technische Bundesanstalt, Germany;
- *Advanced Hall Magnetic Sensing and Measurement in Industry and Physics Laboratories*, by Dragana Popovic Renella, SENIS AG, Switzerland.

The sessions cover the whole spectrum of electrical measurements, from primary metrology to topics shared with other disciplines. The oral sessions titles are:
- Quantum metrology
- Voltage measurements
- Resistance and impedance measurements
- Measurements for power and energy (two sessions)
- Measurements by radiofrequency (two sessions)
- Instrumentation
- Sensors
- Dielectrics, Conductors, Magnetics
- Biomedical measurements (two sessions)
- Signal processing and machine learning

In order to allow the attendees to enjoy the beauties of the historical center of Brescia, the first day of the Symposium was organized in the center of Brescia, specifically in the wonderful San Barnaba Auditorium. The following days will be held instead at the University of Brescia.
As Technical Program Chairs, we would like to thank all the members of the Technical Program Committee and the Reviewers, who allowed to improve the level of the contributions even in a short time.

Luca Callegaro, Istituto Nazionale di Ricerca Metrologica, Italy
Platon Sovilj, University of Novi Sad, Serbia

IMEKO TC-4 2022 **Technical Program Chairs**

IMEKO TC-4 2022 Committe

GENERAL CHAIRS
Luca De Vito, *University of Sannio, Italy*
Emilio Sardini, *University of Brescia, Italy*

TECHNICAL PROGRAMME CO-CHAIRS
Luca Callegaro, *Istituto Nazionale di Ricerca Metrologica - INRiM, Italy*
Platon Sovilj, *University of Novi Sad, Serbia*

SPECIAL SESSION CO-CHAIRS
Paolo Bellagente, *University of Brescia, Italy*
Jakub Svatos, *Czech Technical University (CTU) Prague, Czech Republic*

TUTORIAL CHAIRS
Domenico Giordano, *Istituto Nazionale di Ricerca Metrologica - INRiM, Italy*
Jan Saliga, *Technical University of Kosice, Slovakia*

INDUSTRY LIAISON CHAIR
Dragana Popovic-Renella, *SENIS AG, Switzerland*

PUBLICATION CHAIRS
Martina Marzano, *Istituto Nazionale di Ricerca Metrologica - INRiM, Italy*
Dominique Dallet, *University of Bordeaux, France*

AWARD CHAIR
Alexandru Salceanu, *Technical University of Iasi, Romania*

"I. GORINI" SCHOOL LIAISONS
Consolatina Liguori, *University of Salerno, Italy*
Michela Borghetti, *University of Brescia, Italy*

EXHIBITOR AND DEMO CHAIR
Alessandro Cultrera, *Istituto Nazionale di Ricerca Metrologica - INRiM, Italy*

INTERNATIONAL PROGRAM COMMITTEE
TC-4 Chair
Alexandru Salceanu, *Technical University of IAŞI, Romania*

TC-4 Scientific Secretary
Jan Saliga, *Technical University of Košice, Slovakia*

TC-4 Deputy Chair
Dušan Agrež, *University of Ljubljana, Slovenia*

TC-4 Honorary Chair
Mario Savino, *Politecnico di Bari, Italy*

TC-4 Past Chairs
Linus Michaeli, *Technical University of Kosice, Slovakia*
Pasquale Daponte, *University of Sannio, Italy*

CONFERENCE PROGRAM

Monday, September 12

Session 1-1 - Quantum Metrology

Room: Auditorium San Barnaba
Chairs: Luca Callegaro, *Istituto Nazionale di Ricerca Metrologica, Italy*
Blaise Jeanneret, *METAS, Switzerland*

1 **Towards a novel programmable Josephson voltage standard for sampled power measurements**
Bruno Trinchera, Istituto Nazionale di Ricerca Metrologica, Italy
Danilo Serazio, Istituto Nazionale di Ricerca Metrologica, Italy
Paolo Durandetto, Istituto Nazionale di Ricerca Metrologica, Italy
Luca Oberto, Istituto Nazionale di Ricerca Metrologica, Italy
Luca Fasolo, Istituto Nazionale di Ricerca Metrologica, Politecnico di Torino, Italy

7 **Direct Comparison of Quantum Hall Resistance in Graphene and Gallium Arsenide in Liquid Helium**
Ngoc Thanh Mai Tran, Istituto Nazionale di Ricerca Metrologica, Politecnico di Torino, Italy
Jaesung Park, Korea Research Institute of Standards and Science, Republic of Korea
Dong-Hun Chae, Korea Research Institute of Standards and Science, Republic of Korea

13 **Memristive devices as a potential resistance standard**
Vitor Cabral, Instituto Português da Qualidade, Portugal
Alessandro Cultrera, Istituto Nazionale di Ricerca Metrologica, Italy
Shaochuan Chen Chen, RWTH-Aachen university, Germany
João Pereira, INESC Microsistemas e Nanotecnologias, Portugal
Luís Ribeiro, Instituto Português da Qualidade, Portugal
Isabel Godinho, Instituto Português da Qualidade, Portugal
Luca Boarino, Istituto Nazionale di Ricerca Metrologica, Italy
Natascia De Leo, Istituto Nazionale di Ricerca Metrologica, Italy
Luca Callegaro, Istituto Nazionale di Ricerca Metrologica, Italy
Susana Cardoso, INESC Microsistemas e Nanotecnologias, Portugal
Ilia Valov, RWTH-Aachen University, Research Centre Juelich, Germany
Gianluca Milano, Istituto Nazionale di Ricerca Metrologica, Italy

18 **Advancements in quantum voltage standards for time-dependent signals**
Paolo Durandetto, Istituto Nazionale di Ricerca Metrologica, Italy
Danilo Serazio, Istituto Nazionale di Ricerca Metrologica, Italy
Andrea Sosso, Istituto Nazionale di Ricerca Metrologica, Italy

23 **AC Quantum Voltmeter used for Impedance Comparison**
Damir Ilić, University of Zagreb, Croatia
Ralf Behr, Physikalisch-Technische Bundesanstalt, Germany
Jinni Lee, Physikalisch-Technische Bundesanstalt, Germany

Session 1.2 - Measurements for Power and Energy - PART 1

Room: Auditorium San Barnaba
Chair: Damir Ilić, *University of Zagreb, Croatia*

29 **Laboratory reproduction of on-field low power quality conditions for the calibration/verification of electrical energy meters**
Alessandro Cultrera, Istituto Nazionale di Ricerca Metrologica, Italy
Gabriele Germito, Istituto Nazionale di Ricerca Metrologica, Italy
Danilo Serazio, Istituto Nazionale di Ricerca Metrologica, Italy
Flavio Galliana, Istituto Nazionale di Ricerca Metrologica, Italy
Bruno Trinchera, Istituto Nazionale di Ricerca Metrologica, Italy
Giulia Aprile, Istituto Nazionale di Ricerca Metrologica, Italy
Martino Chirulli, VERIFICA S.p.A., Italy
Luca Callegaro, Istituto Nazionale di Ricerca Metrologica, Italy

34 **On Data Compression Algorithms for Power Measurements in Distributed Energy Systems**
Paolo Bellagente, University of Brescia, Italy

39 **Simple method for calibration of PMU calibrators**
Martin Šíra, Czech Metrology Institute, Czech Republic
Stanislav Mašlán, Czech Metrology Institute, Czech Republic

45 **PMU-based metrics for Power Quality Assessment in Distributed Sensor Networks**
Guglielmo Frigo, Swiss Federal Institute of Metrology, Switzerland
Federica Costa, Swiss Federal Institute of Metrology, Switzerland
Federico Grasso Toro, Swiss Federal Institute of Metrology, Switzerland

51 **Temperature Rise in MV Switchgears: the Role of Loose Busbar Joints**
Susanna Spinsante, Polytechnic University of Marche, Italy
Grazia Iadarola, Polytechnic University of Marche, Italy
Gianmarco Mazzocchi, IMESA SpA, Italy
Claudio Romagnoli, IMESA SpA, Italy

Tuesday, September 13

Session 1-3 - Voltage Measurements

Room: Aula Magna - University of Brescia
Chair: Martina Marzano, *Istituto Nazionale di Ricerca Metrologica, Italy*

57 **Design and Characterisation of 1 kV Multirange Resistive Voltage Divider**
Stanislav Mašlán, Czech Metrology Institute, Czech Republic
Martin Šíra, Czech Metrology Institute, Czech Republic

63 **Feasibility of a digital counterpart of thermal-converter-based current step up**
David Peral, Spanish Center of Metrology, Spain
Yolanda A. Sanmamed, Spanish Center of Metrology, Spain
Javier Díaz de Aguilar, Spanish Center of Metrology, Spain

68 **DMMs as voltage ratio standards: a 20 years report**
Pier Paolo Capra, Istituto Nazionale di Ricerca Metrologica, Italy
Claudio Francese, Istituto Nazionale di Ricerca Metrologica, Italy
Flavio Galliana, Istituto Nazionale di Ricerca Metrologica, Italy
Marco Lanzillotti, Istituto Nazionale di Ricerca Metrologica, Italy
Luca Roncaglione Tet, Istituto Nazionale di Ricerca Metrologica, Italy
Andrea Sosso, Istituto Nazionale di Ricerca Metrologica, Italy
Paolo Durandetto, Istituto Nazionale di Ricerca Metrologica, Italy

Session 2-3 - Signal Processing and Machine Learning

Room: Hall N1 - University of Brescia
Chair: Jakub Svatos, *Czech Technical University, Czech Republic*

73 **Identification and Mitigation of Intermodulation Products Using a Baseband Polynomial Distortion Model with Instantaneous Frequency Dependence**
Stanislas Dubois, University of Bordeaux, Thales DMS, France
Bruno Lelong, Thales DMS, France
Jean-Michel Hodé, Thales DMS, France
Guillaume Ferré, University of Bordeaux, France
Dominique Dallet, University of Bordeaux, France

79 **Floating-Point Roundoff Error Analysis in Artificial Neural Networks**
Hussein Al-Rikabi, Budapest University of Technology and Economics, Hungary
Balázs Renczes, Budapest University of Technology and Economics, Hungary

84 **Engine rotational speed estimation using audio recordings and machine learning algorithms**
Cristian Fosalau, "Gheorghe Asachi" Technical University of Iasi, Romania
George Maties, "Gheorghe Asachi" Technical University of Iasi, Romania
Cristian Zet, "Gheorghe Asachi" Technical University of Iasi, Romania

90 **Lithium-Ion Batteries state of charge estimation based on electrochemical impedance spectroscopy and convolutional neural network**
Emanuele Buchicchio, University of Perugia, Italy
Alessio De Angelis, University of Perugia, Italy
Francesco Santoni, University of Perugia, Italy
Paolo Carbone, University of Perugia, Italy

Poster Session

Room: University of Brescia - Engineering Department
Chair: Alessandro Cultrera, *Istituto Nazionale di Ricerca Metrologica, Italy*

96 **Evaluation results of COOMET Key Comparison of Power**
Oleh Velychko, State Enterprise Ukrmetrteststandard, Ukraine
Tetyana Gordiyenko, State University of Telecommunications, Ukraine

102 **Research of Long-Term Drift of the National High-Voltage DC Standard**
Oleh Velychko, State Enterprise Ukrmetrteststandard, Ukraine
Ruslan Vendychanskyi, State Enterprise Ukrmetrteststandard, Ukraine

107 **Automatic Detection System of New Energy Vehicle Charging Pile Based on Image Recognition**
Jianbo Liu, Shandong Institute of Metrology, China
Wenqiang Li, Shandong Institute of Metrology, China
Weizhao Wang, Shandong Institute of Metrology, China
Xuefeng Ma, Shandong Institute of Metrology, China
Mei Yang Bin Deng, Shandong Institute of Metrology, China
Xinyan Wang, Shandong Institute of Metrology, China

113 **Online SFRA characterization of a batch of induction motors for predictive maintenance**
Giovanni Bucci, University of L'Aquila, Italy
Fabrizio Ciancetta, University of L'Aquila, Italy
Andrea Fioravanti, University of L'Aquila, Italy
Edoardo Fiorucci, University of L'Aquila, Italy
Simone Mari, University of L'Aquila, Italy
Andrea Silvestri, University of L'Aquila, Italy

119 **Design and validation of a reference multi-sensor cinemometer for law enforcement applications**
Seif Ben-Hassine, Laboratoire National de métrologie et d'Essais, France
Dominique Renoux, Laboratoire National de métrologie et d'Essais, France
Catherine Yardin, Laboratoire National de métrologie et d'Essais, France
Jabran Zaouali, Laboratoire National de métrologie et d'Essais, France
Jimmy Dubard, Laboratoire National de métrologie et d'Essais, France
Jean-Marie Lerat, Laboratoire National de métrologie et d'Essais, France
Pierre Betis, Laboratoire National de métrologie et d'Essais, France
Isabelle Blanc, Laboratoire National de métrologie et d'Essais, France

161 **Instrumentation for EEG-based monitoring of the executive functions in a dual-task framework**
Leopoldo Angrisani, University of Naples Federico II, Italy
Andrea Apicella, University of Naples Federico II, Italy
Pasquale Arpaia, University of Naples Federico II, Italy
Andrea Cataldo, University of Salento, Italy
Anna Della Calce, University of Naples Federico II, Italy
Allegra Fullin, University of Campania "Luigi Vanvitelli", Italy
Ludovica Gargiulo, University of Naples Federico II, Italy
Luigi Maffei, University of Campania "Luigi Vanvitelli", Italy
Nicola Moccaldi, University of Naples Federico II, University of Salento, Italy
Andrea Pollastro, University of Naples Federico II, Italy

166 **Latest Advancements in SSVEPs Classification for Single-Channel, Extended Reality-based Brain-Computer Interfaces**
Leopoldo Angrisani, University of Naples Federico II, Italy
Pasquale Arpaia, University of Naples Federico II, Italy
Egidio De Benedetto, University of Naples Federico II, Italy
Nicola Donato, University of Messina, Italy
Luigi Duraccio, Polytechnic University of Turin, Italy

Session 1-4 - Measurement for Power and Energy - PART 2

Room: Aula Magna - University of Brescia
Chairs: Cristian Fosalau, *"Gheorghe Asachi" Technical University of Iasi, Romania*
Bruno Trinchera, *Istituto Nazionale di Ricerca Metrologica, Italy*

171 **Improvement of calibration capabilities with an a posteriori evaluation of the lighting impulse international comparison EURAMET.EM-S42**
Stefano Emilio Caria, Istituto Nazionale di Ricerca Metrologica, Politecnico di Torino, Italy
Paolo Emilio Roccato, Istituto Nazionale di Ricerca Metrologica, Italy

177 **Design of integrated multi-user electric energy meter**
Jianbo Liu, Shandong Institute of Metrology, China
Wenqiang Li, Shandong Institute of Metrology, China
Mei Yang, Shandong Institute of Metrology, China
Xiao Liu, Shandong Institute of Metrology, China
Bin Deng, Shandong Institute of Metrology, China
Weizhao Wang, Shandong Institute of Metrology, China
Xuefeng Ma, Shandong Institute of Metrology, China

181 **Characterization of a method for transmission line parameters estimation with respect to PMU measurement error modeling**
Paolo Attilio Pegoraro, University of Cagliari, Italy
Carlo Sitzia, University of Cagliari, Italy
Antonio Vincenzo Solinas, University of Cagliari, Italy
Sara Sulis, University of Cagliari, Italy

187 **Measurement issues on harmonic analysis according to the IEC 61000-4-7**
Giovanni Artale, Università degli Studi di Palermo, Italy
Giuseppe Caravello, Università degli Studi di Palermo, Italy
Antonio Cataliotti, Università degli Studi di Palermo, Italy
Valentina Cosentino, Università degli Studi di Palermo, Italy
Vito Ditta, Università degli Studi di Palermo, Italy
Dario Di Cara, INM - National Research Council, Italy
Nicola Panzavecchia, INM - National Research Council, Italy
Giovanni Tinè, INM - National Research Council, Italy
Nunzio Dipaola, STMicroelectronics S.r.l., Italy
Marilena G. Sambataro, STMicroelectronics S.r.l., Italy

193 **Bidirectional electricity meter metrological evaluation**
Marcelo M Costa, Eletrobras Eletronorte, Brazil

Session 2-4 - Biomedical Measurements - PART 1

Room: Hall N1 - University of Brescia
Chairs: Ján Šaliga, *Technical University of Košice, Slovakia*
Mario Savino, *Politecnico di Bari, Italy*

198 **Application Scenarios for Gait Analysis with Wearable Sensors and Machine Learning**
Mauro D'Arco, University of Naples Federico II, Italy
Martina Guerritore, University of Naples Federico II, Italy
Annarita Tedesco, University of Bordeaux, France

204 **Human exposure in a 5G cellular base station environment in residential districts of Iasi city**
Marius-Vasile Ursachianu, National Authority for Management and Regulation in Communications, Romania
Catalin Lazarescu, National Authority for Management and Regulation in Communications, Romania
Ovidiu Bejenaru, National Authority for Management and Regulation in Communications, Romania
Alexandru Salceanu, "Gheorghe Asachi" Technical University of Iasi, Romania

210 **Gaussian-based analysis for accurate compressed ECG trace streaming**
Alessandra Galli, University of Padova, Italy
Giada Giorgi, University of Padova, Italy
Claudio Narduzzi, University of Padova, Italy

215 **Multiwavelet-based ECG compressed sensing with samples difference thresholding**
Jozef Kromka, Technical University of Kosice, Slovakia
Ondrej Kovac, Technical University of Kosice, Slovakia
Jan Saliga, Technical University of Kosice, Slovakia
Linus Michaeli, Technical University of Kosice, Slovakia

221 **Numerical Modelling of the Magnetic Fields Generated by Underground Power Cables with Two-point Bonded Shields**
Eduard Lunca, "Gheorghe Asachi" Technical University of Iasi, Romania
Silviu Vornicu, "Gheorghe Asachi" Technical University of Iasi, Romania
Alexandru Salceanu, "Gheorghe Asachi" Technical University of Iasi, Romania

---

Session 1-5 - Resistance and Impedance Measurements

Room: Aula Magna - University of Brescia
Chairs: Luca Callegaro, *Istituto Nazionale di Ricerca Metrologica, Italy*
Jaesung Park, *Korea Research Institute of Standards and Science, South Korea*

227 **Interlaboratory Comparison of Low Impedance for Impedance Spectroscopy**
Stanislav Mašlán, Czech metrology institute, Czech Republic
Hans He, Research Institutes of Sweden, Sweden
Tobias Bergsten, Research Institutes of Sweden, Sweden
Steffen Seitz, Physikalisch-Technische Bundesanstalt, Germany
Tom Patrick Heins, Physikalisch-Technische Bundesanstalt, Germany

233 **Comparison of DC current comparator bridges for resistance metrology**
Martina Marzano, Istituto Nazionale di Ricerca Metrologica, Italy
Pier Paolo Capra, Istituto Nazionale di Ricerca Metrologica, Italy
Cristina Cassiago, Istituto Nazionale di Ricerca Metrologica, Italy
Vincenzo D'Elia, Istituto Nazionale di Ricerca Metrologica, Italy
Enrico Gasparotto, Istituto Nazionale di Ricerca Metrologica, Italy
Luca Callegaro, Istituto Nazionale di Ricerca Metrologica, Italy

238 **Mutual validation of PTB's Josephson and INRIM-POLITO's electronic impedance bridges for the realization of the farad from graphene quantum standards**
Martina Marzano, Istituto Nazionale di Ricerca Metrologica, Italy
Yaowaret Pimsut, Physikalisch-Technische Bundesanstalt, Germany, National Institute of Metrology, Thailand
Mattias Kruskopf, Physikalisch-Technische Bundesanstalt, Germany
Yefei Yin, Physikalisch-Technische Bundesanstalt, Germany
Marco Kraus, Physikalisch-Technische Bundesanstalt, Germany
Massimo Ortolano, Politecnico di Torino, Istituto Nazionale di Ricerca Metrologica, Italy
Stephan Bauer, Physikalisch-Technische Bundesanstalt, Germany
Ralf Behr, Physikalisch-Technische Bundesanstalt, Germany
Luca Callegaro, Istituto Nazionale di Ricerca Metrologica, Italy

243 **A New Impedance Metrology Infrastructure at GUM**
Krzysztof Musioł, Silesian University of Technology, Poland
Maciej Koszarny, Central Office of Measures, Poland
Marian Kampik, Silesian University of Technology, Poland
Krzysztof Kubiczek, Silesian University of Technology, Poland
Adam Ziółek, Central Office of Measures, Poland
Jolanta Jursza, Central Office of Measures, Poland

Session 2-5 - Instrumentation

Room: Hall N1 - University of Brescia
Chairs: Linus Michaeli, *Technical University of Košice, Slovakia*
Jan Holub, *Czech Technical University in Prague, Czech Republic*

248 **Bias-induced Impedance of Current-carrying Conductors: Measurements Simulation Using FRA**
Sioma Baltianski, Israel Institute of Technology, Israel

254 **Increasing of Sampling Rate of Internal ADC in Microcontrollers by Equivalent-Time Sampling**
Jakub Svatos, Czech Technical University in Prague, Czech Republic
Jan Fischer, Czech Technical University in Prague, Czech Republic
Jan Holub, Czech Technical University in Prague, Czech Republic

260 **Antennas Comparison Applied to Detect Partial Discharges Coupled via Dielectric Window and Oil Valve in Power Transformers**
Arthur Silva Souza, Federal University of Campina Grande, Brazil
Raimundo Carlos Silveiro Freire, Federal University of Campina Grande, Brazil
Luiz Augusto M. M. Nobrega, Federal University of Campina Grande, Brazil
Felipe Alexandre Da Silva Bento, Federal University of Campina Grande, Brazil
George Victor Rocha Xavier, Federal University of Sergipe, Brazil
Marlo Andrade, Federal University of Campina Grande, Federal Institute of Pernambuco, Brazil, University of Bordeaux, France

266 **Iterative Interpolated DFT-based Frequency Estimator for Electrical Waveform Affected by Decaying DC Offset**
Daniel Belega, University Politehnica Timisoara, Romania
Dario Petri, University of Trento, Italy
Dominique Dallet, University of Bordeaux, France

271 **Cascaded H-Bridges Multilevel Inverter Drive: Active Power Analysis in Frequency Domain**
Antonino Oscar Di Tommaso, University of Palermo, Italy
Rosario Miceli, University of Palermo, Italy
Claudio Nevoloso, University of Palermo, Italy
Gioacchino Scaglione, University of Palermo, Italy
Giuseppe Schettino, University of Palermo, Italy
Ciro Spataro, University of Palermo, Italy

Wednesday, September 14

Session 1-6 - Biomedical Measurements - PART 2

Room: Aula Magna - University of Brescia
Chairs: Luca De Vito, *University of Sannio, Italy*
Susanna Spinsante, *Università Politecnica delle Marche, Italy*

277 **A Preliminary Study on Flexible Temperature Sensors for Eskin Medical Devices**
Tiziano Fapanni, University of Brescia, Italy
Emilio Sardini, University of Brescia, Italy
Mauro Serpelloni, University of Brescia, Italy

282 **A novel CS-based measurement method for radial artery pulse wave estimation**
Jozef Kromka, Technical University of Kosice, Slovakia
Jan Saliga, Technical University of Kosice, Slovakia
Ondrej Kovac, Technical University of Kosice, Slovakia
Luca De Vito, University of Sannio, Italy
Francesco Picariello, University of Sannio, Italy
Ioan Tudosa, University of Sannio, Italy

288 **Comparison between a PPG Wearable Device and an AFE4403-Based Pulse Oximeter**
Erika Pittella, Sapienza - University of Rome, Italy
Alice Bologni, EsseDH S.r.l., Italy
Roberta Cervoni, Sapienza - University of Rome, Italy
Vincenzo Fortunato, EsseDH S.r.l., Italy
Emanuele Piuzzi, Sapienza - University of Rome, Italy

293 **Design, metrological analysis and optimization of solenoid for homogenization of electromagnetic fields in biomedical experiments**
Slavica Gajić, University of Banja Luka, Bosnia and Herzegovina
Platon Sovilj, University of Novi Sad, Serbia

Session 1-7 - Measurements by Radiofrequency - PART 1

Room: Aula Magna - University of Brescia
Chairs: Gábor Hegyi, *Bay Zoltán Nonprofit Ltd. for Applied Research, Hungary*
Kostiantyn Torokhtii, *Roma Tre University, Italy*

298 **Material Characterization at Millimeter Wave Frequencies in TUBITAK UME**
Erkan Danaci, TUBITAK National Metrology Institute, Turkey
Emre Cetin, Spark Ölçüm Teknolojileri A.Ş., Turkey

304 **An electro-optic system implementing an accurate phase measurement method for sinewave signals**
Luca De Vito, University of Sannio, Italy
Francesco Picariello, University of Sannio, Italy
Sergio Rapuano, University of Sannio, Italy
Ioan Tudosa, University of Sannio, Italy

310 **Compact Monopole Antenna for Smart Meter Applications in ISM Band 900 MHz**
Marlo Andrade, University of Bordeaux, France, Federal Institute of Pernambuco, Brazil, Federal University of Campina Grande, Brazil
Raimundo C.S. Freire, Federal University of Campina Grande, Brazil
Paulo Fernandes da Silva Júnior, State University of Maranhão, Brazil
Ewaldo E.C. Santana, State University of Maranhão, Brazil
Eduarda Froes dos Santos, State University of Maranhão, Brazil
Maria G.A. de Souza, Federal University of Campina Grande, Brazil
Arthur S. Souza, Federal University of Campina Grande, Brazil
Alexandre J.R. Serres, Federal University of Campina Grande, Brazil

Session 2-7 - Sensors

Room: Hall N1 - University of Brescia

Chairs: Platon Sovilj, *University of Novi Sad, Serbia*
Massimo Ortolano, *Politecnico di Torino, Italy*

315 **Static Characterization of the X-Hall Current Sensor in BCD10 Technology**
Gian Piero Gibiino, University of Bologna, Italy
Marco Crescentini, University of Bologna, Italy
Marco Marchesi, STMicroelectronics, Italy
Marco Cogliati, STMicroelectronics, Italy
Aldo Romani, University of Bologna, Italy
Pier Andrea Traverso, University of Bologna, Italy

320 **Image quality comparison of two different experimental setups for MEMS actuators functional evaluation: a preliminary study**
Gabriele Bocchetta, Roma Tre University, Italy
Giorgia Fiori, Roma Tre University, Italy
Andrea Scorza, Roma Tre University, Italy
Salvatore Andrea Sciuto, Roma Tre University, Italy

325 **A preliminary study on the blind angle estimation for Quality Assessment of Color Doppler ultrasound diagnostic systems**
Giorgia Fiori, Roma Tre University, Italy
Andrea Scorza, Roma Tre University, Italy
Maurizio Schmid, Roma Tre University, Italy
Jan Galo, IRCCS Children Hospital Bambino Gesù, Italy
Silvia Conforto, Roma Tre University, Italy
Salvatore A. Sciuto, Roma Tre University, Italy

330 **Development and Prototyping of a Capacitive Oil Level Sensor for Aeronautical Applications**
Francesco Adamo, Polytechnic University of Bari, Italy
Filippo Attivissimo, Polytechnic University of Bari, Italy
Sergio de Gioia, Polytechnic University of Bari, Italy
Attilio Di Nisio, Polytechnic University of Bari, Italy
Daniel Lotano, Polytechnic University of Bari, Italy
Mario Savino, Polytechnic University of Bari, Italy

Session 1-8 - Measurements by Radiofrequency - PART 2

Room: Aula Magna - University of Brescia

Chairs: Erkan Danaci, *TUBITAK UME, National Metrology Institute of Turkey, Turkey*
Erika Pittella, *Sapienza University of Rome, Italy*

335 **EMC Case Study: Using Resistors Instead of Ferrite Ring to Reduce Emis s ion of Battery Powered Equipment**
Tamás Bodolai, Bay Zoltán Nonprofit Ltd. for Applied Research, Hungary
Gábor Hegyi, Bay Zoltán Nonprofit Ltd. for Applied Research, Hungary
Angéla Váradiné Szarka, Bay Zoltán Nonprofit Ltd. for Applied Research, Hungary

340 **Using a Simulation of ALSE Long Wire Method to Lower Measurement Uncertainty in EMC Measurements**
Gábor Hegyi, Bay Zoltán Nonprofit Ltd. for Applied Research, Hungary
Tamás Bodolai, Bay Zoltán Nonprofit Ltd. for Applied Research, Hungary

346 **Design and test of an inkjet-printed microwave interdigital capacitor on flexible Kapton substrate**
Giovanni Gugliandolo, University of Messina, Italy
Andrea Alimenti, Roma Tre University, Italy
Kostiantyn Torokhtii, Roma Tre University, Italy
Nicola Pompeo, Roma Tre University, Italy
Giuseppe Campobello, University of Messina, Italy
Giovanni Crupi, University of Messina, Italy
Enrico Silva, Roma Tre University, Italy
Nicola Donato, University of Messina, Italy

Session 2-8 - Dielectrics, Conductors, Magnetics

Room: Hall N1 - University of Brescia

Chairs: Dragana Popovic Renella, *SENIS AG, Switzerland*
Dragana Naumovic-Vukovic, *Electrical Engineering Institute Nikola Tesla, Serbia*

25th IMEKO TC4 International Symposium
23rd International Workshop on ADC and DAC Modelling and Testing
IMEKO TC-4 2022
Brescia, Italy / September 12-14, 2022

Towards a novel programmable Josephson voltage standard for sampled power measurements

Bruno Trinchera[1], Danilo Serazio[1], Paolo Durandetto[1], Luca Oberto[1], Luca Fasolo[1,2]

[1] *Istituto Nazionale di Ricerca Metrologica - INRiM, Strada delle Cacce 91, 10135-Turin, Italy*
e-mail b.trinchera@inrim.it
[2] *Politecnico di Torino, DET, Corso Duca degli Abruzzi 24, 10129-Turin, Italy*

***Abstract* – The paper deals with recent progress at INRiM towards the setting up and preliminary characterization of a novel programmable Josephson voltage standard (PJVS) operating in a small liquid helium dewar. The PJVS setup is based on a 1-V superconductor-normal metal-superconductor (SNS) binary-divided array of 8192 Josephson junctions. To ensure proper operating conditions of the PJVS chip a custom short cryoprobe was designed, built and successfully tested. The overall system is being developed in the framework of EMPIR project 19RPT01-QuantumPower. The goal is to establish a new quantum voltage standard for sampled power measurement and to gain confidence in running quantum voltage standards for precise calibration of digital sampling multimeters and arbitrary waveform digitizers used in the ac-voltage and power metrology community.**

I. INTRODUCTION

In the era of clean energy transition, the electrical power system is assisting a rapid growth of renewable energy sources with unprecedented levels of integration and rapid decarbonisation of the electricity supply. For stable operation of smart grids, precise and traceable electrical power measurements are required to guarantee stable supply, prevent blackouts, identify the origin and causes of the disturbances, and ensure a fair electricity market. National metrological institutes (NMIs) are working closely with network operators to face the electricity system and grid paradigm shift in response to the EU energy transition and clean energy target.

Presently, in most NMIs, the primary electrical power has traceability to the volt and ampere using a long calibration chain, which involves the use of thermal converters, voltage and current transducers and digitizers. Most recent implementations show that, through a complicated calibration chain, it is possible to achieve sampling-based power measurements with a relative uncertainty ranging from 1 µW/VA to 10 µW/VA (coverage factor k=1) at power-line frequency and at any power factor [1]-[3].

More complex experimental setups aim to integrate ac-quantum voltage standards with sampling power standards [4]- [6] to provide more direct traceability routes of active, reactive and apparent power components to the SI-volt with reduced uncertainty.

In particular, in the framework of the EMPIR project 19RPT01 - QuantumPower, a strong collaboration is taking place between several NMIs to deliver the necessary infrastructure for validated quantum-referenced power measurements and its availability to industry. The initiative brings together the experience gained during the last two decades from the involved NMIs in the field of quantum voltage and electrical power. The project aims to design and build an open-access quantum sampling electrical power standard, which will lead to increased confidence in power measurements used for calibration and validation of standard wattmeters, static energy meters, phantom power sources, power analyzers and new emerging equipment for monitoring and identification of electricity-grid stability parameters where the confidence and traceability are crucial. The new quantum power standard will benefit from the use of quantum voltage standard based on programmable Josephson voltage standard (PJVS) which plays a crucial role in the redefinition of the SI-volt unit.

The research activity being developed at the Istituto Nazionale di Ricerca Metrologica (INRiM) in the framework of 19RPT01 project foresees the integration of two main key components into its modular digital sampling power standard (DSPS) [3]: i) an ac-quantum voltage standard; ii) a synchronous coaxial multiplexer. This will allow to shorten as much as possible the traceability chain employed for the calibration of DSPS constituents by ensuring a direct link of sampled power measurements to the SI-volt, and therefore a reduction in the measurement uncertainty.

The present paper focuses on recent progress towards the development of a novel programmable quantum-based voltage standard which will be integrated into the INRiM modular digital sampling power standard [3].

As the development of such a programmable Josephson voltage standard (PJVS) as a whole is new, it was necessary to carefully design and characterize almost all constituents of the experimental setup. With respect to conventional PJVS, our intent was to develop a compact and transportable experimental bench based on a small liquid helium (LHe) dewar and a home-made short cryoprobe equipped with all essentials parts to ensure suitable operating conditions of the PJVS array.

The maximum output voltage of the PJVS array was chosen to be close to the output voltage level of voltage and current transducers in use at the primary power and energy laboratory of INRiM, which never exceeds 800 mVrms applying nominal quantities to the voltage and current transducers inputs.

II. PJVS SYSTEM DETAILS

It is well known that binary-divided Josephson arrays provide quantized voltages according to fundamental Josephson equation for quantum voltage metrology,

$$U(t) = n\,M(t)\,\frac{h}{2e}f \qquad (1)$$

where n denotes the order of the Shapiro step, M represents the number of Josephson junctions in the "active" state, h and e are the Planck constant and elementary charge, and f the microwave frequency. For proper operation of a PJVS device, two additional conditions must be fulfilled: a) cooling down the array to cryogenic temperatures, e.g. around 4.2 K, and b) rapidly biasing different sub-arrays containing different number of junctions.

At present, both low-frequency current bias and microwave radiation are provided by conventional electronics operating at room temperature, so the connection between the cryogenic environment and room-temperature electronics is performed by using purposely-designed cryoprobes. In the following we report details about the main equipment used for running the PJVS array.

A. Consideration on the small LHe dewar

A LHe dewar designed and manufactured by Precision Cryogenic Systems, Inc. has been used in the proposed experimental setup. The dewar was dimensioned to contain 30 l of LHe and its overall height is about 67 cm. The internal vessel is made of aluminum and the lower inner part is similar to a cylindrical glass with diameter of about 7.73 cm and about 20.3 cm high. This is the useful part dedicated to the experiment and it is wrapped out with a cylindrical AD-MU-80 magnetic shield.

First experiments showed that the small dewar performances in terms of boil-off features and normal evaporation rate are compliant to conventional dewars.

Fig. 1 reports the dewar equipment and the top part of the custom home made cryoprobe.

Fig. 1. Photograph of the dewar with the short cryoprobe inserted end equipment to ensure safety operation during its use.

B. Custom short cryoprobe design

Fig. 2 reports a picture of the custom short LHe-cryoprobe properly designed to host the 1 V PJVS array. Its main support is a low conductivity stainless steel tube with diameter of about 28 mm and length of 700 mm. Internally, an oversized circular waveguide with diameter of about 14 mm and length of 80 mm has been installed. The key parameters of the oversized circular waveguide are: low-microwave loss (attenuation 1 - 3 dB/m at 70 - 75 GHz); low thermal conductivity; temperature operating range from 1 K to 400 K; frequency range from 60 GHz to 90 GHz. The waveguide is plugged at the chip carrier mount flange, see Fig. 2c for details, by a thin polyethylene sheet inserted between the WR-12 flanges.

Since the cryoprobe is significantly shorter than cryoprobes for common higher-capacity dewars, particular attention has to be paid to both its design and the choice of the materials employed for its construction for minimizing the thermal load and, hence, to prevent excessive LHe consumption. The outermost stainless steel hollow tube of the cryoprobe acts itself as an RF shielding and, at the lower end, a 1.5 mm thick magnetic shield made of CRYOPERM 10 is mounted. In fact, in the present setup, the Josephson device is completely shielded to reduce as much as possible electromagnetic interferences, as well as the occurrence of magnetic flux trapping within the Josephson junctions.

Additional key features of the cryoprobe include:

i) top sealed cryoprobe to allow sample cooling using a conventional two-step cooling process leaving the

sample inserted in the dewar, i.e. pre-cooling with liquid nitrogen (LN) and then cooling with liquid Helium (LHe) after removing all the LN;

ii) helium gas escapes from the dewar through a plumbing system of ball valve and pressure release valve located on the top of the LHe dewar.

The pressure inside the dewar is kept constant by using either the pressure-released valve or a flow impedance realized with a small diameter hose using gas hose couplings (quick connectors). As a result, variations of thermal electromotive forces (EMFs) and junctions temperature-dependent electrical parameters during operation are largely damped.

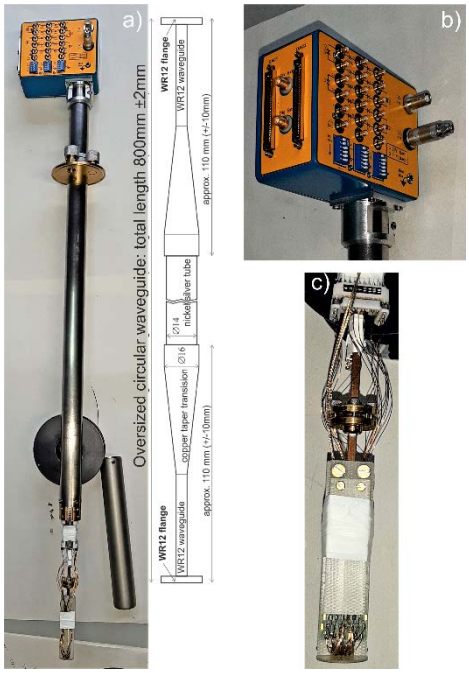

Fig. 2. Home-made short cryoprobe designed for hosting the PJVS chip: a) photograph of the short cryoprobe and cryoperm shield; b) head box with connectors; c) chip carrier with installed PJVS array plugged with WR-12 flange to the oversized waveguide.

C. SNS programmable Josephson array

The PJVS chip is a binary-divided array containing 8192 Josephson junctions fabricated by Supracon[1]. The N-material is an amorphous Nb_xSi_{1-x} alloy near the metal-insulator transitions tuned for operation at about 70 GHz. The array presents quite similar features to those fabricated in the framework of NIST-PTB collaboration [7]. Its main parameters can be summarized as follow:

- $V_C = I_C R_N \approx 160\ \mu V$, with V_C the characteristic voltage, I_C the critical current and R_N the normal resistance, which corresponds to a characteristic frequency of about $f_C = 77$ GHz;
- Critical current $I_C \approx 4.9$ mA at 4.2 K; 0th order Shapiro step width ≤ 4.3 mA; 1st order Shapiro steps width and center for all-subsections ≤ 3.6 mA and ≤ 5 mA, respectively.

The array contains 14 sub-sections of series-connected Josephson junctions, each of which can be independently current-driven to a given quantum step, usually zero and first order. Starting from the low-voltage terminal, the number of junctions in the sub-arrays follows the sequence 32, 16, 8, 4, 2, 1, 1, 64, 128, 256, 512, 1024, 2048, 4096. Two separate single-junction sub-arrays are necessary to perform a highly accurate quantization test and to determine the PJVS quantum operating margins. To this aim, half array (4096 junctions) is current-biased to the n = +1 Shapiro step, whereas the second half is biased to the n = -1 step. The PJVS output voltage is then exactly zero and is measured with a nanovoltmeter, working as a null-detector.

D. Wiring and connectors

Wiring of the PJVS chip to room temperature electronic instruments requires some precautions to avoid as much as possible phenomena due to flux trapping, electromagnetic interference and electrical noise propagation to the measurement setup. The cryoprobe has been equipped with suitable cryogenic wires as follows:

- 12 twisted-pairs of beryllium-copper (BeCu) wires of 100 µm diameter and 10 Ω/m resistance (independent of temperature) are used for biasing of PJVS sub-sections. Relying on theoretical assumptions, the thermal load of such a twisted-pair cable compared to conventional twisted-pair Cu cable leads to a LHe vaporization rate reduction by a factor of 10.
- The PJVS device is suitably installed on a chip-carrier and bonded on finished gold PCB pads with aluminum wires. 14 pads are used to provide connection of the single sub-sections to the biasing electronics. High (V_H) and low (V_L) voltage Josephson array terminals are bonded on two separate PCB pads. Two ultra-miniature coaxial cryogenic cables with inner conductor of stranded copper isolated in Teflon from its outer conductor, made of braided gold-plated copper, were used to transfer the Josephson quantized voltage from 4.2 K to the room temperature environment. In the first configuration, each coaxial cable has been directly soldered to the PCB pads dedicated to the Josephson voltage. However, it is possible to redefine the connections using the inner conductor of both coaxial cables to bring out the Josephson voltage, which seems the most promising configuration to ensure greater immunity from EMI interferences and phenomena related to the generation

[1] Brand names are used for identification purposes and such use implies neither endorsement by INRiM nor assurance that the equipment is the best available in the market.

of thermal electromotive forces between the wires and the PCB pads.

- The cryoprobe head is fixed to the main stainless steel tube with a removable sealing mechanism and, in order to avoid the escape of cold helium vapors, its upper side is sealed with a bicomponent epoxy resin. It is equipped with both 16 coaxial SMB connectors and two 68 pin I/O connectors for quick connection to the biasing electronics. A triaxial LEMO connector was used to bring out the Josephson voltage output. Its fixing ensures a good electrically and thermally decoupling from the cryoprobe head, thus avoiding unwanted thermal gradients, which could give rise to thermal electromotive forces.

III. EXPERIMENTAL SETUP FOR ARRAY CHARACTERIZATION

A photograph of the overall experimental setup employed for testing the PJVS array is shown in Fig. 3. It is composed as follows.

Fig. 3. Photograph of the experimental setup for PJVS array characterization.

A. I-V fast monitoring setup

The current-voltage (*I-V*) characteristics of the single sections of the PJVS array, with and without microwave radiation, have been recorded using a fast-tracking fully digital system. The tracking system was used for the first time in the work reported in [8]. Both high-speed digitizers or precision sampling digital multimeters, such as DMM-3458A, can be used for the recording of voltage and current signals.

B. RF-microwave generation and measuring system

During the first experiment run, the array was irradiated using alternatively two Gunn oscillators, capable of covering a frequency range from 70 GHz to about 73 GHz. The microwave power at the input flange of the circular waveguide was about 30 mW, which seems to be a promising value to ensure almost equal width of zero and first order Shapiro steps. Unfortunately, for an unexpected malfunction of the RF frequency counter sensor it was not possible to lock and stabilize the Gunn frequency to the distributed 10 MHz clock reference coming from INRiM atomic clock. Further investigations using non conventional equipment are in progress and details will be matter of future discussions.

IV. RESULTS AND DISCUSSIONS

First characterization of the system and PJVS array concerned the determination of *I-V* characteristics with and without microwave radiation. The *I-V* characteristic of the full array under no microwave radiation is reported in Fig. 5, where it is clearly observed that I_C at 4.2 K spans from – 4.9 mA to +4.9 mA.

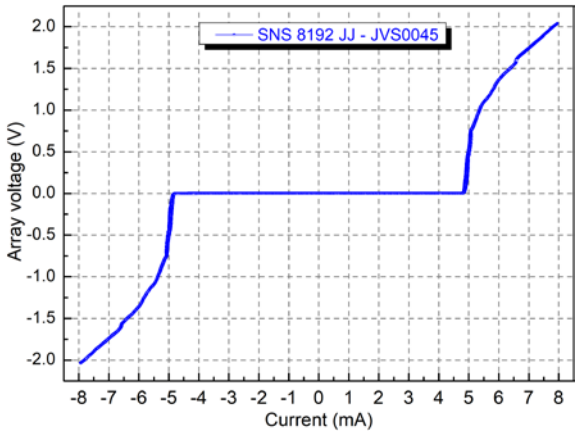

Fig. 4. I-V characteristic for the determination of 1-V PJVS array critical current in in LHe.

The second series of tests were focused on the determination of current-width and flatness of the quantized voltages across each PJVS sub-array. The array has been irradiated from 70 GHz to about 73 GHz.

Fig. 5 reports only the results obtained at 72 GHz.

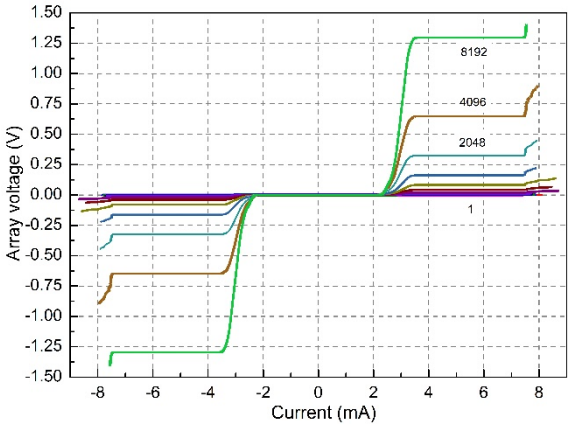

Fig. 5. I-V characteristic of PJVS sub-sections under microwave radiation at about 72 GHz.

As shown, quantized voltage corresponding to n = -1, 0, +1 Shapiro steps are clearly visible for all the PJVS subsections. The RF power has been trimmed for ensuring

almost similar operational current margins for each section. The operational current margins for Shapiro steps -1, 0 and 1 result to be within 3 mA, which are large enough to simplify proper operations of the array for future experiments on the synthesis of sinusoidal staircase waveforms as required for EMPIR project 19RPT01-QuantumPower

Fig. 6 reports a high-resolution plot as a demonstration of the flatness of n=+1 Shapiro steps.

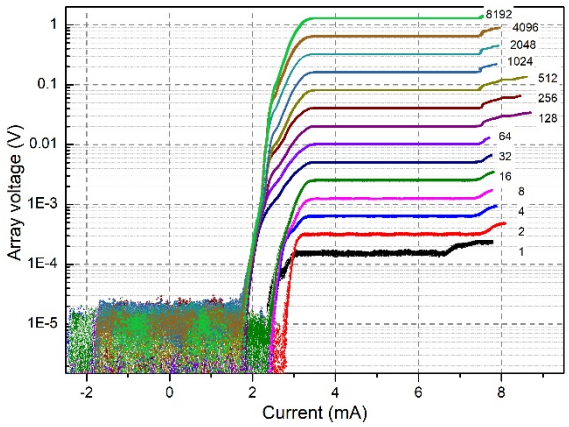

Fig. 6. I-V characteristic of PJVS sub-sections at 72 GHz; logarithmic voltage scale.

The excess of noise observed is due to the fast I-V tracking setup. During the first experiment run, we observed a significant thermal EMF (about 50 µV) superimposed to the Josephson voltage output wired with the cryogenic coaxial cable. Instead, the thermal offset across the BeCu twisted-pair was lower than 1 µV. Further tests have been carried out with a short piece of the same coaxial cable, short-circuited at one end, mounting the same end on the 4 K stage of a pulse-tube cryocooler. The experiment confirmed that large thermal EMF appears, probability due to the different material composition and Seebeck coefficient between center conductor and shield of the coaxial cable.

A. Step flatness quantization test

For demonstrating that the programmable Josephson voltage standard is working properly we perform the so called quantization test.

The test consists of individually biasing the overall binary sub-sections of the PJVS chips under microwave radiation at the first Shapiro step, so that the overall voltage generated by the array is zero. Several biasing sequences were generated and loaded to the biasing electronics. Each sequence corresponds to a well-defined current biasing value chosen in according to the operating margins observed for all subsections as shown in Fig. 6. The biasing current ranging from 4.4 mA to 6.4 mA. The output array was recorded with a digital nanovoltmeter.

The results are reported in Fig. 7. The nanovoltmeter readings at the specific bias current have been corrected by the value of the thermal EMF. It is worth mentioning that after further improvements of the cryoprobe wiring the residual thermal EFM measured at the PJVS output is now reduced by a factor of more than 300 and recent experiments confirm a value of about 153±6 nV.

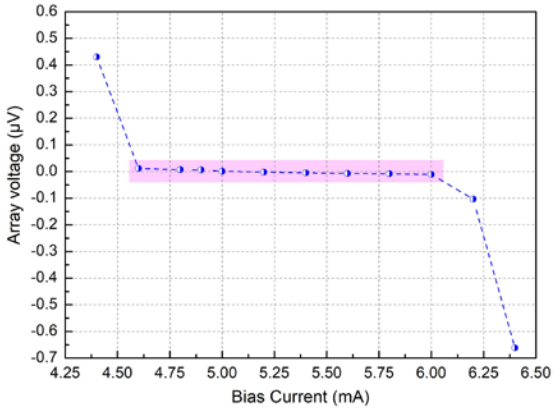

Fig. 7. Step flatness quantization test of the 1-V PJVS SNS chip irradiated at 73 GHz.

B. Synthesis of quantum staircase sine waves

A second round of testing has been conducted in order to validate the experimental setup as a whole, for the direct synthesis of quantum staircase sine waves.

Fig. 8 shows four different sine waves composed of 10 steps at a frequency of about 53 Hz, which differ manly by the bias current used to switch on/off the PJVS sections.

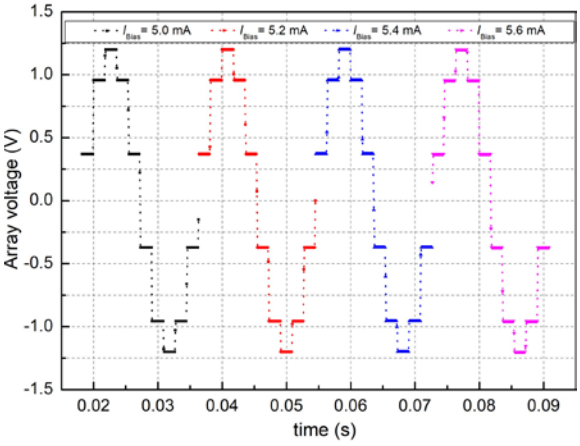

Fig. 8. Staircase sine waves synthesized at different

Comparing the various voltage steps sampled by means of a high precision sampling digital multimeters, e.g. Keysight 3458A, at 10 kS/s and aperture time 90 µS, we found that the relative voltage difference between the

quantized voltage steps at different biasing currents are lower than 1 µV/V.

The results obtained confirm once again that the PJVS system is really working and it will be used by INRiM within the 19RPT01 QuantumPower project in the experimental setup of the quantum power sampling standard.

V. CONCLUSION AND FUTURE WORK

We demonstrated the fully operation of a new setup recently employed at INRiM for the generation of quantized voltage steps using a 1-V programmable Josephson array. All the segments of the binary-divided array have been successfully tested without and with microwave radiation at frequencies ranging from 70 GHz to about 73 GHz using a home-made short cryoprobe designed for working in a small liquid helium dewar.

Next experiments will be focused more in detail on the metrological application of the PJVS setup and its full validation against the maintained national dc voltage standard at 1.018 V. A first comparison shown an agreement with 0.4 ppm.

Further extensions of the presented PJVS for the synthesis of staircase approximated waveforms within the 19RPT01-QuantumPower project are planned and the most relevant achievement will be matter of discussion during the conference.

ACKNOWLODGMENTS

This project (19RPT01 QuantumPower) has received funding from the EMPIR programme co-financed by the Participating States and from the European Union's Horizon 2020 research and innovation.

REFERENCES

[1] W. G. K. Ihlenfeld, E. Mohns, and K. Dauke, “Classical nonquantum ac power measurements with uncertainties approaching 1 µW/VA”, *IEEE Trans. Instr. Meas*., vol. 56, no. 2, pp. 410–413, 2007.

[2] C. Mester, “Sampling primary power standard from dc up to 9 kHz using commercial off-the-shelf components”, *Energies*, vol. 14, no. 8, 2021. [Online]. Available: https://www.mdpi.com/1996-1073/14/8/2203.

[3] B. Trinchera and D. Serazio, “A Power Frequency Modular Sampling Standard for Traceable Power Measurements: Comparison and Perspectives” *IEEE Trans. on Instrum. and Meas*, vol. 71, pp. 1-8, 2022.

[4] L. Palafox et al., “The Josephson-Effect-Based Primary AC Power Standard at the PTB: Progress Report,” *IEEE Trans. Instrum. And Meas.*, vol. 58, no. 4, pp. 1049-1053, April 2009.

[5] Bryan C. Waltrip et al., “AC Power Standard Using a Programmable Josephson Voltage Standard”, *IEEE Trans. Instrum. and Meas.*, vol. 58, no. 4, pp. 1041-1048, April 2009.

[6] B. Djokic, “Low-Frequency Quantum-Based AC Power Standard at NRC Canada”, *IEEE Trans. Instrum. and Meas.*, vol. 62, no. 6, pp. 1699-1703, June 2013.

[7] F. Muller et al., “1 V and 10 V SNS programmable voltage standards for 70 GHz”, *IEEE Trans. Appl. Supercon.*, vol. 19, no. 3, pp. 981-986, June 2009.

[8] B. Trinchera, V. Lacquaniti, A. Sosso, M. Fretto, P. Durandetto and E. Monticone, “On the Synthesis of Stepwise Quantum Waves Using a SNIS Programmable Josephson Array in a Cryocooler”, *IEEE Trans. Appl. Superc.*, vol. 27, no. 4, pp. 1-5, June 2017.

25th IMEKO TC4 International Symposium
23rd International Workshop on ADC and DAC Modelling and Testing
IMEKO TC-4 2022
Brescia, Italy / September 12-14, 2022

Direct Comparison of Quantum Hall Resistance in Graphene and Gallium Arsenide in Liquid Helium

Ngoc Thanh Mai Tran[1,2], Jaesung Park[3], and Dong-Hun Chae[3*]

[1] *Politecnico di Torino, Corso Duca degli Abruzzi 24, 10129 Torino, Italy*
[2] *Istituto Nazionale di Ricerca Metrologica, Strada delle Cacce, 91, 10135 Torino, Italy*
[3]*Korea Research Institute of Standards and Science, Daejeon 34113, Republic of Korea*
N.T.M. Tran and J. Park contributed equally to this work.
[*]Corresponding author. e-mail:dhchae@kriss.re.kr

***Abstract* – Direct comparison of quantum Hall resistance in the same or different materials requires demanding experimental resources, such as two separate cryostats or a specially designed dual-socket probe operating far below the temperature of liquid helium. Here we experimentally demonstrate an efficient direct comparison of quantum Hall resistance in graphene and gallium arsenide/aluminium gallium arsenide heterostructure in liquid helium at 4.2 K with a standard probe from the practical point of view. To perform the direct comparison with one probe, we stacked two Hall devices with a printed circuit board and mating pins and employed a gallium arsenide Hall device with a high electron density. The direct comparison shows that the relative difference in quantized Hall resistance between the two materials in liquid helium is as small as 5 nΩ/Ω.**

I. INTRODUCTION

Precision comparisons of quantum Hall resistance such as the on-site comparison (BIPM.EM K-12) are of paramount importance in resistance metrology to verify the international coherence of primary resistance standards [1,2]. In such a comparison, two quantum Hall resistances (QHRs) in two separate cryostats are compared with each other via an artifact resistance reference. The transfer resistor exhibits instability with respect to temperature as well as intrinsic temporal drift. To avoid the relevant uncertainties, direct comparisons of QHRs in different materials have been performed below a temperature of 1 K for universality tests of QHRs, either in two separate cryostats [3-5] or in one cryostat hosting two Hall devices [6], since 1990. To simultaneously satisfy the quantization conditions of silicon metal–oxide–semiconductor field-effect transistor (Si-MOSFET) and gallium arsenide/ aluminium gallium arsenide (GaAs/AlGaAs) heterostructure Hall devices mounted in one probe under the same magnetic field, one of the two devices needs to be tilted with respect to the magnetic field direction [6], presenting an experimental challenge.

More recently, precise comparisons of the QHRs in graphene and GaAs/AlGaAs heterostructure have been accomplished either directly in two separate cryostats [4], or indirectly, in one cryostat with dual sockets via a resistance reference [7,8]. The required temperature is below 2 K to avoid dissipation in the quantum Hall state in GaAs/AlGaAs heterostructure, even though graphene exhibits good metrological quantization above 4.2 K [9], stemming from the linear energy-momentum dispersion [10,11] of massless Dirac fermions. To date, such a precision comparison has required demanding resources, such as two separate cryostats or a specially designed dual-socket probe operating below the temperature of liquid helium.

Here, we experimentally demonstrate a direct comparison of the QHRs in graphene and GaAs/AlGaAs heterostructure in liquid helium at 4.2 K with a standard probe. National metrology institutes commonly have a probe with a 12-pin transistor outline (TO-8) socket. We used such an ordinary probe to host two Hall devices. A graphene Hall device was mounted on a TO-8 chip carrier, made by printed circuit board (PCB) and mating pins. A GaAs/AlGaAs Hall device was stacked on top of the graphene Hall device with a PCB spacer. The pins of the TO-8 socket were shared by the two stacked Hall devices. To perform the direct comparison at 4.2 K, we employed a GaAs/AlGaAs Hall device with a high electron density whose quantization for a filling factor 2 is achieved above a magnetic field of 10 T [12]. The direct comparison of the QHRs in graphene and GaAs/AlGaAs heterostructure at 4.2 K showed that the relative difference between the two is smaller than 5 nΩ/Ω. We also showed that at 2.8 K, this relative difference is reduced to 2 nΩ/Ω, comparable to the expanded measurement uncertainty, due to dissipation reduction in the quantum Hall state in GaAs/AlGaAs heterostructure.

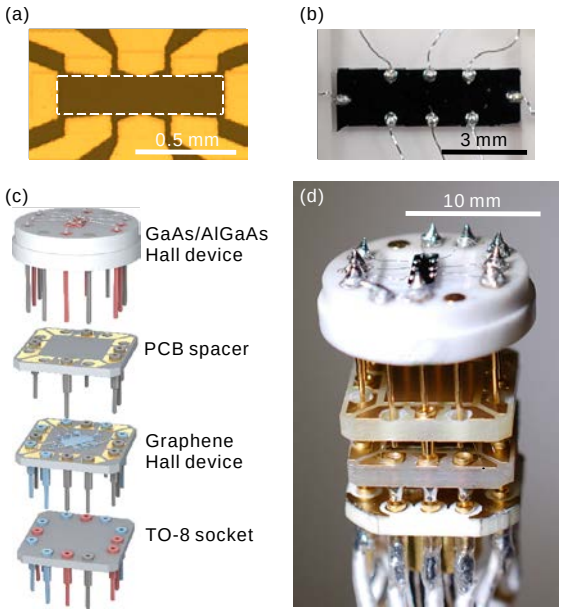

Fig. 1. Stacked Hall devices on the TO-8 socket. (a) Optical image of the graphene Hall device. The dashed line illustrates the boundary of the graphene channel. (b) Photograph of the GaAs/AlGaAs Hall device. (c) Schematic illustrations of the TO-8 socket, graphene Hall device, PCB spacer and GaAs/AlGaAs Hall device. The pins of the TO-8 socket were shared by the graphene and GaAs/AlGaAs Hall devices through stacking, as shown by color coding in blue and red, respectively. (d) Photograph of the two stacked Hall devices mounted on the TO-8 socket.

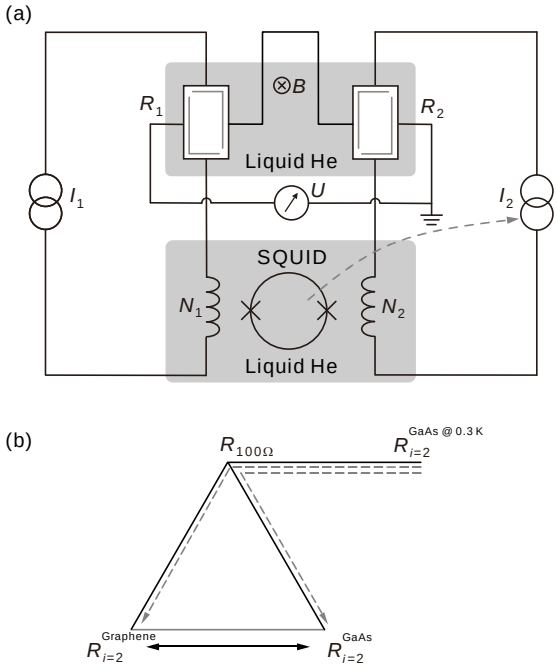

Fig. 2. Schematic of the direct comparison of the QHRs in the graphene and GaAs/AlGaAs Hall devices. (a) Circuit diagram of the cryogenic current comparator bridge for direct comparison. (b) The solid arrow represents the direct comparison between the QHRs realized in the graphene and GaAs/AlGaAs Hall devices. The dashed lines represent traceable measurements via a 100 Ω resistance reference with respect to a QHR standard operating at 0.3 K.

II. DEVICE AND EXPERIMENTAL SETUP

The graphene Hall device was fabricated with epitaxial graphene grown on silicon carbide (SiC). For graphene synthesis on SiC, the SiC substrate was heated to 1600 °C in a hot-wall reactor to sublimate the Si atoms [13]. High-quality graphene with a low step height, typically below 1 nm, and large monolayer coverage is essential for the realization of a graphene-based quantum Hall resistance standard. We used a modified graphite susceptor with a small gap [14] and the polymer-assisted growth technique [15] to prevent step bunching, resulting in a smooth graphene morphology on the SiC. Electron-beam lithography for the patterning of the graphene channel and electron-beam evaporation for the metal contact were applied to fabricate the graphene device. Polymer-assisted hole-doping of the graphene was adopted to fulfill the quantization condition of a filling factor 2 at a lower magnetic field [16]. We also employed a GaAs/AlGaAs Hall device (PTB 130-20) with a high electron density, fabricated by the Physikalisch-Technische Bundesanstalt (PTB), for operation at liquid helium temperature [12]. The carrier type, density and mobility of the graphene device were hole, 2.3×10^{11} cm^{-2} and 5 290 cm^2 V^{-1} s^{-1}, respectively. The carrier type, density and mobility of the GaAs/AlGaAs Hall device were electron, 5.3×10^{11} cm^{-2} and 585 000 cm^2 V^{-1} s^{-1}, respectively. These parameters were evaluated via magnetoresistance measurements in the classical Hall regime. Figure 1(a) and (b) show images of the graphene and GaAs/AlGaAs Hall devices, respectively. The contact resistance was determined in three terminal configuration [17] at the quantum Hall state. The contact resistances of graphene and GaAs devices were approximately 1 Ω and 2 Ω, respectively.

For direct comparison of the QHRs in graphene and GaAs/AlGaAs heterostructure, the graphene and GaAs/AlGaAs Hall devices are loaded into an ordinary probe with a 12-pin TO-8 socket. The GaAs/AlGaAs Hall device was stacked on top of the graphene device, as depicted in Fig. 1(c) and (d). The graphene Hall device was mounted on the TO-8 PCB carrier using 6 selected pins, color coded in blue in Fig. 1(c). The other 5 pins of the TO-8 socket, color coded in red, were connected to the 5 leads of the GaAs Hall device. A PCB adaptor with only 5 mating pins and 7 through-holes, as illustrated in Fig. 1(c), was stacked on the graphene TO-8 carrier. The standard GaAs/AlGaAs Hall device was finally plugged into the PCB adaptor, with only 5 pins electrically connected to the

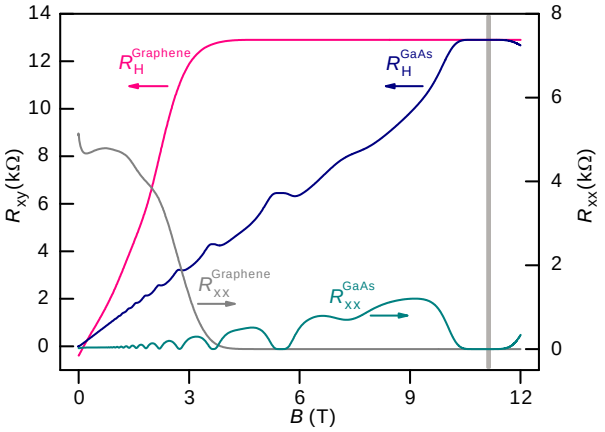

Fig. 3. Magnetoresistance measurements of the graphene and GaAs/AlGaAs Hall devices immersed in liquid helium at 4.2 K. The Hall and longitudinal resistances of the graphene (GaAs/AlGaAs) device are represented by the red (blue) and gray (teal-gray) traces, respectively. The center of the quantized Hall resistance plateau for a filling factor 2 in GaAs/AlGaAs corresponds to a magnetic field of 11 T. The left and right vertical axes display the Hall and longitudinal resistances, respectively.

red-colored pins in the TO-8 socket. The pins of the TO-8 socket were accordingly shared by the two Hall devices through this stacking method.

We employed a helium bath cryostat with a 12 T superconducting magnet. Most of the experiments were performed at 4.2 K. If necessary, the liquid helium temperature can be lowered with a λ-point refrigerator with which the superconducting magnet is equipped. Direct comparison of the QHRs in the graphene and GaAs/AlGaAs Hall devices was performed with a cryogenic current comparator (CCC) bridge [18]. The two Hall devices were loaded in a standard probe with one TO-8 socket immersed in liquid helium. The schematic bridge circuit is shown in Fig. 2(a). The direct comparison was confirmed by an indirect comparison based on conventional traceable resistance measurements via a transfer resistor [18], as illustrated by dashed lines in Fig. 2(b).

III. EXPERIMENTAL RESULTS

A. Magnetoresistance Measurements of the Graphene and GaAs/AlGaAs Hall Devices

Figure 3 shows the Hall resistances and the longitudinal resistances of the graphene and GaAs/AlGaAs Hall devices as functions of the magnetic field in liquid helium at 4.2 K. The Hall resistance ($R_H^{Graphene}$) of the graphene starts to be quantized above a magnetic field of approximately 4 T. The wide Hall plateau for a filling factor 2 (i = 2) in epitaxial graphene, stemming from the magnetic-field-dependent charge transfer between the SiC and graphene [19], is distinct from that of exfoliated

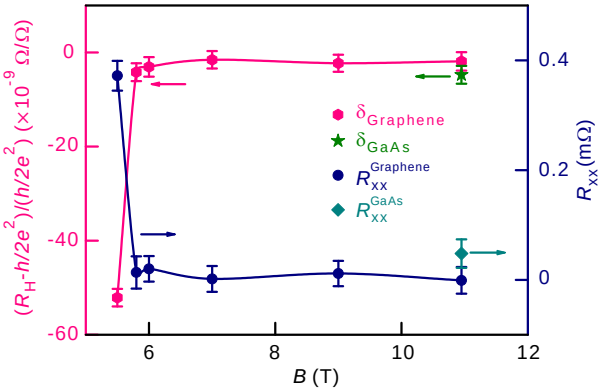

Fig. 4. Relative deviation of the Hall resistance from $\frac{h}{2e^2}$ and the longitudinal resistance measured at 4.2 K. The measurements of the relative deviation and longitudinal resistance in the graphene device are plotted as red hexagons and blue circles, respectively. The green star and teal-gray diamond depict the relative deviation and longitudinal resistance, respectively, of the GaAs/AlGaAs device at 11 T. Error bars of R_{xx} and relative deviation indicate the expanded measurement uncertainty (k=2).

graphene. The corresponding longitudinal resistance ($R_{xx}^{Graphene}$) for i = 2 is suppressed above 4 T. The measured Hall (R_H^{GaAs}) and longitudinal (R_{xx}^{GaAs}) resistances of the GaAs/AlGaAs device overlap with the magnetoresistance traces of the graphene device. The center of the quantized Hall plateau at i = 2 corresponds to a magnetic field of 11 T. The precise direct comparison of the two QHRs was performed at this magnetic field. We note that the common quantization condition for the graphene and GaAs/AlGaAs heterostructure under the same magnetic field can be easily satisfied thanks to the wide quantized Hall resistance plateau of epitaxial graphene, unlike in the direct comparison of Si-MOSFET and GaAs/AlGaAs heterostructure [6].

B. Traceable Measurements of the QHRs in Graphene and GaAs/AlGaAs heterostructure

Prior to the direct comparison, precision measurements of the QHRs in the graphene and GaAs/AlGaAs heterostructure were performed with the CCC bridge by comparing the QHR against a 100 Ω resistance reference, which was precalibrated with respect to a QHR standard realized in GaAs/AlGaAs heterostructure operating at 0.3 K [18]. For these conventional traceable measurements, an auxiliary winding and current source were included in the bridge circuit [18, 20], although this is not shown in Fig. 2(a). The longitudinal resistance was also measured with the CCC bridge. The difference between the ordinary Hall resistance and a Hall resistance measured with a diagonal contact pair corresponds to the longitudinal resistance [21].

Figure 4 shows the relative deviation of the measured Hall resistance from the nominal QHR ($\frac{h}{2e^2}$) at i = 2 with

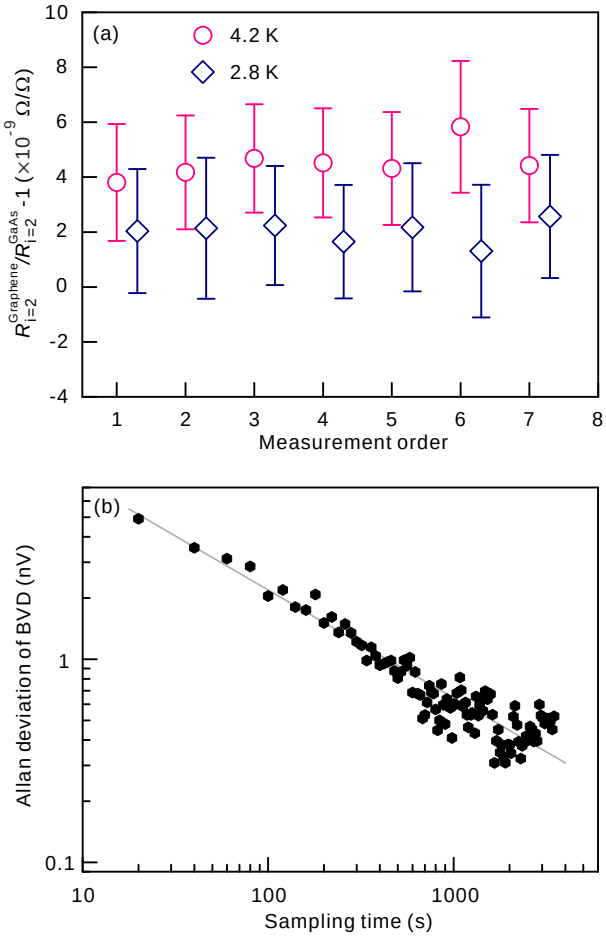

Fig. 5. Direct comparison of the QHRs in the graphene and GaAs/AlGaAs heterostructure and the Allan deviation of the bridge voltage difference. (a) Repeated measurements of the relative difference between the QHRs in the graphene and GaAs/AlGaAs Hall devices in liquid helium under a magnetic field of 11 T at 4.2 K and 2.8 K, represented by circular and diamond symbols, respectively. (b) Allan deviation of the bridge voltage difference for direct comparison from a data set acquired for 4 hours at 4.2 K. The inverse square root time dependence ($1/\sqrt{\tau}$) of white noise overlaps with the Allan deviation plot.

respect to the magnetic field at 4.2 K. The longitudinal resistance is also depicted. The red hexagons and blue circles represent the measurements of the relative deviation and longitudinal resistance, respectively, in the graphene Hall device. The quantized Hall resistance starts to deviate from the nominal value below a magnetic field of 6 T. The Hall resistances in the plateau are equivalent to $\frac{h}{2e^2}$ within the measurement uncertainty. The longitudinal resistance accordingly becomes larger than the measurement uncertainty of 23 μΩ below 6 T. The deviation and longitudinal resistance acquired at the central value (11 T) of the filling factor 2 Hall plateau in the GaAs/AlGaAs Hall device are depicted by star and diamond symbols, respectively. The finite relative deviation of approximately 4.8 nΩ/Ω from the nominal quantized resistance and the finite longitudinal resistance of 48 μΩ are observed at the plateau center. A ratio of the relative deviation to the longitudinal resistance is defined as the *s*-parameter [21]. The *s*-parameter can be also evaluated using a dip at the edge of the Hall plateau and the corresponding longitudinal resistance. It turns out that the *s*-parameter is approximately -0.8. The estimated *s*-parameters with the above two methods are comparable. It implies that the deviation is attributed to a dissipation in the quantum Hall state at the given temperature, which will be discussed in detail later.

C. Direct Comparison of the QHRs in Graphene and GaAs/AlGaAs heterostructure in Liquid Helium

The direct comparison of the QHRs in the graphene and GaAs/AlGaAs Hall devices in liquid helium was performed with the CCC bridge as illustrated in Fig. 2(a). A magnetic field of 11 T was applied because this value lies at the center of the quantized Hall resistance plateau at $i = 2$ for the GaAs/AlGaAs Hall device and simultaneously lies within the wide Hall resistance plateau at $i = 2$ for the epitaxial graphene device.

The circular symbols in Fig. 5(a) represent repeated measurements of the relative difference in the QHRs of the graphene and GaAs/AlGaAs devices in liquid helium at 4.2 K. The acquisition time for each measurement was approximately 16 minutes. The mean relative difference from 7 data sets is approximately 4.5 nΩ/Ω. From the traceable measurements of the QHRs in the graphene and GaAs/AlGaAs heterostructure, as illustrated in Fig. 2(b) and Fig. 4, the relative difference was indirectly determined via the 100 Ω resistance reference, yielding a value of approximately 3.5 nΩ/Ω, consistent with that found in the direct comparison within the measurement uncertainty.

To identify the origin of the finite relative difference at 4.2 K, as plotted in Fig. 5, we also performed a direct comparison at a lower temperature. As shown in Fig. 4, the Hall resistance of the GaAs/AlGaAs heterostructure deviates from the nominal resistance at $i = 2$, and there exists a corresponding longitudinal resistance larger than the measurement uncertainty. These observations indicate that the dissipation in the GaAs/AlGaAs heterostructure at this temperature may lead to a Hall resistance deviation and a finite longitudinal voltage drop. The diamond symbols in Fig. 5 represent the relative differences measured at a lower temperature of 2.8 K, which was achieved by means of the λ-point refrigerator at the superconducting magnet. This experiment clearly shows that the relative difference is reduced to 2 nΩ/Ω at this temperature. This indicates that the relative difference can be attributed to dissipation in the quantum Hall state in the GaAs/AlGaAs heterostructure, which is inefficiently cooled at the given temperatures. Nevertheless, the direct

Table 1. Uncertainty budge for a typical measurement of the resistance ratio via direct comparison

Contribution	Uncertainty (nΩ/Ω)
Winding ratio error	0.6
Insulation	0.4
SQUID resolution	0.1
Miscellaneous	<0.1
ΔU (type A)	0.5
Expanded measurement uncertainty (k = 2)	1.7

comparison in liquid helium at 4.2 K shows that the relative difference in the QHR in the graphene and GaAs is smaller than 5 nΩ/Ω. Note that this stacking method can be employed to compare QHRs in GaAs/AlGaAs heterostructure and other materials, including graphene, for universality tests in an ultimate precision with an existing metrological probe at lower temperatures.

We performed a long direct comparison measurement to investigate the Allan deviation in the setup. Figure 5 (b) shows the Allan deviation of the bridge voltage difference from a data set acquired for 4 hours at 4.2 K. The Allan deviation follows an inverse square root time dependence ($1/\sqrt{\tau}$) up to a sampling time of a few thousand seconds. This indicates that uncorrelated white noise is predominant in the direct comparison measurement. Additionally, the statistical measurement uncertainty can be reduced to a few parts in 10^{10} for the employed acquisition time scale. Note that error bar indicates the expanded measurement uncertainty (k=2).

D. Uncertainty Budget for Direct Comparison

Table I summarizes the contributions to the uncertainty budget for a typical measurement of the resistance ratio via the direct comparison. The overall expanded measurement uncertainty (k = 2) at the 95% confidence level is typically smaller than 2 nΩ/Ω. A significant contribution comes from the winding ratio error. Although the winding ratio error test showed an uncertainty of approximately a few nΩ/Ω, we conservatively assume an error of one part in 10^9. This leads to a value of 0.6 nΩ/Ω when the rectangular distribution is taken into account. The electric insulation of 20 TΩ results in an uncertainty of approximately 0.4 nΩ/Ω. We note that the electrical insulation resistance was measured between a lead and an outer chassis of probe shorted to ground with all the other leads shorted to the chassis. The flux resolution limit of the employed SQUID also contributes to the uncertainty. The flux via the 2048-turn coil induced by a driving current of 38.74 μA is determined by the flux linkage [23] of 11 $\mu A \cdot \text{turns}/\phi_o$ to be approximately $7200\phi_o$. Here, ϕ_o is the quantum of the flux ($h/2e$). There is some evidence from ratio error tests on CCCs that rectification of noise can cause flux errors at the level of $1\ \mu\phi_o$ in SQUIDs similar to the one used in this study [24]. We therefore assign an uncertainty of $1\ \mu\phi_o$ to the SQUID output, and the corresponding flux error becomes $1\mu\phi_o/7200\phi_o$. When the rectangular distribution is considered, the relative uncertainty becomes close to 0.1 nΩ/Ω. Other minor uncertainties include the voltage measurement error of the nanovoltmeter in the bridge, which is smaller than 0.1 nΩ/Ω. The statistical type-A uncertainty of the bridge voltage difference is typically close to 0.5 nΩ/Ω for the employed data acquisition time.

IV. SUMMARY

In summary, we have demonstrated a direct comparison of quantized Hall resistance at a filling factor 2 in graphene and GaAs/AlGaAs heterostructure by a single standard metrological probe at the liquid helium temperature of 4.2 K with less demanding resources from the practical point of view. For this direct comparison, we employed a gallium arsenide Hall device with a high electron density stacked on top of a graphene Hall device with a printed circuit board adaptor to share the limited pins of a standard socket. This direct comparison shows that the difference between the quantum Hall resistances in graphene and GaAs/AlGaAs heterostructure in liquid helium is as small as 5 nΩ/Ω. This difference, which is reduced at the lower temperature, is attributed to the dissipation of the quantum Hall state in gallium arsenide in liquid helium. We note that this paper is about the impementation of the comparison method with a single conventional probe, not about the result itself of the comparison.

ACKNOWLEDGMENT

This research was supported by the Research on the Redefinition of SI Base Units project (Grant No. KRISS-2022-GP2022-0001) funded by the Korea Research Institute of Standards and Science. This work was supported in part by the Joint Research Project GIQS (18SIB07). This project also received funding from the European Metrology Programme for Innovation and Research (EMPIR) co-financed by the Participating States and from the European Union's Horizon 2020 research and innovation programme. In Korea, this collaborative work was supported by the National Research Foundation of Korea (Grant No. NRF-2019K1A3A1A78077479).

REFERENCES

[1] F. Delahaye and D. Dominguez, "Precise comparisons of quantized Hall resistances," in *IEEE Trans. Instrum. Meas.*, vol. IM-36, no. 2, pp. 226-229, Jun. 1987.

[2] F. Delahaye, T. J. Witt, F. Piquemal, and G. Geneves, "Comparison of quantum Hall effect resistance standards of the BNM/LCIE and the BIPM," in *IEEE Trans. Instrum. Meas.*, vol. 44, no. 2, pp. 258-261, Apr. 1995-

[3] B. Jeckelmann, B. Jeanneret, and D. Inglis, “High-precision measurements of the quantized Hall resistance: Experimental conditions for universality,” in *Phys. Rev. B*, vol. 55, iss. 19 – 15, May 1997.

[4] T. J. B. M. Janssen, *et al.*, “Precision comparison of the quantum Hall effect in graphene and gallium arsenide,” in *Metrologia*, vol. 49, pp. 294, Feb. 2012.

[5] F. J. Ahlers, M. Götz, and K. Pierz, “Direct comparison of fractional and integer quantized Hall resistance,” in *Metrologia*, vol. 54, pp. 516, Jun. 2017.

[6] A. Hartland, *et al.*, “Direct comparison of the quantized Hall resistance in gallium arsenide and silicon,” in *Phys. Rev. Lett.*, vol. 66, pp. 969, Feb. 1991.

[7] D. G. Jarrett *et al.,* "Transport of NIST Graphene Quantized Hall Devices and Comparison with AIST Gallium-Arsenide Quantized Hall Devices," in *2018 Conference on Precision Electromagnetic Measurements (CPEM 2018),* Paris, 2018, pp. 1-2.

[8] S. U. Payagala *et al.,* "Comparison Between Graphene and GaAs Quantized Hall Devices With a Dual Probe," in *IEEE Trans. Instrum. Meas.,* vol. 69, no. 12, pp. 9374-9380, Dec. 2020.

[9] R. Ribeiro-Palau, F. Lafont, J. Brun-Picard, *et al.*, “Quantum Hall resistance standard in graphene devices under relaxed experimental conditions,” in *Nat. Nanotechnol*, vol. 10, pp. 965–971, Nov. 2015.

[10] K. Novoselov, A. Geim, S. Morozov *et al.*, “Two-dimensional gas of massless Dirac fermions in graphene,” in *Nature*, vol. 438, pp. 197–200 Sep. 2005.

[11] Y. Zhang, Y-W. Tan, H. Stormer, *et al.*, “Experimental observation of the quantum Hall effect and Berry's phase in graphene,” in *Nature*, vol. 438, pp. 201–204, Sep. 2005.

[12] J. Kučera, P. Svoboda, and K. Pierz, "AC and DC Quantum Hall Measurements in GaAs-Based Devices at Temperatures Up To 4.2 K," in *IEEE Trans. Instrum. Meas.*, vol. 68, no. 6, pp. 2106-2112, Jun. 2019.

[13] M. Ostler, F. Speck, M. Gick, and T. Seyller, “Automated preparation of high-quality epitaxial graphene on 6H-SiC(0001),” in *Phys. Status Solidi B*, vol. 247, pp. 2924 – 2926, Dec. 2010.

[14] J. Park, W.-S. Kim, and D.-H. Chae, “Realization of $5h/e^2$ with graphene quantum Hall resistance array”, in *Appl. Phys. Lett*. vol. 116, 093102, Mar. 2020.

[15] M. Kruskopf, M. D. Pakdehi, K. Pierz, S. Wundrack, R. Stosch, T. Dziomba, M. Götz, J. Baringhaus, J. Aprojanz, C. Tegenkamp, J. Lidzba, T. Seyller, F. Hohls, F. J. Ahlers, and H. W. Schumacher, “Comeback of epitaxial graphene for electronics: large-area growth of bilayer-free graphene on SiC,” in *2D Materials*, vol. 3, 041002, Jun. 2016.

[16] H. He, K.H. Kim, A. Danilov, *et al.*, “Uniform doping of graphene close to the Dirac point by polymer-assisted assembly of molecular dopants,” in *Nat Commun*, vol. 9, 3956, Sep. 2018.

[17] G. L. J. A. Rikken, *et al.*, “Two-terminal resistance of quantum Hall devices” in *Phy. Rev. B* vol. 37, 6181, Apr. 1988.

[18] P. Gournay, B. Rolland, D.-H. Chae and W.-S. Kim, “On-site comparison of quantum Hall effect resistance standards of the KRISS and the BIPM: ongoing key comparison BIPM.EM-K12,” in *Metrologia Tech. Suppl*., vol. 57, 01010, 2020.

[19] T. J. B. M. Janssen, *et al.*, “Anomalously strong pinning of the filling factor ν=2 in epitaxial graphene,” in *Phys. Rev. B*, vol. 83, 233402, Jun. 2011.

[20] D.-H. Chae, W-S. Kim, T. Oe and N.-H. Kaneko, “Direct comparison of 1 MΩ quantized Hall array resistance and quantum Hall resistance standard”, in *Metrologia*, vol. 55, 645, Jul. 2018.

[21] F. Delahaye and B. Jeckelmann B, “Revised technical guidelines for reliable dc measurements of the quantized Hall resistance”, in *Metrologia*, vol. 40, 217, Sep. 2003.

[22] D. Drung and J. Storm, “Ultralow-noise chopper amplifier with low input charge injection”, in *IEEE Trans. Instrum. Meas*, vol. 60, no. 7, pp. 2347-2352, Jul. 2011.

[23] D. Drung, *et al.*, “Improving the stability of cryogenic current comparator setups”, in *Supercond. Sci. Technol.*, vol. 22, no. 11**,** 114004, Oct. 2009.

[24] D. Drung, M. Götz, E. Pesel, and H. Scherer, "Improving the Traceable Measurement and Generation of Small Direct Currents," in *IEEE Trans. Instrum. Meas*., vol. 64, no. 11, pp. 3021-3030, Nov. 2015.

25th IMEKO TC4 International Symposium
23rd International Workshop on ADC and DAC Modelling and Testing
IMEKO TC-4 2022
Brescia, Italy / September 12-14, 2022

Memristive devices as a potential resistance standard

V. Cabral[1], A. Cultrera[2], S. Chen[4], J.Pereira[6], L. Ribeiro[1], I. Godinho[1], L. Boarino[3], N. De Leo[3], L. Callegaro[2], S.Cardoso[6], I. Valov[4, 5], G. Milano[3]

[1] IPQ-Instituto Português da Qualidade, Monte da Caparica, Portugal, vcabral@iqp.pt
[2] Quantum Metrology and Nanotechnologies, INRIM - Istituto Nazionale di Ricerca Metrologica, Turin, Italy
[3] Advanced Materials and Life Sciences Division, Istituto Nazionale di Ricerca Metrologica (INRiM), Turin, Italy, g.milano@inrim.it
[4] RWTH-Aachen university, IWE2, Sommerfeldstr. 24, 52074 Aachen, Germany
[5] Research Centre Juelich, PGI-7, Wilhelm Johnen-Str, 52425 Juelich, Germany, i.valov@fz-juelich.de
[6] INESC Microsistemas e Nanotecnologias, Lisboa, Portugal, Susana Cardoso Freitas, scardoso@inesc-mn.pt

***Abstract* – The EMPIR [1] project 20FUN06 MEMQuD --- "Memristive devices as quantum standard for nanometrology" [2] has as one of its fundamental goals the development of technical capability and scientific knowledge for the implementation of a quantum resistance standard based on memristive devices characterized by high scalability down to the nanometer scale, CMOS compatibility and working in air at room temperature. In this work it is presented an overview of the project and highlighted relevant characteristics and working principles of memristive devices, applications as well as the last revision of the International System of Units (SI) that is the motivation and background for the aim of this project.**

I.INTRODUCTION

The redefinition of the SI units in 2019 [3] turns possible that all measurement units are now defined through fixed values of fundamental constants of nature, representing a significant and historic step forward where, for the first time, the definition of the 7 base units of the SI are based on fixed constants and not depending on any artefact, material properties or measurement descriptions. For electrical units, all units are now defined on the value of the elementary charge, e, and the Planck's constant, h, and are realized and disseminated via the Quantum Hall Resistance standard (QHRS) and the Josephson Voltage Standard [4]. The required systems for the implementation of a QHRS are complex and time consuming to operate, demanding high magnetic fields and low temperature values, near 1 K.

Memristive devices or memristors (from the contraction of memory + resistor) are a new class of nanoscale devices where ionics is coupled with electronics and where device functionalities rely on nanoionic effects. Initially theorized in 1971 from Prof. Chua [5], the ideal concept of memristor, was associated with the so-called resistive switching devices in 2008 by the group of Stanley Williams at HP labs [6]. These are two terminal devices where a switching film (usually a metal-oxide) is sandwiched in between two metal electrodes in a metal-insulator-metal (MIM) structure (Figure 1).

In these devices, the internal state of resistance depends on the history of applied voltage and current exhibiting the typical hysteretic loop in the *I-V* plane (Figure 1.b and 2.b). By exploiting these characteristics, it was demonstrated that memristive devices can have applications in next-generation memories, in-memory computing architectures and neuromorphic architectures. In particular, memristive devices under specific conditions of operation can show low resistance states activated in the device corresponding to values multiple (or half-integer multiples) of the fundamental conductance value, $G_0 = 2e^2/h$. This means that these devices offer a promising platform to observe and generate quantum resistance values in air, at room temperature, and without the need of any applied magnetic field as it is needed for the QHRS. Moreover they also can work at harsh conditions as low/high temperatures, presence of electromagnetic waves and X-ray and are high energy particles resistant. These quantum values of resistance are in line with the spirit and fundamental characteristic of the redefinition of the SI, depending only on the fixed values of the constants e and h.

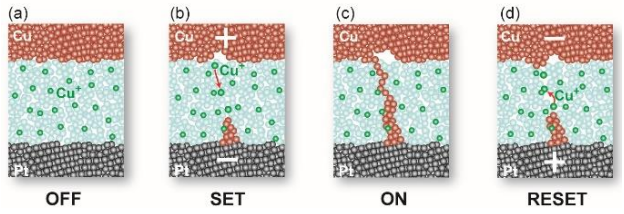

Figure 1. Schematic presentation of the operation principles of cation based ReRAM memory cells with a Cu active electrode and Pt counter electrode. (a) depicts the initial or OFF state. (b) shows the dissolution of metallic Cu to Cu+ ions and the formation of the metallic filament in the 'program' or 'set' operation. (c) is the short-circuited ON state. (d) shows the dissolution of the filament in the 'erase' or 'reset' step under reverse bias and the return to the OFF state. [7]

The project MEMQuD aims to study in details quantum effects in memristive devices and to investigate fundamental aspects underpinning memristive technology. The simpler way to operate this new device, its particular characteristics as low scalability and on-chip integration open the possibility of new applications with relevant impact in metrology field and industry, meeting the challenges opened by the revised SI where new experiments and devices can be explored for allowing integration of fundamental units as internal standard references.

II.OVERVIEW OF THE MEMQUD PROJECT

The three year duration (2021-2024) MEMQud project is formed by a consortium of 15 european participantes [2]: 6 National (or Designated) Metrology Institutes and 9 research and university institutes gathering diverse technical and scientific knowledge that bring to project the needed interdisciplinary skills to implement and underpinning the defined project activities and goals.

The project activities are grouped in three workpackages: *1)* Memristive device fabrication and characterisation, *2)* Nanoelectrical and nanodimensional characterisation of memristive devices and *3)* Development of a quantum-based standard of resistance based on memristive devices.

The first group of activities is focused on manufacturing of memristive cells by the combination of depositing functional layers, structuring methods, surface treatment and engineering supported by traceable analytical and dimensional characterisation techniques.

The second workpackage investigates nanoionic processes by advancing reliable nanoelectrical and nanodimensional characterisation at near atomic scale of the physical mechanism of the memristive, including the development of a traceable quantification of chemical, structural and ionic/electronic properties of memristive devices through microscopy techniques such as Atomic Force Microscopy (AFM), Scanning Electron Microscopy (SEM), Secondary Ion Mass Spectroscopy (SIMS), X-ray Spectrometry including X-ray Diffraction (XRD) and Energy Dispersive X-ray Spectroscopy (EDS).

The third group of activities is focused on metrological electrical characterisation of quantized conductance levels in memristive devices including the investigation of quantized state stability, influence of ambient conditions and noise analysis. Also, a statistical approach and protocols for analysing quantum conductance phenomena, modeling and experimental evaluation of uncertainty associated with quantized states, device-to-device variability and inter laboratories variability will be addressed. Finally, it will be assessed the possibility to develop and test a resistance standard demonstrator in a CMOS circuit, meeting the challenges opened by the revised SI where new experiments and devices can be explored for allowing integration of fundamental units as internal standard references.

III.CHARACTERISTICS AND OPERATION OF MEMRISTIVE DEVICES

The operation of memristive devices is achieved with an electrical stimulus applied to its terminals that is responsible for the transition between an high resistive (HRS) state and a low resistive state (LRS). This resistive switching mechanism is related to the formation/rupture of a conductive path (filament) bridging the two electrodes that is responsible for an increase/decrease of the device conductivity (Figure 1 and Figure 2a).

Among several different types memristors redox-based memory cells (ReRAMs) show particluar promises. Depending on the materials, mobile ions and redox reactions one can distinguish between electrochemical metalization cells ECM (also called CBRAM or PMC); valence change memories VCM or OxRAM and thermochemical memroies (TCM). In the case of ECM, the formation of the conductive filament has been shown to be related to redox reactions involving dissolution of metal atoms from active electrode (Ag, Cu, Ni, Fe etc.) to form metal ions that migrate in the insulating matrix (e.g. an oxide), under the action of the applied electric field. In the case VCM cells, the variation of the internal state of resistance is related to reactions and transport of oxygen-related defects such as oxygen vacancies.

A relevant characteristic of this mechanism is observed when the size of filament is reduced to the atomic scale. In this case, the conductive filament bridging the two electrodes results in a ballistic electron conduction path constituted by discrete conductive channels [9,10]. Each of these conduction channels contributes with a maximum amount of one fundamental quantum of conductance G_0 ($G_0^{-1} \approx 12.9\ \mathrm{k\Omega}$) to the total conductance, G:

$$G = TNG_0 \qquad (1)$$

Where T is the transmission coefficient and N is an integer number representing the number of conducitve channels. However, half-integer multiples of G_0 were also observed for certain types of memristive devices configuration.

The control of the conductance states it is possible with different types of external electrical stimulation: voltage and current sweeps, pulse or constant voltage or current signals. By properly adjusting the external electrical stimulation signal it is possible to control the filament formation/dissolution and the related quantum conductance states achievable in that process [8,9].

The current compliance value of the electrical signal applied to the device (in a sweep voltage signal) to define the transition of the resistive state of the device from the HRS to the LRS will determine the obtained ON resistance value corresponding to the LRS. Experimental data obtained in exploratory measurements made within the scope of this project and presented in Figure 2.b, for a crossbar cell of Pt/SiO2/Cu/Pt, show that the value of the ON resistance decreases with the value of the applied current compliance. This shows that current compliance determines the size of the conducting filament in the switching layer and the corresponding conductance (or resistance) of the device in the LRS. Current compliance adjustment will therefore be one of the external electrical signal parameters to be controlled to induce resistive states corresponding to multiples of G_0.

In this framework, the materials used as electrodes as well as switching layers play an important role in the electrochemistry of the cell and ionic transport properties.

Figures of merits and recommended methods are being discussed at the scientific level in ref. [10],[11]. Already identified figures of merit in the scientific community include device reliability (memristive endurance), state retention (time that device remains in a conductive state after being programmed), switching time, energy consumption, variability and scalability to cite a few. These figures of merit could be in the future recognised as key control characteristics for industrial electrotechnical products based on, or involving, memristive devices. From the point of view of a potential metrological application, as a quantum standard of resistance, retention times of the order of some seconds or minutes (conductive filaments can spontaneously dissolve over time) as has already been demonstrated are sufficient to access and transfer (e.g. by potentiometric method) the quantum resistance value.

More relevant and challenging is the intrinsic stochasticity process associated with the filament formation/rupture and dynamics due to the atomic

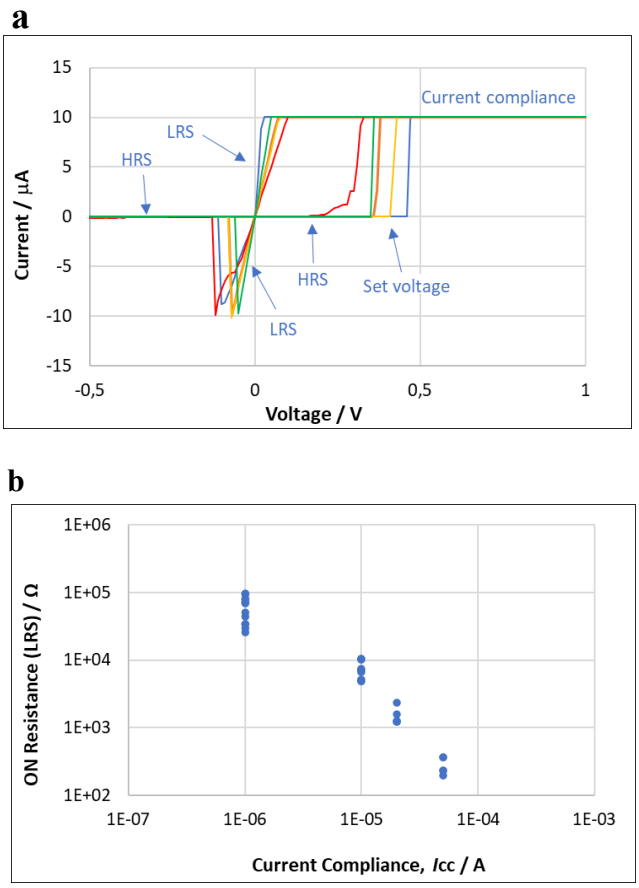

Figure 2. (a) I-V curve characetristic of a crossbar cell based on Pt/SiO₂/Cu PT (30nm/30nm/50nm/30nm) obtained for a sweep voltage signal and a current compliance of 10 µA. The different curves correspond to several consequent set/reset cycles. (b) Value of the ON Resistance obtained as function of the current compliance (I_{cc}) applied in the activation of the low resistve state (LRS) of the device. Crossbar cell fabricated and experimental data obtained in exploratory measurements done in the framework of the MEMQud project.

rearrangement phenomenon. Another source of variability is observed as electronic noise due atomic fluctuations near the point contact.

The combination of the sources of variability affects the repeatibility and the reproducibility of these devices as can be seen with the dispersion of the values obtained for the ON resistance corresponding to each current compliance value and resulting from several activations of the device (Figure 2.b).

Besides these relevant sources of uncertainty, the presence of parasitic resistances [9] should also be taken into account in the assessment of quantum resistance value. Figure 3 schematically shows an equivalent

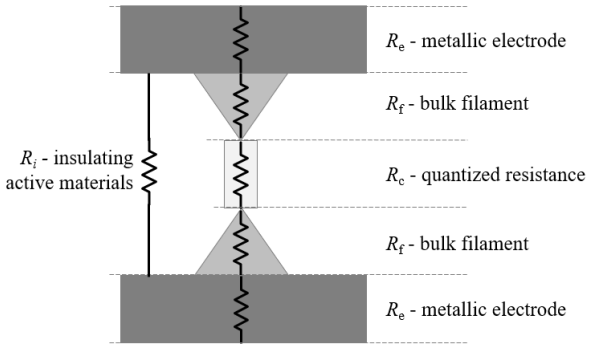

Figure 3. Equivalent electrical circuit of a memristive cell. Besides the quantized contact resistance R_c, the equivalent circuit is composed of the bulk filament resistance R_f, the resistance of the insulating active materials R_i and the resistance of the metallic electrodes R_e.

electrical circuit for memristive cell where the quantized resistance R_c due to the filament constriction is associated to parasitic resistances.

An overall uncertainty estimation will have to take into account these contributions: the systematic error of parasitic resistances should be estimated and corrected (the uncertainty of that estimate will be accounted for as one of the uncertainty components of the combined uncertainty); the variability corresponding to the resistance value obtained at each activation of the device could be first reduced with programming techniques to validate before accessing the desired quantum level of resistance.

IV.METROLOGICAL AND OTHER APPLICATIONS

The properties of memrisitve devices as scalability, high operational speed, compatibility with CMOS technology (both in terms of materials and processes) have been exploited and demonstrated in applications as a new generation of nonvolatile memories as well as in the emulation of neural and synaptic processes.

The integration of memrisitve devices in CMOS circuits also opens the possibility of obtaining a “zero chain traceability” resistance standard available in situ and with the capacity to be integrated in any type of electronic measurement instrumentation to support auto-adjustment and auto-calibration process.

Other specific relevant applications are being identified with the help of the stakeholders of this project. In sensors networks, the calibration of each sensor is usually difficult and a distributed and statistical approach is exploited, where the traceability is propagated among sensors. In this context, the traceability of each sensor can be achieved by integrating memristive devices.

The use of devices in harsh environments (ionizing environments and cosmic rays can strongly affect not only active components such as transistors but also passive components, including resistors. As an example, neutron irradiation damages the material crystallinity (embrittlement effect), thus strongly modifying its resistance. This strongly affects the functionalities of integrated circuits and sensors. The nature of the memristive devices and its application as resistance standard is promising to overcome these effects and to be stable in ionizing environments and under cosmic ray irradiation.

In certain kind of programmable gain amplifiers, its gain (or also the cut-off frequency of a filter) can be modified by changing the value of an associated resistor. The internal programmable resistance state of the memristive devices can also be exploited for programming the gain of amplifiers in analog circuits.

V.CONCLUSION

The potential of the quantum conductance effect in memrisitve devices is for the first explored to be applied in the metrology field as a quantum resistor standard. This specific application highlights the need to improve the control and domination of quantum conductance levels to obtain stable and reproducible steps of resistance. To achieve that, the proper operation parameters (voltage/current stimulation modes) related to the materials used (for electrodes and switching films), the effects of temperature and moisture and device engineering still have to be investigated and tested.

Improving the understanding of the relationship between this quantum phenomenon and the discrete atomic structures of the conductive filaments also need further investigation.

All these aspects will be investigated throughout the activities planned in the MEMQuD project in an integrated multidisciplinary technical and scientific approach.

Aknoledgements: This project (EMPIR 20FUN06 MEMQud) has received funding from the EMPIR programme co-financed by the Participating States and from European Union’s Horizon 2020 research and innovation programme.

VI. REFERENCES

[1] European Metrology Programme for Innovation and Research, https://www.euramet.org/research-innovation/research-empir/
[2] https://memqud.inrim.it/
[3] BIPM, “The International System of Units, 9th edition, SI brochure (EN), 2019. https://www.bipm.org/en/publications/si-

brochurehttps://www.bipm.org/en/publications/si-brochure/
[4] Mise en pratique for the definition of the ampere and other electric units in the SI, 9th edition, SI Brochure – Appendix 2, 2019.
[5] Chua, Leon. "Memristor-the missing circuit element." IEEE Transactions on circuit theory 18.5 (1971): 507-519.
[6] Strukov, Dmitri B., et al. "The missing memristor found." nature 453.7191 (2008): 80-83.
[7] Chen, Shaochuan, and Ilia Valov. "Design of Materials Configuration for Optimizing Redox-Based Resistive Switching Memories." Advanced Materials 34.3 (2022): 2105022
[8] Milano, Gianluca, et al. "Quantum conductance in memristive devices: fundamentals, developments, and applications." Advanced Materials (2022): 2201248.
[9] Milano, Gianluca, et al. “Memristive Devices for Quantum Metrology” Adv. Quantum Technol. 2020.
[10] Lanza, Mario, et al. "Recommended methods to study resistive switching devices." Advanced Electronic Materials 5.1 (2019): 1800143.
[11] Lanza, Mario, et al. "Standards for the characterization of endurance in resistive switching devices." ACS nano 15.11 (2021): 17214-17231.

25th IMEKO TC4 International Symposium
23rd International Workshop on ADC and DAC Modelling and Testing
IMEKO TC-4 2020
Brescia, Italy / September 12-14, 2022

Advancements in quantum voltage standards for time-dependent signals

Paolo Durandetto, Danilo Serazio, Andrea Sosso

INRiM - Istituto Nazionale di Ricerca Metrologica, Strada delle Cacce 91, Turin, Italy
E-mail: p.durandetto@inrim.it, d.serazio@inrim.it, a.sosso@inrim.it

***Abstract* – Quantum voltage standards based on ac Josephson effect are in use in metrology since just a few years after the discovery of the physical effect. The role of quantum standards is now crucial following the SI redefinition in 2019 [1]: electrical units are now defined in function of the fundamental constants e (elementary charge) and h (Planck's constant). The extremely low uncertainty in dc measurements, that can be below 1 nV/V at 10 V [2], is stimulating research to extend application to ac and signals arbitrarily changing with time. Approaching the dc accuracy is challenging, however. The two main technologies used for the generation of non-steady voltage signals are programmable and pulsed Josephson junction arrays. In the following we discuss the main advancements obtained with both technologies and the most recent developments, in particular the advantages of He-free device cooling techniques.**

I. INTRODUCTION

Josephson array voltage standards represent one of the most relevant achievement in superconducting integrated electronics and are fabricated only in few laboratories worldwide. Dc Josephson arrays with tunnel junctions operated at $4.2\,\mathrm{K}$ can generate steady voltages up to 10 V [3], but rapidly setting a voltage value and generating waveforms with quantum accuracy is very difficult. Josephson junctions in dc voltage standard applications are based on highly hysteretic Superconductor-Insulator-Superconductor (SIS) junctions with zero-crossing steps i.e. overlapping voltage steps with current range that spans positive and negative values, hence including the condition of zero dc bias. The current-voltage (IV) relationship is then not one-to-one [4] and it is not possible to control the voltage through electrical bias.

This is otherwise possible in Programmable Josephson Voltage Standards (PJVS) with junctions showing non-hysteretic behavior. Their IV curve under microwave irradiation is a staircase function, thus the output voltage is univocally defined by the current sent through the bias circuit. Such arrays are generally subdivided in sub-circuits with series-connected junctions generating voltages following a power-of-two rule: combining the voltage across all sections it is thus possible to source binary programmed voltages equivalent to the technique used in electronic digital-to-analog converters. Many approaches to junction fabrication have been developed, and several different technologies have proven successful in generating voltages up to 10 V, with good metrological properties: SINIS [5], SNIS [6], [7] with respectively Nb, Al and AlO_x as superconducting (S), normal (N) and insulating (I) elements, and the more recent SNS junctions with Nb_xSi_{1-x} barriers [8], and $NbN/TiN_x/NbN$ junctions for higher temperature operation [9]. The most relevant limitation of PJVS devices is to be found in the time for step switching, when junctions are not operating in a quantized state. During these transients, the array voltage is not accurately known, thus programmable arrays can match primary metrology uncertainties requirements only for signals up to few hundreds Hz.

To get rid of the limitations of programmable standards, arrays operating with a pulsed, square wave, radiofrequency signal have been developed. Making use of short pulses in place of a continuous sinusoidal wave it is possible to suitably modulate the signal period spanning a wide range of frequencies. Fundamental accuracy follows from the control of the flux quanta associated to a single pulse going through a junctions. It follows that the output voltage of the array is exactly calculable in terms of fundamental constants if the number of the quanta per unit time, i.e. the pulse repetition rate, is known. Since the determination of the repetition rate is basically a frequency measurement, this can be done with extreme accuracy and the Josephson effect brings the accuracy of time and frequency measurement into voltage calibrations [10]. Pulsed standards can synthesize arbitrary waveforms with quantum accuracy, taking advantage of the $\Sigma\Delta$ technique for digital-to-analog conversion developed for semiconductor electronics, providing very high spectral purity. However, both operation and fabrication of pulsed standards set very challenging problems.

The extremely low temperatures required for the operation of superconducting devices is generally regarded as the major limitation to a widespread usage. To cool down ordinary superconductors at $4.2\,\mathrm{K}$ the standard technique is based on liquid helium refrigeration (LHe), where all the experiment is immersed, isothermally, in a helium bath. On the other side, more recent He-free systems are

interesting because of ease of use, the savings over high costs of LHe, the absence of risk of shortages [11], and the negligible concerns for operators safety. Yet, proper cryocooler operation necessitates a very specific thermal design to face with problems that are not of concern with liquid coolants, e.g., minimization of thermal gradients to allow uniform operation of the chip. Moreover, the He-free refrigerator has reduced cooling power, thus the rf signal transmission to the chip must be carefully designed in order to limit the heat load on the low temperature stage of the cooler without compromising signal transmission. Additionally, cryocooled standards are particularly interesting for pulsed standard applications, where frequency dependent unwanted effects in the synthesized waveforms are due to the loading of voltage leads. It is possible to reduce these errors by using shorter cables, but this condition cannot be fully realized in LHe system, where cables are more than one meter long, while they can be more than halved in a mechanical cooler.

II. QUANTUM STANDARDS FOR AUDIOFREQENCIES

In Josephson junctions where dissipative effect dominates, the junction capacitance can be neglected. These show non hysteretic behavior in the IV curve that allows changing the output voltage through control of the bias current. In other words, the IV curve under irradiation is a one to one staircase, thus the output voltage is univocally defined by the current fed through the controlling circuit. This is totally different from the case of hysteretic junctions used in dc standards, were steps are overlapping and all share approximately the same interval of currents. This property is exploited in the so-called programmable standards, where the junctions bias currents are used to activate/deactivate array sections. Programmable arrays are subdivided in sections with series connected junctions generating voltages following a power of two sequence. Combining the sections it is then possible to source binary programmed voltages in a way that is very similar to the technique used in electronic digital to analog converters [12] Programmable Josephson arrays are so far the most effective result extending metrological applications of Josephson standards beyond dc, have been used for several applications and provide output voltages up exceeding 10 V [13] In programmable standards, a crucial role is played by the measurement program that controls the bias of array sections, undertakes first data processing (e.g. step verification), and evaluates data validity. The high complexity of quantum based devices, places software in a fundamental role. We developed a Python package for automated measurements with a modular and expandable structure [14] suited to different calibration and testing purposes. The open source approach adopted offers a well known and tested framework for these needs, based on a collaborative effort and improved by shared information and the updates contributed by the community.

INRiM started developing a custom technology for fabrication several years ago. Low hysteresis (overdamped) junctions developed at INRiM can be derived from hysteretic Nb/Al-AlO_x/Nb SIS junctions technology, but the thickness of the Al layer is significantly higher. These junctions can be described as SNIS, since the thick aluminum film is a normal metal at liquid helium temperature. An essential feature is that, at $4.2\,\mathrm{K}$, a transition from the hysteretic to the non-hysteretic state can be induced by changing AlO_x exposure. An interesting feature of SNIS junctions for metrological applications and quantum computing is the high value of current densities achievable and, consequently, of characteristic voltage. This makes SNIS junctions advantageous with respect to other technologies, facilitating the operation of PJVS arrays above $4.2\,\mathrm{K}$ in compact cryocoolers, in the view of the future substitution of expensive and complex LHe refrigeration systems and the consequent diffusion of voltage standards to the private companies. Indeed, present Josephson junctions technologies with high temperature superconductors, like YBCO or MgB_2, are not yet proven effective in providing the integration levels required for large array fabrication [15]. On the other side, the use of SNIS junctions at temperatures close to $4.2\,\mathrm{K}$ is favorable for the generation of wide high order steps, again thanks to the large characteristic voltages [16].

We deeply investigated the development of programmable standards operating at step orders above the first one, making it possible to synthesize stepwise quantum voltage waveforms with fewer bias lines and fewer Josephson junctions, without losses in terms of performances [17]. In particular, we proposed to simultaneously exploit zero, first and second Shapiro steps to reduce junctions and bias lines by two.

III. PULSED STANDARDS TOWARD RF

Pulse-driven arrays of Josephson junctions has proven successful in generating ac voltage waveforms with very pure frequency spectra. They are the basis for the Josephson Arbitrary Waveform Synthesizer (JAWS). Compared to PJVS, JAWS is capable of synthesizing waveforms at much higher frequencies (up to the MHz range) and with rms output voltages up to 2 V [18, 19]. JAWS principle of operation is based on the irradiation of arrays with a train of sub-nanosecond pulses with rise-time of few tens of picoseconds: fundamental accuracy follows from the control of the flux quanta transferred through the junctions in each pulse. The output voltage is then exactly calculable from fundamental constants from:

$$V_n = \Phi_0 \cdot N \cdot n \cdot f_{rep} \tag{1}$$

where $\Phi_0 = h/2e \simeq 2.07 \cdot 10^{-15}$ Wb is the magnetic flux quantum, N is the number of junctions in the array and n is the Shapiro step number, i.e. the number of flux quanta transferred for each current pulse. N and n being fixed, the voltage depends only on the instantaneous pulse repetition frequency f_{rep}. It is possible then to synthesize arbitrary waveforms with quantum accuracy by continuously varying this frequency, which is generally in the range of microwaves. The waveform to be synthesized is encoded into a 0/1 or 1/0/-1 bitstream by means of $\Sigma\Delta$ modulation techniques. In our setup, schematically represented in Fig. 1, the $\Sigma\Delta$ code is generated with a program written in Python and then loaded into the circulating memory of two pulse generators, one for positive and one for negative pulses, properly phased and sharing the same reference clock.

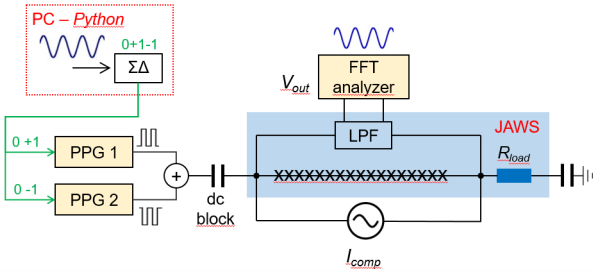

Fig. 1. Schematic representation of JAWS setup.

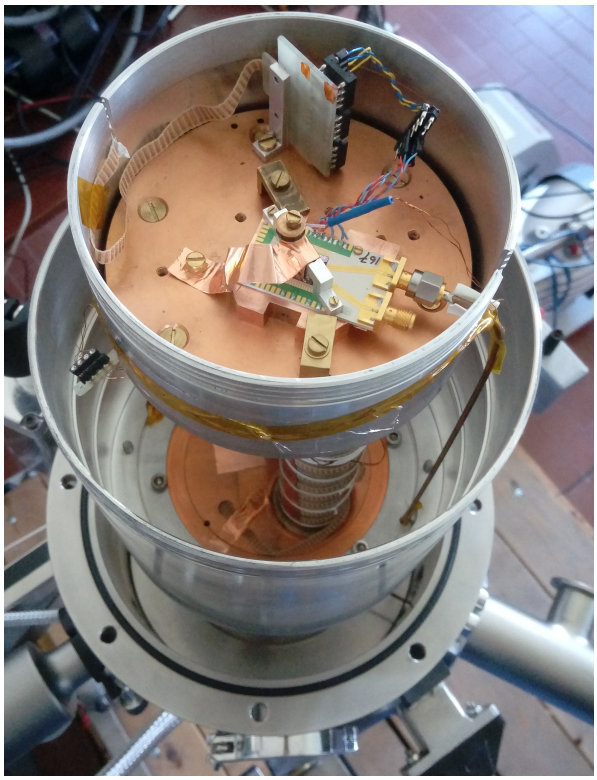

Fig. 2. JAWS standard installed on the coldplate of a pulse-tube cryocooler.

It is widely recognized that, approaching the MHz-range, the most relevant uncertainty contribution in JAWS standards is due to frequency-dependent errors originated by the loading effect of voltage leads [20, 21]. One way to reduce these erros is to use shorter cables, though this condition cannot be fully realized in LHe system, where cables are more than one meter long. Using compact cryocooler, the cable length can be at least halved.

We developed and tested thoroughly a cryogen-free refrigeration system capable of operating a pulsed standard were cable length is halved with respect to helium cooled setups [22].

IV. CRYOCOOLER OPERATION

In the last decade, we have set up two flexible cryogen-free refrigeration systems suited for operation of both programmable and pulsed standards. These are built on two-stage cryocoolers with 1 W cooling power at 4 K and minimum temperature below 3 K (without thermal loads). The second stage of the coolers is fitted with an additional disk (the coldplate) made of oxygen-free copper. In both systems, the coldplate hosts a thermometer and a heater to finely monitor and control its temperature. A second thermometer is free to be installed wherever is necessary, as onto the carrier, in proximity of the Josephson chip. Either a stainless-steel WR-12 waveguide, for PJVS 70 GHz rf transmission, or a low thermal conductivity coaxial cable made of beryllium-copper, for JAWS pulsed bias up to 30 GHz (see Fig. 2), can be installed to reduce the thermal link between the cold region and the outer stages of the cryocooler and the laboratory environment. The apparatus can be easily switched between the two available ac Josephson voltage standards.

As described previously, junctions fabricated with SNIS technology lend themselves as a good option for operation at temperatures above 4.2 K. In particular they show some specific properties with regard to temperature stability of its electrical parameters, measured as the temperature derivative of I_c and V_c vs. temperature [23–28]. SNIS arrays are interesting candidates for a cryocooled standard, providing a compromise between device and refrigerator requirements [29].

Proper operation of a Josephson standard in cryocooler is always a challenging task, owing to the tight thermalization requirements [30, 31] alongside the need of supplying non negligible dc and rf power for proper operation. We addressed the issue of designing an optimized cryopackage for maximizing the thermal contact between the chip and the cooling surface [32]. It takes advantage of a soft indium foil with a corrugate surface for optimal transmission, achieved by filling the voids between rough surfaces. This approach avoids soldering the parts, a solution that is

prone to cracks and surface damage with thermal cycling. Moreover, a highly-conductive, electrical insulating, sapphire lamina is placed on the top of the chip, thus further contributing to the total heat conduction. Thorough tests of thermal conduction, using some junctions as temperature sensors, showed better performance than different methods reported in literature. A specially designed structure guarantees the reproducibility of results and strict control of mechanical parameters.

REFERENCES

[1] M. Stock, R. Davis, E. de Mirandés, and M. J. Milton, "The revision of the SI – the result of three decades of progress in metrology," *Metrologia*, vol. 56, no. 2, p. 022001, 2019.

[2] R. Behr and A. S. Katkov, "Final report on the key comparison EUROMET. BIPM. EM-K10. a: Comparison of Josephson array voltage standards by using a portable Josephson transfer standard," *Metrologia*, vol. 42, no. 1A, p. 01005, 2005.

[3] F. Müller, T. J. Scheller, J. Lee, R. Behr, L. Palafox, M. Schubert, and J. Kohlmann, "Microwave design and performance of PTB 10 V circuits for the programmable Josephson voltage standard," *World Journal of Condensed Matter Physics*, vol. 4, no. 03, p. 107, 2014.

[4] V. Lacquaniti and A. Sosso, "Josephson Junctions for Present and Next Generation Voltage Metrology," in *Modern Metrology Concerns*. InTech, 2012.

[5] H. Schulze, F. Müller, R. Behr, J. Kohlmann, J. Niemeyer, and D. Balashov, "SINIS Josephson junctions for programmable Josephson voltage standard circuits," *IEEE Trans. Appl. Supercond.*, vol. 9, no. 2, pp. 4241–4244, 1999.

[6] V. Lacquaniti, N. De Leo, M. Fretto, S. Maggi, and A. Sosso, "Nb/Al-AlO_x/Nb overdamped Josephson junctions above 4.2 K for voltage metrology," *Appl. Phys. Lett.*, vol. 91, no. 25, p. 252505, 2007.

[7] V. Lacquaniti, C. Cagliero, S. Maggi, R. Steni, D. Andreone, and A. Sosso, "RF properties of overdamped SIS junctions," *IEEE Trans. Appl. Superconduct.*, vol. 15, no. 2, pp. 114–116, 2005.

[8] P. D. Dresselhaus, M. M. Elsbury, D. Olaya, C. J. Burroughs, and S. P. Benz, "10 volt programmable Josephson voltage standard circuits using NbSi-barrier junctions," *IEEE Trans. Appl. Supercond.*, vol. 21, no. 3, pp. 693–696, 2011.

[9] H. Yamamori, M. Ishizaki, H. Sasaki, and A. Shoji, "Operating Margins of a 10 V Programmable Josephson Voltage Standard Circuit Using NbN/TiN_x/NbN/TiN_x/NbN Double-Junction Stacks," *IEEE Trans. Appl. Supercond.*, vol. 17, no. 2, pp. 858–863, 2007.

[10] S. Benz, C. Hamilton, C. Burroughs, L. Christian, and T. Harvey, "AC and DC voltage source using quantized pulses," in *Precision Electromagnetic Measurements Digest, 1998 Conference on*, 1998, pp. 437–438.

[11] D. Kramer, "Helium users are at the mercy of suppliers," *Phys. Today*, vol. 72, no. 4, pp. 26–29, Apr. 2019. [Online]. Available: https://physicstoday.scitation.org/doi/10.1063/PT.3.4181

[12] C. Hamilton, C. Burroughs, and R. Kautz, "Josephson D/A converter with fundamental accuracy," *IEEE Trans. Instrum. Meas.*, vol. 44, no. 2, pp. 223–225, 1995.

[13] H. Yamamori, T. Yamada, H. Sasaki, and A. Shoji, "A 10 V programmable Josephson voltage standard circuit with a maximum output voltage of 20 V," *Supercond. Sci. Technol.*, vol. 21, no. 10, p. 105007, 2008.

[14] P. Durandetto and A. Sosso, "A modular and customizable open-source package for quantum voltage standards operation and control," *PLOS ONE*, vol. 13, no. 12, 2018.

[15] A. M. Klushin, J. Lesueur, M. Kampik, F. Raso, A. Sosso, S. K. Khorshev, N. Bergeal, F. Couëdo, C. Feuillet-Palma, P. Durandetto, M. Grzenik, K. Kubiczek, K. Musiol, and A. Skorkowski, "Present and future of high-temperature superconductor quantum-based voltage standards," *IEEE Instrumentation Measurement Magazine*, vol. 23, no. 2, pp. 4–12, 2020.

[16] B. Trinchera, V. Lacquaniti, A. Sosso, M. Fretto, P. Durandetto, and E. Monticone, "On the synthesis of stepwise quantum waves using a SNIS programmable Josephson array in a cryocooler," *IEEE Trans. Appl. Supercond.*, vol. 27, no. 4, pp. 1–5, 2017.

[17] P. Durandetto and A. Sosso, "Non-Conventional PJVS Exploiting First and Second Steps to Reduce Junctions and Bias Lines," *IEEE Trans Instrum Meas*, pp. 1–1, 2019.

[18] S. Benz, S. Waltman, A. Fox, P. Dresselhaus, A. Rufenacht, L. Howe, R. Schwall, and N. Flowers-Jacobs, "Performance improvements for the NIST 1 V Josephson Arbitrary Waveform Synthesizer," *Applied Superconductivity, IEEE Transactions on*, vol. 25, no. 3, pp. 1–5, June 2015.

[19] O. F. Kieler, R. Behr, R. Wendisch, S. Bauer, L. Palafox, and J. Kohlmann, "Towards a 1 V Josephson Arbitrary Waveform Synthesizer," *IEEE Trans. Appl. Supercond.*, vol. 25, no. 3, pp. 1–5, 6 2015.

[20] D. Zhao, H. E. van den Brom, and E. Houtzager, "Mitigating voltage lead errors of an AC Josephson voltage standard by impedance matching," *Meas. Sci. Technol.*, vol. 28, no. 9, p. 095004, 2017.

[21] J. M. Underwood, "Uncertainty analysis for ac–dc difference measurements with the ac Josephson volt-

age standard," *Metrologia*, vol. 56, no. 1, p. 015012, 2018.

[22] A. Sosso, P. Durandetto, B. Trinchera, O. Kieler, R. Behr, and J. Kohlmann, "Characterization of a Josephson array for pulse-driven voltage standard in a cryocooler," *Measurement*, vol. 95, pp. 77–81, 2017.

[23] V. Lacquaniti, D. Andreone, N. D. Leo, M. Fretto, S. Maggi, A. Sosso, and M. Belogolovskii, "Analysis of the Temperature Stability of Overdamped Nb/Al-AlO_x/Nb Josephson Junctions," *IEEE Trans. Appl. Superconduct.*, vol. 17, no. 2, pp. 609–612, Jun. 2007.

[24] V. Lacquaniti, N. De Leo, M. Fretto, A. Sosso, and M. Belogolovskii, "Nb/Al-AlO_x-Nb superconducting heterostructures: A promising class of self-shunted Josephson junctions," *J. Appl. Phys.*, vol. 108, no. 9, pp. 093 701–093 701, 2010.

[25] V. Lacquaniti, M. Belogolovskii, C. Cassiago, N. De Leo, M. Fretto, and A. Sosso, "Universality of transport properties of ultrathin oxide films," *New Journal of Physics*, vol. 14, no. 2, p. 023025, 2012.

[26] V. Lacquaniti, N. De Leo, M. Fretto, C. Cassiago, R. Rocci, A. Sosso, and M. Belogolovskii, "Controlling the interface properties of submicrometric Nb/A-AlO_x-Nb Josephson junctions," *IEEE Trans. Appl. Superconduct.*, vol. 25, no. 3, pp. 1–4, Jun. 2015.

[27] M. Belogolovskii, E. Zhitlukhina, V. Lacquaniti, N. De Leo, M. Fretto, and A. Sosso, "Intrinsically shunted Josephson junctions for electronics applications," *Low Temperature Physics*, vol. 43, no. 7, pp. 756–765, 2017.

[28] V. Lacquaniti, C. Cassiago, N. D. Leo, M. Fretto, A. Sosso, P. Febvre, V. Shaternik, A. Shapovalov, O. Suvorov, M. Belogolovskii, and P. Seidel, "Analysis of Internally Shunted Josephson Junctions," *IEEE Trans. Appl. Supercond.*, vol. 26, no. 3, pp. 1–5, 2016.

[29] V. Lacquaniti, D. Andreone, N. De Leo, M. Fretto, A. Sosso, and M. Belogolovskii, "Engineering Overdamped Niobium-Based Josephson Junctions for Operation Above 4.2 K," *IEEE Trans. Appl. Superconduct.*, vol. 19, no. 3, pp. 234–237, 2009.

[30] A. Sosso and P. Durandetto, "Experimental analysis of the thermal behavior of a gm cryocooler based on linear system theory," *Int. J. Refrig*, vol. 92, pp. 125–132, 2018.

[31] P. Durandetto and A. Sosso, "Using a Josephson junction as an effective on-chip temperature sensor," *Superconductor Science and Technology*, vol. 34, no. 4, p. 045008, 2021.

[32] P. Durandetto, E. Monticone, D. Serazio, and A. Sosso, "Thermal Performances of an Improved Package for Cryocooled Josephson Standards," *IEEE Trans. Compon. Packag. Manuf. Technol.*, vol. 9, no. 7, pp. 1264–1270, Jul. 2019.

25th IMEKO TC4 International Symposium
23rd International Workshop on ADC and DAC Modelling and Testing
IMEKO TC-4 2022
Brescia, Italy / September 12-14, 2022

AC Quantum Voltmeter used for Impedance Comparison

Damir Ilić[1], Ralf Behr[2] and Jinni Lee[2]

[1] *Faculty of Electrical Engineering and Computing, Primary Electromagnetic Laboratory (FER-PEL), Zagreb, Croatia, damir.ilic@fer.hr*
[2] *Physikalisch-Technische Bundesanstalt (PTB), Braunschweig, Germany, ralf.behr@ptb.de*

***Abstract* – This paper describes the experimental application of the AC quantum voltmeter, developed at PTB, for impedance ratio measurements at voltages up to 5 V and frequencies up to 1 kHz, as continuation of previous work. In such an application the AC quantum voltmeter is not directly measuring the output voltage of an AC source (as in ordinary use), but measures the voltage drop on the impedance, raising the requirements for synchronisation, grounding, and load influence of the used AC voltage source. Therefore, three types of AC sources were tested, a calibrator Fluke 5720A, a new version of an Aivon DualDAC3, and PTB's PDWQ mk2[1]. As impedances, two temperature stabilized Vishay resistors of nominal values of 10 kΩ are used. They are measured in a potentiometric way, i.e., the AC quantum voltmeter measures the RMS voltages on each resistor in a time sequence. The measurement results for different set-ups are described and presented.**

I. INTRODUCTION

The AC quantum voltmeter (AC-QVM), based on the programmable Josephson voltage standard (PJVS), is developed and implemented in recent years as a verified and established system for the measurement of RMS values for frequencies in the kilohertz range and with amplitudes up to 10 V [1] - [4]. The PJVS generates a stepwise sinusoidal waveform of the same frequency and (approximately) amplitude as the AC voltage under investigation, and the residual voltage differences are measured by the fast digitizer. In standard usage, the measured output voltage of an AC voltage source is connected directly to the input of the AC-QVM. In such a direct measurement set-up, it is easier to fulfil the necessary requirements, such as synchronisation between the measured source and AC-QVM and the definition of the grounding point.

On the other hand, the method in which the AC-QVM measures the voltage drop on an impedance gives the possibility for extension of its use to the measurement of DC or AC voltage ratios, i.e., for resistance (or impedance) comparisons or current measurements in the kilohertz frequency range [5] – [9]. In this paper we are presenting resistance comparisons in potentiometric measurement, where only one PJVS is used. The AC-QVM measures the RMS value of voltage drops on each resistor in a time series. This requires the implementation of an AC voltage source (ACVS) which can generate a stable output (voltage and frequency). Furthermore, it should be resistible on load or frequency changes, has a low harmonic distortion, and could be synchronised with the AC-QVM. Therefore, three types of AC sources were tested, a widely used multifunction calibrator Fluke 5720A, a new version of an Aivon DualDAC3, and PTB's PDWQ mk2. The last two are based on digital-to-analog converters and generate stepwise sinusoidal waveforms. Furthermore, the measurement procedure should enable a voltage ratio measurement by minimising the influence of swapping the connections (needed for measurement of voltages in a time series), synchronisation limits and grounding problems.

II. MEASUREMENT SET-UP

The basic set-up is given in Fig. 1, where two nominally equal resistors are chosen for this experiment and form the divider set-up and are connected in the series with ACVS.

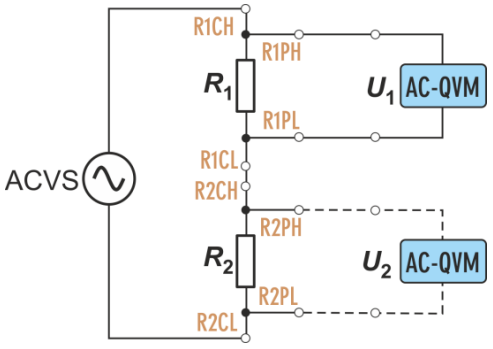

Fig. 1. Schematics of the measurement set-up; here R1CH means current high of R_1, R1PH means voltage high of R_1, etc. (other details are described in the text).

[1] The identification of commercial equipment does not imply the endorsement of either FER-PEL or PTB that it is the best equipment for this purpose, but for the completeness of the information given.

First the AC-QVM measures the voltage U_1 and then voltage U_2. During all measurements the ACVS is left floating, while the shield of the BNC connector of PXI digitizer input defines the grounding point in each measurement. The resistance ratio R_1/R_2 is determined from the measured voltages U_1 and U_2, and can be expressed as correction (in 10^{-6}) of the nominal value equal to 1:

$$r/10^{-6} = \left(\frac{R_1}{R_2} - 1\right) \cdot 10^6 = \left(\frac{U_1}{U_2} - 1\right) \cdot 10^6 \qquad (1)$$

A. AC-QVM

In this experiment the PJVS works at a frequency of 70.00 GHz, while the array is biased by a LeCroy ArbStudio 1104 1 GS/s Arbitrary Waveform Generator (four units each with four output channels for altogether 16 channels, plus one unit for triggering purposes that controls the other four). It generates 20 steps per period of the chosen voltage, while the amplitude is set accordingly. A sampler (PXI NI 5922) digitizes the difference voltage, and operates with the 1 MΩ differential input, up to 10 MSa/s sample rate [2]. The 48-tap standard finite impulse response (FIR) filter is selected due to its flattest frequency response. During all measurements the helium dewar was grounded.

A Keithley 3390 50-MHz arbitrary waveform generator is used for synchronisation purposes and is driven by an external 10 MHz reference. When the Fluke 5720A is used as ACVS, the generator sets the phase between the synthesized waveform and the calibrator waveform by locking its output for a chosen phase difference (usually it is -9° or +171°). In such way the zero-crossing point of the calibrator's output is exactly in the middle point of zero step. When the Aivon DualDAC3 and PTB's PDWQ mk2 are used as ACVS, the Keithley 3390 waveform generator supplies the clock frequency for synchronisation (10 MHz or 20 MHz).

The calculation of an RMS value (to be taken as measured value) is based on the settings of different parameters, adjusted accordingly for the chosen frequency. These parameters are the number of Josephson voltage steps per period according to the voltage to be measured (for all the experiments here it was fixed to 20 steps), the selected number of measured points at each step (NMPSJV), defined by the number of deleted starting points (NDSP), the number of deleted ringing points (NDRP) at the beginning of each voltage step, the sampling rate, and the number of periods captured (NPC). The sampling rate of the PXI NI 5922 was set to 10 MSa/s for 1 kHz and for lower frequencies always to 4 MSa/s. The representative data are given in Table 1. As an example, for a frequency of 31.25 Hz the values are: 4 MSa/s sampling rate, the number of points per Josephson voltage step NPSJV = 6400, NDSP = 0, NDRP = 200, and NMPSJV = NPSJV-NDSP-2×NDRP = 6000 to be used for calculation. An NPC = 15 with the phase difference = –9.0° gives a calculated value and corresponds to a measurement time of 0.48 s (which is a multiple of the measured voltage periods and of power line periods, too). The number of repetition loops NL = 200 corresponds for all frequencies to the total of approximately 2-minute measurement time.

Table 1. Settings of the AC-QVM for the RMS voltage measurements at different frequencies – explanations of parameters are given in the text.

f/Hz	31.25	62.5	125	400	1000
NDSP	0	0	0	0	50
NDRP	200	200	200	100	50
NMPSJV	6000	2800	1200	300	350
NPC	15	30	60	192	480

The final RMS value taken as measurement result is the mean value of described 2-minute measurement sequence. The so-called "standard measurements procedure" (SMP) means five repetitions of such 2-minute measurement sequences.

B. Resistance box

The resistance box, developed at PTB, contains two Vishay 10 kΩ standards, regulated with a thermostat in which the temperature is maintained at 29.95 °C [6]. The output connectors are of BPO type, where the four "inner" connecting pins of each resistor are for current and voltage connections, and all "outer" connecting pins are shorted and grounded. Such grounding has no influence on the measurement of RMS value. For the measurements all connections are rearranged to BNC connectors.

C. Measurement of resistance ratio

Considering the connection of the ACVS and grounding of the system, in our previous experimental work [10] different procedures were tested, and it was found out that procedure marked as P2 was the best one. In that procedure the ACVS HI is connected to R2CL and ACVS LO is connected to R1CH. During U_1 voltage measurements the grounding point is R1PH (ACVS LO is grounded), while during U_2 measurements it is R2PL (ACVS HI is grounded). For any settings in which the middle point of the divider is led to the ground the results are off for different reasons, and such set-up cannot be used.

III. MEASUREMENT RESULTS

We will start the presentation of the results with the direct measurement of the ACVS output voltage to investigate their frequency dependence (or load dependence), and to confirm the level of standard deviations which are reachable by using the SMP. It is worth to mention that the standard deviation, when

measuring voltage drops on the resistors, is expected to be higher than for direct measurement of ACVS output. In Table 2 are given the results for the calibrator Fluke 5720A, where U_r is the relative correction of the nominal output voltage, and *s* is the standard deviation for SMP (both expressed in μV/V).

Table 2. Frequency dependence of the Fluke 5720A – explanations of parameters are given in the text.

U/V	*f*/Hz	31.25	62.5	125	400	1000
1 V	U_r/(μV/V)	2.84	1.07	0.57	-1.18	-3.21
	s/(μV/V)	0.60	0.14	0.42	0.31	1.19
2 V	U_r/(μV/V)	6.51	2.30	2.41	-0.28	-0.80
	s/(μV/V)	0.36	0.61	0.63	0.45	0.52
5 V	U_r/(μV/V)	4.40	0.95	0.60	0.00	-1.61
	s/(μV/V)	0.37	0.51	0.55	0.58	0.51

The relative standard deviation of the RMS value during a 2-minute sequence varies from 1 μV/V @ 62.5 Hz up to 4 μV/V @ 1 kHz and is approximately similar for all voltages. These results show that the frequency dependence is rather small for the calibrator Fluke 5720A, while the loading effect, at least for 10 kΩ, is expected to be neglected due to its specifications.

The Aivon DualDAC3 source is an improved version of the Aivon DualDAC2 [11], for which the source output resistance was measured to be about 70 mΩ, causing a loading effect at a level of -10 μV/V with the 10 kΩ load (although in this measurement set-up with a nominal ratio of 1 such loading effect does not directly produce an error). Besides the load dependence this source exhibits a significant frequency dependence. It has two outputs, but for this experiment only one output was used, while the optical input trigger is connected to the trigger output of PXI system. The external 10 MHz reference frequency is supplied by the Keithley 3390 waveform generator. Despite powering from DC sources, the GND connector of the Aivon DualDAC3 source is always grounded. In Table 3 the results are given, similar as in Table 2. For the Aivon DualDAC3 source only at 1 V nominal output voltage, where U_r is the correction of the nominal output voltage in μV/V, and *s* the standard deviation for SMP. The standard deviation of the RMS value during a 2-minute sequence varies from 0.11 μV/V @ 80 Hz up to 0.35 μV/V @ 1 kHz. This is one order of magnitude smaller than for the Fluke 5720A. The same relates to *s* in Table 3, the standard deviation for SMP, which is also significantly smaller. The load dependence (LD) is calculated as the relative change of the output voltage with the 10 kΩ load, and according to the results the source resistance is about 47 mΩ. The frequency dependence (FD) is calculated as relative change of the output voltage in comparison to the voltage at 20 Hz. Both parameters are significantly larger than those of the Fluke 5720A.

Table 3. Frequency and loading dependence of the Aivon DualDAC3 source – explanations of parameters are given in the text.

f/Hz	20	80	250	625	1000
U_r/(μV/V)	235.92	235.96	227.48	206.72	168.42
s/(μV/V)	0.02	0.03	0.04	0.02	0.03
LD/(μV/V)	-4.79	-4.57	-4.78	-4.69	-4.68
FD/(μV/V)	0.00	0.04	-8.43	-29.19	-67.49

As mentioned before, in the measurement set-up according to Fig. 1 the measurement of voltage ratios (for impedance ratio measurements) consists of two measurements: one of voltage U_1 on R_1 and, without delay by one of voltage U_2 on R_2. There is no multiplexing and no automatization of such procedure, and the manual reconnection is needed after each sequence, as well as for balancing the differential voltage. The results, obtained after long periods of testing, improvement of the measurement set-up and measurement sequences, will be presented in the following subsections. All previous explanations regarding the SMP, set-up, grounding, synchronization, etc. are applied. Since two 10 kΩ standards compared are of the same type, same characteristics and mounted in the same thermostat, it is expected that their ratio should be stable and independent of frequency.

A. Impedance ratio measurements using the Fluke 5720A as ACVS

In Table 4 and Fig. 2 are the results of impedance ratio measurements using the Fluke 5720A as ACVS, where *r* is defined by (1) and *s*(*r*) is the associated standard deviation; both are expressed as relative values in 10^{-6}. The ACVS was set to 2 V. The relative standard deviation of the RMS value during a 2-minute sequence varies from 1.2 μV/V @ 31.25 Hz up to 4 μV/V @ 1 kHz, which is very similar to the results of the direct Fluke 5720A measurement. These results conclude that the set-up is at its optimum (when the Fluke 5720A is used as ACVS) and shows almost no distinction with the standard deviation taken from the direct measurement. The measured ratios are also in very good agreement with former measurements [6], [10].

Table 4. Results of the Fluke 5720A impedance ratio measurements at 2 V – explanations are given in the text.

f / Hz	*r* / 10^{-6}	*s*(*r*) / 10^{-6}
31.25	-3.22	0.47
62.5	-3.01	0.14
125	-3.48	0.41
400	-3.41	0.45
1000	-3.60	0.65

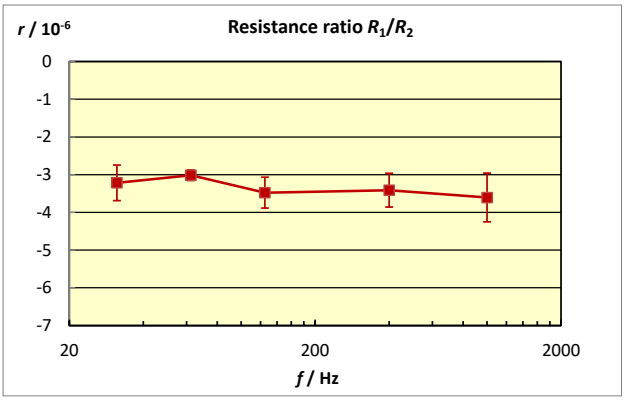

Fig. 2. Graphical presentation of data given in Table 4. Error bars indicate relative standard deviations (k = 1).

B. Impedance ratio measurements using the Aivon DualDAC3 source as ACVS

In Table 5 and Fig. 3 are the results of impedance ratio measurements, using the Aivon DualDAC3 as ACVS with the same parameters as the previous paragraph (subsection III.A). The ACVS was set to 0.5 V. The standard deviation of the RMS value during a 2-minute sequence varies from 0.8 µV/V @ 80 Hz up to 2 µV/V @ 1 kHz (with the unexpectedly high value of 10 µV/V @ 320 Hz).

Table 5. Results of impedance ratio measurements using the Aivon DualDAC3 at 2 V – explanations are given in the text.

f / Hz	r / 10^{-6}	$s(r)$ / 10^{-6}
20	-3.72	0.32
80	-4.42	0.15
160	-4.22	0.23
320	-3.98	0.60
640	-3.82	0.17
1000	-2.47	0.54
2000	-5.59	0.72

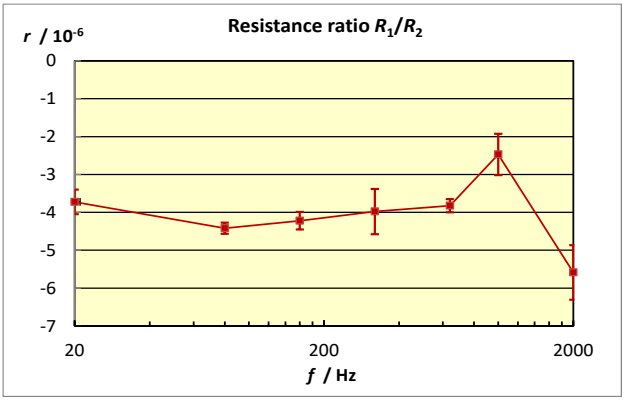

Fig. 3. Graphical presentation of the data given in Table 5 Error bars indicate relative standard deviations (k = 1).

As mentioned in section III, the standard deviation of the direct output measurement on the Aivon DualDAC3 is 0.35 µV/V @ 1 kHz. This is significantly smaller than the 2 µV/V @ 1 kHz measured now with this set-up. In comparison with the Fluke 5720A, the disparity in standard deviation for the Aivon DualDAC3 is much larger between the direct and ratio measurement set-up.

However, it is important to emphasized that the measured ratios r and associated standard deviation $s(r)$ for all frequencies presented in Table 5 and Fig. 3 are in good agreement with the results given in Table 4 and Fig. 2.

C. Impedance ratio measurements using PTB's PDWQ mk2 source as ACVS

In some way this source is similar to the Aivon DualDAC3 source because it generates stepwise approximated sinewave voltages. The source has two outputs, but for this measurement only one output is used. A low-pass filter is mounted on the output to eliminate glitches in the generated voltage. It is synchronised to the PJVS system by using a 20 MHz clock signal generated by a Keithley 3390 waveform generator which is delivered to the clock input by an optical link.

The source was tested by resistance ratio measurements at 1 V and 1250 Hz using different connection and grounding procedures of the ACVS in the circuit. The results are given in Table 6, where r is defined by (1) and $s(r)$ is associated relative standard deviation; both are expressed in 10^{-6}. Sequence identifiers contain ordinal numbers for easier identification of measurement. The explanation of the procedures is as follows:

- **P1:** CAL HI to R1CH, CAL LO to R2CL; PXI ground on R1PH for U_1 and on R2PL for U_2
- **P2:** CAL HI to R2CL, CAL LO to R1CH; PXI ground on R1PH for U_1 and on R2PL for U_2
- **P6:** The goal is that LO of ACVS is connected to PXI ground during measurements of each voltage; connection P2 is used for measurements of U_1 (LO of ACVS to R1CH) and P1 for U_2 (LO of ACVS to R2CL). It is not needed to synchronize the source again after changing the connection.

Based on these descriptions, the result under sequence identifier M42 should be comparable to the results obtained with the other two sources (Tables 4 and 5, Figs. 2 and 3). As it is obvious, the measured r = -56.3, which is completely off from the values given in Tables 4 and 5, and this is also valid for all values in Table 6. The results are showing that this source, at least the tested item, cannot be used in this measurement set-up as ACVS. It has glitches in the generated voltage, is less robust for the reconnection during the measurement sequence (that means maintaining the output voltage at the same level without loss of synchronisation or even after an off-on procedure of the generated voltage) and more sensitive on the grounding connection. All these effects have consequences on the measured RMS value of each voltage,

resulting in a non-repeatable ratio measurement in a time-series way.

Table 6. Results of impedance ratio measurements using PTB's PDWQ mk2 at 1 V – explanations are given in the text.

Sequence identifier	M42	M43	M44	M45	M46
r / 10^{-6}	-56.30	-42.91	-25.12	11.82	15.59
$s(r)$ / 10^{-6}	1.86	1.86	2.05	0.39	0.77
procedure	P2	P2	P2	P1	P1
Helium dewar grounded	X			X	
Outer BPOs grounded	X	X		X	X

Sequence identifier	M47	M48	M49	M50	M51
r / 10^{-6}	18.19	2.36	-5.65	-10.57	2.77
$s(r)$ / 10^{-6}	1.46	0.50	0.81	0.70	1.78
procedure	P1	P6	P6	P6	P6
Helium dewar grounded		X		X	
Outer BPOs grounded		X	X		

IV. CONCLUSIONS

The results show that the Fluke 5720A calibrator is a robust source which can generate sinusoidal waveforms with very stable amplitude and is not sensitive on the applied load (at least for the tested one). The measurement of RMS values is limited due to the phase-lock requirement when the AC-QVM is used. The standard deviation of the RMS value during a 2-minute sequence for a 1 V output voltage could be as low as 1.2 µV/V @ 31.25 Hz (associated standard deviation of the mean can be calculated as $s/\sqrt{n}$) and is almost the same when its output is measured directly with AC-QVM, or when it is used as ACVS for ratio measurement and voltage drop is measured on the divider. The impedance ratio was measured with a standard deviation varying from 0.14 µV/V to 0.65 µV/V for the tested frequency range up to 1 kHz.

When the output voltage of an Aivon DualDAC3 is measured directly by the AC-QVM, the standard deviation of the RMS value during a 2-minute sequence could be as low as 0.11 µV/V @ 80 Hz. However, when it is used as ACVS and the voltage drop is measured on the divider, the same parameter is 0.8 µV/V @ 80 Hz. The impedance ratio was measured with the standard deviation from 0.15 µV/V to 0.72 µV/V for the tested frequency range up to 2 kHz. In comparison to a Fluke 5720A this source is less robust and exhibit a larger frequency and load dependence. In addition, it is more complicated to control and more sensitive when changing the connections during the standard measurement procedure.

It was shown that both calibrator Fluke 5720A and Aivon DualDAC3 could be used as ACVS in the measurement set-up which include the AC-QVM for resistance ratio measurements. Careful settings of the parameters and measurement sequences are always required. It is also worth to emphasize that a previous version, the Aivon DualDAC2, as found in [10], was not useful for such experiments, while in contrary the new version Aivon DualDAC3 could be, as shown in this paper. The obtained ratio r results for the resistance standards in the used resistance box are in good agreement with previous work [6].

Lastly, the measurement results described in subsection III.C conclude that PTB's PDWQ mk2 source is not suitable to be used as ACVS for such purposes.

ACKNOWLEDGEMENTS

This work was co-funded by the EMPIR joint research project 17RPT03 DIG-AC. The EMPIR initiative is co-funded by the European Union's Horizon 2020 research and innovation programme and the EMPIR Participating States. D. Ilić would like to extend his gratitude to the PTB colleagues for their continuous support.

REFERENCES

[1] A. Rüfenacht, C. J. Burroughs, P. D. Dresselhaus, and S. P. Benz, "Differential Sampling Measurement of a 7 V RMS Sine Wave with a Programmable Josephson Voltage Standard", IEEE Trans. Instrum. Meas., vol. 62, no. 6, June 2013.

[2] J. Lee, R. Behr, L. Palafox, A. Katkov, M. Schubert, M. Starkloff, and A.C. Böck, "An ac quantum voltmeter based on a 10 V programmable Josephson array," Metrologia, vol. 50, pp. 612-622, Dec. 2013.

[3] M. Schubert, M. Starkloff, J. Lee, R. Behr, L. Palafox, A. Wintermeier, A.C. Böck, P. M. Fleischmann, and T. May, "An AC Josephson Voltage Standard up to the Kilohertz Range Tested in a Calibration Laboratory," IEEE Trans. Instrum. Meas., vol. 64, no. 6, pp. 1620-1626, June 2015.

[4] J. Lee, J. Nissilä, A. Katkov, R. Behr, "A quantum voltmeter for precision AC measurements", CPEM 2014 Conference Digest, pp. 732-733, June 2014.

[5] J. Lee, R. Behr, B. Schumacher, L. Palafox, M. Schubert, M. Starkloff, A.C. Böck and P.M. Fleischmann, "From AC Quantum Voltmeter to Quantum Calibrator," CPEM 2016 Conference Digest, June 2016.

[6] J. Lee, "Programmable Josephson Arrays for Impedance Measurements," Dissertation, Technische Universität Carolo-Wilhelmina zu Braunschweig, Germany 2010.

[7] M. Starkloff, M. Bauer, M. Schubert et al., “The AC Quantum Voltmeter used for AC Current Calibrations”, CPEM 2018 Conference Digest, July 2018.
[8] D. Ilić, L. Lüddecke, A. Heinrich, J. Meisner, R. Behr, “Calibration of a precision current measurement system for high AC voltages using an AC Quantum Voltmeter”, Conf. Dig. CPEM 2020 Conference Digest, August 2020.
[9] D. Ilić, R. Behr, J. Lee, “Stability of AC current measurements using AC-DC shunts and the AC Quantum Voltmeter”, Proc. of 24th IMEKO TC4 International Symposium, September 2020.
[10] D. Ilić, M. Bauer, J. Lee, R. Behr, “Application of AC Quantum Voltmeter for Impedance Comparison” Conf. Dig. CPEM 2018 Conference Digest, July 2018.
[11] J. Nissilä et al, “A precise two-channel digitally synthesized AC voltage source for impedance metrology,” CPEM 2014 Conference Digest, pp. 768-769, June 2014.

25th IMEKO TC4 International Symposium
23rd International Workshop on ADC and DAC Modelling and Testing
IMEKO TC-4 2022
Brescia, Italy / September 12-14, 2022

Laboratory reproduction of on-field low power quality conditions for the calibration/verification of electrical energy meters

A. Cultrera[1,*], G. Germito[1], D. Serazio[1], F. Galliana[1], B. Trinchera[1], G. Aprile[1], M. Chirulli[2], L. Callegaro[1].

[1] *INIRM - Istituto Nazionale di Ricerca Metrologica, strada delle Cacce, 91 10135 - Torino, Italy.*
[2] *VERIFICA S.p.A. Via S. Annibale M. Di Francia, 29 70010 - Locorotondo, Italy.*

**e-mail: a.cultrera@inrim.it*

***Abstract* – In this work we present a method for testing static active energy meters in low power quality conditions recorded at installation sites. Voltage and current waveforms recorded on the field with a calibrated portable instrument were reproduced with an accurate phantom power generator up to the 40th harmonic. The error on the active energy measurement of an energy meter under test (W_{DUT}) in conditions reproduced from the on-field measurements was evaluated in comparison with a reference meter (W_{REF}). On-field data were recorded at a 50 kW self production photovoltaic facility. This method allows the laboratory reproduction of realistic (distorted) on-field conditions in a metrologically traceable framework.**

I. Introduction

Devices such as electric vehicles charging stations, consumer electronics, renewable energy sources and electronically driven workshop tools, to cite a few, inject disturbances in the network, producing distortion of the sinusoidal voltage and current waveforms which may affect the accuracy of static energy meters when measuring active electrical energy [1, 2, 3, 4].

Such an ubiquitous presence of nonlinear loads and electronic equipment in the electrical network, demands to pay particular attention to the effects of low power quality conditions when performing calibration and verification of household and industrial electrical power and energy meters.

Active energy meters installed within the European Union must comply with the Directive 2014/32/EU Measuring Instruments (MID) [5]. Energy meters complying with the MID are calibrated and verified on the basis of international and national documentary standards (national standards are specific to each country).

Concerning the calibration/verification of newly manufactured energy meters, the international reference documents for EU/MID active energy meters are (i) the EN 50470 [6, 7] series that is the harmonized standard in force for electricity metering equipment; (ii) the IEC 62052 and IEC 62053 series [8, 9], with amendments in order to be compliant with the MID. These standards deal with both sinusoidal and distorted (low power quality) situations and prescribe tests in both conditions, specifying simple waveform shapes intended to be generically representative of possible real-world situations.

On the other hand, the calibration/verification of already deployed energy meters is quite different from the testing of newly manufactured units. For example there could be constraints in the insertion of the verification instrumentation or impediments to burden simulation. Concerning the verification of meters already in service in Italy for example, the task is fulfilled following the guide CEI 13-71 [10]. The guide distinguishes two main cases: tests carried out with phantom power, which are performed with portable generators in sinusoidal regime; and tests made with real burden, where no particular waveforms are prescribed.

Several methods have been proposed to test static meters in non-sinusoidal conditions beyond the ones considered in the presently available standards. Some authors proposed to use waveforms with fixed or time-varying random harmonic content to test static energy meter accuracy in realistic conditions [11]; other approaches consist in looking for an ideal waveform which could be considered the the “best” one for

calibrating meters [12], or using multiple non-sinusoidal waveforms, generated in random sequence [13].

In this work we show that the accurate phantom power generator implemented at INRIM [14] can be used to reproduce power quality waveforms and conditions that have been previously recorded on the field. In our setup, the amplitude phase and frequency of the generated waveforms are kept under control by means of a feedback loop with a high class three-phase comparator, so these can be accurately reproduced compared to the ones previously recorded on the field; this capability is not reported for other similar power generation systems previously presented in literature [15, 16, 17] where the generation of the waveforms was performed with stable but stand-alone calibrators. This approach represents one possibility to test energy meters in specific conditions, e.g. those found at the site where the static meter is installed, while reproducing these conditions in a metrologically traceable framework, hence representing a test in both realistic and representative conditions.

II. Power waveforms recording

The on-field measurements took place in September 2021, at the self production photovoltaic (PV) generation facility of a small factory in Italy. The facility is connected to a low voltage cabin of the national distribution network, and the installed energy meter accounts for both energy injection and absorption by the factory, depending on the moment and solar irradiation of the PV modules. The energy meter installed at the site is a GESIS 2020 OM 330, reference current 1 A, maximum current 20 A, EN class B for active energy measurement. The meter is installed in semi-direct insertion, with TA transducers of ratio 125/5 A/A of IEC class 0.5s.

During the plant operation, the waveforms were sampled with a calibrated ZERA portable reference wattmeter MT-310, having a nominal power measurement accuracy of 0.1 % in direct insertion and of 0.2 % when inserted with amperometric clamps. The instrument was inserted in 4WA mode, with amperometric clamps, and set to the voltage range of 250 V and the current range of 100 A.

The instrument recorded both the waveforms and the harmonic content of the three voltage and the three current channels. Data were stored in the instrumentàs memory in the form of an `xml` format table, which was downloaded and analyzed later.

III. Power waveforms reconstruction

A schematic of the three phase experimental setup used to calibrate a commercial energy meter with the reconstructed waveforms is shown in Fig. 1.

G is a ZERA MTS310 power and energy meters test system, described in detail in [14]. The output of G spans up to 320 V and 120 A per phase, with a frequency of the fundamental from 40 Hz to 70 Hz. The unit G includes a photodetector to measure the pulsed optical output of W_{DUT}. W_{REF}, is a ZERA COM5003 three-phase energy meter, accuracy 0.005 %. Voltage input ranges up to 480 V, current input up to 160 A, with capability of setting up to the 40th harmonic, with a bandwidth of up to 6 kHz.

W_{DUT} is the unit under test, in this case a DPEE TH40C multifunction static three-phase meter. The specifications give a reference current of 1 A, a maximum current of 10 A. The meter is in EN class C and IEC class 0.5s concerning the measurement of active energy.

To reconstruct waveforms on the voltage and current channels on the basis of their measured harmonic content measured by the MT-310, the amplitude and phase of the 40 harmonic components, relative to the fundamental, of each channel were used as input parameters for the software WinSAM™ that controls the ZERA MTS 310. W_{DUT} and W_{REF} were connected to G in 4WA configuration, similarly to the on-field verification.

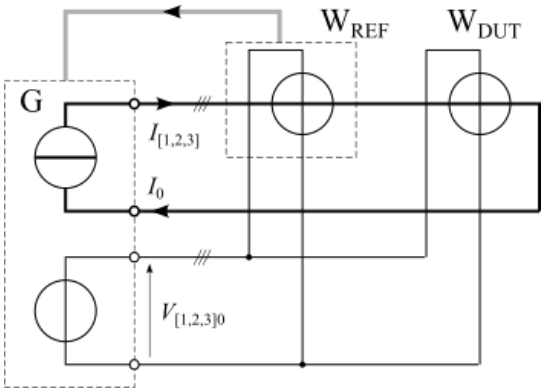

Fig. 1. Simplified schematic diagram of the testbed system for calibration / verification of static electricity meters. See Sec. III for details.

IV. Results: on-site recording

The waveforms recorded on the field, and considered in this work, had voltages of 229.97 V, 231.52 V and 231.19 V for the three phases, and currents of 10.57 A, 10.26 A and 10.41 A at the secondary TA current transducers. The influence of TA transducers, already installed at the verification site, is not discussed in the prest work.

An example of current waveform captured on the TA secondary phase 1 of the facility at the verification site is

shown in Fig. 2. The plot shows the waveform in the time domain, which appears strongly distorted with total harmonic distortion (THD) of 27.25 %; double zero-crossings are clearly visible at about 0 ms and 10 ms. The corresponding voltage waveform, not shown, appears less distorted with THD = 1.16 %.

Fig. 3 shows the corresponding amplitude of the 40 recorded harmonics of the waveform given in Fig. 2; the inset shows a detail of the first 10 harmonics, the most relevant, for the three phases. The amplitudes of the harmonic components relative to each phase are normalized to the corresponding fundamental. It can be seen that mainly odd harmonics were present and that the load was non-symmetric.

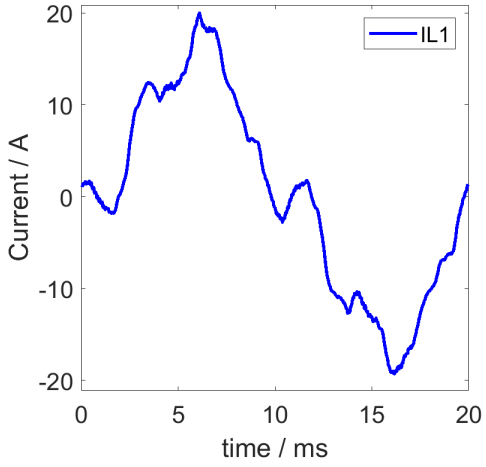

*Fig. 2. Current waveform on the phase 1 (*IL1*) recorded at the facility. Samples were stored in an* MT-310 *verification instrument.*

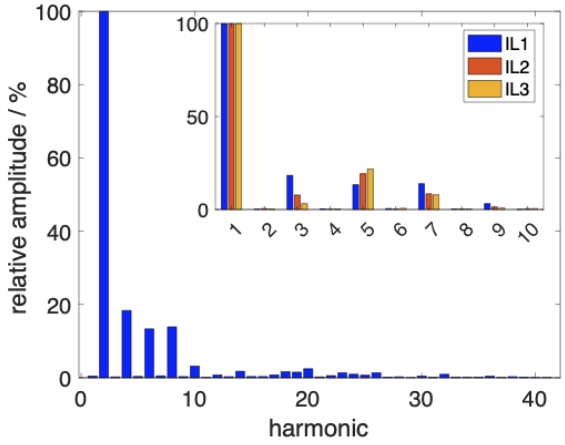

*Fig. 3. Harmonic content of the current waveform of FIg. 1 (main plot). The first 10 harmonics of all the three current channels (*IL1, IL2, IL3*) of the energy meter installed at the facility, are shown in the inset.*

V. Results: Reproduction in the Lab

The amplitude of the fundamental harmonic component of the voltage waveforms reproduced in the laboratory was set to 230 V, standard reference voltage defined in the EN 50470-1 (clause 4.1), since the on-field voltage waveforms were compatible with that, considering the EN 50470-3 (table 12). The amplitude of the fundamental harmonic of the current waveforms has been scaled down to comply with the specifications of W_{DUT} (the DPEE TH40C has a maximum current of 10 A).

According to the on-field measurements, the relative phase between the fundamental components of the voltage and current waveforms were set to -95.09 °, -68.55 ° and -64.04 ° respectively for the phases 1, 2 and 3. The burden was of capacitive type for all the 3 phases.

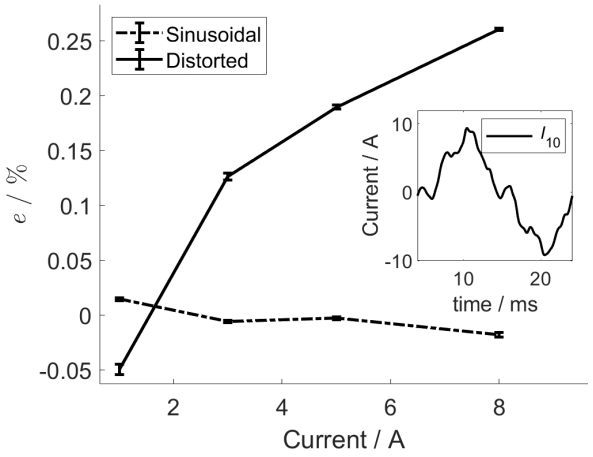

Fig. 4. Relative error, e, between W_{REF} *and* W_{DUT} *for measurements performed with the* DPEE TH40C *(main plot). The solid line represents the error on the measurement of reproduced waveforms; the dashed line corresponds to the error in sinusoidal conditions, given as a reference. The inset shows the reproduction of the on-field waveform shown in Fig. 2, generated on channel* I_{10} *of the presented setup.*

Following the standard EN 50470-1 we define the active energy relative error as

$$e = 100 \frac{E_{A,DUT} - E_{A,REF}}{E_{A,REF}} \%, \quad (1)$$

where $E_{A,DUT}$ is the active energy measurements of W_{DUT} and $E_{A,REF}$ is the active energy measurements of the W_{REF}. Using the direct insertion scheme of Fig. 1, we measured the relative error e in both sinusoidal and distorted regimes, at fixed voltage, as a function of the supplied current level I of the fundamental harmonic within the range 1 A to 8 A. For each measurement point, the fictitious power generated by G was integrated for 20 s for the sinusoidal waveforms and 40 s for the reproduced distorted waveforms to get $E_{A,DUT}$ and $E_{A,REF}$ in each of the two conditions; measurements were repeated 6 times.

Results reported in Fig. 4 show the energy measurement error e for sinusoidal conditions (dashed line, as a reference), and the distorted conditions (solid line). The inset shows the reproduction of the real waveform of Fig. 2. The error bars represent the type A uncertainty (coverage factor $k = 1$) evaluated as the standard deviation of the mean. A full expression of uncertainty of the measurement is under evaluation.

VI. Discussion and conclusions

Fig. 4 shows that the error e of the W_{DUT} spans between $e = -0.0178$ % and $e = 0.0145$ % for the sinusoidal conditions, falling within the range prescribed by the corresponding standards EN 50470 and IEC 62053 for the class of W_{DUT}. On the other hand, the error e corresponding to the distorted conditions is substantially larger, spanning a much larger range from $e = -0.0497$ % to $e = 0.2601$ %. Hence, under the power quality conditions recorded on the field, the measurement error e of W_{DUT} is larger than in sinusoidal conditions, yet the DUT is still performing reasonably compared to W_{REF}.

Note that since there are no prescriptions concerning the limits for the error e in generic low power quality situations in the present standards [7, 9], the results obtained in the reproduced distorted conditions can not be formally compared with any of the defined forms of permissible error found in the normative EN/IEC. Anyway, the error in the present distorted conditions is even within the permissible error prescribed for sinusoidal conditions in the standards EN 50470 and IEC 62053 for the class of W_{DUT}.

In conclusion, this work shows that the presented setup allows to generate arbitrary distorted waveforms based on the harmonic content of real waveforms sampled on the field. Moreover, results suggest that the measurement of arbitrary distorted waveforms can be roughly compared with reference conditions, provided the generation of the reproduced waveforms is under control. This approach can be considered complementary to the others presented above based on statistical methods. Future work will consider other types of on-field installations, both in terms of insertion schemes, nominal power and generation systems.

References

[1] M. R. Khalid, M. S. Alam, A. Sarwar, M.S. J. Asghar, “A comprehensive review on electric vehicles charging infrastructures and their impacts on power-quality of the utility grid”, eTransportation, vol. 1, pp. 100006, 2019.

[2] J. Silva Ortega, V. Sousa Santos, P. Sarmiento Crespo, J. Gómez Sarduy, P. Viego Felipe, E. Quispe, “Effects of power electronics devices on the energy quality of an administrative building”, International Journal of Power Electronics and Drive System, vol. 10, no. 4, pp. 1951-1960, 2019.

[3] W.A.A. Salem, W. G. Ibrahim, A. M. Abdelsadek, A. A. Nafeh “Grid connected photovoltaic system impression on power quality of low voltage distribution system” Cogent Engineering, vol. 9, n. 1, pp. 2044576, 2022.

[4] D. Lumbreras, E. Gálvez, A. Collado, J. Zaragoza, “Trends in Power Quality, Harmonic Mitigation and Standards for Light and Heavy Industries: A Review” Energies , vol. 13, no. 21, pp. 5792, 2020.

[5] Directive 2014/32/EU of the European Parliament and of the Council of 26 February 2014 on the harmonization of the laws of the Member States relating to the making available on the market of measuring instruments.

[6] EN 50470-1:2006+A1:2018, “Electricity Metering Equipment (A.C.) — Part 1: General Requirements, Tests and Test Conditions — Metering Equipment (Class Indexes A, B and C)”, CENELEC: Brussels, Belgium, 2018.

[7] EN 50470-3:2006+A1:2018, “Electricity Metering Equipment (A.C.) — Part 3: Particular Requirements — Static Meters for Active Energy (Class Indexes A, B and C)”, CENELEC: Brussels, Belgium, 2018.

[8] IEC 62052-11:2020, “Electricity metering equipment - General requirements, tests and test conditions — Part 11: Metering equipment”, IEC: Geneve, Switzerland, 2020.

[9] IEC 62053-21:2020, “Electricity metering equipment - Particular requirements — Part 21: Static meters for AC active energy (classes 0,5, 1 and 2)”, IEC: Geneve, Switzerland, 2020

[10] CEI 13-71 “Sistemi di misura dell'energia elettrica (c.a.) — Guida alla composizione, installazione e verifica”, CEI: Milano, Italia, 2015.

[11] L. Bartolomei, D. Cavaliere, A. Mingotti, L. Peretto, R. Tinarelli, “Testing of Electrical Energy Meters Subject to Realistic Distorted Voltages and Currents”, Energies, vol. 13, no. 8, pp. 2023, 2020.

[12] A. Ferrero, C. Muscas, "On the selection of the "best" test waveform for calibrating electrical instruments under nonsinusoidal conditions," in IEEE Transactions on Instrumentation and Measurement, vol. 49, no. 2, pp. 382, 2000.

[13] A. Ferrero, M. Faifer, S. Salicone, "On Testing the Electronic Revenue Energy Meters”. IEEE Trans. Instrum. Meas., vol. 58, no. 9, pp. 3042 , 2009.

[14] L. Callegaro, G. Aprile, A. Cultrera, F. Galliana, G. Germito, D. Serazio, B, Trinchera, “A calibration-verification testbed for electrical energy meters under low power quality conditions”, Measurement: Sensors, vol. 18, pp. 100118, 2021.

[15] D. Gallo et al., “A new methodological approach to quality assurance of energy meters under nonsinusoidal conditions”, IEEE Trans. Instrum. Meas., vol. 56, no. 5, pp. 1694-1702, 2007

[16] A. Olencki and P. Mróz, “Testing of energy meters under three-phase determined and random nonsinusoidal conditions”, Metrology and Measurement Systems vol. 21, no. 2, pp. 217-232, 2014.

[17] L. Bartolomei et al, “Testing of electrical energy meters subject to realistic distorted voltages and currents”, Energies vol. 13, n. 8, pp. 2023, 2020.

25th IMEKO TC4 International Symposium

23rd International Workshop on ADC and DAC Modelling and Testing

IMEKO TC-4 2022

Brescia, Italy / September 12-14, 2022

On Data Compression Algorithms for Power Measurements in Distributed Energy Systems

Paolo Bellagente[1]

[1] *University of Brescia, Department of Information Engineering Via Branze 38, 25123 Brescia, Italy, paolo.bellagente@unibs.it*

***Abstract* –The diffusion of renewable energy sources is heavily affecting all aspects of modern power grids equipped by distributed energy resources and Battery Energy Storage Systems. Suitable Key Performance Indicators (KPI) have been developed, to find optimal storage capacity and control algorithms, which are resulted to be really dependent on data recording time interval. The aim of this paper is to analyze, on real data, which effect the time resolution of measurement data has on energy KPIs and to investigate how to select a proper compression algorithm to enhance the efficiency of the data collection process. Results shows that the KPI will be underestimated by the 40% if the sampling time rises from 5 s to 10 s, making lossy algorithms not interesting. Furthermore, lossless compression algorithms are effective but the tuning of those algorithms is all but intuitive.**

I. INTRODUCTION

The increasing penetration of distributed generation from Renewable Energy Sources (RESs) is heavily affecting the design and operation of modern distribution networks [1]. In particular, the intermittent nature of renewables, such as Photovoltaic (PV) systems, is calling for improved monitoring and control functions over Distributed Energy Resources (DERs) [2]. The uncertainty of distributed RES generation has indeed a relevant impact on the active power profiles of prosumers, i.e., end-users equipped with RES generators [3], [4]. To mitigate this drawback, the adoption of distributed battery storage systems has been recently proposed, with the aim of increasing the self-consumption of intermittent PV generation [5]. Nevertheless, the adoption of storage capabilities at prosumers' premises is only half of the story, and advanced DER control algorithms must be adopted to reduce the impact of the uncertain generation of RESs [6], [7]. The choice of the optimal storage capacity and of the most suitable control algorithm is generally carried out by referring to specific Key Performance Indicators (KPIs). These KPIs, however, strongly depend on the prosumer's generation and consumption profiles [8], and require power data gathered from heterogeneous measuring devices, such as smart meters and inverters. Data recorded by such devices, however, are usually stored in time-series databases as average values with time intervals ranging from 15 min to 1 h. Even though this temporal aggregation is typically used in power system analyses, recent works in the literature demonstrated the need for measurements with higher time resolution, and that the selection of the proper measurement time resolution is crucial for the assessment of the performance of RES installations [9]. In particular, the study published in [10] demonstrated that, if compared to the original time series sampled every 5 s, the adoption of the 15 min aggregation time interval could lead to relevant errors in the computation of some energy KPIs. Even though it is apparent that increasing the time resolution of measurements would surely help to increase the accuracy energy KPIs, the trade-off between the associated costs and benefits is not obvious, and further work should be done to assess the trade-off between data storage and transmission costs and KPI accuracy. On the other side of the advantages of the extensive use of meters for power grid management, there is the massive amount of data generated which should be transmitted to supervisory systems and often stored for further analysis. To reduce the transmission pressure and storage overhead, various compression techniques for smart meter big data, both lossless as lossy, have been proposed in literature [11] showing their effectiveness. The aim of this research work is to analyze in detail which effect the time resolution of measurement data has on energy KPIs on real data and to investigate how to select a proper compression algorithm to enhance the efficiency of the data collection process. The paper is organized as follow: section II introduces the reference use case on which analyzed data has been collected. Among all the KPIs used in literature section III contains the definitions of the one selected as reference for this study and how variations in the aggregation time interval between 5 s and 15 min affect them. Suitable reference compression algorithms are introduced in section IV, how they have been tested is described in section V. Test results are reported in section VI. Finally section VII contains some conclusions.

II. THE REFERENCE USE-CASE

The power flow data analyzed in this study have been collected by the supervisory system of the eLUX laboratory [12] on a public building of the University of Brescia, Italy which houses classrooms and offices as well as student services (i.e., dorms, reading rooms, a cafeteria). The facility, equipped with a 64 kWp PV plant and a 13.8 kWp/25.2 kWh $LiFePO_4$ battery energy storage system (BESS), represents a significant scenario as its power demand is similar to that of a big residential building. To exchange power with the grid, the BESS Power Conversion System (PCS) uses three single-phase bidirectional inverters with one configured as master device. Charge and discharge of batteries are controlled with requests t to the BESS PCS by means of a BESS Controller. All requests are forged on the base of the PV active power generation and the active power measurement at the Point of Common Coupling (PCC) between PV, BESS and the grid. Modbus TCPI/IP is used to let communicate the BESS Controller with the BESS Master Inverter, for charge-discharge control, and the two meters (PCC Meter and PV Meter) to measure the power flow. Further details about the system architecture are available in [13].

III. KEY PERFORMANCE INDICATORS

Different sets of KPI for power plant management have been proposed in literature for the optimal operation of BESSs (including residential PV-BESS installations). Among those, in [8], a system-independent set of KPIs able to measure the effects of the PV and BESS operation at the PCC with the main grid have been proposed to evaluate: i) the impact of distributed PV generators on the uncertainty of prosumers' net active power flows with the distribution grid; ii) the ability of BESS control strategies in reducing the power flow uncertainties caused by distributed PV systems; iii) the ability of a BESS rule-based control approach in reducing the power flow uncertainties introduced by a PV system.

A. Absolute Active Power Flow Ramp

Commercial meters collect data with their own sampling time, usually in the orders of seconds. DSOs use to consider time intervals of 15 min for grid control and monitoring. So a day d is divided into i time intervals $T_{i,d}$ each having k measured samples. Let $P_{i,d}^{U}$ be the Power exchanged with Utility in the i-th time slot of day d, positive taken, negative injected into. The average of the absolute ramp of the active net power flow at the PCC during the i-th time interval of day d, with the BESS in operation is reported in (1).

$$PR_{i,d}^{U} = \frac{|P_{i,d}^{U} - P_{i-1,d}^{U}|}{T_{i,d}}, i = 2 \dots n \quad (1)$$

Let be, now $P_{i,d}^{BESS}$ the Power exchanged with storage in the i-th time slot of day d, positive charge, negative discarge. The Power exchanged with Utility in the i-th time slot of day d without the contribution of the BESS is reported in (2).

$$P_{i,d}^{U*} = P_{i,d}^{U} - P_{i,d}^{BESS} \quad (2)$$

The average of the absolute ramp of the active net power flow at the PCC during the i-th time interval of day d, without the BESS in operation is reported in (3).

$$PR_{i,d}^{U*} = \frac{|P_{i,d}^{U*} - P_{i-1,d}^{U*}|}{T_{i,d}}, i = 2 \dots n \quad (3)$$

B. Impact of Time resolution on KPIs

Using the data collected by the same system of section II, for 24 consecutive hours on April the 15th, 2020, authors in [10] demonstrated that, when evaluating the effect of BESSs in reducing the absolute power ramps in prosumers' PV-BESS installations, the classical sampling time resolution of 15 minutes would lead to misleading results which reduce the average values of power ramps by up to 20% respect to the same KPI calculated using a sampling time of 5 s. Lower sampling time shall improve the phenomenon representation but, at the same time, shall increase the amount of data to be collected, transmitted and stored. In the case studied in [10], moving from a 15 min sampling time to 5 s raises the data amount 180 times.

To better estimate this phenomenon and see if it is possible to find a suitable compromise between accuracy and data volume, in this work 5 s samples between April the 8th 2020 and April the 13th 2020 have been considered. These samples have been aggregated to simulate sampling time resolutions between 5 s and 15 m in steps of 5 s. For each simulated sampling time both PR^{U} and PR^{U*} have been calculated. Results are shown in Fig. 1. The estimated PR^{U} drops from 110 W/s to 65 W/s using only a 10 s sampling time. Results normalized by PR^{U} calculated with sampling time of 5 s are shown in Fig. 2. The value of PR^{U} is underestimated by 40% with a sampling time of 10 s reaching an underestimation of 80% with sampling time over 35 s. Following these results, to be accurately monitor the power flow at the PCC samples should be collected using sampling time of 5 s.

IV. COMPRESSION ALGORITHMS

As the number of available compression algorithms is high, in this work a couple of them have been chosen as reference. In particular, lossy algorithms have been ignored as, accordingly with section III. B, errors in the measure representation have a major impact on the KPI effectiveness. Among lossless algorithms the LZ family is one the most common as it is used by the 7-Zip archiver, a program publicly available under the terms of the GNU Lesser General Public License and commonly embedded

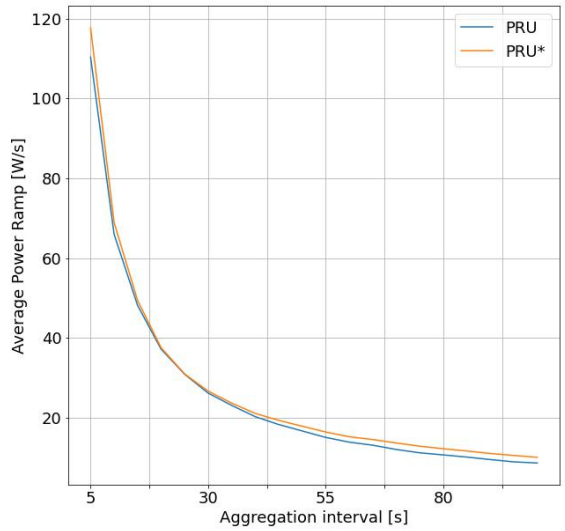

Fig. 1. Average Absolute Power Ramp.

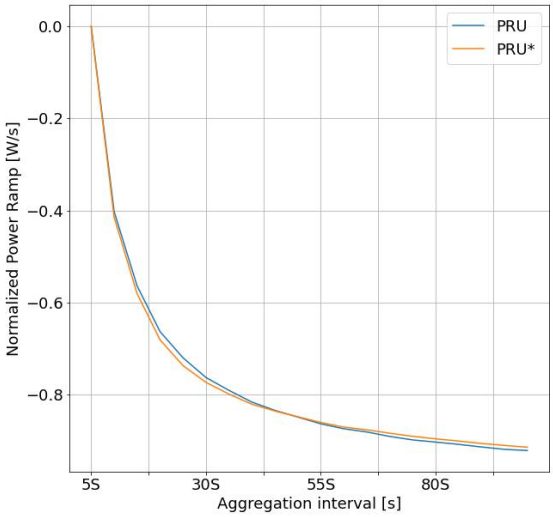

Fig. 2. Average Absolute Power Ramp normalized on its value in a 5s aggregation interval.

in many operating systems since 2009 [14]. Among the format supported by 7-Zip two interesting algorithms have been identified: i) DEFLATE: it is a combination of the LZ family progenitor LZ77 and Huffman coding. ii) LZMA: is a modified version of LZ77 already used in literature for smart meter data compression [15].

A. Huffman Coding and LZ77

The Huffman code maps each symbol to a variable number of bits. The number of bits depends on the frequency of occurrence of the considered symbol. The compression algorithm works creating a binary tree in which symbols result stored in leaves nodes. Links between nodes are labelled as '0' or '1' respectively for link connecting the left child or the right child. Following the tree allows to obtain the bit string representing the desired character [16]. LZ77 [17] compress a data stream mapping a repeated occurrences of data to a reference of the same data present earlier in the uncompressed stream. It stores a couple (length, distance) for each match. The stored match works as coordinates of the matched data from the position back to the actual data. The algorithm uses a sliding window of fixed, programmable, size to save the most recent data in which look for a new match.

B. DEFLATE Compressor and LZMA

DEFLATE creates a series of compressed blocks. Each block is composed by a 3 bit header, which defines the stream start/stop blocks and the encoding method, followed by a chunk of compressed data. The data is compressed in a two stage process first involving Huffing coding, giving the bit code for each symbol, and then LZ77 to further compress eventual duplicated series of bytes [18]. LZMA (Lempel-Ziv-Markov chain Algorithm) adds further compression steps to LZ77. In particular a LZ77 stage is followed by a Markov-Chain-based range encoder [19]. Both algorithms implementations can be tuned in run time by means of a specific parameter, which varies as integer number in the range 1-12 for DEFLATE and 0-9 for LZMA.

V. METHODS

To test the two compression algorithms, the system described in section III has been considered to collect data every 5 s while the control system needs them every 15 m as usual for DSO management. Thus, the measures of Active Power generated by the PV, power flow with the grid and power flow with the BESS, collected every 5 s between April the 8th 2020 and April the 13th 2020, have been aggregated in separate chunks of 15 min. Each chunk has been separately compressed and decompressed using both DEFLATE and LZMA algorithms with each value of their tuning parameters. For each run it has obtained the compression ratio in percentage, as defined in (4), and the compression speed expressed in MB/s.

$$C_r = \frac{CompresedSize}{OriginalSize} \cdot 100 \qquad (4)$$

All the tests have been performed using the lzbench in-memory benchmark of open-source LZ77/LZSS/LZMA compressors [20] using the provided official docker image. This approach has a big advantage of using the same compiler with the same optimizations for all compressors. The container has been hosted on a Dell Precision Tower 1700 MT Workstation equipped with quad-core intel Xeon E3-1220 v3 and 16GB RAM with CentOS 8 Stream. The container has been ran without the Docker daemon leveraging the deamonless, open-source, tool podman included in CentOS 8.

VI. RESULTS AND DISCUSSION

Results of all chunk of data, for each couple algorithm-

parameter have been grouped. Fig. 3 and Fig. 4 show respectively mean compression ratio and the mean compression speed of all data chunks for each couple algorithm-parameter. Compression Ratio of chunks results to be between the 13,4% to the 19.7%. As saved space (SP) is defined as in (5):

$$SP = 1 - \frac{CompresedSize}{OriginalSize} = 1 - C_r \qquad (5)$$

Fig. 3 shows also SP between 86,6% and 80,3%. The compression speed lays within 0.78 MB/s and 82.5 MB/s. It is worth of noting, more than the absolute performance of the algorithms which could not be the best available, the role of the tuning parameter. It is clear from Fig. 3 that the algorithm with the best (lower) compression ratio depends on the tuning parameter as DEFLATE-11 compress more than LZMA-2 making difficult to choose the right algorithm without considering the tuning parameter. The tuning parameter have a huge effect also in the performance of the same algorithm as DEFLATE-8

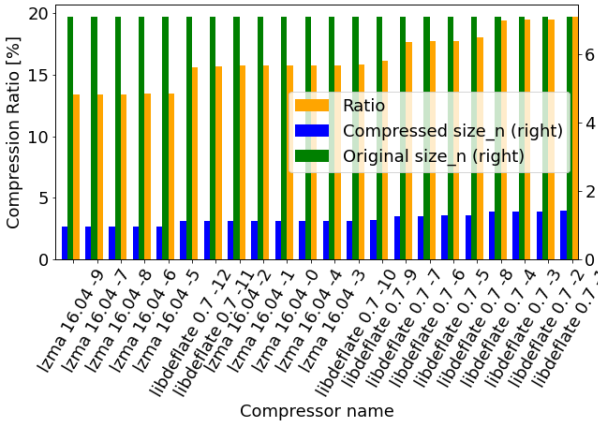

Fig. 3. Compression Ratio varying the algorithm compression parameter.

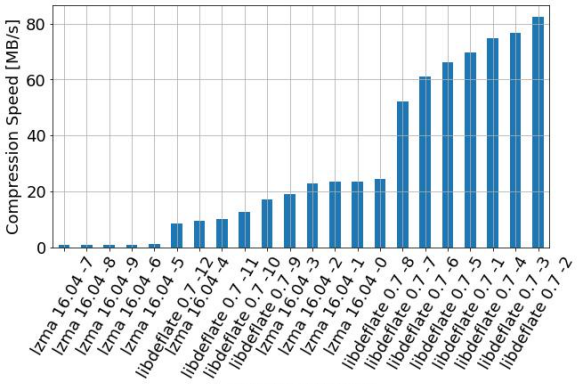

Fig. 4. Compression Speed varying the algorithm compression parameter.

compress less than DEFLATE-5 or LZMA-0 compress more than LZMA-4. A similar behavior could be observed also for Compression Speed in Fig. 4. The same results of Fig. 3 and Fig. 4 are reported together in Fig. 5 using circles to mark DEFLATE results while squares are used to mark LZMA results. The tuning parameter is represented by the color of the marker. It could be observed as LZMA obtains absolutes better results in compression ratio while DEFLATE has better absolute performance in compression speed. It is also evident as DEFLATE depends more on the tuning parameter as DEFLATE-5/6/7 compress more than DEFLATE-8. It is also interesting as LZMA with low parameter values performs really similar to DEFLATE with high parameter values

VII. CONCLUSIONS

The uncertainty of distributed RES generation on active power flows at the prosumer's side has a relevant impact on the operation of power grids and the classical sampling time resolution of 15 minutes would lead to misleading results. In this paper, using 6 days of data produced by a PV+BESS plant at the University of Brescia, Italy, the impact of the variation of the sampling time between 5 s and 15 min on the Absolute Average Power Rate has been evaluated. Results shows as the KPI will be underestimated by the 40% if the sampling time rises from 5 s to only 10 s, making necessary a 5 s sampling time and thus raising the overall amount of data generated. The use of lossless compression algorithm is a common proposed solution to try to reduce the data volume impact, but select the right algorithm could be difficult. For this reason two common lossless algorithms, DEFLATE and LZMA, have been selected and tested on the 6 days long, 5 s sampled dataset already used. Measures have been grouped in 15 min chunks as they would be transferred in a usual

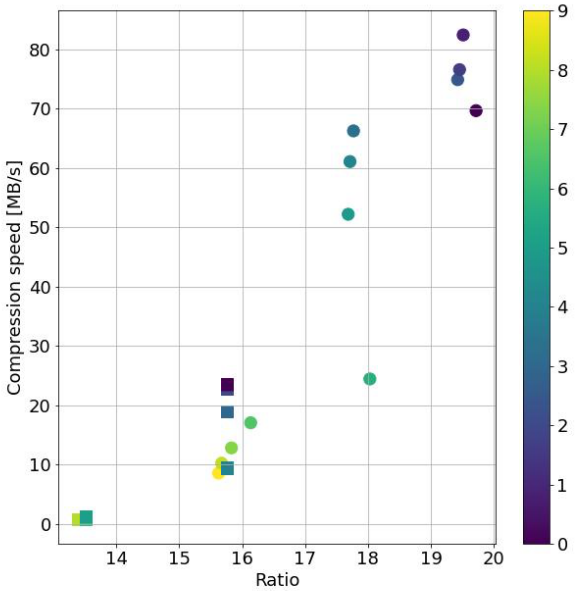

Fig. 5. Performance of couples algorithm-parameter. Circles are DEFLATE results while squares are LZMA results.

configurations. Results shows that as the compression algorithms are somehow effective as expected the tuning of the compression parameter is all but intuitive. This behavior makes try-and-error assessment or offline simulation needed to find the best compromise. In future works, has been already planned to experiment different algorithms aggregating data, sampled each 5 s, in chunk bigger than 15 m to find a suitable compromise between accuracy of KPIs and the overall size of the collected data.

ACKNOWLEDGEMENTS

Author should thanks Dr. Marco Pasetti for the valuable discussions about power grids.

REFERENCES

[1] S. Howell, Y. Rezgui, J. L. Hippolyte, B. Jayan, and H. Li, "Towards the next generation of smart grids: Semantic and holonic multi-agent management of distributed energy resources," *Renewable and Sustainable Energy Reviews*, vol. 77, no. September 2017, pp. 193–214, 2017, DOI: 10.1016/j.rser.2017.03.107.

[2] M. Pasetti, P. Ferrari, D. R. C. Silva, I. Silva, and E. Sisinni, "On the Use of LoRaWAN for the Monitoring and Control of Distributed Energy Resources in a Smart Campus," *Applied Sciences*, vol. 10, no. 320, pp. 1–27, 2020, DOI: 10.3390/app10010320.

[3] S. Liu, P. X. Liu, X. Wang, Z. Wang, and W. Meng, "Effects of correlated photovoltaic power and load uncertainties on grid-connected microgrid day-ahead scheduling," IET Generation, Transmission and Distribution, vol. 11, no. 14, pp. 3620–3627, 2017, DOI: 10.1049/iet-gtd.2017.0427.

[4] V. Sharma, S. M. Aziz, M. H. Haque, and T. Kauschke, "Effects of high solar photovoltaic penetration on distribution feeders and the economic impact," Renewable and Sustainable Energy Reviews, vol. 131, no. June, p. 110021, 2020, DOI: 10.1016/j.rser.2020.110021.

[5] D. Kucevic et al., "Standard battery energy storage system profiles: Analysis of various applications for stationary energy storage systems using a holistic simulation framework," Journal of Energy Storage, vol. 28, no. November 2019, p. 101077, 2020, DOI: 10.1016/j.est.2019.101077.

[6] M. Baumann, M. Weil, J. F. Peters, N. Chibeles-Martins, and A. B. Moniz, "A review of multi-criteria decision making approaches for evaluating energy storage systems for grid applications," Renewable and Sustainable Energy Reviews, vol. 107, no. January, pp. 516–534, 2019, DOI: 10.1016/j.rser.2019.02.016.

[7] C. Jankowiak, A. Zacharopoulos, C. Brandoni, P. Keatley, P. MacArtain, and N. Hewitt, "Assessing the benefits of decentralised residential batteries for load peak shaving," Journal of Energy Storage, vol. 32, p. 101779, 2020, DOI: 10.1016/j.est.2020.101779.

[8] M. Pasetti, "Assessing the Effectiveness of the Energy Storage Rule-Based Control in Reducing the Power Flow Uncertainties Caused by Distributed Photovoltaic Systems," *Energies*, vol. 14, no. 8, p. 2312, 2021, DOI: 10.3390/en14082312.

[9] V. Papadopoulos, J. Knockaert, C. Develder, and J. Desmet, "Investigating the need for real time measurements in industrial wind power systems combined with battery storage," Applied Energy, vol. 247, no. January, pp. 559–571, 2019, DOI: 10.1016/j.apenergy.2019.04.051.

[10] M. Pasetti *et al.*, "Impact of the Measurement Time Resolution on Energy Key Performance Indicators for Distributed Energy Resources: An Experimental Analysis," *AMPS 2021 - 2021 11th IEEE Int. Work. Appl. Meas. Power Syst. Proc.*, Sep. 2021.

[11] L. Wen, K. Zhou, S. Yang, and L. Li, "Compression of smart meter big data: A survey," *Renew. Sustain. Energy Rev.*, vol. 91, pp. 59–69, Aug. 2018.

[12] A. Flammini *et al.*, "A Living Lab and Testing Infrastructure for the Development of Innovative Smart Energy Solutions: the eLUX Laboratory of the University of Brescia," in *2018 AEIT International Annual Conference*, 2018, pp. 1–6.

[13] M. Pasetti, S. Rinaldi, and D. Manerba, "A Virtual Power Plant Architecture for the Demand-Side Management of Smart Prosumers," *Applied Sciences*, vol. 8, no. 3, p. 432, 2018, DOI: 10.3390/app8030432.

[14] I. Pavlov, "7-zip History." [Online]. Available: https://www.7-zip.org/history.txt. [Accessed: 22-Apr-2022].

[15] F. M. Dahunsi, O. A. Somefun, A. A. Ponnle, and K. B. Adedeji, "Compression Techniques of Electrical Energy Data for Load Monitoring: A Review," *Niger. J. Technol. Dev.*, vol. 18, no. 3, pp. 194–208, Nov. 2021.

[16] D. A. Huffman, "A Method for the Construction of Minimum-Redundancy Codes," *Proc. IRE*, vol. 40, no. 9, pp. 1098–1101, 1952.

[17] J. Ziv and A. Lempel, "A universal algorithm for sequential data compression," *IEEE Trans. Inf. Theory*, vol. 23, no. 3, pp. 337–343, May 1977.

[18] L. P. Deutsch, "DEFLATE Compressed Data Format Specification version 1.3," 1996. [Online]. Available: https://www.w3.org/Graphics/PNG/RFC-1951. [Accessed: 23-Apr-2022].

[19] I. Pavlov, "LZMA SDK." [Online]. Available: https://www.7-zip.org/sdk.html. [Accessed: 23-Apr-2022].

[20] "lzbench Github repository." [Online]. Available: https://github.com/dblalock/lzbench. [Accessed: 23-Apr-2022].

25th IMEKO TC4 International Symposium
23rd International Workshop on ADC and DAC Modelling and Testing
IMEKO TC-4 2020
Brescia, Italy / September 12-14, 2022

Simple method for calibration of PMU calibrators

Martin Šíra[1] and Stanislav Mašláň[1]

[1]*Czech Metrology Institute, Okružní 31, 638 00 Brno, msira@cmi.cz*

***Abstract* – The number of Phasor Measurement Units (PMU) is growing rapidly. The metrological institutes and calibration laboratories has to calibrate not only PMUs, but also calibrators of PMUs. To achieve this goal, several reference PMU systems have been built. These systems use costly time synchronization units. The paper shows another method to trace a digitizer to a standard of time. The advantage of the method is removing a need to obtain a time synchronization unit. Setup of a reference PMU system using the method is described and uncertainty budget is shown. The budget shows out the presented method achieved sufficiently low uncertainties required for calibration of PMU calibrators.**

I. INTRODUCTION

The number of Phasor Measurement Units (PMUs) installed around the world and the number of vendors have been growing rapidly. The industry recognized that phasor measurements and wide-area monitoring have significant impact on the power system security. The PMU device measures synchrophasor of alternate voltage and current at a high sample rate (up to 1 phasor per cycle), thus providing the transmission system's dynamic observability. Every PMU is equipped with a GPS (Global Positioning System) receiver, so that all the measurements in the system can be time-aligned.

The measurement of synchrophasor requires measurement of amplitude and phase of an alternate voltage or current signal. The phase has to be referenced to a time standard, thus results in a measurement of absolute phase. PMU consists of a transducer and an analogue to digital converter (ADC) to record a waveform. The sampled data is processed by data processing algorithm, a synchrophasor value is calculated and usually reported to a Phasor Data Concentrator (PDC). PDC can collect streams from multiple PMUs using chosen communications network technology and it is responsible for providing data to analyse.

Calibration of a PMU is a task accomplished by generating a waveform with defined properties of amplitude and absolute phase in both static and dynamic modes. Typical PMU calibrator (e.g. a Fluke 6105A with Fluke 6135A) is a phantom voltage and current generator tied to the control system, standard of time and frequency, control computer and network hub. A PMU calibrator can generate various waveforms to test and validate multiple properties of the PMU according the IEEE standard C37.118.1-2011 [1].

The error of a PMU is expressed as a Total Vector Error (TVE). Maximal TVE of a PMU, as specified by IEEE standard, should be 1 %. So uncertainty of PMU calibrator should be (by using a rule of a thumb 1 to 4) less than 0.25 %.

A calibration of the PMU calibrator is a typical task for National Metrological Institute (NMI) and it is more complex than the calibration of a PMU. A reference PMU is required, and all reference PMU components must be traceable to the national standards. The target uncertainty of the synchrophasor should be less than 0.025 %. Several such PMUs have been developed, e.g. [2], [3]. These reference PMU systems are composed of transducer, digitizer, time standard, time synchronization unit, data processing algorithms, control computer, and control software. The time synchronization unit is used to trace the absolute time of ADC samples. Most of the listed components are common in every NMI. Several international projects aim at calibration of the transducers and digitizer with utmost precision using quantum standards. Contrary the time synchronization unit is not common. It must handle complex time synchronisation signals (e.g. IRIG-B) and can be expensive. However, every NMI own a time standard generating one-pulse-per-second signal (1PPS).

This paper shows a method to trace digital samples to the absolute time and use it for the calibration of synchrophasor without using costly time synchronization unit. A two channel digitizer is used to sample both the voltage signal and a 1PPS signal. This was used to calculate the absolute time of the samples, calculate the synchrophasor and calibrate a PMU calibrator. The advantage of this method is decreased requirements to establish a new calibration service in a NMI.

II. SYNCHROPHASOR CALIBRATION METHOD

The presented calibration method relies on the properties of a two channel digitizer with a time base common to both ADCs. Because of the common time base, time errors of samples acquired by first channel are almost the same as the time errors of the samples acquired by second channel. The first channel is used to calibrate the time base and the second channel is used to sample the synchrophasor waveform.

The method was tested on a measurement setup consisting of:

- transducer,

- two channel digitizer,
- time standard,
- data processing algorithm,

The schematic diagram of the measurement setup is shown in Fig. 1. PMU calibrator Fluke 6105A and 6135A served as a device under test and was set to generate synchrophasor waveform. Selected PMU calibrator cannot work without a connected PMU, thus a PMU was part of the setup. The values measured by the PMU were not taken into account. The transducer of CMI own design scaled the voltage down to the full scale range of the digitizer National Instruments 5922. The digitizer was powered by external DC battery to prevent ground loops. A time standard Stanford-Research FS740 traceable to national standard of time was used to generate 1PPS signal. Both Fluke 6135A and FS740 used dedicated independent GPS antenna.

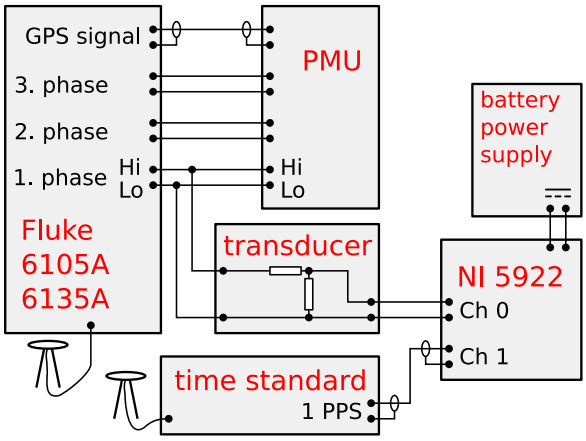

Fig. 1. Schematic diagram of the calibration setup. Both Fluke 6135A and reference time standard are connected to its own GPS antennas.

The generated 1PPS signal consists of rectangular pulses of 20 µs duration, one puls every second. The pulses were used for two purposes.

First purpose was to calibrate the sampling frequency of the ADC. Digitizers usually can lock to a reference frequency signal, typically of 10 MHz frequency. Yet the 1PPS gave clear information on the correctness of the lock.

Second purpose was to identify start of a real time second thus providing the absolute time of the samples. Unfortunately, such a simple 1PPS signal can not provide information which second is observed. This problem was solved by recording the time of start of the sampling in the control computer. The maximal clock error of the computer had to be less than 0.5 s. Such precision can be obtained using Network Time Protocol (NTP).

III. REQUIREMENTS FOR THE CALIBRATION METHOD

Using the TVE definition, requirements for the calibration method can be found. TVE is estimated as:

$$TVE = \frac{|X_{\mathrm{meas}} - X_{\mathrm{ref}}|}{|X_{\mathrm{ref}}|}, \qquad (1)$$

where X_{meas} is value of a measured synchrophasor, X_{ref} is value of a reference synchrophasor. A synchrophasor is defined as a complex number with X_{r} real and X_{i} imaginary part: $X = X_{\mathrm{r}} + iX_i$. For a reference, dependence of the TVE on the error of the amplitude and phase measurement is shown in figure 2.

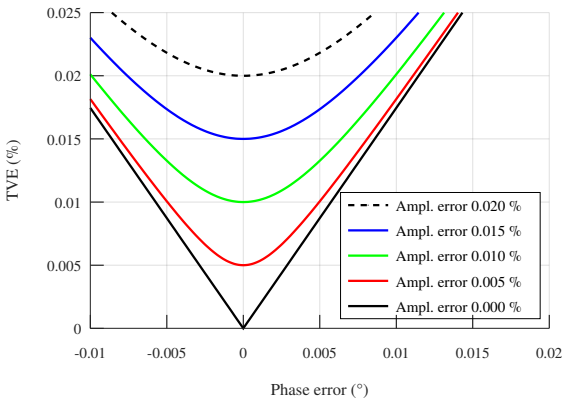

Fig. 2. Dependence of TVE on the errors of the amplitude and phase according Eq 1 for nominal amplitude 1 V and nominal phase 0 °.

To obtain the TVE less than 0.025 % (250 parts per million), the combined relative errors of amplitude and phase measurement must be less than this value. Typical CMCs of NMI for voltage amplitude calibration at range 10 to 300 V is about 10 to 30 µV V^{-1}. This is about one order less than required error of TVE. Because TVE is composed from both amplitude and phase uncertainty, and because the uncertainty is added as square root of sum of squares [4], the uncertainty of amplitude can be the minor component. Thus the uncertainty of phase can be up to 250 µrad (0.0143 °). For typical signal frequency of 50 Hz this results in a maximal possible uncertainty of time measurement 0.8 µs.

IV. ABSOLUTE TIME RESOLUTION USING 1PPS

The 1PPS signal, as generated by a standard of time, usually has got a short transition time in order of nanoseconds. Identification of the beginning of the second depends on the transition time of the signal, resolution and sampling rate of the digitizer and error of the algorithm identifying the actual start of the signal.

The digitizer used in the setup can sample with various rates from 50 to 15 000 kSa s^{-1}. To achieve error less than

0.8 µs, the sampling rate has to be at least 1250 kSa s^{-1}. Sampling rate of 15 MSa s^{-1} was selected during the measurements.

To calculate absolute time of samples, a simple algorithm have been used. The sampling duration was selected to sample at least three pulses of the 1PPS signal, i.e. the length of the record was greater than 3 s. An algorithm found the maximum of the signal, selected voltage at half of the maximum and identified rising slopes of the pulses. Example of identification of a pulse rising slope is shown in Fig. 3. Fig. 4 shows a series of four pulses in one record with marks denoting real time second after 16:21:00 of local time.

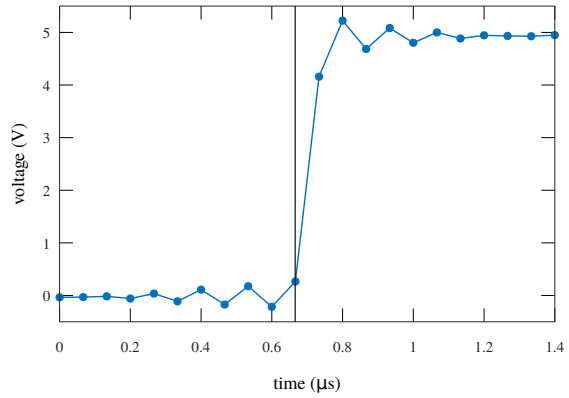

Fig. 3. Rising slope of one pulse denoting start of second as sampled by the digitizer. Vertical line denotes identified start of pulse.

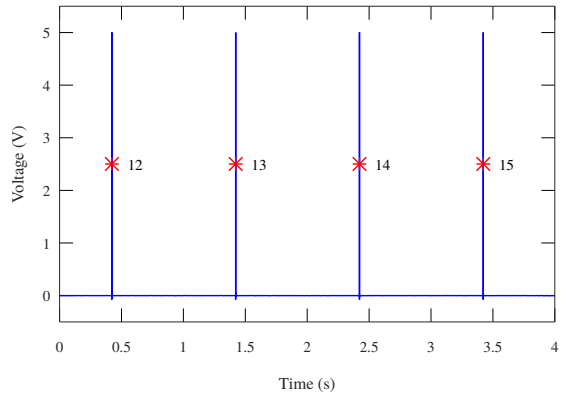

Fig. 4. Record with four pulses per second with marks denoting real time second after 16:21:00 of local time.

Simple linear regression was used to fit the sample indexes of the rising slopes and to obtain information both on the absolute time of every single sample using intercept of the fit and on the sampling rate using slope of the fit. The errors of the linear regression were smaller than 1×10^{-15} s for the case of the digitizer locked to a reference 10 MHz signal. The value of regression errors is at the level of rounding error, see figure 5. This was a good indication and check of proper detection of the rising slopes and of working algorithm.

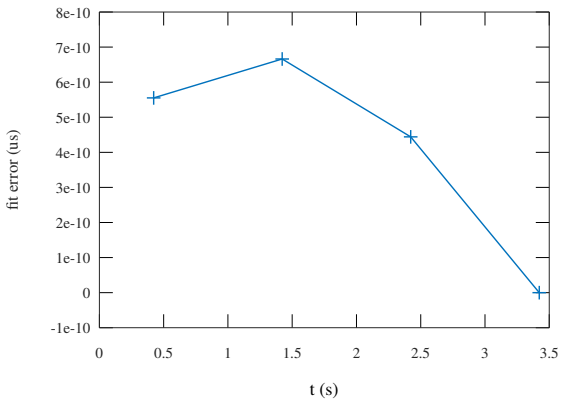

Fig. 5. Linear regression errors of the rising slopes.

Start of the sampling process was recorded by the control computer and the information was used to identify the first pulse of the 1PPS signal and relate it to the actual absolute second of Universal Time Coordinated (UTC). Although operating system Microsoft Windows contain a native tool providing time synchronization using NTP, the reliability was bad with errors repeatably greater than several seconds. Therefore software NetTime [5] was used to synchronize the computer time and the time errors decreased to 100 ms or less. However, any error of computer time smaller than 0.49 s was sufficient to correctly identify the actual seconds of the absolute time.

V. UNCERTAINTY BUDGET

The uncertainty budget of the described setup is shown in following tables.

The first table 1 shows uncertainty components affecting estimation of the phase. The second table 2 shows uncertainty components affecting estimation of the amplitude.

A. *Time standard*

The uncertainty contributions of the time standard FS740 are: the error of the time standard, pulse transition time, jitter, phase accuracy and cable delay. Values of errors were based on the specifications and uncertainty, if not stated in the specifications, was selected as half of the maximum error.

B. *Transducer*

The selected transducer was used to convert PMU calibrator voltage amplitude from 50 to 240 V to a value smaller than 5 V range of the digitizer by means of a resis-

Table 1. Uncertainty budget for absolute phase estimation

Uncertainty source	Error or specifications	*TVE*	$u(TVE)$
Contributions of the time standard:			
Traceability to national standard of time	0 ± 10 ns	0	3.1×10^{-6}
Pulse transition time	1 ± 1 ns	0.31×10^{-6}	0.31×10^{-6}
Jitter	25 ± 25 ps	0.79×10^{-9}	0.79×10^{-9}
Phase accuracy	1 ± 1 ns	0.31×10^{-6}	0.31×10^{-6}
Cable delay, 0.1 m	0.5 ± 0.1 ns	0.173×10^{-6}	0.031×10^{-6}
Contributions of the transducer:			
Phase error	12.61 ± 0.11 m°	220.1×10^{-6}	1.9×10^{-6}
Contributions of the digitizer:			
Interchannel phase difference	0 ± 0.1 m°	0	1.7×10^{-6}
Contributions of data processing:			
Pulse start detection	0 ± 33 ns	0	10×10^{-6}
Phase estimation error	0 ± 0.1 mrad	0	100×10^{-6}
Total phase uncertainty contribution			101×10^{-6}

Table 2. Uncertainty budget for amplitude estimation

Uncertainty source	Error or specifications	*TVE*	$u(TVE)$
Transducer ratio error	17 ± 22 µV V^{-1}	17×10^{-6}	22×10^{-6}
Digitizer gain error	-263 ± 42 µV	404×10^{-6}	64×10^{-6}
Digitizer gain stability (10 minutes)	0 ± 10 µV V^{-1}	0	10×10^{-6}
Algorithm error	0 ± 10 µV V^{-1}	0	10×10^{-6}
Total amplitude uncertainty contribution			69×10^{-6}

tive divider. The transducer was built in Czech Metrology Institute. Calibration of a transducer was already described in several papers and is out of focus of this paper [6]. The transducer was calibrated for amplitude ratio at expected signal frequency (approx. 50 Hz) and at defined impedance load at the output. The impedance was determined by the input impedance of the digitizer and a cable connecting the transducer and the digitizer. The error and uncertainty of the transducer was based on the calibration certificate.

C. Digitizer

Amplitude error of the digitizer was calibrated using methods already published [7]–[10]. The error and uncertainty of the digitizer was based on the calibration certificate. Stability of the digitizer was based on [9]. Because the time of the samples was estimated using the first digitizer channel, and the synchrophasor was estimated using the second channel, the phase error between both channels had to be estimated. The error was measured by using a signal of an AC source. The signal was split using T cable connection and lead to both digitizer channels at once. Next a phase of the AC waveform was calculated for both channels. Difference between the two phase values resulted in the inter-channel phase error.

D. Data processing

Sampled ac waveform had to be processed by an algorithm to obtain amplitude and phase and to calculate the synchrophasor. Three main groups of algorithms exists. Based on the algorithm comparisons [11], [12], the PSFE algorithm have been selected to process the sampled data. Using simulations and studies already presented in [13], [14] and tests published in [15], [16] the algorithm error of phase estimation is expected to be less than 0.1 mrad and for amplitude estimation less than 10 µV V^{-1} for sampling frequency 15 MSa s^{-1}, records longer than 10 periods of the signal, and coherent sampling.

VI. CALIBRATION OF PMU CALIBRATOR

The PMU calibrator was set to generate simple three-phase sine waves of nominal amplitude 230 V and nominal frequency 50 Hz. The signals were sampled one phase after another. Tab. 3 shows the measured phase errors and TVE values. Specifications of the Fluke system for TVE is 0.1 %, so the PMU calibrator is well in the specifications. The total uncertainty of the measurement setup is well below required 0.025 % (250×10^{-6}) so the target uncertainty was achieved. The measured data were published in [17].

Table 3. Measured TVE of a three phase PMU calibrator.

	TVE ($\times 10^6$)
Phase 1	192 ± 122
Phase 2	4 ± 122
Phase 3	133 ± 122

VII. DISCUSSION

The presented paper shows an easy method to trace the sampled records to the absolute time. Simple reference PMU system was set up and the presented method was used to calibrate a PMU calibrator. The system and the method circumvents the need to buy costly time synchronization time units used in other reference PMU meters. The uncertainty contribution to the TVE caused by phase errors was estimated to be 101×10^{-6} (0.0101 %).

The presented system does not implement full online reference PMU meter because of the many complexities of the real PMU meter fulfilling whole IEEE standard. The purpose of the system was only to measure synchrophasor using fully traceable methods and devices and to establish a direct traceability link between national standards of time, voltage and PMU calibrator.

VIII. ACKNOWLEDGEMENT

This research was done in the scope of the QuantumPower (19RPT01) project, which have received funding from the EMPIR programme co-financed by the Participating States and from the European Union's Horizon 2020 research and innovation programme.

IX. REFERENCES

[1] *C37.118.1-2011 - IEEE Standard for Synchrophasor Measurements for Power Systems*, Dec. 28, 2011.

[2] J.-P. Braun and C. Mester, "Reference grade calibrator for the testing of the dynamic behavior of phasor measurement units", in *2012 Conference on Precision Electromagnetic Measurements*, Jul. 2012, pp. 410–411. DOI: 10.1109/CPEM.2012.6250977.

[3] H. Ndilimabaka and I. Blanc, "Development of a reference Phasor Measurement Unit (PMU) for the monitoring and control of grid stability and quality", *EPJ Web of Conferences*, vol. 77, p. 00 009, 2014, ISSN: 2100-014X. DOI: 10.1051/epjconf/20147700009.

[4] JCGM, *Evaluation of measurement data - Supplement 1 to the "Guide to the expression of uncertainty in measurement" - Propagation of distributions using a Monte Carlo method*, JCGM, Ed. Bureau International des Poids et Measures, 2008.

[5] Graham Mainwaring and Mark Griffiths, *NetTime - Network Time Synchronization Tool*. [Online]. Available: https://www.timesynctool.com.

[6] S. Mašlán, M. Šíra, and V. Nováková Zachovalová, "Design, stability analysis and uncertainty contribution of a voltage divider designed for a phase meter", in *Proceedings of the 20 Th IMEKO TC4 International Symposium "Research on Electrical and Electronic Measurement for the Economic Upturn" and 18th IMEKO TC-4 International Workshop on ADC and DAC Modelling and Testing*, Benevento, Italy, Sep. 2014, pp. 942–946, ISBN: 978-92-990073-2-7.

[7] T. R. McComb, J. Kuffel, and R. Malewski, "Measuring characteristics of the fastest commercially-available digitizers", *Power Delivery, IEEE Transactions on*, vol. 2, no. 3, pp. 661–670, 1987.

[8] G. Rietveld, D. Zhao, C. Kramer, E. Houtzager, O. Kristensen, C. de Leffe, and T. Lippert, "Characterization of a Wideband Digitizer for Power Measurements up to 1 MHz", *IEEE Transactions on Instrumentation and Measurement*, vol. 60, no. 7, pp. 2195–2201, Jul. 2011, ISSN: 0018-9456, 1557-9662. DOI: 10.1109/TIM.2011.2117330.

[9] M. Šíra, O. Kieler, and R. Behr, "A Novel Method for Calibration of ADC Using JAWS", in *2018 Conference on Precision Electromagnetic Measurements (CPEM 2018)*, Paris, France: IEEE, Jul. 2018, pp. 1–2, ISBN: 978-1-5386-0973-6. DOI: 10.1109/CPEM.2018.8501009.

[10] R. Lapuh, *Sampling with 3458A: Understanding, Programming, Sampling and Signal Processing*, 1st. Ljubljana: Left Right d.o.o., 2018, ISBN: 978-961-94476-0-4.

[11] D. Slepicka, D. Agrez, R. Lapuh, E. Nunzi, D. Petri, T. Radil, J. Schoukens, and M. Sedlacek, "Comparison of nonparametric frequency estimators", in *Instrumentation and Measurement Technology Conference (I2MTC), 2010 IEEE*, IEEE, 2010, pp. 73–77.

[12] R. Lapuh, "Estimating the fundamental component of harmonically distorted signals from non-coherently sampled data", *IEEE Transactions on Instrumentation and Measurement*, vol. 64, no. 6, pp. 1419–1424, Jun. 2015, ISSN: 0018-9456. DOI: 10.1109/TIM.2015.2401211.

[13] M. Šíra, S. Mašláň, and T. Skalická, "Uncertainty of Phasor Measurement Unit Calculated by Means of Monte Carlo Method", in *2018 Conference on Precision Electromagnetic Measurements (CPEM 2018)*, Paris, France: IEEE, Jul. 2018, pp. 1–2,

ISBN: 978-1-5386-0973-6. DOI: 10.1109/CPEM.2018.8500896.

[14] M. Šíra, S. Mašláň, V. Nováková Zachovalová, G. Crotti, and D. Giordano, "Modelling of PMU Uncertainty by Means of Monte Carlo Method", in *Conference on Precision Electromagnetic Measurements Digest*, Ottawa, Canada, Jul. 2016, p. 2, ISBN: 978-1-4673-9133-7. DOI: 10.1109/CPEM.2016.7540660.

[15] R. Lapuh, "Estimating the Fundamental Component of Harmonically Distorted Signals From Noncoherently Sampled Data", *IEEE Transactions on Instrumentation and Measurement*, vol. 64, no. 6, pp. 1419–1424, Jun. 2015, ISSN: 0018-9456. DOI: 10.1109/TIM.2015.2401211.

[16] R. Lapuh, M. Šíra, M. Lindič, and B. Voljč, "Uncertainty of the Signal Parameter Estimation from Sampled Data", in *Conference on Precision Electromagnetic Measurements Digest*, Ottawa, Canada, Jul. 2016, p. 2, ISBN: 978-1-4673-9133-7. DOI: 10.1109/CPEM.2016.7540770.

[17] M. Šíra, *Dataset of PMU calibrator calibration.* Version 1, Jun. 2022. DOI: 10.5281/zenodo.6670032. [Online]. Available: https://doi.org/10.5281/zenodo.6670032.

25th IMEKO TC4 International Symposium
23rd International Workshop on ADC and DAC Modelling and Testing
IMEKO TC-4 2022
Brescia, Italy / September 12-14, 2022

PMU-based metrics for Power Quality Assessment in Distributed Sensor Networks

Guglielmo Frigo [1], Federica Costa [1], Federico Grasso Toro [1]

[1] *Swiss Federal Institute of Metrology METAS*
Lindenweg 50, 3003 Bern-Wabern, Switzerland
E-mail addresses: {guglielmo.frigo, federica.costa, federico.grasso}@metas.ch

***Abstract* – In modern power systems, the measurement infrastructure represents the backbone of any monitoring and control application. Indeed, the ever-increasing penetration of renewable energy sources and distributed generation has produced an operating scenario prone to instability and rapid variations. Power quality assessment procedures must evolve in order to address these challenges. In this regard, the use of phasor measurement units (PMUs), which measure the phasor values of current and voltage with high precision time stamp, presents a significant opportunity to evolve current power quality assessment procedures. This position paper suggests the inclusion of novel PMU-based metrics in order to extend quality power assessment procedures at each sensitive network node towards the further use of aggregated data at both local and/or central level. The proposed PMU-based metrics will provide a better description of the behavior of the system, allowing to take control actions as part of the extended quality power assessment procedures.**

I. INTRODUCTION

Power quality (PQ) has been an acknowledged problem in power systems for decades. Power quality can have a large detrimental effect on industrial processes and the commercial sector [1]. While industrial processes typically differ in their requirements, from a power quality perspective, each specific industrial process has particular 'weaknesses' in terms of power quality attributes [2]. Hence, the importance of power quality assessment procedures entails significant considerations to be accounted for to the industrial end-user regarding costs associated with machine down-time, clean-up costs, product quality and equipment failure [3].

Power Quality Assessment Procedure (PQAP) can involve the combination of measurements as well as simulations focusing in the required cooperation between all of the involved parts [4]. From surveys performed to assist in identifying the most important concerns reported by customers on the system, the current focus is advancing the new technologies have been developed under the framework of Smart Grid [5].

One example is the phasor measurement unit (PMU). Considered the most important measuring devices in the future of power systems, PMUs present the unique ability to provide synchronized phasor measurements of voltages and currents from widely dispersed locations in an electric power grid [6].

PMUs measure phasor values of current and voltage with high precision time stamp and together with the values of power frequency, power frequency change rate and optional binary data that are also time stamped are transmitted to a central analysis station [7]. Using PMUs to assess the PQ in the power system is becoming more relevant in context of increasing level of power electronic devices in the grid, e.g. HVDC, FACTS, wind and solar power plants, etc., due to increasing installations and use of PMU measurements [8]. Several test cases were developed and assessments were made based on criteria defined in the IEEE Standards [9]. Early results indicate that PMU data is suitable for some indicative steady-state PQ assessment [8].

For wide-area measurement systems and smart grids, PMUs have become key elements since they provide synchronized information related to the fundamental frequency components of voltages and currents. In recent years, some works have extended the concept of PMU to harmonic analysis due to the proliferation of nonlinear loads [10]. In [11], reference model for P-class and M-class PMUs provided by [9] were expanded with the aim of obtaining the harmonic information and electric power quantities. This approach of global harmonic parameters for PMUs introduced unified quantities regarding the overall harmonic content of voltages and currents signals. With these parameters, the estimation of power quality indices (PQIs) according to the IEEE Standard 1459 [12] was proposed to be carried out with the advantage of a reduced amount of data, reducing correspondent requirements of management, storage, and analysis [11].

This position paper suggests the inclusion of novel PMU-based metrics in order to extend quality power assessment procedures at each sensitive network node towards the further use of aggregated data at both local and/or central level.

II. PMU-BASED METRICS APPROACH

Modern power systems are characterized by an ever-increasing integration of renewable energy sources and distributed generation [13]. In such scenario, the measurement infrastructure is the backbone of any situational awareness application [14], and it consists of a distributed sensor network where, in each node of interest, a Phasor Measurement Unit (PMU) provides time-stamped measurements of voltage and current phasors with an update rate of tens Hz [13].

By means of dedicated communication channels, these measurements are aggregated at local level (digital substation) or central level (control room), in order to guarantee prompt and effective reactions to possible unfortunate events.

In the recent IEC Std 60255-118-1 [9] (briefly, IEC Std), the compliance limits are expressed in terms of Total Vector Error (TVE), Frequency and Rate-of-Change-of-Frequency Error (FE and RFE, respectively).

More precisely, two performance classes are envisioned: P- and M-class for protection and measurement applications, respectively [15], with specific focus on fast responsiveness and high accuracy.

The National Metrological Institutes are responsible for the calibration and characterization of PMUs' performance in laboratory conditions [16, 17]. Once deployed on the field, though, the interoperability between different PMU data streams is questionable [18].

As proven in [18], the PMU measurements might suffer from inconsistencies in the presence of transients. Indeed, the phasor signal model consists of a combination of few narrow-band spectral tones. If such assumption is no more valid, as the signal energy is spread all over its spectrum, a definitional uncertainty issue arises [19].

In the metrology and digital transformation context, this represents a valuable test case for establishing new features and extended characterization techniques, to guarantee a full comparability of the results provided by any type of sensor, even after calibration.

In view of a massive deployment of similar devices in the power system, the development of tools and metrics for the on-line assessment of measurement reliability is necessary, and new regulatory efforts for the standardization of such procedures must be envisioned.

In the following sections, we will discuss the current format employed for the transmission of PMU measurement results and propose a minor yet effective amendment to include a reliability index, computed on-line and thus not significantly affecting the data reporting latency.

Following the same approach, same information employed to refine the results of a state estimation application in a realistic power system scenario can allow us to perform better power quality assessment procedures (PQAP).

III. SIGNAL MODEL AND RELIABILITY INDEX

A generic power signal can be represented by a non-linear dynamic model:

$$\mathrm{x(t)} = \mathrm{A}\left(1 + \varepsilon_{\mathrm{A}}(\mathrm{t})\right)\cos\left(2\pi\,\mathrm{f\,t} + \varphi + \varepsilon_{\varphi}(\mathrm{t})\right) + \eta(\mathrm{t}) + \mathrm{z(t)} \quad (1)$$

where A, f, and φ are the amplitude, frequency and initial phase of the fundamental component, respectively. The time-varying terms ε_A and ε_φ account for amplitude and phase dynamics, in terms of polynomial, exponential or modulation trends. The additive terms η and z represent the spurious contribution of narrow- and wide-band disturbances: the first one refers to the combination of (inter-)harmonic terms, while the second one account for continuous-spectrum components as white or coloured noise, decaying DC or transients.

In any PMU-based measurement system, the first step of the measurement chain consists in the acquisition process:

$$\mathrm{x[n]} \simeq \mathrm{x(t} = \mathrm{nT_s}), \mathrm{T_s} = \mathrm{F_s^{-1}}, \mathrm{n} = 1, \ldots \mathrm{N_s} \quad (2)$$

where F_s is the sampling rate and N_s is the sample length.

Given the acquired sample series, the PMU is required to estimate the synchrophasor $\hat{p}$, frequency $\hat{f}$ and ROCOF $\hat{R}_f$ associated to the fundamental component:

$$\hat{p}[m] = \hat{A}[m]\, e^{-j\left(2\pi\left(\hat{f}[m]-f_0\right)mT_r + \hat{\varphi}[m] + \pi\hat{R}_f[m]T_r^2\right)} \quad (3)$$

where the superscript indicates the estimated parameters, while T_r and m are the reporting period and the reporting index, respectively. The subtraction by the system rated frequency f_0 allows for expressing the phase contribution due to off-nominal signal frequencies.

The phasor signal model relies on the assumption that the signal energy is stationary within the considered observation interval and that the signal energy is mostly concentrated in a narrow bandwidth around the fundamental frequency.

When these assumptions are not met (e.g. during an instantaneous step change of amplitude or phase), the PMU estimates suffer from the definitional uncertainty due to the model inconsistency between the spectral properties of the signal under test and its phasor representation.

Consequently, the recent literature has discussed the metrological significance of standard performance metrics in real-world operating conditions and proposed alternative approaches for the assessment of the PMU reliability during transient conditions.

In particular, novel metrics have been introduced in [19], defined in the time domain and not relying on the phasor signal model, thus do not introduce any constraint regarding the spectral bandwidth of the observed phenomenon.

Based on the PMU estimates, it is possible to recover the time-domain trend of the fundamental component as:

$$\hat{x}[n] = \hat{A}\cos\left(2\pi\hat{f}nT_s + \hat{\varphi} + \pi\hat{R}_f(nT_s)^2\right) \quad (4)$$

and define its discrepancy with respect to the corresponding acquired sample series in terms of Normalized RMSE:

$$\text{nRMSE} = \sqrt{\frac{\sum(\hat{x}[n]-x[n])}{N_S}} \quad (5)$$

If we consider the PMU estimation as a non-linear fit process, the nRMSE quantifies the residuals' energy, which can be interpreted as an assessment of the signal energy (and thus signal information content) that has been neglected or misrepresented due to the inconsistency between phasor model and acquired sample series.

IV. SUMMARY OF PREVIOUS RESEARCH

As further explained in [19], a correct interpretation of the nRMSE metric requires a preliminary characterization of its variation range and sensitivity to typical grid disturbances.

For this analysis, we simulated test waveforms representative of real-world operating conditions, either normal or critical, and we reproduced a measurement data stream, as provided by a well-known phasor estimation algorithm, namely the Compressive Sensing Taylor-Fourier Model (cs-TFM) [20].

In particular, during our research we considered the following four scenarios:

1. a normal operating condition with steady-state amplitude and phase, while the frequency varies with a "random walk"-like trend (as measured in the EPFL campus) [21];
2. an instantaneous frequency step of -2 Hz followed by a steep frequency ramp of 8 Hz/s until coming back to 50 Hz;
3. a signal characterized by phase and amplitude modulations whose period is in the order of 10 s, as inspired by the inter-area oscillation that was recorded in Lausanne in December 2016 [22];
4. a three-phase fault at the transformer secondary winding (ungrounded terminal) of the bus feeder in the IEEE 34-bus test grid [18].

Table 1 reports the mean μ and standard deviation σ of the nRMSE metric in the four considered test cases.

Based on the reported distributions, the nRMSE metric proves to be able to discriminate between "good" and "bad" data, i.e. data relying on an inconsistent signal model; as in test case 2 and 4, where step changes occur.

Table 1. Mean and standard deviation of the selected performance metrics in the current test waveforms

Test case	Alg.	nRMSE (%)	
		μ	σ
1	cs-TFM	18.22	0.07
2	cs-TFM	66.63	27.94
3	cs-TFM	18.56	0.05
4	cs-TFM	78.94	45.35

V. SUMMARY OF CURRENT RESEARCH

Previous publications have presented very promising early results [19] [21] [22]. However, as suggested in [23], during practical real-time implementations it might be advantageous to calculate at least two sets of phasors to adequately cover slow and fast transients.

During this stage of research, we are aware that the suggested PMU-metrics do not take into account the influence of higher harmonics in the power grid.

In the present position paper, we focus on the evaluation of the proposed PMU-based metrics power quality assessment procedure for real world scenarios.

REAL WORLD SCENARIO 1: SOUTH AUSTRALIA BLACKOUT 2016

To further evaluate the proposed PMU-based metrics power quality assessment procedure for real world scenarios and to assess the sensitivity of nRMSE in real-world scenarios, as well as its dependence on reporting rate, we used the well-known dataset South Australia Blackout 2016 [24]. This dataset consists of the recording of the South Australia blackout on 28th September 2016.

Results are presented in Figure 1. It is worth noticing that, in Figure 1 upper graph, at 3.75 seconds the loss of some wind power plants causes an abrupt fall of the frequency. In Figure 1 lower graph, nRMSE metric is computed with the CS-TFM PMU in P-class configuration with 4 different reporting rates (from 100 frames per second to 10 frames per second, i.e. the configurations suggested by the IEC Std).

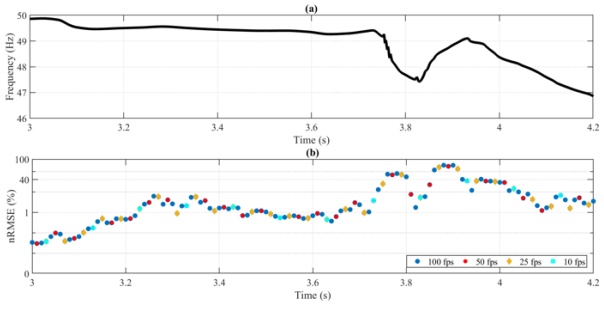

Fig. 1. Evaluation for real world scenario 1
Upper graph: Frequency evolution as function of time.
Lower graph: nRMSE metric computed.

Table 2. Rep. rate and delays for real world scenario 1

Rep. Rate (fps)	10	25	50	100
Delay (ms)	N.A.	55	35	25

As seen in Figure 1, the reporting rate does not affect the computation itself of the nRMSE. However, the higher the reporting rate, the higher the probability to capture promptly an event.

Hence, by using the threshold suggested in [19] (i.e., 40%), we can see how 10 fps are not sufficient to detect the event, whereas the other configurations provide a detection delay that is inversely proportional to the reporting rate, as presented in Table 2.

REAL WORLD SCENARIO 2: TRIP 1.5 GW GENERATOR IN MODIFIED IEEE 39 BUS SYSTEM

For further evaluation, the dataset used for this real world scenario can be found in [25]. In the cited paper, the Authors take the IEEE 29 bus system and replace some of the traditional generators with some wind power plant to mimic the penetration of inertialess generation units. Then they trip some generator (for a total loss of 1.5 GW) and they observe the effects. First contingence at 0.15 s, then nearly 600 ms of a dampened oscillation, then a new contingence at 0.8 s.

As in the previous dataset it is evident that the nRMSE discriminates easily the normal steady-state conditions from the contingencies, but if we look at the delay of the first contingency detection we see how much the reporting rate affects the responsiveness. Related Rep. rates and delays are displayed in Table 3.

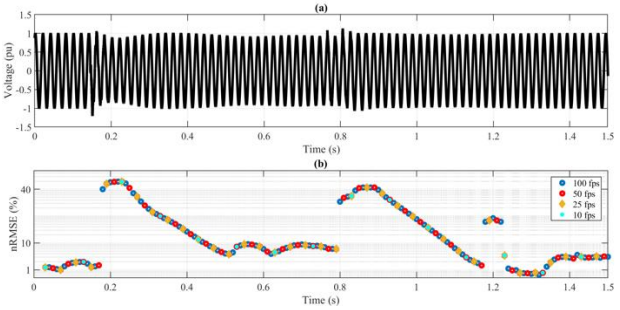

Fig. 2. Evaluation for real world scenario 2
Upper graph: Voltage as function of time.
Lower graph: nRMSE metric with different reporting rates.

Table 3. Rep. rate and delays for real world scenario 2

Rep. Rate (fps)	10	25	50	100
Delay (ms)	85	65	45	35

It can be concluded that the PMU-based proposed seem to be enough, in both simulation [19] and comparison with real world scenarios, seen above, to be consider a valuable approach to further develop toward proper power quality assessment procedures.

VI. STANDARD AMENDMENT PROPOSAL

The IEC Std defines the structure of the measurement data packet as provided by a compliant PMU, as shown in Fig. 3. Focusing on the measurement data field, we can identify six main subfields (byte size in brackets).

All values are in 32-bit floating-point and phasors are in polar format. Analog and digital subfield refer to specific input/output ports, whereas STAT contains bit-mapped flags defining current state and quality info (e.g. internal state, sensor malfunction).

In view of integrating PMU data in more sophisticated control strategies, we propose two possible amendment to the packet structure, as derived from the proposed metrics.

Possible amendment 1:

If a local control application is envisioned, the PMU could verify the bad data detection internally and use a single extra bit as a Boolean flag, where 1 indicates the packet carries potential bad data (i.e., due to model inconsistency and not only on internal malfunction).

Possible amendment 2:

In case of a more centralized approach, an extra subfield of 4 bytes could be dedicated to transmit the nRMSE.

These amendments would not affect the overall packet size in any significant way; neither would request an excessive effort from the computation and transmission capabilities.

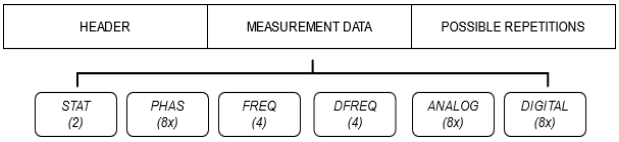

Fig. 3. Measurement data packet structure as defined in [3].

VII. CONCLUSIONS

This position paper suggested the inclusion of novel PMU-based metrics in order to extend PQAP at each sensitive network node towards the further use of aggregated data at both local and/or central level.

The proposed PMU-based metrics provide a better description of the behaviour of the system, as presented in previous research [18-22], allowing to take control actions as part of the extended quality power assessment procedures, while exploiting the advantage of PMUs that require a reduced amount of data.

This position paper focused on the determination of confidence interval associated to metrics for a robust approach for their application in measurement-based controlling efforts. In this preliminary stage of the research, we consider only the systematic error contributions, as we assume that the non-linear effects are covered by noise and harmonics.

The summarized results from previous research proved the scarce accuracy of the PMU-based estimates in dynamic conditions, since nRMSE distributions present inconsistent trends. In addition, due to the present results utilizing well-known datasets from real world scenarios, we can conclude that these proposed metrics would be a new tool for investigating the actual comparability and interoperability of measurements taken from different sensors, and thus quantifying in a more rigorous way the uncertainty in many control applications. Further work regarding its evaluation as performance assessment across the grid is needed.

VII. OPEN SCIENCE

Towards open science, i.e., efforts aimed at achieving more openness in science and the necessary paradigm shift, the current paper follows FAIR principles [26] by the Zenodo community for Sensor Network Metrology: https://zenodo.org/communities/sensornetworkmetrology

REFERENCES

[1] J Stones, in Electrical Engineer's Reference Book (Sixteenth Edition), 2003

[2] S. Mark Halpin, Angela Card, in Power Electronics Handbook (Third Edition), 2011

[3] Shailendra Jain, in Modeling and Control of Power Electronics Converter System for Power Quality Improvements, 2018

[4] McGranaghan, M. Power quality assessment procedure. United States: N. p., 1991. Web.

[5] Rahman, Md & Bin, et al. (2013). Summary of Smart Grid: Benefits and Issues. International Journal of Scientific and Engineering Research. 4. 7.

[6] Yilu Liu et al., "State Estimation and Voltage Security Monitoring Using Synchronized Phasor Measurement". ABB Power T&D Company, CiteSeerX 10.1.1.2.7959

[7] Phadke, A.G. (2002). "Synchronized phasor measurements-a historical overview". IEEE/PES Transmission and Distribution Conference and Exhibition. Vol. 1. pp. 476–479.

[8] Loper, Mari & Trummal, Tarmo & Kilter, Jako. (2018). Analysis of the Applicability of PMU Measurements for Power Quality Assessment. 1-6.

[9] IEEE/IEC 60255-118-1-2018 -International Standard - Measuring relays and protection equipment - Part 118-1: Synchrophasor for power systems, 2018.

[10] Sharma, Rajesh & Dhole, G.M.. (2016). Wide Area Measurement Technology in Power Systems. Procedia Technology. 25. 718-725.

[11] Granados-Lieberman, D. Global Harmonic Parameters for Estimation of Power Quality Indices: An Approach for PMUs. Energies 2020, 13, 2337.

[12] IEEE Std 1459-2010 (Revision of IEEE Std 1459-2000) , vol., no., pp.1-50, 19 March 2010

[13] G. Rietveld *et al.*, "Measurement Infrastructure to Support the Reliable Operation of Smart Electrical Grids," in *IEEE Trans on Instr and Meas*, vol. 64, no. 6, pp. 1355-1363, June 2015.

[14] G. Frigo *et al.*, "Characterization of uncertainty contributions in a high-accuracy PMU validation system," in *Measurement*, vol. 146, pp. 72-86, 2019.

[15] G. Frigo *et al.*, "Definition of Accurate Reference Synchrophasors for Static and Dynamic Characterization of PMUs," in *IEEE Trans on Instr and Meas*, vol. 66, no. 9, pp. 2233-2246, Sept. 2017.

[16] G. J. Fitz Patrick and E. Y. Song, "Interoperability Test of IEEE C37.118 Standard-based PMUs," *2016 International Synchrophasor Symposium*, Mar. 2016.

[17] A. J. Roscoe *et al.*, "The Case for Redefinition of Frequency and ROCOF to Account for AC Power System Phase Steps," *2017 IEEE AMPS*, Liverpool, UK, 2017, pp. 1-6.

[18] G. Frigo *et al.*, "Impact of Fundamental Frequency Definition in IpDFT-based PMU Estimates in Fault Conditions," *2019 IEEE AMPS*, Aachen, Germany, 2019, pp. 1-6.

[19] G. Frigo, F. Grasso-Toro, "On-line performance assessment for improved sensor data aggregation in power system metrology," *XXIII IMEKO World Congress*, Yokohama, JP, 2021, pp. 1-4.

[20] G. Frigo *et al.*, "Taylor-Fourier PMU on a Real-Time Simulator: Design, Implementation and Characterization," *2019 IEEE Milan PowerTech*, 2019, pp. 1-6.

[21] G. Frigo, A. Derviškadić, A. Bach and M. Paolone, "Statistical Model of Measurement Noise in Real-World PMU-based Acquisitions," *2019 IEEE SGSMA*, College Station, TX, USA, 2019, pp. 1-8.

[22] G. Frigo, A. Derviškadić, Y. Zuo and M. Paolone, "PMU-Based ROCOF Measurements: Uncertainty Limits and Metrological Significance in Power System Applications," in *IEEE Trans on Instr and Meas*, vol. 68, no. 10, pp. 3810-3822, Oct. 2019.

[23] A. Ghanavati, H. Lev-Ari and A. M. Stanković, "Sub-Cycle Dynamic Phasors With Adjustable Transient Response," in IEEE Transactions on Power Delivery, vol. 35, no. 4, pp. 1886-1894, Aug. 2020, doi: 10.1109/TPWRD.2019.2956637.

Australian Energy Market Operator, Mar. 2017, [online] Available: http://www.aemo.com.au/media/Files/Electricity/NEM/Market_Notices_and_Events/Power_System_Incident_Reports/2017/Integrated-Final-Report-SABlack-System-28-September-2016.pdf.

[24] Y. Zuo et al., "Impact of Synchrophasor Estimation Algorithms in ROCOF-Based Under-Frequency Load-Shedding," in IEEE Trans on Pow Sys, vol. 35, no. 2, pp.1305-1316, March 2020

[25] Wilkinson, M. D., et al. 2016. "The FAIR Guiding Principles for scientific data management and stewardship." Scientific Data. Nature.

25th IMEKO TC4 International Symposium
23rd International Workshop on ADC and DAC Modelling and Testing
IMEKO TC-4 2020
Brescia, Italy / September 12-14, 2022

Temperature Rise in MV Switchgears: the Role of Loose Busbar Joints

Susanna Spinsante[1], Grazia Iadarola[1], Gianmarco Mazzocchi[2], Claudio Romagnoli[2]

[1]*Department of Information Engineering, Polytechnic University of Marche, Ancona, Italy, {s.spinsante,g.iadarola}@staff.univpm.it*
[2]*IMESA SpA, Jesi, Italy, {gianmarco.mazzocchi,claudio.romagnoli}@imesaspa.com*

***Abstract* – The identification of the different causes of a Medium Voltage (MV) switchgear failure is a complex task. Among the conditions contributing to failure, thermal cycling due to loose joints and electrical components may act as a trigger for fault. This paper presents an experimental analysis of temperature variation taking place in 27 different points of a MV switchgear and originating from loose mechanical and electrical joints in the busbars, compared to the normal operating condition. The loose joints - due to improper installation, vibrations, or ageing of components - are obtained by applying a controlled clamping below the recommended operational value of 45 Nm torque, to six busbar joint screws (two for each phase). Results show that when the applied clamping goes below 10% of the recommended value, temperature does not rise significantly in points other than the loose ones, while the main circuits exhibit a detectable variation of their electrical resistance.**

I. INTRODUCTION

Faulty joints are counted among the major causes of switchgear failure, that not only disrupts power production, transmission, distribution, or conversion, but may also lead to dangerous accidents. A faulty or loose connection, in fact, can increase electrical resistance and, as a consequence, heat-dissipated power. Temperature rise due to increase in heat may escalate until the joint or nearby insulation completely fails, thus resulting in a fault. Estimates supported by experience of well-established industrial operators report that around 25% of Medium Voltage (MV) switchgear faults are determined by loose joints or hot spots in the switchgear [1]. Thermal monitoring, together with Circuite Breaker (CB) drive and partial discharge monitoring, is one of the main tasks nowadays addressed by predictive maintenance solutions designed for switchgears [2, 3]. In fact, in order to reduce costs, more and more electrical equipment operators are changing their traditional approach to maintenance, moving from reactive and preventive maintenance, towards embedded monitoring systems, typically based on Internet of Things (IoT) systems, joint with Artificial Intelligence (AI) and Machine Learning (ML) approaches, able to interpret sensor-measured data inside the switchgear, and provide a prediction of incoming fault. Unfortunately, continuous temperature measurements that could be very helpful in training predictive maintenance algorithms, are extremely rare or even not existing at all for the switchgear, over its long lifetime [4, 5].

In current practice, infrared inspections of the switchgear are performed regularly through ad-hoc viewing ports in the enclosure, using handheld thermal cameras [6]. In order to implement predictive maintenance systems exploiting real-time measurements, proper temperature sensors should be installed inside switchgears, where several electrical connections are established by mechanically screwing together with metal conductors, such as busbars. As Joule's first law states, $P \propto I^2R$, so both current and resistance contribute to generated heat from current circulating in a conductor. Loose joints, corrosion, and deterioration increase the resistance of electrical contacts; as a consequence, the detection of hot spots allows to identify the possible points from which a fault could originate.

Loose joints may be due to improper action by the operator, such as a wrong torque applied to screws after a maintenance operation; or they may be due to ageing of components, or mechanical stress, such as vibrations, determined by the operational environment where the switchgear is located. A real-time thermal monitoring system should be equipped with enough temperature sensors to monitor all possible faulty joints inside the switchgear, but this could rapidly increase the number of sensing units needed, thus increasing also cost and complexity. As a consequence, this study focuses on the effective role of loose joints in causing temperature rise inside the switchgear. To this aim, loose joints are established on purpose in six busbar screws, two for each phase, and the variation of the temperature relative to the ambient temperature is measured both at the loose screws and in other 21 different points inside the switchgear, by means of type K thermocouples. The attained temperature variations are compared to those registered during normal operation of the switchgear, in the same positions. Additionally, the variation of the electrical resistance of the switchgear main circuits, before and after the simulation of the fault, is analysed. This analysis is different from the one found in [7], where the temperature

rise in MV switchgears compliant to the IEC 62271-1:2011 standard was verified, based on the procedure indicated by the norm. In this study, the tested switchgear is already certified according to IEC 62271-200:2021: the analysis of the temperature variation is aimed at the possible implementation of an IoT sensor-based thermal monitoring system to support enhanced maintenance services of the switchgear.

The paper is organized as follows. Section ii. describes the measurement setup, and the switchgear chosen for tests. Experiments are presented in Section iii., while Section iv. discusses the obtained results. Finally, conclusions are drawn in Section v..

II. MEASUREMENT SETUP

Figure 1 shows a graphical representation of the single-panel, air-insulated MINIVER-C MV switchgear chosen for experiments [8]. This metal-enclosed switchgear selected for experimental tests is manufactured by IMESA SpA and responds to the characteristics fixed in accordance to IEC 62271-200:2021: 12 kV operating voltage, 630 A continuous current, 50-60 Hz frequency.

Figure 2 shows the locations of the type K thermocouples inside the switchgear enclosure. The thermocouples used (Nickel-Chromium/Nickel-Alumel, model SR30KX, manufactured by TC Srl) can operate in the temperature range from 0 °C to 1100 °C in the continuous measurement mode, and in the range from -180 °C to 1350 °C in the short time measurement mode. They are cabled as twisted pairs, in EN IEC 60332-1 compliant flame-resistant silicone rubber. About the position of the temperature sensors, thermocouples numbered from 1 to 24 (denoted by red labels, in Fig. 2) are mechanically fixed onto the switchgear point at which the temperature measurement has to be performed, while thermocouples numbered from 25 to 27 (identified by blue labels, in Fig. 2) are used to measure internal air temperature in cables compartment, busbars compartment, and LV compartment used for auxiliary equipment, respectively. The thermocouples numbered from 19 to 24 are applied onto M10 screws that join flat copper omnibus bars: they are made loose on purpose, reducing the applied torque with respect to the prescribed one, by means of a calibrated torque screwdriver (accuracy of applied torque value: $\pm 1\%$). Temperature values at the different switchgear points, and ambient temperature, are measured once every 2.5 min.

A National Instruments NI Compact DAQ 9178 system has been used for the automatic measurements, equipped with an NI 9208 Current Analog Input Board (featuring 16 analog input channels, with a minimum input range of ± 21.5 mA, and a conversion time per channel of 2 ms in high-speed mode) and NI 9214 16-Channel Isothermal Thermocouple Input Modules (featuring a conversion time per channel of 735 μs in high-speed mode, a voltage measurement range of ± 78.125 mV, and a temperature sensitivity of 0.01 °C). Table 1 details the position of each thermocouple inside the switchgear, while pictures in Fig. 3

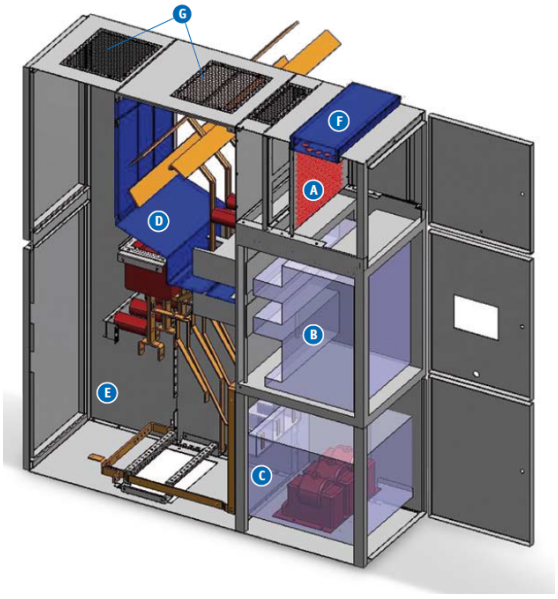

Fig. 1. The MINIVER-C MV switchgear chosen for experiments. The different compartments are: A) Low Voltage (LV) auxiliary instruments; B) circuit breaker (CB); C) voltage transformers (VT); D) busbars; E) lines; F) interconnection channel; G) gas vent slot (from [8]).

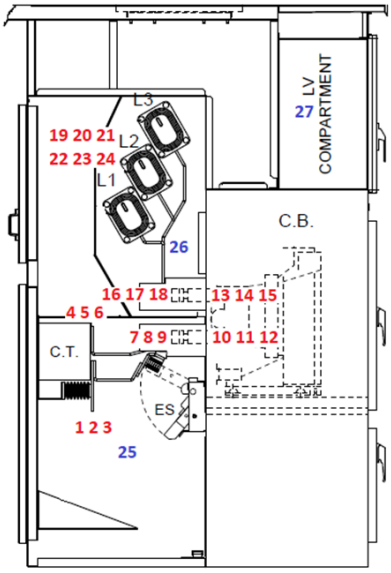

Fig. 2. Position of the 27 type K thermocouples in the MV switchgear. Each of the 3 phases (L1, L2, L3) at the indicated locations has its dedicated thermocouple.

Table 1. Position of each thermocouple inside the switchgear

Label	Position	Phase
T1,T2,T3	Outgoing cable joint	L1,L2,L3
T4,T5,T6	Top contact CT	L1,L2,L3
T7,T8,T9	Lower pole	L1,L2,L3
T10,T11,T12	Lower CB tulip	L1,L2,L3
T13,T14,T15	Upper CB tulip	L1,L2,L3
T16,T17,T18	Upper pole	L1,L2,L3
T19,T20,T21	Omnibus bar joint	L1,L2,L3
T22,T23,T24	Omnibus bar joint	L1,L2,L3
T25	Internal cables compartment	
T26	Internal busbars compartment	
T27	Internal LV compartment	

show some sample installations of the type K thermocouples, labeled according to Table 1.

III. EXPERIMENTS

A. Measurements in standard operational conditions

In standard operational conditions, omnibus bars joints are mechanically obtained with M10 screws nominally clamped at a standard torque of 45 Nm. Rated clamping of M12 screws on current transformers (CT) amounts to 60 Nm; lower and upper pole joints M16 screws are clamped at 165 Nm torque.

Based on these settings, a first experiment consists in measuring the overtemperature, with respect to the external ambient temperature, at the different points of the switchgear, when operated with a rated current of 630 A provided by a calibrated three-phase current generator. Current is maintained until a stable thermal regime is obtained, meaning that all the measured points do not exhibit a temperature variation greater than 1 °C over the last hour of the measurement interval. The overtemperature values of interest for this study are obtained as the difference between the highest temperature measured at each position and the average external ambient temperature. The last one equals 19.1 °C, measured by two additional type K thermocouples located at a 1 m distance from the closed switchgear, in oil bath to avoid perturbations, during a measurement interval of 8 hours and 7 min. As temperature values are sampled every 2.5 min, there are 194 temperature measurements collected from each of the 27 thermocouples.

Before and after the temperature measurement session in standard operational conditions, the electrical resistance of each phase main circuits (IN-OUT, column, CB and CT) is also measured. This way, it is possible to check if the resistance changed because of the thermal behavior of the switchgear.

B. Measurements with loose busbars joints

In a second experiment, the omnibus bars joints, corresponding to thermocouples numbered from 19 to 24, are made loose on purpose, by reducing their effective applied torque from 45 Nm to 4 Nm, i.e. less than 10% of the prescribed value. This condition simulates what would happen, in practice, if the operator forgets to clamp the busbars screws in the switchgear. The temperature measurement session lasts 8 hours and 2 min, so that a total amount of 192 overtemperature values are measured by each thermocouple, with respect to the average ambient temperature of 18. 0 °C. For the applied torque value at the busbar joints, the overtemperature is measured in all the positions listed in Table 1, in order to evaluate how much the loose busbars joints affect the thermal behavior of the switchgear, in the different points monitored. All the other joints are maintained at their rated clamping values, as described in subsection III.A..

Again, the electrical resistance of each phase main circuits (in-out, column, CB and CT) is measured as well, before and after the loose joints measurement session, to check if the resistance values changed or not.

IV. RESULTS AND DISCUSSION

Figure 4 shows the temperature values measured in the first experiment, when the switchgear is operated in standard conditions with the correct torque applied to all the joints. For better reading, curves are grouped based on the measured phase, namely L1 in Fig. 4a), L2 in Fig. 4b), and L3 in Fig. 4c). In all these graphs, the highest curves indicating the greatest increase in temperature, correspond to thermocouples applied onto the top contact of the CT, the lower and upper poles, the lower and the upper CB tulip. The lowest increase in temperature (curves located on the bottom part of each graph) is registered on the outgoing cable joints and on the omnibus bars joints, for all the phases. The last graph in Fig. 4d) shows the time change of the ambient temperature, both inside the switchgear enclosure (T25, T26, and T27) and outside it (T28). It is visible how the highest increase in air temperature takes place inside the busbars compartment, corresponding to thermocouple T26. Temperature measured in standard operational conditions follows the same trend already observed in [9].

The fourth column of Table 2 reports the results obtained from the first experiment: in standard operating conditions, the highest overtemperature values are measured at the phase L3 lower pole (37.9 °C), the phase L2 lower CB tulip (37.8 °C), and the phase L2 lower pole (37.7 °C), respectively. These values are well below the temperature rise limits set by IEC 62271-200:2021 common specifications, irrespective of the specific part, media, type of material, and applied surface treatment of the MV switchgear under test. Table 3 reports the values of the electrical resistance of each phase main circuits (IN-OUT, column, CB

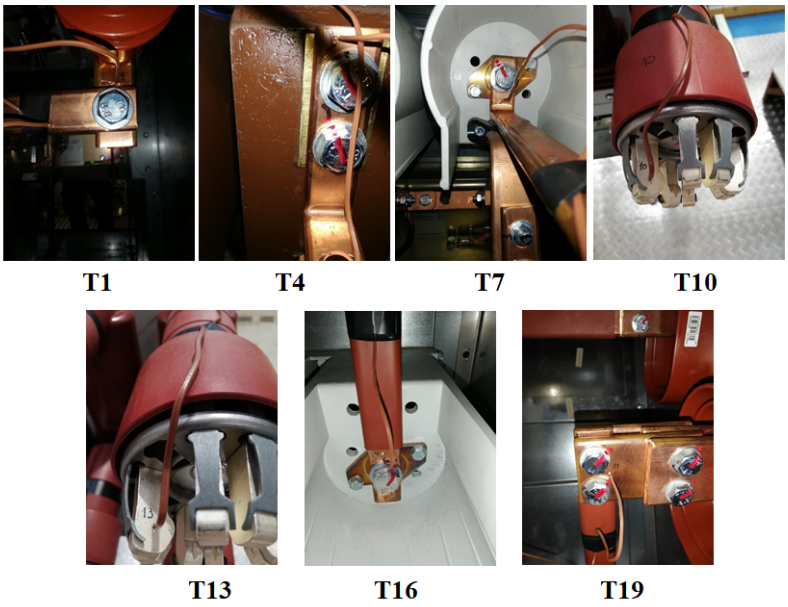

Fig. 3. Some of the type K thermocouples listed in Table 1 and installed inside the switchgear.

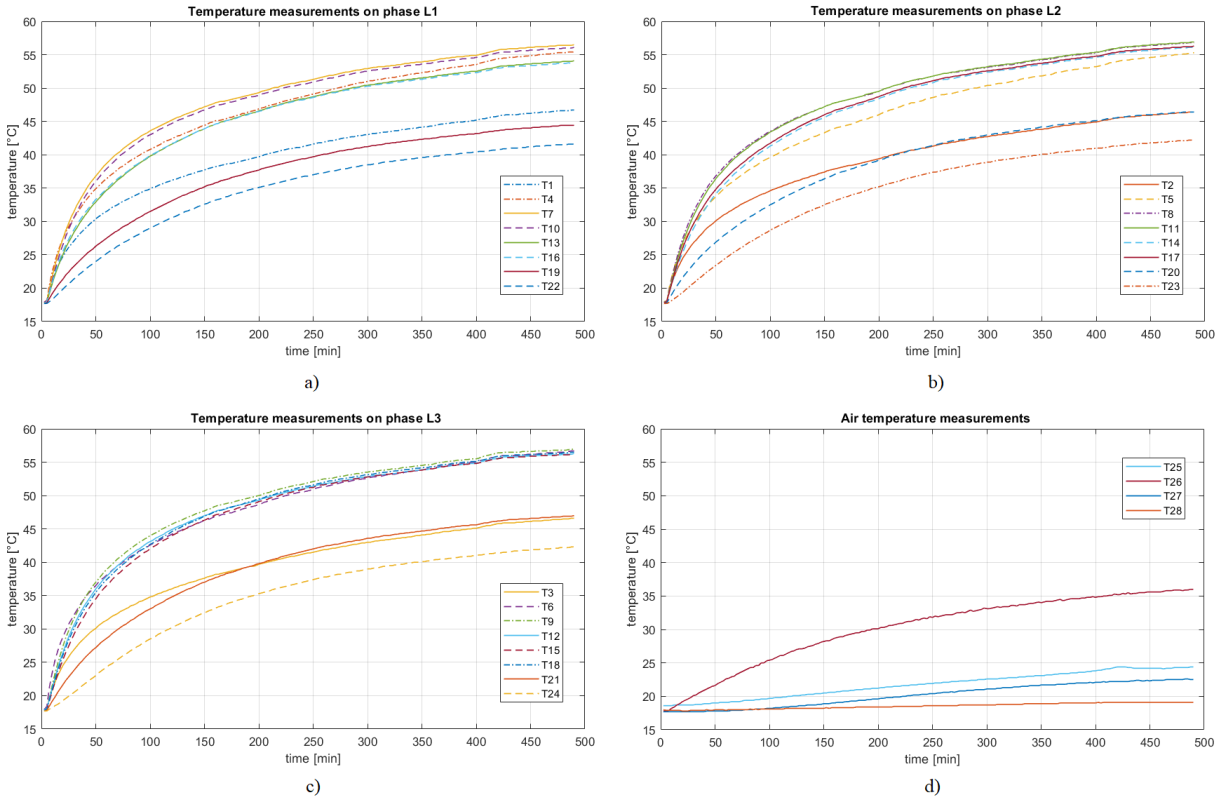

Fig. 4. Temperature measurements in standard operational conditions: a) phase L1, b) phase L2, c) phase L3, d) internal and external air.

Table 2. Measured overtemperature values in standard operational conditions of the MV switchgear, with ambient temperature = (19.1±0.4) °C, and in the loose busbars joints conditions (4 Nm applied torque), with ambient temperature = (18.0±0.4) °C

Thermocouple	Position	Phase	Overtemperature [°C] (normal conditions)	Overtemperature [°C] (loose joints)
T1	Outgoing cable joint	L1	27.6	27.5
T2	Outgoing cable joint	L2	27.3	27.2
T3	Outgoing cable joint	L3	27.5	27.3
T4	Top contact CT	L1	36.3	36.5
T5	Top contact CT	L2	36.2	34.9
T6	Top contact CT	L3	37.6	36.6
T7	Lower pole	L1	37.4	37.5
T8	Lower pole	L2	37.7	36.3
T9	Lower pole	L3	37.9	37.7
T10	Lower CB tulip	L1	37.0	37.2
T11	Lower CB tulip	L2	37.8	37.9
T12	Lower CB tulip	L3	37.2	37.1
T13	Upper CB tulip	L1	35.0	35.9
T14	Upper CB tulip	L2	37.0	37.7
T15	Upper CB tulip	L3	37.1	37.5
T16	Upper pole	L1	34.7	36.1
T17	Upper pole	L2	37.2	38.1
T18	Upper pole	L3	37.4	37.9
T19	Omnibus bar joint	L1	25.3	**29**
T20	Omnibus bar joint	L2	27.3	**30.7**
T21	Omnibus bar joint	L3	27.9	**30.5**
T22	Omnibus bar joint	L1	22.5	**25.5**
T23	Omnibus bar joint	L2	23.1	**24.9**
T24	Omnibus bar joint	L3	23.2	**25.7**
T25	Internal air, cables compartment		5.3	4
T26	Internal air, busbars compartment		16.9	17.4
T27	Internal air, LV compartment		3.4	3.5

Table 3. Electrical resistance values (in $\mu\Omega$) before and after the thermal test in standard operational conditions, for each phase (L1, L2, L3) main circuits (± 1 $\mu\Omega$ uncertainty)

	IN-OUT		Column		CB		CT	
Phase	Before	After	Before	After	Before	After	Before	After
L1	185	179	156	152	56	53	36	35
L2	189	186	160	157	57	56	31	31
L3	205	202	175	172	55	54	38	36

and CT), measured before and after the execution of the standard operational conditions test. As shown, the main circuits resistance values do not show significant variations, as reasonably expected for the standard operation conditions of the certified switchgear.

The last column of Table 2 provides the overtemperature values measured in the second experiment, when the torque applied to omnibus bars joints is less than 10% of the recommended one. The most significant increase in overtemperature is measured by thermocouples located in the loose joints (from T19 to T24): on average, it amounts to 2.8 °C, with the highest increase of 3.7 °C in the omnibus bar joint of phase L1 (T19). In all the other positions, the overtemperature determined by the loose busbars joints varies less than ±1.4 °C, with respect to the one measured in standard operational conditions. On average, the variation amounts to 0.2 °C, that is irrelevant. Table 4 shows the variations of the resistance values, after and before the test. The most relevant ones are found in the IN-OUT (-4.8%) and column (-7.8%) circuits of phase L1 (versus -3.2% and -2.6%, respectively, found after the normal conditions test), and in the IN-OUT circuit of L2

Table 4. Electrical resistance values (in $\mu\Omega$) before and after the experiment with loose busbar joints, for each phase (L1, L2, L3) main circuits (± 1 $\mu\Omega$ uncertainty)

	IN-OUT		Column		CB		CT	
Phase	Before	After	Before	After	Before	After	Before	After
L1	205	195	167	154	55	53	36	35
L2	204	197	162	160	57	55	31	31
L3	216	215	176	171	53	52	37	37

(-3.4%, versus -1.6% found after the normal operational conditions test). In all cases, the measured resistance decreases following the thermal conditioning due to the experiment performed, with respect to its original value.

V. CONCLUSION

Temperature rise of MV switchgear primary circuits has a relevant impact on the switchgear insulation lifetime that, in its turn, may rapidly lead to faults. A practical rule of thumb states that insulation lifetime halves for each rise of 10 °C in average temperature. While loose joints are usually deemed responsible for hot spots in MV switchgears, this paper has shown, by extensive measurements, that even when omnibus bars joints are kept at an extremely low clamping (less than 10% of the recommended one), temperature does not rise significantly in those joints (less than 4 °C), and even less in other points of the switchgear. On the contrary, even limited thermal variations may affect the main circuits resistance values. These results suggest the need to reconsider the effective role of loose joints in predictive maintenance models applied to MV switchgears.

VI. ACKNOWLEDGMENT

This research activity was supported by IMESA SpA and partially by the POR MARCHE FESR project *Marche Innovation and Research fAcilities for Connected and sustainable Living Environments (MIRACLE)* - CUP B28I19000330007.

REFERENCES

[1] M. W. Hoffmann, S. Wildermuth, R. Gitzel, A. Boyaci, J. Gebhardt, H. Kaul, I. Amihai, B. Forg, M. Suriyah, T. Leibfried, et al., "Integration of Novel Sensors and Machine Learning for Predictive Maintenance in Medium Voltage Switchgear to Enable the Energy and Mobility Revolutions", Sensors 2020, vol. 20, 2099, 10.3390/s20072099.

[2] J. I. Aizpurua, V. M. Catterson, I. F. Abdulhadi and M. S. Garcia, "A Model-Based Hybrid Approach for Circuit Breaker Prognostics Encompassing Dynamic Reliability and Uncertainty", IEEE Transactions on Systems, Man, and Cybernetics: Systems, vol. 48, no. 9, pp. 1637-1648, Sept. 2018, doi: 10.1109/TSMC.2017.2685346.

[3] M. Chevalier and V. Boutin, "Heading to Models of Failure Rate Evolution, with Respect to Environmental and Usage Conditions in Time", 2019 Annual Reliability and Maintainability Symposium (RAMS), 2019, pp. 1-6, doi: 10.1109/RAMS.2019.8768942.

[4] M. S. Jadin, S. Taib, "Recent progress in diagnosing the reliability of electrical equipment by using infrared thermography", Infrared Physics & Technology, Volume 55, Issue 4, 2012, pp. 236-245, ISSN 1350-4495, doi: 10.1016/j.infrared.2012.03.002.

[5] A.S. Nazmul Huda, S. Taib, "Application of infrared thermography for predictive/preventive maintenance of thermal defect in electrical equipment", Applied Thermal Engineering, Volume 61, Issue 2, 2013, pp. 220-227, ISSN 1359-4311, doi: 10.1016/j.applthermaleng.2013.07.028.

[6] K. Gitzel, J. Gebhardt and T. Kozel, "Automatic Analysis of thermograms - challenge in thermal monitoring of switchgears using infrared cameras", CIRED 2021 - The 26th International Conference and Exhibition on Electricity Distribution, 2021, pp. 395-399, doi: 10.1049/icp.2021.1581.

[7] S. Iderus and G. Peter, "Temperature Rise Test on Medium Voltage Switchgear Assembly Based on IEC Standard", 2020 8th International Conference on Orange Technology (ICOT), 2020, pp. 1-5, doi: 10.1109/ICOT51877.2020.9468746.

[8] IMESA SpA, "MINIVER/C Medium Voltage Switchgears", [online] `https://www.imesaspa.com/media/multimedia_prodotto/19/MV%20SWITCHBOARD_MINIVER%20C.pdf`, retrieved on April, 22^{nd}, 2022.

[9] K. Perdon, M. Scarpellini, S. Magoni, L. Cavalli, "Modular online monitoring system to allow condition-based maintenance for medium voltage switchgear", CIRED - Open Access Proceedings Journal, 2017, (1), p. 346-349, DOI: 10.1049/oap-cired.2017.0415.

25th IMEKO TC4 International Symposium
23rd International Workshop on ADC and DAC Modelling and Testing
IMEKO TC-4 2022
Brescia, Italy / September 12-14, 2022

Design and Characterisation of 1 kV Multirange Resistive Voltage Divider

Stanislav Mašláň[1] and Martin Šíra[1]

[1]*Czech Metrology Institute (ČMI), Okružní 31, 638 00 Brno, smaslan@cmi.cz*

***Abstract* – The paper describes design of a new multirange AC resistive voltage divider (RVD) for input voltage up to 1 kV for measurement of LF power and power quality parameters. Two prototypes were constructed and characterised in terms of temperature dependence, power dependence of gain and phase errors and AC transfer. The new RVD reached phase change below 0.5 µrad and gain change below 8 µV/V at 53 Hz for voltage step from 100 V to 1 kV with time constant below 2.5 minutes. Voltage dependence and DC ratio stability are under evaluation.**

I. INTRODUCTION

National metrology institutes (NMIs) and some of the higher level commercial calibration labs are using digital sampling techniques for precision measurement of power and power quality (PQ) for several decades now. One of the best known representatives of the kind is commercially available wattmeter DSWM [1]. Expanded uncertainties achievable using these setups reach order of µW/VA. Two key components of such measurement setups are voltage and current transducers used to scale the input voltage and current to low voltages which can be digitized by the precision digitizers. Principle connection of such setup is shown in Fig. 1. Typical digitizers for precision measurements are Agilent 3458A which are suitable for industrial frequencies up to at least 400 Hz. Current transducers are usually coaxial current shunts [2] which can be calibrated at least up to 100 kHz even for 100 A current ratings. Alternatively, precision current ranging transformers can be used such as [3]. These are mainly dedicated for industrial frequencies. Benefit of current transformers is a possibility of remote range switching and shorter settling times for high currents.

Whereas the current can be digitized only via current transducers, the voltage can be digitized directly using the digitizer in case of Agilent 3458A. However, stability of internal dividers of the Agilent 3458A for high voltage ranges is not satisfying for precision measurements (see characterizations in [4]). Thus, even the measured voltage is usually scaled down using some kind of external voltage divider. The most accurate solution is use of the multistage inductive voltage dividers [5]. These can reach uncertainties much lower than 1 µV/V and also have negligible settling times, however they are quite expensive and complicated to construct. Also, they cannot be used to measure signals with a DC component. Therefore, most labs are using simple resistive voltage dividers (RVD). Disadvantage is slower settling for high voltages. On the other hand, they can be operated even above 100 kHz if properly compensated and/or equipped by buffers [6].

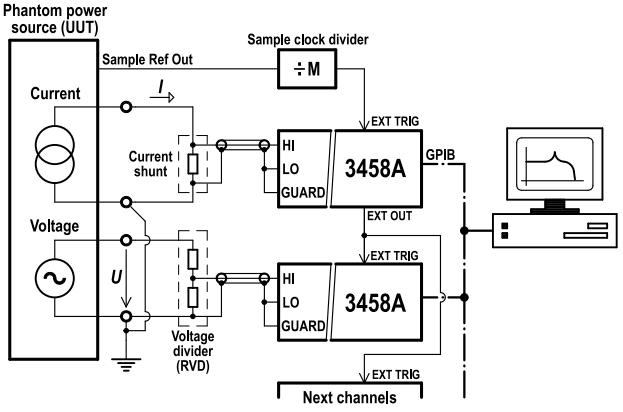

Fig. 1. Basic diagram of digital sampling wattmeter with Agilent 3458A digitizers calibrating phantom power source (e.g. Fluke 6100).

Common problem of any practical measurement with such digital sampling setups is automation of measurements. It is not practical to calibrate phantom power sources or analyzers manually and replacing either current shunt or voltage divider every few measurement points to obtain best resolution on the digitizers. In the past, Czech Metrology Institute (ČMI) lab partially automated this process using set of coaxial current shunts switched via a coaxial multiplexer to cover current range up to 20 A. Later, the multiplexed shunts were replaced by an automatic ranging transformer [3]. However, the problem remained with the RVDs. Experimental measurements at ČMI showed, the Agilent 3458A multimeters set to the aperture time of 150 µs have AC linearity deviations below 1 µV/V and 1 µrad down to roughly 10% of fullscale input for frequencies up to few hundred hertz (see Fig. 2). Thus, about one decade of voltage (and current) can be measured using the same transducer without loss of accuracy. However, that still typically means to replace the RVD several times per calibration session by operator to cover full range of calibration. This was still not satisfying, so a decision

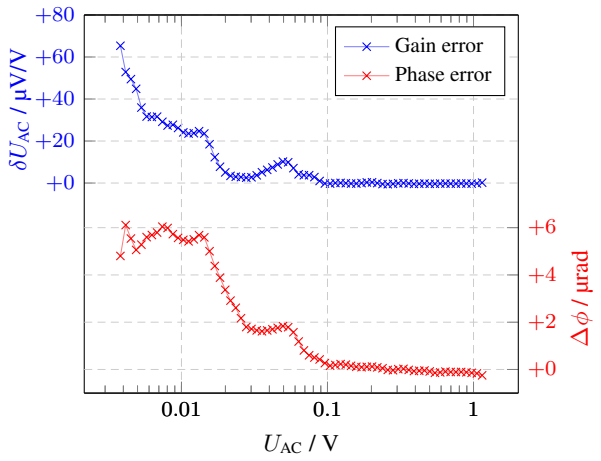

Fig. 2. Relative gain error and absolute phase error of Agilent 3458A as function of applied AC amplitude. Agilent 3458A was configured to range of 1 V, sampling rate of 5 kSa/s, aperture of 150 µs.

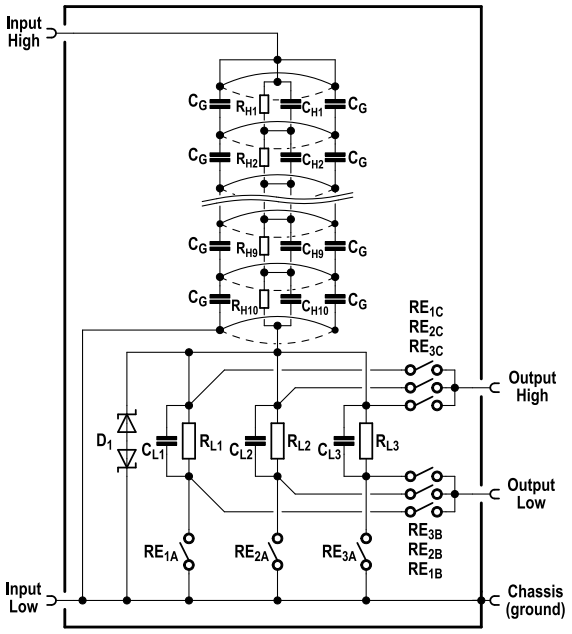

Fig. 3. Principle connection of multi-range RVD up to 1 kV.

to design a multi-range RVD was made in order to further automate the calibration procedures.

II. DESIGN OF THE NEW 1 KV RVD

ČMI is using set of RVDs designed and manufactured by RISE Sweden NMI (former SP) covering range from 4 V up to 560 V. All of these RVDs were designed for 800 mV nominal output at nominal input voltage, i.e. almost fullscale of Agilent 3458A input at 1 V range. No 1 kV RVD was available at ČMI low voltage labs till 2021. Thus, a decision was made to design a new RVD covering voltage range up to 1 kV and at the same time to design it as multi-ranging to further increase the automation of measurements.

Several approaches of the multi-range solution were considered. First, insertion of several taps to the high-side resistors chain was considered. This would have benefit of having a constant output impedance and a possibility to cover wide range of voltages. However, it would require a use of precision HV signal relays and an eventual fail in the relay switch would overload the RVD. Also, insertion of taps and relays would disrupt the guarding of the resistors chain for higher ranges, which would result in quite complex frequency dependencies of RVD transfer. Second considered approach was to keep the ratio of the RVD constant and try to switch the ranges by active amplifiers or buffers with switchable subdivides. Although this solution would certainly work with uncertainties well below 5 µV/V for at least industrial frequencies, it was not chosen because of complexity and need for persistent power supply of RVD. Thus, the third option was chosen. The high-side resistor chain is fixed for all ranges and only the low-side resistors are switched. Advantage is a simple construction of the high-side divider part. Also, this RVD cannot be overloaded by wrong range selection, because the high-side resistor is designed for a full load. Disadvantage is variable output impedance and thus higher sensitivity to capacitive load variation for the lowest range.

Principle connection is shown in Fig. 3. The high-side chain of resistors is formed of ten series groups of resistors R_{H1} to R_{H10}. Each group contains five parallel 10 kΩ resistors, i.e. 200 kΩ in total. That is 100 mW of power dissipation per resistor. Each series group is equiped with parallel 8.2 pF capacitor C_{H1} to C_{H10} needed for phase compensation. The chain of resistors is shielded by 12 guard rings supplied from a capacitive divider composed of capacitors C_G of 470 pF each, i.e. total input capacitance of the RVD is approx. 100 pF. The guarding rings were absolutely necessary as even small movement of the RVD chain in the metal box changed the series capacitance of the chain by few percent. That effect resulted to considerable changes in phase errors. No variation above typical standard deviation of measurement was observed with the guarding rings despite the distribution of their electric fields is still somewhat affected by the deformation of the RVD metal case walls. This could be potentially improved by addition of secondary guard stage around the existing one.

Low side resistors R_{L1}, R_{L2} and R_{L3} are separate for each range to make frequency compensation easier. Each low side resistor is compensated by a separate capacitor tuned so the RVD is slightly under-compensated when connected to Agilent 3458A via 1 m coaxial cable (approx. 375 pF of loading capacitance for our Agilent 3458A units). Therefore, the amplitude transfer should not contain any resonant peak exceeding the input range of the

Table 1. Low-side components and nominal parameters of 1 kV RVD ranges for high-side resistor 200 kΩ and nominal output voltage 600 mV.

Range V	Ratio V/V	P_{LOSS} W	I_{IN} mA	R_{Lx} Ω
240	401	0.288	1.2	500
600	1001	1.8	3	200
1000	1667	5	5	120

digitizer. Particular values of the low-side resistors together with nominal ratios of the new RVD are shown in Tab. 1. The ranges were chosen in step 240 - 600 - 1000 V with nominal output voltage of 600 mV so the RVD is usable for both Agilent 3458A and wideband NI PXI 5922 at ±1 V range. Considering our linearity measurements of Agilent 3458A, it means this RVD can cover rms voltages from 45 V to 1 kV without entering the strongly nonlinear part of the Agilent 3458A amplitude transfer for apertures above 150 µs and frequencies below 400 Hz. That covers vast majority of customer calibrations of power and PQ analyzers and calibrators and thus eliminating need for operator interaction during calibration.

The automation of the RVD is ensured by relay switching of the low-side resistors. In order to minimize the effect of relays, the outputs are connected in 4-terminal arrangement. Three relays were used for each range. First relay RE_{xA} is connecting the current from low-side to ground. The other two relays RE_{xB} and RE_{xC} are connecting potential outputs of the low-side resistor. Three relays are closed for each range, the others are opened. No damage can be done if incorrect relays are switched. Eventual damage of the digitizer during "hot" range switch is prevented by low leakage diode chain D_1. All the relays are small signal relays with two parallel contacts ensuring contact resistance below 50 mΩ. Assuming the worst case end of life contact resistance of 100 mΩ, the current path relay RE_{xA} can cause ratio errors up to 0.5 µV/V, which is insignificant for the purpose. Resistance of potential sensing relays RE_{xB} and RE_{xC} can only cause angular errors at high frequencies, however considering loading capacitance of 375 pF (Agilent 3458A input and 1 meter coaxial cable), the effect can be only as high as 24 µrad at 50 kHz which is acceptable for ČMI purposes.

The relays are controlled by a simple microcontroller unit designed to have idle current of 2 µA. The circuit only wakes up when operator presses a range button or SCPI command is received via isolated RS232 port. Thus, the RVD device is supplied from two small lithium cells with expected life time of at least 5 years and no other external supply or charging is needed for operation. The whole RVD circuit was routed to a single printed circuit board (PCB) made of Rogers 4350b substrate. This material was chosen to reduce the loss tangent of the PCB

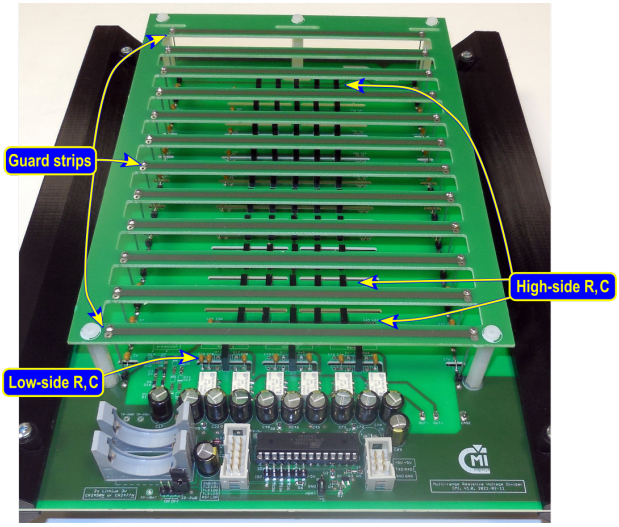

Fig. 4. PCB of the new 1 kV RVD. The smaller PCB on top of main PCB contains guarding strips.

parallel capacitances of the high-side resistors. Furthermore, the space between the leads of the high-side resistors was milled out to reduce the capacitance contribution of the PCB and improve air flow via the PCB. The guarding rings must be stable in geometry as even small change in a field distribution will alter apparent capacitance of the high-side resistors chain. Two approaches of the guarding were tested. First, a 3D printed holders for guarding ring wires were made. Second prototype used guarding rings on another two PCBs placed above on under the main PCB. Both had about the same stability, although the PCB solution seems easier. The picture of the PCBs is shown in Fig. 5. The PCB of the RVD was placed to metal box with milled venting holes on all sides. High voltage input and control buttons were placed to front as they are likely to be accessed. Output and isolated RS232 control port were placed to output. All terminals are banana sockets in standard spacing of 19 mm. The RVD was intended for frequencies mostly up to 10 kHz, so no coaxial connections were considered.

A. *Choice of components*

The older ČMI RVDs and current shunts were always made from combinations of Vishay resistors S102K and S102C [7] which have opposite temperature coefficients (TCR). Combination of those two types lead to acceptable effective TCR in relatively wide range of temperatures. However, it still resulted to TCRs well over 1 ppm/K and thus significant settling times after voltage (or current) was applied. Thus, for the new RVD, it was decided to use more expensive Vishay Z-foil through-hole resistors Z201 [8]. These types claim TCR below ±0.2 ppm/K in typical operating temperatures. The Z-foil resistors were used for all high-side and low-side resistors. All capac-

Fig. 5. Front panel of the new RVD.

itors were of NP0 ceramic dielectric with claimed TCR below ±30 ppm/K. Capacitors for highest available voltage (up to 500 V) were used assuming they provide lowest loss/leakage and nonlinearities.

III. CHARACTERISATION

Most of the AC measurements were performed using setups with Agilent 3458A. Some measurements were performed using pair of synchronized Agilent 3458A. The setups requiring high long term inter-channel transfer stability were built using single Agilent 3458A and a multiplexer with passive inputs based on [9]. That reduced drifts of gain below 0.1 µV/V per day. All measurements were performed using universal digital sampling SW tool TWM [10]. Sampling was coherent, hence ordinary FFT transform with rectangular window was used for obtaining the complex voltages and their ratios. All the high voltage AC setups used Fluke 5215A amplifier as measurement voltage source as it provides high power and bandwidth with reasonable noise. The amplifier internal circuits were analyzed and a simulator of a Fluke calibrator digital signals was made in order to switch the amplifier into the stand alone operation. Signal source for the amplifier was a DDS function generator with 1:2 amplifying transformer at the output to reach required rms voltage of 10 V for 1 kV output of Fluke 5215A. The DDS and digitizer(s) were always synchronized using clock divider between 10 MHz reference and trigger input of Agilent 3458A in order to achieve coherent sampling.

A. Temperature dependence

The temperature dependence was measured by comparing the two RVD prototypes connected in parallel by AC ratio sampling setup with Agilent 3458A. The changes in the ratio were barely in order of 10^{-6} and microradians, so a time-multiplexed measurement was used in order to mitigate the gain and phase instability of Agilent 3458A.

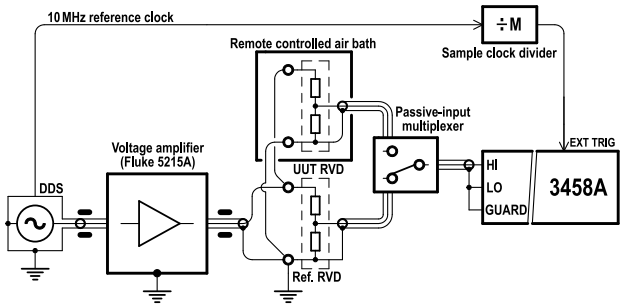

Fig. 6. Measurement setup for RVD temperature coefficient evaluation.

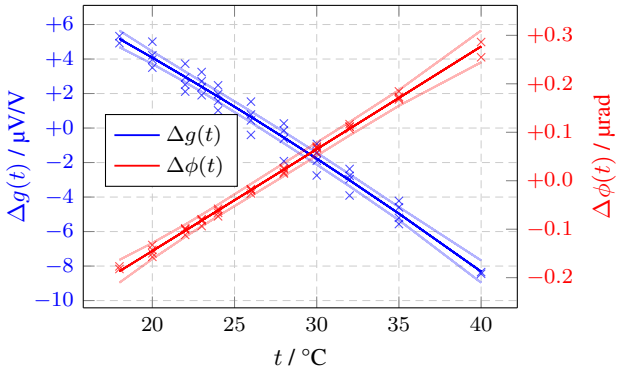

Fig. 7. Temperature dependence of gain and phase error of new RVD for frequency of 53 Hz. The solid lines are second order polynomic fits with calculated expanded uncertainty limits (thin lines).

The setup is shown in Fig. 6. One RVD was placed into the air bath while the other one was left outside as a reference in ambient conditions (23.0 ± 0.5) °C. Temperature of the airbath was cycled from 18 to 40 °C several times in both directions. Settling was about two hours per step to let the RVD settle. The measurement was performed with full input voltage of 1 kV and several frequencies. Example for the worse of the two RVDs is shown in Fig. 7. The measured coefficients at 23 °C for the two RVD prototypes were (−0.191 ± 0.025) ppm/K and (−0.608 ± 0.025) ppm/K for ratio modulus and (0.021 ± 0.002) µrad/K for phase error at 53 Hz (both RVD prototypes). Almost identical coefficients were achieved for other ranges of the RVDs, which suggests the main contribution is of the common high-side resistors chain.

B. Power dependence

Next, the power coefficients were measured for several voltages and frequencies. Analysed RVD was connected in parallel with a reference C-R impedance divider (ZVD) formed of gas dielectric capacitors IET 1404 and Z-foil resistor at low-side. Setup is shown in Fig. 8. The capacitors were modified by removing their internal ceramic capacitance trimmers to reduce their voltage dependence to bare

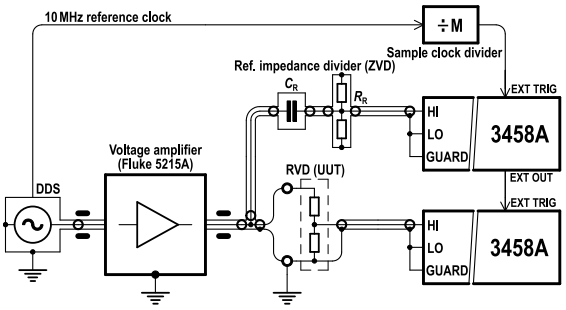

Fig. 8. Measurement setup for RVD power and voltage dependence evaluation.

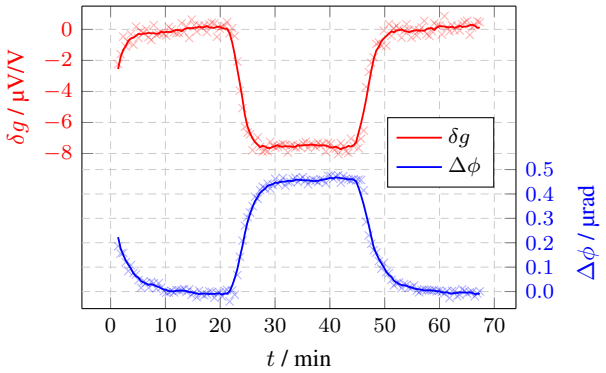

Fig. 9. 100 V - 1 kV - 100 V step response of new RVD for frequency of 53 Hz. δg is relative change of divider ratio, $\Delta\phi$ is absolute change of phase error.

minimum. Frequency and R-C ratios were chosen so the ratios of measured RVD and ZVD were equal to order of 10^{-5} to prevent nonlinearity influence of the digitizers. Interchannel errors of Agilent 3458A pair were corrected by connecting them in parallel and measuring their gain/phase differences for both step voltages. Input voltage was then cycled in about 25 minute steps between idle 100 V and target voltage. Example of the measurement for 1 kV with phase expressed for 53 Hz is shown in Fig. 9. Measured phase response was about (9 ± 1) frad/V^2/Hz. Gain response was about (-8 ± 1) ppm/kV. Very close values were obtained for other frequencies in range up to 2 kHz. Time constant of the step transition was obtained by fitting the step responses by first order exponential functions. Phase shift response time constant was 2 vs 2.5 min for rise vs fall time. Gain response time constant was 1.2 vs 1.6 min.

IV. FREQUENCY TRANSFER

Frequency transfer of the new RVD was measured with modified digital impedance bridge setup [11] using step-up method. The setup is shown in Fig. 10. First, the absolute transfer of auxiliary 24 V RVD was measured (ratio of 1:30). Next, the new RVD on all its ranges was compared to the auxiliary RVD. The setup measured voltage ratios up to 1:55. The linearity of the bridge was traceable to ratio of the calculable resistance standards as described in [11], so the gain errors even for the high ratios were below 3 µV/V. The loading effect of the RVDs by impedance bridge input impedance was corrected numerically using known input impedances of a bridge channels and output impedance of the RVD. The results expressed for the expected loading capacitance of 375 pF are shown in Fig. 11. Note the transfers were fitted by second order polynomes to smooth the noise in the measured data at low frequencies. The ratio was also measured directly using pair of ACMS Fluke 5790 and the difference from the bridge method at 10 kHz was less than 40 µV/V which is within the assigned uncertainties. The bridge setup was also used to measure phase shift of the RVD.

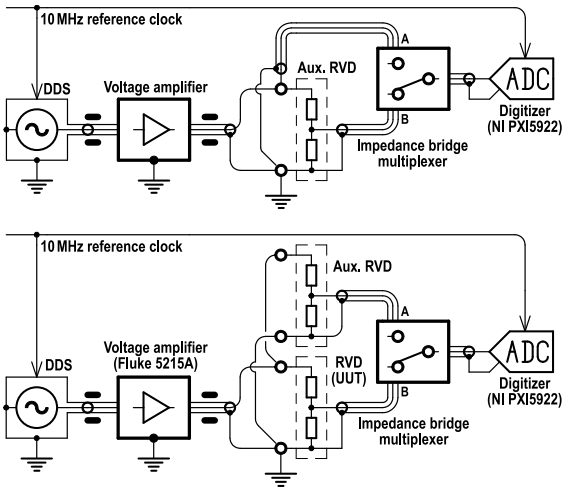

Fig. 10. Measurement setup for step-up measurement of RVD AC transfer. Upper diagram is for first step when calibration input-to-output ratio directly. Lower diagram is for next steps when comparing two RVDs.

V. CONCLUSION

Simple three-range RVD with remote control was constructed. The RVD is suitable to cover voltage range at least 45 to 1000 V in typical setup with Agilent 3458A at industrial frequencies. Measurements of two RVD prototypes showed the Vishay Z-foil resistors reduced temperature dependence of the divider about three times compared to the designs with older Vishay S102C/S102K resistors to approx 0.2 and 0.6 ppm/K. Measured power time constant of RVD is below 2.5 minutes (below 4 minutes to settle within 1 µV/V and 0.1 µrad at 53 Hz) which suits well practical measurements. Power dependence of the divider was measured to be below 8 ppm/kV and 0.5 µrad/kV^2 at 53 Hz for the worse of the two RVD prototypes. The power dependence of the gain is about one third of our older RVD designs, whereas the phase dependence is almost identical to ČMI and older RISE RVDs. Settling time constant was at least halved compared to older designs. Measurement of

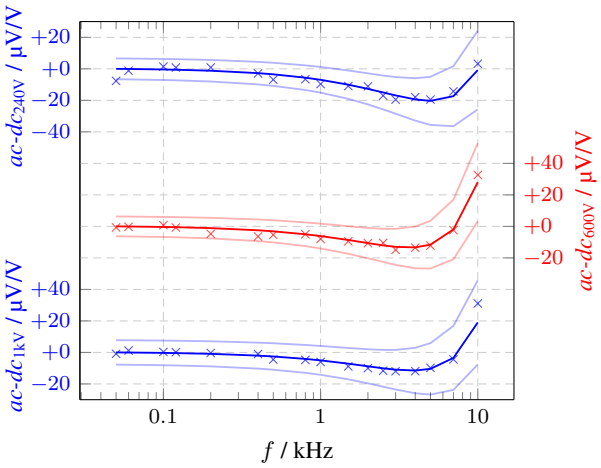

Fig. 11. Measured input-to-output ac-dc transfers of the new RVD for all three ranges. The thick lines are polynomic fits with the assigned expanded uncertainties (thin lines).

voltage dependence and DC ratio stability are in progress and will be presented at the conference.

REFERENCES

[1] Stefan Svensson. "Power measurement techniques for non-sinusoidal conditions". PhD thesis. Göteborg Sweden 1999: Chalmers University of Technology, 1999.

[2] Věra Nováková Zachovalová et al. "Development of high current shunts of cage design with active cooling". In: *2016 Conference on Precision Electromagnetic Measurements (CPEM 2016)*. 2016, pp. 1–2. DOI: 10.1109/CPEM.2016.7540485.

[3] Ilya Budovsky et al. "Precision multi-range current transformer for the automation of electrical power standards". In: Aug. 2014, pp. 412–413. DOI: 10.1109/CPEM.2014.6898434.

[4] Rado Lapuh. *Sampling with 3458A*. Ljubljana: Left Right, 2018. ISBN: 978-961-94476-0-4.

[5] G.W. Small et al. "Precision three-stage 1000 V/50 Hz inductive voltage divider". In: *IEEE Transactions on Instrumentation and Measurement* 54.2 (2005), pp. 600–603. DOI: 10.1109/TIM.2004.843377.

[6] Tobias Bergsten, Valter Tarasso, and Karl-Erik Rydler. "Precision measurement system for characterisation of phase displacement of voltage dividers up to 1 MHz". In: *CPEM 2010*. 2010, pp. 259–260. DOI: 10.1109/CPEM.2010.5545107.

[7] Vishay Foil Resistors (VFR) - Vishay Precision Group (VPG). *S-Series - Datasheet*. [online]. URL: http://www.vishaypg.com/docs/63001/63001.pdf.

[8] Vishay Foil Resistors (VFR) - Vishay Precision Group (VPG). *Z series (Z Foil) - Datasheet*. [online]. URL: http://www.vishaypg.com/docs/63187/zseries.pdf.

[9] Stanislav Mašláň et al. "Digital Sampling Setup for Measurement of Complex Voltage Ratio". In: *IEEE Transactions on Instrumentation and Measurement* 66.6 (2017), pp. 1355–1363. DOI: 10.1109/TIM.2017.2649899.

[10] Stanislav Mašláň. *TWM - TracePQM Wattmeter*. Czech Metrology Insitute. URL: https://github.com/smaslan/TWM.

[11] S. Mašláň et al. "Four-Terminal Pair Digital Sampling Impedance Bridge up to 1MHz". In: *IEEE Transactions on Instrumentation and Measurement* 68.6 (June 2019), pp. 1860–1869. DOI: 10.1109/TIM.2019.2908649.

25th IMEKO TC4 International Symposium
23rd International Workshop on ADC and DAC Modelling and Testing
IMEKO TC-4 2020
Brescia, Italy / September 12-14, 2022

Feasibility of a digital counterpart of thermal-converter-based current step up

D. Peral[1], Y.A. Sanmamed[1], J. Díaz de Aguilar[1]

[1]*Spanish Center of Metrology (CEM), Tres Cantos, Madrid, Spain,*
dperal@cem.es, jdiaz@cem.es

***Abstract* – The development of a new traceability step-up chain using digital instruments (digitisers) with direct traceability to SI would allow dynamic measurements of current and voltage waveforms. CEM has studied the feasibility of a digital counterpart for the traditional thermal-converter-based step up, which is limited to provide the RMS values of monotone signals. This paper describes and validates this new digital method, obtaining a complete set of calibrations shunt-digitizer for currents up to 1 A. The performed measurements show very promising results, comparable to the well-established thermal-converter approach results, with differences between both techniques lower than 2 μA/A up to 1 kHz.**

I. INTRODUCTION

The International System of Units (SI) base unit of electric current, the ampere, A, after the 2019 SI redefinition, is defined by taking the fixed numerical value of the elementary charge e to be $1.602\,176\,634{\cdot}10^{-19}$ when expressed in the unit C which is equal to A·s, and where the second is defined in terms of caesium frequency $\Delta\nu_{\mathrm{Cs}}$ [1].

The ampere can be realized by using Ohm's law, the unit relation A=V/Ω, and practical realizations of the SI derived units, the volt V and the ohm Ω, which are based on the Josephson and quantum Hall effects, respectively. This practical realization is widely adopted in the metrology community. As the values of the elementary charge e and the Planck constant h are fixed in the current SI, the Josephson and von Klitzing constants $K_{\mathrm{J}} = 2e/h$ and $R_{\mathrm{K}} = h/e^2$ have also fixed numerical values.

Although the traditional realization of alternating current (ac), based on the so called thermal transfer from direct current (dc) by means of thermal converters [2] and used by most of the National Metrology Institutes (NMI), allows to obtain accuracies of the order of 1 μV/V, these are limited to Root Mean Square (RMS) values not being valid for dynamic measurements, which are the kind of measurements found in the industry. Furthermore, thermal converters methods are lengthy and laborious.

A new traceability chain based on digitisers directly traceable to SI would allow to measure voltage and electric current waveforms dynamically. The inclusion of this digital traceability chain in NMIs, has to be preceded by a thorough validation.

The Spanish Metrology Centre (CEM) together with other NMIs have been working on this topic for some time: from the characterization of analog-to-digital converters (ADC) [3-5], to the description of quantum standards [6-9] and the combined use of ADC and quantum standards on the same measurement arrangement [10-14].

The research in this paper is divided into two sections. The first section (section II) presents the measurement setup and results of a digital counterpart of the traditional thermal-converter-based step up, using a combination of shunts and digitisers in the ranges 20 mA - 1 A, and 10 Hz - 10 kHz. This digital counterpart can be directly traceable to the SI definition. The second section (section III) includes the measurement setup and results for the validation of the new digital traceability chain. This chain is validated by comparing the measurements against historical thermal-converters-based step up data.

The measurements obtained in this paper show comparable results to the well-established thermal-converter approach for currents up to 1 A when the frequency is lower than 1 kHz.

II. DIGITAL-BASED CURRENT STEP UP

A. *Theory*

The digital based current step up method consists in providing the same series current to two combinations of shunt-digitiser connected in parallel: the shunt-digitizer under test and the standard shunt-digitiser (Figure 1). The output voltage of the shunts is sampled independently and simultaneously by each digitiser.

By comparing these outputs and knowing the correction of the standard shunt-digitiser (calibrated against Josephson voltage standard), the correction of the shunt-digitizer under test can be known. Repeating this process with higher current shunts, and taking the calibrated combination of shunt-digitizer under test as the standard combination of shunt-digitiser for the next step, a complete digital traceability chain can be established.

B. *Measurement setup*

The measurement setup for the 20 mA to 50 mA step is represented in Figure 1, where two digitisers Keysight

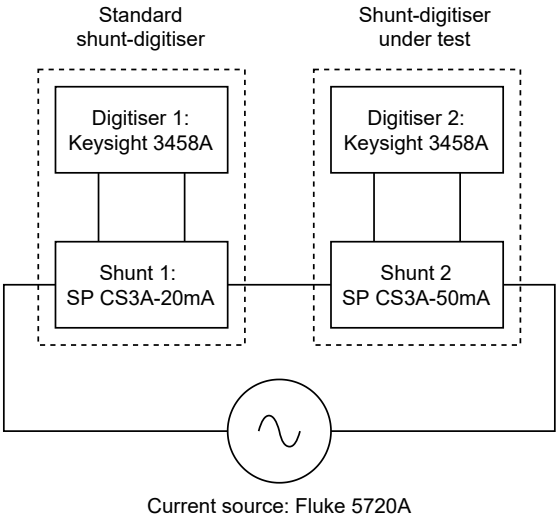

Fig. 1. Setup of the digital step up.

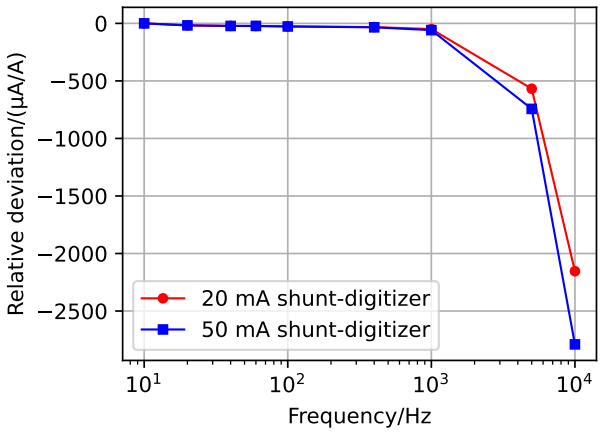

Fig. 2. Frequency response normalized with 10 Hz *response for the* 20 mA *to* 1 A *step up.*

3458A and a current source Fluke 5720A working in voltage mode are used. Further setup information regarding noise reduction, shielding and guarding can be found elsewhere [15].

The same setup and procedure have been used to step up from 20 mA to 1 A in five steps. Nine frequencies, from 10 Hz to 10 kHz and dc have been considered. The aperture time (T_a) during which digitisers are reading the current signal is 200 µs up to 100 Hz. Aperture time decreases for higher frequencies since it is limited by the necessary sampling frequency. Further details about selected parameters can be found in Tables 1 and 2.

An in-house developed software based on four parameter sine-fitting has been used for processing the digitised data [16].

C. *Measurement results*

Regarding the first step up (20 mA - 50 mA), Figure 2 represents shunt-digitiser frequency responses. The values has been represented as the relative deviation from the values at 10 Hz, therefore, the quantity unit is µA/A.

Responses include the contribution of both, shunts and digitisers.

D. *Discussion*

Figure 2 shows that the normalized frequency response has a moderately constant value up to 1 kHz. For higher frequencies, differences are much bigger.

The frequency response is mainly due to the digitizers, as obtained in a previous work [10].

The main reason for the variation of the frequency response is due to the input impedance of the digitiser. Also, at higher frequencies the aperture time must be lower, which means lower accuracy and higher noise on the measurements.

As stated previously, by knowing the response of the 20 mA shunt-digitizer combination it is possible to obtain the response of the 50 mA combination one.

III. VALIDATION

A. *Theory*

The validation can be achieved comparing shunt ac-dc differences obtained by thermal and digital methods. To remove the digitizer influence, two set of measurement are needed: one with the configuration shown in Figure 1 and another swapping digitisers.

Contrary to thermal-converters-based realizations of ac current, for a digital-based step up of shunts, dc measurements are not required. However, in this validation dc measurements are performed since the traditional thermal converters approach provides just ac-dc difference.

The diagram on Figure 3 represent schematically the relationship between inputs and outputs (in general, currents or voltages) of combinations of shunt-digitiser. For narrow input ranges, the relationship can be represented by two parallel straight lines, one for ac (upper line, in blue) and the other for dc (lower line, in green). Considering the setup shown in Figure 1, the following steps are taken:

1. ac current is applied to the standard shunt-digitiser and shunt-digitiser under test. The output of both digitisers is recorded at the same time.

2. dc current is applied to the standard shunt-digitiser and shunt-digitiser under test. The output of both digitisers is recorded against the same time.

3. ac-dc measurement differences (δ_s and δ_t) are calculated substracting recordings from step 2 to record-

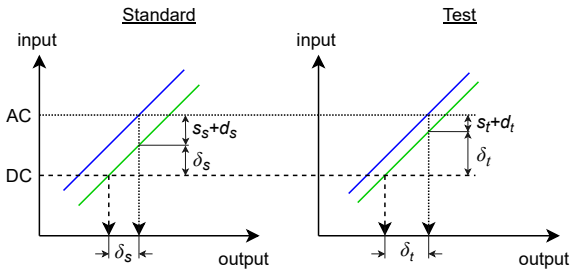

Fig. 3. Diagram of the validation method.

ings from step 1. Sub index s refers to the standard equipment and t to the equipment under test.

Considering a unitary slope of the ac and dc response of shunt-digitiser combinations, the following system of two equations can be written:

$$\begin{cases} AC_1 = DC_1 + \delta_s + (s_s + d_s) \\ AC_1 = DC_1 + \delta_t + (s_t + d_t) \end{cases} \quad (1)$$

Where s is the difference ac-dc of the shunt and d is the difference ac-dc of the digitiser. AC and DC are the input magnitudes which, in the general case, can be voltage or current. Note that the key factor here is that the input to both combinations of shunt-digitiser is the same, and that combining the equations from system 1, AC and DC dependency is removed:

$$\delta_s + (s_s + d_s) = \delta_t + (s_t + d_t) \quad (2)$$

If digitisers are swapped, and considering that ac-dc difference of shunts and digitisers (s_t, s_s, d_t and d_s) are the same after the swap, since applied current has always a similar level and measurements are taken in a short period of time, the following system of equations can be written:

$$\begin{cases} AC_2 = DC_2 + \delta'_s + (s_s + d_t) \\ AC_2 = DC_2 + \delta'_t + (s_t + d_s) \end{cases} \quad (3)$$

And analogously to equation 2:

$$\delta'_s + (s_s + d_t) = \delta'_t + (s_t + d_s) \quad (4)$$

Combining equations 2 and 4, the next expression is achieved:

$$(s_t - s_s) = \frac{(\delta_s + \delta'_s) - (\delta_t + \delta'_t)}{2} \quad (5)$$

From where the difference between test and standard shunts ac-dc difference, $(s_t - s_s)$, can be obtained, since digitiser influence is removed.

This value will be compared to the one obtained by thermal converter characterization.

B. *Measurement setup*

Two set of measurements are taken here. For the first one, the results of section II are used providing that dc measurements, with its respective aperture times, are also performed.

For the second set of measurements, the digitisers are swapped, and the same procedure described in section II.B is followed. As well, dc measurements have to be included.

C. *Measurement results*

Table 1 shows the numerical values of $(s_t - s_s)$, described in section III.A, for the first step up (20 mA - 50 mA). The analogous quantity due just to the contribution of digitisers, $(d_t - d_s)$, is also included for comparison purposes. It was calculated subtracting equation 4 from equation 2.

Table 2 includes the equivalent historical results for a thermal-converters-based realization of ac current [16] together with the results of the digital step up (extension of Table 1) and the differences between both techniques. In the thermal converters columns, blank spaces indicate that, for certain frequencies, there are not historical results .

Table 1. Numerical values of the difference between test and standard shunts ac-dc difference, $(s_t - s_s)$, described in section III.A for the step up 20 mA *to* 50 mA.

f/Hz	T_a/µs	$(s_t - s_s)$/(µA/A)	$(d_t - d_s)$/(µA/A)
10	200	-0.3	-0.9
20	200	-0.2	-1.1
40	200	-0.5	-0.5
60	200	-0.2	-0.5
100	200	0.2	-1.2
400	140	-0.8	0.6
1 000	60	-1.9	7.8
5 000	12	-20.3	164.8
10 000	12	-69.4	631.1

D. *Discussion*

$(s_t - s_s)$ in Table 1 shows a similar performance to the frequency response represented in Figure 2, with very low differences (lower than ±2 µA/A up to 1 kHz). Also, $(s_t - s_s)$ is lower than $(d_t - d_s)$, especially for higher frequencies. This result is expected, since the influence of ac signals in complex devices as digitisers is higher than the influence of ac signals in relatively simple low reactance devices as shunts.

Table 2 shows very small differences for the $(s_t - s_s)$ of the thermal converter step up approach, as expected. This is true for the whole range of currents and frequencies (the higher discrepancy is -2.4 µA/A at 10 Hz for the 200 mA to 500 mA step up).

Table 2. Difference between test and standard shunts ac-dc difference, $(s_t - s_s)$, for the equivalent historical results of a thermal-converters-based realization of ac current, the digital step up measured in this paper and the differences between both techniques.

	Thermal converters step up $(s_t - s_s)$/(μA/A)					Digital step up $(s_t - s_s)$/(μA/A)					Techniques difference (μA/A)				
Step up /mA → / f/Hz ↓	20 - 50	50 - 100	100 - 200	200 - 500	500 - 1000	20 - 50	50 - 100	100 - 200	200 - 500	500 - 1000	20 - 50	50 - 100	100 - 200	200 - 500	500 - 1000
10	-2.2	-1.8	-2.0	-2.4	-1.7	-0.3	0.6	0.5	1.2	1.7	1.9	2.4	2.5	3.7	3.4
20	-0.6	-0.7	-0.1	-0.9	0.0	-0.2	0.6	0.7	1.4	0.5	0.4	1.4	0.8	2.3	0.5
40	-0.6	0.0	-0.5	0.0		-0.5	0.5	1.1	1.4	1.0	0.0	0.5	1.6	1.5	
60	0.0	-0.1	0.0	-1.3		-0.2	0.0	0.5	0.9	1.4	-0.2	0.1	0.5	2.2	
100	0.1	-0.1	-0.1	0.3		0.2	0.4	0.7	1.1	0.5	0.1	0.5	0.9	0.8	
400	0.8	0.2	0.2	0.2		-0.8	0.9	2.0	0.3	0.3	-1.6	0.8	1.8	0.1	
1 000	0.0	0.2	0.0	-0.1	0.0	-1.9	-0.6	-0.8	0.5	0.4	-1.9	-0.9	-0.8	0.6	0.5
5 000	0.7	0.9	0.1	-1.4		-20.2	4.9	5.7	-2.1	5.7	-20.9	4.1	5.7	-0.6	
10 000	-0.7	1.4	-0.1	-1.3	-0.6	-69.4	12.7	17.1	-4.2	12.5	-68.7	11.3	17.2	-2.9	13.1

In the case of the digital step up, $(s_t - s_s)$ is also very low for the whole current range when the frequency is lower than 1 kHz. In this instance, the maximum discrepancy is 2.0 μA/A at 400 Hz for the 100 mA to 200 mA step up.

Regarding frequencies between 5 kHz and 10 kHz, some differences are also very low, however, this does not occur for all the step ups: some step up differences present moderately high positive values, others present high negative ones, showing high variability for higher frequencies.

The data from the difference of both techniques shows small differences up to 1 kHz for all step ups. This means that, knowing the digitiser error from a quantum calibration, equivalent results to thermal converter can be achieved with the advantage of not performing dc measurements and with the possibility of dynamic measurements analysis.

IV. CONCLUSION

This paper explains how to perform a digital based current step up using a combination of shunts and digitisers. The measurements obtained using this method show very good results, comparable to the well-established thermal-converter approach results: differences of less than ±2 μA/A between both techniques. This is true when the current ranges from 20 mA to 1 A and when the frequency is lower than 1 kHz. For these ranges the technique could be considered as validated. For bigger frequencies deviations get higher and, therefore, accuracy is limited.

Although, compared to the thermal converter method, the bandwidth of the digital method is narrower, it provides important advantages. The promising results described here will allow NMIs to establish a digital traceability chain for ac current in the near future, allowing high accuracy dissemination for complex waveforms that vary with time or have a decent amount of harmonic content. At the same time this digital chain will simplify and shorten calibration procedures.

V. ACKNOWLEDGMENT

This work was carried out with funding by the European Union within the EMPIR project 17RPT03 DIG-AC. The EMPIR initiative is co-funded by the European Union's Horizon 2020 research and innovation programme and the EMPIR Participating States.

REFERENCES

[1] CCEM, "Mise en pratique for the definition of the ampere and other electric units in the SI", Appendix 2 of the SI Brochure, May 2019. Online: https://www.bipm.org/documents/20126/41489676/SI-App2-ampere.pdf

[2] R. Caballero, J.D. de Aguilar, Y.A. Sanmamed, M. Neira, "Calibration of non quadratic sensibility thermal converters", 18th IMEKO TC4 Symposium on Measurement of Electrical Quantities, September 2011, pp. 138-141.

[3] J.D. de Aguilar, J.R. Salinas, R. Lapuh, A. Méndez, F.G. Lagos, Y.A. Sanmamed, "Characterization of the amplitude frequency response of analog-to-digital converters", Conference on Precision Electromagnetic Measurements (CPEM), 2016, pp. 1-2, doi: 10.1109/CPEM.2016.7540455.

[4] Y.A. Sanmamed, J.D. de Aguilar, R.C. Santos, J.R. Salinas, "Temperature influence on the establishment of a digital voltage reference", Conference on Preci-

sion Electromagnetic Measurements (CPEM), 2020, pp. 1-2, doi: 10.1109/CPEM49742.2020. 9191820.

[5] J.R. Salinas et al., "Study of Keysight 3458A Temperature Coefficient for Different Aperture Times in DCV Sampling Mode", Conference on Precision Electromagnetic Measurements (CPEM), 2018, pp. 1-2, doi: 10.1109/CPEM.2018.8500883.

[6] D. Ilić, R. Behr, J. Lee, "Stability of AC current measurements using AC-DC shunts and the AC Quantum Voltmeter", 24th IMEKO TC4 Symposium on Measurement of Electrical Quantities, September 2020, pp. 369-373.

[7] P. Durandetto, A. Sosso, "A modular and customizable open-source package for quantum voltage standards operation and control", Plos one, 2018, vol. 13, No. 12, e0209246. https://doi.org/ 10.1371/journal.pone.0209246.

[8] "Good Practice Guide on the operation of AC quantum voltage standards", First Edition, Czech Metrology Institute, Brno, Czech Republic, 2018, ISBN: 978-80-905619-2-2.

[9] J. Ireland et al., "Real-time quantum-accurate voltage waveform synthesis", Conference on Precision Electromagnetic Measurements (CPEM), 2020, pp. 1-2, doi: 10.1109/CPEM49742.2020.9191715.

[10] J.D. de Aguilar, J.R. Salinas, O. Kieler, R. Caballero, R. Behr, Y.A. Sanmamed, A. Méndez, "Characterization of an analog-to-digital converter frequency response by a Josephson arbitrary waveform synthesizer", Meas. Science and Technology, 2019, vol. 30, No. 3, 035006, https://doi.org/10.1088/1361-6501/aafb27.

[11] M. Šíra, O. Kieler and R. Behr, "A Novel Method for Calibration of ADC Using JAWS", IEEE Trans. on Instrum. and Meas., vol. 68, No. 6, pp. 2091-2099, June 2019, doi: 10.1109/TIM.2018.2888918.

[12] H. Malmbekk, C.D. Shelly, J.M. Williams, "Calibrating a Voltmeter with a PJVS Using a DAC as a Real-Time Calibrated Transfer Standard", Conference on Precision Electromagnetic Measurements (CPEM), 2018, pp. pp. 1-2, doi: 10.1109/CPEM.2018.8500872.

[13] J.D. de Aguilar, "Caracterización de convertidores digitales mediante patrones cuánticos" (Doctoral dissertation), 2020 https://doi.org/10.20868/UPM. thesis.63766.

[14] T. C. Öztürk, S. Ertürk, A. Tangel and M. Arifoviç, "Using Programmable Josephson Voltage Standard for Static and Dynamic Gain Characterization of Integrating ADC", IEEE Trans. on Instrum. and Meas., vol. 69, No. 7, pp. 4425-4435, July 2020, doi: 10.1109/TIM.2019.2941360.

[15] P. S. Filipski and M. Boecker, "AC-DC Current Shunts and System for Extended Current and Frequency Ranges", IEEE Instrum. and Meas. Tech. Conf. Proc., 2005, pp. 991-995, doi: 10.1109/IMTC.2005.1604287.

[16] J.R. Salinas, J.D. de Aguilar, F. García-Lagos, G. Joya, F. Sandoval, M.L. Romero, "Spectrum analysis of asynchronously sampled signals by means of an ANN method", 29th Conference on Precision Electromagnetic Measurements (CPEM), 2014, pp. 422-423, doi: 10.1109/CPEM.2014.6898439.

[17] J.D. de Aguilar, R. Caballero, Y.A. Sanmamed, "Realization and Validation of the 10 mA-100 A Current Standard at CEM", IEEE Trans. on Instrum. and Meas., vol. 63, No. 7, pp. 1753-1759, July 2014, doi: 10.1109/TIM.2013.2293229.

25th IMEKO TC4 International Symposium
23rd International Workshop on ADC and DAC Modelling and Testing
IMEKO TC-4 2022
Brescia, Italy / September 12-14, 2022

DMMs as voltage ratio standards: a 20 years report

Pier Paolo Capra[1], Claudio Francese[2], Flavio Galliana[3], Marco Lanzillotti[4], Luca Roncaglione Tet[5] ,Andrea Sosso[6] and Paolo Durandetto[7].

[1,2,3,4,5,6,7] *National Institute of Metrological Research INRIM), str. delle Cacce 91, 10135 Turin, Italy*
[1]p.capra@inrim.it
[2]c.francese@inrim.it
[3]f.galliana@inrim.it
[4]m.lanzillotti@inrim.it
[5]l.roncaglione@inrim.it
[6]a.sosso@inrim.it
[7]p.durandetto@inrim.it

***Abstract* – At the National Institute of Metrological Research a convenient setup to verify the DMMs linearity has been developed. It consists in a top-class calibrated DC Voltage calibrator supplying directly the DMMs under test. Some Keysight 3458A, a Fluke 8508A and an 8588A DMMs are being enrolled in the tests. This setup is also compared with another setup with a Digital Analog Converter (R – 2R DAC) in place of the calibrator. The DMMs linearity is being verified both when DMMs are just switched on and at thermal regime. The interference of the input stages of the DMMs connected in parallel during the linearity measurements and the linearity by inverting the plug of one of the DMMs connected in parallel are currently under verification.**

I. INTRODUCTION

Modern commercial high precision digital multimeters (DMMs) are widespread in primary and secondary calibration laboratories acting in very large fields of the five electrical quantities in low frequency (dc and ac voltage and current and dc resistance). They play a strategic role in the traceability transfer from National standards to secondary electrical laboratories, acting as primary reference standard for all quantities or as a traceability transfer [1]. Another important and useful feature of DMMs is their excellent linearity, mainly in the DC Voltage function, that in some cases is two orders of magnitude better than their accuracy specifications [2]. In addition, the linearity, or better, the deviation from linearity of a DMM, is not subjected to changes or drift, but it is instead an invariant parameter [3]. To measure the residual deviation from linearity of DMMs, the best method consists in directly connecting a Josepshon Array Voltage Standard (JAVS), acting as voltage reference, to a DMM under test and measuring the voltage values read by the DMM given increasing and decreasing of exactly known voltage steps provided by the JAVS [3, 4]. Unfortunately, this method is time consuming and not available in many laboratories and National Metrological Institutes (NMIs). For laboratories without JAVS, one or more JAVS-calibrated DMMs can be used to maintain a DC voltage ratio standard and used for voltage ratio traceability in mutual comparisons with a low noise digital to analog converter (DAC) [5,6,7] as common voltage source.

To that aim, two high precision voltage dividers and a measurement setup for calibration of DC voltage sources were developed at INRIM taking advantage of the linearity calibration of DMMs [8-10].

II. MULTIMETERS LINEARITY VS JOSEPHSON ARRAY

The linearity of modern digital multimeters requires, in order to be determined with sufficient accuracy, a system that generates DC voltages with stability better than $1 \cdot 10^{-8}$ during the measurement. The Josephson voltage standard is a quantum-based system capable of, generating accurate and low noise waveforms useful for characterization up to 10 V. While the accuracy specifications of multimeters are subject to deterioration over time and require regular calibration, linearity is maintained without deteriorating. The linearity shape of a multimeter is specific and uniquely identifies an instrument, exactly as fingerprints for humans. Figures 1 show the linearity shape of an HP3458 with option A measured against a Josephson array after 15 years. The graphs represent two fits where the reference voltage appears on the abscissa, while the ordinate is the measurement of the multimeter. After so many years the characteristics of the DMM did not change significantly and voltage measurements performed with a replacement technique, without a prior calibration of the multimeter

would lead to results with uncertainties of a few parts in 10^{-7}. In the following paragraphs, the comparison of linearity between different multimeters calibrated against the Josephson effect will be shown.

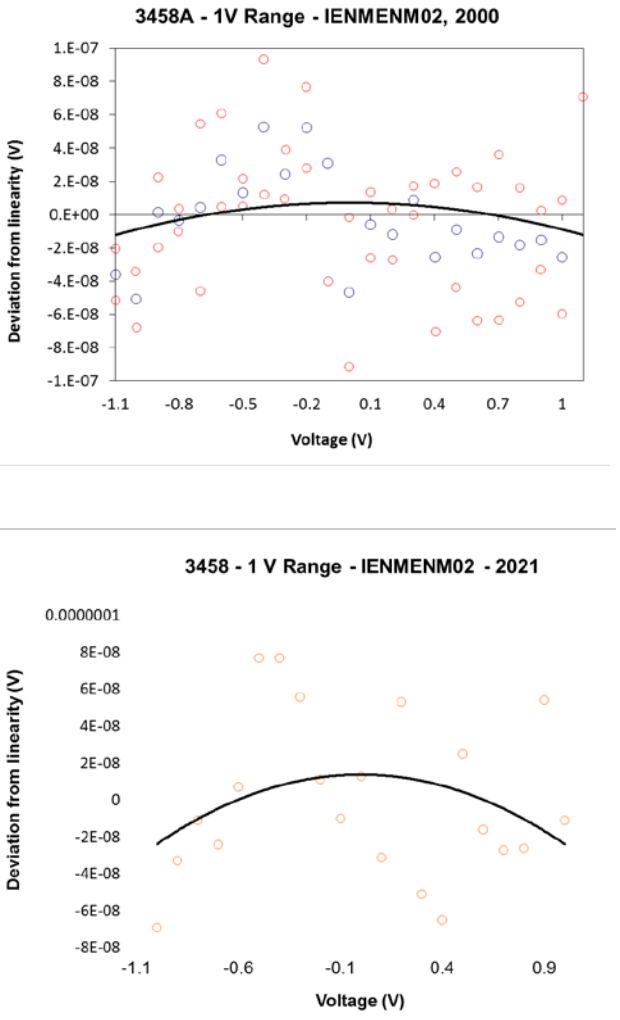

Fig. 1 (a & b). Linearity error of the same DMM measured over a time span of more than twenty years

II. MEASUREMENT METHOD

The circuit in our measurements is very straightforward: the output of the calibrator is applied to all DMMs under test connected in parallel. Then, for all relevant values, we generate several stable voltages and take the readings from all instruments. Assuming first, for the sake of simplicity, that offsets and thermal e.m.f.s. are constant, the voltages on all DMMs inputs are equal except for mutual offsets that are not changing in the measurement. Then, clearly all voltmeters are observing the same voltage increments.

The relative nonlinearity error is determined by first fitting linearly the readings of one DMM vs. one of the others. The nonlinear part of the relationship between the readings is then obtained as the difference from the actual and the fit values. A secondary outcome of this method is an estimate of the DMM relative gain (gain error) and of the total voltage offset (constant term in the fit).

In reality, offsets and thermal e.m.f.s cannot be considered as constant at the sensitivity level required to estimate nonlinearities. Offsets drifting linearly with time can appear as a modified DVM gain or even nonlinear contributions if samples are not evenly spaced in time, and should be eliminated from result. In this case, the apparent contribution to slope due to drift can be canceled by taking a first set of readings with positive increments, then, a second one, backwards, with negative increments. This is basically the usual procedure for canceling offsets and linear drifts in measurements, applied to the fitting. For proper application of the method, any relevant drift should be checked to be linear and samples must be read with equal time interval separation to preserve linearity over time in sample sequence numbering. Averaging the forward-backward results, the only effect of the drift in the result is a change in the offset of the fit. However, since the DVM offset continuously changes with time, this is not a relevant parameter. For proper usage of a calibrated multimeter as ratio standard it must be either evaluated or canceled out in every measurement.

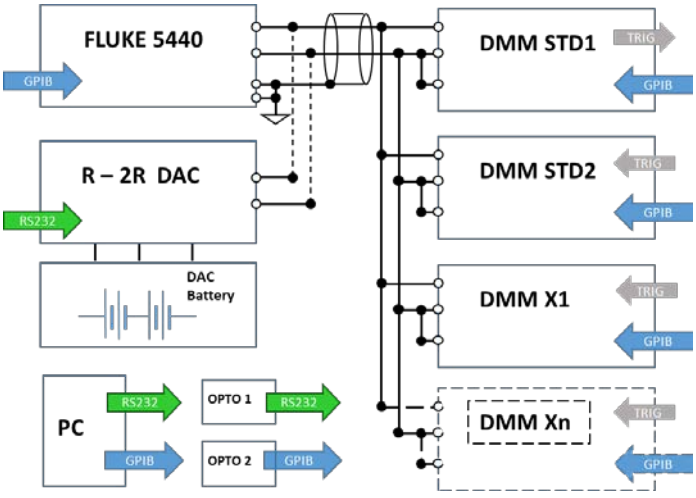

Fig. 2. Block diagram of the measuring system. The direct voltage is generated by two dc sources used alternately. The battery-powered R-2R DAC can generate low noise and fully floating voltages of ±12 V while the FLUKE 5440 calibrator can operate up to 1000 V. All multimeters have the LO terminal connected to the guard system, while the ground reference is distributed by the calibrator. The measurement system is controlled by a computer via the IEEE4-488 BUS or the serial, both equipped with optical decoupling systems.

III. SETUP

The system used for the characterization of the multimeters is shown in Fig. 3**.** The station includes two units for the generation of dc voltage, one of the commercial type and the second specially designed at INRIM.

Fig. 3. The whole apparatus has been built inside a rack and, for clarity reasons, all the devices are shown together. In real measurement situations, to reduce both electrical and thermal noise, only the operative units are connected and powered. The side shields of the rack are normally removed to help with normal thermal cooling of the instruments

The FLUKE 5440 type dcv calibrator was chosen as the commercial unit. It is a DC voltage source with high stability and low noise, equipped with a GPIB connection. The second unit is a R-2R Digital to Analog Converter (R-2R DAC) controlled via an HC74595 shift-register connected to a microcontroller with an optical decoupling system and a serial port. This unit, by means of optical decoupling, is considerably quieter than normal commercial calibrators and the stability of the generated dc voltage is appropriate for the purposes described in the article. The two HP 3458 reference multimeters are placed in the rack (at the top) and alternatively at the bottom are the multimeters being calibrated, all connected in parallel. The ground connection is distributed by the generator, while the multimeters are arranged in a floating manner with the Lo terminal connected to the Guard terminal. The cables used are shielded with connections with low thermo-electromotive forces.

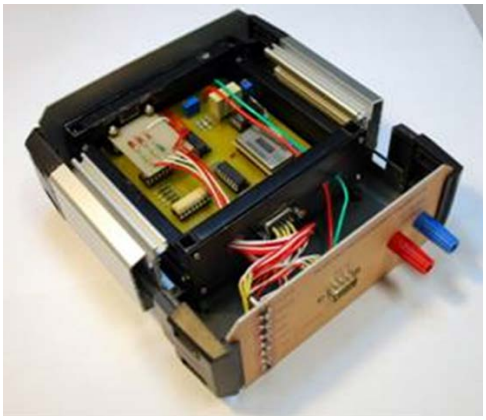

Fig. 4. The R-2R A/D converter unit is fully battery supplied and the digital control subcircuit is connected to the A/D conversion IC trough opto-isolators. Thus the output wires, connecting the source to the voltmeters under test, are the only galvanic link to the outside environment in order to avoid ground loops.

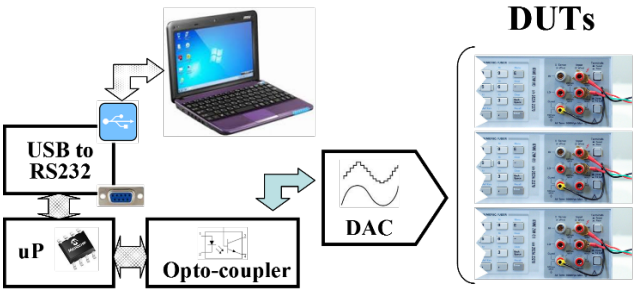

Fig. 5. The control system of the DAC consists of a USB-RS232 converter and a microcontroller, which generates the 16-bit control parameters. The digital part is powered through the computer's USB port. The 16-bit codes are sent serially to two 74LS595 shift registers connected directly to the DAC. The two Bytes stored in the shift registers are dumped with a single clock stroke in the DAC which updates the output voltage. The decoupling of the power supply is achieved by the opto-couplers, placed between the microprocessor and the shift registers. The connection of the DAC to the DMMs takes place with a connection as short as possible and equipped with terminations with low thermo-electromotive forces.

IV. DMMS COMPARISON

The two sample multimeters, calibrated against the

Josephson effect, are periodically compared with each other to verify that the linearity specifications are maintained. The graph in Fig 4 shows the linearity of two instruments, on the 10 V range and with the same settings used in the calibration phase. The linearity results obtained with a simple comparison measurement confirm the data derived from the JAVS calibration and do not change after months and after repeated “on and off” cycles.

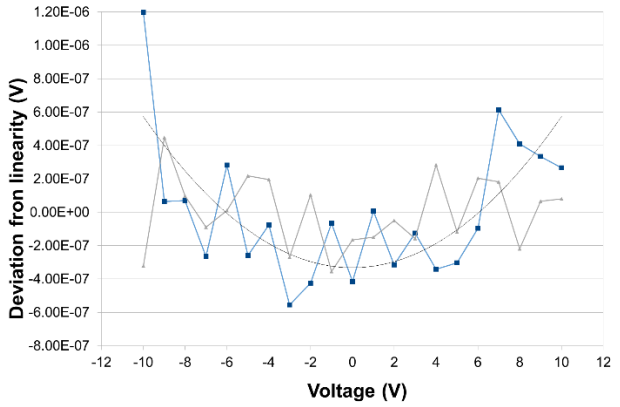

Fig. 6. Linearity comparison chart between two multimeters, both calibrated against JAVS. The linearity of the multimeters can therefore be verified not only with JAVS but also with calibrated instruments, obtaining uncertainties of about $5 \cdot 10^{-8}$.

V. SOFTWARE

The measurement system is completely automatic and is fully controlled by the IEEE-488 BUS except for the DAC which requires a dedicated controller. Starting from one / two multimeters calibrated against a JAVS system, up to 4 multimeters can be calibrated at the same time. Furthermore, the same system can also be used for verifying the linearity of the dc source used for the generation of the reference signal. The program developed can accept all the most common metrology grade DMMs.

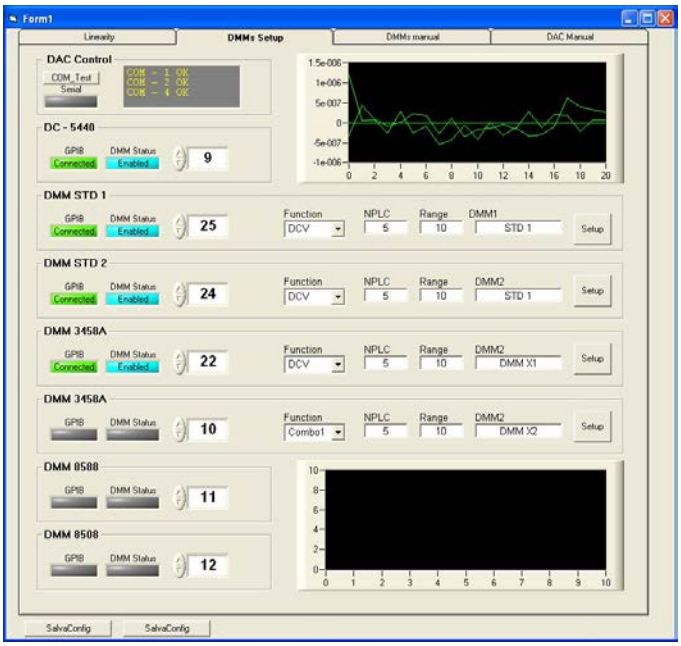

Fig. 7. The control program handles 1 or 2 multimeters calibrated by the JAVS and up to 4 under calibration. The settings are identical for all multimeters, but can be changed individually. The trigger signal can be managed via software or, more accurately, using the "Trigger" inputs the instruments are equipped with.

VI. CONCLUSIONS

The presented system allows to determine the linearity of high precision digital multimeters. The system is suitable both for laboratories equipped with a sample generation system based on the Josephson effect and for laboratories that do not have one and are working with DMMs calibrated vs JAVS.

The comparison of test carried out over about 20 years was presented and shown. We observed that the linearity characteristics of the multimeters do not change significantly over time, and always remains within the specifications declared by the manufacturers. The non-linearity values obtained on the DMMs tested are of a few parts in 10^{-8} and require reference signals of adequate stability. There is no evidence of cross-talk in connecting multiple multimeters in parallel, but experiments are still ongoing.

REFERENCES

[1] C. Cassiago, G. La Paglia, U. Pogliano, “Stability evaluation of high-precision multifunction instruments for traceability transfer”, IEEE Trans. Instrum. Meas. Vol. 50, No.6, December 2000, pp. 1206-1210.

[2] Agilent Technologies, 3458A Multimeter-User's Guide, Revision: B.01, March 2001.
[3] Helko E van den Brom et al, "Voltage linearity measurements using a binary Josephson system" Meas. Sci. Tech. Vol. 18, No. 11, September 2007, pp.3316-3320.
[4] I. Giem, "Sub-ppm linearity testing of a DMM using a Josephson junction array," IEEE Trans. Instrum. Meas., Vol. 40 No. 2, 1991pp. 329-332.
[5] R. Cerri, A. Sosso, P. P. Capra and L. Roncaglione, Programmable source for DC voltage ratio calibration of DVMs" 17th Int. Cong. Metrology, 12008 (2015).
[6] R. Cerri, A. Sosso, P. P. Capra "A low noise source for DC voltage ratio calibration of DVMs", in Prec. Elec. Conf. CPEM 2014, pp. 136–137.
[7] A. Sosso and R. Cerri, "Calibration of multimeters as Voltage Ratio Standards", in Prec. Elec. Conf. CPEM 2000, pp. 375–376.
[8] F. Galliana et al., "Automated precision DC voltage fixed ratios divider" Measurement 122, March 2018, pp. 291-296.
[9] F. Galliana et al, "Automated setup to accurately calibrate electrical dc voltage generators", Measurement 123, July 2018, pp. 1291-134.
[10] F. Galliana, R. Cerri, D. Corona, "Automatic DC voltage precision resistive divider with ratios between 10:1 and 10^7:1, Measurement 183 October 2021, pp:1-10.

25th IMEKO TC4 International Symposium
23rd International Workshop on ADC and DAC Modelling and Testing
IMEKO TC-4 2020
Brescia, Italy / September 12-14, 2022

Identification and Mitigation of Intermodulation Products Using a Baseband Polynomial Distortion Model with Instantaneous Frequency Dependence

Stanislas Dubois[1], Bruno Lelong[2], Jean-Michel Hodé[3], Guillaume Ferré[4], Dominique Dallet[5]

[1,4,5]*Univ. Bordeaux, Bordeaux INP, CNRS, IMS, UMR 5218, Talence (FRANCE), forename.name@ims-bordeaux.fr*
[1,2,3]*Thales DMS, Elancourt (FRANCE), forename.name@fr.thalesgroup.com*

***Abstract* – The linearization of active electronic components such as the PA or the ADC, is a vast subject. Many issues come into play, including behavioral modeling with the selection of a relevant model in terms of accuracy and complexity, the identification of this model, and the correction of defects by compensation. In this article, we propose a baseband model of non-linearity defects observed at the digitization output and after IQ demodulation, with a focus on order 3 intermodulation. We then introduce a refinement of this model by adding a dependence on the variation of the instantaneous frequency of the signal. We describe a method suitable for calibration of the model, by identification on a two-tone signal. We finally present a measurement bench adapted to the calibration of the coefficients of the model, followed by some results of linearization.**

I. INTRODUCTION

This paper deals with the baseband modeling of the distortion at the output of a high speed (2 GHz) and high resolution (14 bits) commercially available ADC. This ADC features IQ demodulation, filtering and decimation, making it possible to select and reduce the useful frequency band of the signal thus digitized. We will use these capabilities later, and we are therefore interested in modeling distortion defects on complex signals, at the digitization output and downstream processing stages of the ADC.

The objective is thus to propose a model on a complex analytical signal applicable at the output of the digitization chain (ADC, digital IQ amplitude/phase demodulation, and decimation) suitable for calibration and linearization. Although the targeted application is narrow band here, we propose to take into account the frequency dependence, analogous to a memory effect, with a view to versatility. Finally, these models aim to intervene at the end of the digital chain for practical reasons: limitation in flow due to decimation, and therefore in energy consumption, and ease of implementation. The targeted application of this work is indeed an embedded application. The models envisaged must then present a limited complexity, facilitating their identification and the implementation of the linearization.

In this paper, we propose an extension of a baseband polynomial model by involving the derivative of the sampled analytical signal, and thus by adding an instantaneous frequency dependence to our model. This writing thus makes it possible to model to a certain extent the variation of the non-linearity with the frequency. This method has been patented in 2015 [1].

This paper is organized as follows. We will first develop the distortion model on an analytical signal, and the instantaneous frequency dependence. Afterwards, the identification of these models will be studied, from spectral observations of the distortion of two-tone signals. We will then see a measurement bench allowing the calibration of our ADC, and finally results of identification and linearization by compensation.

II. MODELING

Any active analog or mixed system generates distortion spurs on its output. This is called a non-linear system. The simplest model allowing to illustrate this phenomenon is the polynomial model, or in series of powers, describing a non-linear distortion. A polynomial model links the real input $x(t)$ of a nonlinear system to its output $y(t)$ by the following relation:

$$y(t) = \sum_{n=0}^{N} a_n x^n(t) \approx x(t) + D\left[x(t)\right] = x(t) + \sum_{n=2}^{N} a_n x^n(t) \quad (1)$$

with N the order of non-linearity of the system, and the a_n the coefficients of the model. The 0th order coefficient is an offset ($a_0 \approx 0$), and the 1st order coefficient is the linear gain of the system ($a_1 \approx 1$). The nonlinear distortion is then contained in the higher order terms. This separation in the distorted signal between the input signal and a function (here D) of distortion depending on the input signal allows

a compensation of the defects by subtracting this part of distortion from the signal at the output of the system to be linearized.

A. *Baseband distortion modeling*

We find an expression for distortion defects on an analytical signal in [2, 3, 4]. This model is described in these papers as coming from the polynomial expansion of the complex envelope of an RF signal: $x_{RF}(t) = 2\Re\left[x(t)e^{j\omega_0 t}\right]$, where ω_0 is the pulse of the RF carrier frequency of the signal (using the notation of [2]).

Our distortion model is based on the Order 3 Volterra Base Band Series model, with no memory effect [4]:

$$\tilde{D}^{(3)}(x) = x\alpha\,|x|^2 \tag{2}$$

This model can be extended to the order $2N+1$ as follows:

$$\tilde{D}^{(2N+1)}(x) = x\sum_{k=1}^{N}\alpha_k|x|^{2k} \tag{3}$$

The model presented so far does not present a frequency dependence, i.e. it does not allow to model a memory effect, being a variation of the non-linear distortion as a function of frequency. This point will be dealt with in the next subsection.

B. *Adding and instataneous frequency dependence*

We here propose to add a dependence of the distortions on the instantaneous frequency of the signal. This instantaneous frequency will be noted f_i. It is expressed as follows for a sinusoidal signal of natural frequency f_0:

$$x(t) = ae^{j\psi(t)} \qquad \text{with } \psi(t) = 2\pi f_0 t + \phi \tag{4}$$

$$f_i(t) = \frac{1}{2\pi}\frac{\partial\psi(t)}{\partial t} = \frac{1}{2\pi}\frac{\partial}{\partial t}\left(2\pi f_0 t + \phi\right) = f_0 \tag{5}$$

The instantaneous frequency of a sinusoidal signal therefore corresponds to its natural frequency, the instantaneous frequency of a signal made up of two tones of the same level, to the average of the frequencies of the two tones.

We have,

$$\frac{x'}{x} = \frac{\frac{\partial x}{\partial t}}{x} = j\frac{a2\pi f e^{j(2\pi f_0 t+\phi)}}{ae^{j(2\pi f_0 t+\phi)}} = j2\pi f_0$$

Thus :

$$f_i(t) = \frac{1}{2\pi}\Im\left[\frac{x'}{x}\right] = \frac{1}{2\pi}\frac{\Im\left[x'x^*\right]}{|x|^2} \tag{6}$$

We therefore propose the following refinement to the 3rd order distortion model:

$$\tilde{D}_i^{(3)}(x) = x\left(\alpha + \beta f_i\right)|x|^2 \tag{7}$$

i.e.

$$\tilde{D}_i^{(3)}(x) = x\left[\alpha|x|^2 + \frac{1}{2\pi}\beta\Im\left(x'x^*\right)\right] \tag{8}$$

C. *Synoptic view in blocks of the model*

This model can be represented by a block diagram view (see Fig. 1). The differentiator filter is called h_D and its delay is written τ_D. It is compensated on the other channels so that the following operations are synchronous. We can also see here linearization by compensation, by reconstructing the distortions from the input signal and then subtracting them from the signal. This point will be discussed in section v..

III. IDENTIFICATION

The identification of this model is done here from frequency observations of a well-known two-tone CW (Continuous Wave) signal, i.e. whose frequencies are known. The frequency identification of this model follows the work of [5]. This method is suitable for a model calibration phase.

A. *Two-tone reference signal*

In this paper, we will focus on the response of a commercially available ADC to the excitation of a two-tone signal. This signal used for the calibration of the model, indeed makes it possible to reveal the defects which interest us here, namely the near-carrier inter-modulation. A two-tone signal also has several interesting advantages, an ease in the practical implementation of its generation, and a good coverage of the phase space allowing the excitation of the full dynamic range of the ADC [6, 7, 8, 9].

For the calibration of the model, we look at the excitation of the ADC by a two-tone signal of the form:

$$x(t) = a_1e^{j2\pi f_1 t} + a_2e^{j2\pi f_2 t}$$

with a_1 and a_2 the complex amplitudes of the tones of frequencies f_1 and f_2 respectively.

B. *Identification of the model*

The response of our distortion model to the excitation of a two-tone signal develops as follows:

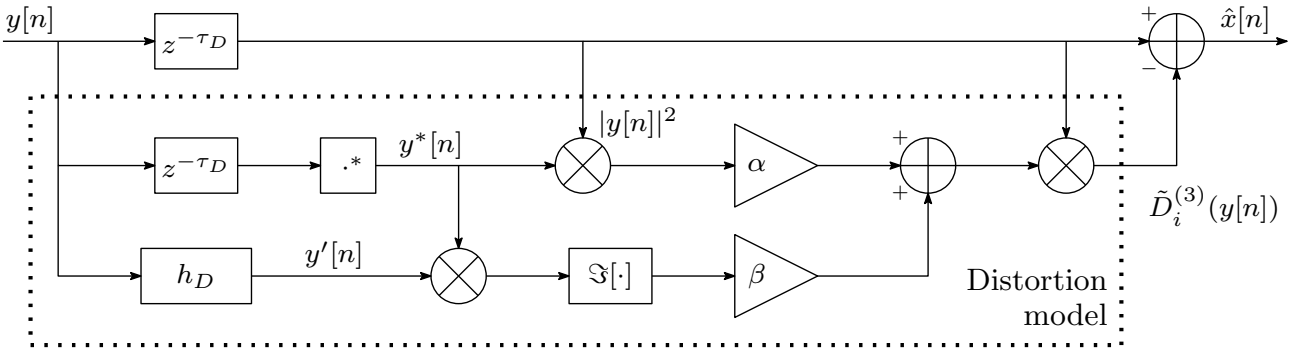

Fig. 1. Synoptic model (order 3 with instantaneous frequency dependence) of reconstruction of distortion and compensation

$$
\begin{aligned}
y(t) &= x(t) + \tilde{D}_i^{(3)}(x(t)) \\
&= x(t) + x(t)\left(\alpha + \beta f_i\right)|x(t)|^2 \\
&= a_1 e^{j2\pi f_1 t} + a_2 e^{j2\pi f_2 t} \\
&+ \left(\alpha + \beta f_i\right)\Big[\left(a_1^3 + 2a_2^2 a_1\right)e^{j2\pi f_1 t} \\
&\qquad + \left(a_2^3 + 2a_1 a_2\right)e^{j2\pi f_2 t} \\
&\qquad + a_1^2 a_2^* e^{j2\pi(2f_1 - f_2)t} \\
&\qquad + a_1^* a_2^2 e^{j2\pi(2f_2 - f_1)t}\Big]
\end{aligned}
$$

We then observe the following tones at the output of the ADC, and on the model (cf. Fig. 2).

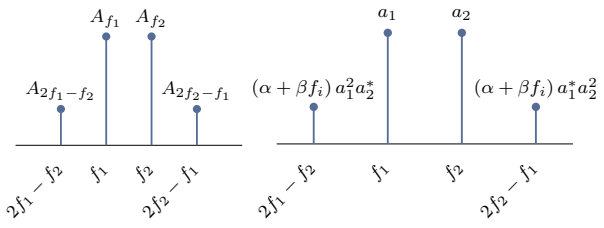

(a) ADC output *(b) Model expression*

Fig. 2. Model identification from spectral observation

For the identification of the coefficients α and β, we will use the results of two measurements, around the instantaneous frequencies f_{i_a} and f_{i_b}. These two frequencies will be chosen as the extremities of the band in which the ADC will be modeled.

In our case, the modeling will be performed in a band B of a few hundreds kHz to a few MHz, around the RF carrier f_0. So we will have $f_{i_a} = f_0 - \frac{B}{2}$ and $f_{i_b} = f_0 + \frac{B}{2}$.

We then have to solve the following system. The coefficients are obtained by averaging a redundant observation of the model:

$$
\left(\alpha + \beta f_{i_a}\right) = \frac{1}{2}\left[\frac{A_{2f_{1_a}-f_{2_a}}}{A_{f_{1_a}}^2 A_{f_{2_a}}^*} + \frac{A_{2f_{2_a}-f_{1_a}}}{A_{f_{2_a}}^2 A_{f_{1_a}}^*}\right] = R_a \quad (9)
$$

$$
\left(\alpha + \beta f_{i_b}\right) = \frac{1}{2}\left[\frac{A_{2f_{1_b}-f_{2_b}}}{A_{f_{1_b}}^2 A_{f_{2_b}}^*} + \frac{A_{2f_{2_b}-f_{1_b}}}{A_{f_{2_b}}^2 A_{f_{1_b}}^*}\right] = R_b \quad (10)
$$

This system then resolves to:

$$
\alpha = \frac{f_{i_a} R_b - f_{i_b} R_a}{f_{i_a} - f_{i_b}} \quad (11)
$$

$$
\beta = \frac{R_a - R_b}{f_{i_a} - f_{i_b}}; \quad (12)
$$

During this identification phase, the frequencies of the two tones being known, the instantaneous frequencies f_{i_a} and f_{i_b} are obtained as follows:

$$
f_{i_a} = \frac{a_1^2 f_{1_a} + a_2^2 f_{2_a}}{a_1^2 + a_2^2} \quad (13)
$$

$$
f_{i_b} = \frac{a_1^2 f_{1_b} + a_2^2 f_{2_b}}{a_1^2 + a_2^2} \quad (14)
$$

with f_{1_a} and f_{2_a} the frequencies of the two-tones of the first measurement, around f_{i_a}, and f_{1_b} and f_{2_b} the frequencies of the two-tones of the second measurement, around of f_{i_b}.

IV. EXPERIMENTAL SETUP

To validate the theoretical concepts developed in the previous sections, we build the following experimental setup (see Fig. 3).

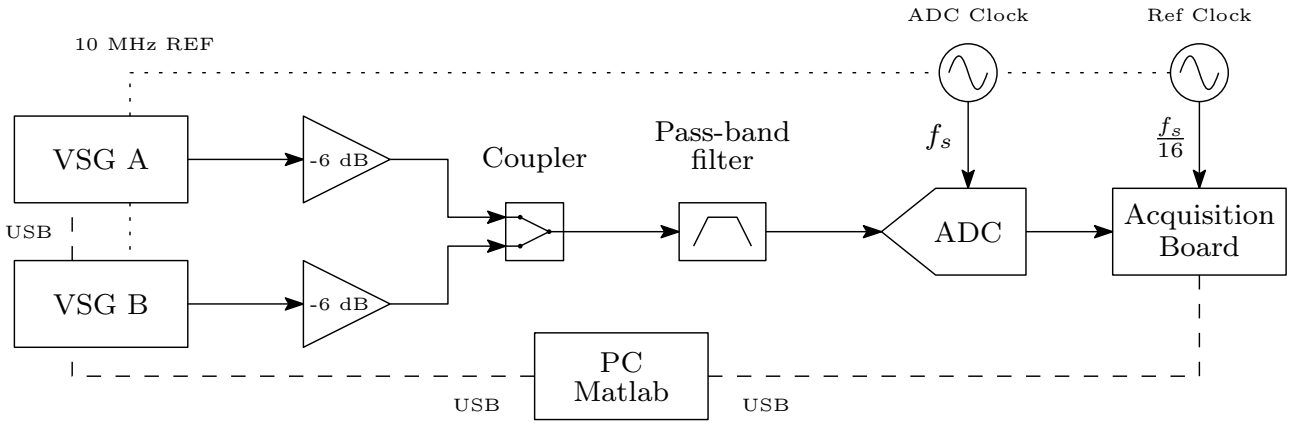

Fig. 3. Experimental setup synoptic

The two-tone signal used as a reference for the calibration is generated by two vector signal generators (VSG A and VSG B). Each sends a CW signal, one at frequency f_1, and the other at frequency f_2, and the two-tone signal is then assembled by a coupler. This signal could be generated by only one of these instruments, but the linearity of the input signal would not be sufficient for the precision required by our measurements. The presence of attenuation in the assembly, between the VSGs and the coupler, also makes it possible to improve the linearity of the reference signal during calibration, by attenuating twice (due to the goings and comings routes), any bounces in the assembly.

A band-pass filter is then used to remove out-of-band noise that can fall back during digitization. Finally, the ADC studied is a commercially available ADC (AD9689, 14 bit, 2 Gsps), mounted on its acquisition card. The latter is used to configure the ADC and to recover the points captured at the PC level. Two clock generators are used, one for the ADC clock, and the other for the acquisition card reference clock, for data transfer.

The various measurement and generation instruments are controlled from MATLAB via USB. Finally, all the instruments share the same reference (10 MHz) which allows them to operate synchronously.

V. LINEARIZATION

We present in this section linearization results of an ADC using the model, the identification method, and the measurement bench, described in the previous sections.

To linearize the signal at the output of the ADC from the proposed model, the distortions are reconstructed from the distorted signal itself (cf. Fig. 1). Indeed, the signal is assumed to be weakly non-linear, that is to say that

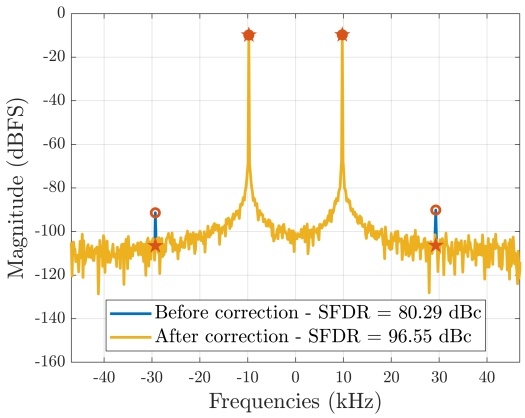

Fig. 4. Linearization results using model $\tilde{D}_i^{(3)}$ with fundamentals both at -10 dBFS

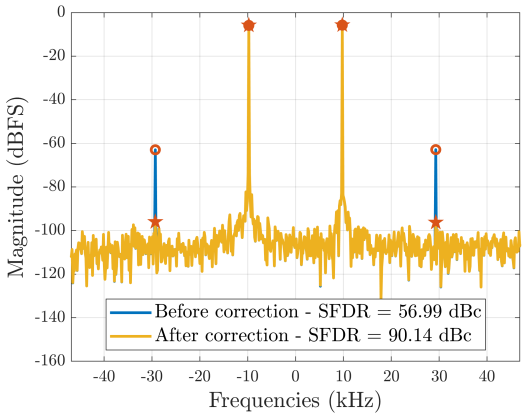

Fig. 5. Linearization results using model $\tilde{D}_i^{(3)}$ with fundamentals both at -6 dBFS

the parasitic spurs are at a sufficiently low level for their contribution in the reconstruction of the distortions to be

negligible.

We thus observe some linearization results in Fig. 4 and 5 using our 3rd order model with instantaneous frequency dependence. In these figures, the amplitudes of the fundamentals and of the IMD3 products are characterized by cirle markers on the signal before correction, and by stars on the signal after correction.

These figures demonstrate the effectiveness of the compensation with the proposed model. The SFDR (Spurious Free Dynamic Range) is indeed pushed to the noise floor (15 to 24 dB amelioration).

To illustrate the relevance and efficiency of the model depending on the instantaneous frequency, it is necessary to observe the variation of IMD3 (Order 3 intermodulation) in a frequency band. It is then necessary to calibrate the compensation model (here simply to order 3) and note that a simple coefficient α alone cannot translate a variation in frequency of the IMD3, i.e. a memory effect. The instantaneous frequency model is then calibrated on this same band, so as to reproduce this behaviour. The calibrated coefficients can be seen in Fig. 6 and the compensation results in Fig. 7.

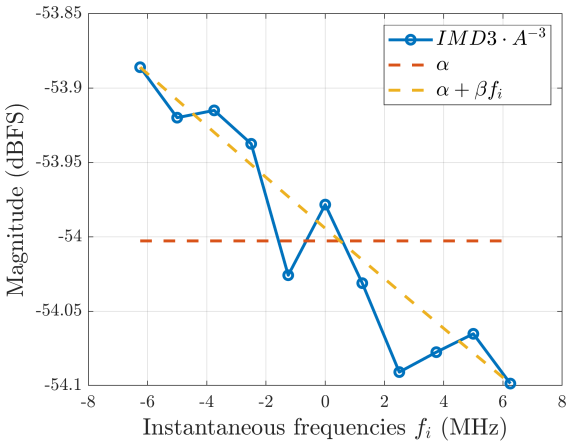

Fig. 6. Coefficients of order 3 compensation models. A is the magnitude of the fundamentals (assuming they are at the same level)

This model is limited here to a linear variation of the IMD3 as a function of the instantaneous frequency, which can be associated with a narrow band behaviour of the ADC. To model more complex behaviours of the IMD3 with regards to frequency, this model would then have to be extended to a polynomial frequency dependence.

We finally note that although the studied ADC presents

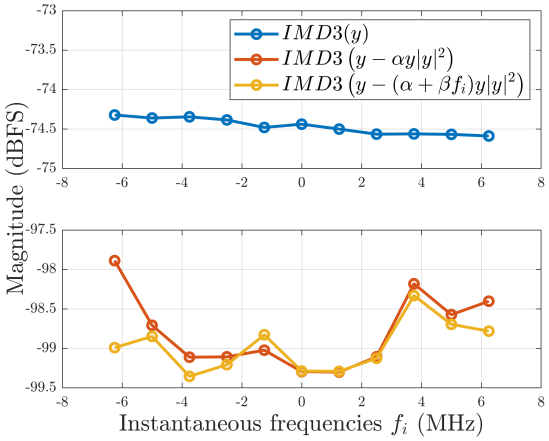

Fig. 7. Linearization results using order 3 compensation models with and without instantaneous frequency dependence

an IMD3 varying with the instantaneous frequency, this variation is here too weak in the studied band so that the gain brought by this new contribution is significant during the linearization (less than 1 dB of improvement compared to a simpler model without memory effect). This approach nevertheless seems promising for systems with more frequency dependence of nonlinearities, or for a study on a wider band.

VI. CONCLUSION

In this paper, we have presented a baseband distortion model, with an instantaneous frequency dependence, in order to model a nonlinear frequency evolving behavior. A method for identifying this model, based on a frequency observation of the application of a two-tone signal, is then presented. We finally built a measurement bench adapted to the implementation of the identification of this model.

The results of modeling and linearization present effective mitigation of intermodulation products. The frequency variation of the distortion is modeled by the instantaneous frequency (f_i) dependence.

When trying to improve the accuracy of the modeling or identifying models going to higher orders, in order to acount for higher order intermodulation products, limiting dynamic range, it quickly appears crucial to get out of the noise floor. Indeed, the higher the distortion order observed, the lower the amplitude of the intermodulation products will be, approaching the noise floor. The solution is then to observe on longer time intervals, in order to integrate this measurement noise and to make the noise floor go down spectrally.

To go further, the model with a dependence in instantaneous frequency could be studied for signals more complex than a two-tone signal, not allowing to lift the correlation of the model on a single measurement. One could be inspired by the identification of Volterra kernels from white noise [10].

Finally, the model presented has certain limitations inherent in its structure. A distortion model going to order 3 with a simple instantaneous frequency dependence is in fact only able to model defects that vary linearly with the level, and with the instantaneous frequency. This model is therefore initially suitable for narrow-band modeling of components with relatively basic behavior. Subsequently, a wider-bandwidth behavior can be modeled by a polynomial variation of the instantaneous frequency. Similarly, identifying a model at higher orders of non-linearities can also allow modeling of a polynomial variation of the intermodulation with respect to the level.

REFERENCES

[1] J-M. Hodé. "Method for Correcting Intermodulation Errors of a Conversion Circuit". EP3235137. 2015.

[2] M. Grimm et al. "Joint Mitigation of Nonlinear RF and Baseband Distortions in Wideband Direct-Conversion Receivers". In: *IEEE Transactions on Microwave Theory and Techniques* 62.1 (2014).

[3] E. Ward and B. Mulgrew. "Baseband Equivalent Volterra Series for Modelling Cross-Channel Nonlinear Distortion". In: (2019).

[4] B. Fehri and S. Boumaiza. "Baseband Equivalent Volterra Series for Behavioral Modeling and Digital Predistortion of Power Amplifiers Driven With Wideband Carrier Aggregated Signals". In: *IEEE Transactions on Microwave Theory and Techniques* (2014).

[5] S. Dubois et al. "Frequency Identification of a Memory Polynomial Model for PA Modeling". In: *IEEE International Instrumentation and Measurement Technology Conference* (2022).

[6] P. S. Liam et al. "Performance Comparison of Various Multisine Excitation Signals in ADC Testing". In: *IEEE International Symposium on Electronic Design, Test and Application* (2011).

[7] C. L. Moneiro, P. Arpaia, and A. C. Serra. "Dual Tone Analysis for Phase-Plane Coverage in ADC Metrological Characterization". In: (2003).

[8] M. S. Ong et al. "Optimal Dual-Tone Frequency Selection for ADC Sine-Wave Tests". In: *IEEE Transactions on Instrumentation and Measurement* 60.5 (2011).

[9] J. J. Blair. "Selecting Test Frequencies for Two-Tone Phase-Plane Analysis of ADCs: Part II". In: *IEEE Transactions on Instrumentation and Measurement* 56.4 (2007).

[10] R. D. Nowak and B. D. Van Veen. "Random and Pseudorandom Inputs for Volterra Filter Identification". In: *IEEE Transactions on Signal Processing* 42.8 (1994).

25th IMEKO TC4 International Symposium
23rd International Workshop on ADC and DAC Modelling and Testing
IMEKO TC-4 2020
Brescia, Italy / September 12-14, 2022

Floating-Point Roundoff Error Analysis in Artificial Neural Networks

Hussein Al-Rikabi and Balázs Renczes

Department of Measurement and Information Systems
Budapest University of Technology and Economics
Budapest, Hungary

***Abstract* – In this paper, roundoff errors in Artificial Neural Networks (ANNs) are analyzed on a model for Solid-State Power Amplifiers (SSPAs). Calculations are carried out on 32-bit Floating-Point (FP32) arithmetics, and results are verified using 64-bit floating-point representation as reference. Besides the modeling of quantization noise at every operation, error propagation is also taken into consideration when calculating the cumulative Quantization Noise Power (QNP) after each stage and at the final output. By this means, the predictability of roundoff errors in the ANN is demonstrated. Consequently, it can be determined whether the FP32 arithmetic is sufficient instead of applying the computationally more demanding 64-bit calculations.**

***Keywords* – Artificial Neural Networks, Quantization Noise, Floating-Point Number Representation, Solid-State Power Amplifier.**

I. INTRODUCTION

Over the last decades, the evolution of deep learning algorithms has been noticeable, as they have been used in various applications, starting with video processing, voice enhancement, and generally in digital signal processing [1]. Recently, improving the performance of Artificial Neural Networks (ANNs) has been an essential scope of research. The main parameters to investigate are size, speed, performance, and power consumption of the ANN architectures as they have been used extensively in current applications [2]. Using a finite number of bits to represent the data and the coefficients is called quantization. The quantization of ANNs has been an important scope of study recently as this technique is widely used in large models and systems such as artificial intelligence chips. The quantization process of weights, biases, and operations in ANNs significantly reduces the storage size of the system. Furthermore, the reduction in the number of bits can also substantially accelerate the ANNs [1]. In this paper, a nonlinear model of Solid-State Power Amplifiers (SSPAs) is used as an example for the proposed analysis to predict its behavior using ANNs. SSPAs have been used in a variety of applications recently, especially in mobile communication systems, due to their small size and low phase distortion [3].

There have been similar studies in the literature that are summarized in the following part. Nichols et al. [4] studied the feasibility of using the 32-bit Floating-Point (FP32) format for ANNs on Field Programmable Gate Arrays (FPGAs), and they compared this representation with the 16-bit fixed-point representation. They showed that the FP32 arithmetic makes the system thirteen times bigger in size than the 16-bit fixed-point format; hence it would be area consuming for the hardware implementations. Lian et al. [5] presented an implementation of a Convolutional neural network (CNN) accelerator on an FPGA device with Block Floating-Point (BFP) arithmetic. They mixed the 16-bit Floating-Point (FP16) and the FP32 formats in their architecture. They showed that the BFP can efficiently reduce the size, signal traffic, and hence energy as this method provided all these merits with only 0.12% accuracy loss. Peric et al. [6] have made a comparison between 32-bit fixed-point and FP32 representations in terms of quantization noise and signal to noise ratio. They concluded that the accuracy of the floating-point quantizer is the same as that of the fixed-point quantizer.

In this study, our contribution is to investigate the effect of FP32 quantization on ANNs theoretically. This means that we do not compare experimental results, but the QNP is predicted in advance without launching the network structure. For the investigation, an example of an SSPA model is used in this paper. The analysis includes a comparison between theoretical and simulated results. Simulations were carried out using MATLAB 2021b. The remainder of this paper is organized as follows. Fundamental concepts about the investigated structures are presented in Section II, including ANNs and SSPAs. Section III gives a background on the IEEE floating-point standard and the quantization noise. Simulation results and the discussion are presented in Section IV, while Section V concludes the paper.

II. INVESTIGATED STRUCTURES

This section presents a theoretical overview of the ANNs and the SSPAs.

A. *Artificial Neural Networks*

ANNs have been used for many applications recently. It is important to implement them with a small size, complexity, and with low energy while maintaining acceptable performance. ANNs are effective tools for tackling complex nonlinear problems and identifying universal input-output mappings. An ANN consists of inputs, outputs, and hidden layers. Each link between two neurons, or between an input and a neuron, has its own weight. Furthermore, each neuron has its own bias. Weights are considered through multiplication, while biases are added to the sum of input-weight products [7]. An activation function is applied to the summation result in each neuron. Nonlinear activation functions are essential in artificial neural networks because they allow them to learn complex mappings between their inputs and outputs [8].

The accuracy of the ANN is determined by the weights and biases established throughout the training phase. Fig. 1 depicts a simplified ANN architecture [7].

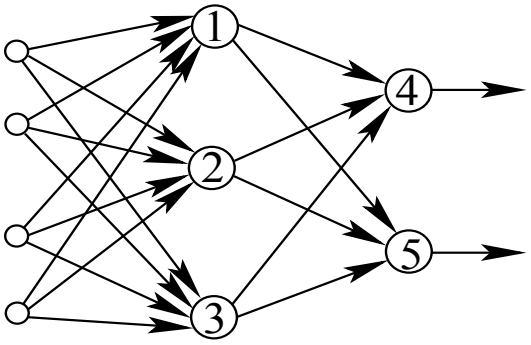

Fig. 1. A basic ANN architecture [7].

B. *Solid-State Power Amplifier Model*

High Power Amplifiers (HPAs) are utilized in mobile communications and base stations to transmit suitable power levels. The performance of Orthogonal Frequency-Division Multiplexing (OFDM) systems is greatly influenced by HPA nonlinearities [9]. Traveling-Wave Tube Amplifiers (TWTAs) and SSPAs are the two most prevalent types of HPAs. In this study, SSPA is preferred since the phase distortion of typical SSPAs is significantly smaller than that of TWTAs. The SSPA model can be described as follows [9]:

$$F_A(x) = \frac{x}{\left[1 + (x/A_o)^{2p}\right]^{-2p}}, \tag{1}$$

where $F_A(x)$ is the output of the SSPA, x is the SSPA input, p is the smoothness from the linear region to the saturation region and A_o is the output maximum saturation level.

III. BACKGROUND OF THE ERROR ANALYSIS

A basic overview of floating-point number representation systems, and modeling of quantization noise in these systems will be presented in this section.

A. *IEEE floating-point Standard*

Computer manufacturers utilized incompatible floating-point representations for a long time. The output of one computer could not be directly translated by another. The IEEE 754 Floating-Point Standard, which defines floating-point numbers, was created in 1985 by the Institute of Electrical and Electronics Engineers (IEEE). This is the floating-point format that is described in this section because it is now nearly universally used [10].

The IEEE 754 Standard defines the FP32 representation [11]. It uses one bit for the sign s, 8 bits for the exponent e, and 23 bits for the mantissa m. The first bit of the mantissa (to the left of the binary point) is always 1 in floating-point and hence does not need to be stored. It's referred to as the implied leading one. Round down, round up, round toward zero, and round to nearest are the four rounding modes. Round to nearest is the default rounding mode [10].

This format is also called full-precision, contrary to the FP16 format, which is referred to as half-precision. The FP32 representation is also known as single precision compared to the double precision, which is the 64-bit Floating-Point (FP64) format. The bitmap of the FP32 representation is illustrated in Fig. 2.

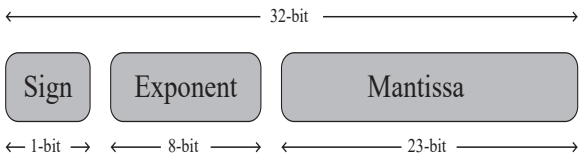

Fig. 2. Bitmap of the FP32 representation.

Based on the binary number system, the FP32 format represents a real number x as follows [6]:

$$x = (-1)^s \cdot 2^e \cdot \left(1 + \frac{m}{2^{23}}\right). \tag{2}$$

In this case, the exponent e and the mantissa m can have values in the following ranges:

$$e \in \{-128, -127, \ldots, -1, 0, 1, \ldots, 126, 127\}, \tag{3}$$

$$m \in \{0, \ldots, 2^{23} - 1\}. \tag{4}$$

Similar to the fixed-point 32-bit representation, the single precision, which is the FP32 representation gives discrete values. However, the difference is that the FP32 representation has variable step size. A smaller step size makes the FP32 representation very efficient to represent small values, while a large step size makes the presentable range wide [6].

B. Floating-Point Quantization Noise

Scientists mostly overlook roundoff errors in computations because of the success of the IEEE double precision standard. We usually expect that a simple personal computer's precision is infinite. However, roundoff errors can readily ruin a calculation's outcome, even if it appears fair. As a result, even with IEEE double precision representation, it is worthwhile to investigate them.

Using floating-point numbers to represent physical quantities enables a vast dynamic range to be covered with a small number of digits. Roundoff errors are usually proportional to the amplitude of the depicted quantity when using this type of representation. In most applications, floating-point representation is better than fixed-point representation from a point of numerical accuracy. The adoption of floating-point numbers is speeding up as the speed of floating-point calculations improves and the cost of implementation decreases. As a result, having a modeling approach for the propagation of Quantization Noise Power (QNP) is needed to simulate or predict the accuracy of the applied implementations.

The difference between the quantizer output (x') and input (x) is the roundoff error of the floating-point quantizer v_{FL}, which is represented by the following equation [12]:

$$v_{\mathrm{FL}} = x' - x. \tag{5}$$

An approximation has been derived in [12] to calculate the QNP, and it is demonstrated by the following equation:

$$E\{v_{\mathrm{FL}}^2\} = 0.18 \cdot 2^{-2p} \cdot E\{x^2\}, \tag{6}$$

where $E\{x^2\}$ is the expected value of the quantizer input power, and p is the number of mantissa bits plus the hidden bit, which in total is 24 bits for FP32 format. When the mantissa is 16 bits or more, the QNP is given by (6); otherwise, the following theoretical bounds present it [12]:

$$\frac{1}{12} \cdot 2^{-2p} \cdot E\{x^2\} \leq E\{v_{\mathrm{FL}}^2\} \leq \frac{1}{3} \cdot 2^{-2p} \cdot E\{x^2\} \tag{7}$$

IV. SIMULATION RESULTS AND DISCUSSION

A small ANN was trained and built in simulation that has one input, one output, and one hidden layer with three neurons. Hyperbolic Tangent Sigmoid (TanSig) activation function has been used in the proposed analysis. The SSPA model of (1) has been built using an ANN for prediction application. The practical range and values for the SSPA considered in this study are [0,1] for x, 0.8 for p, and 1 for A_o.

An FP32 quantizer was used for each operation and for the input of the ANN. The double precision floating-point format was assumed to be the reference to our calculations and simulations. The quantization of the weights and the biases is not included in this study as all of them have been set to FP32 representation. By this means, we can obtain the actual roundoff error during each operation. Coefficient quantization is a subject of further investigation.

Table 1. Propagation of error formulas.

Function	Variance
$F = A + constant$	$\sigma_F^2 = \sigma_A^2$
$F = A \cdot constant$	$\sigma_F^2 = constant^2 \cdot \sigma_A^2$
$F = e^A$	$\sigma_F^2 = F^2 \cdot \sigma_A^2$
$F = \frac{1}{A}$	$\sigma_F^2 = F^2 \cdot (\sigma_A^2 / A^2)$

Table 2. QNP after each quantizer taking the error propagated from previous operations into consideration.

No.	Designator	Theoretical	Simulation
1	Input	2.13E-16	1.69E-16
2	m1	5.21E-16	4.72E-16
3	m2	2.42E-16	2.21E-16
4	m3	3.84E-15	3.54E-15
5	s1	6.00E-16	6.41E-16
6	s2	9.03E-16	1.20E-15
7	s3	1.22E-14	1.71E-14
8	Ag1	2.40E-15	2.56E-15
9	Ag2	3.61e-15	4.82E-15
10	Ag3	4.87e-14	6.85E-14
11	Ae1	1.13E-14	2.30E-14
12	Ae2	1.14E-16	8.82E-17
13	Ae3	2.03E-06	5.89E-06
14	As1	1.64E-14	2.98E-14
15	As2	9.63E-16	1.33E-15
16	As3	2.05E-06	5.89E-06
17	Ar1	5.61E-16	4.39E-16
18	Ar2	1.04E-15	1.06E-15
19	Ar3	1.36E-18	5.77E-19
20	Agg1	2.24E-15	1.76E-15
21	Agg2	4.16E-15	4.25E-15
22	Agg3	5.42E-18	2.31E-18
23	Af1	2.31E-15	1.82E-15
24	Af2	4.52E-15	4.25E-15
25	Af3	6.37E-16	2.97E-16
26	mm1	5.83E-17	4.64E-17
27	mm2	3.11E-14	2.97E-14
28	mm3	9.31E-16	5.14E-16
29	ss	3.27E-14	3.12E-14
30	y	3.29E-14	3.12E-14

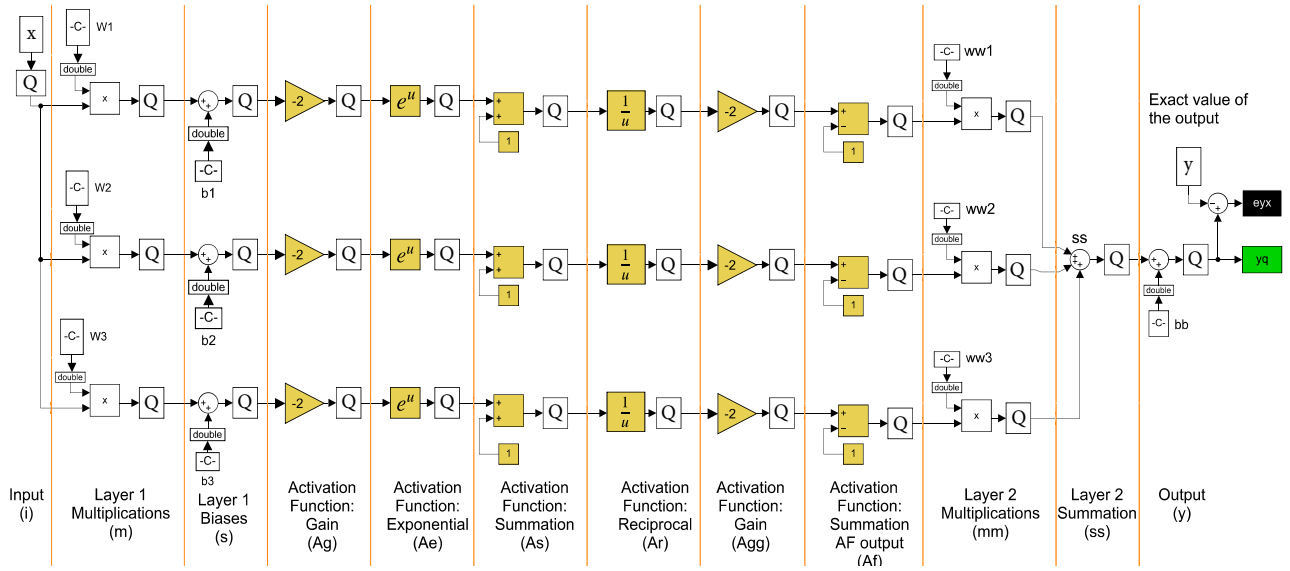

Fig. 3. Block diagram of the SSPA ANN model including the quantizers.

For statistical calculations, 10000 samples were injected into the ANN that spread in the range [0,1]. Fig. 3 shows the ANN architecture including the quantizers denoted by the letter Q that are placed after each operation.

TanSig activation function have been used for each neuron in the ANN. The QNP was calculated for each quantizer, using (6), and added to the propagated QNP from previous operations. The variances, which apply for the QNP, of the error transformation through a function are presented in Table 1. Table 2 shows the cumulative QNP after each operation.

The QNP was also calculated in the simulation by finding the difference between the input and the output of each quantizer. The QNP propagates through stages, and it can increase or decrease according to the operation. If the operation is, for example, a division or a reciprocal, the QNP will decrease while it increases if the operation is a summation or a multiplication operation. The same designator abbreviations were used in Table 2 and in Fig. 3.

For the inserted inputs, the QNP of each quantizer has been investigated considering the bounds of (7). The investigation showed that every QNP value was in the theoretically given range. However, due to the limits of this paper, these results are not presented in detail. The quantizer stages Ag and Agg have zero QNP because the input values are already quantized and a multiplication by two of a quantized number introduces no extra quantization error by this operation quantizer. But the increase that can be seen from Table 2 is caused by a multiplication of the QNP from previous stages by a constant according to the second function in Table 1.

The total QNP values of the model have been calculated theoretically and in simulation. They are 3.29E-14 and 3.12E-14, respectively. The theoretical QNP at the output of the ANN using the FP64 format is 1.14E-31. This small value indicates that the FP64 format is a valid choice to be considered as a reference. Since the theoretical and actual values are really close to each other, the acquired results show the effectiveness of the presented method. Furthermore, it can be seen that these errors are sufficiently small so that the FP32 arithmetics can be used instead of an FP64 arithmetics. By this means, the cost and size of implementation can be decreased significantly, as it was highlighted in Section I.

V. CONCLUSION

Analysis of the 32-bit Floating-Point (FP32) quantization in an Artificial Neural Network (ANN) has been presented in this study taking the double precision floating-point representation as a reference. The ANN have been trained to model a Solid-State Power Amplifier (SSPA) as a practical example. The Quantization Noise Power (QNP) after each operation was calculated theoretically and in simulation.

It can also be concluded that when the QNP propagates through the different stages of the ANN, it can increase or decrease. We encountered two cases when it increased: the exponential and the multiplication operations. It can also decrease when multiplying by a number smaller than one or when it is a reciprocal operation.

Results show that the presented method is effective in giving an estimation of the error that would be generated when using the FP32 quantization. The total error calculated for the presented example is small compared to

the data values. Therefore, using half the number of bits, the FP32 representation, for such small ANNs is a valid choice.

VI. ACKNOWLEDGMENT

This research was funded by the National Research, Development, and Innovation Fund of Hungary under Grant TKP2021-EGA-02.

REFERENCES

[1] M. Kiyama, Y. Nakahara, M. Amagasaki, M. Iida, "A quantized neural network library for proper implementation of hardware emulation", 2019 Seventh International Symposium on Computing and Networking Workshops (CANDARW), 2019, pp.136-140.

[2] A. Gholami, S. Kim, Z. Dong, Z. Yao, M. W. Mahoney, K. Keutzer,"A survey of quantization methods for efficient neural network inference", arXiv preprint arXiv:2103.13630, 2021.

[3] F. Gregorio, T. Laakso, "The performance of OFDM-SDMA systems with power amplifier non-linearities", Proceeding of the 2005 Finnish Signal Processing Symposium-FINSIG, vol.5, 2005.

[4] K. R. Nichols, M. A. Moussa, S. M. Areibi, "Feasibility of floating-point arithmetic in FPGA based artificial neural networks", In CAINE Conference, 2002.

[5] X. Lian, Z. Liu, Z. Song, J. Dai, and W. Zhou, X. Ji, "High-performance FPGA-based CNN accelerator with block-floating-point arithmetic", IEEE Transactions on Very Large Scale Integration (VLSI) Systems, vol.27, No.8, 2019, pp.1874-1885.

[6] Z. Peric, M. Savic, M. Dincic, N. Vucic, D. Djosic, S. Milosavljevic, "Floating Point and Fixed Point 32-bits Quantizers for Quantization of Weights of Neural Networks", IEEE, 2021 12th International Symposium on Advanced Topics in Electrical Engineering (ATEE), 2021, pp.1-4.

[7] K. Du, M. Swamy, "Neural Networks and Statistical Learning", 2nd edition, Springer, London, 2019.

[8] I.A.D. Williamson, T. W. Hughes, M. Minkov, B. Bartlett, S. Pai, S. Fan, "Reprogrammable Electro-Optic Nonlinear Activation Functions for Optical Neural Networks", IEEE Journal of Selected Topics in Quantum Electronics, vol.26, No.1, pp.1-12, Jan.-Feb. 2020.

[9] P. Gautam, P. Lohani, B. Mishra, "Peak-to-Average Power Ratio reduction in OFDM system using amplitude clipping", 2016 IEEE Region 10 Conference (TENCON), 2016, pp.1101-1104.

[10] D. Harris, S.L. Harris, "Digital design and computer architecture",Morgan Kaufmann, 2016.

[11] "IEEE Standard for Floating-Point Arithmetic", IEEE Std 754, 2019.

[12] B. Widrow, I. Kollár, "Quantization Noise: Roundoff Error in Digital Computation, Signal Processing, Control, and Communications", Cambridge University Press, Cambridge, 2008.

25th IMEKO TC4 International Symposium
23rd International Workshop on ADC and DAC Modelling and Testing
IMEKO TC-4 2022
Brescia, Italy / September 12-14, 2022

Engine rotational speed estimation using audio recordings and machine learning algorithms

Cristian Fosalau[1], George Maties[1], Cristian Zet[1]

[1] *"Gheorghe Asachi" Technical University of Iasi, Romania, cfosalau@tuiasi.ro*

***Abstract* – There are many situations in practice when the value of the rotational speed of an engine is needed to be known and a direct instrument for measuring it is not available or, if present, it is decalibrated. One can use instead a non-contact method for estimating the speed. The paper presents such a non-contact method for estimating the rotational speed of a heat engine based on audio recordings and machine learning algorithms. The method principle, experimental validation and a discussion upon the optimal parameters and factors that lead to the best performances are presented.**

I. INTRODUCTION

In the automotive industry, measuring engine speed is essential both in operation and in troubleshooting and maintenance process. There are numerous methods of measuring engine speed in the automotive industry, presented both as a principle in the literature and as functional commercially available devices mounted on cars. The basic principles on which analog and digital tachometers operates, based on either electrical, magnetic, or optical methods, are well known [1-4]. These devices require coupling to the motor shaft and are most often mounted into the car gearbox. There are also non-contact solutions for measuring the engine speed, based on the analysis of engine vibration [5], on the electrical noise produced by the spark plug during ignition over the battery voltage [6], or on various digital image processing methods applied to video recordings over rotating elements [7]. An interesting method of analyzing the automotive engine sound is depicted in [8]. It uses a deterministic - stochastic signal decomposition approach through which the quality of the engine sound may be assessed and then synthesized according to the customer needs and claims. In this approach, the deterministic component of the audio signal is extracted using the synchronous discrete Fourier transform, whereas the stochastic one is modeled using a new suboptimal multipulse excitation approach. A similar approach is discussed in [9], in which sound and vibration measurements are utilized to estimate journal bearing performances of electric motors. In this research, 1/3 octave band analysis techniques are employed for training three unsupervised types of ML algorithms, namely Random Forest Classifier, k-Nearest Neighbours Classifier and Gradient Boosting Regressor. It was proved in the paper that the best results are obtained using sound and z acceleration sets of data for the KNN algorithm, thus obtaining an accuracy of 98 %.

The present paper aims to describe a new method of measuring / classifying the speed values of the heat engine of a car based on processing the sound waveform recordings of the engine using machine learning (ML) algorithms. The method is presented only as a principle in order to provide a very simple solution for estimating engine speed, being useful if the vehicle's tachometer is defective or decalibrated, but it can also be successfully used to determine the speed of any moving element in rotation which produces a characteristic sound whose features are related to speed.

II. METHOD PRESENTATION

In this section, the main steps of the method along with the operations to be performed in each step are presented. Fig. 1 shows schematically the steps to be accomplished for practically implementing the method.

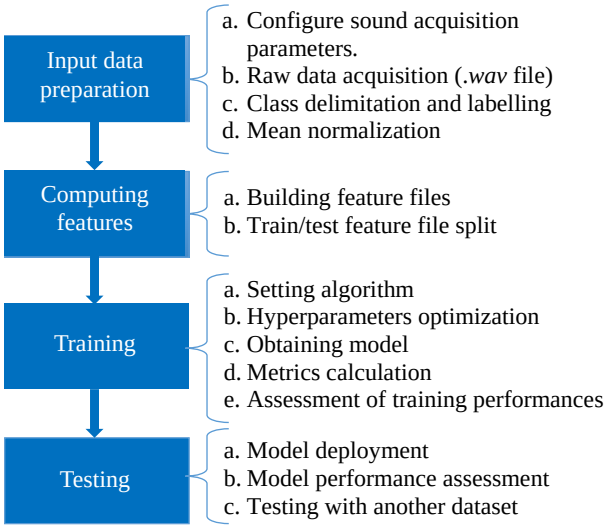

Fig. 1. Main steps of the method dataflow

A. Input data preparation

The preparation of the training set, as well as the test set, is a very important task because the success of the

experiment essentially depends on this stage. The recording of the sound produced by the engine is carried out with the help of a mobile phone that is equipped with a built-in sound acquisition hardware system. Recording is done either with the phone's default software or with a sound recording application downloaded from specific application market. It is important to specify that the application be able to record sound continuously, as any delay in recording process causes desynchronization between the timeline and the sound track.

a) *Configure sound acquisition parameters*. This operation consists of setting the resolution, sample rate, number of channels and bitrate in the application chosen for sound recording. It is advisable that the recording is done with a high sampling rate, but not very high because it is directly related to delaying the processing time.

b) *Raw data acquisition.* The sound is recorded at a distance of 1 m from the engine in operation, in two situations: with the hood open and the hood closed. The records are saved in *.wav* format. There are accomplished N_1 records with the hood open and N_2 records with the hood closed, with a mobile phone, for a speed range between idle speed (800 rpm) and 3200 rpm when the engine speed is increased progressively between these two limits and then decreased. Speed recordings in the increasing sense are used for building the training dataset whereas those corresponding to the decreasing slope are for building the testing dataset.

The synchronization of the speed values with the engine sound can be done by video recording of the car's tachometer with a second phone and processing of the two tracks using a common video processing software for delimiting the classes (VideoPAD Editor for example). In this case, the car's tachometer is the only measurement instrument in this approach, all other results being estimations of the measured quantity. A second more precise solution achieves synchronization by using a specialized device for reading the parameters of the car such as an OBDII, manufactured by ELM Electronics, which is plugged into the dedicated Data Link Connector of the car. Using this solution, the speed values are recorded at a sample rate of 10 samples / s, but precise synchronization of the OBDII start-up time and sound recording are still required. It must be noted here that the accuracy of angular speed measurement using an OBDII device is less than 2 %, as reported by the manufacturer, whereas the tachometer precision is not better than 5 %. However, this solution was chosen for simplicity as it does not require specialized devices.

c) *Class delimitation and labeling*. The delimitation of classes is achieved with the help of video graphics processing software, according to which the moments of time in which the tachometer indicates a certain speed is demarcated. It should be noted here that a very precise delimitation of the speed values is not necessarily to be done, the indications of the car's tachometer being sufficient with an accuracy up to 5%. The *.wav* files corresponding to the classes are thus converted to spreadsheet data files containing the sample values.

d) *Mean normalization*. In order to make the amplitudes of all the records comparable, the data strings are normalized according to the formula:

$$s_{in} = \frac{s_i - \mu}{S_{max} - S_{min}} \quad (1)$$

where s_{in} is the i-th normalized sample, μ is the mean of the class module and S_{max} and S_{min} are the maximum and minimum values of the record.

B. Computing features

The second step is to prepare the feature files for both training and testing. The feature file is built for each of the N_1 + N_2 waveform recordings, after which they are concatenated to form a compound feature dataset. It should be noted from the beginning that, due to numerous mechanical components of the motor the emitted sound depends on, such a sound waveform is very complex, containing a lot of time varying frequencies, as well as multiple influence factors that cannot be neglected. In the second section, a sample of such as waveform will be depicted and discussed.

Within a recording represented by a *.wav* file, for each feature class, a comma separated value (csv) file is built. This file will be used for training / testing the ML algorithm. The construction of the features is based on a series of statistical parameters calculated on batches that are cut from the spectrum of the signal corresponding to each class. Fig.2 schematically describes the process of feature computing algorithm.

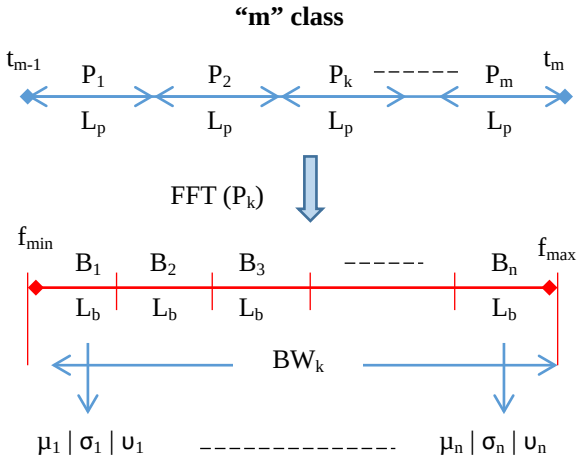

Fig.2. Schematic of feature computing algorithm

The file representing the "m" labeled class is divided into N_m packets of length L_P, which is one of the feature computing parameters and which is common to all classes. For each packet the signal spectrum is calculated by applying a windowed Fast Fourier Transform (FFT). The Flat-Top window was chosen for this due to its property to provide the best amplitude accuracy. A frequency band comprised between f_{min} and f_{max}, BW_k, is cut from the spectrum. Each BW_k is divided into a number of batches, N_{bk} of equal lengths, L_{bk}. Hence, each batch B_k represents a sub-band within BW_k so that

$$BW_k = N_{bk} L_{bk} \tag{2}$$

Next, the statistical parameters mean (μ), standard deviation (σ) and variance (υ) are calculated for each batch, obtaining the k-th feature line in the "m" class feature file. The files thus obtained for each record are concatenated to form the *general feature file*. The final operation in the feature computing stage consists in splitting the general feature file in training and testing datasets (usually the training is assigned to increasing speed whereas the second part of the feature file, corresponding to decreasing speed, is assigned for testing the speed estimator). From the training set, 20% is assigned to cross validation operation devoted to optimizing the hyperparameters of the training ML algorithm.

C. Model training

To obtain the ML model, three well-known algorithms were included for analysis, namely Support Vector Machine (SVM), Neural Network (NN) and Logistic Regression (LR). A comparison was made between the performances offered by them in various conditions and different values of their training parameters.

Table 1 lists the variables that accompany the training model operation. The hyperparameters specific to every algorithm are optimized using the *grid exhaustive search algorithm*, in which a series of manually set values for hyperparameters are scanned successively, and their performances are compared to minimize the training accuracy using cross validation method. The optimization algorithm uses for cross validation 20% of each training class.

Table 1. Feature parameters and hyperparameters for ML algorithms

Algorithm	**Feature parameters**	**Hyperparameters**
SVM	Building class: # of classes, f_{min}, f_{max}, BW, L_P, N_b Statistical: μ, σ, υ	SMT type, Kernel type, c, nu, degree, γ, C_0.
NN		# of hidden neurons, hidden layer type, output layer type, cost function type.
LR		tolerance, max iteration.

After optimizing the hyperparameters and training the algorithm, the model is obtained in .json format, for which the metrics are determined and the performance is evaluated on the testing dataset.

D. Model testing

The model testing is completed in two ways:

a) On the test datasets built together with the training datasets from the same *.wav* records, defined as supervised testing records with known class labels. In this case, the model deployment for testing is accomplished for every feature dataset built using initially acquired waveforms. For each dataset, the accuracy is calculated after which the average is assessed. A discussion is, however, performed according to special conditions such as open or closed hood.

b) Live testing with datasets acquired and processed on-line and in real time. For testing in live conditions, an appropriate software was built in LabVIEW which performs in real time the following chain of tasks: sound acquisition - building feature set - model deployment - class estimation - accuracy computing. This test is unsupervised as the class labels are not known a priori, but only the result indication.

III. EXPERIMENTAL VALIDATION

To experimentally validate the method, a number of 10 recordings in *.wav* files were acquired with a mobile phone placed 1 meter from the engine running, 5 with the hood open and other 5 with the hood closed. The recordings have been accomplished with a Samsung Galaxy A52 smart phone using the built-in sound recording application on the engine of an Opel Crossland car, 3 cylinders, 1.2 dm^3 volume, gasoline. The sound acquisition parameters were: sample rate 44100 sample / second, 2 channels, bit rate 256 kbit / s, resolution 16 bits. The recordings were made during approx. 8 minutes, 4 minutes in increasing speed between 800 and 3200 rpm, and 4 minutes when the speed decreases. The speed increase and decrease were approximately linear. Each *.wav* file was divided into 12 classes labeled 1, 2, 3,…, 12, for which the range 800 - 3200 rpm was divided into 12 segments, corresponding to a range of 200 rpm each segment.

Feature building, model training and model testing were carried out using the LabVIEW program and the Analytics and Machine Learning toolkit that is endowed with specific ML libraries and functions. In Fig. 3 is given a fragment of a sound recording containing raw data extracted from a *.wav* file within the range of a packet of 30,000 samples (0.68 s) and for the 3rd class, viz. for the interval of speeds from 1200 rpm to 1400 rpm. In Fig.4, the corresponding spectrum of the signal calculated for a bandwidth BW = 5000 Hz along with a detail up to 500 Hz is given, which represents the pattern for this packet. One may notice the richness of the

spectral components, even in the field of high frequencies.

Unfortunately, in the low frequency range, the spectrum is limited to about 30 Hz by the phone's microphone. This may be a serious source of errors as it makes the task of determining features more difficult because the range of fundamental frequencies for this kind of recorded sound is located in this band. Finally, the pattern is segmented in N_b batchs using rectangular windows.

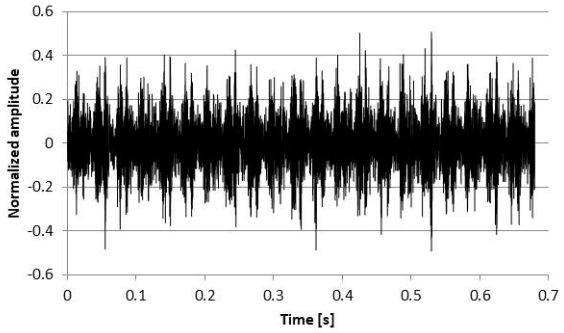

Fig. 3. A fragment of raw data for the 3rd class

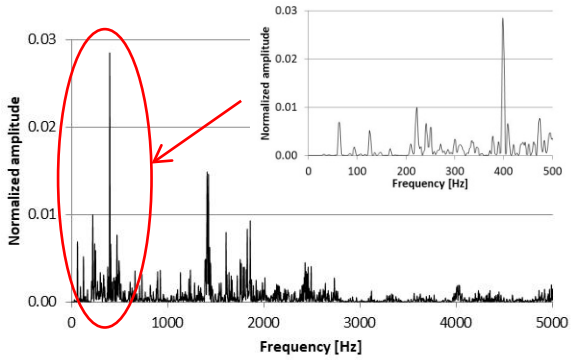

Fig.4. Example of a signal spectrum

It is known that in any ML application, setting the model features is the most important and difficult task because the success of the algorithm essentially depends on the ability to perform this action. It is, nevertheless, practically impossible to establish from the very beginning a set of features that provide maximum or optimal performance. The present paper aims to carry out a study upon the model performance when varying a series of parameters that define the training features.

These parameters are: ML algorithm type, L_P, N_b, f_{max} and the statistical parameters, μ, σ and υ employed, considering the hyperparameters for each algorithm already optimized using the grid exhaustive search method. The minimum frequency f_{min} was considered less than 30 Hz, having no influence over the bandwidth length, The metrics chosen for assessing the algorithm goodness is the accuracy, defined as:

$$Accuracy = \frac{TN + TP}{N} \tag{3}$$

where TN and TP represent the true negative and the true positive results respectively, and N is the total number of trials for a certain class. We tested also other metrics for assessing the performances of the algorithm such as precision, recall and F1-score, but very similar results were obtained and we retained for our reports only the accuracy, which is the most comprehensive and relevant. The frequency resolution *df* for a packet *k* of length L_{Pk} is calculated as:

$$df = \frac{sampling\ frequency}{L_{pk}} \tag{4}$$

IV. RESULTS AND DISCUSSION

There were performed a large number of trials (training and test) in order to draw a conclusion regarding the best set of feature parameters to be engaged for obtaining the best results.

Table 2 presents some of these trials underlying the most significant lines that may lead to a relevant conclusion. The effectiveness of the algorithm is assessed by the calculated accuracy as a metric score, but also a discussion is undergone regarding the computation time. An exact computation time has not been determined for a dataset, but estimation can be made according to the quantity of features to be calculated. By analyzing the lines of the tables, we can conclude the following:

- From lines 1, 4 and 7 one may observe that the increase of L_P improves the resolution in frequency and therefore the accuracy in both training and testing stages, because the features are more differentiated by their individual value of the spectral components, than by their statistical behavior in the range of a batch. Nevertheless, too high an L_P (lines 19 and 20), i.e. too low a resolution, mainly under 1 Hz, decreases the overall performance leading to overfitting, that is obtaining excellent accuracy in the training stage while testing with new data provides poor results.
- SVM and NN algorithms provide comparable results, but the benefits brought by LR are unsatisfactory.
- Comparing the lines 7 and 9 or 8 and 10, it is observed that increasing the batch number, i.e. narrowing the bandwidth of a batch on which the statistical parameters are calculated improves the selectivity of the features. The drawback is a bigger computing effort and hence a delay in obtaining the result.
- The best results are obtained by using the statistical parameters μ and σ. In this case, adding the variance υ does not significantly change the accuracy, but also increases the features computing time.
- By analyzing the lines 15 to 19, it is found that widening the frequency range (increasing f_{max}) leads to enlarging the dispersion of the features with maximum performance around 300 Hz, after which the accuracy drastically decrease. This also reduces the accuracy of new recordings that are not part of the test dataset.

Table 2. The most significant trials (training + testing) containing the significant parameters and their results

# trial	Algorithm type	L_p [samples | s]	df [Hz]	f_{max} [Hz]	N_b	L_b [Hz]	Statistical params	Training accuracy	Testing Accuracy
1.	SVM	10000 | 0.22	4.4	200	5	39.7	μ	0.88	0.58
2.	NN	10000 | 0.22	4.4	200	5	39.7	μ	0.79	0.63
3.	LR	10000 | 0.22	4.4	200	5	39.7	μ	0.65	0.55
4.	SVM	30000 | 0.68	1.4	200	5	39.7	μ	0.90	0.64
5.	NN	30000 | 0.68	1.4	200	5	39.7	μ	0.86	0.71
6.	LR	30000 | 0.68	1.4	200	5	39.7	μ	0.7	0.54
7.	SVM	50000 | 1.13	0.9	200	5	39.7	μ	0.93	0.71
8.	NN	50000 | 1.13	0.9	200	5	39.7	μ	0.89	0.75
9.	SVM	50000 | 1.13	0.9	200	10	20.2	μ	0.94	0.75
10.	NN	50000 | 1.13	0.9	200	10	20.2	μ	0.89	0.78
11.	NN	50000 | 1.13	0.9	200	10	20.2	μ, σ	0.99	0.87
12.	NN	50000 | 1.13	0.9	200	10	20.2	μ, σ	0.99	0.87
13.	NN	50000 | 1.13	0.9	200	10	20.2	μ, σ, υ	0.99	0.88
14.	NN	50000 | 1.13	0.9	200	30	7	μ, σ	1	0.90
15.	NN	50000 | 1.13	0.9	200	40	5.3	μ, σ	1	0.91
16.	NN	50000 | 1.13	0.9	300	40	5.3	μ, σ	1	0.93
17.	**SVM**	**50000 | 1.13**	**0.9**	**300**	**40**	**7.9**	**μ, σ**	**1**	**0.95**
18.	SVM	50000 | 1.13	0.9	400	40	9.7	μ, σ	1	0.89
19.	SVM	60000 | 1.36	0.7	300	40	7.9	μ, σ	1	0.86
20.	SVM	60000 | 1.36	0.7	300	30	10.3	μ, σ	0.97	0.83

- If reduced response times, that is sampling on periods below 0.2 s are desired, this can be done by reducing L_P, but at the cost of significantly diminishing the accuracy, even below 80%. This can be counterbalanced by reducing N_b and possibly adding a new statistical parameter (in this case υ may be efficient).
- From the example presented in Fig.5, it is observed that the reduction of score is mainly present during the transition zones between classes. It is therefore necessary to make this transition area as smooth as possible.

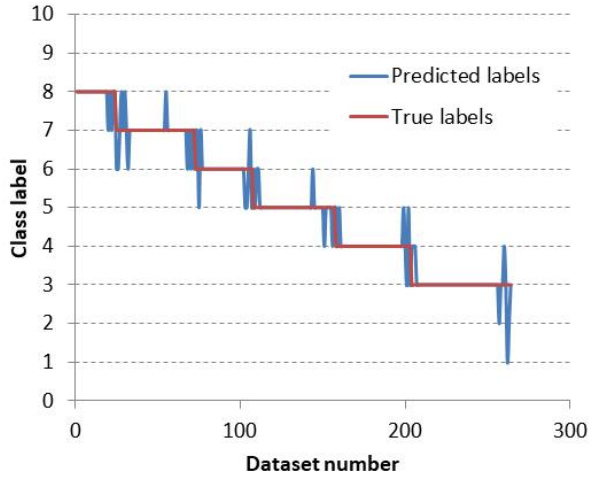

Fig.5. A sequence of testing results where inaccuracies at transition regions may be remarked

- Better results are obtained for longer records for each class, so widening the training records (minimum 30 seconds).
- There is an optimum of the feature parameters represented by the thicker line in the table (line 17) for which one obtained the best score.

As a general conclusion drawn over the above observations, a trade-off between the sampling period, the resources involved, the accuracy and the time computing must be done in order to optimize the feature parameters and to obtain a satisfactory result for further deploying the algorithm in practice.

V. CONCLUSIONS

In the paper, a method based on machine learning algorithms devoted to estimate de rotational speed of a heat engine based on recordings of the sound emitted by the engine was presented. The method was illustrated only as a working principle and has been implemented only on a portable computer for now, being planned to be deployed on smartphones to increase its usability and portability. The main benefits of the method are:

- it is simple, cheap and easy to implement as an application on a device equipped with a sound acquisition system (tablet, mobile phone, laptop, etc.);
- its performance expressed as accuracy in testing stage is satisfactory if a sufficiently large number of classes is considered, with the reverse that important resources for computing are needed;
- it can be used as a method of measuring speed for other rotating or cyclic objects, such as electric motors,

drive mechanisms, etc.;

The method has also some downsides:

- because of the large number of mechanical elements contributing to a specific sound of an engine, in the present study, training and deploying were performed on a single type of car. Training on an engine from one type of car and deploying on another car did not give satisfactory results using the presented feature parameters;
- the method is limited by the computing resources of the device used.

We plan for the future to implement the method as application for smartphones able to estimate speeds for any type of engine, even for electric motors. For this, new types of features are to be utilized using Short Time Fourier Transform and Wavelet Transform. The development of the method is also being considered for detecting malfunctions of an engine.

REFERENCES

[1] J. Marek, H.-P. Trah, Y. Suzuki, I. Yokomori (Editors.), “Sensors for Automotive Applications”, Wiley, 2003.

[2] F. Gustafsson, “Rotational speed sensors: limitations, pre-processing and automotive applications”, IEEE Instrum. & Meas.Magazine, vol. 13, no. 2, April 2010, pp. 16-23.

[3] Z. Shi et al., “Design and Development of a Tachometer Using Magnetoelectric Composite as Magnetic Field Sensor”, IEEE Trans. on Magnetics, vol. 54, no. 7, July 2018, pp. 1-4.

[4] G. H. Choi, W. S. Ra, T. S. Yoon and J. B. Park, “Low-cost tachometer based on the recursive frequency estimation for automotive applications”, SICE Annual Conference 2007, vol. 1, pp. 46-49.

[5] X. Shan, Lu Tang, He Wen, R. Martinek and J. Smulko, “Analysis of Vibration and Acoustic Signals for Noncontact Measurement of Engine Rotation Speed”, Sensors, vol.20, Jan. 2020, pp.1-10.

[6] J.M. Chicharro, A.L. Morales, R. Moreno, A.J. Nieto, P. Pintado, “Sensorless automotive engine speed measurement by noise analysis”, IEEE International Conference on Mechatronics, 2009. Malaga, Spain, pp.14-17.

[7] F.J.T.E. Ferreira, A.F.F.Duarte and F.J.P.Lopes, “Experimental Evaluation of a Novel Webcam-Based Tachometer for In-Situ Rotational Speed Measurement”, IEEE International Conference on Industrial Technology (ICIT), 2020, pp. 917-924.

[8] S.A. Amman and M. Das, “An Efficient Technique for Modeling and Synthesis of Automotive Engine Sounds”, IEEE Trans. on Ind. El., Vol. 48, No. 1, Feb. 2001.

[9] M. Moschopoulos, G.N.Rossopoulos, and C.I. Papadopoulos, "Journal Bearing Performance Prediction Using Machine Learning and Octave-Band Signal Analysis of Sound and Vibration Measurements" Polish Maritime Research, vol.28, no.3, 2021, pp.137-149.

25th IMEKO TC4 International Symposium
23rd International Workshop on ADC and DAC Modelling and Testing
IMEKO TC-4 2020
Brescia, Italy / September 12-14, 2022

Lithium-Ion Batteries state of charge estimation based on electrochemical impedance spectroscopy and convolutional neural network

Emanuele Buchicchio[1], Alessio De Angelis[1], Francesco Santoni[1], Paolo Carbone[1]

[1]*Department of Engineering University of Perugia, Via G. Duranti, 93 - 06125 - PERUGIA, emanuele.buchicchio@studenti.unipg.it, alessio.deangelis@unipg.it, francesco.santoni@unipg.it, paolo.carbone@unipg.it*

***Abstract* – Estimating the state of charge of batteries is a critical task for every battery-powered device. In this work, we propose a machine learning approach based on electrochemical impedance spectroscopy and convolutional neural networks. A case study based on Samsung ICR18650-26J lithium-Ion batteries is also presented and discussed in detail. A classification accuracy of 80% and top-2 classification accuracy of 95% were achieved on a test battery not used for model training.**

I. INTRODUCTION

Many battery-powered devices such as laptops, smartphones, cameras, tablets, cordless shavers, lawnmowers, drones, and even electric cars are now part of our daily life. In most battery-operated systems, knowing the remaining charge within the battery is essential for end-users. In addition, the knowledge of the remaining battery capacity is fundamental for its management because states of extremely high or extremely low state-of-charge (SOC) can irreversibly damage the battery [1]. The relationship between the battery's observable signals and the estimated SOC is highly non-linear, varying with temperature and discharge/charge currents [2].

There is no practical method for SOC direct measurement outside laboratory settings [3]. Therefore, many research works have been conducted over the last decades to develop a secure, practical, and reliable method for SOC estimation [4, 5].

The data-driven SOC estimation approaches require limited knowledge about internal battery characteristics. In contrast, model-driven approaches require an in-depth understanding of the battery's internal chemical ed electrical characteristics. Model-based methods also require the assumption that the battery model is accurately established. This condition is hard to realize in real applications due to the effect of measurement noise and model parameter drifts with aging, and temperature [3]. Combining some a-priori information, embedded in physical electrochemical models or electrical equivalent circuit models, with experimental data, model-based approach can result in reliable and accurate predictions [6]. However, they require extensive domain knowledge and relatively long development times. Common model-based approaches in recent publications include the usage of Sliding Mode Observer, Luenberger Observer, Kalman filters, Electrochemical Model, Equivalent Circuit Model, Electrochemical Impedance Model [7].

Data-driven approaches, such as those based on machine learning (ML), are becoming more popular for estimating the SOC and battery state-of-health (SOH) due to the greater availability of battery data and improved computing power capabilities. SOC estimators based on neural networks (NN) have been studied extensively in the literature. When using the NN model, a large amount of known input data and expected output data obtained from the battery charging and discharging experiments is required to train the network and extract the fitting relationship without an a-priori model of the battery.

Traditional ML techniques contain no more than one or two layers of non-linear and linear transformations. With the advent of faster computational power and an abundance of available real-world data, more complex architectures were investigated, which, in many cases, allowed researchers to make striking improvements in many applications. The deep learning architecture used in this work, called a deep residual network, won the 2015 ImageNet challenge with an error rate of 3.57% which even surpasses human-level accuracy valued at 5.1% [8] for the same task.

II. MATERIALS AND METHODS

A. *SoC estimation using Electrochemical impedance spectroscopy and Convolutional Neural Networks*

Electrochemical impedance spectroscopy (EIS) is a powerful tool for monitoring SOC and SOH of rechargeable batteries [9]. It provides an estimate of the equivalent battery impedance $Z(f)$ by, e.g., measuring the voltage variations at the battery contacts after a varying input current is applied. Visual representation of the results is often obtained by plotting the negative imaginary part of $Z(f)$ vs its real part.

Although it is easy to observe that different SOC values generate different shapes in EIS visual representations, the relationships between SOC and $Z(f)$ are not obvious. This

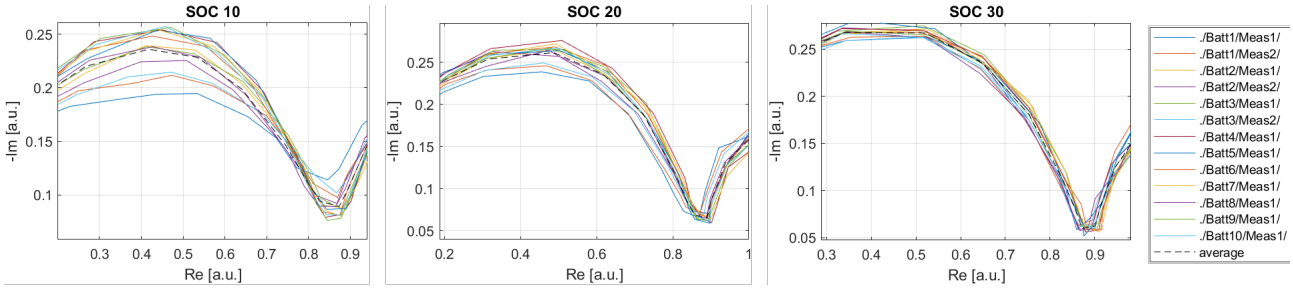

Fig. 1. Normalized EIS curve comparison. The shape of the curve is specific for each SOC internal state

is shown in figure 1 that is based on measurements of the $Z(f)$ of ten rechargeable batteries, characterized by three different SOCs.

Finding a closed-form derivation of this relationship appears an unfeasible task. However, we can approximate this unknown function by extracting information from experimental results. We can easily spot some differences in the visual representation of experimental data from different SOC conditions. EIS curves measured at the same SOC level show similar shape patterns, but exhibit translations in the complex plane. The magnitude of the translation varies for different batteries and even for the same battery across different measurements (figure 2). Using an ML-based approach to relate SOC to EIS-derived data requires the assumption that the EIS shape patterns depend on SOC and are invariant given the same battery type.

Convolutional Neural Networks (CNN) provide the three primary advantages for image processing [10] over the traditional feed-forward neural network with fully connected layers. Firstly, they have sparse connections instead of fully connected connections, which lead to reduced parameters and allow for processing high-dimensional data. Secondly, weight sharing across the entire image reduce memory requirements and causes translational equivariance property. Thirdly pooling layer bring invariance to the local translation property. The invariance and equivariance properties make CNN an ideal candidate for performing classification tasks on EIS curves such as those graphed in figure 2. Given that deep CNNs are the de-facto

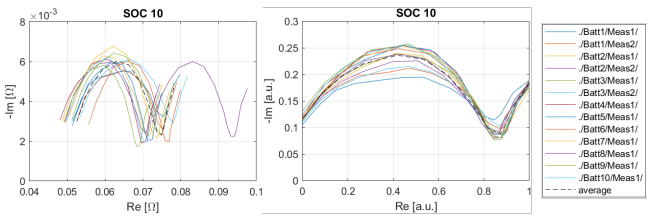

Fig. 2. Comparison of measured EIS curves at SOC 10%. *Original data (on the left) and normalized (on the right). EIS curves are similar in shape, but are translated. In one case, the translation is much more relevant*

industry standard solution for image classification tasks, with many well-known architectures and pre-trained models available, we developed a CNN-based SOC estimator for EIS curves visual representation images.

B. *Electrochemical impedance spectroscopy data acquisition*

We are using a Keysight U2351A data acquisition board to provide the excitation signal by means of a 16-bit digital to analog converter (DAC) and to acquire the current and voltage signals by means of two 16-bit analog to digital converter (ADC) channels. The excitation signal is a random-phase multisine, i.e. the sum of harmonically-related sinusoids [11] that allows to simultaneously excite the battery at a wide range of frequencies. In this case, the excited frequencies are 0.05, 0.1, 0.2, 0.4, 1, 2, 4, 10, 20, 40, 100, 200, 400, and 1000 Hz in all measurements. The excitation signal generated by the DAC is converted to a current signal by a voltage-to-current converter custom circuit [12]. The current signal is measured across a known shunt resistor. The voltage signal across the battery is also measured by a second INA connected to the second ADC channel. The current and voltage signals acquired by the ADC channels are transferred to a PC to compute the discrete Fourier Transform (DFT) and calculate the complex impedance value at each excited frequency. The current amplitude at each excited frequency was 50 mA, which resulted in a measurement uncertainty of approximately 0.1 mΩ, as characterized in [13].

C. *SOC estimation as a machine learning classification task*

In machine learning, *classification* is the task of predicting the class to which an object belongs. Each object is uniquely represented by a set of values $x1, x2, \ldots, xl$, known as *features* in ML jargon. The l feature values, stacked together, in the common ML notation are labeled as the *feature vector* $x \in R^l$. The goal is to design a classifier $f(x)$, so that given a values in a feature vector x we will be able to predict the class of witch the object belong. To formulate the task in mathematical terms, each class is

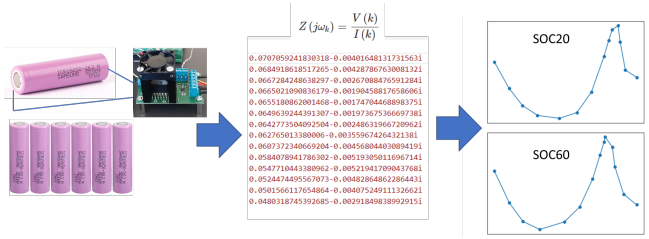

Fig. 3. EIS of battery is measured at different SOC using the system presented in [13]. The complex impedance values are then encoded in 2D visual representation to feed the convolutional neural network.

represented by the class label variable y and $\hat{y}$ denotes the predicted class given the value of x and the set of possible predicted classes in the so-called *vocabulary*:

$$\hat{y} = \Phi(f(x)), \tag{1}$$

where $\Phi(\cdot)$ is a nonlinear function that maps any possible $f(x)$ values to one on the class labels.

The set of possible SOC class *vocabulary* considered in this work is 100%, 90%, 80%, 70%, 60%, 50%, 40%, 30%, 20%, and 10%.

The raw features vectors is made by complex impedance values measured at frequencies $[0.05, 0.1, 0.2, 0.4, 1, 2, 4, 10, 20, 40, 100, 200, 400, 1000]$ Hz for a specific SOC. A two-dimensional visual representation of the impedance curve in the complex plane is used to build a 2D feature vector for each measured EIS (Figure 3).

D. Training and test dataset

We compiled and published two open-access dataset [14],[15] of data obtained through EIS, by measuring ten brand new Samsung ICR18650-26J lithium-Ion batteries at different SOCs. A detailed description of the measurement system is available in [13].

Two sets of EIS measurements have been kept out from training and validation as a test dataset for the final system performance assessment. These two test cases are representative of two different scenarios: 1) a new set of EIS data on battery that was originally included in model training; 2) A set of EIS originating from a battery never seen by the model during training and validation.

For the *new battery* test case we randomly choose one of the ten batteries. Battery 10 was among data in [14] and battery 06 among data in [15] For the *new measurement* test case we randomly choose a set of EIS from one measurement cycle. Measurement 10 on battery 01 was selected among data in [14] and measurement 8 on battery 05 among data in [15]

E. Training and validation workflow

We have developed a fully automated pipeline for training deep learning-based classifiers using the open-source libraries PyTorch and FastAI [16]. The workflow consists of three steps (Figure 4):

1. Step 1: data acquisition;
2. Step 2: data selection;
3. Step 3: model training.

The *Data acquisition* step produces a CSV file containing EIS spectra at each SOC. In *Data selection* the available data are split in training ad test datasets. The test dataset will only be used for test and not for training. The training dataset will be further split to hold out 20% data for validation. We implemented different training strategy for the *model training step*. In this work, we performed two different experiments adopting the *validation hold* strategy for the first one and the *leave k-out cross validation* strategy for the second one. In the *validation hold* experiment we trained a single model using 80% of the available data, while 20% of the data was set aside and used exclusively for validation. The performance of the model was then verified using the test dataset containing completely new measurements. In the second experiment we implemented the *leave k-out* strategy as *leave one battery out* to investigate the model performance dependency from a particular choice of training data-set and effects of specific battery inclusion in the training process. We run ten training sessions excluding data related to one of the batteries each time. This experiment produced ten trained models that can be used alone or combined in an *ensemble model* for SOC inference.

We published all the algorithms developed for this work in the open-source python *ML Measurement library* [17]. We also created several Jupyter notebooks with the high-level experiment workflow orchestration script executable on free *Google Colab* machine learning compute platform for easy experiment repeatability. The notebooks take advantage of the free Google Drive private storage associated with the user's account to store all trained models and generated images. While paid service subscriptions include more computational resources, the hardware and software configuration available with the free service allows running all experiments from scratch within a few hours. The notebook itself provides the installation of missing software components in the *setup* phase.

F. Efficient deep CNN training for SoC estimation

Many pre-trained deep learning models have proven adequate for image/video classification tasks. We chose the ResNet18 CNN because the residual network architecture achieves good results in image classification tasks and is

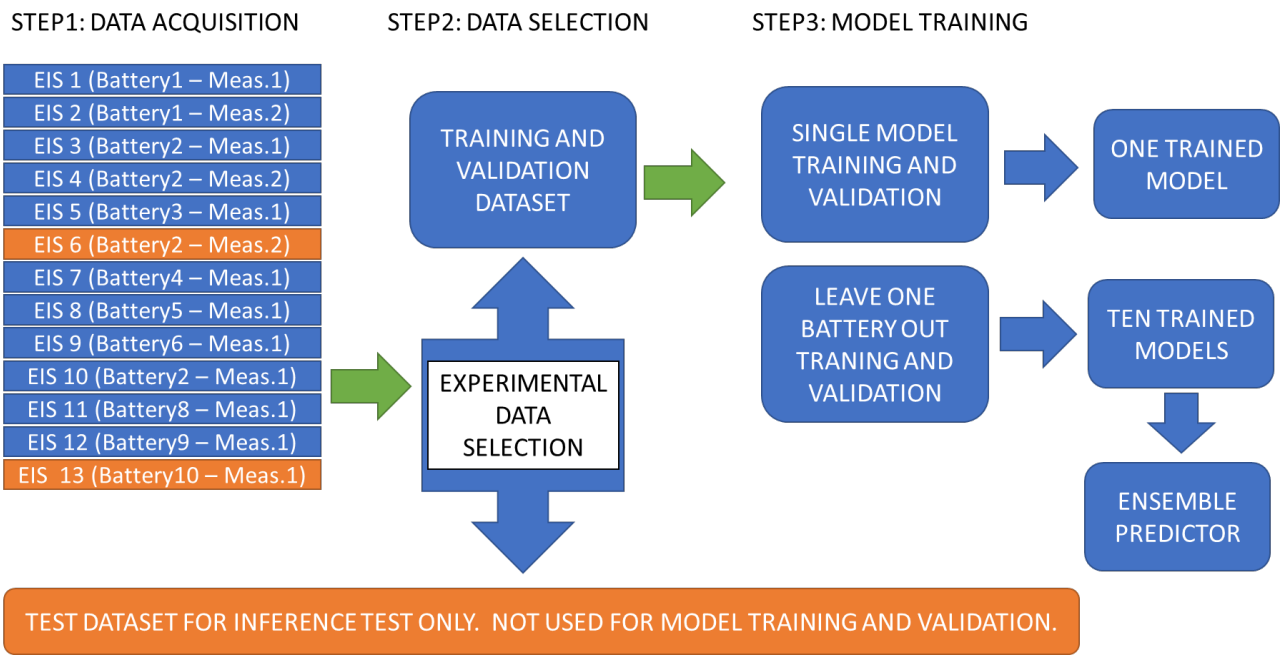

Fig. 4. SOC estimator training and validation workflow overview. The same workflow was applied to both dataset [14] and [15]

relatively fast to train [18]. Transfer learning from general-purpose image classification pre-trained models allows fast fine-tuning training of the deep CNN model. The optimal learning rate for training has been estimated with the Cyclical Learning Rates method [19] to avoid time-consuming multiple runs to perform hyper-parameters sweeps. The algorithm implementation in the FastAI library suggested a learning rate in the range $10^{-2} - 10^{-3}$. We perform the model fine-tuning with a sequence of freeze, fit-one-cycle, unfreeze, and fit-one-cycle operations using the *discriminative learning rate fine tuning* method developed in [20] and implemented in FastAI library [16].

After some tests, we set the training script to run for fifty epochs, although, in many case cases, few epochs would suffice.

G. Data Augmentation

For model training, we developed an *ad-hoc* data augmentation technique based on simulating additional measurements by adding white Gaussian noise within the uncertainty band estimated in [13]. The training pipeline generates for each available EIS spectrum K different visual representations with K equal to the augmentation factor parameter set in the experimental setup. The results shown in this article were obtained with $K = 10$.

H. System calibration

Experimental data revealed high variability across different batteries and also significant differences between measurements on the same battery at different times. For a field application, it is, therefore, necessary to tune the estimation model each time the battery is replaced and periodically to compensate for changes in the internal state of the battery that occur over time. This procedure can be performed as part of a periodic calibration procedure using hardware onboard the device or a dedicated external instrument that may be included in the docking station of the device. (e.g., in the charging station of an electric vehicle).

III. RESULTS

A. SOC curve analysis

Observing the visual representation of the EIS data resulting from the data pre-processing (Figure 3), we can see that are shape variations across different SOC for the same battery but also for the same SOC across different batteries (Figure 5).

B. Model validation

The SOC estimator model trained in the *validation hold* experiment achieves up to 100% accuracy score on the validation dataset. The accuracy depends on the amount of measurement noise used for data augmentation. Using a realistic amount of AWG noise according to the uncertainty band of the impedance measurement system estimated in [13], the model trained using data from the second dataset achieves an overall 87% accuracy The three models trained in the *leave one battery out* experiment achieved accuracy scores between 88% and 89%.

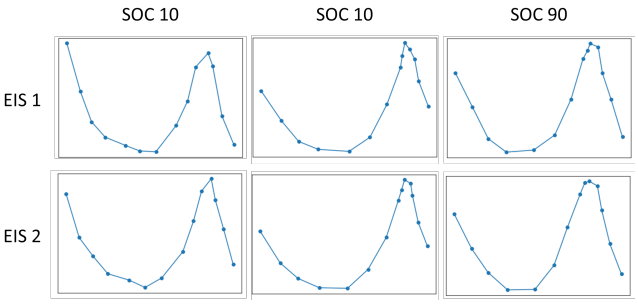

Fig. 5. EIS curves of two battery at SOC 10% *,* 30% *and* 90% *with differences across SOC for the same battery and across batteries for the same SOC.*

To verify that the SOC estimation produced is based on a reasonable set of image features, we compute the *class activation map* (CAM) [21] on some inference results using the implementation we published in [17]. CAMs allow to visually highlight the image areas that were more relevant to the final classification performed by a specific image classification neural network. The resulting heat map (Figure 6) shows that the main contributions to the SOC classification came from the peak and valley areas of the curves, whose shape changes with SOC.

C. Test in a SOC measurement system

We deploy the training model in an inference pipeline to simulate the usage in a real SOC estimation system. In a real application, the model training should be performed during the system calibration procedure to fine-tune the model on the actual battery that must be monitored. To evaluate the SOC estimator performance on realistic conditions we arrange two different test cases, representative of several use cases of the system:

1. New battery test: SOC estimation of a battery similar (same model) to the batteries used for model training but never connected to the system before.

2. New measure test: SOC estimation of one of the batteries used for training a few days after initial system calibration.

Model trained during both in *leave one battery out* and *validation hold* experiments was evaluated on the two test cases. In the real-world use of a battery system, an accurate estimate of SOC is often not necessary. In addition, impedance measurements are affected by several factors (such as temperature) that prevent accurate data from being obtained. Based on this consideration, k-accuracy in addition to accuracy, was used to evaluate the models. Multi-class classification metrics was computed using functions implemented of SciKit Learn [22] open-source library. The model trained in *validation hold* experiment

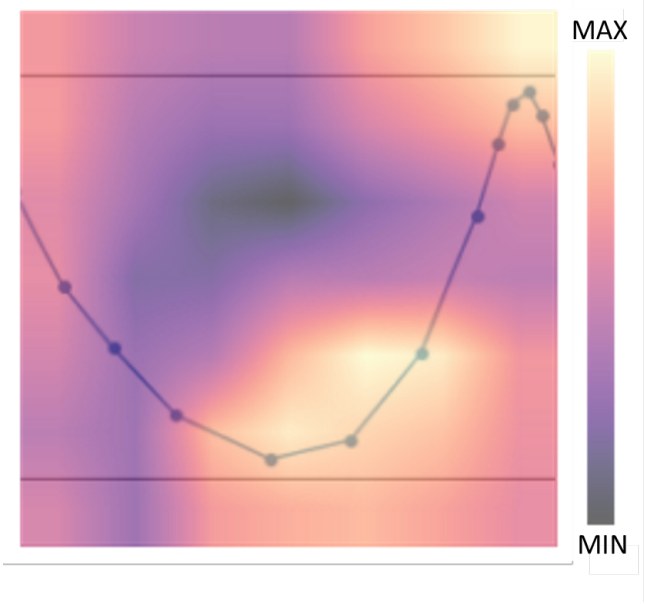

Fig. 6. Overlay of 7x7 class activation map on an EIS curve measured at SOC 40% *on battery 06. The brighter colors indicate a relative more significant contribution of feature (image pixels) in the area to the final classification.*

achieves 0.68 accuracy and 0.87 top2-accuracy on *new battery* test and 0.90 accuracy and 0.100 top2-accuracy on *new measure* test. The ensemble model trained in *leave one battery out* experiment achieves 80% overall classification accuracy and 95% top2-accuracy on *new battery* SOC estimation test and 90% accuracy and 100% top2-accuracy on *new measure* test.

IV. CONCLUSIONS

Experimental results confirm that the relationship between EIS and SOC can be leveraged to estimate the SOC of a battery from impedance measurements. Although the analytical relationship is unknown, deep neural networks can be used as an approximated model to estimate SOC. We develop a SOC estimator based on CNN and a training pipeline that allows for fast system calibration on the specific battery to compensate for the variation in EIS present in each specific battery and the battery aging over time. The proposed system achieves 90% and 100% top-2-accuracy accuracy in SOC estimation for a battery included in the training. On an unknown battery the system scores a 62% accuracy and 80% top-2-accuracy.

REFERENCES

[1] Y. Chen, Y. Kang, Y. Zhao, L. Wang, J. Liu, Y. Li, Z. Liang, X. He, X. Li, N. Tavajohi, and B. Li, "A review of lithium-ion battery safety concerns: The issues, strategies, and testing standards," *Journal of Energy Chemistry*, vol. 59, pp. 83–99, 2021. doi:

10.1016/j.jechem.2020.10.017.

[2] E. Chemali, P. J. Kollmeyer, M. Preindl, and A. Emadi, "State-of-charge estimation of li-ion batteries using deep neural networks: A machine learning approach," *Journal of Power Sources*, vol. 400, pp. 242–255, 10 2018. doi: 10.1016/j.jpowsour.2018.06.104.

[3] C. Hu, L. Ma, S. Guo, G. Guo, and Z. Han, "Deep learning enabled state-of-charge estimation of lifepo4 batteries: A systematic validation on state-of-the-art charging protocols," *Energy*, vol. 246, p. 123404, 5 2022. doi: 10.1016/J.ENERGY.2022.123404.

[4] I. Babaeiyazdi, A. Rezaei-Zare, and S. Shokrzadeh, "State of charge prediction of ev li-ion batteries using eis: A machine learning approach," *Energy*, vol. 223, p. 120116, 2021. doi: 10.1016/j.energy.2021.120116.

[5] M. Galeotti, L. Cinà, C. Giammanco, S. Cordiner, and A. Di Carlo, "Performance analysis and soh (state of health) evaluation of lithium polymer batteries through electrochemical impedance spectroscopy," *Energy*, vol. 89, pp. 678–686, 2015. doi: 10.1016/j.energy.2015.05.148.

[6] K. J. M. C. J.-Y. Y. W.-S. Choi Woosung, Shin Heon-Cheol, "Modeling and applications of electrochemical impedance spectroscopy (eis) for lithium-ion batteries," *J. Electrochem. Sci. Technol*, vol. 11, no. 1, pp. 1–13, 2020. doi: 10.33961/jecst.2019.00528.

[7] M. A. Hannan, D. N. How, M. B. Mansor, M. S. H. Lipu, P. Ker, and K. Muttaqi, "State-of-charge estimation of li-ion battery using gated recurrent unit with one-cycle learning rate policy," *IEEE Transactions on Industry Applications*, vol. 57, pp. 2964–2971, 5 2021. doi: 10.1109/TIA.2021.3065194.

[8] K. He, X. Zhang, S. Ren, and J. Sun, "Deep residual learning for image recognition," in *Proceedings of the IEEE Computer Society Conference on Computer Vision and Pattern Recognition*, vol. 2016-December, 2016. doi: 10.1109/CVPR.2016.90.

[9] A. Guha and A. Patra, "Online estimation of the electrochemical impedance spectrum and remaining useful life of lithium-ion batteries," *IEEE Transactions on Instrumentation and Measurement*, vol. 67, 2018. doi: 10.1109/TIM.2018.2809138.

[10] I. Goodfellow, Y. Bengio, and A. Courville, *Deep Learning*. MIT Press, 2016. `http://www.deeplearningbook.org`.

[11] R. Pintelon and J. Schoukens, *System identification: a frequency domain approach*. John Wiley & Sons, 2012.

[12] A. D. Angelis, P. Carbone, A. Moschitta, M. Crescentini, R. Ramilli, and P. A. Traverso, "A fast and simple broadband eis measurement system for li-ion batteries," in *24th IMEKO TC4 International Symposium and 22nd International Workshop on ADC and DAC Modelling and Testing*, 2020. `https://www.imeko.org/publications/tc4-2020/IMEKO-TC4-2020-30.pdf`.

[13] A. De Angelis, E. Buchicchio, F. Santoni, A. Moschitta, and P. Carbone, "Uncertainty characterization of a practical system for broadband measurement of battery EIS," *IEEE Transactions on Instrumentation and Measurement*, vol. 71, pp. 1–9, 2022. doi: 10.1109/TIM.2022.3156994.

[14] E. Buchicchio, A. De Angelis, F. Santoni, and P. Carbone, "Data for: Dataset on broadband electrochemical impedance spectroscopy of lithium-ion batteries for different values of the state of charge." *Mendeley Data*, 2022. doi: 10.17632/ch3sydbbrg.3.

[15] E. Buchicchio, A. D. Angelis, F. Santoni, and P. Carbone, "Dataset on broadband electrochemical impedance spectroscopy of lithium-ion batteries for different values of the state of charge." *Mendeley Data*, 2022. doi: 10.17632/MBV3BX847G.3.

[16] J. Howard and S. Gugger, "FastAI: A layered API for deep learning," *Information (Switzerland)*, vol. 11, 2020. doi: 10.3390/info11020108.

[17] E. Buchicchio, "Machine learning for measurement: v0.2.0." *Zenodo*, June 2022. doi: 10.5281/zenodo.6484862.

[18] K. He, X. Zhang, S. Ren, and J. Sun, "Deep residual learning for image recognition," in *2016 IEEE Conference on Computer Vision and Pattern Recognition (CVPR)*, pp. 770–778, 2016. doi: 10.1109/CVPR.2016.90.

[19] L. N. Smith, "Cyclical learning rates for training neural networks," in *Proceedings - 2017 IEEE Winter Conference on Applications of Computer Vision, WACV 2017*, 2017. doi: 10.1109/WACV.2017.58.

[20] J. Howard and S. Ruder, "Universal language model fine-tuning for text classification," in *Proceedings of the 56th Annual Meeting of the Association for Computational Linguistics (Volume 1: Long Papers)*, (Melbourne, Australia), pp. 328–339, Association for Computational Linguistics, July 2018. doi: 10.18653/v1/P18-1031.

[21] B. Zhou, A. Khosla, A. Lapedriza, A. Oliva, and A. Torralba, "Learning deep features for discriminative localization," in *2016 IEEE Conference on Computer Vision and Pattern Recognition (CVPR)*, pp. 2921–2929, 2016. doi: 10.1109/CVPR.2016.319.

[22] F. Pedregosa, G. Varoquaux, A. Gramfort, V. Michel, B. Thirion, O. Grisel, M. Blondel, P. Prettenhofer, R. Weiss, V. Dubourg, J. Vanderplas, A. Passos, D. Cournapeau, M. Brucher, M. Perrot, and E. Duchesnay, "Scikit-learn: Machine learning in Python," *Journal of Machine Learning Research*, vol. 12, pp. 2825–2830, 2011.

25th IMEKO TC4 International Symposium
23rd International Workshop on ADC and DAC Modelling and Testing
IMEKO TC-4 2022
Brescia, Italy / September 12-14, 2022

Evaluation results of COOMET Key Comparison of Power

Oleh Velychko[1], Tetyana Gordiyenko[2]

[1] State Enterprise "All-Ukrainian state research and production center for standardization, metrology, certification and consumers' rights protection" (SE "Ukrmetrteststandard"), Metrologichna Str., 4, 03143, Kyiv, Ukraine
velychko@ukrcsm.kiev.ua
[2] State University of Telecommunications, Solomianska Str., 7, 03110, Kyiv, Ukraine
t_gord@hotmail.com

***Abstract* – The Agreement on Mutual Recognition of the International Committee on Weights and Measures plays a key role for the mutual recognition of the measurement results that are carried out in the National Metrology Institutes from different countries. The COOMET Key Comparison of Power was conducted between thirteen National Metrology Institutes and Designated Institutes from five Regional Metrology Organizations. Traditional results of comparison are published in the Key Comparison Database of International Bureau for Weights and Measures. Results of comparative analysis of this comparison in the context of Regional Metrology Organizations and metrological traceability are presented. For checking consistency of Key Comparison data was used E_n number and z scores. Results for all participants of comparison are satisfactory for E_n number and z scores.**

I. INTRODUCTION

The special agreements on the mutual recognition (MRA) of measurements and tests at the international level are very important to overcome technical barriers to trade between countries. This contributes to the establishment of global metrological traceability [1, 2]. In this case, the main role is have by the National Metrology Institutes (NMIs) and Designated Institute (DIs), in which the national measurement standards are keeping. These measurement standards are subject to periodic international comparisons to establish and further confirm their equivalence to other similar measurement standards.
The Agreement on Mutual Recognition of the International Committee on Weights and Measures (CIPM) [3] plays a key role for the mutual recognition of the measurement results that are carried out in the NMIs of different countries. The main basis for ensuring this process is the results of international comparisons of national measurement standards, which are carried out in accordance with the requirements of the CIPM MRA. The results of such comparisons, in particular of key comparisons (KC), are published in a special key comparison database (KCDB) of the International Bureau of Weights and Measures (BIPM) [4, 5, 6].
KC is conducted both by the consultative committees (CC) of the CIPM, BIPM, and within the regional metrology organizations (RMO), which are distributed on a continental basis, mainly. There are six such RMOs now (EURAMET, APMP, COOMET, SIM, AFRIMET and GULFMET) and all of them organize and conduct KCs according to established procedures. Evaluation of data and results of comparisons includes the establishment of a reference value (RV) of comparisons and it corresponding uncertainty and the degree of equivalence (DoE) of national standards also its corresponding uncertainties [7, 8]. Only Euro-Asian Cooperation of National Metrological Institutions (COOMET) has recommendations for the evaluation of comparison data and results [9, 10].
Comparative analysis of KC results for NMI/DI both in the context of each RMO and metrological traceability to specific NMI/DIs is relevant and important. Carrying out those analysis is connected with the need to take into account the geographical location of the leading institutes. This minimizes the costs of NMI/DIs to achieve the required metrological traceability.

II. THE TRADITIONAL EVALUATION OF KC DATA

CC KC results are interpreted in terms of KC RV and DoE [11, 12]. The RMOs organize the corresponding RMO KCs with a number of common participants and with protocols allowing it results to be linked to the CC KC results after the equivalence of the NMI benchmarks of the participants has been established (calculation of KC RV and DoE). The RMO KC data evaluation procedures are designed to provide linkage to the last CC KC data [7, 13, 14].
Distribution of six RMOs by World map is shown on Fig. 1.

Fig. 1. Distribution of RMOs by World map.

The COOMET KC of active power of low-frequency 50/60 Hz (COOMET.EM-K5) was conducted from 2016 to 2018 between thirteen NMI/DI: State Enterprise (SE) "Ukrmetrteststandard" (UMTS, Ukraine); BelGIM (Belarus); VNIIM (Russia); GEOSTM (Georgia); CMS (Kyrgyzstan); UME (Turkey); SMU (Slovakia); LEM-FEIT (North Macedonia); NIM (China); MASM (Mongolia); QCC EMI (United Arab Emirates); SASO-NMCC (Saudi Arabia), and NIS (Egypt) from five RMOs: COOMET; EURAMET; APMP; GULFMET, and AFRIMET. UMTS was as the pilot laboratory of this KC. The traditional results of KC (DoE) are published in KCDB [4, 15] for power factor (PF) 1.0, 0.5 Lag, 0.5 Lead, 0.0 Lag, 0.0 Lead at frequencies of 50/53 Hz. Results for PF 1.0 at frequencies of 53 Hz (for example) are shown on Fig. 2. Results for PF (0.5 Lag, 0.5 Lead, 0.0 Lag, 0.0 Lead) at frequencies of 50/53 Hz are similar to those for PF 1.0, so they are not considered further.

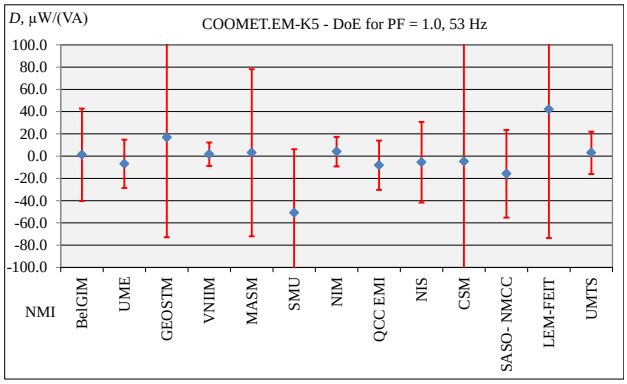

Fig. 2. DoE for NMI/DI participants for PF = 1.0, 53 Hz.

The correlations in traceability between the NMI/DI participants have been neglected for calculating the KC RV. Because three NMI/DIs have the lowest standard uncertainties then they determine the KC RV. NIM and VNIIM was participants of CCEM-K5 KC [16], and UME was pilot laboratory of EURAMET.EM-K5.1 KC [17] and they have different traceability source.

The KC RV x_{ref} is calculated as the mean of NMI/DI participant results with COOMET.EM-K5 data and is given by formula:

$$x_{ref} = \sum_{i=1}^{N} \frac{x_i}{u_c^2(x_i)} \Big/ \sum_{i=1}^{N} \frac{1}{u_c^2(x_i)} \qquad (1)$$

and combine standard uncertainties

$$u_c^2(x_{ref}) = 1 \Big/ \sum_{i=1}^{N} \frac{1}{u_c^2(x_i)}, \qquad (2)$$

where x_i is result of i-th NMI/DI participant; $u_c(x_i)$ is standard uncertainty of i-th NMI/DI participant; N is the total number of NMI/DI participants.

KC RV and expanded uncertainties (k = 2) for PF 1.0, 53 Hz are x_{ref} = -2.1 µW/(VA) and U_{ref} = 5.8 µW/(VA).

The DoE of i-th NMI/DI D_i and its combined standard uncertainties $u_c(D_i)$ with respect to the KC RV are estimated as

$$D_i = x_i - x_{ref}, \qquad (3)$$

$$u_c^2(D_i) = u_c^2(x_i) + u_c^2(x_{ref}). \qquad (4)$$

NMI/DI participant results of RMO KCs of power (EUROMET.EM-K5&K5.1, SIM.EM-K5, and COOMET.EM-K5) are linked to those of CCEM-K5 KC and shown on Fig. 3 for PF 1.0, 53 Hz [4].

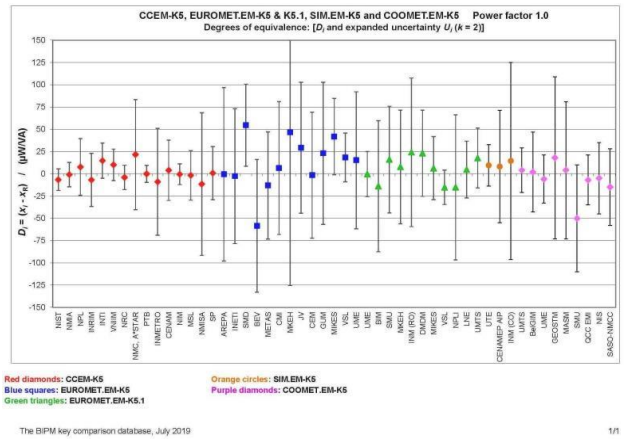

Fig 3. Linked DoE for NMI/DI participants of RMO KCs of power for PF = 1.0, 53 Hz.

DoE of i-th NMI/DI participants of COOMET.EM-K5 with respect to linking to CCEM-K5 is estimated as

$$d_i = D_i + \Delta, \qquad (5)$$

where: d_i is best estimate of result from i-th NMI/DI to linking to CCEM-K5; D_i is DoE from COOMET.EM-K5 for NMI/DI participant in COOMET.EM-K5 only; Δ is correction factor with respect to linking to CCEM-K5.

Measurements from the linking NMIs provide estimates

$$\Delta_{iLINK} = d_{iLINK} - D_{iLINK}, \quad (6)$$

where Δ_{iLINK} is correction factor for *i*-th linking NMI/DI; d_{iLINK} is DoE for *i*-th linking NMI/DI from CCEM-K5; D_{iLINK} is DoE for *i*-th linking NMI/DI from COOMET.EM-K5.
NIM and VNIIM were linking NMIs (see Fig. 3). The correction factor Δ is 0.9 for PF 1.0, 53 Hz (for example) [4, 15].

III. THE EVALUATION OF KC RESULTS IN THE CONTEXT OF RMOS

COOMET.EM-K5 KC was conducted between NMI/DI participants from five RMOs: COOMET; EURAMET; APMP; GULFMET, and AFRIMET. NMI/DI participant results (D_i is DoE of *i*-th NMI/DI participant, $U(D_i)$ is expanded uncertainty of D_i) in the context of RMOs are shown in Table 1 and on Fig. 4 for PF 1.0, 53 Hz.

TABLE 1. NMI/DI RESULTS OF COOMET.EM-K5 IN THE CONTEXT OF RMOS FOR PF 1.0, 53 HZ.

NMI	D_i, 10^{-6}	$U(D_i)$, 10^{-6}	E_{ni}	z_i
		COOMET		
VNIIM	1.7	10.6	0.16	0.08
BelGIM	1.2	41.5	0.03	0.06
GEOSTM	16.7	89.6	0.19	0.81
CSM	-4.9	158.1	0.03	0.24
UMTS	3.0	19.0	0.16	0.15
		EURAMET		
UME	-6.9	21.7	0.32	0.34
SMU	-50.9	57.2	0.89	2.48
LEM-FEIT	42.0	115.6	0.36	2.04
		APMP		
NIM	4.0	13.3	0.30	0.19
MASM	3.1	75.1	0.04	0.15
		GULFMET&AFRIMET		
QCC EMI	-8.2	22.2	0.37	0.40
SASO-NMCC	-15.9	39.4	0.40	0.78
NIS	-5.5	36.3	0.15	0.27

E_{ni} number and z_i scores [18-20] are most often used to check the consistency of KC data, which are presented in Table 1 and on Fig. 5 (for E_{ni} number) and Fig. 6 (for z_i score).
E_{ni} number is calculated as:

$$E_{ni} = |D_i| / 2u_c(D_i). \quad (7)$$

z scores are calculated by the formula:

$$z_i = |D_i| / \sigma, \quad (8)$$

where σ is the standard deviation for qualification assessment.

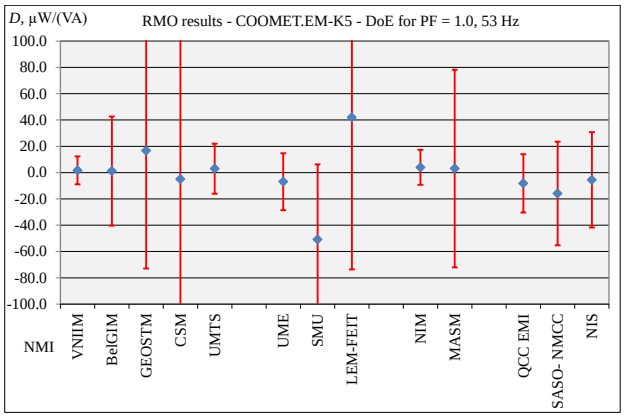

Fig. 4. DoE for NMI/DI participants in the context of RMOs for PF 1.0, 53 Hz.

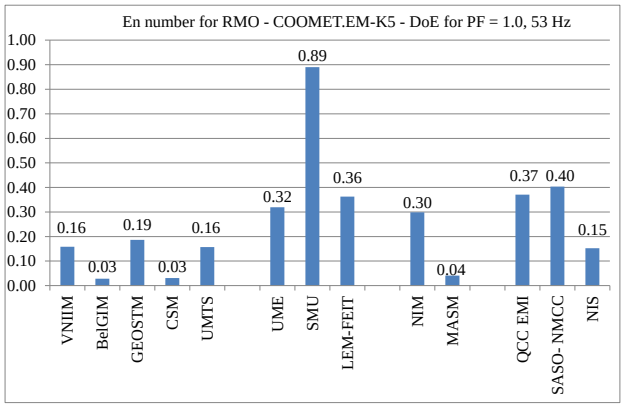

Fig. 5. E_{ni} number for NMI/DI participants in the context of RMOs for PF 1.0, 53 Hz.

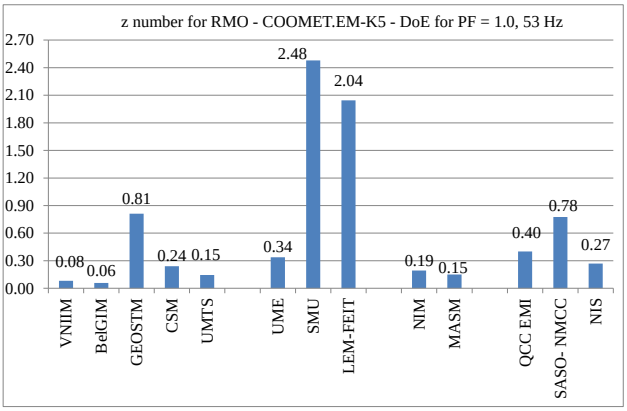

Fig. 6. z score for NMI/DI participants in the context of RMOs for PF 1.0, 53 Hz.

Values of E_{ni} number for COOMET NMI/DI participants of COOMET.EM-K5 are vary from 0.03 to 0.19, EURAMET – from 0.32 to 0.89, APMP – from 0.04 to 0.30, GULFMET&AFRIMET – from 0.15 to 0.40.
The highest values of E_{ni} number are fixed for EURAMET NMI/DI participants, and the smallest – for COOMET. Results for all NMI/DI participants of COOMET.EM-K5

are satisfactory for E_{ni} number (< 1.0), but value of E_{ni} number for SMU from EURAMET several times more than values for all other NMI/DI participants.

Values of z_i scores for COOMET NMI/DI participants are vary from 0.06 to 0.81, EURAMET – from 0.34 to 2.48, APMP – from 0.15 to 0.19, GULFMET&AFRIMET – from 0.27 to 0.78.

The highest values of z_i scores are fixed for EURAMET NMI/DI participants, and the smallest – for COOMET and APMP. Results for all NMI/DI participants of COOMET.EM-K5 are satisfactory for z_i scores (< 3.0), but value of z_i scores for SMU and LEM-FEIT from EURAMET ($2.0 < z_i < 3.0$) indicate a dubious performance characteristic and require precautionary measures.

IV. THE EVALUATION OF KC RESULTS IN THE CONTEXT OF METROLOGICAL TRACEABILITY

In KC of power took part NMI/DIs, which had metrological traceability to the three main NMIs: PTB (Germany), UME, and NIM. PTB, NIM and VNIIM had own traceability as CCEM-K5 KC participants. PTB was a pilot laboratory for EUROMET.EM-K5 KC also. QCC EMI traceabile to NMIA (Australia), which was a pilot laboratory for APMP.EM-K5.

Fig. 7 shows the traceability of NMI/DI participants of COOMET.EM-K5 KC. Cells on Fig. 6 with a dashed line show NMI that did not participate in COOMET.EM-K5 KC.

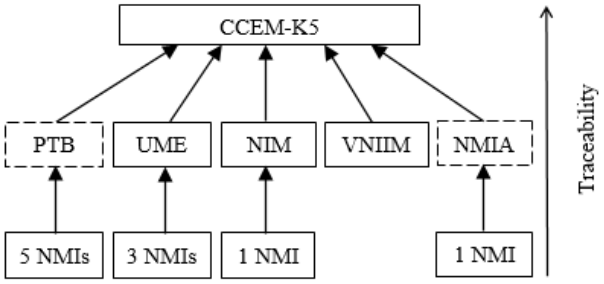

Fig. 7. The metrological traceability for NMI/DI participants.

NMI/DI results of COOMET.EM-K5 in the context of metrological traceability are shown in Table 2 and on Fig. 8. E_{ni} score and z_i score for NMI/DI participants are presented in Table 2 and on Fig. 9 (only for E_{ni} number) and Fig. 10 (for z_i score).

Values of E_{ni} number for NMI/DI participants which traceable to PTB from EURAMET are vary from 0.03 to 0.89, UME from EURAMET – from 0.03 to 0.40, NIM from APMP – from 0.04 to 0.30, other NMI – from 0.16 to 0.37.

The highest values of E_{ni} number are fixed for NMI/DI participants which traceable to PTB, and the smallest – for NIM and UME. Results for all NMI/DI participants are satisfactory for E_{ni} number (< 1.0), but value of E_{ni} number for SMU may indicate the time drift of the power standard since its last calibration in the PTB. In general, NMI/DI participants of comparison may be encouraged to calibrate it standards immediately before of comparison.

Table 2. NMI/DI results in the context of metrological traceability to NMI/DI.

NMI	D_i, 10^{-6}	$U(D_i)$, 10^{-6}	E_{ni}	z_i
		PTB		
UMTS	3.0	19.0	0.16	0.15
BelGIM	1.2	41.5	0.03	0.06
GEOSTM	16.7	89.6	0.19	0.81
SMU	-50.9	57.2	0.89	2.48
LEM-FEIT	42.0	115.6	0.36	2.04
		UME		
UME	-6.9	21.7	0.32	0.34
SASO- NMCC	-15.9	39.4	0.40	0.78
NIS	-5.5	36.3	0.15	0.27
CSM	-4.9	158.1	0.03	0.24
		NIM		
NIM	4.0	13.3	0.30	0.19
MASM	3.1	75.1	0.04	0.15
		Other NMI/DI		
VNIIM	1.7	10.6	0.16	0.08
QCC EMI	-8.2	22.2	0.37	0.40

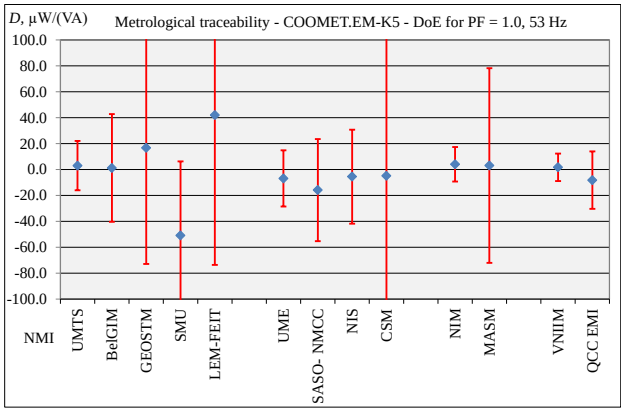

Fig. 8. DoE for NMI/DI participants in the context of traceability for PF 1.0, 53 Hz.

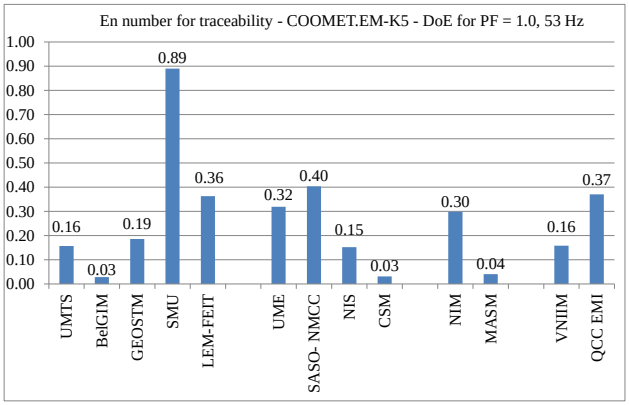

Fig. 9. E_{ni} number for NMI/DI participants in the context of traceability for PF 1.0, 53 Hz.

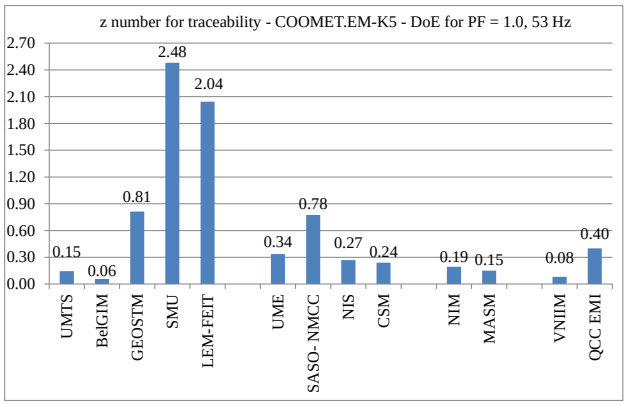

Fig. 10. z_i number for NMI/DI participants in the context of metrological traceability for PF 1.0, 53 Hz.

Values of z_i scores for NMI/DI participants which traceable to PTB from EURAMET are vary from 0.06 to 2.48, UME from EURAMET – from 0.24 to 0.78, NIM from APMP – from 0.15 to 0.19, other NMI – from 0.08 to 0.40.

The highest values of z_i scores are fixed for NMI/DI participants which traceable to PTB, and the smallest – for NIM. Results for all NMI/DI participants are satisfactory for z_i scores (< 3.0). Value of z_i scores for SMU and LEM-FEIT ($2.0 < z_i < 3.0$), which traceable to PTB, indicate a dubious performance characteristic and require precautionary measures. In both cases, the specified NMI/DI participants also need to pay attention to improving the level of practical training of staff.

V. THE POSSIBILITY OF IMPLEMENTATION OF THE CIPM MRA

BelGIM, UME, SMU, and UMTS checked COOMET.EM-K5 KC results against CMC entries in the KCDB and confirmed that the results support these CMC entries for active power.

GEOSTM, MASM, QCC EMI, SASO-NMCC, and NIS are had not CMC entries in the KCDB. COOMET.EM-K5 results of these NMI/DIs may be basis for preparing of CMC entries draft for active power.

NMIs Kyrgyzstan and North Macedonia are not signatories of the CIPM MRA, therefore, CSM and LEM-FEIT do not have possibility to prepare CMC entries draft for AC active power.

Results this KC can become the basis for recognizing quality management systems of NMI/DI participants (MASM, QCC EMI, and SASO-NMCC) for internationally recognized calibration service – CMC in field of electrical and magnetism.

VI. CONCLUSION

In general, there is good agreement of results of NMI/DI participants of KC for AC active power from five RMOs. This comparative analysis of KC results in the context of each RMO is shown the geographical context of NMI/DI participants.

All NMI/DI participants of this KC reported metrological traceability of the unit of AC active power. Traceabile of NMI/DI participants was provided through the NMIs that participated in the CCEM-K5 KC (PTB, NIM, and VNIIM), and NMIs, which was pilot laboratories of KC RMOs (UME, and NMIA). This comparative analysis can make it possible to minimize the cost of NMI/DI to achieve the required metrological traceability for AC active power. For such RMOs as COOMET, EURAMET, APMP, and GULFMET the results of this KC can become the basis for conducting a peer-review of NMIs/DIs in order to recognize its quality management systems for calibration service in framework of the CIPM MRA. It is expected that this comparison will be able to provide support for NMI/DI participants' entries in Appendix C of the CIPM MRA. Five NMI/DI participants KC (GEOSTM, MASM, QCC EMI, SASO-NMCC, and NIS) which do not have CMC entries in the KCDB got such opportunity.

REFERENCES

[1] O. N. Velichko, "Traceability of measurement results at different levels of metrological work", Measurement Techniques, 52, 11, 2009, pp. 1242–1248.

[2] JCGM 200, International vocabulary of metrology, Basic and general concepts and associated terms (VIM), 3-rd edition, 2012, 105 p.

[3] Text of the CIPM MRA, 1999, 28 p.

[4] The BIPM key comparison database (KCDB), Available from: http://kcdb.bipm.org.

[5] CIPM MRA-G-13, Calibration and Measurement Capabilities in the context of the CIPM MRA, Guidelines for their review, acceptance and maintenance, 2021, 24 p.

[6] O. N. Velichko, "Calibration and measurement capabilities of metrological institutes: features of preparation, examination, and publication", Measurement Techniques, 53, 6, 2010, pp. 721–726.

[7] CIPM MRA-G-11, Measurement comparisons in the CIPM MRA, Guidelines for organizing, participating and reporting, 2021, 26 p.

[8] JCGM 100, Uncertainty of measurement, Part 3: Guide to the expression of uncertainty in measurement (GUM), 2008, 134 p.

[9] COOMET R/GM/14, Guidelines for data evaluation of COOMET key comparison, 2016, 6 p.

[10] T. Yandayan, A. M. Dahlan, "Promotion of Cooperation Activities in Metrology between Europe and South East Asia", International metrology conference CAFMET, 2010, 8 p.

[11] M. G. Cox, "The evaluation of key comparison data", Metrologia, 39, 2002, pp. 589–595.

[12] G. Mana, E. Massa, M. Predescu, "Model selection in the average of inconsistent data: an analysis of the measured Planck-constant values", Metrologia, 49, 2012, pp. 492–500.

[13] F. Delahaye, T. J. Witt, “Linking the results of key comparisons CCEM-K4 with the 10 pF results of EUROMET.EM-K4”, Metrologia, 39, 01005, 2002.
[14] O. Velychko, “Proposals for linking the results of key comparisons CCEM-K4 and COOMET.EM-K4”, In: Proceedings of the Conference on Precision Electromagnetic Measurements (CPEM 2010), Daejeon, South Korea, 5545263, 2010, pp. 414-415.
[15] O. Velychko, S. Karpenko, “Final report on COOMET Key Comparison of Power (COOMET.EM-K5)”, Metrologia, 56, 1A, 01010, 2019.
[16] N. Oldham, T. Nelson, N. F. Zhang, H.-K. Liu, “Report of CCEM-K5 Comparison of 50/60 Hz Power”, Metrologia, 40, 1A, 01003, 2003.
[17] H. Çaycı, “EURAMET.EM-K5.1 Key Comparison of 50/60 Hz Power Final Report”, Metrologia, 48, 01009, 2011.
[18] O. Velychko, “Possibilities of linking results of key and supplementary comparisons in field of electricity and magnetism”, Measurement, 2019, pp. 144, 167.
[19] O. Velychko, T. Gordiyenko, “Metrological Traceability at Different Measurement Levels, Standards, Methods and Solutions of Metrology”, IntechOpen, 2019, pp. 1-21.
[20] ISO/IEC 17043:2010, “Conformity assessment – General requirements for proficiency testing”.

25th IMEKO TC4 International Symposium
23rd International Workshop on ADC and DAC Modelling and Testing
IMEKO TC-4 2022
Brescia, Italy / September 12-14, 2022

Research of Long-Term Drift of the National High-Voltage DC Standard

Oleh Velychko[1], Ruslan Vendychanskyi[2]

State Enterprise "All-Ukrainian state research and production center for standardization, metrology, certification and consumers' rights protection" (SE "Ukrmetrteststandard"), Metrologichna Str., 4, 03143, Kyiv, Ukraine
[1] velychko@ukrcsm.kiev.ua, [2] vendychanskyi@gmail.com

***Abstract* – The high-voltage direct current (DC) technology is widely used in electrophysical, environmental, electrical, power plants and systems. Power transmission DC is more economical than on alternating current, therefore high DC lines are built in many countries. The high-voltage DC is used for testing of the insulation of capacitors, cables, rotating machines, etc. For these types of insulation, the detection of significant defects is effective at high direct voltage. The National high-voltage DC standard of Ukraine has already undergone several modernizations to improve its metrological characteristics and reliability during operation from 1999. Research of the metrological characteristics of the this standard allows to increase the accuracy and reliability of calibration of high-voltage DC working standards of accredited calibration laboratories.**

I. INTRODUCTION

The high-voltage direct current (DC) technology is widely used in electrophysical, environmental, electrical, power plants and systems. Power transmission on DC is more economical than on alternating current, therefore high DC lines are built in many countries of the world. It is possible to transmit large powers with less losses through them [1,2].

The high-voltage DC is used for acceptance or maintenance testing of the insulation of capacitors, cables and rotating machines. For these types of insulation, the detection of significant defects is effective at high direct voltage, at which there is no danger of powerful partial discharges and there is practically no destructive effect on defect-free insulation [2].

An urgent task is to ensure the metrological traceability of high-voltage DC working standards and measuring instruments. An important role in this is played by the national standards of different countries. They provide the highest level of working standard calibrations for accredited calibration laboratories [3,4].

II. NATIONAL HIGH-VOLTAGE DC STANDARDS

Less than twenty countries have high-voltage DC standards that have voltages above 150 kV. In addition, these standards differ significantly in their accuracy. The best such standards include the national standards of such countries as Sweden, Finland, Australia, Turkey, Canada, Germany, France, Spain [5].

The State Primary Standard of a Unit of DC Electric Voltage of range from 1 kV to 180 kV (National High-Voltage DC Standard) functions in State Enterprise "Ukrmetrteststandard" (UMTS, Kyiv, Ukraine) since 1999. During operation, the National High-Voltage DC Standard has already undergone several modernizations to improve its metrological characteristics and reliability. The standard has a long-term history of research of its characteristics.

Metrological characteristics of National High-Voltage DC Standard:

- range of reproduction of nominal values of high-voltage DC from 1 kV to 180 kV;
- standard deviation of the measurement result when reproducing a unit of high-voltage DC does not exceed $5 \cdot 10^{-5}$;
- expanded measurement uncertainty is $3.6 \cdot 10^{-4}$;
- instability for the year does not exceed is $3 \cdot 10^{-4}$.

During the COOMET.EM-S7 supplementary comparison [6] was established metrological characteristics of National High-Voltage DC Standard have high stability and a reserve for improvement.

A general view of the national standard is presented on Fig. 1.

III. RESEARCH OF THE NATIONAL HIGH-VOLTAGE DC STANDARD OF UKRAINE

The basis of the National High-Voltage DC Standard is the combined measures of high-voltage DC (CMs). These measures consist (Fig. 2) of unambiguous DC measures (UMs) with a nominal voltage of 1 kV on Zener diode (VD), a current stabilization unit for the measuring circuit (BS) and a voltmeter (V). UMs are implemented on Zener diodes, which are selected and tested according to special methods [7].

Metrological characteristics of UM:

- nominal voltage value for (U_{UMn}):

Fig. 1. The general view of National high-voltage DC standard.

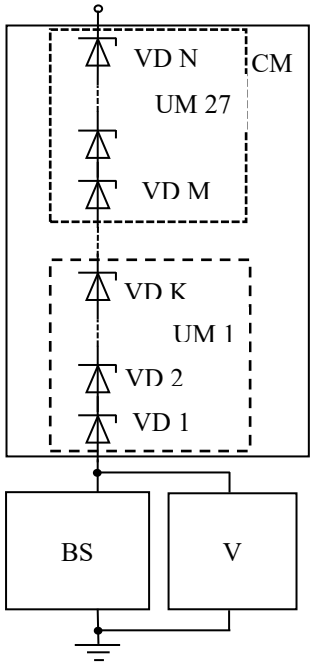

Fig. 2. The generalized structural scheme of CM.

unambiguous measure of type I (UM1… UM10) is 1 kV; unambiguous measure of type II (UM11… UM27) is 10 kV;
- deviation of the actual voltage value from the nominal value of the voltage measure is $1 \cdot 10^{-4}\ U_{UMn}$;
- instability of the actual voltage value of unambiguous measure not more than is $2 \cdot 10^{-4}\ U_{UMn}$.

Metrological characteristics of BS:
- the range of stabilization of the operating current of UMs: range I is from 10 to 100 V;
range II is from 100 to 1000 V;
- nominal value of stabilization current is 5 mA;
- deviation of the actual value of the stabilization current from the nominal value is ±5 μA.

Measurement of the high-voltage DC is based on the differential method of measurement. The value of DC voltage is calculated by the equation:

$$U_{SS} = U_{SSs} + \Delta U_{SSV}, \qquad (1)$$

where $U_{SSs} = \sum_{k=1}^{N} U_{OS\,k}$ is the true value of the high-voltage DC of CMs at 180 kV, in volts; $U_{OS\,k}$ is the DC voltage of k-th UM, N is numbers of UMs in the combined measure ($N = 180$); ΔU_{SSV} is the measured value of DC voltage of a precision voltmeter, in volts [7].

The combined standard measurement uncertainty of high-voltage DC of the National High-Voltage DC Standard is calculated by the equation:

$$u_{c\ SSs} = \frac{1}{U_{SSs}} \sqrt{\left(\sum_{k=1}^{N} u_{OS\,k}^2 + u_{SSV}^2 \right)}, \qquad (2)$$

where $u_{OS\,k}$ is the standard measurement uncertainty of k-th UM; u_{SSV} is the standard measurement uncertainty of measurement high DC voltage by precision voltmeter [7,8].

IV. RESEARCH OF LONG-TERM DRIFT OF THE NATIONAL STANDARD

The National High-Voltage DC Standard has been constantly researched since 1999. Its modernizations have improved metrological characteristics.

Table 1 and in Figs 1–3 show the results of determining the standard deviation (SD) reproduction of the CM output voltage of the standard from 1999 to 2021. The value of SD in relative units is in the range from $0.04 \cdot 10^{-6}$ to $10.4 \cdot 10^{-6}$.

The following remarks can be made from Figs 1–3:
- with increasing voltage, the relative value of SD decreases;

Table 1. Change of SD for voltage range from 1 kV to 180 kV.

U_n	Year/SD								
	2021	2019	2016	2013	2010	2007	2004	2000	1999
1	0.89	1.23	0.50	2.46	1.33	1.19	2.85	10.40	2.20
2	0.71	0.74	0.83	1.24	0.95	1.46	1.60	5.05	1.20
3	0.45	0.5	0.55	1.02	0.70	0.97	1.54	3.37	0.77
4	0.4	0.42	0.46	0.80	0.57	0.81	1.18	2.53	0.70
5	0.38	0.41	0.44	0.72	0.56	0.76	0.97	2.05	0.62
6	0.3	0.35	0.39	0.63	0.53	0.67	1.02	1.71	0.67
7	0.28	0.32	0.35	0.55	0.46	0.61	0.88	1.47	0.47
8	0.28	0.3	0.33	0.51	0.42	0.62	0.78	1.29	0.44
9	0.26	0.29	0.33	0.51	0.44	0.61	0.72	1.15	0.39
10	0.27	0.3	0.35	0.52	0.47	0.62	0.68	1.04	0.36
20	0.14	0.17	0.19	0.28	0.27	0.33	0.60	0.85	1.10
30	0.09	0.12	0.14	0.19	0.21	0.24	0.42	0.69	0.83
40	0.07	0.09	0.11	0.15	0.17	0.19	0.35	0.60	0.68
50	0.07	0.08	0.09	0.13	0.14	0.16	0.29	0.52	0.66
60	0.08	0.07	0.08	0.12	0.12	0.14	0.33	0.46	0.55
70	0.08	0.06	0.07	0.10	0.11	0.13	0.29	0.42	0.52
80	0.08	0.06	0.07	0.10	0.10	0.11	0.25	0.39	0.56
90	0.07	0.05	0.06	0.09	0.09	0.10	0.23	0.36	0.54
100	0.05	0.05	0.06	0.08	0.09	0.10	0.21	0.35	0.50
110	0.04	0.04	0.06	0.08	0.08	0.09	0.19	0.33	0.47
120	0.04	0.04	0.05	0.07	0.08	0.09	0.20	0.31	0.44
130	0.04	0.04	0.05	0.07	0.07	0.08	0.31	0.30	0.42
140	0.04	0.04	0.05	0.06	0.07	0.08	0.35	0.29	0.39
150	0.04	0.04	0.04	0.06	0.07	0.07	0.41	0.27	0.37
160	0.03	0.03	0.04	0.05	0.06	0.07	0.45	0.26	0.35
170	0.03	0.03	0.04	0.05	0.06	0.07	0.45	0.24	0.34
180	0.03	0.03	0.04	0.05	0.06	0.06	0.45	0.23	0.34

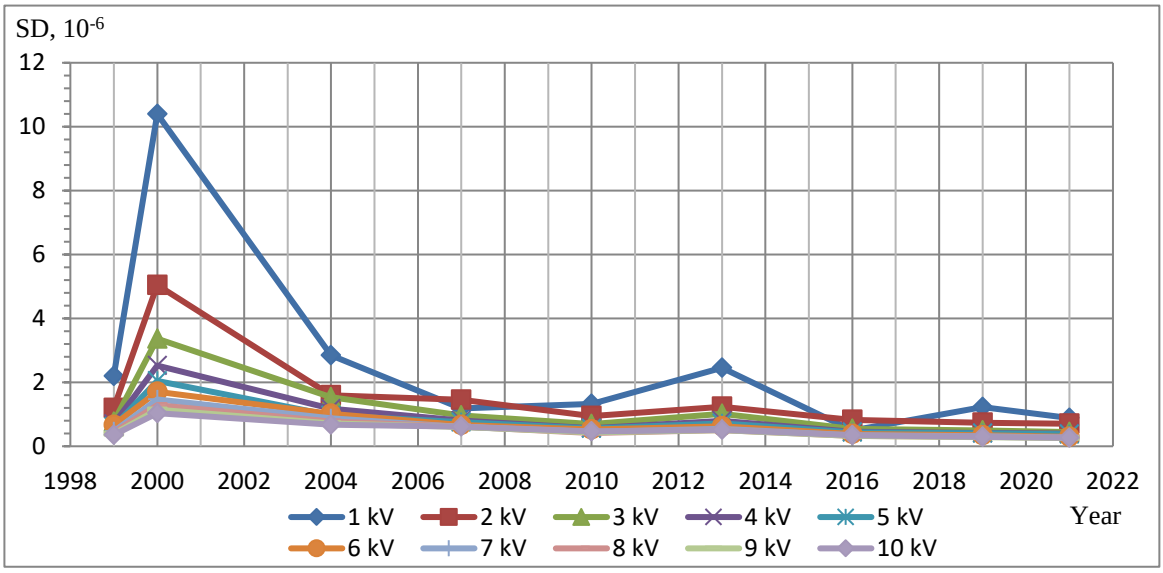

Figure 1. Change of SD for voltage range from 1 kV to 10 kV.

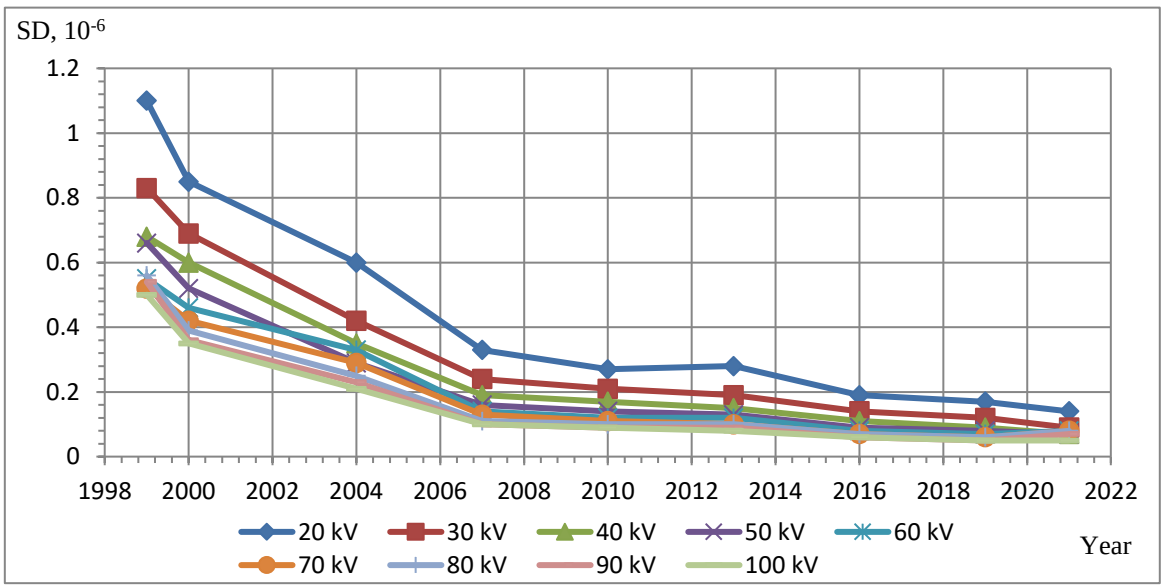

Figure 2. Change of SD for voltage range from 20 kV to 100 kV.

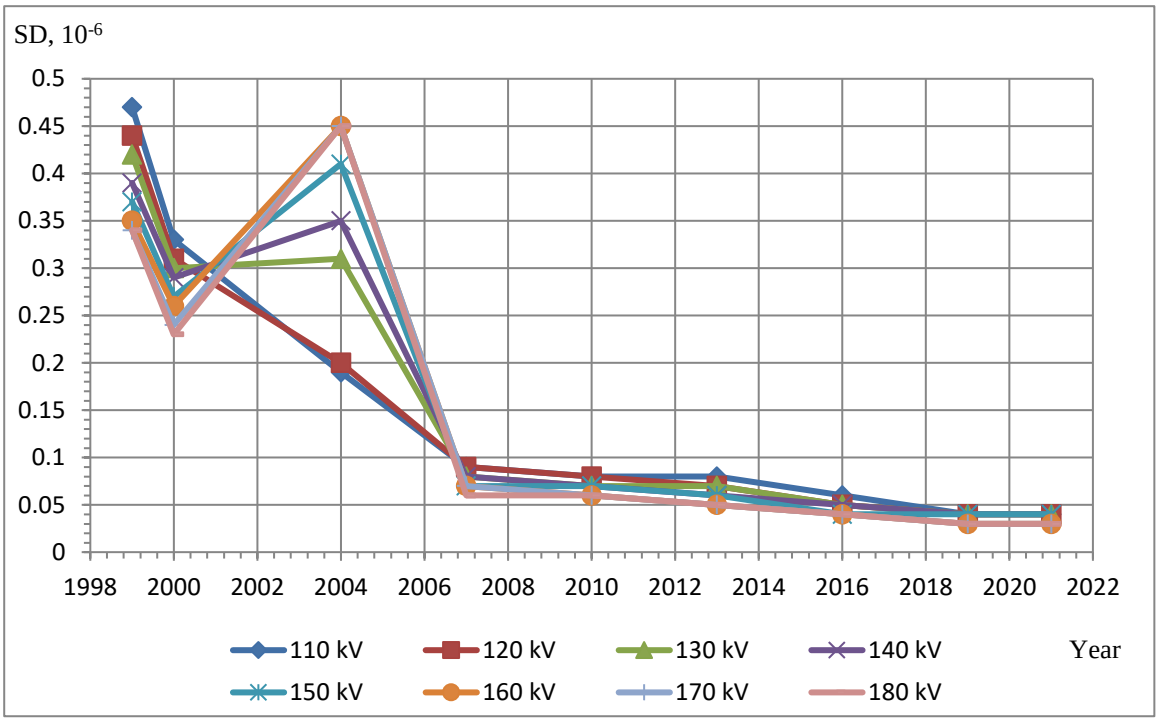

Figure 3. Change of SD for voltage range from 110 kV to 180 kV.

- in the period from 1999 to 2007 there was a significant decrease of SD;
- for the voltage range from 130 kV to 180 kV in 2004 there was a significant increase in SD, with its further decrease in subsequent years.

Analysis of research results for this period indicates the following reasons:
- since 2007 the Fluke 9100 E calibrator, which has much higher metrological characteristics than the calibrator previously used, has been used to research of UMs of types I and II;

- significant reduction of SD, which was observed in the period from 1999 to 2007, caused by the natural aging of low-voltage Zener diodes and the stabilization of its electrical characteristics;
- the decrease in the value of SD with increasing voltage is associated with a decrease in the impact of high-voltage electric fields on UM of type II, which are used for voltages above 100 kV;- a significant increase in SD for the voltage range from 130 to 180 kV is due to the high value of instability of one section of the UM, which corresponds to the nominal voltage of the standard 130 kV, after its repair the nature of SD change in subsequent years.

V. CONCLUSION

The research of the National High-Voltage DC Standard for long-term period allows you to constantly monitor it metrological characteristics. Accurate determination of the characteristics of the this standard allows to increase the accuracy and reliability of calibration of high-voltage DC working standards of accredited calibration laboratories.

REFERENCES

[1] K.Schon, High Voltage Measurement Techniques. “Fundamentals, Measuring Instruments, and Measuring Methods”, Springer Nature Switzerland AG, 2019, 466 p. doi: 10.1007/978-3-030-21770-9_1

[2] A.Küchler, “High Voltage Engineering. Fundamentals-Technology-Applications”, Springer Vieweg, Berlin, 2018, 650 p. doi: 10.1007/978-3-642-11993-4.

[3] JCGM 200:2012. International vocabulary of metrology – Basic and general concepts and associated terms (VIM). 3rd edition. JCGM, 2007. 108 p.

[4] Velichko O. N., “Traceability of measurement results at different levels of metrological work”, Measurement Techniques, vol. 52, 2009, No. 11, p. 1242–1248. doi: 10.1007/s11018-010-9428-7.

[5] The BIPM key comparison database (KCDB), http://kcdb.bipm.org.

[6] RMO comparison COOMET.EM-S7, https://www.bipm.org/kcdb/comparison?id=1393.

[7] Velychko O., Vendychanskyi R., “Research of the National Primary Standard of the High DC Voltage”, Digest of 2018 Conf. on Precision Electromagnetic Measurement. Paris, France. 2018 (June 8–13), 2 p.

[8] JCGM 100:2008 (GUM 1995 with minor corrections) “Evaluation of measurement data – Guide to the expression of uncertainty in measurement”. JCGM, 2008. 134 p.

25th IMEKO TC4 International Symposium
23rd International Workshop on ADC and DAC Modelling and Testing
IMEKO TC-4 2022
Brescia, Italy / September 12-14, 2022

Automatic Detection System of New Energy Vehicle Charging Pile Based on Image Recognition

Jianbo Liu,Wenqiang Li, Weizhao Wang, Xuefeng Ma, Mei Yang, Bin Deng, Xinyan Wang

Shandong Engineering Research Center of Reliability Evaluation for Electric Energy Metering Devices，Shandong Institute of Metrology, No.28, Qianfoshan East Road, 250014 Jinan, China
18553159166@163.com

***Abstract* –In this paper, the active electric energy value of the charging pile and its change time scale are obtained through the image recognition algorithm, and the low-pass filter algorithm is used to filter out the time scale jitter. By calculating the active electric energy value (*Ex*) of the charging pile in the time scale interval and the standard electric energy value (*Eb)* in the same interval, the active electric energy error is calculated according to the electric energy comparison method. Compared with the traditional energy comparison method, the verification time is related to the minimum quantitative value of active electric energy, The verification time of this method is only related to the jitter of time scale and the quantization error of camera, which can greatly improve the verification efficiency of low-power charging pile.**

***Keywords* –image recognition, the charging pile, the jitter of time scale**

I. INTRODUCTION

The important basis for trade settlement of charging piles is active electric energy[1]. Most of the charging piles in stock have no pulse detection output of hardware, and only the accuracy of active electric energy can be measured by electric energy comparison method, This method must meet the requirements of "the standard meter shall operate synchronously with the tested charging pile, and the ratio (%) of the electric energy value represented by the last word (or minimum Division) of the tested charger display to the accumulated shall not be greater than 1/10 of the grade index of the tested charger"[2]. Since the resolution of the active electric energy value of the charging pile is mostly 0.01 degrees, in order to meet the requirements, the minimum cumulative electric energy will reach 10kWh, resulting in very slow measuring speed. Under small working current, it takes more than 30min for a single test point. The regulation also requires that "the average value of two errors is taken as the verification result", then the verification time will be doubled; The verification time of other items in the regulation is about 10min[3][4]. In addition, the on-site operation seriously restricts the work efficiency and cannot complete the verification task. The detection technology based on image recognition algorithm adopted in this paper can ensure that a point can be verified within 17min regardless of the detection current, which greatly improves the verification efficiency of charging pile under small current[5][6].

II. TECHNICAL SCHEME

In order to solve the problem of slow measuring speed, the image recognition technology is used to read the active electric energy of the charging pile. Combined with the filtering algorithm, the full-automatic and rapid verification of the charging pile can be realized, the work efficiency can be improved and the human error can be reduced. It can be applied to the laboratory, on-site detection and the factory detection of the charging pile equipment.

The active energy value displayed by the camera on the charging pile is obtained through the convolution neural network (CNN) algorithm, and the digital active energy value and change time scale value are obtained. The delay jitter is filtered through the low-pass filter algorithm, And reconstruct the time scale value of the active power value collected by the camera, calculate the standard power value (*Eb*) collected by the AD acquisition module in the interval from the $M + 1$ time scale value (M is the screen refresh rate) to the nth time scale value (n is the cut-off frequency of the filter), compare the power value (*Ex*) collected by the camera in the same time zone, and calculate the active power error according to the power comparison method.

As shown in *Figure 1*, the detection system is composed of USB camera, DSP processing motherboard, computer, USB to serial port, electric vehicle analog load, vehicle DC charging interface circuit simulator, current sensor, power module, proportional partial voltage resistance and AD acquisition module.

Among them, the USB camera can manually adjust the focal length, which can be well focused to the active power data. Its magnification is 20 ~ 220 times, continuously adjustable, and the frame rate is 45fps; DSP processing motherboard adopts DSP-BF609 EZ-KIT Lite of ADI, which meets the calculation performance and interface requirements of the system; The analog load of electric vehicle adopts equivalent resistance or electronic load or directly adopts rechargeable battery, and the resistance value of the load can be set through CAN bus; The electric vehicle charging interface circuit simulator adopts the charging pile control guidance detection device for simulation, or other equipment meeting the requirements of relevant standards can be used to simulate the communication and interoperability between electric vehicle and charging pile; The current sensor is used to convert the current signal into voltage signal for AD acquisition module to collect; The power module outputs customized power supplies of ±5V and ±3.3V, and the current output capacity is 2A; The proportional voltage dividing resistance is composed of 2kΩ, 0.01% precision resistance and 998kΩ, 0.01% precision resistance, and the transformation ratio is 500:1.

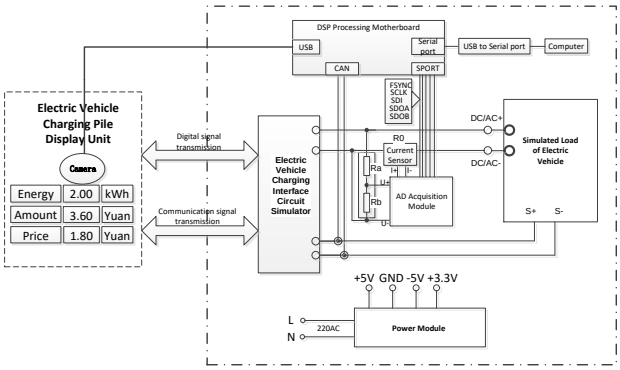

Fig. 1. Block diagram of detection system.

III. WORKING PRINCIPLE

The proportional voltage divider reduces the voltage signal by 500 times, and the current sensor converts the current signal into a voltage signal and inputs it to the AD acquisition module. The AD acquisition module continuously collects the signal values of voltage and current channels at a sampling rate of 1ksps, calculates the current standard electric energy value EBI according to equation 1, and saves the corresponding time scale value T_{bi} (unit: Second).

$$Eb_{\mathrm{i}} = \sum_{m=1}^{i} \frac{U_m \times I_m \times T_s}{3600 \times 1000} \tag{1}$$

T_{s}: refers to the sampling time interval. The sampling rate of the system is 1ksps, so the sampling interval is 0.001 seconds; U_{m}: sampling value of voltage, unit: V; I_{m}: sampling value of current, unit: A; *I*: Is the current sampling point; *m*: Is a historical sampling point.

At the same time, continuously receive the image signal, analyze the electric degree value of active electric energy (*Ex*) through CNN algorithm, and save the corresponding time scale value (T'_{n}), after passing through the low-pass filter, reconstruct the time scale value (T''_{n}) according to formula 10.The low-pass filter M = 20th order, the cut-off frequency is 0.01fs (Fs sampling rate which is the time interval for the camera to read the change value of electric energy each time), Through the reconstructed time scale value *Ex* of the electric energy value of the tested electric energy meter in the corresponding interval of $T''_{M+1}$to T''_{n}, and the standard electric energy meter value *Eb* of the corresponding time period of AD acquisition module, calculate the active electric energy error of the charged pile according to formula 4. The calculation of standard electric energy meter *Eb* (referring to the electric energy calculated by AD acquisition module according to Formula 1) is shown in formula 2.

$$Eb = Eb_{m2} - Eb_{m1} \tag{2}$$

Eb_{m1} is the electric energy value Ex_{M+1} of the standard electric energy meter at the corresponding time of the tested charging pile; Eb_{m2} is the electric energy value Ex_n of the standard electric energy meter at the corresponding time of the tested charging pile.

The electric energy value of the tested charging pile in this time period is

$$Ex = Ex_n - Ex_{M+1} \tag{3}$$

So as to calculate the error value of active electric energy γ by

$$\gamma = \frac{Ex - Eb}{Eb} \times 100\% \tag{4}$$

IV. PRINCIPLE OF IMAGE RECOGNITION

Image recognition only involves the recognition of numbers 0 ~ 9. In order to simplify the design, as shown in *Figure 2*, we only need to manually frame the individual, tenth and percentile images of active electric energy through the mouse, and then classify them according to 0 ~ 9 respectively. Since the maximum electric value tested by the charging pile based on image recognition does not exceed 9.99kwh, generally 1.00 kwh can meet the requirements of test accuracy.

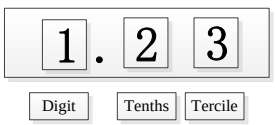

Fig. 2. Image analysis diagram.

Manually framing three numbers can greatly reduce the boundary recognition of the image. After framing, the data matrix (U8 RGB_Digit [m_1][n_1][3],U8 RGB_Tenths[m_2][n_2][3],U8 RGB_Tercile [m_3][n_3][3] ,

m_1,m_2 and m_3 are the total pixels of the row of the image intercepted by the mouse, and n_1,n_2 and n_3 are the total pixels of the column of the image framed by the mouse) of three digital images can be obtained by reading the images of three numbers, RGB pixels are stored in the array, and the color pixels are converted into gray pixels (U8 Gray_Digit[m1][n1], U8 Gray_Tenths[m2][n2]、 U8 Gray_Tercile [m3][n3]) through RGB to gray function, which coexists in the digital matrix, True color image is m × n × 3 numerical array, grayscale image is m × n numerical array, evenly extract the three digital pixel matrices into 28 × 28 digital matrices, the purpose is to match the existing MNIST dataset, the extracted array is U8 Mnist_Digit[28][28],U8 Mnist_Tenths[28][28], U8_UnitTercile[28][28]. As the background color of the active electric energy of the charging pile and electric value of the electric degree value displayed are basically fixed in two colors, according to this known information, we can store the gray level of 28 × 28 digital matrices are further binarized, if the gray value of and 4 edges and corners which is within ± 50 is 0, otherwise the gray value is 1,as shown in formula 5. Then, the numerical classification of individual Digit, tenth and Tercile is recognized by CNN, and the electric energy value recognized by the current image is obtained according to equation 6.

$$f(v)=\begin{cases}0 & \mathrm{Mod}(v+256-vb)\le 50\\ 1 & \mathrm{Mod}(v+256-vb)>50\end{cases} \quad (5)$$

vb is the average gray value of the four corners, and *v* is the gray value of the current pixel color.

$$Ex_i=\mathrm{Digit}\times 1+\mathrm{Tenths}\times 0.1+\mathrm{Tercile}\times 0.01 \quad (6)$$

The frame rate of the camera is 45Hz, so there will be one frame of image every 22ms. If the image value of this frame is different from that of the previous frame (the first frame is directly stored), store the current electrical value Ex_i and the current time scale T_i', as shown in *Figure 3*, the charging pile interface displays electric energy and time scale.

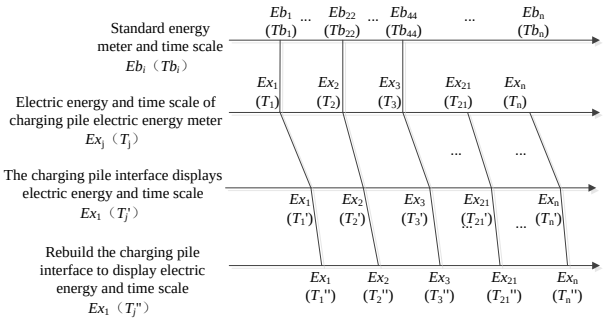

Fig. 3. Principle of time synchronization between electric energy and time scale.

CNN needs to use MNIST data set for training before use. It can also binarize MNIST data set according to the middle value of gray level for training. The program will save the learned parameters and can be used directly without training next time. There are 70000 pictures in MNIST dataset, including 60000 for training CNN and 10000 for testing CNN. Each picture is a 28 ×28 Handwritten digital pictures of 0 ~ 9 pixels. Each sample is a 28 × 28 pixel gray handwritten digital picture with white characters on black background.

V. TIME SCALE JITTER PROCESSING

The camera can obtain a time scale with a time standard accuracy of 22ms. Because the charging pile displays the electric energy by acquiring the data of the metering module in the pile, the inconsistent communication time of the read data will cause the time scale of image recognition to shake, as shown in *Figure 4*. The time interval of electric energy measurement of the metering module in the tested charging pile is even, but the time scale displayed on the charging pile interface is uneven. Therefore, the detection time of the charging pile must be prolonged to obtain sufficient accuracy, Assuming that the maximum jitter of the time scale is 0.5s, and just the last jitter time scale is 0.5s, In this way, according to the system control error of 0.1%, the detection time is 0.5s×1000=500s. Since the power output of the charging pile is very stable and the power calculation is shown in formula 7, the difference between each active electric energy value and the last active electric energy value is taken as the input, If $\Delta T_i=Tx_i-Tx_{i-1}>0$, formula 7 can be rewritten into formula 8. A low-pass filter is designed to conduct low-pass filtering for the function Δ T, filter out the time scale jitter, so as to restore to the time scale of the metering module in the tested charging pile, and reduce the influence of jitter by 10 times or less. As shown in *Figure 4* and *Figure 5*.

$$P_i=\begin{cases}\dfrac{Ex_i-Ex_{i-1}}{Tx_i-Tx_{i-1}} & i>0\\ \dfrac{Ex_0-0}{Tx_0-0} & i=0\end{cases} \quad (7)$$

$$\Delta T_i=\begin{cases}\dfrac{Ex_i-Ex_{i-1}}{P_i} & i>0\\ \dfrac{Ex_0-0}{P_0} & i=0\end{cases} \quad (8)$$

ΔT_i adopts FIR finite impulse filter, and its difference equation is shown in formula 9.

$$\mathrm{y}(n)=\sum_{k=0}^{M}b_k x(n-k) \quad (9)$$

y(*n*) is the output value of the filter; *x*(*n*-*k*) is the input value of the filter; *M*: Is the order of the filter: 20; *b*: Is the filter coefficient.

The coefficient of filter is the key of FIR filter. Various filters can be generated by modifying the coefficient. The order of filtering is designed as M = 20, and the cut-off frequency is set to the sampling rate of

0.01. The filter coefficient is obtained by fir1 of MATLAB: Set M = 20, W_n=0.02% (W_n corresponds to half of the sampling frequency), b=fir1(M， W_n,, 'low'), The filter coefficient of B is

b=[0.0070,0.0090,0.0149,0.0243, 0.0361,0.0494, 0.0627,0.0749,0.0845,0.0908, .09290,0.0908, 0.0845,0.0749,0.0627,0.0494,0.0361,0.0243, 0.0149,0.0090,0.0070]. The input data of FIR filter is $\Delta T_j'$, as shown in *Figure 4*, and the output data of FIR filter is $\Delta T_j''$, as shown in *Figure 5*. Since the phase shift of FIR filter is m / 2 = 10, as shown in Figure 5, the first 10 numbers are invalid.

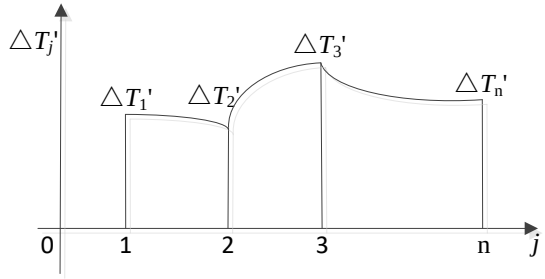

Fig. 4. Camera reading time scale interval.

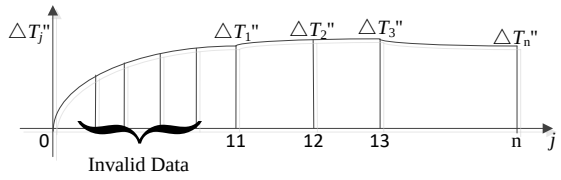

Fig. 5. Time scale interval after filter.

As shown in *Figure 3*, reconstructing the time scale of the charging pile display interface according to the output result of the filter is actually filtering out the reading delay jitter and restoring the real time scale close to the metering module in the tested charging pile, as shown in formula 10.

$$T_n'' = \sum_{k=2}^{n} \Delta T''_{n+M/2} + T_1' \qquad (10)$$
$$T_1'' = T_1' \text{且} n>1$$

The filter output is delayed by M/2 points. After T_n' passes through the low-pass filter, the purpose is to reduce the impact of time scale jitter on the measurement error. The time scale interval of T_n'' 'after filtering is closer to the real time scale T_n of the metering module in the charging pile. M sampling points are required to completely restore the FIR filter. In this system, the start of intercepting data starts from T_{11}' and the corresponding filter output is T''_{M+1}.

VI. PRINCIPLE OF ELECTRIC ENERGY CALIBRATION

As shown in *Figure 6*, search the time scale Tb_{m1} closest to T''_{M+1} in the time scale Tb[0,m] of the standard electric energy meter, the retrieval method is to find the number of I with $Tb_i - T''_{M+1}$ as the minimum value, and the number is $m1$. Then search the time scale Tb_{m2} closest to T_n'' in the time scale Tb[0,m] of the standard electric energy meter. The search method is to find the number of i with $Tb_i - T_n''$ as the minimum value, and the number is $m2$. The value of n is related to the charging power of the charging pile. The value algorithm is that the test time is greater than 100 seconds, that is, assuming that the time jitter after filtering is less than 0.1 seconds and the additional error is less than 0.1%. According to the requirements of the regulations, it can only reach the additional error of 0.1%. The time resolution of Tb_i is 1ms, and the time resolution of the electric energy meter of the charged pile is 22ms. Relative to the operation error of 0.1s, it can be ignored. In this way, in the same time interval, the electric degree value of the standard electric energy meter is calculated according to equation 2, the electric degree value of the electric energy meter of the tested charging pile is calculated according to equation 3, and the active electric energy error value calculated by comparing the standard and the tested electric energy meter value is calculated according to equation 4.

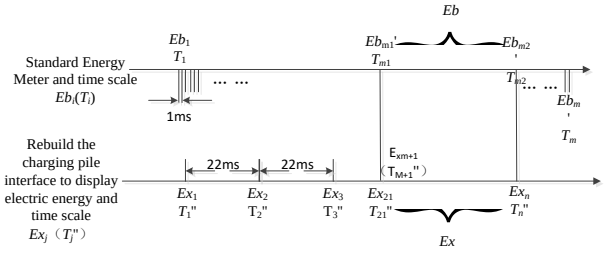

Fig. 6. Acquisition of electric energy and time scale.

VII. TEST RESULTS AND ANALYSIS

As shown in *Figure 7*, the field test is carried out according to the method in this paper.

The traditional electric energy comparison method and the method based on image recognition are measured respectively. The test time takes the level 1 charging pile as an example. The duration of one-time verification of an error verification point (for the stock pile with the current resolution of 0.01 degrees) is shown in the table below. According to the requirements of the verification regulation, the measurement is carried out when the output current of the charging pile is Imin, 0.5imax and IMAX respectively. The comparison results are shown in Table 1, Table 2 and Table 3:

Fig. 7. Field test picture.

Table 1. Comparison of verification time of DC charging pile.

Output Power	Electric Energy Comparison Method	Image Recognition Method
570 V 5 A(I_{min})	210 min	16.7 min
570 V 120 A(0.5I_{max})	8.7 min	16.7 min
570 V 250 A(I_{max})	4.2 min	16.7 min
Total Time	222.9min	50.1 min

Table 2. Comparison of verification time of Single-phase AC charging pile.

Output Power	Electric Energy Comparison Method	Image Recognition Method
220 V 0.5 A(I_{min})	2727 min	16.7 min
220 V 16 A(0.5I_{max})	85 min	16.7 min
220 V 32 A(I_{max})	43 min	16.7 min
Total Time	2885 min	50.1 min

Table 3. Comparison of verification time of Three-phase AC charging pile.

Output Power	Electric Energy Comparison Method	Image Recognition Method
220 V 1 A(I_{min})	909 min	16.7 min
220 V 32 A(0.5I_{max})	28.4 min	16.7 min
220 V 63 A(I_{max})	14.4 min	16.7 min
Total Time	951.8 min	50.1 min

The experimental data show that through the error verification of charging pile based on image recognition, The efficiency of off-board charger is increased by 4.5 times, the efficiency of single-phase AC charging pile is increased by 57 times, and the efficiency of three-phase AC charging pile is increased by 19 times. For the verification of low power output points of AC charging pile or DC charging pile, the time advantage is obvious, so this method is recommended for verification. When the output power of DC charging pile is large, there is no obvious efficiency advantage, but the total verification time is significantly shortened and the efficiency is significantly improved.

VIII. CONCLUSION

By designing a low-pass filter with a cut-off frequency of 0.01fs (sampling rate), the random time jitter returned by the DC electric energy meter is effectively filtered, the detection time scale is reconstructed, the random time jitter is reduced, and the rapid detection of active electric energy of the charging pile is realized.

The charging pile error verification based on image recognition does not change the verification method of the national metrological verification regulation, nor does it violate the principle of making the system error meet 1 / 10 of the grade index and ignoring the influence of the system error. Its verification time is greatly shortened and the efficiency of charging pile verification is greatly improved.

REFERENCES

[1] Ge Jun, Discussion on verification of AC charging pile of electric vehicle [J] China's strategic emerging industries, 2020 (4): 131.

[2] Che Renbo, Discussion on metrological verification of electric vehicle charging pile [J] Exploring science, 2020 (4): 14.

[3] Zhang Hongbao, Peng Lu, Xu Pengfei, et al Research on metrological verification of electric vehicle charging pile [J] Measurement and testing technology, 2019,46 (3): 29-31 DOI:10.15988/j.cnki. 1004-6941.2019.3.009.

[4] Chen Yongqiang, LV Guowei, Qiu Qiaodan, Some suggestions on the current situation of metrological verification of in-service electric vehicle charging pile [J] Household appliances, 2019 (9): 14-19 DOI:10.3969/j.issn. 1673-6079.2019.09.005.

[5] Wei Dong, Dong bochen, Liu Yiqing, Design and hardware implementation of image recognition system based on improved neural network [J] Journal of electronics and information, 2021,43 (7): 1828-1833 DOI:10.11999/JEIT200202.

[6] Qi Yanrong, Zhou XiaBing, Li Bin, et al

Acceleration and optimization of CNN image recognition based on FPGA [J] Computer science, 2021,48 (4): 205-212 DOI:10.11896/jsjkx. two hundred million six hundred thousand and eighty-nine

25th IMEKO TC4 International Symposium
23rd International Workshop on ADC and DAC Modelling and Testing
IMEKO TC-4 2022
Brescia, Italy / September 12-14, 2022

Online SFRA characterization of a batch of induction motors for predictive maintenance.

Giovanni Bucci, Fabrizio Ciancetta, Andrea Fioravanti,

Edoardo Fiorucci, Simone Mari, Andrea Silvestri

Department of Industrial Engineering Information and Economics, Monteluco di Roio, 67100, L'Aquila (AQ), { giovanni.bucci, fabrizio.ciancetta, edoardo.fiorucci, andrea.silvestri1}@univaq.it {simone.mari, andrea.fioravanti}@graduate.univaq.it

***Abstract* – Asynchronous motors represent a large percentage of motors used in industry. Implementing predictive maintenance techniques can be justified in the case of engines that are of critical importance in the processes despite being of low cost. In these cases, the continuous monitoring of the motors requires non-invasive and online techniques, which allow the monitoring of motor characteristics over time to highlight potential trends that tend toward the condition of catastrophic failure. Online SFRA may be of interest in this scenario. In this article, this technique has been applied to a set of new asynchronous motors. They have been characterized under different load conditions. The results were used to determine transfer functions (TFs) with which it is possible to compare the TFs acquired by an engine to be monitored. The test system and the first experimental results are presented.**

I. INTRODUCTION

The role of electric motors in the industrial sector is increasingly central if we consider the current increase in the use of electric systems for efficiency and the development of intelligent systems. Although the purchase cost of mains-powered asynchronous motors is low compared to the cost of the energy they consume during their life, it is nevertheless of interest to investigate their state of health during normal operating conditions [1-5]. It is possible to use online techniques based on the injection of test signals on the stator windings and carry out the frequency response processing, with different methodologies as, for example, the online SFRA (Sweep Frequency Response Analysis). It can avoid the costly and challenging decommissioning of motors that can power complex and critical processes [6-9].

These techniques have numerous advantages, including the low cost of the measuring equipment; however, these techniques are based on evaluating the variations of the characteristic curves of an engine. These variations can occur over time due to normal aging and wear or as an initial symptom of impending failures as a result of conditions such as overload, bearing damage, and the effects of improperly performed maintenance.

Therefore, it is necessary to acquire information on a sufficient number of new motors in different operating conditions to identify reference curves for the processing of deviations and identify normal operating conditions from that symptom of a possible initial failure.

For this purpose, ten new induction motors were acquired from the same production batch and were connected to a dynamometer for nominal and variable load tests. The characteristics were achieved with a mains power supply, without the interposition of transformers or other systems, to reproduce the normal operating conditions of mains-powered asynchronous motors. Moreover, the dynamometer itself is of the passive type, without energy recovery, so as not to disturb the power supply network during the tests.

II. THE TESTING SYSTEM

The measurement technique used is the SFRA[10], in online mode. SFRA is based on injecting a sinusoidal signal with a typical amplitude of a few volts, with frequencies ranging from a few Hz to 2 MHz, between the two terminals of an electrical winding, both in rotating electrical machines in transformers. The traditional SFRA is used on non-powered devices, which requires them to be put out of service; for online monitoring, it is necessary to carry out measurements without interruption of operation and without the stimulus signals interfering with the normal functioning of the equipment.

Previous works [10-12] have carried out various experimental measurement campaigns on different devices, and ad hoc systems have been developed for standard SFRA and online.

The SFRA online was developed for this need, with the adoption of coupling filters with the electrical network, suitably designed to operate as a band-pass in the 2 kHz - 1.5 MHz range to stop the fundamental component at 50. Hz and voltage harmonics up to the 40th and allow the application of the stimulus signal.

The SFRA signal generation and the acquisition were performed with the Digilent Analog Discovery 2 NI

Edition board with BNC Adapter [10], controlled by a PC running the testing software designed in the NI LabVIEW Environment. This device is a two-channel oscilloscope with differential inputs, 14-bit resolution, ±25 V input range, 30-MHz bandwidth, and 100 MSample/s sampling frequency, equipped with a two-channel arbitrary function generator with ±5 V output range, 20-MHz bandwidth, and 100 MSample/s sampling frequency.

The overall cost of the whole testing system, including the coupling filters and cables, is less than €400, to which the software development cost is to be added.

The measurement software has been developed to evolve the version proposed in [10], implemented in the NI LabVIEW environment. The S/N reduction was the most critical objective during the design of the proposed system due to the high electromagnetic noise generated by the motor under test, which can lead to different SFRA measurement problems.

The measurement procedure is based on the following steps: 1) simultaneous acquisition of input Vin and output Vout signals; 2) application of Hanning window to both the signals; 3) Fast Fourier Transform (FFT) processing of Vin and identification of its amplitude and frequency (bin position) in the spectrum; and iv) FFT processing of Vout and the identification of the component having the same bin position of Vin.

The test bench used must reproduce the actual operating conditions of a mains-powered asynchronous motor, without an inverter, without energy recovery systems introducing disturbances on the power supply line that would make the test results unacceptable.

The load has been carried out adopting the Magtrol HD 815 hysteresis brake dynamometer equipped with a Magtrol TM 108 torque and speed transducer. In addition, the brake has been controlled with a Magtrol DSP 6001 unit that also performed the acquisition of torque and rotational speed (Figs. 1 and 2)

III. EXPERIMENTAL RESULTS

The experimental tests have been performed on a set of 10 new three-phase induction motors model BE 90 LA4 produced by Bonfiglioli; the rated features @50 Hz are the following: i) voltage 230/400 V Δ/Y, ii) current 6.1/3.5 A Δ/Y; iii) power 1.5 kW; iii) speed 1430 rpm; iv) power factor 0.74; v) efficiency 82.5% at 100% load, complying IE2 according to IEC EN 60034; vi) insulation class F, IP 55.

The motor under test can be considered parallel connected to the network, composed of cables, power transformer, and power mains; the input signal is applied to both the motor under test and the supply system.

Therefore, a diagnostic system must separate the effects of the motor from those external to it.

To this aim, we first applied the SFRA to the supply system with the motor circuit breaker open (Fig. 3).

The line-to-line terminals selected for further acquisitions are wu because of only one resonance peak in the range 800-1500 kHz.

In Fig. 4, the SFRA TF for motor #1, at various load percentages after 1 hour of full load service, are shown; no effects of the motors are appreciable below 100 kHz. Therefore, the following figures will refer to the band 100 kHz, 1.5 MHz. 5 TFs were acquired for each motor, for mechanical load varying from 100% to 0%, after one hour of operation at full load.

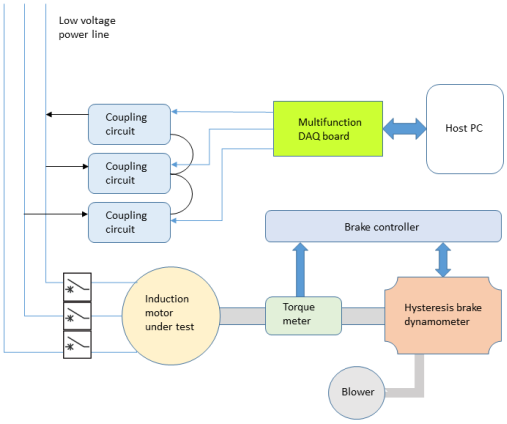

Fig.1 – Block diagram of the experimental setup

Fig. 2. The testing bench.

The reference curves have been processed by considering firstly. The definition of the reference curves was first performed considering the TFs corresponding to the same working point, and the envelope TFs in figures 5 to 9 were obtained. In each one, there are: i) the TF of the envelope of the maximum values, ii) the mean TF, iii) the envelope TF of the minimum values, iv) the TF obtained as the mean plus the standard deviation, v) the TF obtained

as the mean minus the standard deviation. This choice allows for identifying different degrees of deviation of a subsequent experimental TF. For example, the standard deviation allows defining a region that includes 68 percent of all the data points around the mean TF. In Fig.10, the total reference TFs, obtained with the dataset of 50 acquisitions, are reported in the complete range of 3 kHz - 1500 kHz and in detail in the range of interest 100 - 1500 kHz. It is observed that below 100 kHz, the TFs remain almost similar, confirming that the effect of the presence of the motor is not relevant in this band.

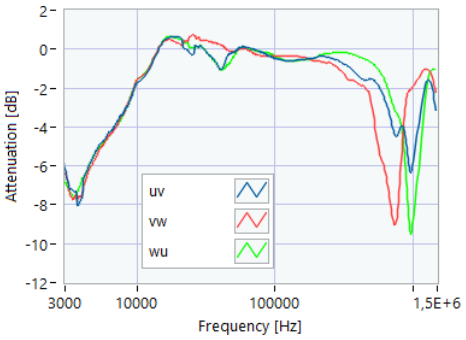

Fig.3 - SFRA online TF of the supply system only, measured on terminals line to line.

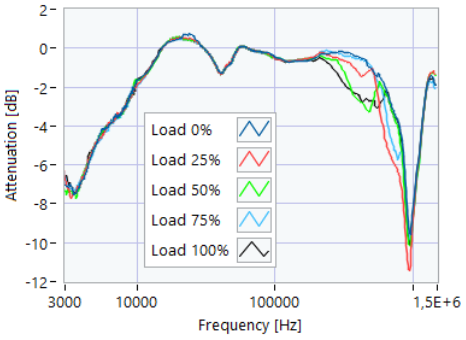

Fig.4 - SFRA online motor #1, at various load percentages after 1 hour of full load service.

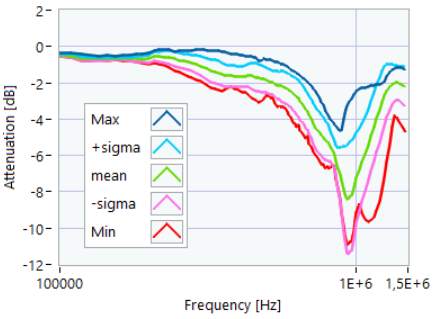

Fig. 5 - Reference TF processed at 0 % load

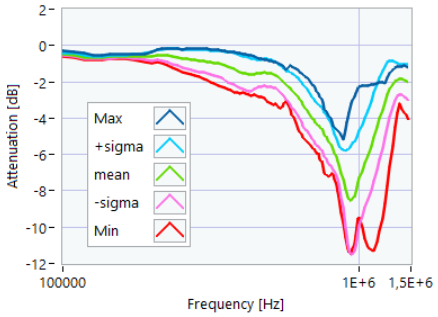

Fig. 6 - Reference TF processed at 25 % load

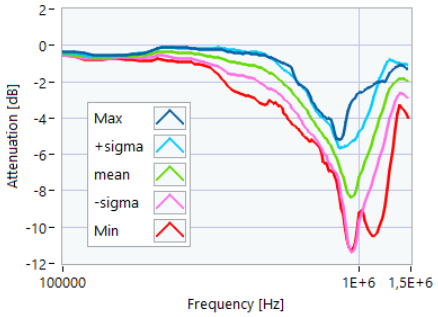

Fig. 7 - Reference TF processed at 50 % load

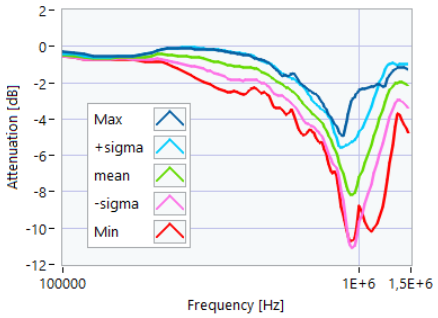

Fig. 8 - Reference TF processed at 75 % load

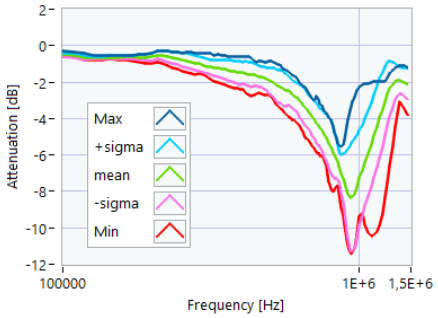

Fig. 9 - Reference TF processed at 100 % load

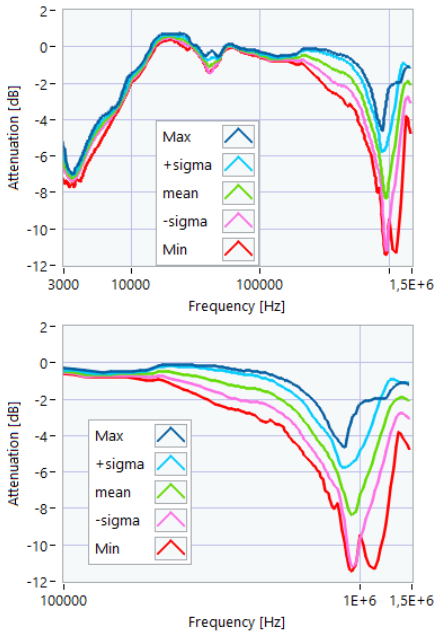

Fig. 8 – Overall reference TFs processed with the whole dataset

IV. DATA ANALYSIS: A PROPOSAL

The evaluation of the data obtained with the SFRA technique is usually carried out with a qualitative approach by displaying the reference TFs compared to the current TF, with the support of numerical indicators, which can be of a statistical type. It is generally possible to use the correlation methods on the whole extension of the TF and subsections deemed significant. In this article, two correlation indices have been considered; the first index is Pearson's correlation ρ:

$$\rho = \frac{n\sum x_i y_i - \sum x_i \sum y_i}{\sqrt{n\sum x_i^2 - (\sum x_i)^2}\sqrt{n\sum y_i^2 - (\sum y_i)^2}} \quad (1)$$

where n is the number of TF values, x_i and y_i are the values of the X and Y TFs (for i[th] sample). The Pearson's correlation is the most commonly used in the SFRA contest.

The second is Spearman's rank r correlation coefficient; it is helpful if the compared TFs make the Pearson's correlation coefficient undesirable or misleading. Spearman's correlation measures the strength and direction of monotonic association between the two TF, according to the equation:

$$r = 1 - \frac{6\sum d_i^2}{n(n^2-1)} \quad (2)$$

where d_i is the difference in paired ranks and n = the number of values. Kendall's τ and other correlation coefficients have been neglected as they cannot provide further information than these two. The coefficient evaluation procedure is based on the qualitative observation that the motor effect is not significant for frequencies lower than 100 kHz. Therefore, it is possible to carry out correlation tests with ρ and r in the 3 -100 kHz band to mainly observe variations in the supply network impedance in the motor connection node.

The correlation test can start from the following observation: in the range 100 kHz - 1.5 MHz, there may be more resonance peaks; in the case of the motor considered, only one is present at about 950 kHz, if we consider the mean TF of the motors set. To use Spearman r correctly, monotonous, increasing, and decreasing sections of TF must be isolated. Therefore, an algorithm was implemented that can divide the TF into monotonous sections and then perform the calculation of the ρ and r coefficients in the identified sections. The appearance of additional peaks or the shift of the primary resonance peak is detected concurrently by ρ and r. Five reference TFs are available, respectively, envelope TF of the maxima, mean TF plus one standard deviation, mean TF, mean TF minus one standard deviation, and TF envelope TF of the minima. We suggest calculating the ρ and r of the TF acquired for all TFs, to identify the best similarity.

As a preliminary test, a reversible malfunction condition was implemented by inserting in series on one of the motors a power resistor of 1 ohm in series with one of the line conductors. According to the rated values of the motor, the average phase impedance is about 38 ohm; the inserted resistance involves a variation on a phase of 2.6% of impedance. The acquired TF is in black in Figs. 9 - 12; the correlation factors obtained compared with the reference TFS are in Tables 1-4.

The results in Table I refer to the whole frequency range 3 kHz-1.5 MHz; the correlation with all five curves is high, with higher values for both indices relative to the mean TF. In reality, the engine is apparently functioning normally, even if there is a fault in the connection. The correlation across the range does not seem capable of providing helpful information.

The results in Table II relate to the 3-100 kHz band; the correlation with all five curves is very high; therefore, there are no variations in the characteristics of the power supply network during the test.

Table III shows the correlation results in the frequency range lower than the resonant frequency at 950 kHz. A better correlation is observed with the envelope TF of the maxima, considering both the values of p and r. This may suggest an anomalous condition, even if within the limits of regular operation. Table IV shows the correlation values for the frequency range higher than the resonance peak. In this interval, the considered TF realigns itself with the mean TF.

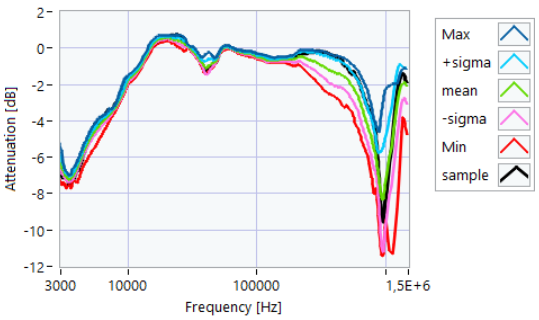

Fig. 9- TF of a motor with a 1-ohm resistance in series on a phase conductor: comparison with the reference TFs on the whole bandwidth

Table 1. Correlation factors on the whole TF range.

Reference TF	Pearson's ρ	Spearman r
Max	0.8863	0.9466
+ sigma	0.9619	0.9869
mean	0.9843	0.9883
-sigma	0.9699	0.9782
Min	0.9332	0.9592

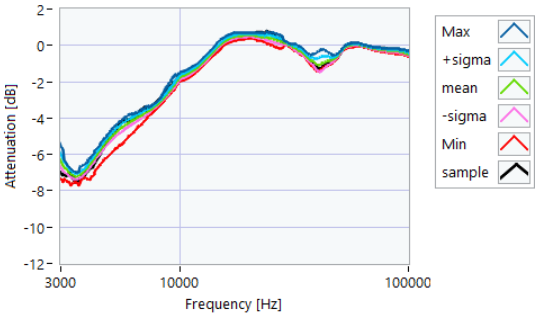

Fig. 10- TF of a motor with a 1-ohm resistance in series on a phase conductor: comparison with the reference TFs in the range 3-100 kHz

Table 2. Correlation factors in the range 3-100 kHz.

Reference TF	Pearson's ρ	Spearman r
Max	0.9443	0,9599
+ sigma	0.9820	0.9908
mean	0.9922	0.9971
-sigma	0.9964	0.9987
Min	0.9915	0.9968

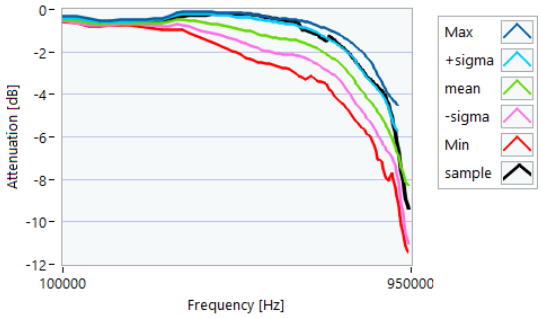

Fig. 11- TF of a motor with a 1-ohm resistance in series on a phase conductor: comparison with the reference TFs in the range 100-950 kHz

Table 2. Correlation factors in the range 100-950 kHz.

Reference TF	Pearson's ρ	Spearman r
Max	0.9885	0.9861
+ sigma	0.9947	0.9695
mean	0.9769	0.9146
-sigma	0.9772	0.8974
Min	0.9582	0.8939

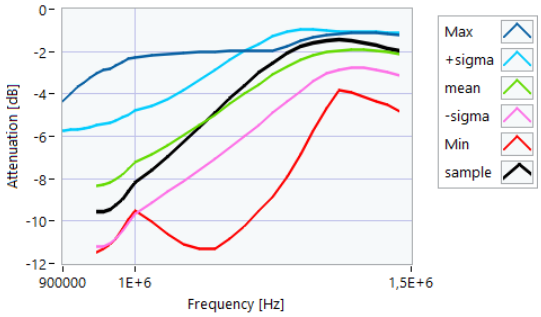

Fig. 10- TF of a motor with a 1-ohm resistance in series on a phase conductor: comparison with the reference TFs in the range 950-1500 kHz

Table 2. Correlation factors in the range 950-1500 kHz.

Reference TF	Pearson's ρ	Spearman r
Max	0.7771	0.8687
+ sigma	0.9795	0.8693
mean	0.9973	0.9795
-sigma	0.9914	0.9754
Min	0.8023	0.8544

V. CONCLUSIONS

In this article, the characterization of a batch of new asynchronous motors was carried out using the SFRA online technique. The goal is to identify a predictive diagnostic technique for mains-powered motors, capable of recognizing possible deviations from regular operation characteristics before catastrophic failures occur. With the aid of correlation indices determined in specific areas of the TFs, it is proposed to support the qualitative analysis of the TFs with data to be included in predictive diagnostic algorithms. In the future, reversible and non-reversible

damages will be implemented on the same motors, and the new TFS will be compared with the reference TFs obtained.

REFERENCES

[1] H. Henao et al., "Trends in fault diagnosis for electrical machines: A review of diagnostic techniques," IEEE Ind. Electron. Mag., vol. 8, no. 2, pp. 31–42, Jun. 2014.

[2] F. C. Trutt, J. Sottile, and J. L. Kohler, "Detection of AC machine winding deterioration using electrically excited vibrations," IEEE Trans. Ind. Appl., vol. 37, no. 1, pp. 10–14, Jan. 2001.

[3] G. Betta, C. Liguori, A. Paolillo, and A. Pietrosanto, "A DSP-based FFTanalyzer for the fault diagnosis of rotating machine based on vibration analysis," IEEE Trans. Instrum. Meas., vol. 51, no. 6, pp. 1316–1322, Dec. 2002.

[4] L. M. Contreras-Medina, R. de Jesus Romero-Troncoso, E. Cabal-Yepez, J. de Jesus Rangel-Magdaleno, and J. R. Millan-Almaraz, "FPGAbased multiple-channel vibration analyzer for industrial applications in induction motor failure detection," IEEE Trans. Instrum. Meas., vol. 59, no. 1, pp. 63–72, Jan. 2010.

[5] A. Glowacz, "Diagnostics of DC and induction motors based on the analysis of acoustic signals," Meas. Sci. Rev., vol. 14, no. 5, pp. 257–262, 2014.

[6] Di Pasquale, A., Fiorucci, E., Ometto, A., Rotondale, N. "Frequency characterization of cast-resin transformers" (2012) SPEEDAM 2012 - 21st International Symposium on Power Electronics, Electrical Drives, Automation and Motion, art. no. 6264464, pp. 1045-1050.

[7] Dolce, S., Fiorucci, E., Bucci, G., D'Innocenzo, F., Ciancetta, F., Di Pasquale, A. "Test instrument for the automatic compliance check of cast resin insulated windings for power transformers" (2017) Measurement: Journal of the International Measurement Confederation, 100, pp. 50-61.

[8] Bucci, G., Ciancetta, F., Fiorucci, E., Mari, S., Fioravanti, A. A non-intrusive load identification system based on frequency response analysis (2021) 2021 IEEE International Workshop on Metrology for Industry 4.0 and IoT, MetroInd 4.0 and IoT 2021

[9] Bucci, G., Ciancetta, F., Fioravanti, A., Fiorucci, E., Prudenzi, A. “Application of SFRA for diagnostics on medical isolation transformers” (2020) International Journal of Electrical Power and Energy Systems, 117, art. no. 105602.

[10] Bucci, G., Ciancetta, F., Fiorucci, E. "Apparatus for online continuous diagnosis of induction motors based on the SFRA technique" IEEE Transactions on Instrumentation and Measurement, 69 (7), art. no. 8843945, pp. 4134-4144.

[11] Bucci, G., Ciancetta, F., Fiorucci, E., Mari, S., Fioravanti, "Deep Learning Applied to SFRA Results: A Preliminary Study" (2021) ACM International Conference Proceeding Series, pp. 302-307.

[12] Fioravanti, A., Prudenzi, A., Bucci, G., Fiorucci, E., Ciancetta, F., Mari, S. "Non intrusive electrical load identification through an online SFRA based approach" (2020) 2020 International Symposium on Power Electronics, Electrical Drives, Automation and Motion, SPEEDAM 2020, art. no. 9161856, pp. 694-698.

25th IMEKO TC4 International Symposium
23rd International Workshop on ADC and DAC Modelling and Testing
IMEKO TC-4 2022
Brescia, Italy / September 12-14, 2022

Design and validation of a reference multi-sensor cinemometer for law enforcement applications

Seif Ben-Hassine[1], Dominique Renoux[1], Catherine Yardin[1], Jabran Zaouali[1], Jimmy Dubard[1], Jean-Marie Lerat[1], Pierre Betis[1], Isabelle Blanc[1]

[1]*Laboratoire National de métrologie et d'Essais (LNE), France, Seif.Benhassine@lne.fr*

***Abstract* – This paper describes a new reference multi-sensor cinemometer designed for the purpose of the homologation of radars dedicated to road traffic control. It is intended to replace the actual reference cinemometer deployed in France, which is not longer adapted to the new generation of radars as it delivers less measurement parameters and has less detection capabilities. The new multi-sensor cinemometer system is presented by detailing the operation of its processing units. The fusion of measurements provided by the various sensors is explained. The computation of the reference speed and its associated uncertainty is exposed. Finally, on-site measurement results are presented by comparing the system with the actual reference cinemometer.**

I. INTRODUCTION

The rapid evolution of cinemometer technology with the use of multi-target tracking functions, that enables high rate of target detection and curvilinear speed measurement, requires an evolution of the verification techniques and reference cinemometer. Currently, the method used to assess the speed accuracy of traffic cinemometers in France is the comparison to a standard system based on a single Continuous-Wave (CW) radar, called HADER. This one delivers an instantaneous speed measurement whose traceability to the International System of Units (SI) is ensured by the calibration of the emitted RF frequency and of the measured Doppler shift of the echoed RF wave. This reference system, operating at 24 GHz, is equipped with a static parabolic antenna emitting a narrow electromagnetic beam and is used at a 25° angle with the road. This system is limited in application with respect to new devices as it does not allow the speed measurement on curvilinear roads. Furthermore, it is hightly sensitive to masking effects on multiple lane roads.

In this paper, we present a new multi-sensor cinemometer system of increased capacities and facilities while keeping the required level of uncertainty. This system allows to compete with the features of new cinemometer technologies:

- Multi-lane measurement without masking effect.
- Multi-target measurement.
- Configurable infraction zone.
- Curved track measurement.
- Speed gradient measurement in the infraction zone.

Section II presents the device and its main processing units. Section III deals with the data acquisition unit and describes the different sensor subsystems. Section IV describes the data processing unit which combines the measurement results provided by the various sensors and computes the reference speed. The latter is then compared to the device under test (DUT) measurements by taking into account the measurement uncertainty. Section V discusses the reliability of the designed cinemometer system and gives some results based on the comparison with the reference system HADER. Finally, Section VI concludes this development.

II. OVERALL DESCRIPTION

The system is based on a multi-sensor configuration in order to improve the reliability of the system measurements and to reduce the overall uncertainty. The system consists of an acquisition and processing unit controlling four radars and one lidar speed sensors. The different system components are represented on the diagram in Figure 1.

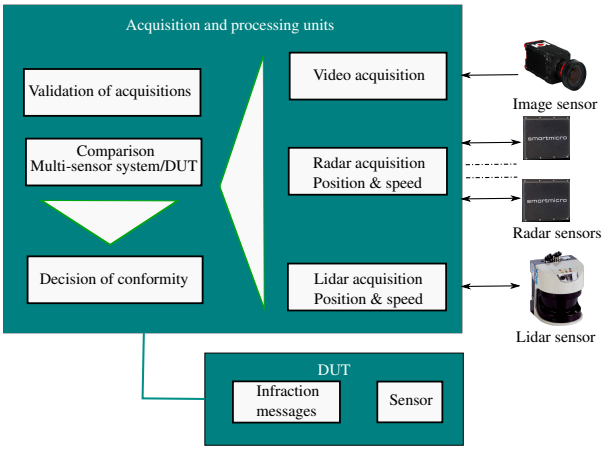

Fig. 1. System block diagram.

The system continuously acquires the speed, time and position information from the lidar and radar

sensors. Concurrently, the alive stream of the camera is timestamped and recorded. The processing unit calculates the reference speed value, its associated uncertainty, and the time for each infraction. The reference time is dispatched by an NTP (Network Time Protocol) server connected to a GPS receiver. The processing unit also enables to extract the associated image at this reference time.

Automatic DUT provides, for each violation a speed value, time and picture that can be compared to those of the developed system. This comparison is made easy by means of a dedicated developed software which displays side by side information of time sorted infractions that can be checked by the pictures display of the vehicle provided both by the system and the DUT.

III. DATA ACQUISITION

A. *Radar subsystem*

The instantaneous speed measurement of the vehicles is carried out by using the Doppler phenomenon in the microwave domain, this is the principle of the radar system [1]. The emitted electromagnetic wave radiates its energy in a privileged direction by means of a directional antenna. After reflection on a moving target, a part of the wave received by the antenna is combined in an electronic mixer circuit with a fraction of the transmitted wave. The Doppler frequency (F_d) obtained from this mixer is proportional to the mobile speed (v) and to the cosine of an angle between the mobile trajectory and the radiation axis of the antenna [2], *i.e.*:

$$F_d = \frac{2v\cos(\alpha)}{\lambda}. \quad (1)$$

with

- v the mobile speed in m/s.
- α the angle between the mobile trajectory and the radiation axis of the antenna in rad.
- λ the emission wavelength in m.

The radars sensors are of type FMCW MIMO (Frequency Modulated Continuous Wave Multiple Input Multiple Output) system. This type offers the target tracking feature. The tracking function of the radar sensor is supported by a B-Spline model to approximate the traffic lane. The parameters used for the configuration of the sensors are the control points of the B-Spline interpolation curve. These control points are calculated from the X-Y coordinates of the points measured at the road middle points [3]. Figure 2 shows a graphical representation of the B-Spline curve associated to the control points. The coordinates of the control points are defined with respect to a reference point located on the mechanical structure of the system.

The radar subsystem is composed of four sensors of type

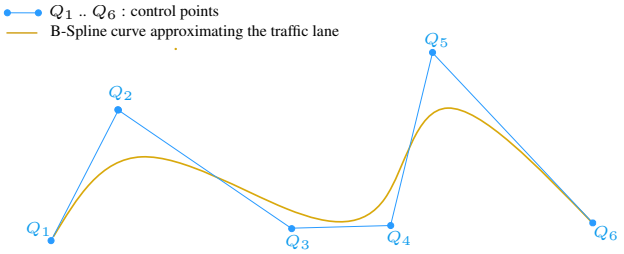

Fig. 2. Graphical representation of B-Spline curve associated to the control Points.

Smartmicro UMRR-11 T132. This type of sensor, with an operating frequency range of 76 GHz to 77 GHz, is designed for multi-lane, multi-object traffic management applications with 4D/HD$^+$ technology [4]. The HD$^+$ resolution means that the sensor allows separating objects according to their speed and their distance from the sensor. The use of a 77 GHz sensor guarantees the absence of interference between a DUT Doppler radar (operating at 24 GHz) and the designed reference cinemometer system. The 77 GHz allows achieving better performances in range, speed accuracy and resolution compared to 24 GHz radar.

Figure 3 presents the electrical architecture of the radar subsystem. The radars perform the position and speed measurements simultaneously on the same target. The use of multi-sensors allows:

- to reduce the cases of masking by positioning the radars at a height between 2,4 m and 2,6 m,
- to increase the redundancy on the detection zone,
- to provide a compromise between the blind zone and the redundancy zone.

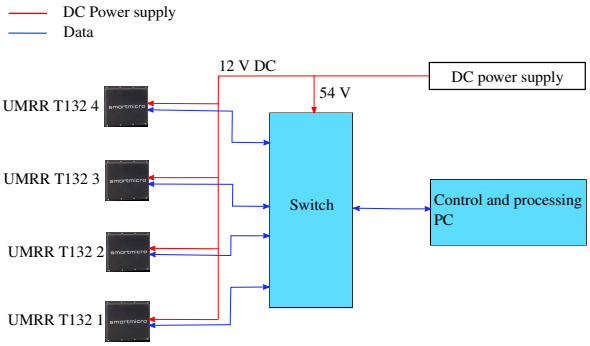

Fig. 3. Electronic architecture of the radar subsystem.

The data are provided by the radar units on an Ethernet UDP bus, with target positions and speed defined with respect to the reference point used for B-Spline definition.

B. *Lidar subsystem*

Lidar (Light detection and ranging) is an opto-electronic measurement device that derives the distance between the

surface of an object and the device (emitter/receiver) from the measurement of the time of flight of a laser pulse. The cinemometer is a 2D lidar based on a rotary pulsed laser emitter/receiver and the velocity can be determined by the difference of distances acquired for several rotations. The rotation frequency is 75 Hz and the angular resolution is 0.5°. The laser emits light at a wavelength of 905 nm.

The lidar cinemometer is integrated by CES Ag from a commercial lidar. It is composed of a 2D lidar unit SICK LMS511-12100, an industrial PC and a customized software for data acquisition and processing.

The data, as a sampled target horizontal profile of the vehicle, recorded by the lidar subsystem for each five rotations and provided by the CESag software are post-processed by a LNE software to provide a set of measured speeds over an interval around the infraction line.

C. *Vision subsystem*

The vision subsystem is composed of a camera, a video recorder from IO industries and a ruggedized PC tablet with IO controlling software. The recorded images are accurately time stamped using transmitted digital NEMA ZDA frames to the tablet and an analog PPS (Pulse Per Second) signal provided to the recorder. These two times information, via serial and analog interface, are provided by the GPS unit. The camera resolution is 4112x2176 and the frame rate is 30 Hz. The optimal exposure time is around 100 μs to avoid kinetic blur. The camera is equipped with a F1/4 20 mm lens. All these features enable to identify the number plate of vehicles under cloudy weather, four lanes highway and high speed up to 300 km/h.

D. *Synchronization of acquisitions*

Lidar and radar acquisitions are time stamped by the clocks of two driving different PCs which are synchronized to the NTP server of the GPS unit, all being connected to the same Ethernet local network. The video recorded stream is also time stamped by two signals, as described in the vision subsystem, provided by the same GPS unit.

Data analysis was performed on trials in order to determine the synchronization of acquisitions. It showed a stable 160 ms time shift between lidar and radars data. The stability of this time shift has been evaluated on acquisitions with short and long durations on several sessions. It is consistent with the specified processing time of the radar sensors and the system design which sets the lidar as a time reference for all acquisitions.

IV. DATA PROCESSING

A. *Data fusion*

The radar and lidar subsystems perform speed measurements independently of each other. These measurements are then combined to improve the reliability of the measurements produced by the system and to decrease the overall uncertainty.

The data are provided in the system reference frame. The fusion process is carried out in steps by considering at each step only two set of sensor's targets. It is firstly applied to the radars. A radar being taken as the initial set of targets, the process consists in associating it with data from a second radar according to a temporal criterion and a spatial criterion applied to each target. This new enlarged set, of fused data for each target, is then compared to the data from the third radar using the same criteria. The process continues until the lidar data are fused. At each step, the unfused targets are kept in the group. The fusion reliability is tested by initializing the process on different sensors.

B. *Computation of the reference speed and its associated uncertainty*

The reference speed value is evaluated in three steps represented in Figure 4.

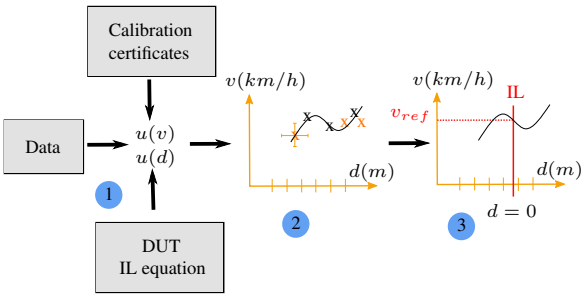

Fig. 4. Computation steps for establishing the reference speed value and the associated uncertainty.

The first step, described before, deals with the input data: the measurement line which is defined according to the infraction line of the DUT, and the fused data issued from the fusion algorithm and their associated uncertainties. These uncertainties have been evaluated separately for each sensor and they take into account the trueness and fidelity components. The radar and lidar uncertainties are decomposed into a constant part and a variable part. These parts correspond to the short and long term uncertainties. In the case of distance measurements d, we have propagated the uncertainties associated to the coordinates x,y returned by the sensors by using the measurement line equation and the measurement model of the distance from the target to the infraction line.

In the second step, a regression model is applied to represent for each target the relationship between the measured speed values v and the distances to the measurement line d. This model is a polynomial of maximum degree 3, quite often degree 0 (constant speed)

or degree 1 (monotonic variation), and its expression is given by:

$$G(d) = b_0 + b_1 d + b_2 d^2 + b_3 d^3. \quad (2)$$

with b_0, b_1, b_2 and b_3 being the model coefficients. They are estimated with GLS (Generalized Least Squares) methods [5] that enables to propagate the uncertainties associated to the data.

In the third step, the model is used to evaluate the reference speed value of the target at the infraction line. This prediction is computed by setting d = 0 and then its expression corresponds to the intercept b_0 of the model whatever the degree of the polynomial:

$$v_{ref} = G(0) = b_0. \quad (3)$$

It follows that the uncertainty associated to the reference speed value is the uncertainty associated to the term b_0.

V. TESTS AND VALIDATION

Different test campaigns were carried out, including lab's simulation tests and tests performed on various real traffic sites, to adjust the system and to assess its performances through comparative and statistical analysis of all collected data. The accuracy of the measured speeds by the system has been assessed using the HADER cinemometer as a reference.

A comparison campaign is performed with the HADER on a two-lane road located in the suburb of Paris. Only the receding lane is used for the test. A photograph of the test setup is presented in Figure 5. The HADER is approximately placed at 7 m from the origin point of the new system, with an orientation angle set at 25° between its main beam and the road axis. This distance and this angle are measured using a tacheometer device. A subsequent correction is then applied on the speed measurements accounting for the measured angle value. Table 1 presents the radar and lidar uncertainties taken as hypotheses for the computation of the reference speed and its associated uncertainty.

Table 1. Radar and Lidar uncertainties used to test the computation algorithm of the reference speed and its associated uncertainty.

	$u(d)$	Constant $u(v)$	Variable $u(v)$
Radar ($v \leq 100$ km/h)	1 m	0.31 km/h	0.36 km/h
Radar ($v > 100$ km/h)	1 m	0.2 %	0.45 %
Lidar	0.04 m	0.2 %	0.22 %

Figure 6 presents the X-Y positions of objects detected by radar 1. We observe that the vehicles trajectories are

Fig. 5. Measurement campaign on a two-lane road located in the suburb of Paris.

centered on the B-Spline curve calculated by the radar sensor.

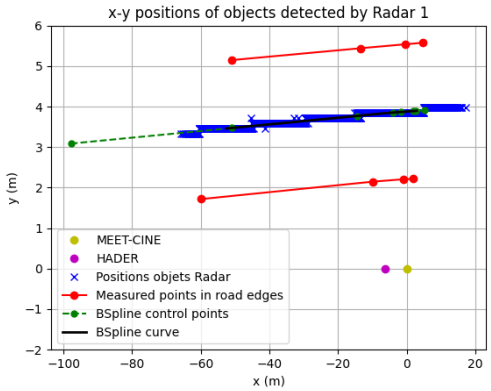

Fig. 6. X-Y positions of objects detected by radar 1.

The data pairing between HADER and the system is performed at the infraction position determined from the actual orientation of HADER antenna and the distance between HADER and the system. The system measurements are interpolated at this position. The time shift between the HADER and the system is evaluated by comparing the timestamps corresponding to the maximum

speeds recorded by both systems. All HADER timestamps are then corrected according to this time shift. The pairing of HADER speed values to the speed values measured by the system is carried out by matching the HADER corrected timestamps with those of the designed system.

The performance of the multi-sensor cinemometer system is evaluated by using the relative difference between HADER speed values and those of each sensor at the intersection coordinate between the HADER radar beam and the road center axis. Table 2 gives a statistical summary of results obtained for several measurement sessions performed the same day with the mean value of the relative difference and its associated standard deviation.

Figures 7 and 8 provide the comparison of the speed values measured by HADER and the sensors (radar 1 and lidar) on the targets detected during the first 10 min measurement session. This comparative study shows a high degree of agreement between the HADER and the multi-sensor cinemometer system. The mean values of differences between each system's sensors and the HADER are all lower than 0.21 %. The associated standard deviations are all lower than 0.57 %. The standard deviations do not vary from one test to another, which reveals that there is no test effect.

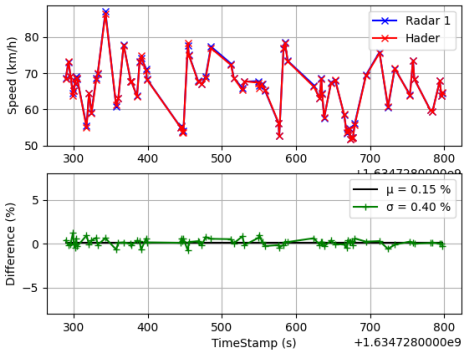

Fig. 7. Pairing results HADER-Radar 1.

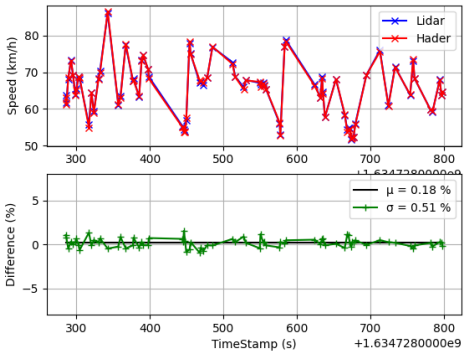

Fig. 8. Pairing results HADER-lidar.

Figure 9 shows the computation results of the reference speed and its associated uncertainty from the multiple sensors output using the data fusion and polynomial interpolation modules. We observe a good matching between HADER measurements and the reference speed values. The absolute differences do not exceed the uncertainty level of the system assigned at 0.34 km/h, except for 10 % of the measurements. It is assumed that is due to a false pairing of targets between HADER and the multi-sensor cinemometer system.

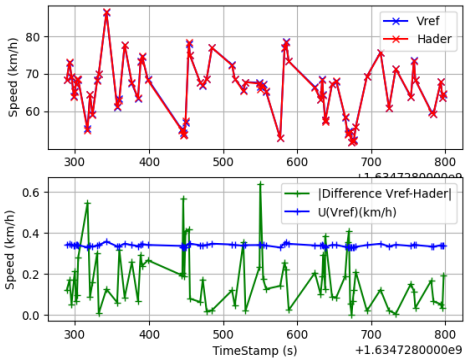

Fig. 9. Computation results of the reference speed and its associated uncertainty.

VI. CONCLUSION

In this article, the design of reference multi-sensor cinemometer is described. The system performance has been verified by comparison to the actual reference cinemometer. The system uses a multi-sensor approach already implemented for traffic control applications [6]. The data acquisition and processing units of this system provide an extended set of features with the combination of radar and lidar technologies capabilities. The processing unit includes sensor's data fusion, regression model and predictions of the speed values before, after and at the infraction line. The localization of this measurement point is software-defined within the measurement range of the sensors, which allows a greater flexibility for the exploitation of the measurement results. The data processing module allows to compute the measurement uncertainty associated to the reference speed value. On-site measurements have been performed to compare the system with the reference system HADER. The results show a good agreement with the existing reference cinemometer.

REFERENCES

[1] M.I.Skolnik, "Introduction to radar", Radar handbook, 1962, vol. 2, p. 21.

[2] K.K.M Shariff, E.Hoare, L.Daniel, et al., "Comparison of adaptive spectral estimation for vehicle speed

Table 2. Mean (μ) and standard deviation (σ) of relative difference of paired speed values of HADER and the multi-sensor cinemometer system with varying test conditions.

		Test 1 10min	Test 2 10 min	Test 3 10 min	Test 4 20 min	Test 5 30 min
HADER-Radar 1	$\mu(\%)$	0.15	0.19	0.21	0.13	0.18
	$\sigma(\%)$	0.4	0.4	0.47	0.39	0.47
HADER-Radar 2	$\mu(\%)$	-0.05	-0.1	0	-0.09	0.03
	$\sigma(\%)$	0.33	0.46	0.38	0.42	0.49
HADER-Radar 3	$\mu(\%)$	-0.21	-0.2	-0.11	-0.23	-0.27
	$\sigma(\%)$	0.39	0.48	0.44	0.43	0.49
HADER-Radar 4	$\mu(\%)$	-0.01	-0.12	0.1	-0.02	-0.08
	$\sigma(\%)$	0.43	0.44	0.44	0.43	0.52
HADER-Lidar	$\mu(\%)$	0.18	0.06	0.08	0.13	0.16
	$\sigma(\%)$	0.51	0.52	0.47	0.54	0.57

measurement with radar sensors", Sensors, 2017, vol. 17, no 4, p. 751.

[3] Q.Agrabat, A.Batailly, "Cubic and bicubic spline interpolation in Python", Doctoral dissertation, École Polytechnique de Montréal, 2020.

[4] P.Hindle, "Comprehensive Survey of 77, 79 GHz Automotive Radar Companies-Sensors and ICs", Microwave Journal, March 2020.

[5] M.J.T.Milton, P.M.Harris, I.M.Smith, et al., "Implementation of a generalized least-squares method for determining calibration curves from data with general uncertainty structures", Metrologia, 2006, vol. 43, no 4, p. S291.

[6] M.Wang, L.Jiang, W.Lu, et al., "Detection and tracking of vehicles based on video and 2D radar information", International Conference on Intelligent Transportation. Springer, Singapore, 2016. p. 205-214.

25th IMEKO TC4 International Symposium
23rd International Workshop on ADC and DAC Modelling and Testing
IMEKO TC-4 2022
Brescia, Italy / September 12-14, 2022

Using historical data to improve electrical resistance standards measurement uncertainty

Marcelo M Costa[1], André L C França[2]

[1] *Eletrobras Eletronorte, Rod. Arthur Bernardes, 2172, Belém, Brazil, marcelo.melo@eletronorte.gov.br*
[2] *Eletrobras Eletronorte, Rod. Arthur Bernardes, 2172, Belém, Brazil, andre.franca@eletronorte.gov.br*

***Abstract* – This paper presents methodologies for the evaluation of historical data of electrical resistance standards in order to improve their performance in relation to manufacturer's specification, in order to improve test uncertainty ratio and measurement uncertainty.**

I. INTRODUCTION

Calibration of electrical resistance measurement instruments, such as ohmeters, earth meters and Kelvin bridges, together with voltage and current measurement instruments, is a significant part of the workload of electrical calibration laboratories. Some of these instruments are highly accurate, as resistance measurements instruments used for accurate temperature measurements and precision digital multimeters.

For these measurement instruments, sometimes metrological performance of the standards specified by their manufacturers is overestimated when compared to the actual performance, leading to low test uncertainty ratios (TURs). In such a case, it is recommended for the calibration laboratories to evaluate alternatives for TUR improvement, such as purchasing new higher accuracy standards or evaluation of methodologies to improve the performance of their standards. Purchasing new higher accuracy standards usually envolves significative amount of financial resources, that might not be available for the calibration laboratory. A less expensive alternative is to characterize the performance of the standards, based on their historical data, using statistical and other techniques of data analysis. The behaviour over time of the values assigned to the measurement standards can follow a well-defined drift that can be modelled in order to predict the values, for a given moment, with certain uncertainty [1].

This paper presents application of methologies to improve metrological performance of electrical resistance standards. Historical calibration data of the standards are analysed and used to define new performance parameters better than manufacturer's specifications, leading to higher TUR and lower measurement uncertainties.

II. RESISTANCE STANDARDS

Electrical calibration laboratories have several options of resistance standards depending on the measurement uncertainty level. Standard resistors are often used by primary or high level calibration laboratories, while secondary or lower level calibration laboratories use precision digital multimeters. For both laboratories' types, working standards are usually decade boxes and multi-function calibrators.

In this paper, the reference standard considered is a precision digital multimeter from Fluke, model 8588A. Working standards are a multi-function calibrator (MFC) from Fluke, model 5720A and a resistance decade box, from Tettex, model 1108-B GR. Figure 1 shows the Fluke 8588A digital multimeter, Figure 2 shows the Fluke 5720A multifunction calibrator and the Tettex 1108-B GR resistance decade box and Figure 3 shows their traceability chain.

Fig. 1. Fluke 8588A DMM reference standard.

Fig. 2. Tettex 1108-B GR decade box and Fluke 5720A MFC working standards.

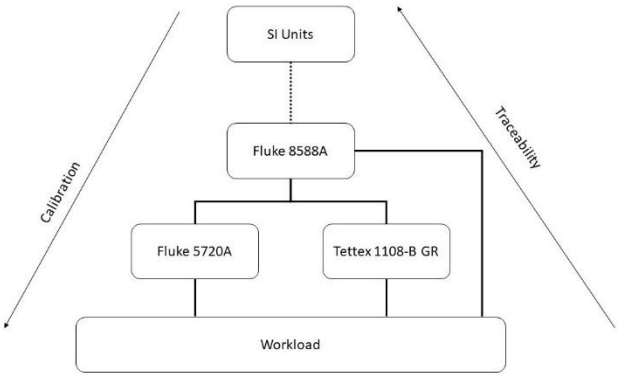

Fig. 3. Resistance standards traceability chain.

Fluke 8588A precision DMM, as a reference standard, should be calibrated at regular intervals at the National Metrology Institute (NMI) or at a 17025 standard accredited laboratory. It also can be used as working standard. This instrument is new, so there is a low quantity of avaliable historical data. According to its manufacturer, accuracy performance relative to the standards is as low as 7.5 μΩ/Ω at 100 Ω (1-year, 2σ) [2].

Fluke 5720A MFC and Tettex 1108-B GR are working standards, calibrated by the Fluke 8588A reference standard and used to calibrate the main part or the laboratory's workload. 5720A MFC has a set of discret resistors from 1 Ω, 1.9 Ω, 10 Ω to 100 MΩ. Absolute uncertainty defined by its manufacturer is 27 μΩ/Ω at 10 Ω (1-year, 2.58σ) [3]. Tettex 1108-B GR has resistors in decade values from 0.1 Ω to 100 kΩ, and 0.01 % accuracy from 1 Ω to 100 kΩ.

III. DATA ANALYSIS

The historical calibration data of an instrument can be useful when describing the normal variation of the instrument or a population of substantially identical instruments. The use of historical data is recommended when the laboratory has a considerable amount of data that allows the estimation of the standard uncertainty due to the variability of the readings, to confidently characterize the drift of instruments and standards. This use must be done with great caution, as some occurrences, such as overload, maintenance, adjustment and natural aging itself, may invalidate the use of the accumulated data. By using standards historical data, a calibration laboratory can improve performance specifications of them. Also, standards calibration intervals may be lengthened or shortened by performing a technical and statistical analysis using their calibration history, thus reducing costs with traceability maintenance in the case of calibration interval lengthening [4, 5, 6].

Data analysis techniques are applied to identify patterns, relations and trends that help interpret data and extract explicit and implicit information. [7]. One of these techniques is the regression. Regression problems occur in many metrological applications. Such problems arise when the quantity of interest cannot be measured directly, but has to be inferred from measurement data (and their uncertainties) using a mathematical model that relates the quantity of interest to the data. This is the case for estimating the drift or long-term stability of standards or measuring instruments. Nowadays, regression is also often used in supervised machine learning field [8].

Linear regression is often used for the prediction of values assigned to measurement standards whose behaviour over time is linear, and the function that predicts this behaviour is the simple model described by a straight line. One of the most common methods to estimate a straight line that best fits a set of data is the least squares method. The goal is to find the straight line $y = Ax + B$ that best fits the measurements, that is, to find the best estimates for the constants A and B based on the data [9]. Uncertainty of the data fit to the straight line can also be evaluated by the regression method.

Other simpler data analysis techniques can be used instead of regression or other sophisticated techniques for standards performance evaluation, depending on the target uncertainty or reliability, or on the amount of available historical data. One simple technique is the estimation of the standards drift by subtraction of successive calibration values.

IV. PERFORMANCE ANALYSIS

This section presents the performance analysis of the 5720A MFC and 1108-B GR decade box working standards, based on their historical calibration data. Before analysis, it was ensured that both standard were not submitted to maintenances, adjustments or other occurrences that could impair the quality of the analysis. All the calibrations used in the analysis were performed with controlled temperature of (23 ± 3) °C.

Table 1 and Figure 5 show last five calibration results of the 1108-B GR decade box, at 100 Ω (dial position 1x100 Ω), where R is the measured resistance, U is the uncertainy at 95.45% confidence and drift was calculated by subtracting the measured resistance of a calibration from the measured resistance of the previous calibration. All these calibrations were performed in the laboratory, using the standards Fluke 8588A DMM (2022), Fluke 8508A (2021 and 2019) and Agilent 3458A (2018 and 2017) precision digital multimeters. Before performing the measurements, the switches were rotated several times, in order to reduce the effect of the contact resistance. In this calibration point, accuracy defined by the manufacturer is 0.01 %. As it can be seen, the highest drift value is almost three times lower than accuracy specified by the manufacturer.

Table 1. Tettex 1108-B GR 100 Ω calibration history.

Date	R (Ω)	U (%)	Drift (%)
07-feb-22	100.000 0	0.0015	0.003 0
21-jan-21	100.003 01	0.000 93	0.003 5
02-sep-19	100.006 5	0.0013	0.000 5
10-jan-18	100.007 0	0.0029	0.002 0
06-jan-17	100.009 0	0.0029	

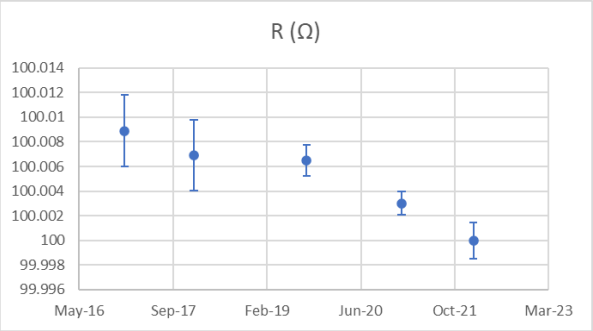

Fig. 5. Tettex 1108-B GR 100 Ω calibration history.

Applying linear regression to the calibration data of Table 1, it is possible to fit the data to the straight line shown on Figure 6. Uncertainty of the 1-year predicted resistance value is 0.0012 % (95.45%, k=2.87), about eight times lower than manufacturer's specification.

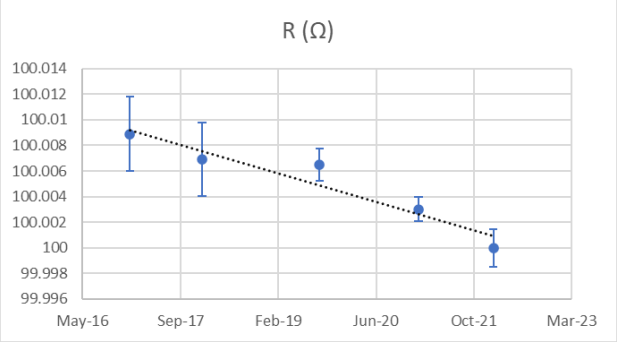

Fig. 6. Tettex 1108-B GR 100 Ω calibration history linear regression.

Table 2 and Figure 7 show last five calibration results of the 5720A MFC, at 10 Ω. All these calibrations were performed in the laboratory, using the standard Fluke 8588A DMM (2021) and Fluke 8508A DMM (the significant difference in uncertainty values in each year for this DMM is due to the fact that this standard was calibrated in different laboratories with different measurement capabilities). In this calibration point, absolute uncertainty defined by the manufacturer is 27 μΩ/Ω (1-year, 2.58σ).

Table 2. Fluke 5720A 10 Ω calibration history.

Date	R (Ω)	U (μΩ/Ω)	Drift (μΩ/Ω)
12-mar-21	10.000 50	11	6.2
06-jun-19	10.000 43	22	13
06-apr-18	10.000 57	13	14
08-jun-16	10.000 43	15	4.1
08-apr-15	10.000 47	19	

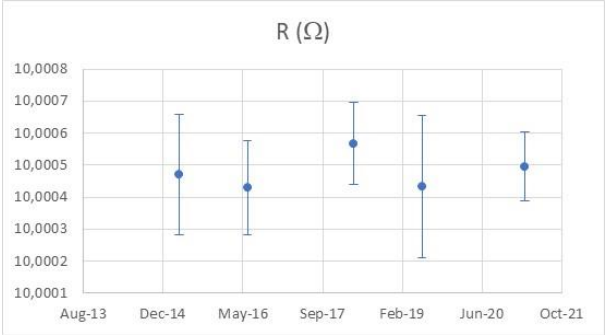

Fig. 7. Fluke 5720A 10 Ω calibration history.

Linear regression was used to fit a straight line to the calibration history data of Table 2. Estimated uncertainty of the 1-year predicted resistance value is 6.4 μΩ/Ω (95.45%, k=2.87), about three times lower than performance specified by the standard's manufacturer.

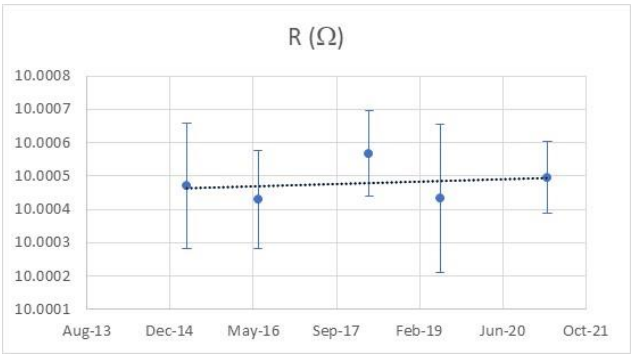

Fig. 8. Fluke 5720A 10 Ω calibration history linear regression.

V. DISCUSSION

After performing analysys of historical calibration data, electrical calibration laboratories can choose between assigning an improved accuracy specification to the characterized instruments, or lengthening their calibration interval, enabling reduction of the maintenance costs of the laboratory.

If the laboratory decides to improve standard's performance specification, first it should check if uncertainty due to it is one of the most significative of the uncertainty sources. In many electrical resistance calibrations, uncertainty due to standard's performance is

the most significative. In this case, after evaluation of the combined measurement uncertainty from the standard uncertainties from all input quantities (uncertainty sources) using the rules defined by [10], laboratory can obtain lower measurement uncertainties. Care should be taken in this case, because the new uncertainty due to standard's performance will replace uncertainty due to standard's performance based on manufacturer's apecification, which usually includes, besides long-term stability or drit, other performance parameters. For example, 5720A MFC manufacturer's performance specification includes stability, but also temperature coefficient, linearity, line and load regulation.

Considering the case of the Tettex 1108-B GR decade box working standard reported on the previous section, there are three performance specifications: the first is the accuracy stated by the manufacturer (I), the second is the highest value from subtraction of successive calibration values (II), and the last is the uncertainty of the predicted value by the linear regression (III). Table 3 and Figure 8 shows a comparison of the uncertainties considering the three cases above. As it can be seen, reduction of the combined standard uncertainty can be as high as 85% in the case III. Still in the case III, there is the accuracy improvement too, as the resistance predicted value is determined.

Table 3. comparison of the uncertainties considering the three cases.

Case	I	II	III
Root of square sum of all other uncertainties except performance/drift (Ω)	7.3E-4		
Standard uncertainty due to performance/drift (Ω)	5.8E-3	2.0E-3	4.2E-4
Combined standard uncertainty (Ω)	5.8E-3	2.2E-3	8.4E-4

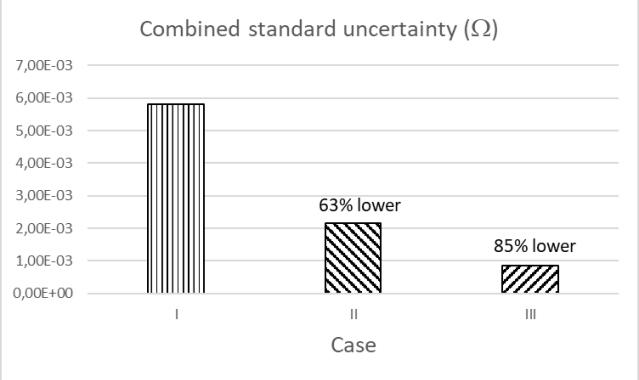

Fig. 8. Combined standard uncertainties comparison.

VI. CONCLUSION

This paper presented evaluation of electrical resistance standards historical calibration data, with the objective of improve manufacturer's performance specification and thus also improving measurement uncertainty and test uncertainty ratio (TUR) when performing accurate measuring instruments calibration. Two methodologies were presented, a simple one and a complex one, based on data analysis methods. Estimated combined standard uncertainty could be reduced at about 85%. For futher work, For future work, the application of other data analysis and prediction methods will be evaluated, such as weighted least squares.

REFERENCES

[1] M. Avellaneda, A. López, "Prediction of measurement standard values to improve uncertainty, under well-defined drift conditions", Measurement: Sensors, V. 18, 2021, 100082. https://doi.org/10.1016/j.measen.2021.100082.

[2] Fluke, "8588A Reference Multimeter – Product Specifications", Rev. F, March 2019.

[3] Fluke, "5700A/5720A Series II Multi-Function Calibrator Operators Manual", Rev. 2, May 1996.

[4] CGCRE/INMETRO DOQ-CGCRE-018, "Guidance for calibration of analog and digital measurement instruments in the electricity area", Rev. 02, September 2018.

[5] P. Reese, "Instrument Adjustment Policies", 10.51843/wsproceedings.2015.09, 2015.

[6] NIST, "GMP 11 Good Measurement Practice for Assignment and Adjustment of Calibration Intervals for Laboratory Standards", 2019.

[7] R. Origuella, "Applying data analytics to decision-making in metrology" [Internet] 2022 [Updated 2021 Mar 3, Cited 2022 Mar 21]. Available from https://certi.org.br/blog/en/applying-data-analytics-to-decision-making-in-metrology/.

[8] Vl. Nasteski. "An overview of the supervised machine learning methods." Horizons. b 4, 2017.

[9] J. Taylor, "An Introduction to Error Analysis", 2nd

edition, University Science Books, Sausalito, USA, 1997.
[10] BIPM Guide JCGM 100:2008, “Evaluation of measurement data — Guide to the expression of uncertainty in measurement”, 2008.

25th IMEKO TC4 International Symposium
23rd International Workshop on ADC and DAC Modelling and Testing
IMEKO TC-4 2022
Brescia, Italy / September 12-14, 2022

Research and application of time relay calibration device

Deng Bin[1], Sun Xiaoyan[1], Li Wenqiang[1], Wang Mingyu[2], Xu Hailong[2], Guan Zexin[1] ,

Wang Dalong[1], Zhang Zhe[2],Wang Weizhao[1]

[1] 1st Shandong Engineering Research Center of Reliability Evaluation for Electric Energy Metering Devices，Shandong Institute of Metrology, 250131, No. 28, QianfoShan East Road,Jinan,Shandong,China ,dengbin0105@sina.com
[2] 4th Shandong Institute of Metrology and Science 250131, No. 28, QianfoShan East Road, Jinan,Shandong,China,guofangjiliang@139.com

Abstract
This paper introduces the design principle and application of time interval measuring instrument. A simple calibration device basing on the powerful data processing ability of single chip microcomputer, has strong data processing capability for time relay is designed Which solves the traceability problem of various types of time relays, and realizes the automatic calibration of time relays, the uncertainty of measurement process is analyzed and studied. Not only be used to calibrate the time relay, but also be used for testing industrial digital electronic detonators and other initiating explosive devices.

Keyword
single chip microcomputer
Time relay
electronic detonator
initiating explosive device
uncertainty

I. INTRODUCTION

Time relay is widely used in delay time control of automatic control circuit, its design principles are different. There are generally four types of time relays.

For example, power on delay type, power off delay type, on delay type, off delay type, etc. Nowadays, although there are time relay delay time detector, digital electric stopwatch, digital millisecond meter, time interval measuring instrument and other equipment with time relay contact on-off time interval detection function[1].

However, in the process of measurement and calibration, different tooling is loaded to calibrate different types of time relays. The operation mode is complex, error prone, low efficiency and low measurement accuracy. The purpose of automatic calibration cannot be achieved.

The device has excellent promotion value, not only be used for the calibration of time relay, but also be used for testing industrial digital electronic detonators and other initiating explosive devices.

II. MEASUREMENT PRINCIPLE

The measurement principle of timing test system is shown in Figure 1.

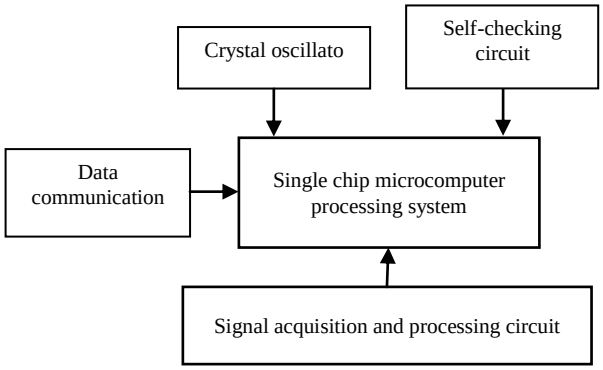

Fig. 1. measurement principle block diagram

According to JJF1282-2011 calibration specification for electronic time relay, calibration device of time relay is studied.The device can calibrate the delay time of time relay.

Test system is mainly composed of signal acquisition and processing circuit, single chip microcomputer processing system, crystal oscillator， self checking circuit，display output, etc.

III. DESIGN IDEAS

A. Calibration of power-on delay time relay

Calibration of power-on time delay type time relay, As shown in Figure 2. It is mainly designed based on the function of closing action time of a switch, when the S switch is closed, start timing, normally closed contact, S

switch off stop timing ,normally closed contact[2].

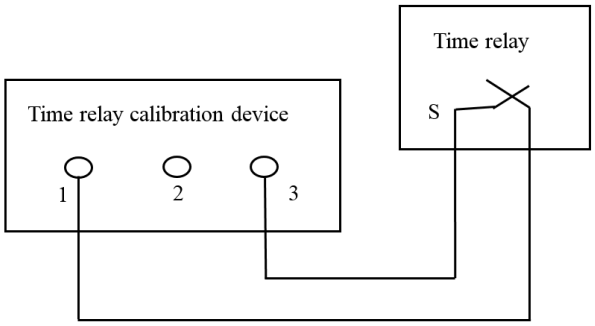

Fig. 2. Calibration diagram of power-on delay

B. Calibration of power-off delay time relay

Calibration of power-off delay time relay, it is mainly designed with the function of the disconnection time difference between the two switches, start timing when S1 switch is off, power on switch, S2 switch off stop timing , normally closed contact, is shown in Figure 3.

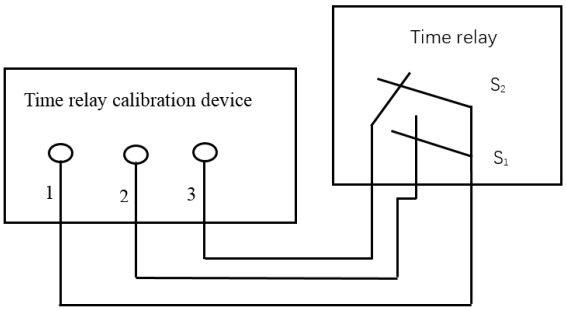

Fig. 3. Calibration diagram of power-off delay time

C. Calibration of on-delay time relay

Calibration of on-delay time relay, the calibration of on-delay time relay is mainly designed based on the function of closing action time of a switch with additional on conditions. The delay does not start when only the relay control power is turned on, only when an additional signal is switched on again, or an electronic time relay that starts delay only after a certain line is connected[3].

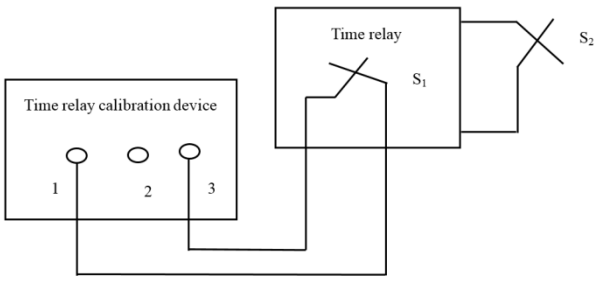

Fig. 4. calibration diagram of on-delay

D. Calibration of disconnect time delay relay

Calibration of disconnect time delay type time relay, it is mainly designed with the function of closing action time of a switch with additional opening conditions, the relay is disconnecting an external signal, or an electronic time relay that starts delaying after a certain line. The control power supply of the relay is continuously switched on during the whole delay cycle[4].

As shown in Figure 4, the relay is connected to the control power supply, when accessory condition switch S2 is off, switch S1 (normally closed contact) is on. The normally closed contact is closed to start timing, and the switch S1 (normally closed contact) is disconnected to stop timing.

E .Test of industrial digital electronic detonator

As shown in Figure 5, we delay the initiation time by setting the tested industrial digital electronic detonator,after completing the identification and detection of digital electronic detonator through network communication,then send the initiation command of digital electronic detonator[5].

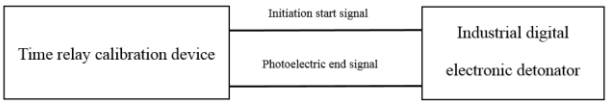

Fig. 5. Test diagram of industrial digital

Measuring the time interval between sending initiation command start signal and initiation end signal,the test of digital electronic detonators is generally completed in a safe blasting box.The industrial digital electronic detonator tester is connected to the blasting box through photoelectric sensor, and connected with it through the data line interface.

The time interval generator outputs the standard time interval, calibrates the industrial digital electric detonator electric parameter tester, and calculates the delay measurement error.

According to the industry standard, the technical requirements for industrial digital electronic detonator products are as follows.

The delay time is not more than 150 ms and the maximum allowable error is not more than ±1.5 ms.

The delay time is more than 150 ms and the maximum allowable error is less than ±1% .

The maximum allowable error of the calibration device for the electric parameter tester of the industrial digital electronic detonator shall at least satisfy the following requirements[6].

when the delay time is less than 150 ms, the maximum allowable error of the measuring standard instrument is ±0.05 ms.

when the delay time is more than 150 ms, the maximum allowable error of the measuring standard instrument is ±0.02% .

IV. SYSTEM DESIGN

The timing test system is mainly composed of front-end signal generation and conditioning module, time measurement circuit module and MCU control

module.The time measurement circuit module is realized by CPLD.The structure of the timing test system is shown in Figure 6.

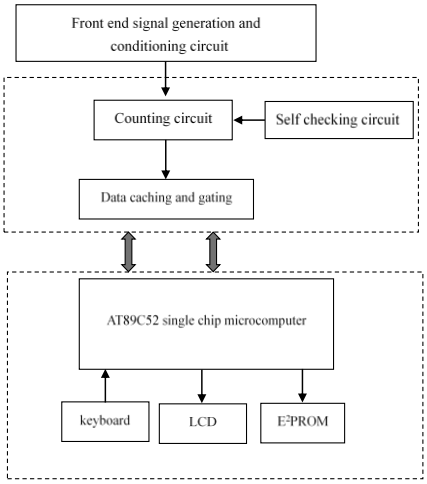

Fig. 6. structure diagram of timing test system

The essence of front-end signal generation and conditioning module measuring time relay is to quickly and accurately measure the hourly interval between multiple adjacent pulses through timing method.

As shown in Figure 7, the existing program-controlled DC power supply output voltage regulation speed is slow (generally in tens of Ms Level) , can not quickly set up the set-up voltage. Based on the existing program-controlled DC voltage, the device can increase the MOS switch control output, and can set up the set-up voltage quickly (in tens of microseconds level) .

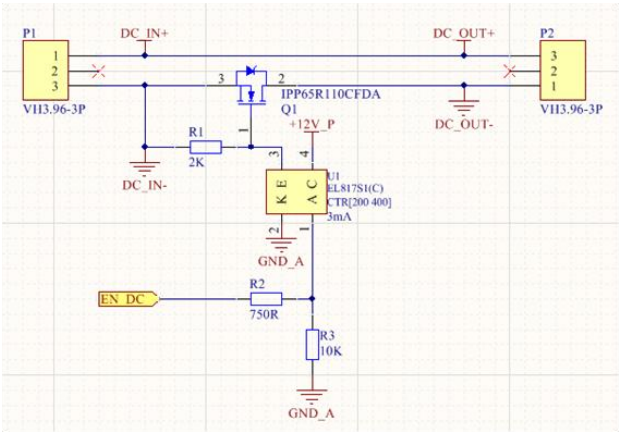

Fig. 7. Quick Power Supply schematic diagram

P1 is the variable DC input.

P2 is variable DC power output Q1 is Mos for switching on and off DC signal.

R1 is MOS discharge resistance (adjustable switching speed).

U1 is optocoupler for isolating control signal.

EN_DC is DC output enable signal.

TTL level, high level effective.

As shown in Figure 8, the trigger circuit is ready to work, timing circuit module,between the start and end of the counter, the time scale pulse enters the corresponding counter through the counting circuit, the counter starts counting .When the contacts are momentarily connected, the first shaping circuit outputs a single pulse as the counting on signal of the first single pulse as the counter, when the contacts are disconnected, the generated signal passes through the single pulse output by the shaping circuit as the counting end signal.

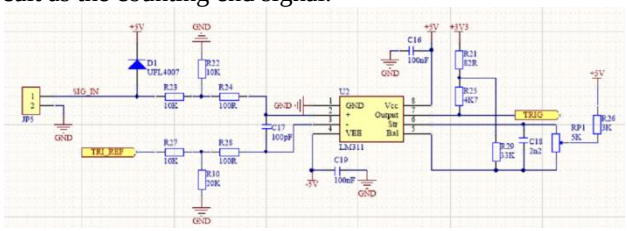

Fig. 8. Trigger circuit

At the same time, send a counting end signal to the single chip microcomputer for inquiry. The counting circuit mainly counts the pulse of contact delay, the number N counted by the counter multiplied by the cycle T of the clock pulse is the time interval between contact delays[7].

The time interval data is stored in each counter respectively before the instrument is reset, the single chip microcomputer gates the counter and collects data. The self-test circuit is mainly moved in by serial, move out the register in parallel and output pulse signal to the counter for counting, so as to detect whether the counting circuit can work normally.

After the measurement is completed,the front-end time measurement count ends,when the single chip microcomputer detects the transmitted signal,it will gate the counting results and collect the data, the collected data is calculated and saved, and then displayed by LCD controlled by keyboard.

V. TEST DATA ANALYSIS

In order to verify the metering characteristics of the time relay calibration device, In this paper, SF2001-1 stopwatch calibrator is selected as the verification standard.

Table 1. test data time relay

Test point	Measured value (s)							
	one	two	three	four	five	six	average value	standard deviation
100ms	0.10000	0.10000	0.10000	0.10000	0.10000	0.10000	0.10000	0.00000
1s	1.00000	1.00000	1.00000	1.00000	1.00000	1.00000	1.00000	0.00000
10s	10.0000	10.0000	10.0000	10.0000	10.0000	10.0000	10.0000	0.0000
100s	100.000	100.000	100.000	100.000	100.000	100.000	100.000	0.000
1000s	1000.00	1000.00	1000.00	1000.00	1000.00	1000.00	1000.00	0.00

The standard has been traceable and qualified by the superior measurement organization for many years and has good stability. From 1ms to 9999 s, according to different time bases, select any test point for 100 ms, 1 s, 10 s, 100 s and 1000 s for calibration.

The test data are shown in Table 1. According to the test data, within the measurement range from 100 ms to 9999

s, the maximum allowable error of the time relay calibration device designed in this paper is better than 1×10^{-6}T, Maximum allowable error and stability of calibration device. All can meet the requirements of measurement standards in calibration specifications.

VI. APPLICATION

A.testing of initiating explosive devices

In initiating explosive device test,the detonation velocity of explosives has always been considered as an important index to measure the performance of explosives. How to accurately measure the detonation velocity of explosives has practical guiding significance in scientific research,high-quality production and rational use.

Through the developed time interval measuring instrument,it can realize the rapid and accurate test of the action time of various products in the civil explosive industry, such as detonator, detonator, electric detonator, explosive, igniter and so on.

The photoelectric conversion circuit uses light as the medium to transmit electrical signals. After photoelectric conversion, the collected electrical signals are amplified, filtered and level converted.After photoelectric conversion, there may be some noise in the output voltage signal, which needs to be suppressed.

The photoelectric sensor designed in this way is generally used to test the detonator. For the test of Nonel Detonator, the other end needs to be a sound sensor, and the test of Nonel Detonator can be realized through the acoustic electric conversion circuit. For the test of explosives and electric detonators, one end is the current trigger circuit and the other end is the sound sensor trigger circui[7].

He design of the calibration delay time of the industrial digital electronic detonator simulator is shown in figure 6

The program memory control module is connected with the high precision time interval measuring instrument as the delay start signal, and the delay time is set. After verifying the password is correct, the start signal starts to time, the delay time ends, and the energy storage capacitor starts to discharge, the analog bridgewire circuit has an instant initiation capacitance current, and the analog bridgewire resistance is connected in parallel with a high-precision time interval measuring instrument to turn on the delay end signal or trigger the end signal through a photoelectric sensor, high precision time interval measuring instrument and industrial digital electronic detonator electric parameter measuring instrument simultaneously measure delay time, calculate delay time error.

B.calibration of time parameters of automatic detection system for fire emergency lamps

According to GB17945-2010 fire emergency lighting and evacuation indication system, the automatic detection system tester of fire emergency lamps is the equipment for detecting the lighting system of fire emergency lamps. The emergency conversion time of fire emergency lighting system shall not be greater than 0.5 s, and that of the system used in high-risk areas shall not be greater than 0.03 s.

This requires that the emergency time of the tester of the automatic detection system of fire emergency lamps is better than that of the fire emergency lighting system. The emergency conversion time of the tester of the automatic detection system of fire emergency lamps is calibrated by using the developed time interval measuring instrument.

For the calibration of emergency switching time, one end is connected with the start switch (solid-state relay). Using the switching response speed characteristics of the solid-state relay, when there is a sudden power failure, trigger the timing start circuit and start the start signal. The other end is connected with a photosensitive triode. When the emergency light is on instantaneously, the timing end circuit is triggered to start the end signal.

Ⅶ. UNCERTAINTY

For example,taking 10s measurement point to analyze the source of uncertainty of time relay calibration device, The allowable error limit of stopwatch calibrator, Uncertainty component caused by inaccurate time base of calibration device and measurement repeatability.

A.Uncertainty component introduced by allowable error limit of stopwatch calibrator

According to the technical indicators of the stopwatch calibrator, the maximum allowable error of the time interval: $\pm(1\times10^{-7}\times T0+3\ \mu s)$, which is qualified after verification and evaluated according to class B. Assuming uniform distribution and inclusion factor *k* be equal to 2, uncertainty is equal to 2.3 μs .

B.Uncertainty introduced by inaccurate time base of calibration device

Since the time relay calibration device in different verification points, it is necessary to select different time bases for measurement. If the time base of the selected 10s point is 0.001 s and the half width of the interval is 0.0005s, according to the class B evaluation method, assuming uniform distribution, *k* be equal to 2, uncertainty is equal to 0.29 ms.

C.Uncertainty component introduced by measurement repeatability

Under the specified conditions, use the stopwatch calibrator to make 6 repeated measurements on the calibration device at 10 s, testing data are shown in Table 1.According to class a evaluation, the standard uncertainty introduced is calculated by Bessel formula, uncertainty is equal to 0.02 ms.

D. Synthetic standard uncertainty

The above standard uncertainty components are not related to each other, so the synthetic standard uncertainty is equal to 0.3 ms.

E.Extended uncertainty

Take k be equal to 2 , Extended uncertainty be equal to

0.6 ms.

Ⅷ. CONCLUSION

This paper designs a simple time relay calibration device according to JJF1282-2011 electronic time relay calibration specification,which is from 0.1 ms to 9999 s, maximum allowable error: $\pm(1\times10^{-6}T+0.1\ \mu s)$, accuracy of crystal oscillator frequency is better than 1×10^{-6}.

The test data results show that the measurement range and maximum allowable error of the instrument can meet the requirements of the measurement standard in the specification.

It can be used to calibrate the delay error of time relays such as power on delay type, power off delay type, upper delay type and lower delay type, and can also be used for the test of industrial digital electronic detonators and other initiating devices.

REFERENCES

[1]Zhang Yan, Huang Peicheng , "Technology and method of high precision time interval measuring instrument ", Advances in astronomy, vol.24, No.1, Mar.2006 ,pp.1-13.

[2]Liu Deliang, Wei Guangjun, "Research on ignition time measurement of a missile based on FPGA", Computer measurement and control, vol.19，No.6, Dec.2011,pp.1394-1396，

[3]Wu Zhen, Wu Jun "Design and application of gap measurement system based on DSP and FPGA ", Instrumentation technology and sensors, vol.68，No.9 Sep.2008, pp.68-69.

[4]Liu Dongbin ,"Design and implementation of high precision time interval measurement system based on FPGA ", Journal of missiles and guidance, vol.29，No.2 Apr.2009, pp.99-302.

[5]Ma Yun, Guo Peng , "Precision time measurement based on FPGA delay time insertion method", Modern navigation, vol.317, NO. 5, Oct.2013,pp.137-321.

[6]Liu Yonggang, Wang Ruitao, " Design and application of general interface between single chip microcomputer and programmable logic device", Measurement technology, vol.25, NO.3,May.2005, pp. 48-50.

[7]Sun Jie, pan Jifei ," Overview of high precision time interval measurement methods",Computer measurement and control, vol.15, NO.2,Feb.2007, pp.145-148

25th IMEKO TC4 International Symposium
23rd International Workshop on ADC and DAC Modelling and Testing
IMEKO TC-4 2022
Brescia, Italy / September 12-14, 2022

Research on online calibration method of refrigerator intelligent inspection line

Deng Bin[1] , Xu Hailong[2] , Ma Xuefeng[1] , Liu Jianbo[1] , Guan Zexin[1] , Wang Weizhao[1] ,

Wang Dalong[1], Sun Xiaoyan[1] , Jia Ru[1] , Sun Xiaojie[1]

[1] 1st Shandong Engineering Research Center of Reliability Evaluation for Electric Energy Metering Devices，Shandong Institute of Metrology ,250131, No. 28, QianfoShan East Road, Jinan,Shandong,China ,dengbin0105@sina.com

[2] 2nd Shandong Institute of Metrology and Science 250131, No. 28, QianfoShan East Road, Jinan,Shandong,China , 1070249558@qq.com

Abstract

In order to solve the problem of measuring and tracing the dynamic line and static line of the wireless intelligent detection line in the assembly line workshop of an enterprise, the on-line measurement method of refrigerator intelligent detection line was studied, and a set of on-line calibration device of refrigerator intelligent detector was established. The test results show that the on-line calibration device of the refrigerator intelligent detector designed in this paper can realize the minimum measuring AC power of 0.5 W and the lowest measuring temperature of -30 ℃. This measurement method solves the real-time online automatic calibration of the refrigerator intelligent testing line, as well as the real-time online measurement supervision of the measured data.

Keyword

wireless intelligent detection line
measurement traceability
online calibration device
refrigerator Simulation System
uncertainty

I. INTRODUCTION

With the continuous development of wireless detection technology, wireless intelligent detection line (dynamic line and static line), which is widely used in the automatic assembly line workshop of home appliance enterprises, and the wireless intelligent detection means are becoming higher and higher. The refrigerator wireless intelligent detector is a measuring instrument specially used to measure the metrological characteristics of refrigerators. It uses modern detection technology to realize real-time online detection, alarm, recording, data storage and query of the refrigerator production line, and can realize centralized control and online supervision of the wireless intelligent detection line[1].

However, when the wireless intelligent detection line (dynamic line or static line) is used for automatic detection, on the one hand, the tested refrigerator moves continuously along with the sliding spool conveyor belt of the production line, and the wireless intelligent detector of the refrigerator also moves synchronously. On the other hand, the production line workshop of the enterprise produces day and night, and the detection cycle of the refrigerator wireless intelligent detector is long, which is prone to the situation that the amount of detection data is out of tolerance, while the refrigerator with abnormal detection data may cause quality accidents. Therefore, it is necessary to carry out real-time online measurement and monitoring on the wireless intelligent detector of the refrigerator, solve the traceability problem of online measurement and detection of the detection line of a refrigerator manufacturing enterprise, and ensure the consistency and accuracy of the detection value of the intelligent detection line.

II. CALIBRATION METHOD

The online calibration of the refrigerator intelligent detection line is realized through the online measurement and monitoring platform. The working principle of the refrigerator intelligent detector is shown in Figure 1.

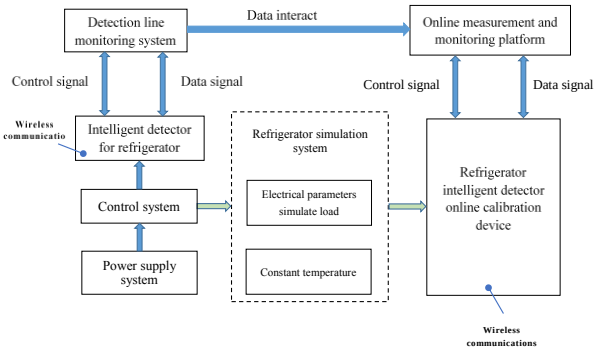

Fig. 1. Measurement schematic diagram

The refrigerator detection system is divided into an electrical parameter detection system and a temperature parameter detection system[2].

It collects the measurement data of the refrigerator detection line detection system and the online calibration device of the refrigerator intelligent detector in real time, collects and stores them in real time through the online measurement and monitoring platform, and then automatically analyzes, processes and queries the uploaded data. For the measurement of the electrical parameter detection system, the standard meter method is used to directly collect the measurement data of AC voltage, AC current, AC power, power factor, frequency and AC energy from the electrical parameter simulation load of the refrigerator simulation system.

The direct measurement method is adopted for the measurement of temperature parameter detection system, without considering the type of configured temperature sensor (thermal resistance sensor or thermocouple sensor), and the temperature parameters are measured through the simulated temperature field provided by the constant temperature device of the refrigerator simulation system. In practical work, the refrigerator intelligent detection system can provide AC power supply, directly detect the measurement performance indicators of the refrigerator, and the refrigerator can also be used as a simulated load.

A. Electrical parameter calibration

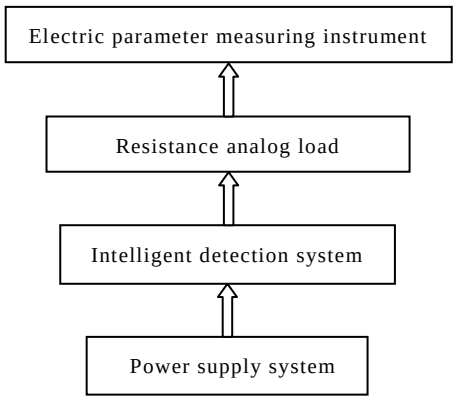

Fig. 2. Electrical parameter measurement

As shown in figure 2, standard table method which is adopted to calibrate AC voltage, AC current, AC power, AC energy and other electrical parameters. At least 5 calibration points are uniformly selected within the measurement range at 50 Hz to calculate the indication error of refrigerator intelligent detector.

The average value of the intelligent detector of the tested refrigerator is Y_x, the standard value of electrical parameter is Y_n , and the value error of the intelligent detector of the tested refrigerator is ΔY, and the value error calculation formula is as follows:

$$\Delta Y = Y_x - Y_n \qquad (1)$$

B. Temperature parameter calibration

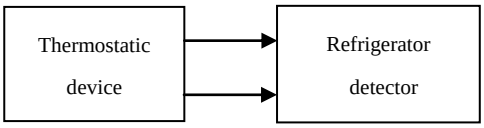

Fig. 3. temperature measurement

As shown in figure 3, with a standard temperature field method refrigerators intelligent detection system, the temperature parameters of calibration intelligent detector temperature sensor in the refrigerator in the constant temperature trough, set the thermostat temperature calibration point, control thermostat (second-class platinum resistance thermometer) temperature T_n, after being stable, record the display value detector T_x, calculation error of measurement.

$$\Delta T = T_x - T_n \qquad (2)$$

III. DESIGN OF OF CALIBRATION DEVICE

A.Operating environment conditions

The operating environment requirements are as follows: Simulated ambient temperature from -25 ℃ to 40 ℃.

Data transmission: communication antennas of more than 4G can be installed independently. Communication antennas are not affected by refrigerator shielding and can normally send data.

Data monitoring: it can install communication interface such as RS485, and can monitor the running status of electrical parameters and temperature parameters of refrigerator intelligent detection system in real time, but it shall not affect its normal communication function.

B. Composition of calibration device

The measurement standard instruments are shown in Table 1.

Table 1. Standard of measurement

Name	Model	Range	Maximum allowable error or accuracy
Electric parameter measuring instrument	CL3112	ACA：10 mA - 100 A	MPE：±0.02%
		ACV：1.5 V - 600 V	MPE：±0.02%
		F：40 Hz - 70 Hz	MPE：±0.005Hz
Ac meter calibration device	JHP-20A	ACV：10 V - 600 V ACA：0.1 A - 20 A	MPE：±0.1%
Standard platinum resistance thermometer	CST6602、CIMM1215	From -196 ℃ to 420 ℃	Second Class
Micro intelligent tank	CF40-A30	From -30 ℃ to 50 ℃	Volatility: ±0.05 ℃, Evenness:0.10 ℃

When the intelligent detection line of refrigerator is a static line, the calibration device is mainly composed of electrical parameter measuring instrument, AC meter

calibration device, second-class standard platinum resistance thermometer, miniature intelligent slot, electrical parameter simulation load, etc.

In the actual running state, the measurement data of the online calibration device of the intelligent detector and the monitoring system are monitored in real time by the remote online measurement method.

When the intelligent detection line of refrigerator is a dynamic line, the measurement standard instrument in Table 1 cannot meet the realtime online measurement and calibration work. It is necessary to design a wireless transmission measurement and calibration device to carry out onsite calibration through the online measurement and detection platform.

C. Electrical parameters simulate load

The AC electronic load will consume the power of the power supply system in the actual calibration environment, which cannot meet the actual power consumption of each functional component in the calibration.Different power consumption of each functional component of refrigerator results in different load resistances[3-4].

Fig. 4. Simulated load test diagram

Based on the power consumption of refrigerator, a set of analog load resistances is designed to replace the refrigerator. It is used to detect the measurement error of electrical parameters of refrigerator detection system, as shown in figure 4.

In this scheme, 100 Ω, 250 Ω, 1 kΩ, 10 kΩ, 100 kΩ and other AC precision resistors are selected, and the AC precision resistors are used to design electrical parameters to simulate the load.

As shown in Figure 5,the rated power of each functional part of the refrigerator is 0.5 W, 5 W, 15 W, 50 W, 300 W and 500 W respectively.

The design electrical parameters simulate the size of the load resistance, which is the rated power, rated voltage and rated current of the load resistance, as well as the influence of the temperature coefficient of the resistance value[3-4].

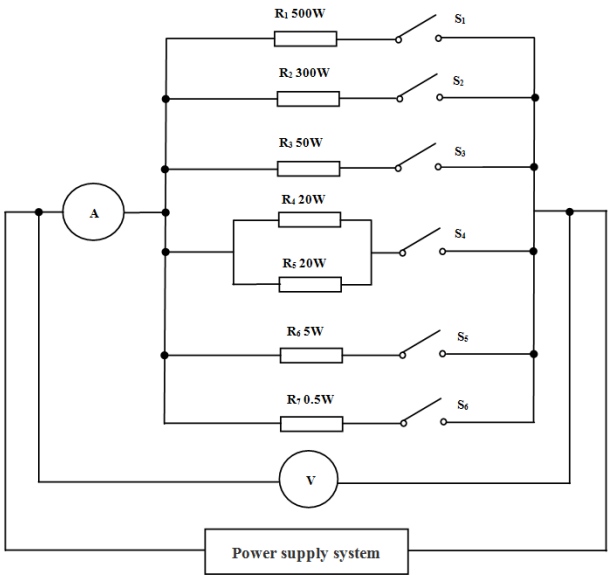

Fig. 5. Analog load resistance block diagram

D. Electric parameter detection system

The electric parameter measuring instrument is used to measure AC voltage, AC current, AC power, AC energy and other parameters,which is mainly composed of power supply,metering module, control module,display and communication module. The power module converts AC voltage to DC voltage that can be used by other modules.

The metering module divides the voltage signal through the resistance, converts the current signal into a signal for sampling through the current transformer and the sampling resistance.

Table 2. Design key components

Name	Model	Technical Index
Metering chip	RN7302	AC voltage, current, power and electric energy , MPE: ±0.1%
MCU	8101	Supply voltage: 2.5 V - 5.5 V, Frequency：32 MHz
LCD touch screen	SDWE080T67	Supply voltage:12 V
Crystal oscillator	HC-49SMD-3	Frequency 6 MHz， MPE: ±0.002%
Manganese copper shunt	FLQ-200-5-CK-110	Resistance：200 μΩ，MPE: ±0.1%
Resistance voltage divider	1206	Resistance：120 kΩ，MPE: ±0.1%
Resistance voltage divider	0603	Resistance：1.5 kΩ；MPE: ±0.1%
transformer	TC-X-195	Coil transformation ratio：135:22:20, Input voltage range：120 V - 320 V
Voltage module	W4726267	17 V / 220 mA ， MPE: ±0.1%

The metering chip completes the signal sampling and data processing. The control module mainly includes CPU, data storage chip, clock chip, etc. The display module includes a LCD driver chip. After receiving the data transmitted by the CPU, the driver chip drives the LCD to complete the display function.

The key parts selected in the design are mainly composed of electric energy metering chip, main control MCU, time base crystal oscillator, resistance voltage divider, current transformer, manganese copper shunt, liquid crystal, etc., as shown in Table 2.

The system control function is realized by single chip microcomputer.Since the measurement accuracy of the system is 0.1%, 16 bit A/D conversion is selected, and the linear error is better than 0.002%. The built-in self calibration circuit can be easily connected with the single chip microcomputer through the serial output interface.

At the same time, it has the characteristics of low power consumption, high precision and strong anti-interference ability. The current measuring circuit converts the measured resistance into the measured voltage, which is integrated into the single chip microcomputer through AD conversion. AC voltage measurement range: (10-300) V, AC current range: (0.1-20) A, active electric energy: (0-99999.99) kWh, measurement accuracy: 0.1%.

E.Temperature parameter detection system

The dynamic line of the refrigerator wireless intelligent detection line. In fact ,the refrigerator moves continuously along with the sliding spool conveyor belt, and the detection instruments andequipment also move synchronously.

The calibration device for temperature parameters should be designed with full consideration of the actual measurement environment.

Fig. 6. Key parts for temperature detection

As shown in Figure 6, the key components of the temperature parameter detection system are mainly composed of const-670 intelligent precision dry body furnace, dy-300s low potential transfer switch, daqm-4301 data acquisition, class A platinum resistance sensor,card DS18B20 temperature sensor, waterproof antenna and other key components.

Daqm-4301 data acquisition card connects DS18B20 temperature sensor or A-level platinum resistance sensor, 2-wire or 3-wire, 8-Channel 128 points, temperature measurement from -55℃ to 125 ℃, maximum allowable error of temperature measurement: ± 0.0625 ℃, communication baud rate: 1200 bps, 2400 bps, 4800 bps, 9600 bps, 38400 bps, etc.

Dy-300s low potential transfer switch is a 10 channel scanning switch. Its switch contact thermal potential is lower than 0.4μV.Computer program control can be realized through RS232 or RS485 interface.

Const670 intelligent precision dry body furnace, temperature control from -40 ℃ to 160 ℃, allowable temperature control error:±0.014 ℃, temperature fluctuation:±0.005 ℃,axial uniformity: 0.035 ℃.

Using the wireless network communication function, this paper selects A-level platinum resistance sensor or DS18B20 temperature sensor for design. Under the dynamic test conditions, the data information of thermocouple or platinum resistance is sent to the data acquisition system through the program-controlled scanning switch. Using the serial port communication technology, the data information is read, analyzed, processed and stored by the computer.

F.Metering monitoring platform system

As shown in Figure 7,The measurement and monitoring platform system realizes the real-time data acquisition of electric parameters and temperature parameters based on data analysis, and can realize the data acquisition of AC voltage, AC current, electric energy, etc., and monitor the measurement data of the intelligent refrigerator detector[5].

Fig. 7. Metering monitoring platform system

The measurement and monitoring platform system will upload the data for processing, including error calculation, display, early warning, alarm, etc.

The measurement and monitoring platform is connected to the Internet in 4G mode, and the

underlying data interaction protocol based on TCP/IP is directly connected to the cloud server. The collected data is received and processed by the front-end service integrated in the cloud server, and stored in the cloud database to ensure the continuity, accuracy and effectiveness of the data. The application layer platform adopts B/S architecture, the mainstream springboo framework, supports database cluster technology, and has the ability of big data analysis.

IV. TEST DATA ANALYSIS

This calibration method is used to calibrate the dynamic line of refrigerator wireless intelligent detection line in a refrigerator manufacturer.

Table 3. Experimental data

AC power			Temperature channel T1		
Display value	actual value	U (k=2)	Display value	Actual value	U(k=2)
0.499 W	0.501W	0.003W	-30.0℃	29.8℃	0.2℃
4.98W	5.01 W	0.02W	-10.0℃	-9.9℃	0.2℃
14.97W	14.99 W	0.02W	0.0℃	0.1℃	0.2℃
49.98W	50.03 W	0.05W	10.0℃	9.9℃	0.2℃
200.1 W	200.3W	0.2W	30.0℃	29.9℃	0.2℃
499.8 W	500.2W	0.5W	/	/	/

Refrigerator intelligent detector model:KF2010-X1.Maximum allowable error: ±1%. Table 3 shows the test data of the power parameters of the dynamic line and the temperature parameters of the temperature channel T1 of the refrigerator wireless intelligent detection line.

According to the test results, the calibration method can meet the requirements of dynamic line quantity traceability of refrigerator wireless intelligent detection line.

The uncertainty of AC power mainly comes from the standard uncertainty components introduced by the maximum allowable error of the electrical parameter measuring instrument, the maximum allowable error of the AC regulated power supply, the measurement repeatability of the tested intelligent detector and other factors[6].

The uncertainty of temperature parameters is mainly derived from the standard uncertainty component introduced by the maximum allowable error of the second-class standard platinum resistance, the uniformity and fluctuation of the temperature field in the constant temperature tank, and the measurement repeatability of the temperature indicator and controller.

V. CONCLUSION

In this paper, through the research on the on-line calibration method of refrigerator intelligent detection line, we have established the on-line measurement calibration device of refrigerator intelligent detection line.

After many field tests and analysis of test data, it shows that the design scheme in this paper meets the online real-time measurement and calibration of the refrigerator wireless intelligent detection line (dynamic line and static line) of a refrigerator manufacturer, and solves the problem of quantity traceability of the enterprise refrigerator intelligent detector.

REFERENCES

[1] Xia Enpin,Qi Xin, “Research on standard of free embeddedstandard refrigerator”,China standardization, vol.577,No.2,Feb. 2021,pp.77-80.

[2] Zhang Sen,Sui Feng, “Development of temperature calibration device with fixed-point method”, Chemometrics, vol.28, No.4, Jul. 2019, pp.107-110.

[3] Zhang Xiaobin,“Study on constant power AC Electronic load”, Power Electronics, vol.44,No.1,Jan. 2010, pp.81-83.

[4] Hao Zhikun, “Research on AC electronic load calibration technology”, Journal of Astronautic Metrology and Measurement,vol.37,No.4,Aug. 2017 ,pp.54-60.

[5] Liu Deliang, Wei Guangjun, “Research on ignition time measurement of a missile based on FPGA”, Computer measurement and control,vol.19,No.6, Dec. 2011,pp.1394-1396.

[6] Liu Fang,Tian MingXing, “Research on three-phase electronic load simulator”, High Voltage Apparatus, vol.46,No.8,Aug. 2010,pp.22-25.

25th IMEKO TC4 International Symposium
23rd International Workshop on ADC and DAC Modelling and Testing
IMEKO TC-4 2022
Brescia, Italy / September 12-14, 2022

Characterization of Energy Harvesting systems from AC power lines

G. Bucci[1], F. Ciancetta[1], E. Fiorucci[1], S. Mari[1], A. Fioravanti[1], A. Silvestri[1]

[1] *Dept. of Industrial and Information Engineering and Economics, University of L'Aquila, Italy*

***Abstract* – In recent years, energy supply has been a worldwide issue. The energy demand has increased enormously and involves all the main areas: industrial, automotive, health, monitoring, home-system, etc. Therefore, using renewable energy sources or other techniques becomes essential to produce energy. Energy harvesting systems are an indispensable alternative for converting ambient energy from the surrounding environment into electrical energy in powering autonomous electronic devices or circuits. This paper presents the characterization of energy harvesting systems for high voltage power lines. The system can recover energy from a source (DC or AC) to supply a load and manage the excess energy to a storage system. Some tests have been performed, and results have been discussed mainly from the energy point of view and self-consumption.**

I. INTRODUCTION

In recent years, there has been an increase in research aimed at recovering any energy that is daily dispersed in the environment and could be reused to meet specific purposes by creating electrical and electronic systems and devices [1]. Energy Harvesting indicates all the techniques used by electronic devices designed to obtain the necessary energy directly from the environment in which they operate [2]. Due to the scarcity of sources and the worsening of environmental pollution, sustainable energy development continues to attract increasing attention. In recent years, research has been explored, providing new approaches for the production of energy from renewable sources such as wind energy [3], thermal energy [4], solar energy [5], mechanical energy [6], and vibration energy [7], etc. The energy produced by this equipment could be used to power the sensors in a large-scale project that involves monitoring the structural health of bridges, tunnels, and buildings and monitoring energy consumption by implanted utilities, medical devices, and IoT systems [8] - [10]. In all these applications, energy harvesting plays a role of fundamental importance as it would allow continuity in operation. It converts non-electrical energy into electrical energy to power the device directly or by storing it in batteries or other storage systems that can operate the sensors. In this way, a self-recharging system is created, and maintenance interventions to be carried out are reduced. This can be advantageous in cases where the replacement of batteries is frequent or not accessible or in any case where the monitoring must take place without interruption of the service. For example, to monitor infrastructures, detect consumption, or monitor the state of health of a patient. In health applications [11], it is necessary to have a sensor suitable for monitoring the state of health, which a battery must power. When the battery runs out, it must be replaced, and this requires an intervention that is not always possible for the patient. Using a system that uses energy harvesting technology, monitoring occurs continuously without external interventions. This architecture can be applied in any field where: i) the device cannot be powered by a direct energy source and, therefore, the use of energy accumulators is required; ii) the replacement of the accumulators requires an intervention that can be carried out by specialized personnel; iii) it is necessary to provide continuous monitoring. For example, another field of application concerns the measurement systems of electricity consumption on power lines transmission lines where sensors can be used to collect information and monitor users' consumption and measure all magnetoelectric parameters such as voltage, current and magnetic field [12]. In such a system, the battery cannot maintain a permanent power supply for the sensors, leading to the sensors' replacement. However, sensors are often located in remote areas, in adverse work environments that reduce battery life, and in places where it is economically disadvantageous to replace them. For these reasons, it is crucial to collect energy from the surrounding environment to obtain a self-powered sensor to solve these problems.

II. CONSIDERATION ON ENERGY HARVESTING SYSTEM FROM AC POWER NETWORK

Conductors in power systems such as overhead lines, cables, and busbars usually carry a large mains frequency load current. In addition, a magnetic field *H* at the same frequency is also associated with this current. Over time, the variability of the electric and magnetic fields can generate an induced voltage on a coil that can be coupled through electromagnetic induction. The energy collected essentially takes place via an inductor, i.e., a Micro Energy Harvesting (MEH) [13], also called an Inductive Energy Harvester (IEH). The induced alternating voltages will subsequently be adapted to power the electronics using energy management and conversion module so that it is

possible to obtain a stable low voltage direct current (DC) capable of supplying the connected loads. Conventionally, the power management module integrates surge protection, rectification, filtering, DC-DC conversion and other submodules. According to the different application modes of the front-end, the MEH can be divided into two categories: high potential MEH and low potential MEH as shown in Fig 1.

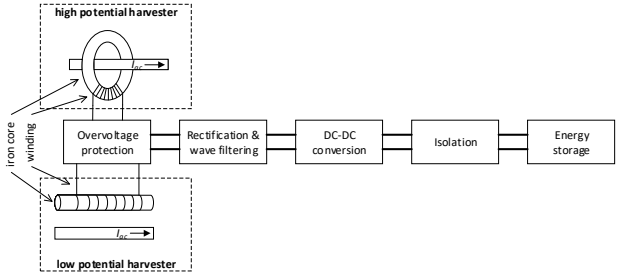

Fig. 1. High and low potential MEH block diagram.

A. Low potential MEH

In this case, the autonomous energy collector is formed by an iron core and a coil. It is positioned away from the HV conductors. There are no installation problems for low potential MEH as long as there is still a variable *H* field distribution in the space where the MEH is present. Conventionally, the collector has low potential as it will not be installed directly on the HV side; therefore, it is also known as the low potential MEH method. The advantage of the low potential MEH is greater installation flexibility which provides greater applicability to different scenarios. Theoretically, it can be used for sensors or systems suitable for monitoring the operating parameters involved as long as the magnetic field is present and the energy supplied by MEH is sufficient, even if the power is low. However, it isn't easy to measure [14]. Furthermore, in a low potential MEH device, the coil can be miniaturized, which can also be compatible with the fabrication of microelectromechanical systems (MEMS). In a low potential MEH device, since the parasitic *H* field is commonly weak, the most critical considerations are focused on designing the coil to improve its performance.

B. High potential MEH

Unlike the low potential MEH, the coil structure of the high potential MEH is of the ring type. In this way, the iron core closed in a ring is clamped on the section of a conductor carried by the current. As a result, the radial *H*-field generated by the current can be recovered in the iron core by the secondary induced voltage. Due to the high permeability of the iron core, the energy density of the high potential MEH is relatively large. Therefore, this type of MEH configuration is also called high potential magnetic field energy harvesting and can be mainly used for devices with transmission line monitoring purposes. The most significant advantage of high potential MEH is that the recovered power is significant; therefore, the application can require energy consumption even on several watts, such as, for example, video monitoring of the conditions of high voltage transmission lines, etc. Also, the state of power produced is stable as long as the line is powered, which is always significant as condition monitoring is only needed when the line is in service. The devices used for energy harvesting in the case of high potential MEH are usually: improved Rogowski coil, current limiting current transformer (CT), and compensating CT [15].

III. SETUP OF MEASUREMENT SYSTEM

The present paper characterizes energy harvesting systems for low potential and high potential MEH. The measurement setup is reported in Fig. 2 where: 1) e-peas AEM30940 energy harvesting has been adopted for managing the flow energy; 2) AGILENT 6613C supplies energy to AEM30940; 3) NiMH (Nickel-Metal-Hydride) rechargeable battery was used as a storage element; 4) via a mechanical switch, an external load of 90 Ω emulates an external system to supply; 5) Yokogawa WT3000 measures the input power from the AGILENT 6613C, the output power over the load and the bi-directional power on the NiMH rechargeable battery; 6) all the measurement has been stored and analyzed on a LabVIEW user interface.

The main parts of the measurement system are reported in detail in the following sections.

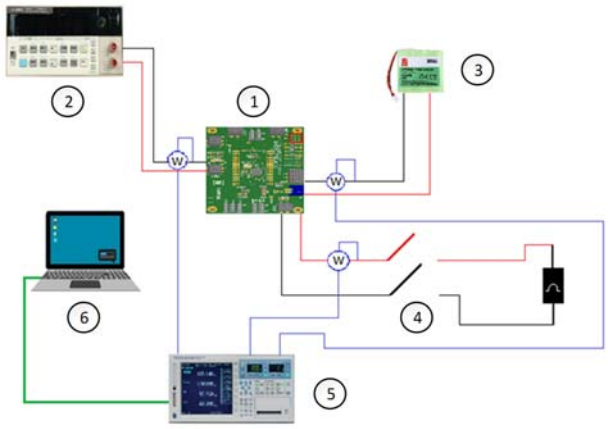

Fig. 2. Measurement system.

A. AEM30940

The AEM30940 is an integrated circuit that manages the energy produced by a piezoelectric generator, a turbine microgenerator, or any high-frequency RF input to store the energy in a rechargeable element and simultaneously power two low power loads with independent regulated voltages. The AEM30940 extends battery life and is used in a wide range of applications such as industrial monitoring, home automation, transportation and smart farming. The AEM30940 collects available input energy

by absorbing up to 110 mA. It integrates an ultra-low-power boost converter to charge an energy storage element, such as a lithium-ion battery, thin-film battery, supercapacitor, or conventional capacitor. The boost converter works with input voltages in the range of 50 mV to 5 V. This device can start operating with empty storage elements, an input voltage of just 380mV, and an input power of only 3 µW. It features a system capable of powering a low voltage device at 1.2 V or 1.8 V (such as a microcontroller) and a high voltage device from 1.8 V to 4.1 V (such as a radio transceiver) simultaneously. LDO (Low Drop-Out) regulators drive both low noise and high stability. Various operating modes can be configured via pins by setting predefined conditions for the energy storage element (overload or over-discharging voltages) and selecting the voltage of the high voltage supply and the low voltage supply. In addition, special modes can be obtained by using some external resistors for the operational configuration of the device [16].

The block diagram is shown below.

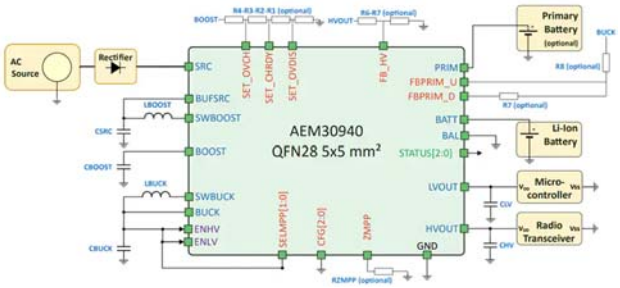

Fig. 3. AEM30940 block diagram.

B. Storage element

A NiMH (Nickel-Metal-Hydride) rechargeable battery was used as a storage element. The nickel-metal hydride accumulator is a type of rechargeable battery in which the cathode is made up of nickel oxyhydroxide (NiOOH), while the anode is made up of a composite hydride of metals, typically mixtures of lanthanides and nickel or other metals of the first series transition and/or aluminum.

NiMH batteries generally work with devices that require moderate power currents, such as digital cameras, cell phones, and consumer electronics.

The main characteristics are: i) technology: NiMH; ii) rated voltage: 3.6 V; nominal energy storage capacity cells type: 2/3AAA; dimensions: 30x30x10 mm;

C. Yokogawa WT3000

Precision Power Analyzer Yokogawa WT3000 has been adopted to measure the input power from the AGILENT 6613C, the output power to a load, and the bi-directional power of the NiMH rechargeable battery. The Yokogawa WT3000 has a power accuracy of ±0.02% reading, DC and 0.1 Hz to1 MHz measurement bandwidths, and up to four input elements.

D. Load

The load used to test the energy harvesting system is a resistive load where the resistance value was obtained considering that the AEM30940low voltage output channel is 1.8 V with a maximum current of 20 mA for the selected configuration. Therefore, a 90 Ω resistance was used. It was decided to use four 90 Ω resistors by connecting them in parallel and then putting them in series To dissipate the maximum deliverable current value. Even if the total resistance is 90 Ω, the energy dissipated on the load for every resistor is reduced to a quarter.

E. LabVIEW

The NI LabVIEW environment has been adopted for acquiring, processing, and saving the measurements. LabVIEW is a development environment for applications mainly oriented to data acquisition and electronic instrumentation management and the analysis and processing of signals. An ad-hoc software has been developed which collects Yokogawa WT3000 measurement data, displays the data in the UI, and saves the data in a CSV file for export to other software, as reported in the following figure.

Fig. 3. The developed UI based on LabVIEW.

IV. TESTS

Different operating conditions have been considered. In detail: i) the behavior of the energy harvesting system in the presence or absence of the source has been examined; ii) the voltage and current values was measured for every element connected to the energy harvesting system, as well as iii) the different behavior of the energy harvesting system for different values of the input voltage. These tests were carried out by connecting and disconnecting the load to the AEM30940. The connection and disconnection of the load are made possible through a mechanical switch. The developed software in LabVIEW has been used to save the measurement data of Yokogawa WT3000 by sampling the data every 100 ms.

A total of five tests have been carried out, as shown in

Table I, in detail: battery charge tests without load with 1 V and 5 V power supplies ((1) and (3)), battery discharge tests with 90 Ω load applied (2), battery charge tests with 5 V and 1 V and applied load of 90 Ω ((4) and (5)).

Table I. Tests carried out.

Test number	Type	Supply (V)	Load (Ω)
1	Charge	Low (1 V)	---
2	Discharge	---	90 Ω
3	Charge	High (5 V)	---
4	Charge	High (5 V)	90 Ω
5	Charge/ Discharge	Low (1 V)	90 Ω

A. Test n.1

In this test, the load has been disconnected from the energy harvesting system while the power supply of the source is 1 V. The recorded values are shown in Figure 4. The starting voltage of the battery is approximately 3.6 V. Subsequently; the input voltage has connected to the AEM30940 board with a value of 1 V. The storage element begins to charge exponentially, reaching an asymptotic voltage value of about 4.1 V while the current value towards the storage system remains almost constant.

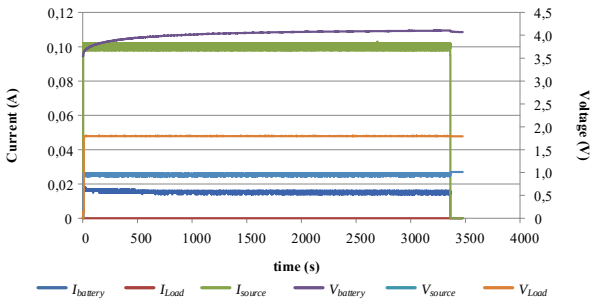

Fig. 4. Measurement results on test n.1.

B. Test n.2

In the second test, the load was connected to the harvester system. First, the power source was interrupted; then, starting from the maximum voltage accumulated in the battery during the charge transient (about 4.2 V), the resistance was connected, closing the mechanical switch. The data acquisition phase began immediately afterward. The battery voltage decreases slightly linearly during the discharge process, while the voltage on the load is constant. Finally, the current delivered to the load is relatively stable (see Figure 5).

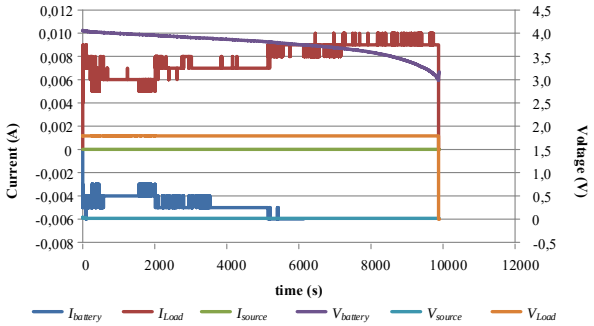

Fig. 5. Measurement results on test n.2.

C. Test n.3

In the third test, the harvester system was powered with a voltage of 5 V corresponding to the maximum input value while the load remained disconnected. As a result, the input supply presents a value higher than the maximum battery voltage. In addition, the current values of either the battery or the input source have a behavior that decays exponentially, unlike Test n.1 where the current values remain practically constant for the entire test duration.

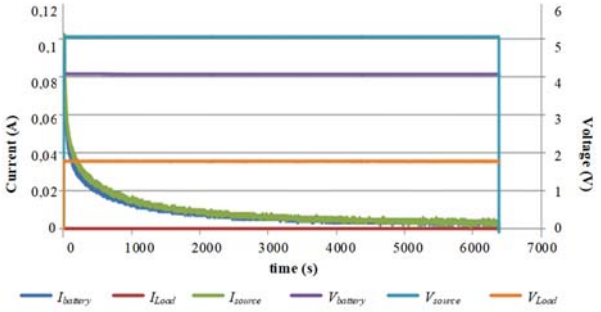

Fig. 6. Measurement results on test n.3.

D. Test n.4

In the fourth test, the harvester system has an input source voltage of 5 V, and the load is connected to the board. The maximum voltage that can be accumulated on the battery is reached in a very short time. The current either of the battery or the source decreases exponentially. There is a greater slope of the battery current ($I_{battery}$) than that of the source (I_{source}) while the current of load (I_{load}) remains constant, absorbing the same amount of power.

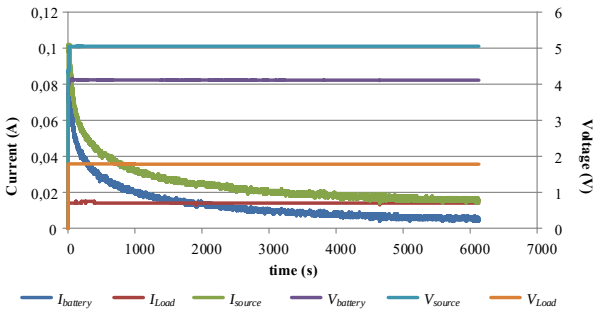

Fig. 7. Measurement results on test n.4.

E. Test n.5

In the fifth and last test, the response of the harvester system was measured during a charge, with a constant power supply at 1 V and a subsequent discharge. The test simulates the availability of energy from the input source for a certain time while it is missing. With a supply voltage of 1 V, the charge on the battery increases from 3.5 V to 3.9 V. Subsequently, the supply of energy is interrupted causing the charge accumulated by the battery to be discharged on the load. It is noted that the current absorbed by the load remains constant, and the board continues to supply energy to the load without interruption, guaranteeing continuity of service with the presence of the battery. Furthermore, the battery voltage (Vbattery) decreases during discharge until it reaches a minimum voltage value (2.8 V); then, the discharge stops. The load is no longer powered as the board disables the output voltage, and the battery voltage value returns to approximately 3.6 V.

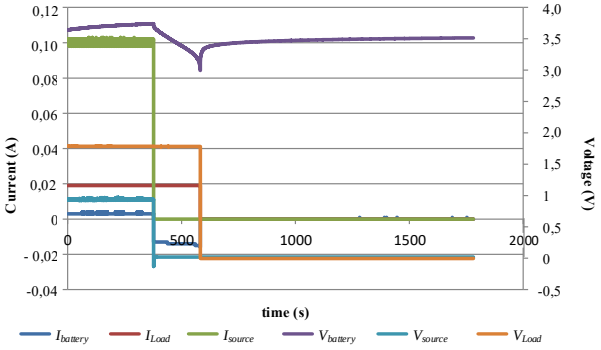

Fig. 8. Measurement results on test n.5.

V. RESULTS

The maximum voltage on the storage element was obtained by powering the system at 5V, corresponding to the maximum applicable input voltage on the board. The value of 4.35V is never exceeded; the voltage remains around 4.1 V in the other tests with an input supply voltage of 1V. During the charging phase, $V_{battery}$ tends to a value of 4.07 V or 4.35V (depending on the input source voltage). With a 1 V input source, the boost converter stops to recharge the battery when the voltage level reaches a value of 4.1 V. On the contrary, with a 5 V input source, a higher value has been reached.

When charging with a 1V input source supply, the voltage on the battery increases at a constant current (see Test 1 and Test 4). On the contrary, in the tests with a 5 V input supply, the charge takes place differently: the voltage increases and the current remains constant until the voltage on the battery reaches its maximum value, after which a reduction in the current is registered (see Test 2 and Test 4).

Finally, the following tables show the energy values recorded during the charging phase at 1V and 5V voltage with and without the connected load.

Table II. Energy comparison in mWh without a load connected.

	Supply (1 V)	Supply (5 V)
Source	89.44	85.82
Battery	57.34	61.29

Table III. Energy comparison in mWh with a load connected.

	Supply (1 V)	Supply (5 V)
Source	113.82	221.54
Battery	31.68	97.02
Load	27.57	42.68

Table II shows that the self-consumption amount regarding the energy supplied by the source without a load connected is 35.89% and 28.58% for the charging phase at 1 V and 5 V, respectively. While in Table III, the self-consumption amount respect on the energy supplied by the source with a load connected is 47.93% and 33.95% for charging phase at 1 V and 5 V, respectively. The results show the conversion efficiency is higher during the charging phase at 5 V, and in any case, the load connected to the energy system decreases the performance by 5%.

VI. CONCLUSIONS

This paper characterized an energy harvesting system in different operating configurations by changing the input supply values and connecting and disconnecting a load.

Using a LabVIEW-based UI that control the measurement performed by the Yokogawa WT3000, currents and voltages of input and output elements connected to the energy harvesting system have been measured and saved. The results show that the system's response under test presented an acceptable behavior, unwanted responses were found only for voltage values close to the operating ranges.

The conversion efficiency depends on the load connected and the supply voltage but can be considered about the 30% of the energy supplied by the input source.

The wide range of applications that these devices will have in the future and the enormous utility they can provide in various fields is expected to develop increasingly sophisticated and functional Harvesting devices.

REFERENCES

[1] S. Ulukus et al., "Energy Harvesting Wireless Communications: A Review of Recent Advances," in IEEE Journal on Selected Areas in Communications, vol. 33, no. 3, pp. 360-381

[2] Energy Harvesting - Clean Technologies - European Union Business Innovation Observatory Contract No 190/PP/ENT/CIP/12/C/N03C01

[3] A. Jushi, A. Pegatoquet and T. N. Le, "Wind Energy Harvesting for Autonomous Wireless Sensor Networks," 2016 Euromicro Conference on Digital System Design (DSD), 2016, pp. 301-308

[4] N. Kumari and M. Rokotondrabe, "Thermal network modelling of hybrid piezo-pyro transducer for application in energy harvesting," 2019 IEEE 5th International Conference for Convergence in Technology (I2CT), 2019, pp. 1-4

[5] H. Sharma, A. Haque and Z. A. Jaffery, "An Efficient Solar Energy Harvesting System for Wireless Sensor Nodes," 2018 2nd IEEE International Conference on Power Electronics, Intelligent Control and Energy Systems (ICPEICES), 2018, pp. 461-464

[6] X. Zhang, Z. Zhang, G. Meng and D. Luo, "Design, modeling, simulation of a novel mechanical road tunnel energy harvesting system with hydraulic transaction," 2015 IEEE International Conference on Information and Automation, 2015, pp. 726-730

[7] S. Balguvhar and S. Bhalla, "Green Energy Harvesting Using Piezoelectric Materials from Bridge Vibrations," 2018 2nd International Conference on Green Energy and Applications (ICGEA), 2018, pp. 134-137.

[8] S. Siskos et al., "Design of a flexible multi-source energy harvesting system for autonomously powered IoT : The PERPS project," 2019 29th International Symposium on Power and Timing Modeling, Optimization and Simulation (PATMOS), 2019, pp. 133-134.

[9] Bucci, G., Ciancetta, F., Fiorucci, E., Mari, S., & Fioravanti, A. (2021). State of art overview of non-intrusive load monitoring applications in smart grids. Measurement: Sensors, 18.

[10] Ciancetta, F., Fiorucci, E., Ometto, A., Fioravanti, A., Mari, S., & Segreto, M. -. (2021). A low-cost IoT sensors network for monitoring three-phase induction motor mechanical power adopting an indirect measuring method. Sensors (Switzerland), 21(3), 1-13.

[11] D. Fan, L. Lopez Ruiz, J. Gong and J. Lach, "EHDC: An Energy Harvesting Modeling and Profiling Platform for Body Sensor Networks," in IEEE Journal of Biomedical and Health Informatics, vol. 22, no. 1, pp. 33-39, Jan. 2018.

[12] Bucci, G., Ciancetta, F., Fiorucci, E., & Ometto, A. (2017). Survey about classical and innovative definitions of the power quantities under nonsinusoidal conditions. International Journal of Emerging Electric Power Systems, 18(3).

[13] Riaz, A., Sarker, M. R., Saad, M. H. M., & Mohamed, R. (2021). Review on comparison of different energy storage technologies used in micro-energy harvesting, wsns, low-cost microelectronic devices: Challenges and recommendations. Sensors, 21(15).

[14] Bucci, G., Fiorucci, E., Ciancetta, F., & Luiso, M. (2014). Measuring system for microelectric power. IEEE Transactions on Instrumentation and Measurement, 63(2), 410-421.

[15] Gallo, D., Landi, C., Luiso, M., Fiorucci, E., Bucci, G., & Ciancetta, F. (2013). A method for linearization of optically insulated voltage transducers. WSEAS Transactions on Circuits and Systems, 12(3), 91-100.

[16] AEM30940 Energy Harvesting. https://e-peas.com/product/aem30940/

25th IMEKO TC4 International Symposium
23rd International Workshop on ADC and DAC Modelling and Testing
IMEKO TC-4 2022
Brescia, Italy / September 12-14, 2022

Regional Interlaboratory Comparison of Measuring Systems for Current Transformers Accuracy Testing

Dragana Naumovic-Vukovic[1], Slobodan Skundric[1], Marko Cukman[2], Darko Ivanovic[2], Ivan Novko[3], Miroslav Bonic[3]

[1] *Electrical Engineering Institute Nikola Tesla JSC, Koste Glavinića 8a, Belgrade, Serbia, draganav@ieent.org*
[2] *Končar – Instrument Transformers Inc, Ulica Josipa Mokrovića 10, Zagreb, Croatia, marko.cukman@koncar-mjt.hr, darko.ivanovic@koncar-mjt.hr*
[3] *Končar – Electrical Engineering Institute Ltd, Fallerovo šetalište 22, Zagreb, Croatia, mbonic@koncar-institut.hr, inovko@koncar-institut.hr*

***Abstract* – The paper describes an intercomparison of measuring systems for current transformers accuracy testing between three laboratories Koncar - Instrument Transformers, Koncar - Electrical Engineering Institute and Electrical Engineering Institute Nikola Tesla. All laboratories are accredited according to EN/ IEC 17025: 2017 standard. The obtained discrepancies in ratio and phase errors are within participant's declared measurement uncertainties. All laboratories have confirmed their competence ($|E_n|\leq 1$) for the applied measurement methods, in accordance with EN ISO/ IEC 17043.**

I. INTRODUCTION

The laboratories accredited according to standard EN/IEC 17025:2017 for calibration and testing, have to demonstrate how they ensure the validity of their results. The best way to fulfil requirements for monitoring the validity of the calibration and testing results, standard EN/IEC 17025:2017, point 7.7, is through the comparison with the results of other laboratories where it is available and appropriate [1]. Comparison can be achieved through participation in proficiency testing (PT schemes) or/and participation in interlaboratory comparison (ILC) [1]. PT/ILC schemes are an important parameter for the test/calibration laboratories to assure the quality of test and calibration results. For accredited laboratories participation in PT/ILC and getting acceptable and successful results in the area of their declared measurements capabilities is a compulsory periodical activity in terms of EN ISO/IEC 17025. This activity is also required from the national accreditation bodies.

In the field of instrument transformers, accredited PT schemes are very rare. From time-to-time key comparisons occurred, organised between national metrology institutes laboratories [2, 3, 4]. Usually, proficiency of the lower rank laboratories, in the national metrology hierarchy, its verified through bilateral or multilateral comparisons organised by National metrology institutes. [5].

This paper describes the results of an ILC organised between regional leading accredited laboratories in the field of current transformers: Koncar – Instrument Transformers Inc. (LAB1), Electrical Engineering Institute Nikola Tesla JSC, (LAB2) and Koncar – Electrical Engineering Institute Ltd, (LAB3). The participating laboratories are accredited according to standard EN/IEC 17025:2017.

II. MEASURING SYSTEMS

All participating laboratories used measuring systems for current transformers accuracy testing based on differential measuring methods. In this method ratio error and phase displacement of chosen artefact (device under test) compares with the errors of standard current transformer. Measuring systems consists of: standard current transformer, measuring bridge (electronic device for accuracy testing of instrument transformers), standard current burden and current supply. In laboratories LAB1, LAB2 and LAB3, measuring systems originating from different manufacturers were used. Measuring equipment from laboratory LAB1 is directly traceable according to the national standards of Germany. Laboratories LAB 2 and LAB3 have measuring equipment that are traceable according to the national standards of Germany, through the national standards of Serbia and the national standards of Croatia, respectively.
The LAB1 was chosen as the reference laboratory by agreement between participants.

III. TRANSFER CURRENT TRANSFORMER

In this ILC commercial current transformer (CT) was

used as a transfer artefact. The transfer CT of the 1000A/5A ratio, class 0.2 was tested at rated burden of 30VA as well as on 7.5VA. Agreed measuring points were 5%, 20%, 100% and 120% of rated current at 50Hz. Transfer CT has remained stable throughout the ILC. Laboratories have measured ratio error and phase displacement of the transfer CT following their usual internal testing procedures.

IV. COMPARISON AND EVALUATION

The measurement results (ratio error and phase displacement) for participation laboratories are shown in Fig. 1, 2, 3 and 4. Numerical values for ratio error and phase displacement with expanded uncertainty of measurement for each laboratory participant are presented in tables from. In te tables from 3 to 8 is also presented En number for all participation laboratories.

A. Results

Results for ratio error, for all laboratories, shown in fig. 1 and 2, for all measurements points, are within interval from -0.076% to 0.039% for the rated burden S and within interval from 0.074% to 0.126% for the burden S/4.

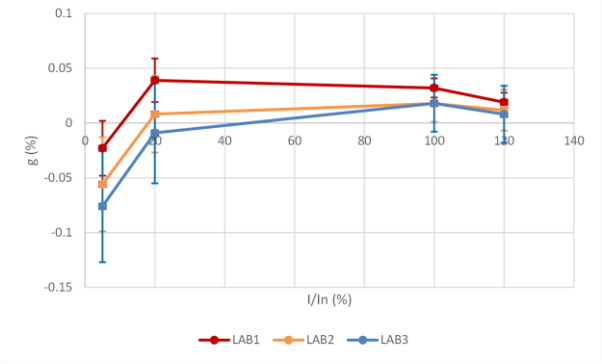

Fig. 1. Ratio error for rated burden 30VA at 50Hz

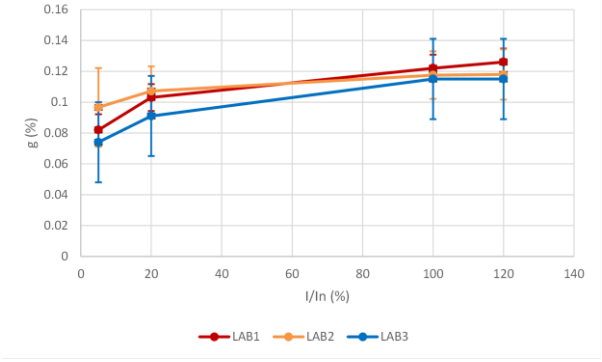

Fig. 2. Ratio error for rated burden 7.5 VA at 50Hz

Results for phase displacement for all laboratories, shown in fig. 3 and 4, for all measurements points, are within interval from 0.32 min to 4,6 min for the rated burden S and within interval from 0.39 min to 3.7 min for the burden S/4. The discrepancy between laboratories in the ratio error is maximum 0.053 % for the rated burden S and 0.02% for the burden S/4. The discrepancy in phase displacement is maximum 2.2 min for the rated burden S and 1.1 min for the burden S/4.

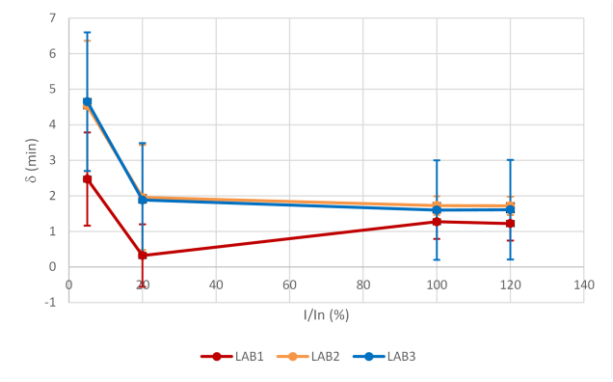

Fig. 3. Phase displacement for 30VA at 50Hz

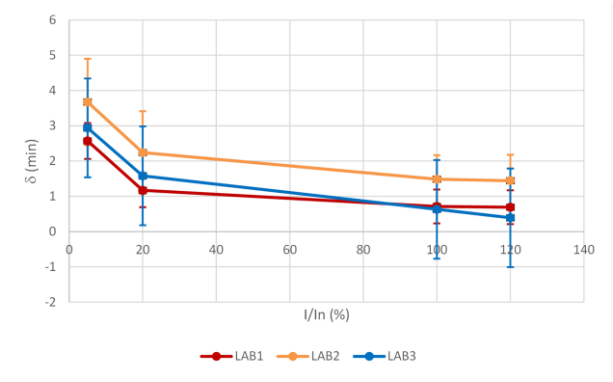

Fig. 4. Phase displacement for 7.5VA at 50Hz

B. Uncertainty budget

The uncertainty budget of the LAB1 and LAB2 results, for ratio error and phase displacement contain five different contributions: type A uncertainty of the measurement, uncertainty of the measuring bridge, uncertainty of the standard CT, burden variations and reference current variation. The uncertainty budget of the LAB3 for ratio error and phase displacement, contain three different contributions: type A uncertainty of the measurement, uncertainty of the measuring bridge and uncertainty of the standard CT. The uncertainty of the primary circuit configuration wasn't considered because all participant laboratories applied pre-agreed disposition for primary circuit.

The expanded uncertainties (k = 2) of all participants laboratories are calculated according to:

$$U(g) = 2 \cdot \sqrt{\sum_i u_i^2(g)} \quad (1)$$

$$U(\delta) = 2 \cdot \sqrt{\sum_i u_i^2(\delta)} \quad (2)$$

The uncertainty budgets for participant laboratories for measuring points 5% and 100% of rated current at rated burden of 30VA are given in the following tables.

Table 1. Type A and B standard uncertainty and expanded uncertainty for ratio error of transfer current transformer (1000A/5A) at rated burden S and measuring points 5%I_n and 100%I_n

Measuring point	Type	*Uncertainty components $u_i(y)$* (%)		
		LAB1	LAB2	LAB3
5% I/I_n	A	0.0115	0.0184	0.0219
	B	0.0050	0.0110	0.0130
Expanded uncertainty (k=2, *p*=95%)		0.0251	0.0430	0.051
100% I/I_n	A	0.00007	0.0026	0.001
	B	0.0087	0.0079	0.0133
Expanded uncertainty (k=2, *p*=95%)		0.0087	0.0167	0.0266

Table 2. Type A and B standard uncertainty and expanded uncertainty for phase displacement of transfer current transformer (1000A/5A) at rated burden and measuring points 5%I_n and 100%I_n

Measuring point	Type	*Uncertainty components $u_i(y)$* (min)		
		LAB1	LAB2	LAB3
5% I/I_n	A	0.603	0.725	0.680
	B	0.255	0.561	0.698
Expanded uncertainty (k=2, *p*=95%)		1.31	1.83	1.95
100% I/I_n	A	0.01	0.08	0.05
	B	0.24	0.11	0.70
Expanded uncertainty (k=2, *p*=95%)		0.48	0.27	1.40

It can be noticed that dominant component of measuring uncertainty at measuring point 5% of rated current, for both ratio error and phase displacement is type A for all participants. At measuring point 100% of rated current dominant component for all participants is type B. The source for the stated trend of uncertainty of measurement is the nature and features of the chosen transfer current transformer.

C. Statistical Evaluation

The statistical method applied for evaluation of the results in this ILC was calculation of En number [6]. For each participant laboratory E_n number is calculated using equation:

$$En = \frac{X_{lab} - X_{ref}}{\sqrt{U_{lab}^2 + U_{ref}^2}} \quad (3)$$

where

X_{lab} is the participant's result, LAB1, LAB2 and LAB3

X_{ref} is te reference assigned value:

$$X_{ref} = \frac{X_{LAB1} + X_{LAB2} + X_{LAB3}}{3} \quad (4)$$

Table 3. Numerical values of ratio error with expanded uncertainty of measurement and En number for LAB1

I/In (%)	g_{ref} (%)	U_{ref} (%)	G_{LAB1} (%)	U_{LAB1} (%)	$\lvert E_{n\ LAB1}\rvert$
S = 30 VA					
5	-0.052	0.024	-0.023	0.0251	0.83
20	0.013	0.020	0.039	0.0198	0.93
100	0.023	0.011	0.032	0.0087	0.68
120	0.013	0.011	0.019	0.0087	0.43
S = 7.5 VA					
5	0.084	0.013	0.082	0.0101	0.14
20	0.100	0.011	0.103	0.0087	0.19
100	0.118	0.010	0.122	0.0087	0.28
120	0.120	0.011	0.126	0.0087	0.46

Table 4. Numerical values of phase displacement with expanded uncertainty of measurement and En number for LAB1

I/In (%)	g_{ref} (%)	U_{ref} (%)	G_{LAB1} (%)	U_{LAB1} (%)	$\lvert E_{n\ LAB1}\rvert$
S = 30 VA					
5	3.88	0.99	2.47	1.31	0.86
20	1.38	0.78	0.32	0.88	0.90
100	1.53	0.50	1.27	0.48	0.38
120	1.52	0.50	1.22	0.48	0.43
S = 7.5 VA					
5	3.06	0.64	2.57	0.51	0.60
20	1.66	0.63	1.17	0.48	0.62
100	0.94	0.54	0.71	0.48	0.32
120	0.84	0.55	0.69	0.48	0.21

U_{lab} is the expanded uncertainty of a participant's results, LAB1, LAB2 and LAB3
U_{ref} is the expanded uncertainty of the reference:

$$U_{ref} = \sqrt{U_{LAB1}^2 + U_{LAB2}^2 + U_{LAB3}^2} \qquad (5)$$

Table 5. Numerical values of ratio error with expanded uncertainty of measurement and En number for LAB2

I/In (%)	g_{ref} (%)	U_{ref} (%)	G_{LAB2} (%)	U_{LAB2} (%)	$\lvert E_{n\ LAB2}\rvert$
S = 30 VA					
5	-0.052	0.024	-0.0559	0.0430	0.09
20	0.013	0.020	0.0081	0.0350	0.11
100	0.023	0.011	0.0177	0.0167	0.24
120	0.013	0.011	0.0117	0.0187	0.05
S = 7.5 VA					
5	0.084	0.013	0.0966	0.0255	0.44
20	0.100	0.011	0.1072	0.0160	0.35
100	0.118	0.010	0.1175	0.0154	0.04
120	0.120	0.011	0.1179	0.0163	0.09

Table 6. Numerical values of phase displacement with expanded uncertainty of measurement and En number for LAB2

I/In (%)	g_{ref} (%)	U_{ref} (%)	G_{LAB2} (%)	U_{LAB2} (%)	$\lvert E_{n\ LAB2}\rvert$
S = 30 VA					
5	3.88	0.99	4.528	1.836	0.31
20	1.38	0.78	1.954	1.478	0.34
100	1.53	0.50	1.726	0.261	0.34
120	1.52	0.50	1.720	0.260	0.36
S = 7.5 VA					
5	3.06	0.64	3.674	1.227	0.44
20	1.66	0.63	2.240	1.174	0.43
100	0.94	0.54	1.484	0.680	0.62
120	0.84	0.55	1.443	0.733	0.66

Table 7. Numerical values of ratio error with expanded uncertainty of measurement and En number for LAB3

I/In (%)	g_{ref} (%)	U_{ref} (%)	G_{LAB3} (%)	U_{LAB2} (%)	$\lvert E_{n\ LAB3}\rvert$
S = 30 VA					
5	-0.052	0.024	-0.076	0.051	0.43
20	0.013	0.020	-0.009	0.046	0.43
100	0.023	0.011	0.018	0.026	0.16
120	0.013	0.011	0.008	0.026	0.17
S = 7.5 VA					
5	0.084	0.013	0.074	0.026	0.35
20	0.100	0.011	0.091	0.026	0.33
100	0.118	0.010	0.115	0.026	0.11
120	0.120	0.011	0.115	0.026	0.17

Satisfactory criterion for measuring results is $|E_n| \leq 1$. Evaluated values for E_n number for each laboratory are presented in tables from 3 to 8. Values for E_n number are also shown in Fig. 5 and 6 for ratio errors and Fig. 7 and 8 for phase displacement.

Table 8. Numerical values of phase displacement with expanded uncertainty of measurement and En number for LAB3

I/In (%)	g_{ref} (%)	U_{ref} (%)	G_{LAB3} (%)	U_{LAB3} (%)	$\lvert E_{n\ LAB3}\rvert$
S = 30 VA					
5	3.88	0.99	4.65	1.95	0.35
20	1.38	0.78	1.88	1.60	0.28
100	1.53	0.50	1.60	1.40	0.05
120	1.52	0.50	1.61	1.40	0.06
S = 7.5 VA					
5	3.06	0.64	2.94	1.40	0.08
20	1.66	0.63	1.58	1.40	0.05
100	0.94	0.54	0.63	1.40	0.21
120	0.84	0.55	0.39	1.40	0.30

As presented in tables from 3 to 8 all participant laboratories have E_n number less than 1.0 for both measured ratio errors and phase displacement. Therefore, all participant laboratories confirmed their competence for the applied measurement methods, in accordance with EN ISO / IEC 17043.

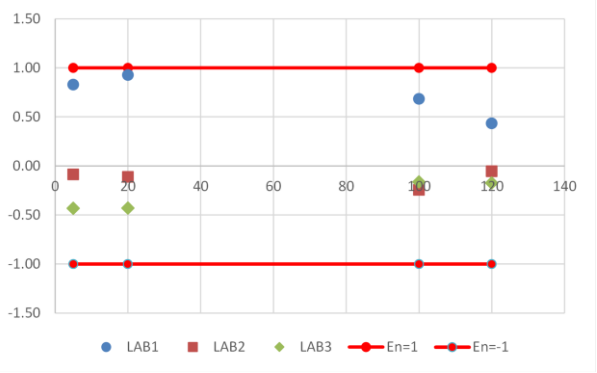

Fig. 5. E_n number for ratio error at S=30VA and measuring points from 5%I_n to 120%I_n for all participant laboratories

V. CONCLUSION

The interlaboratory comparison described in this paper is successfully performed. For ratio error and phase displacement measurement participant laboratories used measurement systems from different manufacturers. Transfer current transformer 1000A/5A, 30VA, class 0.2

remained stable during the comparison. The discrepancy between laboratories in the ratio error measurement is within 0.05 % for the rated burden S and within 0.015% for the burden S/4. The discrepancy in phase displacement measurement is within 2.2 min for *the* rated burden S and 1.1 min for the burden S/4. The obtained discrepancies in ratio and phase errors are within participant's declared measurement uncertainties. The carried out statistical processing of measurement results shows that all laboratories have E_n number less than 1.00. In this way participant laboratories confirmed their competence in accuracy measurement of current transformers and ensured the validity of their results.

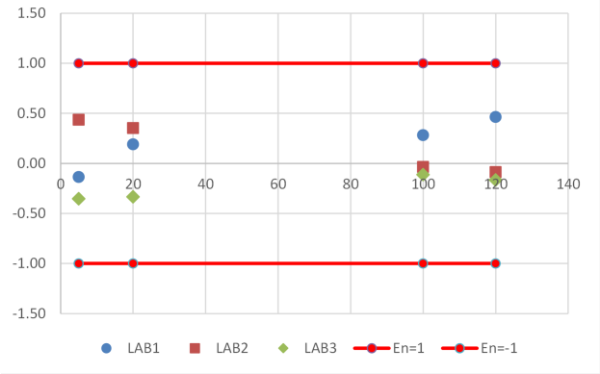

Fig. 6. E_n number for ratio error at S=7.5VA and measuring points from 5%I_n to 120%I_n for all participant laboratories

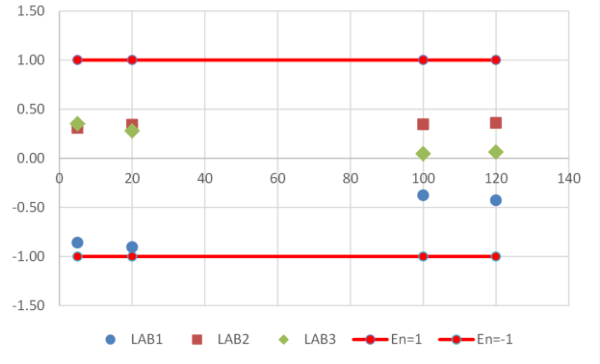

Fig. 7. E_n number for phase displacement at S=30VA and measuring points from 5%I_n to 120%I_n for all participant laboratories

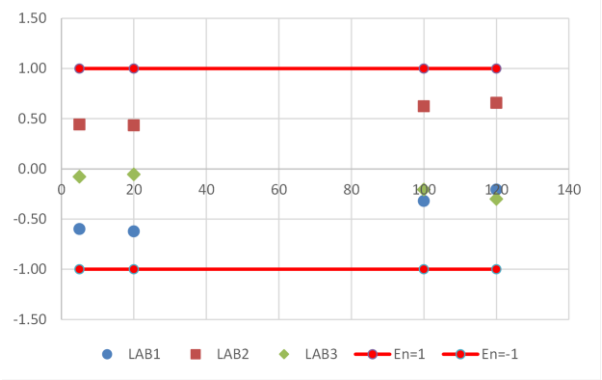

Fig. 8. E_n number for phase displacement at S=7.5VA and measuring points from 5%I_n to 120%I_n for all participant laboratories

REFERENCES

[1] EN ISO/IEC 17025:2017 General requirements for the competence of testing and calibration laboratories

[2] M. Gelovani, B. Schumacher, "Final report on COOMET.EM-S11: Supplementary bilateral comparison of the measurement of current transformers between UNIM and PTB," Metrologia, Vol. 51, No. 1A, January 2014, DOI:10.1088/0026-1394/51/1A/01013

[3] E.Dimitrov, G.Kunamova, R.Styblikova, K.Draxler, E.Dierikx, "Final report EURAMET.EM-S30 on EURAMET Project 1081:Supplementary comparison of measurements of current transformers Metrologia Vol 47, No. 1A, January 2010, DOI:10.1088/0026-1394/47/1A/01001.

[4] A.Santos, D.Slomovitz, G.Aristoy, R.Sandler, J.Luis Casais, P.Casi de Olivera, A.Zipaquira Triana, J.Gonzales, S.Ochoa Marques, E.Mohns, "Supplementary comparison of instrument current transformers", Metrologia, Vol.57, No. 1A, 2020.

[5] B. Djokic, H. Parks, N. Wise, D. Naumovic Vukovic, S. Skundric, A. Zigic, V Poluzanski, A Comparison of Two Current Transformer Calibration Systems at NRC Canada, IEEE Transactions on Instrumentation and Measurement, IEEE Instrumentation and Measurement Society, vol. 66, no. 6, pp. 1628 - 1635, issn: 0018-9456, doi: 10.1109TIM.2017.2631739, 2017.

[6] ISO/IEC 17043:2010 Conformity assessment – General requirements for proficiency testing

25th IMEKO TC4 International Symposium
23rd International Workshop on ADC and DAC Modelling and Testing
IMEKO TC-4 2022
Brescia, Italy / September 12-14, 2022

First results on the functional characterization of two rotary comb-drive actuated MEMS microgripper with different geometry

Gabriele Bocchetta[1], Giorgia Fiori[2], Andrea Scorza[3], Nicola Pio Belfiore[4], Salvatore Andrea Sciuto[5]

Dep. of Industrial, Electronic and Mechanical Engineering, Roma TRE University, Rome, Italy
[1] gabriele.bocchetta@uniroma3.it, [2] giorgia.fiori@uniroma3.it, [3] andrea.scorza@uniroma3.it,
[4] nicolapio.belfiore@uniroma3.it, [5] salvatore.sciuto@uniroma3.it

***Abstract* – Microgrippers (MGs) are Micro Electro-Mechanical System (MEMS) devices able to manipulate cells and micrometric objects. In order to carry out their functional characterization, a comparison between two electrostatic rotary comb-drives actuated prototypes with different geometries through an image analysis-based method is proposed. This study aims at evaluating and comparing the MGs displacement as a function of the supply voltage. The two investigated geometries are equipped with a single rotary comb-drive and a double rotary comb-drive actuation. MGs data have been collected through a trinocular optical microscope with a digital camera and processed by means of an algorithm implemented *ad hoc* in MATLAB. Based on the promising results obtained, further studies are going to be carried out by including other geometries and improving the experimental setup and implemented method.**

I. INTRODUCTION

Microgrippers (MGs) are devices that are part of the class of MEMS (Micro Electro-Mechanical System) devices. These devices require micro-actuators to move the gripper jaws, thus offering a wide range of possible applications, especially in the biomedical sector [1-3]. In literature, there are studies on different types of micro-actuators, based on different operating principles, i.e., electrostatic, electromagnetic, electrothermal, piezoelectric, and shape memory alloys [4-6]. The MG prototypes under examination are equipped with electrostatic rotary comb-drives and Conjugate Surface Flexure Hinges (CSFHs) and fabricated monolithically on a Silicon-on-Insulator (SOI) wafer with an aluminum hard mask, through a process of Deep Reactive Ion Etching (DRIE) [9-10]. Previous studies available in literature [11-12] have presented a theoretical formulation describing the electrostatic torque exerted by rotary comb-drives, which is a function of the geometric characteristics of the micro-actuator, whose nominal values have been reported in Table 1, and the square of the supply voltage and have evaluated the displacement as a function of the latter [13-15]. This preliminary study, based on image analysis method, aims to investigate the design of MG prototypes by analyzing the relationship between gripper tips displacement and the number of active micro-actuators, as a function of supply voltage and to verify if doubling the electrostatic torque applied by the comb-drives, the prototype displacements double, as assumed by the theoretical model [9-12]. In particular, the two Devices Under Test (DUTs) are two new-concept MG prototypes composed of a double four-bar linkage in a mirroring configuration actuated by electrostatic rotary comb-drives. The main difference between the two investigated geometries is the comb-drive number: the first prototype (Fig. 1a) is actuated by a Single Rotary Comb-Drive (SRCD), while the second one (Fig. 1b) by a Double Rotary Comb-Drive (DRCD).

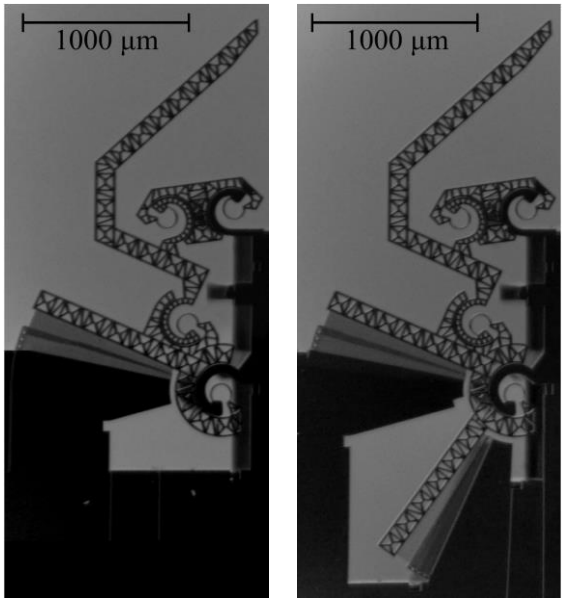

(a) (b)

Fig. 1. Geometry comparison between (a) single and (b) double rotary comb-drive actuated microgripper.

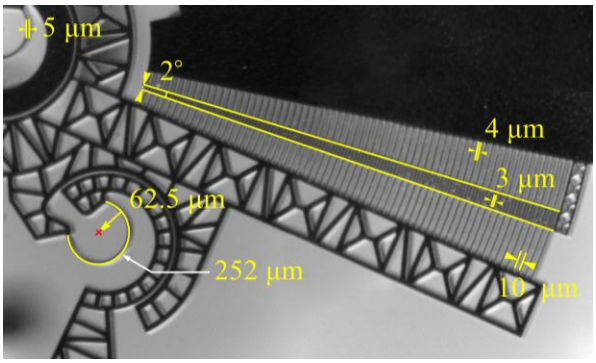

Fig. 2. Microgripper geometric characteristics.

Table 1. Microgripper main specifications

Component		SRCD	DRCD
Number of comb-drives		2	4
Fingers	Number per comb-drive	64	
	Width	4 µm	
	Thickness	40 µm	
	Distance	10 µm	
	Initial overlapping angle	2°	
	Rotor-stator distance	3 µm	
CSFH	Number	8	
	Curved beam length	252 µm	
	Curved beam width	5 µm	
	Curved beam thickness	40 µm	
	Curvature radius	62.5 µm	
SOI Wafer	Device layer thickness	40 µm	
	Insulated layer thickness	5 µm	
	Handle layer thickness	400 µm	

II. MATERIALS AND METHODS

In order to evaluate the functional characteristics of the two DUTs, different videos have been acquired using a trinocular optical microscope equipped with a digital camera and the corresponding data have been processed by a measurement procedure implemented by the Authors in MATLAB. In particular, some videos of the MG jaws and the comb-drive that the two prototype geometries have in common (Fig. 2) have been acquired, for the purpose of evaluating the MG displacement. The two DUTs have been powered by an Arbitrary/Function Generator that supplied a trapezoidal ramp signal, in order to assess the displacement as the supply voltage increases.

A. Experimental setup

The experimental setup is shown in Fig. 3, while its main components have been reported in Table 2, and can be schematized considering two main parts:

- Power supply system, consisting of an Arbitrary /Function Generator and a power amplifier for the MG prototypes supply signal generation.
- Image acquisition system, consisting of a trinocular optical microscope and a digital camera for acquiring videos of the DUTs.

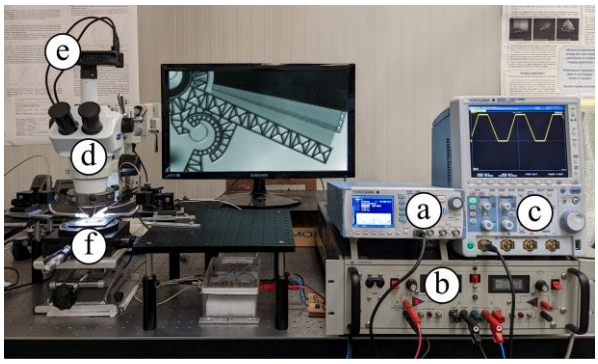

Fig. 3. Experimental setup: (a) Arbitrary/Function Generator, (b) Power Amplifier, (c) Oscilloscope, (d) Light Microscope, (e) Digital Camera, and (f) DUT.

The MG prototypes have been placed under the microscope lens and have been powered through the contact of three tungsten needles, positioned by three micropositioners. The Arbitrary/Function Generator has been configured to generate a trapezoidal ramp signal with a 2 s period, thus obtaining for each period a phase with a duration of 0.5 s corresponding to the maximum supply voltage. The generated signal subsequently has been amplified, thus obtaining a supply voltage between 0 e 20 V peak-to-peak and a digital oscilloscope (Fig. 3c) has been placed in parallel with the supply circuit in order to monitor in real-time the supply voltage powering the DUT. Different videos of the DUTs have been acquired using the microscope-mounted digital camera at a frame rate of 60 fps, and with a duration to capture at least thirty periods of the supply signal and thirty frames for each period showing the MG at the maximum displacement. In particular, videos of the

Table 2. Experimental Setup

Device	Characteristics
Arbitrary/ Function Generator	Amplitude: 0 to ± 10 V peak-to-peak, Frequency: 0.01 µHz to 5 MHz
Power Amplifier	Amplitude: 0 to ± 20 V
Light Microscope	Zoom Range: 16×, 20×, 40×, 60×, 80×, 100×
Light source	LED Ring Light Color temperature: 5600 °K
Digital Camera	23.3 MP, sensor size ½.3 in, maximum image size 5568×4176 pixel
Image Processing Software	In-house algorithm implemented in MATLAB (2021b, MathWorks)
PC	Intel core i7-4790, 32 GB RAM, Nvidia GeForce GTX 960

comb-drive at 40× magnification and videos of the MG jaws at 80× magnification have been acquired for evaluating the angular displacement of the micro-actuators and the gripper tips displacement respectively.

B. Video processing

The collected data have been processed in a MATLAB environment. The comb-drive angular displacement and the gripper tip displacement have been evaluated through a measurement procedure that performs a tracking of virtual markers inserted frame by frame within predetermined Regions Of Interest (ROIs) as shown in Fig. 4 [15-18]. As regards the comb-drive videos, the Instantaneous Center of Rotation (ICR) of the comb-drive has been obtained on the first frame from the intersection of two lines drawn by the operator, and the angular displacement has been evaluated as follows:

$$\vartheta = \frac{s}{r} \tag{1}$$

where ϑ describes the angular displacement made by the comb-drive, that it has been evaluated as the ratio between the markers trajectory which describes an arc of a circle s, and the radius r, calculated as the distance between the ICR and markers x- and y-coordinates. Finally, the comb-drive average angular displacement and the gripper tip displacement have been evaluated as the mean over all acquired periods.

Table 3. Main uncertainty sources

Source	Value
Arbitrary/Function Generator amplitude uncertainty	±(1% of $V_{peak\text{-}to\text{-}peak}$ + 2 mV)
Arbitrary/Function Generator frequency uncertainty	±(3 ppm of setting + 2 pHz) Aging rate: ±1 ppm/year
Power amplifier amplitude uncertainty	2 mV
Optical system uncertainty	1 µm
Video tracking algorithm uncertainty	It depends on the subject of the video and magnification level. It has been estimated as 0.01° for comb-drive videos and 0.1 µm for SRCD gripper tip videos and 0.3 µm for DRCD gripper tip videos respectively

III. UNCERTAINTY ANALYSIS

In order to discuss the obtained results, an uncertainty analysis considering the main sources of uncertainty has been carried out. In according with the approach adopted in [13-15], Type A and Type B uncertainties have been combined [19], following:

$$\sigma_T = \sqrt{\sigma_A^{\,2} + \sigma_B^{\,2}} \tag{2}$$

Type A uncertainties σ_A have been evaluated considering the standard deviation of the obtained results, while Type B uncertainties σ_B have been calculated by taking into consideration the following sources of uncertainty present in the measurement chain, listed in Table 3:

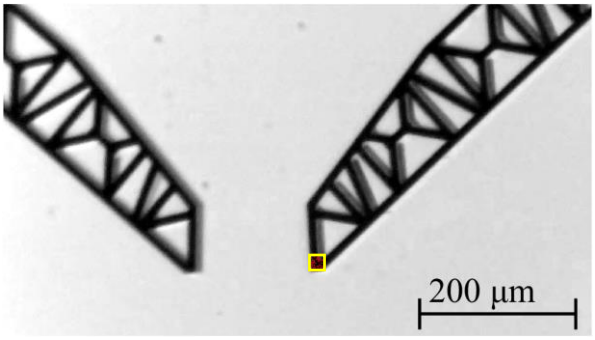

Fig. 4. Virtual marker (red) inserted in the ROI (yellow) for motion evaluation through video tracking.

- Arbitrary/Function Generator on signal amplitude and frequency, reported in the datasheet.
- Power amplifier uncertainty on amplitude, reported in the datasheet.
- Optical system uncertainty has been overall estimated as 1 µm. This contribution considers the lateral resolution that depends on diffraction and the wavelength of the incident light, and the pixel resolution [20-22].
- Video tracking algorithm uncertainty, which varies frame by frame and depends on the type of considered video, i.e., comb-drive or gripper tip.

Table 4. Variable settings in MCS

Data	Parameter	Distribution	
Comb-drive videos	ICR x-coordinate	Normal	x_{ICR} ± 5 px
	ICR y-coordinate	Normal	y_{ICR} ± 1 px
	MC x-coordinate	Normal	x_{MC} ± 2 px
	MC y-coordinate	Normal	y_{MC} ± 2 px
Gripper tip videos	MC x-coordinate	Normal	x_{MC} ± 2 px
	MC y-coordinate	Normal	y_{MC} ± 2 px

x_{ICR}, y_{ICR}, x_{MC} and y_{MC} indicate the ICR and MC average x- and y-coordinates which depend on the video of each investigated device due to a different frame during the acquisition.

The video tracking algorithm uncertainty has been evaluated by the means of a Monte Carlo Simulation (MCS) with 10^4 iterations [23]. At each MCS iteration, the number of markers inserted in the ROI has been made to vary randomly, thus obtaining a variation of the Markers' Centroid (MC) x- and y-coordinates. Concerning the comb-drive angular displacement evaluation, since the implemented algorithm requires a manual step for the ICR assessment, its contribution in

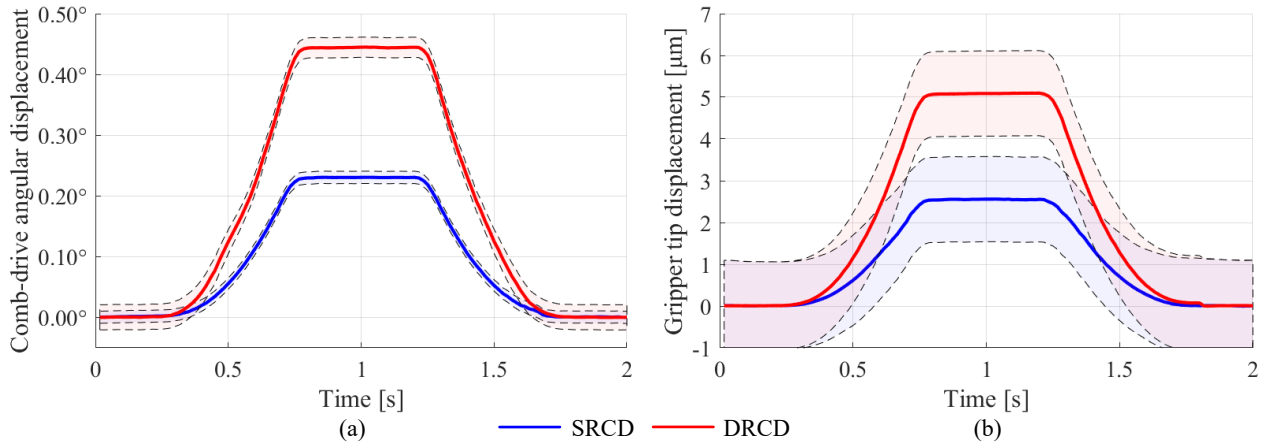

Fig. 5. SRCD and DRCD results: (a) comb-drive angular displacement and (b) gripper tip displacement as a function of the supply voltage.

the uncertainty analysis has been evaluated by varying the ICR coordinates according to the distribution obtained after performing the ICR evaluation process by six different operators, 30 times each. Finally, the evaluated uncertainties have been expressed as the overall calculated standard deviations and have been combined for reporting the measured results referring to a single average period.

Table 5. Experimental results

	SRCD	**DRCD**
Comb-drive angular displacement	0.23° ± 0.01°	0.45° ± 0.02°
Gripper tip displacement	2.5 ± 1.1 µm	5.1 ± 1.1 µm

IV. RESULTS AND DISCUSSION

In this section, the first obtained results correlated by the relative uncertainties are reported and commented. Fig. 5 shows the comb-drive angular displacements and the gripper tip displacement together with their total uncertainties obtained applying to the two MGs a power supply in the range 0-20 V peak-to-peak. The obtained preliminary results reported in Table 5 show that the maximum angular displacement corresponds to 0.23° ± 0.01° and 0.45° ± 0.02° for SRCD and DRCD respectively, while the gripping tip maximum displacement is 2.5 ± 1.1 µm for SRCD and 5.1 ± 1.1 µm for DRCD. Therefore, considering the stationary part of the curves, due to the maximum supply voltage, the average ratio between DRCD and SRCD displacement is very close to 2, i.e., 1.93 ± 0.06 for the comb-drive angular displacement and 2.0 ± 0.4 for the gripper tip displacement.

V. CONCLUSIONS

The present preliminary study focused on the functional characterization of two MG prototypes with different geometry actuated by electrostatic rotary comb-drives. The two investigated devices are made up of a double four-bar linkage in a symmetrical configuration and respectively equipped with SRCD and DRCD micro-actuators. In order to evaluate the prototypes functional characteristics, videos of the two DUTs have been acquired using a trinocular optical microscope equipped with a digital camera. The acquired data have been processed through an in-house algorithm implemented in MATLAB by the authors and the uncertainty analysis has been carried out in order to estimate the quality of the measurements. For the two examined devices, the maximum angular displacement, i.e., at 20 V supply voltage, is 0.23° ± 0.01° for SRCD and 0.45° ± 0.02° for DRCD with a ratio of 1.93 ± 0.06. On the other hand, the maximum gripper tip displacement corresponds to 2.5 ± 1.1 µm and 5.1 ± 1.1 µm for SRCD and DRCD respectively, with a ratio of 2.0 ± 0.4. These preliminary results show that, as a first attempt, duplicating the number of the active micro-actuators reflects in MG double displacements.

In the near future, it will be important to improve the experimental setup and the video processing algorithm and to investigate other MG geometries with the aim to assess if the CSFHs behavior can be assumed linear as a function of the supply voltage, within the considered range of displacements, and moreover, to investigate if different microactuator geometries also correspond to different values of the pull-in voltage [24].

REFERENCES

[1] D.O.Otuya, Y.Verma, H.Farrokhi, L.Higgins, M.Rosenberg, C.Damman, G.J.Tearney, “Non-endoscopic biopsy techniques: a review”, Expert Rev Gastroenterol Hepatol, vol.12, No.2, February 2018, pp. 109-117.

[2] A.Bagolini, P.Bellutti, P.Di Giamberardino, I.J.Rudas, V.D’Andrea, M.Verotti, A.Dochshanov, N.P.Belfiore, “Stiffness characterization of biological tissues by means of MEMS-technology

based micro grippers under position control", Mech. Mach. Sci., July 2017, pp. 939–947.

[3] K.R.Oldham, "Applications of MEMS technologies for minimally invasive medical procedures", in "MEMS for Biomedical Applications", Woodhead Publishing, 2012, pp. 269-290.

[4] P.K.Sekhar, V.Uwizeye, "Review of sensor and actuator mechanisms for bioMEMS", in "MEMS for Biomedical Applications", Woodhead Publishing, 2012, pp. 46-77.

[5] S.Yang, Q.Xu, "A review on actuation and sensing techniques for MEMS-based microgrippers", J Micro-Bio Robot, vol.13,No.1, May 2017,pp. 1-14.

[6] H.Llewellyn-Evans, C.A.Griffiths, A.Fahmy, "Microgripper design and evaluation for automated μ-wire assembly: a survey". Microsystem Technologies, vol.26, No. 6, January 2020, pp. 1745-1768.

[7] N.P.Belfiore, A.Bagolini, A.Rossi, G.Bocchetta, F.Vurchio, R.Crescenzi, A.Scorza, P.Bellutti, S.A.Sciuto, "Design, Fabrication, Testing and Simulation of a Rotary Double Comb Drives Actuated Microgripper", Micromachines, vol.12, No.10, October 2021, p. 1263.

[8] A.Bagolini, S.Ronchin, P.Bellutti, M.Chistè, M.Verotti, N.P.Belfiore, "Fabrication of Novel MEMS Microgrippers by Deep Reactive Ion Etching with Metal Hard Mask", J. Microelectromechanical Syst., vol.26, No.4, May 2017, pp. 926-934.

[9] J.Andrew Yeh, J.-Y.Huang, C.-N.Chen, C.-Y.Hui, "Design of an electrostatic rotary comb actuator", Journal of Micro/Nanolithography, MEMS, and MOEMS, vol.5, No.2, April 2006, 023008.

[10] N.P.Belfiore, G.B.Broggiato, M.Verotti, R.Crescenzi, M.Balucani, A.Bagolini, P.Bellutti, M.Boscardin, "Development of a MEMS technology CSFH based microgripper," Proc. of 23rd International Conference on Robotics in Alpe-Adria-Danube Region, IEEE RAAD, January 2014, pp. 1-8.

[11] H.Chang, H.Zhao, F.Ye, et al., "A rotary comb-actuated microgripper with a large displacement range", Microsystem Technologies, vol.20, No.1, January 2014. pp. 119-126.

[12] L.A.Velosa-Moncada, L.A.Aguilera-Cortés, M.A.González-Palacios, J.P.Raskin, A.L.Herrera-May, "Design of a Novel MEMS Microgripper with Rotatory Electrostatic Comb-Drive Actuators for Biomedical Applications", Sensors, vol.18, No. 5, May 2018, p. 1664.

[13] F.Vurchio, G.Fiori, A.Scorza, S.A.Sciuto, "A comparison among three different image analysis methods for the displacement measurement in a novel MEMS device," Proc. of 24th IMEKO TC4 International Symposium and 22nd International Workshop on ADC and DAC Modelling and Testing, 2020, pp. 327–331.

[14] F.Vurchio, G.Fiori, A.Scorza, S.A.Sciuto, "Comparative evaluation of three image analysis methods for angular displacement measurement in a MEMS microgripper prototype: a preliminary study", ACTA IMEKO, vol.10, No.2, June 2021, pp.119-125.

[15] F.Vurchio, G.Bocchetta, G.Fiori, A.Scorza, N.P.Belfiore, S.A.Sciuto, "A preliminary study on the dynamic characterization of a MEMS microgripper for biomedical applications," Proc. of 2021 IEEE International Symposium on Medical Measurements and Applications (MeMeA), 2021.

[16] J.Shi, C.Tomasi, "Good Features to Track," Proc. of the IEEE Conference on Computer Vision and Pattern Recognition, June 1994, pp. 593–600.

[17] C.Tomasi, T.Kanade, "Detection and Tracking of Point Features", Carnegie Mellon University Technical Report CMU-CS-91-132, April 1991.

[18] Z.Kalal, K.Mikolajczyk, J.Matas, "Forward-Backward Error: Automatic Detection of Tracking Failures," Proc. of the 20th International Conference on Pattern Recognition, August 2010, pp. 2756–2759.

[19] ISO/IEC. Part 3: guide to the expression of uncertainty in measurement (GUM:1995). In Guide 98-3: 2008, Uncertainty of Measurement; ISO/IEC: Geneva, Switzerland, 2008.

[20] P.Prasad, "Introduction to Biophotonics", John Wiley and Sons, Inc, 2003.

[21] X.Heng, D.Erickson, L.R.Baugh, Z.Yaqoob, P.W.Sternberg, D.Psaltis, C.Yang, "Optofluidic microscopy–a method for implementing a high resolution optical microscope on a chip", Lab Chip, vol.6, No.10, October 2006, pp. 1274–1276.

[22] D.S.Zhang, et al., "Displacement/strain measurements using an optical microscope and digital image correlation", Optical Engineering, vol.45, No.3, March 2006, 033605.

[23] G.Fiori, A.Scorza, M.Schmid, J.Galo, S.Conforto, S.A.Sciuto, "A novel method for the gain conversion factor estimation in quality assessment of ultrasound diagnostic systems," Proc. of 2022 IEEE International Symposium on Medical Measurements and Applications (MeMeA), 2022, "in press".

[24] K.Ramakrishnan, H.Srinivasan, "Closed form models for pull-in voltage of electrostatically actuated cantilever beams and comparative analysis of cantilevers and microgripper", Journal of Electrical Engineering, vol.63, No.4, July 2012, pp. 242-248.

25th IMEKO TC4 International Symposium
23rd International Workshop on ADC and DAC Modelling and Testing
IMEKO TC-4 2022
Brescia, Italy / September 12-14, 2022

A first approach to the registration error assessment in Quality Controls of Color Doppler ultrasound diagnostic systems

Giorgia Fiori[1], Andrea Scorza[1], Maurizio Schmid[1], Jan Galo[2], Silvia Conforto[1], Salvatore A. Sciuto[1]

[1] *Dep. of Industrial, Electronic and Mechanical Engineering, Roma TRE University, Rome, Italy*
[2] *Clinical Engineering Service, IRCCS Children Hospital Bambino Gesù, Rome, Italy*

***Abstract* – Color Doppler Imaging (CDI) is widely used in diagnostic imaging, although the Quality Control procedures for Doppler testing have not been standardized yet. Therefore, in the present study, a novel parameter, called Doppler Image Registration Error (DIRE), for the quantification of the color flow superimposition in duplex imaging of CDI diagnostic systems has been proposed. According to the definition, the registration error is expected to be 0% when no colored pixels associated to the flow are outside the flow region. Its estimation has been carried out through a novel semi-automatic method based on the post-processing of ultrasound (US) images from a flow phantom tube. Two new US diagnostic systems, equipped with a linear array probe each, have been used to collect data at different settings. Based on the promising outcomes, further studies are going to be carried out, mainly to make the results independent on the operator subjectivity.**

I. INTRODUCTION

Nowadays, Color Doppler Imaging (CDI) is used routinely in diagnostic imaging and it plays a key role by allowing the real-time visualization of the blood flow overlaid on the grayscale anatomical image [1,2]. The Doppler signal is codified into velocity values according to a color map and displayed as a color inside a region of interest, known as color box. Although in some cases CDI is still assumed to provide qualitative rather than quantitative information [3], to date, a shared worldwide standard on Doppler equipment testing is lacking. The professional organizations involved, e.g., [3,4], disagree about the ultrasound (US) system configuration settings, as well as how many and which performance parameters have to be included in a Quality Control (QC) program for Doppler testing [5]. On the other hand, in literature the demand of proper performance tests has been highlighted in the last years [5-10], also due to the continuous improvement in the technology of the ultrasound equipment. Among the performance tests for CDI proposed by the Institute of Physics and Engineering in Medicine (IPEM), Color/Power Doppler Duplex priority control function is considered [4]. Such test takes into account the action of a specific US system control, usually adjustable by the operator, known as color write priority (CWP) [1,11,12]. This function allows to set a threshold below which Doppler information is displayed in the flow region and above which it is not displayed. When a high CWP is set, color data override the grayscale data (i.e., higher color flow sensitivity), otherwise, when a low CWP is set, the grayscale data override the color data (i.e., lower color flow sensitivity). In the first case, the lumen of the vessel is totally filled but some color bleeding may occur outside the flow region, while in the second case, a poor filling of the blood vessel can be observed [1,11,12].

By considering the degree of color bleeding when CWP setting is maximum, it is possible to determine a novel parameter useful to monitor the US probe color flow sensitivity over time or to compare it among different systems. In literature, the positioning of color flow information at an incorrect location (e.g., outside the vessel lumen) within the color box is defined as misregistration [1]. No recent studies known to the authors have investigated this positioning error with the aim to implement a QC procedure for CDI systems testing. In this regard, the present study would give a contribution by introducing the Doppler Image Registration Error (DIRE) to objectively assess this specific component of the CDI diagnostic systems, through the implementation of a semi-automatic method based on the analysis and processing of US images from tissue mimicking phantoms. In particular, two new ultrasound diagnostic systems, equipped with a linear array probe each, have been used to collect Color Doppler videos from the tube of a flow phantom at different settings. After the description of the method, first experimental results are shown and discussed.

II. REGISTRATION ERROR ASSESSMENT

The assessment of the registration error proposed in the present study has been carried out by post-processing a Color Doppler video acquired on a flow phantom. As a first step, the implemented semi-automatic method excludes all

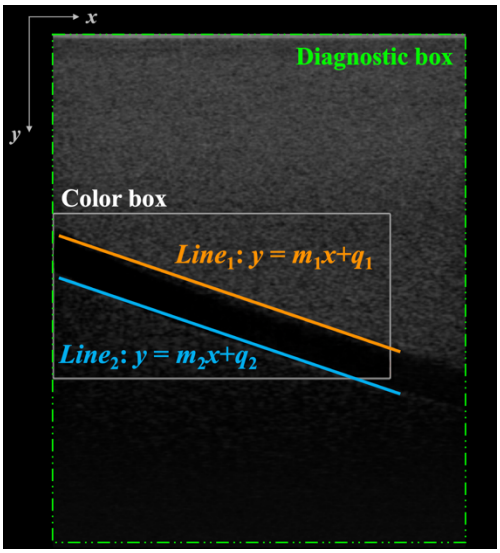

Fig. 1. Example of the straight lines drawn on the upper and lower boundaries of the displayed tube walls. The image $\bar{I}_{gray}$ provided to the operator contains the grayscale-coded information.

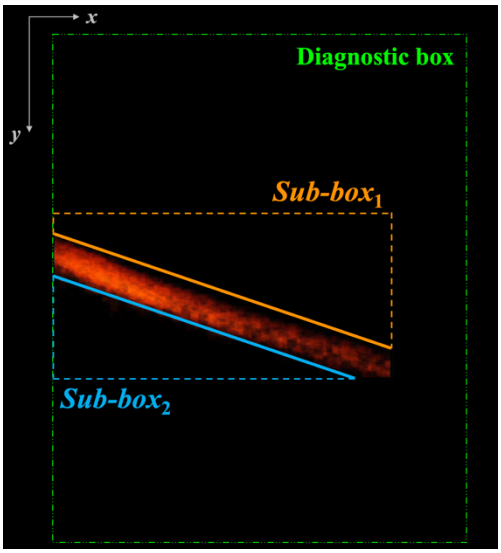

Fig. 2. Example of the average image $\bar{I}_{color}$ cropping according to the endpoints of the two sub-boxes.

the US settings details surrounding the diagnostic box (shown in Fig. 1) through an automatic masking [13], and separates the color-coded information from the grayscale-coded one through a saturation filter [14] based on a threshold th_{sat}, obtaining two distinct images, I_{color} and I_{gray}, respectively. Such procedure is repeated for each frame (j = 1, …, N) of the collected video. Afterwards, the average images $\bar{I}_{color}$ and $\bar{I}_{gray}$ are obtained by averaging all the N frames, and the normalized square sum of the RGB components of $\bar{I}_{color}$ is computed. In the next step, the implemented method provides the operator with the image $\bar{I}_{gray}$ allowing her/him to manually draw a straight line following the upper and lower boundaries of the displayed tube walls ($Line_1$ and $Line_2$ in Fig. 1), to determine the corresponding slope (m_1 and m_2) and y-intercept (q_1 and q_2) values.

The coordinates of the intersecting points between the two lines and the color box (Fig. 1) are retrieved to subdivide the color box into two different sub-boxes: the endpoints of the latter are then used to crop the average image $\bar{I}_{color}$, as shown in Fig. 2. The intensity K of the pixels included in the two sub-boxes is compared with a specific threshold th. If $K \geq th$ the corresponding pixel is assumed as a colored pixel outside the tube walls. Finally, the percentage Registration Error ($RE_{\%}$) is computed as follows:

$$RE_{\%} = \frac{n_{out}}{n_{tot}} \cdot 100 \quad (1)$$

where n_{out} is the number of colored pixels detected outside the tube walls, while n_{tot} the total number of colored pixels in the entire color box which intensity $K \geq th$. According to the definition proposed, $RE_{\%}$ is expected to be 0%. In this case, no colored pixels associated to the flow are positioned outside the tube.

III. MATERIALS AND METHODS

CIRS, Model 069 Doppler phantom has been used in this study to collect Color Doppler videos. The simulator [15] is an easy-to-assemble reference test device able to provide constant or pulsatile flows from 0.5 to 12.5 ml·s^{-1}. It consists of a Tissue-Mimicking Material (TMM) and a sloped echogenic tube with an inner diameter of 4.8 mm, filled with a Blood Mimicking Fluid (BMF).

The tube simulating the blood vessel can be scanned in two configurations (at 70° and 45°) since the simulator has both a top and bottom scan surface. In Table 1 the main characteristics of the US flow phantom are reported together with the specification of the configuration used.

Table 1. CIRS Model 069 flow phantom specifications [15].

Parameter	Characteristics
Scan surface	Saran laminate membrane
TMM	Zerdine®
TMM attenuation coefficient	0.7 dB·cm^{-1}·MHz^{-1}
TMM sound speed	1540 ± 10 m·s^{-1}
BMF sound speed	1570 ± 30 m·s^{-1}
Flow range	0.5 – 12.5 ml·s^{-1}
Nominal tube inner diameter	4.8 mm
Tube slope	70°

Table 2. B-mode and Color Doppler settings and specifications for ultrasound systems A and B.

Parameter	set 1	set 2
B-mode frequency	Penetration	
Field of view (cm)	7	
Nominal Doppler frequency (MHz)	A: 5.5 , B: 5.3	
Color write priority	Maximum	
Wall filter	Minimum	Medium
Color smoothing	Minimum	Medium
Persistence	Minimum	Medium
Line density	Minimum	A: Minimum B: Medium
Transmission power (%)	100	A: 100 B: 90
Acquisition duration (s)	2	
Number of acquired frames	A: 61 , B: 65	A: 62 , B: 59
Frames resolution (px×px)	A: 768×1024 , B: 924×1232	
Color box size (px×px)	A: 223×459 B: 295×400	A: 206×461 B: 268×351

In this study, a constant flow rate Q = 6.0 ml·s^{-1}, corresponding to a nominal average flow velocity v_a = 33.7 cm·s^{-1}, has been set on the simulator. Data acquisition has been carried out on two intermediate technology level US diagnostic systems (namely A and B), equipped with a linear array probe each. A single Color Doppler video lasting 2 s has been acquired at the lowest Doppler frequency of the probes and for two US system settings, i.e., set 1 and set 2 (Table 2). In set 1, pre- and post-processing settings have been reduced, while in set 2 the best settings provided by each US specialist have been maintained.

As a preliminary approach, a semi-automatic method for the registration error assessment has been implemented through an *ad hoc* algorithm developed in MATLAB environment. The processing steps described in the previous section have been applied to each acquired video according to the following specifications. The threshold used to process each frame and separate the color- from the grayscale-coded information has been set to th_{sat} = 0.35 [13,14], and the images $\bar{I}_{color}$ and $\bar{I}_{gray}$ have been obtained by averaging N = 55 consecutive frames. After the action of an operator, required to manually draw two straight lines on the boundaries of the tube walls into the US image, the corresponding slope and y-intercept values have been computed. The threshold used to detect the colored pixels, inside the two sub-boxes and in the whole color box, has been selected on the basis of the minimum gray level difference the human eye may distinguish [16], i.e., th =

Table 3. Monte Carlo Simulations settings.

Parameter	Symbol	Distribution	Mean ± SD
Threshold on color saturation	$th_{sat} \pm \sigma_{sat}$	Uniform	0.35 ± 0.01
Number of averaged frames	$N \pm \sigma_N$	Uniform	55 ± 2
Upper line slope	$m_1 \pm \sigma_{m1}$	Normal	A1: 0.36 ± 0.01 A2: 0.36 ± 0.01 B1: 0.43 ± 0.01 B2: 0.44 ± 0.01
Upper line y-intercept	$q_1 \pm \sigma_{q1}$	Normal	A1: 251 ± 3 px A2: 246 ± 2 px B1: 219 ± 4 px B2: 213 ± 3 px
Lower line slope	$m_2 \pm \sigma_{m2}$	Normal	A1: 0.36 ± 0.01 A2: 0.36 ± 0.01 B1: 0.43 ± 0.01 B2: 0.45 ± 0.01
Lower line y-intercept	$q_2 \pm \sigma_{q2}$	Normal	A1: 309 ± 3 px A2: 308 ± 3 px B1: 280 ± 4 px B2: 275 ± 4 px
Threshold for colored pixels detection	$th \pm \sigma_{th}$	Uniform	10 ± 1

A1 = ultrasound system A in set 1; A2 = ultrasound system A in set 2; B1 = ultrasound system B in set 1; B2 = ultrasound system B in set 2.

10. Finally, the percentage registration error has been computed by applying Eq. (1).

IV. MONTE CARLO SIMULATION

Monte Carlo Simulation (MCS) has been widely used in literature for the measurement uncertainty estimation of image analysis-based methods [17-21]. In this study, a MCS with 10^4 iterations has been carried out for each probe and US system setting to estimate the uncertainty of the $RE_{\%}$ parameter. In Table 3, the distributions assigned to the main parameters involved in the registration error assessment are listed and expressed as mean ± standard deviation (SD). Both the thresholds th_{sat} and th, as well as the number of averaged frames N have been set as uniform distributions. On the other hand, normal distributions have been assigned to the slopes and y-intercepts of the lines drawn on the upper and lower tube walls. In particular, since the implemented semi-automatic method requires the action of an operator, six independent observers without medical expertise were asked to manually select two pairs of lines on the tube walls sixteen times to test and estimate subjects' inter- and intra-variability [22]. The test has been repeated by the same operators providing them with the average image $\bar{I}_{gray}$ obtained for each US system (A and B) and configuration setting (set 1 and set 2).

V. RESULTS AND DISCUSSION

The percentage registration errors $RE_{\%}$ obtained for the two new US systems, both set with two different configuration settings (set 1 and set 2), are reported in Table 4. Mean and standard deviation values have been estimated from the MCSs. By considering the US system A, the results for set 1 and set 2 are compatible. As per the US system B, the $RE_{\%}$ obtained in set 2 is rather low, and the closest to 0% among all 4 US system-set pairs. The latter outcome suggests that the proposed semi-automatic method is quite sensitive to the quantification of the $RE_{\%}$, even if the results are affected by a high uncertainty source likely due to the action of the observers required to manually draw the straight lines on the boundaries of the tube walls. This consideration is supported by the estimation of the percentage error between the nominal tube diameter, reported in Table 1, and the measured one, computed by considering the slopes and y-intercepts of the two lines reported in Table 3. In this case, for the US systems A and B, this error varies between 12% and 19%. Therefore, this overestimation can be considered as one of the causes of the high measurement uncertainties obtained in this study.

Table 4. Percentage registration error outcomes for each US system and configuration setting.

US system	US setting	$RE_{\%} \pm SD_{RE\%}$ (%)
A	set 1	8 ± 5
	set 2	9 ± 5
B	set 1	9 ± 6
	set 2	3.3 ± 2.3

VI. CONCLUSIONS

In the last years, the demand of proper performance tests for Color Doppler imaging has been highlighted, since a shared QC program for Doppler testing is still lacking. In this regard, the present study would give a contribution in the field by proposing a first approach to the assessment of a novel parameter for the monitoring of the US probe color flow sensitivity in CDI diagnostic systems. This parameter named Doppler Image Registration Error (DIRE), has been derived from a performance test already proposed by the IPEM, and assessed as the degree of color bleeding when color write priority setting is maximum. According to the definition, the registration error is expected to be 0% when no colored pixels associated to the flow are positioned outside the flow region.

A novel semi-automatic method based on the post-processing of a Color Doppler video, acquired from the tube of a flow phantom, has been implemented in MATLAB environment. As a first attempt, two new ultrasound diagnostic systems, equipped with a linear array probe each, have been used to collect data at different US settings. Although the implemented method requires the external action of an operator, the results obtained are promising, suggesting that further improvements of the method are needed. In fact, to test and estimate subjects' inter- and intra-variability six independent observers without medical expertise were asked to manually draw the straight lines on the boundaries of the tube walls: their action has been identified as one of the main uncertainty sources in the assessment of the percentage registration error. Therefore, the improvements of the semi-automatic method that are going to be carried out will include: the shift towards a fully automatic method removing the need of the subjective action of an operator, and the introduction of some weights in the computation of the registration error parameter in order (a) to exclude or reduce from its quantification any isolated colored pixel outside the flow region (e.g., due to noise) and (b) to accentuate any groups of pixels detected outside the flow region, for instance on the basis of their distance from the tube lumen. Finally, further studies should be carried out on a higher number of ultrasound diagnostic systems and probe models.

ACKNOWLEDGMENT

The Authors wish to thank SAMSUNG Healthcare and SIEMENS Healthineers for hardware supply and technical assistance in data collection.

REFERENCES

[1] P.R.Hoskins, K.Martin, A.Thrush, "Diagnostic Ultrasound. Physics and Equipment", 3rd edition,

CRC Press, Boca Raton, FL, USA, 2019.
[2] M.A.Pozniak, P.L.Allan, “Clinical Doppler Ultrasound”, 3rd edition, Churchill Livingstone, 2013.
[3] AIUM Technical Standards Committee, “Performance Criteria and Measurements for Doppler Ultrasound Devices”, 2nd edition, USA, 2002.
[4] IPEM – Institute of Physics and Engineering in Medicine, “Report no. 102: Quality assurance of ultrasound imaging systems,” York, UK, 2010.
[5] J.E.Browne, “A review of Ultrasound quality assurance protocols and test devices”, Phys. Med., vol.30, No.7, September 2014, pp.742-751.
[6] S.Balbis, T.Meloni, S.Tofani, F.Zenone, D.Nucera, C.Guiot, “Criteria and scheduling of quality control of B-mode and Doppler ultrasonography equipment”, J. Clin. Ultrasound, vol.40, No.3, March-April 2012, pp.167-173.
[7] E.Samei, D.E.Pfeiffer, “Clinical Imaging Physics: Current and Emerging Practice”, 1st edition, Wiley Blackwell, Hoboken, NJ, USA, 2020.
[8] ACR Guidelines and Standards Committee, “ACR–AAPM Technical standard for diagnostic medical physics performance monitoring of real time ultrasound equipment”, revised 2021 https://www.acr.org/-/media/ACR/Files/Practice-Parameters/US-Equip.pdf (accessed July 2022).
[9] J.M.Thijssen, M.C.van Wijk, M.H.M.Cuypers, “Performance testing of medical echo/Doppler equipment”, Eur. J. Ultrasound, vol.15, No.3, October 2002, pp.151-164.
[10] A.M.Di Nallo, L.Strigari, M.Benassi, “A possible quality control protocol for Doppler ultrasound for organizational time optimization”, J. Exp. Clin. Cancer Res., vol.25, No.3, September 2006, pp.373-381.
[11] L.Terslev, A.P.Diamantopoulos, U.M.Døhn, W.A.Schmidt, S.Torp-Pedersen, “Settings and artefacts relevant for Doppler ultrasound in large vessel vasculitis”, Arthritis Res. Ther., vol. 19, No.167, July 2017.
[12] D.J.Rubens, S.Bhatt, S.Nedelka, J.Cullinan, “Doppler artifacts and pitfalls”, Radiol. Clin. North. Am., vol.44, No.6, November 2006, pp.805-835.
[13] G.Fiori, A.Scorza, M.Schmid, J.Galo, S.Conforto, S.A.Sciuto, “A preliminary study on the Average Maximum Velocity Sensitivity index from flow velocity variation in quality control for Color Doppler”, Measurement: Sensors, vol.18, No.100245, December 2021.
[14] A.Scorza, D.Pietrobon, F.Orsini, S.A.Sciuto, “A preliminary study on a novel phantom based method for performance evaluation of clinical colour Doppler systems,” Proc. of 22nd IMEKO TC4 International Symposium & 20th International Workshop on ADC Modelling and Testing, 2017, pp. 175–179.
[15] CIRS Tissue Simulation & Phantom Technology, “Doppler ultrasound flow simulator – Model 069,” http://www.cirsinc.com/wp-content/uploads/2019/04/069-DS-120418.pdf (accessed July 2022).
[16] G.Fiori, F.Fuiano, A.Scorza, J.Galo, S.Conforto, S.A.Sciuto, “A Preliminary Study on the Adaptive SNR Threshold Method for Depth of Penetration Measurements in Diagnostic Ultrasounds”, Appl. Sci., vol.10, No.18, September 2020.
[17] G.Fiori, F.Fuiano, A.Scorza, J.Galo, S.Conforto, S.A.Sciuto, “A preliminary study on an image analysis based method for lowest detectable signal measurements in PW Doppler ultrasounds”, ACTA IMEKO, vol.10, No.2, June 2021, pp.126-132.
[18] F.Fuiano, G.Fiori, A.Scorza, M.Schmid, S.Conforto, S.A.Sciuto, “A preliminary approach based on numerical simulations for the design of a PWV-varying arterial simulator”, Measurement: Sensors, vol.18, No.100240, December 2021.
[19] F.Vurchio, G.Fiori, A.Scorza, S.A.Sciuto, “A comparison among three different image analysis methods for the displacement measurement in a novel MEMS device,” Proc. of 24th IMEKO TC4 International Symposium & 22nd International Workshop on ADC Modelling and DAC Modelling and Testing, 2020, pp. 327–331.
[20] F.Fuiano, G.Fiori, A.Scorza, S.A.Sciuto, “A novel experimental set-up for Young Modulus Assessment through Transit Time measurements in Biomedical applications,” Proc. of 2021 IEEE International Workshop on Metrology for Industry 4.0 and IoT (MetroInd4.0&IoT), 2021, pp. 117–121.
[21] G. Fiori, A.Scorza, M.Schmid, J.Galo, S.Conforto, S.A.Sciuto, “A novel method for the gain conversion factor estimation in quality assessment of ultrasound diagnostic systems,” Proc. of 2022 IEEE International Symposium on Medical Measurements and Applications (MeMeA), 2022, "in press".
[22] F.Vurchio, G.Bocchetta, G.Fiori, A.Scorza, N.P.Belfiore, S.A.Sciuto, “A preliminary study on the dynamic characterization of a MEMS microgripper for biomedical applications,” Proc. of 2021 IEEE International Symposium on Medical Measurements and Applications (MeMeA), 2021.

25th IMEKO TC4 International Symposium
23rd International Workshop on ADC and DAC Modelling and Testing
IMEKO TC-4 2020
Brescia, Italy / September 12-14, 2022

Instrumentation for EEG-based monitoring of the executive functions in a dual-task framework

Leopoldo Angrisani[1], Andrea Apicella[1], Pasquale Arpaia[1,2], Andrea Cataldo[3], Anna Della Calce[1], Allegra Fullin[4], Ludovica Gargiulo[1], Luigi Maffei[4], Nicola Moccaldi[1,3], Andrea Pollastro[1]

[1]*Department of Electrical Engineering and Information Technology (DIETI), University of Naples Federico II, Naples, Italy*
[2]*Interdepartmental Center for Research on Management and Innovation in Healthcare (CIRMIS), University of Naples Federico II, Naples, Italy*
[3]*Department of Engineering for Innovation, University of Salento, Lecce, Italy*
[4]*Department of Mental and Physical Health and Preventive Medicine, Section of Human Anatomy, University of Campania "Luigi Vanvitelli", Naples, Italy*

***Abstract* – Instrumentation for electroencephalographic (EEG)-based monitoring of the executive functions in a dual-task framework is proposed. The proposed system integrates in a single solution (i) the administration of the cognitive task, (ii) the EEG signal acquisition and processing, (iii) the data storage synchronized whit an external Gait Analysis system. The system is based on a wearable passive brain computer interface solution that allows EEG monitoring during gait, by means of acoustic stimuli. The centralized platform guarantees the synchronization of all the processes, and therefore, improves the state of the art accuracy in measurements related to executive functions and gait. An experimental validation demonstrated the feasibility of the proposed solution in terms of execution of cognitive tasks during gait, real-time monitoring of EEG signals, and synchronized storage of EEG data, gait and cognitive task performances.**

I. INTRODUCTION

The role of executive functions in motor tasks is widely investigated due to their involvement in initiating, planning, organising and regulating behaviour [1]. Dysfunctions in cognitive processes are strongly linked to a decrease in gait performances highlighting the strong interrelation between cognition and gait [2]. In particular, monitoring cognitive disorders helps to predict future loss of mobility or the risk of fall. Among biosignal-based systems, neural-based are the most informative ones in order to monitor cognitive activity due to their high temporal resolution and good real-time performance [3].

The devices currently available to measure neural activity (magnetoencephalography, magnetic resonance imaging, functional near-infrared spectroscopy, traditional electroencephalography) are mostly not compatible with a condition of movement. Only recently, wireless EEG solutions have become commercially available but often not yet approved for clinical use and requiring complex bureaucratic processes for permission to use in experiments. However, nowadays, no integrated instrument allowing a subject to undergo a dual task while the EEG signal is monitored exist. The electroencephalography (EEG) is widely used to study the brain organization of cognitive processes such as perception, memory, attention, language and emotions in healthy adults and children [4]. In particular, the most used signal for EEG-based analysis of executive function are the Event-related potentials (ERP). ERPs are EEG-patterns in time domain occurring after sensorial stimuli recognised by the subject and can be characterized by (i) amplitude and (ii) latency. Amplitude provides an index of the intensity of neural activity and latency reveals the timing of neural activation [5]. Measuring neural activity during walking is a challenging task. A wearable passive brain computer interface solution allow EEG monitoring during gait, by means of acoustic stimuli is proposed. [6]. The proposed architecture guarantees the synchronization of all the processes, and therefore, improves the state of art accuracy in measurements related to executive functions and gait.

The paper is structured as follows: Section ii. reports the system design; Section iii. describes the system realization; Section iv. reports the feasibility experimental campaign.

II. DESIGN

In this Section the architecture and the operation of the system are presented.

A. Architecture

The architecture of the proposed system is shown in Fig. 1. The system can be synchronized with a Gait Analysis system via a trigger input port. A *Cognitive Task Manager* (CTM) can be set by the operator to configure a desired cognitive task. The tasks consist in reacting to acoustic

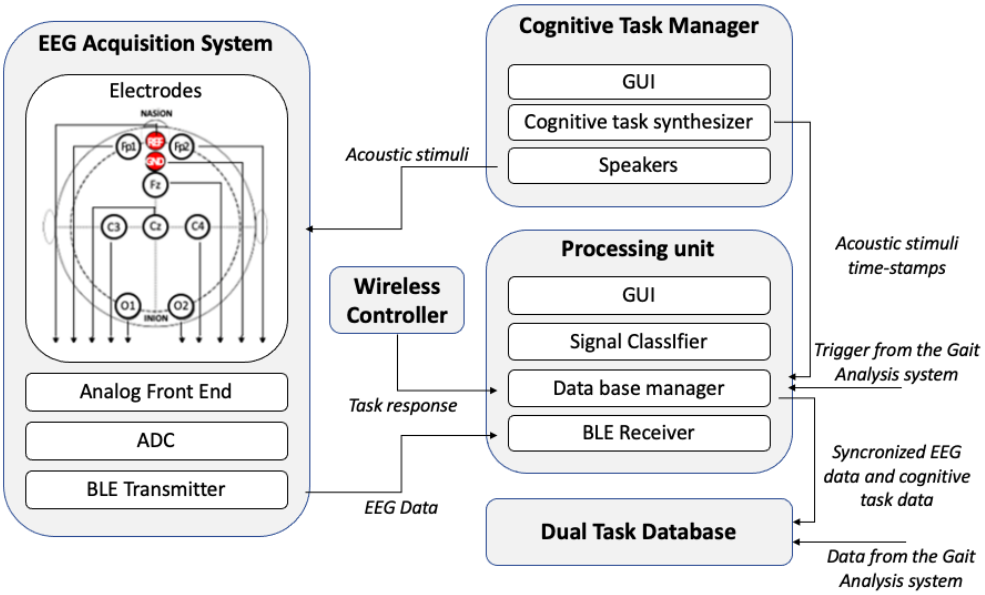

Fig. 1. System architecture.

stimuli by means of a *Wireless Controller* (WC), according to a proper rule. A wireless *EEG Acquisition System* (EAS) acquires user's EEG signal during cognitive task execution and gait. A *Processing Unit* (PU) receives EEG data from EAS, cognitive task responses from WC, acoustic stimuli time-stamp from CTM, and the trigger from the Gait Analysis System. The PU processes data and plots the EEG feature values and the cognitive task scores in real time; in the meanwhile, it manages all the data and send them to the *Dual Task Database* for off-line analysis based also on data from Gait Analysis System.

B. *Operation*

Before starting, the participant is explained the cognitive tasks to be performed.

After the EEG acquisition system montage, the contact impedance of the electrodes is checked and the Wireless Controller is given to the participant for the cognitive task execution. The operator, through the Cognitive Task Manager GUI, can set the type of cognitive task and its difficulty by acting on: stimulus frequencies, stimulus duration, inter-stimuli time interval. The Processing Unit is connected via Bluetooth to the EEG acquisition system and signal acquisition starts just before the cognitive task during gait. In the meantime, the Gait Analysis system starts and a trigger signal is sent to the PU.

III. REALIZATION

In this section, details about hardware and software are provided.

A. *Hardware*

The wireless AB-Medica Helmate system Class IIA is employed for the EEG signal acquisitions [7]. Unlike other wireless EEG signal measurement devices such as the B-Alert X systems [8], the Helmate system acquires the signal through dry electrodes. These electrodes, not requiring conductive gel, are faster to set up and can be used for longer times since there is no loss of transductive properties linked to gel dryness [9]. In addition, the Helmate monitors several cortex areas differently from similar acquisition systems based on few channels.

The electronics of Helmate is mounted on an ultralight structure and the device also includes accessories for use on a single patient: under-helmet, under-throat and electrodes. The under-helmet and under-throat are disposable and both contribute to the stability of the system, so that movement of the patient's head does not risk causing artifacts during signal acquisition.

Ten dry electrodes placed according to the 10/20 International Positioning System are provided: Fp1, Fp2, Fz, Cz, C3, C4, O1, O2, AFz (reference electrode), and Fpz (Ground). The electrodes made of conductive rubber with ends covered in Ag/Ag-Cl. Three different electrode shape are available in order to minimize the contact impedance:

- Electrode with flat contact surface, useful for placement in the frontal area;
- Small electrode with 5 legs, allows each single leg to pass through normal hair;
- Long, rigid 3-leg electrode, useful for passing through particularly thick hair, or for placement in the occipi-

tal area.

The sampling rate of EEG signals is 512 Sa/s. EEG data are transmitted by Bluetooth Low Energy protocol in packets of 32 samples.

The hardware components of the system user interface are:

- a system of Logitech speakers useful to improve the audio of cognitive tasks especially during the walking activity.
- A wireless pen (NORWII N27 Wireless Presenter, Hyperlink Volume Control Presenter RF 2.4GHz) allows the subject to respond to the cognitive task on the move. The subject presses the pen button when required by the specific cognitive task.

B. Software

The software of the system consists in an app developed for the administration of cognitive tasks, the EEG data processing and visualization, and the data synchronization and storage. The software is developed in Python [10]. In the following, the functioning of the app is described.

Firstly, a GUI allows the user to insert information related to the subject's anamnesis, the session information and the data storage directory. Then, biographical data and on the current status of the patient are saved. Thereafter, the GUI allows the selection and the setting of three operating conditions:

- *EEG baseline*: the EEG signal of the patient in resting condition is recorded;
- *N-back task*: a sequence of letters is played and the subject has to indicate when the current stimulus matches the one from N steps earlier in the sequence. The load factor N changes according to the task difficulty;
- *Go-Nogo task*: a sequence of two sounds is presented and the partecipant has to respond to certain frequent stimuli (go stimuli) and makes no response for rare others (nogo stimuli). An example sound of the frequent stimulus is played before trial starts. Task difficulty increases by reducing the inter-stimulus time.

Then, the streaming of data related to the helmate channels and the extracted EEG features are displayed. Afterwards, the streaming of the EEG signals acquired, the communication with the wireless pen, and communication with the external gait analysis system for synchronization are enabled and the trial starts.

Once the trial is completed, all the communications with external devices are disabled. Finally, data are stored on the filesystem, allowing the user to use this information for off-line analysis.

IV. EXPERIMENTAL VALIDATION

In this section an experimental validation of the proposed system is reported. Ethical approval was obtained from the Ethics Committee of Psychological Research of University of Naples Federico II. All experiments were performed in accordance to the declaration of Helsinki. Subjects were asked to sign the informed consent form before their inclusion in the experimental campaign.

A. Experimental protocol

Four experimental sessions were realized and EEG signal was recorded in four conditions:

- In the first session, one minute EEG signal is recorded in resting state;
- In the second session, the subject is seated while performing a Go-Nogo task for the response inhibition assessment; The subject provides his/her answers via the wireless pen.
- In the third session, the subject is required to walk on a platform equipped with force-feeders at their preferred speed;
- In the last session, the subject is required to walk on the platform equipped with force-feeders and, at the same time, performs the cognitive task, providing his or her answers via the wireless pen.

B. Data analysis

Data were filtered by a fourth-order bandpass Butterworth filter [1.5 - 30] Hz; then, grand average method is applied in order to extract the ERP.

A preliminary comparison is carried out between EEG data acquired by AB-Medica Helmate and Mitsar-EEG 201 in order to assess the suitability of the proposed device in acquiring ERPs. Mitsar-EEG 201 is a 19-channel electroencephalographic system. EEG recordings were obtained using a cap with 19 electrodes positioned according to the 10/20 International Positioning System. The two devices differ also in the type of reference adopted: AB-Medica Helmate has Fpz as its reference while Mitsar-EEG 201 has the the earlobes (A1-A2) as its reference. EEG data of a subject (female, 25 years old) while performing a Go-Nogo task using the two devices are acquired. Data are divided in 1 second epochs and ERPs are calculated. Results are shown in fig. 3 and 2. The ERP phenomenon is observable using both devices. Differences in the amplitudes of the two phenomenons are observable and are due to the different referencing system.

Another analysis is carried out to test the AB-Medica system during movement. One subject (male, aged 28) is involved in the system experimental validation.

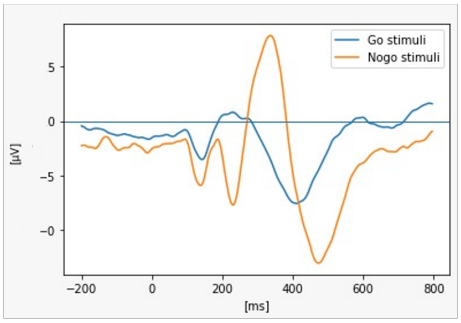

Fig. 2. ERP from 22 channel EEG device at Cz.

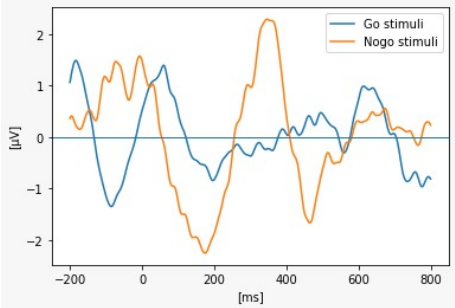

Fig. 3. ERP from Ab-Medica Helmate at Cz.

A visual comparison between EEG data recording during the first and the third session is made in order to demonstrate the usability and the effectiveness of Ab-Medica Helmate in recording EEG signal during gait. Typical signal trends over time in a resting condition and during movement are shown in Fig. 4. Due to motion artefacts, the dynamics of the two signals are significantly different, reaching 300 μV amplitudes during gait. A preliminary analysis is carried out to assess the performance of the system in terms of ERP extraction during gait. Fig 5 and 6 show ERP, in particular the P300 (an ERP potential occurring 300 ms after the sensorial stimulus), acquired during a Go-NoGo tasks sitting and walking, respectively. Despite the evident noise, a peak at 300 ms can be detected in both cases. Furthermore, signal amplitude of EEG recorded during gait is traced back to typical ERP amplitude dynamics, demonstrating that the ERP calculation also acted as a filter for artefact removal.

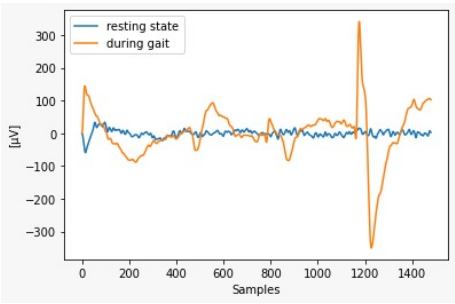

Fig. 4. 3 seconds EEG signal during walking and sitting at Cz.

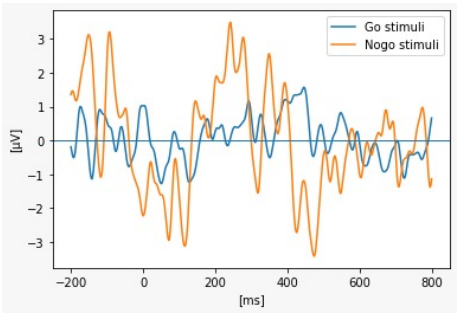

Fig. 5. ERP resulting from Go-Nogo activity while sitting at Cz.

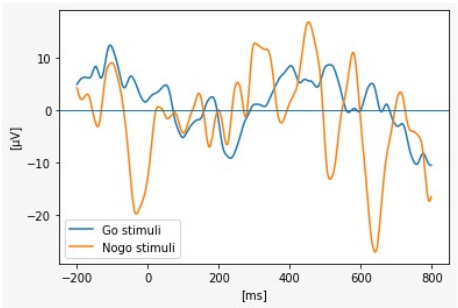

Fig. 6. ERP resulting from Go-Nogo activity while walking at Cz.

V. CONCLUSION

Instrumentation for EEG-based monitoring of the executive functions in a dual-task framework is proposed.

Experimental validation demonstrated the proposed system allows monitoring the EEG of individuals while they perform cognitive tasks during gait. An experimental validation demonstrated the feasibility of the proposed solution in terms of execution of cognitive task during gait, real-time monitoring of EEG signal, and synchronized storage of EEG data, gait and cognitive task performances. In future contributions, the sample size will be increased in order to understand whether the cross-subject influences the result. Another future step will involve the re-referencing of data recorded by the Ab-Medica Helmate to understand the influence of the chosen reference on the ERPs visualisation, as well as improving signal to noise ratio by applying additional filters and using new artifact removal techniques. In particular, the Artifact Subspace Reconstruction (ASR) revealed to be a promising technique for artefact removal with respect to traditional approaches such as Independent Component Analysis and Principal Component Analysis [11, 12].

ACKNOWLEDGMENT

This work was carried out as part of the "ICT for Health" project, which was financially supported by the Italian Ministry of Education, University and Research (MIUR), under the initiative 'Departments of Excellence' (Italian Budget Law no. 232/2016), and the European Union - FSE-REACT-EU, PON Research and Innovation 2014-2020 DM1062/2021 contract number 18-I-15350-2.

REFERENCES

[1] A. Diamond, "Executive functions," *Annual review of psychology*, vol. 64, pp. 135–168, 2013.

[2] M. Montero-Odasso, J. Verghese, O. Beauchet, and J. M. Hausdorff, "Gait and cognition: a complementary approach to understanding brain function and the risk of falling," *Journal of the American Geriatrics Society*, vol. 60, no. 11, pp. 2127–2136, 2012.

[3] C. Berka, D. J. Levendowski, M. N. Lumicao, A. Yau, G. Davis, V. T. Zivkovic, R. E. Olmstead, P. D. Tremoulet, and P. L. Craven, "Eeg correlates of task engagement and mental workload in vigilance, learning, and memory tasks," *Aviation, space, and environmental medicine*, vol. 78, no. 5, pp. B231–B244, 2007.

[4] M. Teplan *et al.*, "Fundamentals of EEG measurement," *Measurement science review*, vol. 2, no. 2, pp. 1–11, 2002.

[5] D. Friedman, Y. M. Cycowicz, and H. Gaeta, "The novelty p3: an event-related brain potential (erp) sign of the brain's evaluation of novelty," *Neuroscience & Biobehavioral Reviews*, vol. 25, no. 4, pp. 355–373, 2001.

[6] L. Angrisani, P. Arpaia, A. Esposito, L. Gargiulo, A. Natalizio, G. Mastrati, N. Moccaldi, and M. Parvis, "Passive and active brain-computer interfaces for rehabilitation in health 4.0," *Measurement: Sensors*, vol. 18, p. 100246, 2021.

[7] "Ab-medica s.p.a." https://www.abmedica.it/, 2020.

[8] "alert-x-series Website," https://www.advancedbrainmonitoring.com/products/b-alert-x-series, accessed: 2019-09-30.

[9] M. A. Lopez-Gordo, D. Sanchez-Morillo, and F. P. Valle, "Dry eeg electrodes," *Sensors*, vol. 14, no. 7, pp. 12 847–12 870, 2014.

[10] G. Van Rossum *et al.*, "Python programming language." in *USENIX annual technical conference*, vol. 41, no. 1, 2007, pp. 1–36.

[11] C.-Y. Chang, S.-H. Hsu, L. Pion-Tonachini, and T.-P. Jung, "Evaluation of artifact subspace reconstruction for automatic eeg artifact removal," in *2018 40th Annual International Conference of the IEEE Engineering in Medicine and Biology Society (EMBC)*. IEEE, 2018, pp. 1242–1245.

[12] M. Plechawska-Wojcik, M. Kaczorowska, and D. Zapala, "The artifact subspace reconstruction (asr) for eeg signal correction. a comparative study," in *International Conference on Information Systems Architecture and Technology*. Springer, 2018, pp. 125–135.

25th IMEKO TC4 International Symposium
23rd International Workshop on ADC and DAC Modelling and Testing
IMEKO TC-4 2022
Brescia, Italy / September 12-14, 2022

Latest Advancements in SSVEPs Classification for Single-Channel, Extended Reality-based Brain-Computer Interfaces

Leopoldo Angrisani[1], Pasquale Arpaia[1,2], Egidio De Benedetto[1], Nicola Donato[3], Luigi Duraccio[4]

[1]*University of Naples Federico II - Department of Information Technology and Electrical Engineering, Naples, Italy*
[2]*University of Naples Federico II - Interdepartmental Research Center in Health Management and Innovation in Healthcare (CIRMIS), Naples, Italy; pasquale.arpaia@unina.it*
[3]*University of Messina - Department of Engineering, Messina, Italy*
[4]*Polytechnic University of Turin - Department of Electronics and Telecommunications, Turin, Italy*

***Abstract* – This work details the latest advancements on a single-channel, reactive Brain-Computer Interfaces developed at the Interdepartmental Research Center in Health Management and Innovation in Healthcare (CIRMIS) of the University of Naples Federico II. The proposed instrumentation is based on Extended Reality (XR) and exploits the acquisition and classification of the Steady-State Visually Evoked Potentials (SSVEPs). In particular, an XR headset is employed for generating the flickering stimuli necessary to the SSVEP elicitation. The users brain signals are captured by means of a highly wearable and portable electroencephalografic acquisition unit, which is connected to a portable processing unit in charge of processing in real time the incoming data. In this way, a deeper interaction between users and external devices with respect to traditional architectures is guaranteed. The classification capability of the proposed instrument has been significantly improved over the years. Currently, in fact, a classification accuracy up to 90 % is obtained with at least 2 s of acquisition time.**

I. INTRODUCTION

A Brain-Computer Interface (BCI) is a technology employed in order to provide a direct communication path between the human brain and external devices [1, 2, 3]. Since a huge amount of information can be extracted from the user brain signals, a distinction is typically made between active, reactive, and passive BCIs [4]. Reactive BCIs rely on the acquisition and processing of brain waves produced in response to external stimuli [5]. Among all the reactive-BCI paradigms, Steady-State Visually Evoked Potentials (SSVEPs) have gained momentum in the development of applications regarding healthcare [6], entertainment [7], and industry [8]. Typically, SSVEPs are a sinusoidal-like waveform with a fundamental frequency equal to that of the observed flickering stimulus. Often, higher harmonics can also be detected [9].

In SSVEP-based applications, N flickering stimuli at different frequencies are associated to specific commands, so that the user can select the desired target by simply looking at the corresponding flickering stimulus. These stimuli are traditionally displayed on LCD monitors. Moreover, multi-channel EEG acquisition units are often adopted [10]. However, this setup is often very bulky and limits the portability of these systems.

For this reason, the Interdepartmental Research Center in Health Management and Innovation in Healthcare (CIRMIS) of the University of Naples Federico II has developed an innovative solution which can facilitate the adoption of BCI-SSVEP in daily-life activities. In particular, the proposed BCI instrumentation is based on a single-channel electroencephalographic (EEG) acquisitions [11] and on the use of Extended Reality (XR) devices to render the flickering stimuli [12] for the SSVEPs elicitation. The number of the stimuli accommodated on the XR display was set to two [8], so that the user was able to take a binary decision by gazing one stimulus out of two. The data coming from the wearable EEG acquisition unit are processed in real time by a portable processing unit, which is in charge of classify the received brain signals and send the related command to external devices.

The classification capability of the proposed system has been significantly improved over the years. The first processing method employed was based on the traditional Power Spectral Density Analysis (PSDA) in frequency domain. It managed to classify one frequency out of two with an accuracy greater than 80 % and an acquisition time of 2 s [8]. More recently, a time-domain approach based on the Canonical Correlation Analysis (CCA) was employed by improving the obtained accuracy of about 5 % [6]. However, the main drawback of these methods was related to the impossibility to detect undesired frame per second (fps) variation of the XR headset during the generation of the flickering stimuli. For the sake of the example, given a refresh rate of 60 Hz, a variation of about 5 % inevitably

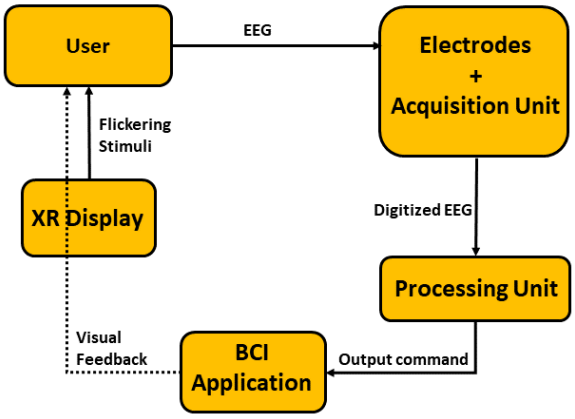

Fig. 1. Major blocks of the system architecture.

leads to a shift of the rendered frequencies from 10.0 Hz up to 9.5 Hz or 10.5 Hz. This means that the elicited SSVEPs are shifted accordingly. Therefore, the classification performance of the proposed algorithms decreases since the acquired signals and the reference ones are no longer consistent.

For this reason, an adaptive strategy to find the actual SSVEP peaks has been employed in recent months [5]. Moreover, the adoption of Machine Learning (ML) clasifers such as K-Nearest Neighbor (K-NN), Support Vector Machine (SVM), and Feed-Forward Neural Networls (NN) has also been performed to further improve the classification of the features which are extracted from the original samples. This new technique, defined *Features Reduction (FR)*, has achieved an accuracy greater than 90 % at 2-s acquisition time.

The paper is organized as follows. Section ii. provides a description of the system architecture, along with the modality of rendering of the flickering stimuli, and the classification algorithm implemented over the years. Therefore, Section iii. shows the obtained experimental results. Finally, conclusions are drawn.

II. MATERIALS AND METHODS

A. System Description

The architecture of the BCI instrumentation is shown in Fig. 1. An *AR Display* renders 2 flickering stimuli to elicit users SSVEPs. Then, three dry *Electrodes* are placed in *Oz*, *Fz*, and *A2* positions, according to the 10-20 International System [6], and capture the user EEG. The electrodes are connected to a portable *Acquisition Unit*, which sends the digitized EEG samples to a portable *Processing Unit*. The processing unit runs the SSVEP classification algorithm, and sends in real time the output command to the *BCI Application*, which actuates the received command and provides a feedback to the User in order to show the desired selection.

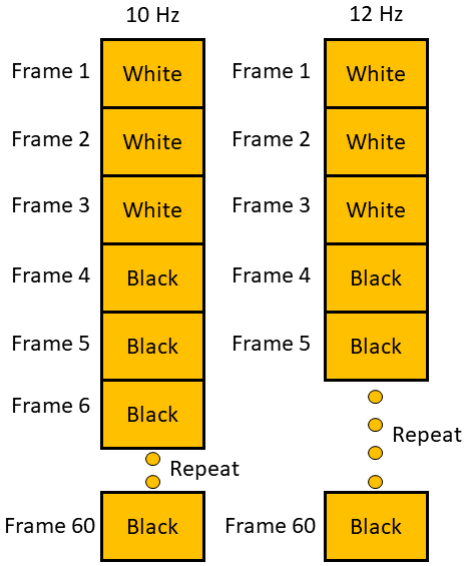

Fig. 2. Rendering of the two flickering stimuli in a 1-s time interval

B. Hardware

The chosen XR device was the *Epson Moverio BT-200*. It is an Optical-See-Through device with a 23Â° diagonal field of view, and a nominal refresh rate of 60 Hz. The selected acquisition unit was the Olimex EEG-SMT, a 10-bit, 256 S/s, open source Analog-to-Digital converter. Finally, the adopted processing unit was the Raspberry Pi 4, a single-board PC connected via USB to the Olimex.

C. Software

The flickering icons on the Epson Moverio glasses were generated by means of an Android application realized with Android Studio. The XR environment consisted of two squares placed at opposite edges of the screen. The two squares reverse black and white according to the chosen flickering frequency (namely, 10 Hz and 12 Hz). Moreover, a software written in Python 3 on the Raspberry Pi 4 was used to (i) acquire the digitized signal via USB from the Olimex, (ii) process it, and (iii) send the output command to the specific target via TCP/IP [6, 12, 13]

D. Rendering of the Flickering Stimuli

With regards to the rendering of the flickering stimuli at 10 Hz and 12 Hz, Fig. 2 shows the implemented pixel alternations. Since 10 Hz is a submultiple of six of Moverio Refresh Rate (60 Hz), the length of the sequence that has to be repeated is equal to six frames (i.e., three frames white, and three frames black). Instead, 12 Hz is a submultiple of five of Moverio Refresh Rate, then the length of the sequence is equal to five frame (i.e., three frames white, and two frames black).

E. SSVEPs Classification

The algorithms implemented over the years were metrologically characterized by analyzing data related to an experimental campaign conducted on 20 untrained and healthy volunteers. For each volunteer, 24 signals were acquired. The chosen flickering frequencies were 10 Hz (rendered on the right side of the screen) and 12 Hz (rendered on the left). Each subject was asked to focus on one stimulus at time, for 10 s. Two metrics are used to evaluate the classification performance: (i) classification accuracy, and (ii) acquisition time. The classification accuracy is defined as the percentage of brain signal correctly classified, while the acquisition time represents the time duration of the signals considered.
In this work, three algorithms are considered.

- *Power Spectral Density Analysis:* The most intuitive approach used to detect and classify the elicited SSVEPs is based on a Power Spectral Density Analysis (PSDA) [14]. First, a Fast Fourier Transform (FFT) is applied to the user EEG. Then, a PSD is performed in the neighborhood of each frequency rendered on the display according to (1).

$$P(f_n) = \frac{1}{2k+1}\left[\sum_{i=k_n-k}^{k_n+k} A^2(i)\right] \tag{1}$$

  Where: $P(f_n)$ is the PSD coefficient for the given frequency f_n, k_n is the corresponding bin in frequency domain, k is the number of neighbours to be considered, and A is the signal amplitude. Finally, the classification is performed based on the hypothesis that the observed stimulus is very likely to be that with the highest PSD [15]. However, this method requires a minimum time duration ΔT of the acquired EEG in order to correctly discriminate the harmonics, since an appropriate frequency resolution Δf is required [16], as explained in (2).

$$\Delta T = \frac{1}{\Delta f} \tag{2}$$

- *Canonical Correlation Analysis:* An alternative way to process SSVEPs is the Canonical Correlation Analysis (CCA) in time domain. It is a multivariate statistical method of correlating linear relationships between two sets of data [17]. CCA is performed between the EEG data and a set of sine waves having the same frequencies of the stimuli, and variable phase. A correlation coefficient ρ_{mn} is extracted for each stimulus frequency f_n. This relation is described by (3).

$$\rho_n = max_\phi \frac{cov(D, \Phi_n(\phi))}{\sigma_D \, \sigma_{\Phi_n(\phi)}} \tag{3}$$

  Where D is the EEG data, Φ_n is the sine wave at the frequency f_n of each rendered stimulus, and ϕ is the phase ranging from 0 to 2π. Therefore, these coefficients are used for SSVEP classification. For the sake of example, in [17] the output of the classification was associated to the frequency with the highest correlation coefficient extracted. Alternatively, in [6, 13] the maximum value among the correlation coefficients ρ_n was compared with given threshold values: the signal was marked as classified only if the chosen correlation coefficient exceeded these thresholds. The classification performance achieved with the use of CCA are typically better than PSDA [15]. However, a band pass filtering for the EEG can be necessary during the pre-processing phase, due to the effect of spontaneous EEG activities not involved in SSVEP events.

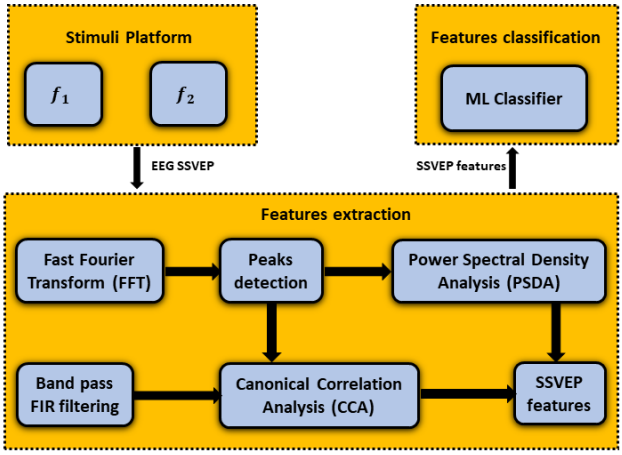

Fig. 3. Features extractions and ML-based classification

- *Features Reduction:* However, none of these two methods detects undesired frame per second (fps) variation of the XR headset during the generation of the flickering stimuli. Given the Moverio Refresh Rate (60 Hz), a variation of about 5 % inevitably leads to a shift of the rendered frequencies from 10.0 Hz up to 9.5 Hz or 10.5 Hz. This means that the elicited SSVEPs are shifted accordingly. Therefore, the classification performance of the proposed algorithms may decrease as the acquired signals and the reference ones are no longer consistent. For this reason, an adaptive strategy to find the actual SSVEP peaks has been employed. The main blocks are shown in Fig. 3. The *EEG Samples* are processed both in frequency and time domains, in order to obtain a reduced number of significant features.
  - In the frequency domain, a fast Fourier transform (FFT) is performed. Then, the actual SSVEPs *Peaks* are detected around the two rendered frequencies. In this way, the uncertainty introduced by the XR device during the generation of the flickering stimuli is mitigated

as the Power Spectral Densities (PSDs) P_1 and P_2 around the two detected peaks are more accurate.

– In the time domain, a *Band pass Filtering* between 5 and 25 Hz is applied by means of a Finite Impulsive Response (FIR) filter with linear phase response. Then, the Canonical Correlation Analysis (CCA) between the filtered signal and a set of sinewaves, having the frequencies of the two detected peaks and variable phase, is performed. As a consequence, also the two canonical correlation coefficients ρ_1 and ρ_2 obtained for each frequency are more accurate.

Ultimately, for a given brain signal of variable length, only four features are extracted and *Normalized*.
The *Classification* is carried out by means of three ML classifiers: in particular, Support Vector Machine (SVM), k-Nearest Neighbour (k-NN), and Artificial Neural Network (ANN) are employed. The FR algorithm was tested on this realized data set by means of Leave One Subject Out Cross Validation (LOSO CV). This validation strategy highlights the inter-individual reproducibility. It divides the data set in 20 folds, where each fold is constituted by a subject. Then, for each combination of the models hyperparameters, the process will run 20 times, each time with a different subject in the test set, taking the remaining ones in the training set.

III. RESULTS

In Table 1, the classification accuracy obtained by the proposed algorithm in function of the acquisition time *T* and the ML model is summarized. The uncertainty is evaluated at 2-σ. Clearly, increasing the duration of *T* leads to an increase of the classification accuracy as more information is given to the Features Reduction block. Overall, the best performance are obtained by ANN, but even a more simple classifier like k-NN reaches comparable accuracy levels.
In Table 2, a comparison between the results achieved by ANN is made with those obtained by the two classification algorithm previously developed (PSDA and CCA). As visible, the proposed ML-based algorithm provides a significant enhancement. The main contribution is given by the peak detection block, which allows to obtain more accurate features both in time and frequency domains, thus mitigating the uncertainty caused by unpredictable frame rate variation of the XR device. It should also be noted that both the CCA and PSDA are characterized by a worse inter-individual 2-σ uncertainty. Hence, the model proposed in this work offers a greater possibility to be generalized to every users.

Table 1. Accuracy Results in function of the Acquisition Time T for the three ML Models

T (s)	k-NN (%)	SVM (%)	ANN (%)
0.5	72.8 ± 4.1	74.8 ± 4.3	$\mathbf{75.0 \pm 4.3}$
1.0	80.7 ± 4.4	82.0 ± 4.4	$\mathbf{82.1 \pm 4.4}$
2.0	88.3 ± 2.6	$\mathbf{89.2 \pm 2.3}$	$\mathbf{89.2 \pm 2.3}$
3.0	93.3 ± 2.6	93.6 ± 2.3	$\mathbf{93.7 \pm 2.5}$
5.0	96.4 ± 2.1	96.4 ± 2.1	$\mathbf{96.7 \pm 1.7}$
10.0	99.0 ± 1.3	99.2 ± 1.3	$\mathbf{99.4 \pm 1.2}$

Table 2. PSDA, CCA, and FR Classification Accuracy in function of the Acquisition Time T

T (s)	PSDA [8] (%)	CCA [6] (%)	FR (%)
0.5	-	70.8 ± 4.5	$\mathbf{75.0 \pm 4.3}$
1.0	-	74.8 ± 8.1	$\mathbf{82.1 \pm 4.4}$
2.0	81.1 ± 7.6	84.9 ± 5.4	$\mathbf{89.2 \pm 2.3}$
3.0	87.7 ± 5.2	91.0 ± 4.2	$\mathbf{93.7 \pm 2.5}$
5.0	96.0 ± 2.6	95.4 ± 2.5	$\mathbf{96.7 \pm 1.7}$
10.0	98.9 ± 1.0	-	$\mathbf{99.4 \pm 1.2}$

IV. CONCLUSION

This work provides a review about the latest advancement on single-channel Brain-Computer Interfaces based on Steady-State Visually Evoked Potentials and Extended Reality. The proposed BCI instrumentation with the adoption of XR guarantees greater immersivity and engagement with respect to traditional setups. Over the years, three different algorithms were implemented to classify users SSVEPs. The current algorithm is based on a combined processing in time and frequency domains and on a ML classification. It reaches a classification accuracy up to 90 % with at least 2 s of acquisition time. These results outperformed the previous ones obtained with traditional processing strategies like Power Spectral Density Analysis and Canonical Correlation Analysis. Moreover, an additional advantage in using ML was the decrease in the inter-individual 2-σ uncertainty. Therefore, such approach can facilitate future developments of ready-to-use systems.

REFERENCES

[1] J. R. Wolpaw, N. Birbaumer, D. J. McFarland, G. Pfurtscheller, and T. M. Vaughan, "Brain–computer interfaces for communication and control," *Clinical neurophysiology*, vol. 113, no. 6, pp. 767–791, 2002.

[2] A. Apicella, P. Arpaia, G. Mastrati, and N. Moccaldi, "Eeg-based detection of emotional valence towards a reproducible measurement of emotions," *Scientific Reports*, vol. 11, no. 1, 2021.

[3] A. Apicella, P. Arpaia, M. Frosolone, and N. Moc-

caldi, "High-wearable EEG-based distraction detection in motor rehabilitation," *Scientific Reports*, vol. 11, no. 1, 2021.

[4] L. Angrisani, P. Arpaia, E. De Benedetto, A. Esposito, N. Moccaldi, and M. Parvis, "Brain-computer interfaces for daily-life applications: a five-year experience report," in *2021 IEEE International Instrumentation and Measurement Technology Conference (I2MTC)*, pp. 1–6, 2021.

[5] A. Apicella, P. Arpaia, E. D. Benedetto, N. Donato, L. Duraccio, S. Giugliano, and R. Prevete, "Enhancement of ssveps classification in bci-based wearable instrumentation through machine learning techniques," *IEEE Sensors Journal*, pp. 1–1, 2022.

[6] P. Arpaia, L. Duraccio, N. Moccaldi, and S. Rossi, "Wearable brain–computer interface instrumentation for robot-based rehabilitation by augmented reality," *IEEE Transactions on Instrumentation and Measurement*, vol. 69, no. 9, pp. 6362–6371, 2020.

[7] I. Martišius and R. Damaševičius, "A prototype SSVEP based real time BCI gaming system," *Computational intelligence and neuroscience*, vol. 2016, 2016.

[8] L. Angrisani, P. Arpaia, A. Esposito, and N. Moccaldi, "A wearable brain–computer interface instrument for augmented reality-based inspection in industry 4.0," *IEEE Transactions on Instrumentation and Measurement*, vol. 69, no. 4, pp. 1530–1539, 2019.

[9] G. R. Müller-Putz, R. Scherer, C. Brauneis, and G. Pfurtscheller, "Steady-state visual evoked potential (SSVEP)-based communication: impact of harmonic frequency components," *Journal of neural engineering*, vol. 2, no. 4, p. 123, 2005.

[10] E. Yin, Z. Zhou, J. Jiang, Y. Yu, and D. Hu, "A dynamically optimized SSVEP brain–computer interface (BCI) speller," *IEEE Transactions on Biomedical Engineering*, vol. 62, no. 6, pp. 1447–1456, 2014.

[11] P. Arpaia, N. Moccaldi, R. Prevete, I. Sannino, and A. Tedesco, "A wearable EEG instrument for real-time frontal asymmetry monitoring in worker stress analysis," *IEEE Transactions on Instrumentation and Measurement*, vol. 69, no. 10, pp. 8335–8343, 2020.

[12] P. Arpaia, E. De Benedetto, L. De Paolis, G. D'Errico, N. Donato, and L. Duraccio, "Highly wearable SSVEP-based BCI: Performance comparison of augmented reality solutions for the flickering stimuli rendering," *Measurement: Sensors*, vol. 18, p. 100305, 2021.

[13] P. Arpaia, E. De Benedetto, and L. Duraccio, "Design, implementation, and metrological characterization of a wearable, integrated AR-BCI hands-free system for health 4.0 monitoring," *Measurement*, vol. 177, p. 109280, 2021.

[14] Y. Wang, R. Wang, X. Gao, B. Hong, and S. Gao, "A practical vep-based brain-computer interface," *IEEE Transactions on neural systems and rehabilitation engineering*, vol. 14, no. 2, pp. 234–240, 2006.

[15] G. Hakvoort, B. Reuderink, and M. Obbink, "Comparison of psda and cca detection methods in a SSVEP-based BCI-system," *Centre for Telematics & Information Technology University of Twente*, 2011.

[16] X. Chen, Y. Wang, M. Nakanishi, X. Gao, T.-P. Jung, and S. Gao, "High-speed spelling with a non-invasive brain–computer interface," *Proceedings of the national academy of sciences*, vol. 112, no. 44, pp. E6058–E6067, 2015.

[17] Z. Lin, C. Zhang, W. Wu, and X. Gao, "Frequency recognition based on canonical correlation analysis for ssvep-based BCIs," *IEEE transactions on biomedical engineering*, vol. 53, no. 12, pp. 2610–2614, 2006.

25th IMEKO TC4 International Symposium
23rd International Workshop on ADC and DAC Modelling and Testing
IMEKO TC-4 2022
Brescia, Italy / September 12-14, 2022

Improvement of calibration capabilities with an *a posteriori* evaluation of the lighting impulse international comparison EURAMET.EM-S42

S.E. Caria[1,2], P.E. Roccato[3]

[1] *Istituto Nazionale di Ricerca Metrologica (INRiM), Strada delle Cacce 91, 10135 Torino, Italy, s.caria@inrim.it*
[2] *Politecnico di Torino, Corso Duca degli Abruzzi 24, 10129 Torino, Italy, stefano.caria@polito.it*
[3] *Istituto Nazionale di Ricerca Metrologica (INRiM), Strada delle Cacce 91, 10135 Torino, Italy, p.roccato@inrim.it*

***Abstract* – By the evaluation of the EURAMET.EM-S42 intercomparison results, the Laboratorio Alte Tensioni e Forti Correnti (LATFC) of Istituto Nazionale di Ricerca Metrologica (INRiM, Italy NMI) starts an analysis of the calibration capabilities with the developed measuring system for lightning impulse voltages.**
This paper addresses the issue of the expanded uncertainty re-evaluation for the INRiM's CMCs up to 200 kV according to a new analysis of the comparison reference value (CRV), without affecting the results of the other participants in the comparison for all the involved lighting impulse parameters.
A validation of the new uncertainty values has been performed by means the calculation, for some test data waveforms extract for reference standard IEC 61083 - 2, of the convolution with the measured divider step response.

I. INTRODUCTION

The INRIM's Laboratorio Alte Tensioni e Forti Correnti (LATFC, High Voltage and High Power Laboratory) has the instrumentation to perform calibrations with lightning impulse (LI) waveforms up to 700 kV.

In 2016 started the Supplementary comparison EURAMET.EM-S42 [1, 2], for lightning impulse voltage measurement systems, in which thirteen institutes worldwide participate to the comparison. During the comparison were analyzed different LI waveforms: from 100 kV to 700 kV of peak value, name of test voltage value, with different polarities and different front time (short and long), from 0,84 µs to 1,56 µs, and with a time to half value of about 60 µs.

The LATFC laboratory of the INRIM was one of the participants of the comparison, in the 2017 springtime, during European circulation of the Transfer reference measurement system (TRMS). The TRMS is based on a commercial divider combined with its acquisition system and others auxiliary equipment.

The aim of this paper is to point out the reasoning that leads to evaluate a reduction in uncertainty of the INRIM's measurement systems up to 200 kV.

II. LIGHTNING IMPULSE MEASURING SYSTEM

The INRIM's LATFC laboratory owns a Lightning Impulse Reference Measuring System that consist in two different voltage dividers, the first is the reference for LI up to 200 kV (subject of this paper) the second one increases the voltage level up to 600 kV, National Instruments' scope card PXIe-5124 and self-made software. The LI source is a generator capable of generate a lightning impulse up to 800 kV, for in-house operations, while on-site measurements are carried out with the customer generation system. Below the components of the system for this work are described.

A. Voltage divider

Fig. 1 shows the SAGI 304, a resistive divider developed by means of lab specification. Due to its dimensions and characteristics, it could be possible to use only up to 200 kV.

B. Digitizer

The digitizer that is used for the data acquisition is the National Instruments' scope PXIe-5124, whose characteristics are:

- Max sampling rate: 200 MS/s
- Resolution: 12 bits

C. Software

The software used for the measurement of lightning impulse in LATFC's laboratory is developed in-house with LabVIEW. It could dialogue with the different acquisition systems used in the laboratory for tests and calibrations.

The algorithm developed according to the IEC 60060-1 [3] and the IEC 61083 series [4, 5]. The algorithm has been validated for all the lighting impulse waveforms with respect to the values reported in the IEC 61083-2 [5].

Fig. 1. SAGI 304 resistive divider up to 200 kV.

D. LI Generator

The LATFC's generator, an HAEFELY SGSA 800/40 shown in Fig. 2, is a multi-stage impulse system, with eight stages where each stage can hold up to 100 kV with a total of 800 kV. It could be partialized if necessary, for the generation below 100 kV.

Fig. 2. LATFC's Haefely Impulse generator.

III. IMPROVEMENT OF UNCERTAINTY TARGET

Starting from comparison performed in the years 2016-2020, the entire measurement system was studied deeper to pursue the objective to reduce the CMCs declared. The uncertainties declared for complete lightning impulse (LI) during the comparison, current CMCs, are reported in Table 1:

Table 1. Expanded uncertainty declared.

Parameter	Expanded uncertainty
Peak Voltage, U_t	0,5%
Front time, T_1	3%
Time to half-value, T_2	3%
Overshoot, β'	1%

Where, as described in IEC 60060 - 1 [3]:

- U_t is the maximum value of the test voltage curve;
- T_1 is a virtual parameter defined as 1/0.6 times the interval T between the instants when the impulse is 30 % and 90 % of the peak value (points A and B, Fig. 3);
- T_2 is the time interval between the virtual origin O1 and the instant when the test voltage has decreased to half the test voltage value;
- β' is the relative overshoot magnitude

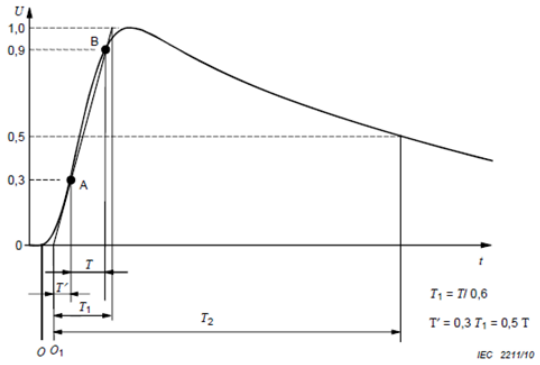

Fig. 3. Lightning impulse time parameters, from IEC 60060-1

The INRiM's comparison results has been reported without any improvement in the uncertainty of time parameters due to the unavailability of the old calibration system due to a failure and the consequent impossibility of a direct verification, before the comparison, to evaluate the extent of the measurement uncertainty.

The objective is to reduce the expanded uncertainty until obtaining the value targets reported in Table 2, requested for commercial operation in the calibration of high voltage lighting impulse measuring systems:

Table 2. Expanded uncertainty targets.

Parameter	Expanded uncertainty
Peak Voltage, U_t	0,5%
Front time, T_1	1,5%
Time to half-value, T_2	1%
Overshoot, β'	0,5%

The parameter reported in Table 2 was hypothesized starting from step response of the entire measurement system obtained during comparison, for an ideal LI waveform.

IV. REANALYSIS OF INTERNATIONAL COMPARISON RESULTS

To support the reduction of the CMCs uncertainty it was performed a complete reanalysis of the comparison results with the expanded uncertainty target.

The reanalysis includes the recalculation of comparison reference value (CRV) as described in the final report [1], which is considered as an estimation of the measurand according to the measurements provided by the participating laboratories [1, 2], reported in equation (1):

$$CRV = \frac{\sum_{i=1}^{N} x_i u^{-2}(x_i)}{\sum_{i=1}^{N} u^{-2}(x_i)} \quad (1)$$

Where:

- x_i are the errors provided by the participants for the TRMS readings
- $u(x_i)$ are the corresponding standard uncertainties.

To not be verbose, in this paper were reported only the results for one significant type of LI, where the higher value in the degree of equivalence has been found for the most critical parameter T_1. Specifically, given that the uncertainty on the test voltage value, peak measurement, does not change, only the measurements relating to times were reported.

All the tables and figures are referred to Short-P100 case, the worst one in this analysis. Short-P100 is the LI with a positive peak voltage of 100 kV and front time of 0,84 µs that is the fastest front time that could be performed according to the IEC 60060-1 [3].

Fig. 4 and Table 3 shown the values relatives to the T_1 measurements performed during the comparison, where:

- Δx_i is the difference percentage between the measurement of the laboratory and the CRV;
- $U(\Delta x_i)$ is the expanded uncertainty related to Δx_i;
- E_n is the degree of equivalence of laboratory, if it is under the value 1 it is considered acceptable; calculated as shown in equation (2):

$$E_n = \frac{x_i - CRV}{2\cdot\sqrt{u^2(x_i) - u^2(CRV)}} \quad (2)$$

- CRV is the comparison reference value;
- U(CRV) is the expanded uncertainty of CRV, calculated as shown in equation (3):

$$U(CRV) = 2 \cdot \frac{1}{\sqrt{\sum_{i=1}^{N} u^2(x_i)}} \quad (3)$$

- Pr denotes "probability of" is a parameter used for consistency check. If Pr is under 5% the check is considered failed. calculated as shown in equation (4, 5):

$$Pr\{\chi^2(\nu) > \chi^2_{obs}\} < 5\% \quad (4)$$

Where:
ν = N -1 is the number of degrees of freedom

$$\chi^2_{obs} = \sum_{i=1}^{N} \frac{(x_i - CRV)^2}{u^2(x_i)} \quad (5)$$

Fig. 4. T1's data results of comparison.

Table 3. T1's data results of comparison.

LAB	Δx_i	$U(\Delta x_i)$	E_n
INRIM	-1,57%	3,43%	-0,46
OTHERS	-0,43%	2,61%	-0,17
	-0,25%	3,03%	-0,08
	0,45%	2,17%	0,21
	-4,95%	3,02%	-1,64
	2,78%	2,61%	1,06

	-0,37%	2,24%	-0,17
	-0,15%	2,61%	-0,06
	-1,11%	2,53%	-0,44

CRV	U(CRV)	Pr
2,41%	0,98%	57%

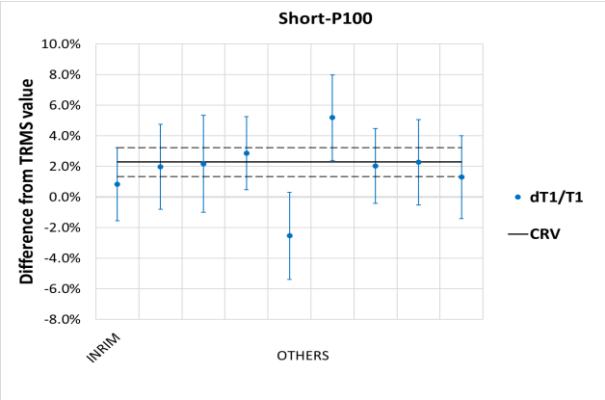

Fig. 5. T1's data after recalculation.

Table 4. T_1's data after recalculation.

LAB	Δx_i	$U(\Delta x_i)$	E_n
INRIM	-1,44%	2,21%	-0,65
OTHERS	-0,30%	2,62%	-0,12
	-0,11%	3,04%	-0,04
	0,58%	2,19%	0,27
	-4,82%	3,00%	-1,61
	2,91%	2,63%	1,11
	-0,24%	2,26%	-0,11
	-0,01%	2,62%	-0,01
	-0,98%	2,54%	-0,38

CRV	U(CRV)	Pr
2,28%	0,94%	47%

Fig. 5 and Table 4 reported the results of the comparison if INRIM reduced the declared expanded uncertainty from 3% to 1,5% for the front time T_1 parameter. It is possible to see that no one of the other partners present a variation in the degree of equivalence that change their status or their compliance with the comparison results. For the INRIM measurements the degree of equivalence is still under the unit value.

The variation in the CRV uncertainty values shows an improvement in the comparison results, due to its reduction, the reduction of the probability Pr is negligible for the analysis, considering that the minimum acceptable value is 5 %.

Comparing the figures, it is possible to notice that the INRIM's uncertainty still intersect the CRV.

Fig. 6 and Table 5 shortly shown the comparison results before and after reanalysis relative of T_2, time to half value.

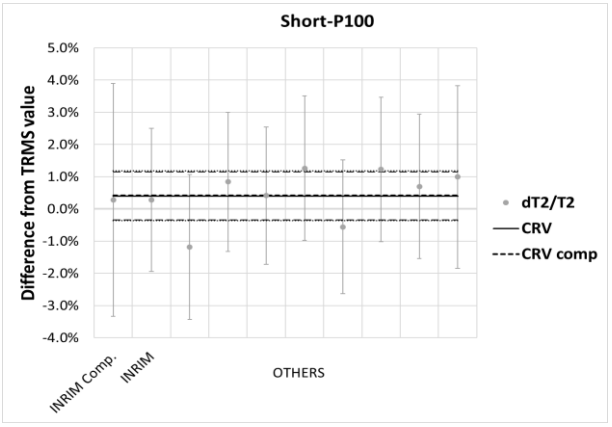

Fig. 6. T_2's comparison and reanalysis data.

Table 5. T_2's INRIM data.

INRiM Lab	Δx_i	$U(\Delta x_i)$	E_n
Comparison	-0,13%	3,53%	-0,04
Reanalysis	-0,12%	2,10%	-0,06

	CRV	U(CRV)	Pr
Comparison	0,35%	0,78%	80%
Reanalysis	0,40%	0,75%	82%

Also, in the case of T_2 it is possible to observe, in Fig. 6, that with the reduction of INRIM's uncertainty the CRV change is negligible and that changes don't affect the compliance for the other participants of the comparison.

V. CONVOLUTION METHOD TO VALIDATE REANALYSIS

To validate the results of the comparison reanalysis, a determination of the dynamic behavior from step response measurements was performed as described in IEC 60060 – 2 [6].

A step generator based on the voltage collapse, by means a relay with mercury-wetted contacts commutation, has been used to perform experimental measurement of dynamic response of the divider. The acquisition system National Instruments' scope card PXIe-5124 used for this evaluation is the same of the LI measurements.

The convolution method consists, as described in Annex D of IEC 60060-2, in a calculation of the output of

the measuring system starting from step response and an impulse, representative of the waveform normally measured during calibration operations.

For this work have been used the most significant reference waveshape, related to calibration, generated from the test data generator (TDG), described in IEC 61083-2 [5], used for the software algorithm validation.

The step response measurements are used to characterize a measuring system, it consists in a measurement of the output of the system's behaviour while a step occur. Voltage step generators are designed and used for this specific tests.

The step response is also used to calculate parameters that are recommended for LI reference measuring systems. Table 6 shown the recommended parameter values that are described in IEC 60060-2 [6] and INRiM's reference measuring system step response values.

Table 6. Step response parameters for LI reference measuring systems.

	Recommended	INRiM's SAGI304
Experimental response TN	≤ 15 ns	10 ns
Settling time t_s	≤ 200 ns	85 ns
Partial response T_α	≤ 30 ns	10 ns

For this validation was used a step response performed during comparison, in the same laboratory layout, and the TDG file was rescaled to be compatible, as test voltage value only, with the voltage that the reference measuring system can measure, up to 200 kV.

In Fig. 7 it is possible to observe the original TDG waveform for LI-A1 [5], solid blue line, and the waveform resulting from the convolution, dashed orange line. The convoluted waveform was translated, in time and value, only to guarantee a better visibility.

In Table 7 were reported the results of the convolution methods, compared, as relative variation, with the value reported in IEC 61083-2 standard, performed for different reference waveforms.

For each waveform it could be appreciated that the results are less than new expanded uncertainty target for all the parameters.

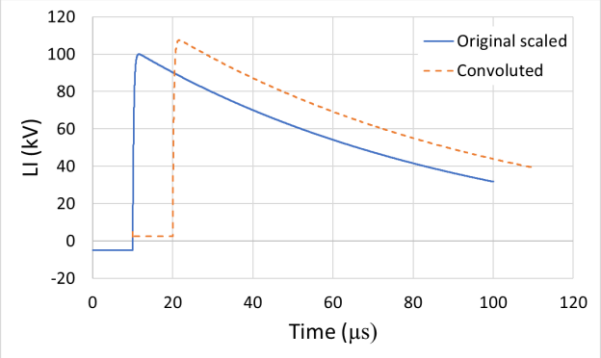

Fig. 7. Comparison between LI A1 reference and convoluted waveforms.

Table 7. Results of convolution method.

TDG	U_t	T_1	T_2	β'
LI A1	0,05%	1,19%	0,25%	0,13
LI A3	0,12%	0,18%	0,44%	0,29
LI A4	0,15%	0,68%	0,48%	0,28
LI A11	0,18%	1,18%	0,46%	0,37
LI M6	0,04%	1,11%	0,07%	0,06
LI M10	0,01%	0,96%	0,03%	0,09

VI. CONCLUSIONS

The new uncertainty targets for lighting impulse parameters have been integrated in the EURAMET.EM-S42 calculation to assure the reliability of the values. The new calculation of the comparison reference value (CRV) has not changed the results for other partners involved in the measurements. The degree of equivalence is, for all the intercomparison levels, E_n<1, assuring a good reliability of the measurements results.

The new uncertainty values have been verified applying a convolution calculation between the measured step response of the high voltage divider and most significant waveforms obtained by the reference standard IEC 61083-2:2014. The calculation of the convolution results by means of INRiM algorithm have been compared with the standard reported value for all the parameters.

In consideration of this reanalysis the LATFC-INRiM laboratory can reconsider the expanded uncertainty for CMCs up to 200 kV, with an important improvement especially for the time parameters T_1 and T_2.

Further analysis could be performed also for the higher voltage levels with the measuring system up to 600 kV.

REFERENCES

[1] https://www.bipm.org/documents/20126/48859014/EURAMET.EM-S42.pdf/9faf30cc-78be-379f-771a-

4e6133ce6a0f.
[2] J. Hällström, A.-P. Elg, J. Havunen and F. Garnacho, Supplementary comparison EURAMET.EM-S42, comparison of lightning impulse (LI) reference measuring systems, Metrologia, 2020.
[3] IEC 60060-1 High-voltage test techniques - Part 1: General definitions and test requirements, 2010-09.
[4] IEC 61083-1 Instruments and software used for measurements in high-voltage impulse tests - Part 1: Requirements for instruments.
[5] IEC 61083-2 Instruments and software used for measurement in high-voltage and high current tests - Part 2: Requirements for software for tests with impulse voltages and currents.
[6] IEC 60060-2 High-voltage test techniques - Part 2: Measuring systems, 2010-11

25th IMEKO TC4 International Symposium
23rd International Workshop on ADC and DAC Modelling and Testing
IMEKO TC-4 2022
Brescia, Italy / September 12-14, 2022

Design of integrated multi-user electric energy meter

Jianbo Liu,Wenqiang Li, Mei Yang, Xiao Liu,Bin Deng,Weizhao Wang, Xuefeng Ma

Shandong Engineering Research Center of Reliability Evaluation for Electric Energy Metering Devices，Shandong Institute of Metrology, No.28, Qianfoshan East Road, 250014 Jinan, China
18553159166@163.com

***Abstract* –In this paper, an integrated multi-user energy meter was designed, which achieves accurate measurement of multi-user energy through circuit sharing and current sampling respectively. The integrated design has the advantages of small size, low cost, easy installation and use, and easy implementation of remote data transmission and intelligent control.**

***Keywords* –Multi-user electric energy meter, energy measurement, integrated design**

I. INTRODUCTION

With the development of electronic technology, static electric energy meters have emerged and been widely used for their advantages such as high accuracy, good stability, and remote data transmission [1-3]. Single-phase static electric energy meters are mainly used for electric energy measurement of residential users. Due to the slow change of power load of residential users, the voltage of all users in each distribution unit is the same. The difference is the current flowing through each user's circuit. The voltage sampling circuit sharing and multi-channel cyclic sampling mode of current circuit are adopted to integrate multiple meters of electric energy meter and realize multi-user electric energy measurement[4-10]. Based on this, an integrated multi-user electric energy meter that can realize multi-channel electric energy measurement was designed, The electric energy meter circularly switches the current signal of each user's loop through the electronic switch with a switching time of less than 1ms, so as to sample the current signal of all users. Multi-user electric energy meter has the characteristics of small volume, low cost and convenient installation and use. Experiments show that the multi-user electric energy meter meets the requirements of IEC 62053. At present, it has been widely used in school, mine and other occasions.

II. PRINCIPLE AND STRUCTURE OF MULTI-USER ENERGY METER

The voltage sampling of the conventional static energy meter uses a voltage transformer to convert a large voltage to a small voltage, and the current sampling uses a micro current transformer to convert a large current to a mA-level small current, and then uses a precision resistor to convert the small current to a small voltage. The two signals directly enter the metering chip to accumulate energy by integration, and achieve accurate energy measurement by calibration.

The multi-user energy meter adopts the same working principle. Due to the slow change of the electricity load of the resident users, the energy measurement of multiple users together is collected, the voltage sampling loop is shared, and the current sampling loop of multiple users is independent, and the current sampling signal is connected to the metering chip through an electronic switch. The principle of the multi-user energy meter is shown in *Figure 1*.

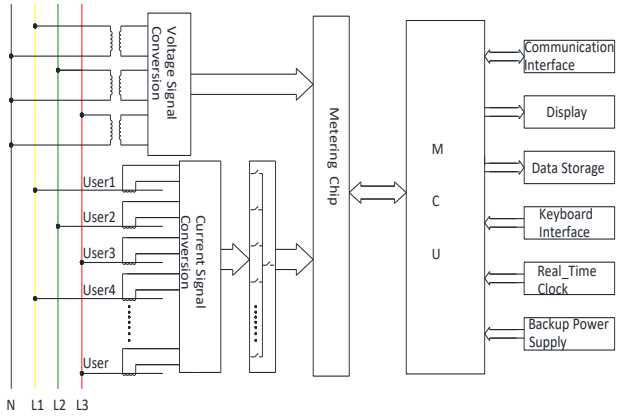

Fig. 1. The principle of the multi-user energy meter.

In the figure above: three voltage transformers are used to collect the voltage signal of the power supply circuit. The current signal output by the current transformer of each user circuit is connected to the signal filter board, and then connected to the metering board together with the voltage signal after filtering. The metering chip on the metering board multiplies the voltage signal and current signal to obtain the power data. The main control CPU reads the power data of each household and multiplies the time data to realize the transformation to the electric

energy signal.

Because the current signal in the user circuit cannot change suddenly, the current signal of the user circuit is obtained by interval acquisition, and then the user current data in the sampling interval is restored by general statistical method. In this way, the obtained user current data can accurately reflect the real data of the user. Three households are switched every 1 second. The average acquisition cycle of each household is 330ms.

Voltage Signal Conversion—Use a voltage transformer to convert a large voltage into a small voltage that can be directly input to the chip; Current Signal Conversion—Use current transformer to convert large current into small current; Metering Chip—Processor for accumulating electric energy through two input signals; MCU—Micro Control Unit; Communication Interface—Interface for transmitting instructions and data.

The household-by-house circulation method belongs to intermittent collection, and the collection speed must be fast to meet the energy measurement requirements. According to Shannon's sampling theorem, the sampling interval of 50Hz (period 20ms) should be less than 10ms. Taking into account the influence of harmonics, the sampling interval is generally not more than 4ms. For multi-user energy meters of 24 households, the sampling interval should not be less than 1/6ms.

The CS5460 sampling chip is used, its conversion frequency is F=MCLK/1024, MCLK is the frequency of the external crystal oscillator, if MCLK=12MHz, then F=11719Hz, that is, the time to complete an acquisition is about 1/12 ms, which is less than 1/6 ms and fully meet the requirements.

The ac energy measurement is realized by measuring the power along with the integral of the time. A high speed Analog to Digital Converter (ADC) in the measurement and processing unit is used for the synchronous sampling of two voltage and current sampling signals. The micro-processing unit computes the energy according to the discrete digital signals. The calculation of the energy is get from equation as follow.

$$W = \frac{1}{T}\sum_{k=1}^{N} u(k) \times i(k) \qquad (1)$$

$$T = N \times \Delta t$$

Where T is the time interval of the sampling, N is the integer sequence.

Phase lock technology is applied to lock the sampling frequency automatically with the multiple of the frequency of the input signals. With this phase lock, the influence for the measurement caused from the drift of the clock signal is eventually avoided [11].

The continuous cyclic switching of the multi-channel current sampling signal through the electronic switch realizes the simultaneous measurement of multi-user electrical energy.

For multi-user energy meters with a large number of users, three-phase four-wire power supply is generally used. Each of the three phases of L1, L2, L3 has an independent metering unit. L1-phase supplies power to No.1, 4 , 7 households, L2-phase supplies power to No.2, 5 , 8 households, and L3-phase supplies power to No.3, 6 , 9 households, etc., multi-user energy meter can realize the energy measurement of 24 households or more. The internal structure of the multi-user energy meter is shown in *Figure 2*.

Fig. 2. Internal structure of multi-user electric energy meter.

III. ENERGY MEASUREMENT ERROR

Due to the multi-cycle sampling mode, the sampling frequency of each household is reduced exponentially compared to the conventional static energy meter, which will affect the accuracy of energy measurement.

In order to verify the accuracy of energy measurement, taking the first 6 households of a multi-user energy meter with a type of 200V , 5 (50) A as an example, according to the requirements of IEC 62053, the energy error of multi-user energy meters of each household at a load current of 0.5A, 5A and 50A and a power factor of 1.0, 0.5L and 0.8C, is measured, respectively [12].

In the experiment, a verification equipment was used, for AC electical energy meters to measure the energy error. Its measurement range is 220 V, (0.1~100) A, and the uncertainty of energy measurement is 0.05% (k = 2). The measurement results are shown in Table 1.

Obtained from Table 1, the maximum error of energy measurement in the first 6 households of multi-user energy meters is -0.34%, which meets the requirements of resident users for level 2 meters. Although the multi-channel cyclic sampling mode reduces the sampling frequency of each household, the multi-user energy meter can still meet the energy measurement needs of

residential users.

Table 1. Energy measurement error of multi-user energy meters.

user	load point	Error (%)		
		cosϕ=1.0	cosϕ=0.5L	cosϕ=0.8C
1	220 V 0.5 A	- 0.22	- 0.13	- 0.14
	220 V 5 A	- 0.23	- 0.11	- 0.12
	220 V 50 A	- 0.19	- 0.15	- 0.17
2	220 V 0.5 A	- 0.23	- 0.23	- 0.21
	220 V 5 A	- 0.16	- 0.19	- 0.17
	220 V 50 A	- 0.21	- 0.24	- 0.23
3	220 V 0.5 A	- 0.22	- 0.34	- 0.22
	220 V 5 A	- 0.20	- 0.30	- 0.14
	220 V 50 A	- 0.15	- 0.17	- 0.18
4	220 V 0.5 A	- 0.21	- 0.28	- 0.23
	220 V 5 A	- 0.18	- 0.13	- 0.16
	220 V 50 A	- 0.21	- 0.16	- 0.15
5	220 V 0.5 A	0.32	0.29	0.28
	220 V 5 A	0.31	0.23	0.26
	220 V 50 A	0.32	0.31	0.33
6	220 V 0.5 A	- 0.23	- 0.28	- 0.07
	220 V 5 A	- 0.11	- 0.10	0.06
	220 V 50 A	- 0.18	- 0.20	0.08

Due to the use of integrated design and circuit sharing technology, compared with conventional static energy meters, the volume of multi-user energy meters is greatly reduced, the cost is also greatly reduced, at the same time it is easy to install and maintain, and has broad application prospects.

IV. OTHER FUNCTIONS

Due to the use of micro-processing technology, multi-user energy meters can achieve multiple functions. It can realize the functions of prepaid use of electric energy, remaining power alarm, and power failure due to arrears by the prepayment function module, the functions of multi-rate by the clock module, the remote load switch can be opened or closed by the control module, and remote data transmission can be realized by the communication module, memory can realize power storage and query of multiple users. The schematic diagram of the functional structure of the multi-user energy meter is shown in *Figure 3*.

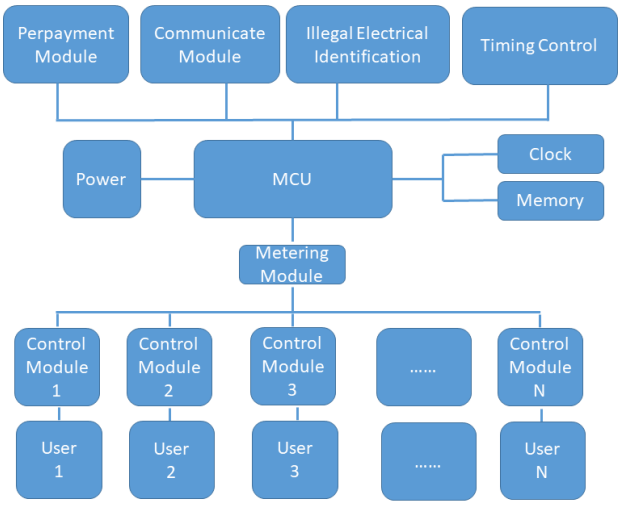

Fig. 3. The schematic diagram of the functional structure of the multi-user energy meter.

V. CONCLUSIONS

In this paper, based on the characteristics of the slow changes in the electricity load of residential users, an integrated multi-user energy meter have been designed, which uses independent sampling of the current loop and sharing with other circuits, which greatly reduces the size and cost of the energy meter and is easy to install and maintain. After actual measurement, the energy measurement error of the multi-user energy meter fully meets the needs of the residents. Due to the use of micro-processing technology, multi-user energy meters can achieve the advantages of prepayment, multiple rates, remote control of load switches, multi-channel data storage, remote data transmission, etc., and have a broad application prospect.

VI. ACKNOWLEDGMENT

During the research, we received the guidance and help from Professor Cao Ruiji of SDIM China. Under the guidance, we have realized the integrated design by circuit sharing technology. We would like to express my admiration and heartfelt thanks to Professor Cao. During this process, we also got the guidance of Dr. Wang Lei of NIM China, and I would like to express our gratitude to Dr. Wang.

REFERENCES

[1] R.F Masnicki, "Some Remarks on the Accuracy of Energy Meters," 2018 IEEE International Conference on Environment and Electrical Engineering and 2018 IEEE Industrial and Commercial Power Systems Europe (EEEIC / I&CPS Europe), Palermo, 2018, pp. 1-5.

[2] A. Cataliotti, V. Cosentino and S. Nuccio, "The metrological characterization of the static meters for

reactive energy in the presence of harmonic distortion" 2007 IEEE Instrumentation & Measurement Technology Conference IMTC 2007, Warsaw, 2007, pp. 1-6.

[3] A. Bernieri, G. Betta, L. Ferrigno and M. Laracca, "Electrical energy metering in compliance with recent european standards," 2012 IEEE International Instrumentation and Measurement Technology Conference Proceedings, Graz, 2012, pp. 1541-1545.

[4] Hu Chang-lun, Wang Xiao-jun, Ma Li-guo, Zuo Ya-nan. Development of Multi-users Multi-function Watt-hour Meter Based on ATT7022B[J]. Electronics Quality, 2014, (2): 21-26 .

[5] GONG Maofa, ZHANG Xuebin, LIU Qingxue, GONG Zheng, WANG Yongqing. Multi-user and multi-functional prepayment meter based on CS5460A [J]. Electric Power Automation Equipment, 2011, 31(9): 121-124.

[6] TANG Qiufang, LUO Meilin, ZHOU Shaowu, ZHOU Minghui. Multi-users Watt-hour Intellectual Meter Based on ARM[J]. MODERN ELECTRONICS TECHNIQUE, 2009, 32(6): 158-161.

[7] TANG Yuan-xin, HE Liang, SUN Zhai-qing, ZENG Yi-qing. The multiuser central electrical energy meter and its selection[J]. CHINA HOUSING FACILITIES, 2006,(4): 45-47.

[8] JI You, TANG Yuan-xin, GONG Mao-fa, GONG Zheng, HUANG He-song. Power Consumption, Functions and Features of Multi User Smart Watt-hour Meter[J]. Science & Technology Information, 2014, (3): 66,89.

[9] YANG Mei, CAO Rui-ji. The Design Features and Causes Interference of Multi-users Electromechanical eter[J]. ELECTRICAL MEASUREMENT & INSTRUMENTATION, 2010, 47(Z2): 95-98.

[10] JIANG Ji Shun. Design of a novelty multi-user single-phase watt-hour meter[J]. MICROCOMPUTER & ITS APPLICATIONS, 2009, 28(11): 77-79.

[11] X. Ma, W. Li, G. Yu, R. Cao, Q. Zhang and X. Zhang, "Development of high voltage ac energy meter," 2012 Conference on Precision electromagnetic Measurements, Washington, DC, 2012, pp. 132-133.IEC 62053-21:2003 Electricity metering equipment(a.c.) - Particular requirements - Part 21: Static meters for active energy(classes 1 and 2).

25th IMEKO TC4 International Symposium
23rd International Workshop on ADC and DAC Modelling and Testing
IMEKO TC-4 2020
Brescia, Italy / September 12-14, 2022

Characterization of a method for transmission line parameters estimation with respect to PMU measurement error modeling

Paolo Attilio Pegoraro[1], Carlo Sitzia[1], Antonio Vincenzo Solinas[1], Sara Sulis[1]

[1]*Department of Electrical and Electronic Engineering, University of Cagliari, via Marengo 2, 09123 Italy, carlo.sitzia@unica.it*

***Abstract* – The line parameters available to the System Operator can be quite different from actual values because of different reasons, such as aging, manufacturing tolerance, environmental conditions, etc. Proposals have been presented in literature to estimate line parameters and monitor their changes. Synchrophasor measurements from PMUs have appeared as a possible breakthrough for accurate estimation. A novel algorithm has been recently proposed to estimate line parameters in presence of realistic systematic errors in PMU-based measurement chains. This paper aims at characterizing the robustness of the algorithm with respect to possible mismatches of the models associated to PMU measurement errors. Systematic and random contributions are considered at different levels. Simulations on an IEEE test network help in investigating method robustness and possible limits.**

I. INTRODUCTION

When dealing with power system management, several applications are involved. Among others, state estimation [1], fault location methods [2], etc. In all these applications, network models play a fundamental role and line parameters are thus the basis of any further processing or evaluation. In practice, line parameter values can significantly differ from data available to Transmission System Operator (TSO) because manufacturing, installation or ageing introduce model mismatches that can result in Energy Management System issues. Measuring line parameters is thus a critical and challenging task, to which phasor measurements units (PMUs) can contribute significantly, since their outputs are direct, accurate and frequent measurements of voltage and current phasors synchronized to Coordinated Universal Time (UTC) and thus associated with an accurate time tag. TSOs have been installing PMUs in the last decade to build the so-called Wide Area Monitoring Systems (WAMSs), i.e., the new generation distributed monitoring infrastructures for power systems.

Even if promising, the PMU is only one element of the measurement chain, which includes also Instrument Transformers (ITs), and thus line parameter estimates are affected by measurement errors at different levels. In the literature, different approaches to PMU-based parameters estimation have been introduced recently. In [3], only the PMU error is considered for a single line estimation, while in [4] also ITs are considered, adopting an estimation method based on direct application of PMU current and voltage measurements available at both ends of the line at a given time instant. In [5] and [6], multiple time instants are considered, but IT errors are modeled as zero mean random noise, thus neglecting systematic errors.

When IT systematic errors are not fully compensated, which is a typical situation, line parameter estimation is strongly affected. In [7], calibrated transducers are used to propagate accuracy while estimating line parameters. In [8] systematic errors of current amplitudes and voltage phase angles are assumed negligible to simultaneously estimate line parameters and other systematic errors, while [9] focuses on the detection of uncalibrated ITs in a preliminary way.

In [10, 11], an algorithm to estimate simultaneously line parameters and systematic errors introduced by ITs was presented, dealing with multiple lines at the same time and with multiple operating conditions of the network. The method relies on the definition of a measurement model that considers both systematic and random measurement errors and on prior knowledge on line parameters, IT and PMU uncertainty. Considering the estimation framework, potential issues can arise when a mismatch between considered prior information and actual deviations occurs.

In this paper, the role of systematic and random errors in PMUs will be investigated. Indeed, PMU specifications do not allow tuning prior information on systematic and random errors in PMU measurement chain. For this reason, the impact of PMU systematic errors on line parameters estimation and their role in the compensation process of the entire measurement chain need to be assessed. Performance and robustness of the method [11] will be examined through simulation on the IEEE 14 bus test system.

II. ESTIMATION FRAMEWORK

In the following, the algorithm proposed in [10] and extended in [11] to address several load scenarios is briefly introduced with a focus on its assumptions and measure-

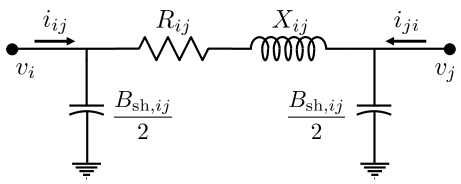

Fig. 1. π-model of a transmission line.

ment model. An equivalent single-phase model is considered (see [9]), which adopts a π-model for each line as that represented in Fig. 1. Fig. 1 also shows the considered measurements, since v_i, v_j, i_{ij} and i_{ji} are the synchronized phasor measurements (synchrophasors) of the start-node voltage of the line (node i), of the end-node voltage (node j), of the branch current from node i and of that from node j, respectively. The measurements are assumed available from two PMUs installed at both ends of the line and correspond to the same time instant $t = nT_{RR}$, which identifies the PMU generic timestamp (T_{RR} is the PMU reporting interval). From Fig. 1, it is clear that the line parameters to estimate are the line resistance R_{ij}, the line reactance X_{ij} and the shunt susceptance $B_{\text{sh},ij}$ (equally split into the two sides of the model).

The line parameter estimation algorithm is based on a set of equations, corresponding to different timestamps and involving the unknown line parameters and the measurement errors. In particular, the four measurements available for each timestamp and for each line allow writing two complex-valued equations: the first one expresses the voltage drop across the line; the second one derives from Kirchhoff's Current Law. In detail, the following two equations are considered:

$$v_i^R - v_j^R = (R_{ij} + jX_{ij}) \left(i_{ij}^R - j\frac{B_{\text{sh},ij}}{2} v_i^R \right) \quad (1)$$

$$i_{ij}^R + i_{ji}^R = j\frac{B_{\text{sh},ij}}{2}(v_i^R + v_j^R) \quad (2)$$

where superscript ^{R} indicates the reference value of the corresponding measured quantity. Equations (1) and (2) define thus constraints for the line parameters based on actual values of voltage and current phasors at a given time.

Since we are dealing with a measurement process, reference values can be rewritten as functions of measured synchrophasors, systematic and random errors as follows:

$$\begin{aligned} v_h^R &= \frac{v_h}{(1 + \xi_h^{\text{sys}} + \xi_h^{\text{rnd}})} e^{j(-\alpha_h^{\text{sys}} - \alpha_h^{\text{rnd}})} \\ &\approx V_h e^{j\varphi_h} \left(1 - \xi_h^{\text{sys}} - \xi_h^{\text{rnd}} - j\alpha_h^{\text{sys}} - j\alpha_h^{\text{rnd}}\right) \quad (3) \\ i_{ij}^R &= \frac{i_{ij}}{(1 + \eta_{ij}^{\text{sys}} + \eta_{ij}^{\text{rnd}})} e^{j(-\psi_{ij}^{\text{sys}} - \psi_{ij}^{\text{rnd}})} \\ &\approx I_{ij} e^{j\theta_{ij}} \left(1 - \eta_{ij}^{\text{sys}} - \eta_{ij}^{\text{rnd}} - j\psi_{ij}^{\text{sys}} - j\psi_{ij}^{\text{rnd}}\right) \quad (4) \end{aligned}$$

where $h \in \{i, j\}$, V_h and I_{ij} are the measured voltage and current magnitudes, respectively, ξ_h and η_{ij} indicate the corresponding measurement errors, φ_h and θ_{ij} are the voltage and current phase angles measured by the PMUs, and α_h and ψ_{ij} are the corresponding errors. Superscripts $^{\text{sys}}$ and $^{\text{rnd}}$ are used to split the measurement errors in their systematic and random components. All the errors are $\ll 1$ (their absolute values) and the approximated expressions in (3) and (4) are obtained considering a first order approximation with respect to measurement errors and thus neglecting terms, even multivariate, with a degree > 1. An equation analogous to (4) can be written also for the other current in the opposite direction.

Systematic errors are unknown like the line parameters and thus multiple pairs of equations corresponding to different timestamps and possibly to different operating conditions of the network can be used to define a set of equations which is the basis for the estimation. In [10] and [11], systematic errors are attributed to ITs, i.e., to voltage transformers (VTs) and current transformers (CTs), while PMUs are considered as affected mainly by random errors.

To simplify the estimation task, (1) and (2) are further modified by considering line parameters as follows:

$$\begin{aligned} R_{ij} &= R_{ij}^0 (1 + \gamma_{ij}) \\ X_{ij} &= X_{ij}^0 (1 + \beta_{ij}) \\ B_{\text{sh},ij} &= B_{\text{sh},ij}^0 (1 + \delta_{ij}) \end{aligned} \quad (5)$$

where superscript ^{0} indicates the known values that are already available to the TSO, and γ_{ij}, β_{ij} and δ_{ij} are the unknown relative deviations from them, which represent the lack of knowledge.

Replacing then (3) and (4) into (1) and (2) and considering first order approximation ($|\gamma_{ij}|$, $|\beta_{ij}|$ and $|\delta_{ij}|$ are also $\ll 1$), a linear system of equations for branch (i, j) can be written as

$$\begin{aligned} \mathbf{b}_{ij} &= \mathbf{H}_{ij} \begin{bmatrix} \xi_i^{\text{sys}} \\ \alpha_i^{\text{sys}} \\ \xi_j^{\text{sys}} \\ \alpha_j^{\text{sys}} \\ \eta_{ij}^{\text{sys}} \\ \psi_{ij}^{\text{sys}} \\ \eta_{ji}^{\text{sys}} \\ \psi_{ji}^{\text{sys}} \\ \gamma_{ij} \\ \beta_{ij} \\ \delta_{ij} \end{bmatrix} + \mathbf{E}_{ij} \begin{bmatrix} \xi_i^{\text{rnd}} \\ \alpha_i^{\text{rnd}} \\ \xi_j^{\text{rnd}} \\ \alpha_j^{\text{rnd}} \\ \eta_{ij}^{\text{rnd}} \\ \psi_{ij}^{\text{rnd}} \\ \eta_{ji}^{\text{rnd}} \\ \psi_{ji}^{\text{rnd}} \end{bmatrix} \\ &= \mathbf{H}_{ij}\mathbf{x}_{ij} + \mathbf{E}_{ij}\mathbf{e}_{ij} = \mathbf{H}_{ij}\mathbf{x}_{ij} + \boldsymbol{\epsilon}_{ij} \end{aligned} \quad (6)$$

where $\mathbf{b}_{ij}$ is the real-valued vector of constant terms (representing equivalent measurements) derived from (1) and (2) when real and imaginary coordinates are considered. $\mathbf{b}_{ij}$ includes multiple sets of equivalent measurements corresponding to (1) and (2) for each considered timestamp. The unknowns are common to all the timestamps and thus

$\mathbf{x}_{ij}$ is the vector of unknown quantities, which are all the parameter deviations and systematic errors. Vector $\mathbf{e}_{ij}$ includes all the random errors, while $\mathbf{H}_{ij}$ and $\mathbf{E}_{ij}$ are the measurement matrix and the random error transformation matrix, respectively. The former links equivalent measurements in $\mathbf{b}_{ij}$ to $\mathbf{x}_{ij}$ and the latter computes the associated equivalent random errors (included in $\boldsymbol{\epsilon}_{ij}$) from $\mathbf{e}_{ij}$.

Using N_t timestamps and four equations for each timestamp, we have $4N_t$ equations for each branch. It is possible to consider also multiple branches (e.g. N_{br} branches) together in the same estimation process. In this case, for the same timestamp, we have all the voltage and current measurements of all the considered branches and thus we can define an augmented model with $4N_tN_{\text{br}}$ equations. Instead of the vector of the unknowns for a single branch, we have a vector $\mathbf{x}$ of N unknown quantities corresponding to all the parameter deviations of the lines ($3N_{\text{br}}$ unknowns if all the branches have the same model as in Fig. 1) and to all the systematic errors of the measured synchrophasors. Since joint branches share the same node voltage measurements, the number of systematic errors in $\mathbf{x}$ can be $< 8N_{\text{br}}$. In addition, prior knowledge on the unknowns can be considered, thus defining an overall model as follows:

$$\mathbf{b}_{\text{tot}} = \begin{bmatrix} \mathbf{b}_{i_1 j_1} \\ \vdots \\ \mathbf{b}_{i_{N_{\text{br}}} j_{N_{\text{br}}}} \\ \mathbf{0}_{N\times 1} \end{bmatrix} = \begin{bmatrix} \mathbf{H} \\ \mathbf{I}_N \end{bmatrix} \mathbf{x} + \begin{bmatrix} \mathbf{E}\mathbf{e} \\ \mathbf{e}_{\text{prior}} \end{bmatrix} \quad (7)$$

$$= \mathbf{H}_{\text{tot}}\mathbf{x} + \boldsymbol{\epsilon}_{\text{tot}} \quad (8)$$

where $\mathbf{b}_{i_k j_k}$ includes the equivalent measurements of the kth considered branch ($k = 1, \ldots, N_{\text{br}}$), while $\mathbf{H}$ and $\mathbf{E}$ are the measurement and transformation matrices obtained considering all the branches and the corresponding equations like those in (6). Vector $\mathbf{e}$ is composed of the random errors for all the measured synchrophasors, $\mathbf{0}_{N\times 1}$ is the N-size zero vector and $\mathbf{I}_N$ is the N-size identity matrix. Prior values are given by $\mathbf{0}_{N\times 1}$ since they are all zeros (best assumption on deviations and systematic errors without further information) and $\mathbf{e}_{\text{prior}}$ includes the corresponding prior errors. Prior errors represent lack of knowledge and can thus be treated as random variables as discussed in Section III.

Starting from the model defined by (8), it is possible to estimate all the unknowns, i.e., to achieve an estimation of line parameters and systematic errors simultaneously for all the lines and measurement channels without requiring a preliminary calibration. A Weighted Least Squares (WLS) solution of (8) can be obtained by solving the following system:

$$(\mathbf{H}_{\text{tot}}^{\text{T}}\mathbf{W}_{\text{tot}}\mathbf{H}_{\text{tot}})\hat{\mathbf{x}} = \left(\mathbf{H}_{\text{tot}}^{\text{T}}\mathbf{W}_{\text{tot}}\right)\mathbf{b}_{\text{tot}} \quad (9)$$

where $\hat{}$ indicates the estimate and $\mathbf{W}_{\text{tot}}$ is the weighing matrix, which is the inverse of the covariance matrix of random vector $\boldsymbol{\epsilon}_{\text{tot}}$, indicated as $\boldsymbol{\Sigma}_{\boldsymbol{\epsilon}_{\text{tot}}}$ in the following.

III. MEASUREMENT ERRORS AND PRIOR INFORMATION

Considering prior information on the unknowns and random errors of PMU measurements as uncorrelated, it is possible to write:

$$\boldsymbol{\Sigma}_{\boldsymbol{\epsilon}_{tot}} = \begin{bmatrix} \boldsymbol{\Sigma}_{\boldsymbol{\epsilon}} & \mathbf{0} \\ \mathbf{0} & \Sigma_{\mathbf{e}_{\text{prior}}} \end{bmatrix} \quad (10)$$

where symbol $\boldsymbol{\Sigma}$ represents a covariance matrix (of the vector reported in the subscript), $\boldsymbol{\epsilon} = \mathbf{E}\mathbf{e}$ and $\mathbf{0}$ stands for a zero matrix of suitable size. From the law of propagation of uncertainty it follows

$$\boldsymbol{\Sigma}_{\boldsymbol{\epsilon}} = \mathbf{E}\boldsymbol{\Sigma}_{\mathbf{e}}\mathbf{E}^{\text{T}}. \quad (11)$$

To define $\Sigma_{\mathbf{e}}$ we have to consider all the random errors $\xi_{i_k}^{\text{rnd}}$, $\alpha_{i_k}^{\text{rnd}}$, $\xi_{j_k}^{\text{rnd}}$, $\alpha_{j_k}^{\text{rnd}}$, $\eta_{i_k j_k}^{\text{rnd}}$, $\psi_{i_k j_k}^{\text{rnd}}$, $\eta_{j_k i_k}^{\text{rnd}}$ and $\psi_{j_k i_k}^{\text{rnd}}$ for all the considered branches (i_k, j_k). In [11], these errors were assumed uncorrelated and associated with PMU uncertainty. Thus $\Sigma_{\mathbf{e}}$ was diagonal and included all the square standard uncertainties derived from PMU specifications (e.g., using maximum magnitude and phase-angle errors from instrument datasheet and assuming uniform distributions). To define $\Sigma_{\mathbf{e}_{\text{prior}}}$, two different considerations can be made:

- Prior variances $\sigma^2_{\gamma_{i_k j_k}}$, $\sigma^2_{\beta_{i_k j_k}}$ and $\sigma^2_{\delta_{i_k j_k}}$ are assumed from general considerations on the uncertainty of line parameters (e.g. relying on the TSO experience). Line parameter deviations are assumed uncorrelated (if further information is available, it can be integrated seamlessly). A mismatch between actual uncertainty and assumed values can occur and in [12] such issue is thus deeply investigated.

- Systematic errors in the measurement chain are considered uncorrelated (also in this case, if any prior knowledge is available it can be integrated). As mentioned above, in [11], systematic errors were attributed mainly to ITs and thus the variance of each error was derived from the IT class specification.

The presented assumptions allow computing $\Sigma_{\mathbf{e}}$ and $\Sigma_{\mathbf{e}_{\text{prior}}}$ and thus solving (9), but they might lead to possible issues in the algorithm configuration. Indeed, the measurement error of PMUs can be actually composed of both systematic and random errors and this would result in a transfer of uncertainty from $\Sigma_{\mathbf{e}}$ representing random error only to $\Sigma_{\mathbf{e}_{\text{prior}}}$. However, the amount of each error contribution is difficult to predict. For this reason, in the next section, the problem of uncertainty model mismatch and the robustness of the method against it are investigated by considering different PMU uncertainty scenarios while keeping the base configuration of the method.

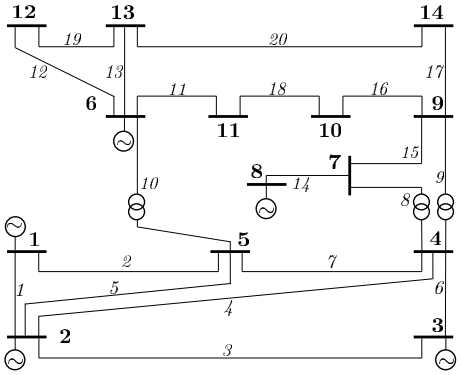

Fig. 2. IEEE 14 bus system with node and branch indices.

IV. TESTS AND RESULTS

A. Test assumptions

Tests have been performed via MATLAB simulations considering the IEEE 14 bus system (Fig. 2, [13]) and limiting the analysis to the first six branches (involving the first five buses). The algorithm is configured to work on all the branches simultaneously, considering $N_t = 100$ measurement timestamps for each estimation. In particular, 10 repeated measurements of the same load condition and 10 different load conditions (10 cases) are used for each test.

To assess the performance in each scenario, $N_{MC} = 10000$ Monte Carlo (MC) trials are used. In each trial, starting from a reference load condition, a powerflow is computed considering the actual line parameters to obtain the reference value of each measured quantity.

For each MC trial, the following conditions are considered:

1. The line parameters R_{ij}, X_{ij} and $B_{\text{sh},ij}$ are extracted from a uniform distribution with a maximum deviation of $\pm 15\,\%$ from R^0_{ij}, X^0_{ij} and $B^0_{\text{sh},ij}$, respectively (i.e., nominal values of the network).

2. All ITs are of Class 0.5 and thus maximum voltage and current magnitude errors are $0.5\,\%$, while maximum phase-angle displacements are 0.6 crad for VTs and 0.9 crad for CTs, respectively. Actual IT errors are extracted from uniform distributions.

3. The PMUs are compliant with the synchrophasor standard IEC/IEEE 60255-118-1:2018 [14]. Maximum errors for magnitudes (Δ_{mag}) and phase angles (Δ_{ang}) for both voltages and currents are assumed to vary from $\Delta_{\text{mag}} = 0.1\,\%$ and $\Delta_{\text{ang}} = 0.1$ crad (PMU accuracy A, in the following) to $\Delta_{\text{mag}} = 0.707\,\%$ and $\Delta_{\text{ang}} = 0.707$ crad (PMU accuracy B), depending on the test[1]. For each test, the values of Δ_{mag} and Δ_{ang} are numerically the same and are referred to as 'PMU accuracy' for the sake of brevity. In the different tests, percentage p ranging from $0\,\%$ to $75\,\%$ of systematic error has been associated with the PMU, for voltage and current measurements. This defines the maximum PMU systematic error of the measured quantity as follows:

$$\Delta^{\text{sys}}_{\text{mag}} = \frac{p}{100}\Delta_{\text{mag}} \tag{12}$$

$$\Delta^{\text{sys}}_{\text{ang}} = \frac{p}{100}\Delta_{\text{ang}} \tag{13}$$

PMU systematic errors are extracted from uniform distributions whose ranges are thus $\pm\Delta^{\text{sys}}_{\text{mag}}$ and $\pm\Delta^{\text{sys}}_{\text{ang}}$ for magnitudes and phase angles, respectively. PMU random errors are instead extracted from uniform distributions for each of the N_t timestamps in the trial and the considered maximum deviations are given by $\Delta^{\text{rnd}}_{\text{type}} = \Delta_{\text{type}} - \Delta^{\text{sys}}_{\text{type}}$, where type $\in \{\text{mag}, \text{ang}\}$.

4. The active and reactive power of loads and generators vary within $\pm 10\,\%$ (uniform distribution) of nominal value for all 10 cases in a trial.

In each MC trial, the systematic errors of the measurements are then the sum of two contributions, from IT and PMU.

B. Systematic errors estimation and compensation

To understand the impact of different values of p, we first focus on systematic error estimation. Figure 3 reports the average percent root mean square errors (RMSEs) of voltage magnitude systematic error estimation, i.e. the average on the nodes of the RMSE of ξ^{sys}_h ($h = 1, \ldots, 5$) estimates. This quantity represents also the root mean square residual compensation error and thus gives an idea of the capability to estimate the systematic component of the measurement chain. The results are obtained with PMU accuracy A and reported for different percentages of the PMU systematic error.

In Fig. 3, the RMSEs are compared with prior standard deviations, i.e., with the original standard uncertainty of ξ^{sys} (the generic node voltage magnitude systematic error), which is computed across all MC trials based on the extracted systematic errors and then averaged on the nodes. Prior values only slightly increase with p because, with $\Delta_{\text{mag}} = 0.1\,\%$, the additional contribution to systematic error brought by the PMU is much lower than IT contribution ($\sigma_{\xi^{\text{sys,VT}}_h} = 0.5/\sqrt{3}\,\%$). Average RMSE slightly decreases instead because PMU random errors decrease with higher p, thus confirming that, notwithstanding the mismatch in prior definition, the algorithm is still able to estimate the overall systematic error (which is reduced with respect to prior of about $49\,\%$, in absence of systematic error in PMU, and of about 52% when $p = 75\,\%$). Similar

[1]PMU accuracy B corresponds to about $1\,\%$ maximum total vector error (TVE) for synchrophasor measurement.

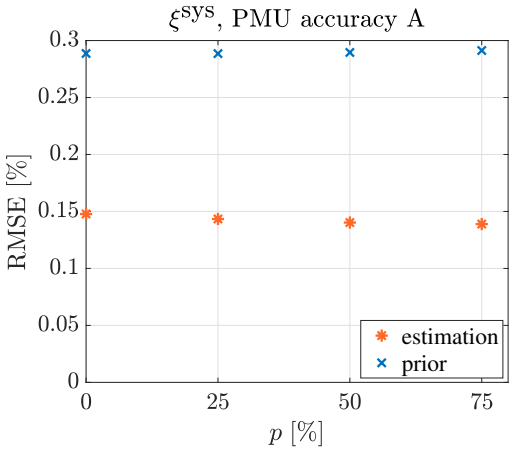

Fig. 3. Average RMSE of voltage synchrophasor magnitude estimation with a varying percentage of the PMU systematic error (PMU accuracy A).

considerations hold true also for voltage phase angles, and for current magnitudes and phase angles.

Figure 4 shows the same type of results obtained with PMU accuracy B. In this case, the contribution of PMU systematic errors is much larger, as proven by increasing prior values. Nevertheless, the algorithm is still able to reduce significantly the overall systematic error and the RMSE reduction with respect to prior is even larger with higher values of p, thanks to the reduced random contribution. In particular, the RMSE reduction is above 37% for $p = 0\,\%$, then it increases with p reaching the maximum improvement of about $44\,\%$ for $p = 75\,\%$.

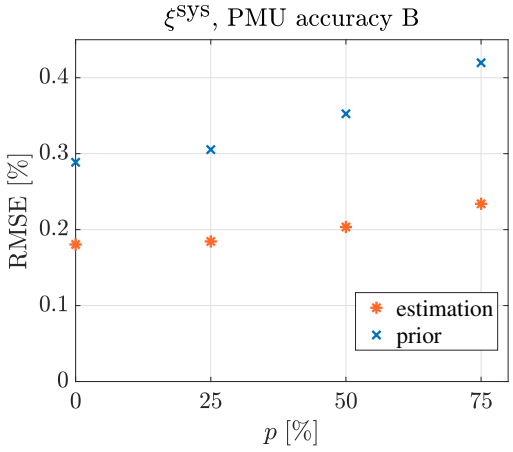

Fig. 4. Average RMSE of voltage synchrophasor magnitude estimation with a varying percentage of the PMU systematic error (PMU accuracy B).

C. *Line parameter estimation*

Previous results have shown that systematic errors in the measurement chain can be reduced significantly regardless of their origin and of possible lack of prior knowledge. However it is important to understand the effect of mismatch on the main target of the estimation, i.e., line parameters.

Figure 5 shows an example of the results on line parameters. Average percent RMSE values are reported for the estimates of γ_{i_k,j_k} $(k = 1, \ldots, 6)$ when PMU accuracy and p vary. As a term of comparison, prior values are always the same and equal to $15/\sqrt{3} = 8.66\,\%$ (with slight variations when deviations are actually extracted during MC trials). The results are extremely interesting and need to be carefully interpreted. First of all, the estimation accuracy increases with PMU accuracy as expected. Second, the impact of p is not straightforward. For low PMU accuracies, as mentioned before, PMU systematic error doesn't affect significantly the overall systematic error and thus the main impact is given by the reduced random contribution (with increasing values of p). It is also important to remember that, since the overall systematic error is the sum of two uniform distributions and the PMU contribution changes with p, the resulting trapezoidal distributions of systematic errors can differ significantly. When PMU accuracy degrades, the contribution of systematic error becomes more relevant and comparable with IT contribution. For this reason, resistance estimation starts to degrade with higher p even if the random contribution is reduced (see PMU accuracy B). However the maximum RMSE increase is less than $6\,\%$ with $p = 75\,\%$ and worst PMU accuracy, thus confirming the robustness of the method also to measurement model tuning degradation (higher prior mismatch).

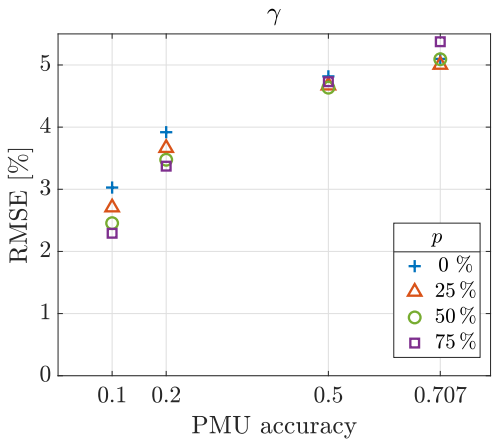

Fig. 5. Average RMSE of line resistance deviation with a varying percentage of the PMU systematic error and varying PMU accuracy.

V. CONCLUSIONS

In this paper, a recently proposed algorithm for transmission line parameters estimation relying on WAMS technology has been analyzed from the viewpoint of PMU measurement error model. Tests performed have shown that the systematic contribution of PMUs can be grasped by the estimation when highly accurate instruments are considered. When less accurate devices are used, the effect of additional systematic errors emerge. However, the impact of model mismatch is still low thus pointing to the algorithm robustness. These results are thus promising for method's applicability in real-word scenarios.

ACKNOWLEDGMENT

Dr. Pegoraro's work was partially funded by Fondazione di Sardegna for the research project "IQSS, Information Quality aware and Secure Sensor networks for smart cities", year 2020.

REFERENCES

[1] C. Muscas *et al.*, "New Kalman filter approach exploiting frequency knowledge for accurate PMU-based power system state estimation," *IEEE Trans. Instrum. Meas.*, vol. 69, no. 9, pp. 6713–6722, Sep. 2020.

[2] J. Fu, G. Song, and B. De Schutter, "Influence of measurement uncertainty on parameter estimation and fault location for transmission lines," *IEEE Trans. Autom. Sci. Eng.*, vol. 18, no. 1, pp. 337–345, Jan. 2021.

[3] A. Xue *et al.*, "Robust identification method for transmission line parameters that considers pmu phase angle error," *IEEE Access*, vol. 8, pp. 86 962–86 971, May 2020.

[4] M. Asprou, E. Kyriakides, and M. M. Albu, "Uncertainty bounds of transmission line parameters estimated from synchronized measurements," *IEEE Trans. Instrum. Meas.*, vol. 68, no. 8, pp. 2808–2818, Aug. 2019.

[5] M. Asprou and E. Kyriakides, "Identification and estimation of erroneous transmission line parameters using pmu measurements," *IEEE Trans. Power Del.*, vol. 32, no. 6, pp. 2510–2519, Dec. 2017.

[6] A. Wehenkel, A. Mukhopadhyay, J.-Y. L. Boudec, and M. Paolone, "Parameter estimation of three-phase untransposed short transmission lines from synchrophasor measurements," *IEEE Trans. Instrum. Meas.*, vol. 69, no. 9, pp. 6143–6154, Sep. 2020.

[7] C. Wang, V. A. Centeno, K. D. Jones, and D. Yang, "Transmission lines positive sequence parameters estimation and instrument transformers calibration based on pmu measurement error model," *IEEE Access*, vol. 7, pp. 145 104–145 117, Oct. 2019.

[8] Y. G. Kononov, O. S. Rybasova, and K. A. Sidirov, "Identification of overhead-line parameters from PMU data with compensation of systematic measurement errors," in *Int. Conf. on Ind. Eng., Appl. and Manuf. (ICIEAM)*, May 2018, pp. 1–5.

[9] H. Goklani, G. Gajjar, and S. A. Soman, "Instrument transformer calibration and robust estimation of transmission line parameters using PMU measurements," *IEEE Trans. Power Syst.*, vol. 36, no. 3, pp. 1761–1770, May 2021.

[10] C. Muscas, P. A. Pegoraro, C. Sitzia, A. V. Solinas, and S. Sulis, "Compensation of systematic measurement errors in PMU-based monitoring systems for transmission grids," in *IEEE Int. Instrum. and Meas. Technol. Conf. (I2MTC)*, 2021, pp. 1–6.

[11] C. Sitzia, C. Muscas, P. A. Pegoraro, A. V. Solinas, and S. Sulis, "Enhanced PMU-based line parameters estimation and compensation of systematic measurement errors in power grids considering multiple operating conditions," *IEEE Trans. Instrum. Meas.*, vol. 71, pp. 1–12, 2022.

[12] C. Muscas *et al.*, "Characterization of a PMU-based method for transmission line parameters estimation with systematic measurement error modeling," in *AEIT Int. Annual Conf.*, 2021, pp. 1–6.

[13] R. Abu-Hashim *et al.*, "Test systems for harmonics modeling and simulation," *IEEE Trans. Power Del.*, vol. 14, no. 2, pp. 579–587, Apr 1999.

[14] IEC, "IEEE/IEC international standard - measuring relays and protection equipment - part 118-1: Synchrophasor for power systems - measurements," *IEC/IEEE 60255-118-1:2018*, pp. 1–78, 2018.

25th IMEKO TC4 International Symposium
23rd International Workshop on ADC and DAC Modelling and Testing
IMEKO TC-4 2022
Brescia, Italy / September 12-14, 2022

Measurement issues on harmonic analysis according to the IEC 61000-4-7

Giovanni Artale [a], Giuseppe Caravello [a], Antonio Cataliotti [a], Valentina Cosentino [a], Vito Ditta [a]
Dario Di Cara [b], Nicola Panzavecchia [b] and Giovanni Tinè [b]
Nunzio Dipaola [c], Marilena G. Sambataro [c]

[a] *Department of Engineering, Università degli Studi di Palermo, 90128 Palermo, Italy; giovanni.artale@unipa.it; giuseppe.caravello02@unipa.it; antonio.cataliotti@unipa.it; valentina.cosentino@unipa.it; vito.ditta@unipa.it;*
[b] *Institute of Marine Engineering (INM), National Research Council (CNR), 90146 Palermo, Italy; dario.dicara@cnr.it; nicola.panzavecchia@cnr.it; giovanni.tine@cnr.it;*
[c] *STMicroelectronics S.r.l., Catania, 95121, Italy; nunzio.dipaola@st.com, marilena.sambataro@st.com*

***Abstract* – The objective of this article is an analysis of measurement issues related to the implementation of digital signal processing techniques for harmonic analysis, by means of FFT algorithm with different interpolation algorithms (linear, quadratic and cubic) and different sampling rates. A comparative analysis is made on errors on harmonics measurement obtained in the various case study analyses. Such errors are compared with the IEC 61000-4-7 limits. The study is supported by both simulation and experimental tests; these last are performed with different acquisition boards for signals acquisition.**

Keywords: harmonic analysis, power quality, power system measurements, IEC 61000-4-7

I. INTRODUCTION

Harmonics measurement of voltage or current is one of the key elements in the framework of power quality (PQ) assessment in power systems and there is an increasing interest in the integration of such measurements in common smart metering platforms. Several techniques can be found in literature for the implementation of spectral analysis for PQ measurements [1]–[4].

One of the most known algorithms is the Discrete Fourier Transform (DFT), which is also the one mainly considered by the IEC 61000-4-7 Standard. This algorithm can be used to estimate the amplitude of the harmonic components of the signal whatever the number of acquired samples available (not necessarily a power of two); this can be useful when the number of samples must be chosen to obtain a given observation window (for example 200 ms according to IEC 61000-4-7), depending on the sampling frequency of the data acquisition device. On the other hand, the main disadvantage of DFT is the computational cost, which is $O(N^2)$, being N the number of samples; in fact, if the measurement need is to obtain the spectral analysis results in a short time, it is necessary to have high-performance hardware. An alternative to DFT is its faster version, i.e. the Fast Fourier Transform (FFT) [5]–[8]. This algorithm has a computational cost lower than the DFT one, being equal to $Nlog_2(N)$; however, it needs N to be equal to a power of 2, to obtain the best computational performance.

This may pose a constraint in terms of sampling frequency, which should be set in accordance with the signal frequency and in order to allow having a proper number of samples for the FFT (in the specified synchronous observation window specified by the IEC Standards [1]-[2]). When this is not possible (for example in already existing devices with fixed or few selectable values for sampling frequency), a possible solution can be to use interpolation or zero padding techniques. In both cases they will cause some approximation of the signal and a consequent error on harmonic analysis (which will be the greater, the less accurate is the signal reconstruction). Limiting such errors is needed for obtaining a more accurate information, within the Standards error limits [1]-[2]. From a practical viewpoint, the implementation of harmonic analysis algorithms on low-cost devices is also a topical issue for PQ measurements; for typical smart metering platforms the optimization of the processing algorithm is crucial to perform the analysis in a short time and to limit the costs related to the hardware components. The FFT is obviously the most suitable algorithm (if compared to DFT); thus, it is necessary to find the best solutions for its implementation in low-cost devices, keeping errors within the limits imposed by the Standards.

In this framework, the aim of this paper is to analyse the performances of harmonic analysis implementation using FFT with different interpolation algorithms and sampling rates. The final aim is to demonstrate how these aspects can impact on the choice of the measurement device and its technical features. The paper is structured as follows: firstly, target measurement issues are considered for harmonic analysis. Secondly, a simulation study is presented to verify analytically how the considered issues impact on harmonic analysis. Finally, to verify the measurement issue impact in a real case implementation, some experimental tests are presented, which have been carried out with two different commercial data acquisition boards.

II. HARMONIC ANALYSIS MEASUREMENT ISSUES

The IEC 6100-4-7 standard imposes limits on the accuracy of harmonics for Class A instruments [2]. For the measurement of voltage harmonics, the Standard provides two different conditions that must be respected, depending on the amplitude of the harmonic measured U_m:

$$\text{Cond. 1: } U_m \geq 1\%\, U_{nom} \rightarrow e < \pm 0.05\, U_m \qquad (1)$$

$$\text{Cond. 2: } U_m < 1\%\, U_{nom} \rightarrow e < \pm 0{,}0005\, U_{nom} \qquad (2)$$

where U_{nom} is the voltage rated value.

The error in measuring the amplitude of the individual harmonics depends on how accurately the single harmonic is detected within the harmonic spectrum.

According to IEC 61000-4-30, the observation window (T_w) must be equal to 200 ms, i.e. 10 cycles of the fundamental frequency at 50 Hz [1], [9]; a maximum synchronization error is allowed of 0.03% of T_w; when such condition is not met, Hanning window can be applied. This may reduce the scallop loss errors in harmonics amplitudes measurement, while it does not have effect on frequencies measurements, unless further processing is made on spectrum samples (such as a frequency domain interpolation). To synchronize the sampling, the IEC 61000-4-30 require a preliminary measurement of the signal frequency; after this, sampling frequency f_s and number of acquired samples n can be set [10], [11]. In this viewpoint, a high sampling frequency allows acquiring more samples in the same T_w and to have a more accurate reconstruction of the signal. However, the processing of a high number of samples can be a problem for low-cost devices, in terms of memory and computational capabilities (to allow obtaining the measurements within the specified time constraints).

As regards the sampling synchronization, usually data acquisition system uses a fixed sampling frequency. This is the case of typical platforms for smart metering purposes, where f_s value is normally obtained by scaling the on-board clock frequency. This may lead f_s to be not suitable for acquiring a number of samples n equal to power of 2 in the considered observation window Tw. A possible solution is to apply an interpolation algorithm to the acquired samples (n), so to obtain the desired number of "interpolated" signal samples (N, equal to a power of 2) and enable the efficient FFT calculation, whatever f_s and n are. However, this introduces an approximation error on the acquired waveform reconstruction. In fact interpolation algorithms act approximating the part of signal between two consecutive points with a given function; their accuracy increases with the order of the approximation function and the number of samples n in the given Tw. So, the accuracy of the signal reconstruction will depend on both f_s, n and the chosen interpolation algorithm. On the other hand, as the order of the interpolation function increases, the computational cost necessary to implement the algorithm increases too.

To evaluate the effects of these parameters on the errors produced by the signal approximation, some case study results (of both simulation and experimental tests) are shown in the following sections.

III. SIMULATION TESTS

Simulations were performed using a LabVIEW software. A Virtual instrument (VI) has been built whose block diagram is shown in Fig. 1; it allows comparing the errors produced by the three proposed interpolation algorithms, in different sampling frequency conditions. In detail, the signal (sum of the fundamental component and its harmonics) is simulated with given sampling parameters (f_s and n, with $n/f_s = T_w$ and $n \neq$ power of 2); then it is interpolated with different algorithms (linear, quadratic and cubic) to obtain the 2-power number of samples (N). The interpolated signal is then processed by FFT. The values of the spectral components are compared with the set values of the individual harmonics (represented by the red arrows in Fig. 1) in order to evaluate the amplitude errors.

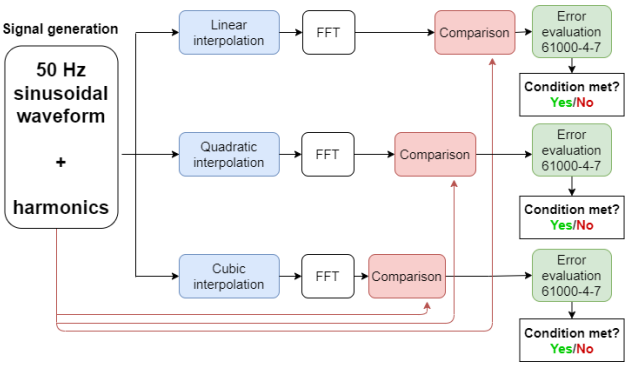

Fig. 1. - Block diagram of the VI used for simulations

Depending on harmonics amplitudes (higher or lower than 1%, see Cond. 1 or Cond. 2 reported above), the VI assesses whether the error limits are fulfilled or not. Since the IEC 61000-4-30 does not give any indication of the test waveform, the test signals used for the simulations were chosen in accordance with the standard IEC 50160 "Voltage characteristics of electricity supplied by public distribution systems" [12], [13]. The test signal had a fundamental frequency of 50 Hz, amplitude of 230 V RMS and added harmonics up to 50th order, with variable amplitudes as summarized in Table 1. The IEC 6100-4-7 imposes that limits on the accuracy of harmonics measurement for Class A must be fulfilled up to the 50th order harmonic; since IEC 50160 provides indications for harmonics up to the 25th, higher order harmonics were added according to the following scheme, similar to IEC 50160, as shown in Table 1:

- Even order harmonics: 0.5% of the fundamental;
- Odd order harmonics: 1.5% of the fundamental.

Simulations were carried out for three different sampling frequencies (f_s = 16, 24 and 32 kHz) and for three different interpolation algorithms (linear, quadratic and cubic). For each case study, the compliance has been verified with the error limits on harmonic analysis imposed by the Standard IEC 61000-4-7. The simulated cases are summarized in Table 2. The signal has an observation window T_w of 200 ms, according to IEC 61000-4-30 and IEC 1000-4-7. The number of signal samples n is given by:

$$n = f_s \cdot T_w \quad (3)$$

Table 1 - Harmonic components amplitude - IEC 50160

Even order harmonics		**Odd order harmonics**			
		three multiples		**no-three multiples**	
Order *h*	Relative amplitude *uh*	Order *h*	Relative amplitude *uh*	Order *h*	Relative amplitude *uh*
2	2,00%	3	5,00%	5	6,00%
4	1,00%	9	1,50%	7	5,00%
6...24	0,50%	15	0,50%	11	3,50%
		21	0,50%	13	3,00%
				17	2,00%
				19, 23, 25	1,50%
uh is the amplitude of the h-order harmonic relative to the amplitude of the fundamental component					

For interpolation and FFT calculation, N equal to 2048 or 4096 has been considered. The errors made with the different algorithms were compared with the IEC 61000-4-7 limit (according to *Cond.* 1 or *Cond.* 2, if measured harmonic amplitude is higher than 1% of the nominal voltage or not, respectively - see Section II). Results of two cases are reported in Fig. 2 and Fig. 3, for f_s equal to 16 kHz and 24 kHz, respectively (N = 2048).

Table 2 - Simulated cases

Case 1: f_s. = 16 kHz	n = 3200	N=2048 N= 4096
Case 2: f_s. = 24 kHz	n = 4800	N=2048 N= 4096
Case 3: f_s. = 32 kHz	n = 6400	N=2048 N= 4096
f_s. = sampling frequency; n= acquired samples; N = number of samples after the interpolation.		

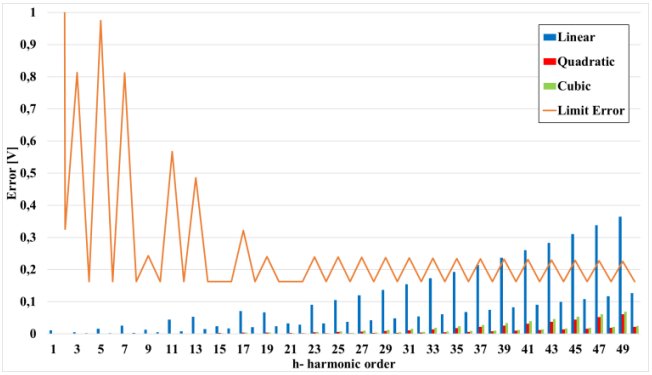

Fig. 2 – Simulation results; f_s = 16 kHz; interpolation with N = 2048 samples

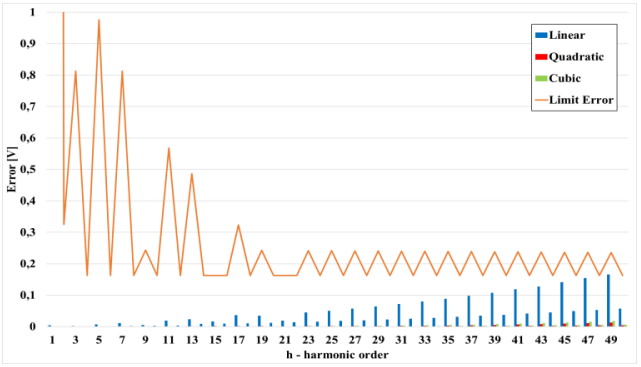

Fig. 3 - Simulation results; f_s = 24 kHz; interpolation with N = 2048 samples

Table 3 – Simulation results; compliance with IEC61000 4-7 limit errors

f_s. [kHz]	***16***	***16***	***24***	***24***	***32***	***32***
N	***2048***	***4096***	***2048***	***4096***	***2048***	***4096***
Linear interpolation	*Not verified*	*Not verified*	*Verified*	*Verified*	*Verified*	*Verified*
Quadratic interpolation	*Verified*	*Verified*	*Verified*	*Verified*	*Verified*	*Verified*
Cubic interpolation	*Verified*	*Verified*	*Verified*	*Verified*	*Verified*	*Verified*

In Fig. 2 it is possible to see that the error exceeds the limits in the case of interpolation with linear algorithm;

therefore, the adoption of this algorithm does not allow fulfilling the Standard requirements. On the contrary, as shown in Fig. 3, with a higher sampling frequency, the error is lower for all interpolation algorithms, including the linear one. The same results are obtained by interpolating at N = 4096 samples. Table 3 summarizes the results obtained. Cases where the error condition is not met are highlighted in red; cases when the error condition is met are highlighted in green, instead.

IV. EXPERIMENTAL TESTS

In order to validate the results previously obtained in simulation with an ideal signal, experimental tests were carried out using a real signal. The scheme of the test system is shown in Fig. 4. The signal was generated by using a Fluke 6100-A calibrator and it was acquired with a data acquisition board (DAQ). The generated signal is sampled at a given f_s and then it is interpolated with the different algorithms (linear, quadratic and cubic) to obtain the 2-power number of points N. Each interpolated signal is then processed by FFT. The values of the spectral components are compared with the respective values set on the power calibrator, in order to evaluate the errors (i.e. the power calibrator values were assumed as reference for errors evaluation).

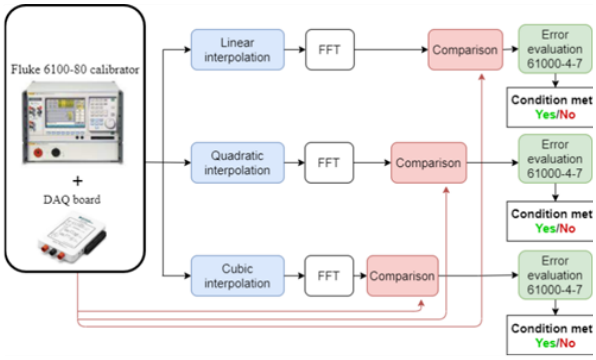

Fig. 4 - Scheme of the measurement setup and VI used for experimental tests

The tests were carried out with two DAQs, to compare the results obtained with different devices and ADC resolutions. The first board is a NI myDAQ board, which has a maximum sampling rate of 200 kHz, an input voltage range of 10 V and a 16-bit ADC. The second board is a NI 9252 board with 24-bit ADC, a maximum sample rate of 50 kHz and an input voltage range of 10 V. The test signal was a signal with a fundamental component (frequency 50 Hz, rms 7 V) and all harmonics up to the 50th, with amplitudes according to Table 1. For the tests with NI myDAQ the same sampling frequencies of previous simulations tests were used (16, 24 and 32 kHz). For NI 9252 the sampling frequency can be set according to the formula $f_s = \frac{f_M}{128 \cdot a}$, where a is an integer number (2,3,4….) and f_M is the DAQ Internal master time base (12.8 MHz). Thus the tests were carried out with signal frequencies of 16.67 kHz, 25 kHz and 33.34 kHz, (respectively for a=3, 4 and 5), in order to use the nearest possible values to those used for simulations and experimental tests with NImyDAQ. For both DAQs, the errors made with the different algorithms were compared with the limit imposed by the standard (as made for simulations). Ù

The errors results for the three interpolation algorithms are shown in Fig. 5 and Fig. 6 (for the NImyDAQ and the NI 9252, respectively). For the lowest sampling frequency, in both cases the errors made with the linear algorithm exceed the IEC 6100-4-7 limits, even if is visible that, with the same algorithm and number of interpolated points, the errors obtained with the NI 9252 board are lower than those obtained with the NImyDAQ (due to the better accuracy specifications). On the other hand, the error limits are fulfilled with both DAQs for the other tested sampling frequencies.

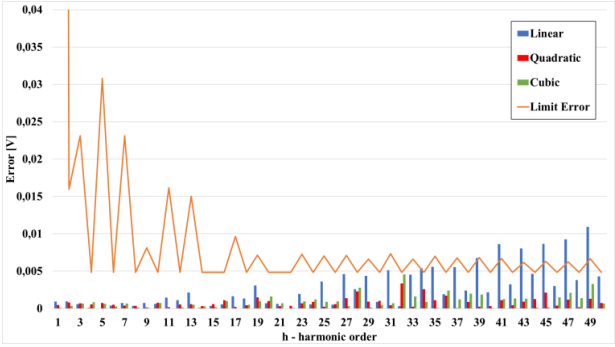

Fig. 5 – Experimental results - NImyDAQ, fs = 16 kHz; interpolation with N = 2048 samples

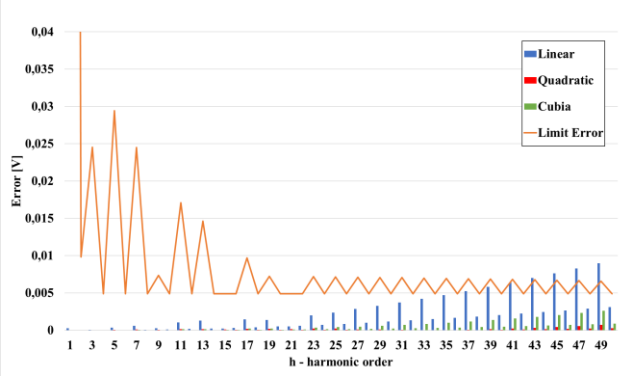

Fig. 6 - Experimental results - NI 9252, f_s = 16.67 kHz; interpolation with N = 2048 samples

Table 4 summarizes the results obtained in all tests. Cases where the error condition is not met are highlighted in red; cases where the error condition is met are highlighted in green, instead. As can be seen, the experimental results are in accordance with the simulations, even considering the different DAQs

accuracies. For the lowest value of f_s (around 16 kHz) the linear interpolation algorithm does not allow to meet the IEC 6100-4-7 limits) for both DAQs and both values of N (2048-samples and 4096-samples interpolation). For all tested sampling frequencies, results within the IEC 6100-4-7 limits were obtained with the quadratic and cubic algorithms, instead.

Table 4 – Experimental results; compliance with IEC61000 4-7 limit errors

NImyDAQ						
f_s. [kHz]	***16***	***16***	***24***	***24***	***32***	***32***
N	***2048***	***4096***	***2048***	***4096***	***2048***	***4096***
Linear interpolation	*Not verified*	*Not verified*	*Verified*	*Verified*	*Verified*	*Verified*
Quadratic interpolation	*Verified*	*Verified*	*Verified*	*Verified*	*Verified*	*Verified*
Cubic interpolation	*Verified*	*Verified*	*Verified*	*Verified*	*Verified*	*Verified*
NI 9252						
Linear interpolation	*Not verified*	*Not verified*	*Verified*	*Verified*	*Verified*	*Verified*
Quadratic interpolation	*Verified*	*Verified*	*Verified*	*Verified*	*Verified*	*Verified*
Cubic interpolation	*Verified*	*Verified*	*Verified*	*Verified*	*Verified*	*Verified*

V. PRELIMINARY ANALYSIS ON COMPUTATIONAL COST

In addition to the impact on harmonic analysis results, the choice of the interpolation function determines also an impact on the overall computation cost of the processing algorithm. Thus, it must be made considering the computational capabilities and performances of the hardware device where the algorithm is meant to be implemented. In fact, the higher the order of the interpolation function, the higher the number of operations needed to perform the interpolation. For a given value of N, the cubic interpolation (third-order polynomial function) will require an higher computational burden than the quadratic one (second-order polynomial function), which in turn will require an higher computational burden than the linear interpolation (first-order polynomial function), Depending on the processing capabilities of the hardware device, this implies more time required to perform all operations and, in some cases, the interpolation implementation can be not feasible, especially in low-cost devices (with limited memory, speed and computational features).

For example, the operations required for each interpolation algorithm (linear, quadratic cubic) are reported in Table 5, for both cases of N = 2048 and N = 4096 points. The total number of required operations for the harmonic analysis computation is given by the sum of interpolation and FFT algorithms operations. It should be noted that the number of operations does not depend on the sampling frequency but only on N value.

Table 5 – Computational cost. Number of operations vs. interpolation algorithm

		Number of operations		
		FFT	**Interpolation algorithm**	**Total**
N = 2048	Linear Algorithm	22528	12288	34816
	Quadratic Algorithm	22528	45056	67584
	Cubic Algorithm	22528	65536	88064
N = 4096	Linear Algorithm	49152	18432	67584
	Quadratic Algorithm	49152	90112	139264
	Cubic Algorithm	49152	131072	180224

CONCLUSIONS

This paper has presented a study on the effectiveness of time-domain interpolation algorithms for the implementation of harmonic analysis on common smart metering platforms, according to IEC 61000-4-7. The study has investigated the feasibility of using such algorithms when the meter sampling frequency does not allow to obtain the synchronous observation window with a suitable number of acquired samples for the efficient FFT implementation (i.e. equal to a power of 2).

The study has been aimed at evaluating how sampling frequency and the interpolation algorithm used for the implementation of FFT can affect the error on harmonics measurement. Different case studies have been analysed and compared, in order to study the impact of the sampling frequency and interpolation function (linear, quadratic and cubic) on both spectral analysis accuracy and algorithm complexity. Actually, a suitable trade-off between such features is crucial for the implementation of PQ measurements, according to IEC 61000-4-30 ad 61000-4-7, even in low cost devices, keeping the errors on harmonics measurement below the limits imposed by such Standards. To reach the performances of the highest accuracy class (Class A) is mandatory to use high efficiency but not complex solutions, to limit the need for expensive hardware components, without worsening the measurement accuracy.

Different simulations were carried out both in LabVIEW environment with an ideal signal and with a real signal acquired with DAQ boards. The results show that, with a given sampling frequency, it is not always possible to use the linear interpolation algorithm, so it is necessary use more complex algorithms, with higher computational cost. This could be not feasible for a commercial device, depending on its speed, computation and memory capabilities. This will result in the need for more powerful data acquisition systems and more memory capabilities for the storage of acquired samples Alternatively, when it is possible to increase the sampling rate, simpler interpolation algorithm can be used (as the linear one).

ACKNOWLEDGEMENT

The research presented in this paper received the financial support of the European Union in the following grants:

- PO FESR Sicilia 2014-2020, Action 1.1.5, Project n. 08000PA90246, Project title: “Smart grids per le isole minori (Smart grids for small islands)”, acronym: I-Sole CUP G99J18000540007;
- Program IEV CT Italie Tunisie 2014-2020, Project n. IS_2.1_131, Project acronym: SInERT, CUP: B74I19001040006 and B74I18014130002, Project title: “Solution innovantes pour l’intégration des énergies renouvelables sur le réseau électrique tunisien”.

The paper contents are the sole responsibility of the authors and they do not necessarily reflect either the point of view of the European Union or that of the Program Managing Authority.

REFERENCES

[1] IEC61000-4-30/ 2015-12-Electromagnetic compatibility (EMC) Part 4-30: Testing and measurement techniques - Power quality measurement methods.

[2] CEI EN 61000-4-7/A1-2010-11 - Electromagnetic compatibility (EMC) Part 4-7: Testing and measurement techniques - General guide on harmonics and interharmonics measurements and instrumentation, for power supply systems and equipment connected thereto.

[3] A. E. Legarreta, J. H. Figueroa, e J. A. Bortolin, “An IEC 61000-4-30 class A Power quality monitor: Development and performance analysis”, in 11th International Conference on Electrical Power Quality and Utilisation, Lisbon, Portugal, Oct. 2011, pp. 1–6.

[4] R. Athiya e Dr. A. K. Sharma, “A review of experimental study of power quality monitor on harmonic measurement”, Int. J. Eng. Technol. Manag. Res., vol. 7, n. 6, 2020, pp. 156–159.

[5] A. Kalair, N. Abas, A. R. Kalair, Z. Saleem, e N. Khan, “Review of harmonic analysis, modeling and mitigation techniques”, Renew. Sustain. Energy Rev., vol. 78, Oct. 2017, pp. 1152–1187.

[6] B. N. Mohapatra e R. K. Mohapatra, “FFT and sparse FFT techniques and applications”, in 2017 Fourteenth International Conference on Wireless and Optical Communications Networks (WOCN), Mumbai, India, Feb. 2017, pp. 1–5.

[7] Hsiung Cheng Lin, “Inter-Harmonic Identification Using Group-Harmonic Weighting Approach Based on the FFT”, IEEE Trans. Power Electron., vol. 23, n. 3, May 2008, pp. 1309–1319.

[8] T. Tarasiuk, “Comparative Study of Various Methods of DFT Calculation in the Wake of IEC Standard 61000-4-7”, IEEE Trans. Instrum. Meas., vol. 58, n. 10, Oct. 2009, pp. 3666–3677.

[9] T. Radil e P. M. Ramos, “Power quality detection and classification method for IEC 61000-4-30 Class A instruments”, in 2010 IEEE Instrumentation & Measurement Technology Conference Proceedings, Austin, TX, May 2010, pp. 691–696.

[10] G. Artale et al., “PQ and Harmonic Assessment Issues on Low-Cost Smart Metering Platforms: A Case Study”, (2020) Sensors (Switzerland), 20 (21), art. no. 6361, pp. 1-27.

[11] D. Kumar e F. Zare, “Harmonic Analysis of Grid Connected Power Electronic Systems in Low Voltage Distribution Networks”, IEEE J. Emerg. Sel. Top. Power Electron., vol. 4, n. 1, pagg. 70–79, mar. 2016, doi: 10.1109/JESTPE.2015.2454537.

[12] CEI EN 50160/A1 - Caratteristiche della tensione fornita dalle reti pubbliche di distribuzione dell’energia elettrica (in Italian).

[13] C. Masetti, “Revision of European Standard EN 50160 on power quality: Reasons and solutions”, in Proceedings of 14th International Conference on Harmonics and Quality of Power - ICHQP 2010, Bergamo, Italy, set. 2010, pagg. 1–7. doi: 10.1109/ICHQP.2010.5625472.

25th IMEKO TC4 International Symposium
23rd International Workshop on ADC and DAC Modelling and Testing
IMEKO TC-4 2022
Brescia, Italy / September 12-14, 2022

Bidirectional electricity meter metrological evaluation

Marcelo M Costa[1]

[1] *Eletrobras Eletronorte, Rod. Arthur Bernardes, 2172, Belém, Brazil, marcelo.melo@eletronorte.gov.br*

***Abstract* – This paper presents metrological evaluation of bidirectional electricity meters, comparing its performance when measuring electrical energy in direct and reverse power flows. Evaluation results shown that the difference between measuring results in both directions is not significant compared to the measurement uncertainty and to the maximum permissible errors. In this evaluation, four IEC 0,2S and 0,5S accuracy classes electricity meters were tested.**

I. INTRODUCTION

Electricity meters have been in use since the late 1800's when electric power began to be used by countries. Today, two types of meter technologies are available: induction electromechanical and static electronic. Both types are considered integrating devices, measuring the power consumed over a period of time. These meters are essentially one way. Figure 1 shows electromechanical and electronic electricity meters.

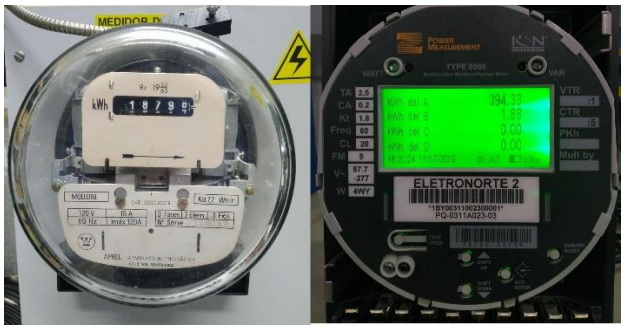

Fig. 1. Electromechanical and electronic electricity meters.

The advance of smart grids, renewable energy and distributed generation of electrical energy require measurement in bidirectional way, as the users take energy from the grid and also supply energy to the grid. Other situation that requires bidirectional measurement is the energy interchange between electrical grids. Traditional electricity meters are not able to measure bidirectional electrical energy, so a special meter is required [1,2]. National and international standards and other metrological policies state that bidirectional electricity meters should meet metrological requirements in both power flow directions [3, 4, 5, 6].

This paper presents metrological evaluation of bidirectional electricity meters in direct and reverse power flow. Test setup is shown, as well as test results, including measurement uncertainty.

II. BIDIRECTIONAL ELECTRICITY METER

A four-quadrant or bidirectional electricy meter measures electrical energy in both power flow directions: direct (delivered active power), or from the source to the load, and reverse, from the load to the source (received active power). Figure 2 shows four-quadrant operation mode. Table 1 shows four-quadrant power flow relationships [7, 8]. This is the case of smart meters, one of the most important devices used in the smart grids.

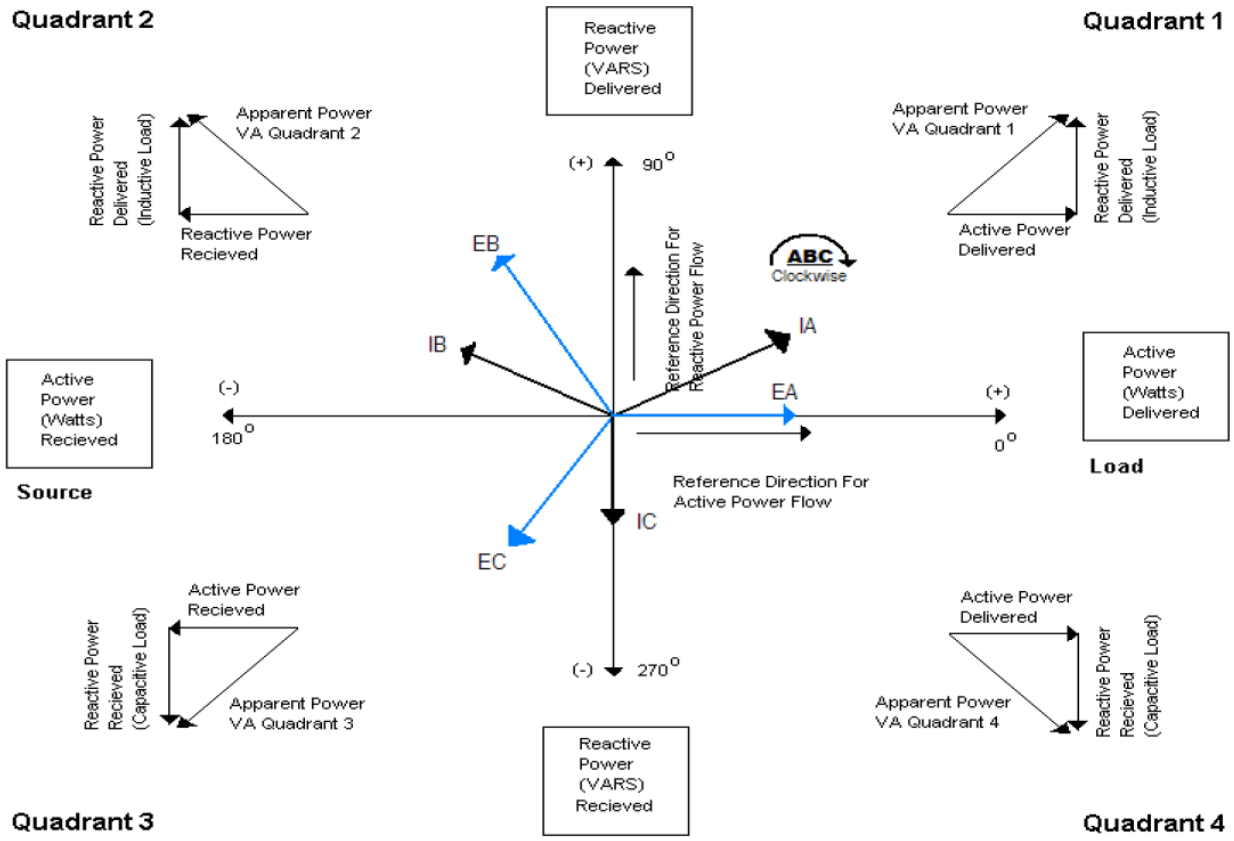

Fig. 2. Four-quadrant electricity measurement [8].

Table 1. Four-quadrant power flow relationships [8].

Apparent power Quadrant	Active power flow direction	Active power flow direction
1	Delivered	Delivered
2	Received	Delivered
3	Received	Received
4	Delivered	Received

Accuracy requirement shoud be met by the meters in both directions, so performance tests must include accuracy evaluation in direct and reverse operation modes.

III. TEST SETUP

In the experimental tests, some electricy meters were calibrated in laboratory conditions, using appropriate methods and standards. Ambient temperatute was (23 ± 2) ºC and relative humidity was (40 ± 10) %. A 3-phase voltage and current source was used to supply electrical energy to the meters under test and to the reference standard. Two power sources were available: one Zera model MT-500 and one Omicron model CMC 256plus.

The reference standard was from Radian Research, model RD-30, which was traceable to the Brazilian standards. Its maximum error is (0.02% / Cos φ) or (0.02% / Sin φ), according to its manufacturer.

Voltage and current from the source were supplied to the meters under test and to the reference standard. After the measurement of a defined amount of energy, meters under test generates a pulse. This amount of energy per pulse is the meter constant, which must be informed to the reference standard. Pulse output of the meters were connected to the reference standard pulse input, which displayed the measurement error of the meters after each integration period of about 50 s. At least 5 readings were taken at each calibration point. Reported measurement uncertainty was estimated using [9]. Figure 3 shows the block diagram of the test setup.

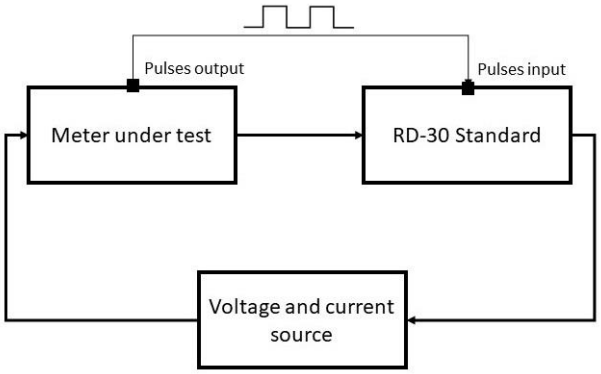

Fig. 3. Block diagram of the test setup.

Calibration points used are shown in Table 2. Frequency was line frequency of 60 Hz, and V_N and I_N are the nominal voltage and current of the meters. Each calibration point was measured in direct and reverse power flow.

Table 2. Calibration points.

Active energy (Wh)			Reactive energy (varh[1])		
Voltage (V)	Current (A)	Cos φ	Voltage (V)	Current (A)	Sin φ
V_N	I_N	1	V_N	I_N	1 i
		0.5 i			0.5 i
		0.8 c			0.8 c
	$0.1I_N$	1		$0.1I_N$	1 i

Four electricity meters were tested: three 0,2S IEC (active energy) and class D INMETRO (active and reactive energy) accuracy class and one 0,5S IEC and class C INMETRO accuracy class. All meters were tested at nominal voltage of 66.4 V and nominal current of 5 A. Figure 4 shows the RD-30 standard and two 0,2S accuracy classe electricity meters, and Figure 5 shows the Omicron CMC 256plus three phase voltage and current source.

Fig. 4. Radian RD-30 standard (left) and two IEC 0,2S accuracy class electricity meters (right).

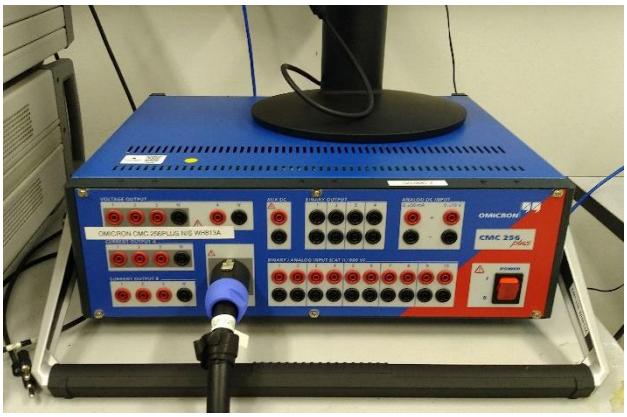

Fig. 5. Omicron CMC 256plus three phase voltage and current source.

IV. TEST RESULTS

This section shows some of the calibration results of the electricity meters under test. The meters were calibrated in active energy and reactive energy, as the meters also meet brazilian metrological requirements and policies for reactive energy meters. Measurement uncertainty was estimated using [10].

Table 3 and Figure 6 show the calibration results for active energy (Wh) of one of the 0,2S and D accuracy class meters, where "D" refers to direct power flow direction and "R" refers to reverse direction, *e* is the measurement error and *U* is the measurement uncertainty (95.45%, 2σ). Maximum permissible error is 0.2 % for cos φ = 1 and 0.3 % for cos φ = 0.5 ind. As it can be seen, absolute error diference is 0.004% in both calibration points, much smaller than measurement uncertainty. For cos φ = 1, the ratio (absolute error diference) / (measurement uncertainty) is 0.2 and measurement uncertainty is $1/10^{th}$ of the maximum permissible error, while for cos φ = 0.5 ind, the ratio (absolute error diference) / (measurement uncertainty) is about 0.11, and measurement uncertainty is about 1/8 of the maximum permissible error.

Table 3. 0,2S and D accuracy class electricity meter calibration results (Wh).

Calibration point	e (%)	U (%)
66.4 V - 5 A – Cos φ=1 (D)	-0.081	0.020
66.4 V - 5 A - Cos φ=1 (R)	-0.085	0.020
66.4 V - 5 A - Cos φ=0.5 ind (D)	-0.094	0.037
66.4 V - 5 A - Cos φ=0.5 ind (R)	-0.098	0.035

[1] Although VARh is used many times, IEC defines varh or varh.h as the unit symbol for reactive power [9].

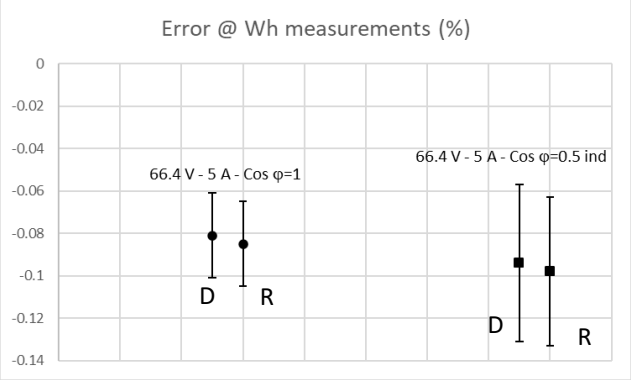

Fig. 6. 0,2S and D accuracy class electricity meter calibration results (Wh).

Table 4 and Figure 7 show the calibration results for reactive energy (varh) of the same ION 8500 electricity meter. Maximum permissible error, according to INMETRO D accuracy class, is 0.4 % for Sin φ = 1 ind and 0.6 % for Sin φ = 0.5 ind. Absolute error difference is quite small for sin φ = 1 ind, but it increases for sin φ = 0.5 ind. For sin φ = 1 ind, the ratio (absolute error diference) / (measurement uncertainty) is 0.25, while for for sin φ = 0.5 ind, the ratio (absolute error diference) / (measurement uncertainty) is about 0.55.

Table 4. D accuracy class electricity meter calibration results (varh).

Calibration point	e (%)	U (%)
66.4 V - 5 A - Sin φ=1 (D)	-0.088	0.020
66.4 V - 5 A - Sin φ=1 (R)	-0.083	0.020
66.4 V - 5 A - Sin φ=0.5 ind (D)	-0.078	0.037
66.4 V - 5 A - Sin φ=0.5 ind (R)	-0.058	0.035

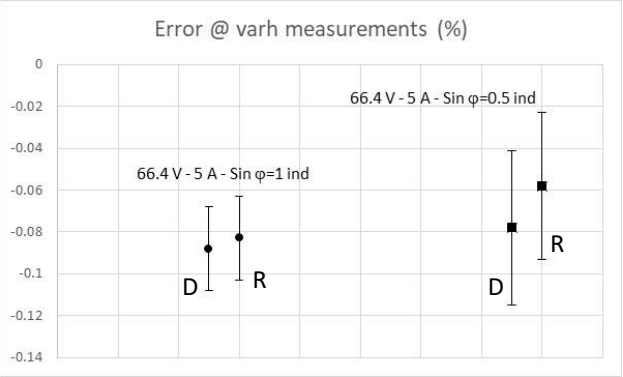

Fig. 7. D accuracy class electricity meter calibration results (varh).

Table 5 and Figure 8 show the calibration results for active energy (Wh) of the IEC 0,5S and INMETRO C accuracy class electricity meter. Maximum permissible error is 0.5 % for cos φ = 1 and 0.6 % for cos φ = 0.5 ind. Absolute error diference is 0.005% and 0.006%, much smaller than measurement uncertainty. For cos φ = 1, the ratio (absolute error diference) / (measurement uncertainty) is 0.25 and measurement uncertainty is about 1/25 of the maximum permissible error, while for for cos φ = 0.5 ind, the ratio (absolute error diference) / (measurement uncertainty) is about 0.16.

Table 5. 0,5S and C accuracy class electricity meter calibration results (Wh).

Calibration point	e (%)	U (%)
66.4 V - 5 A – Cos φ=1 (D)	0.007	0.020
66.4 V - 5 A - Cos φ=1 (R)	0.002	0.020
66.4 V - 5 A - Cos φ=0.5 ind (D)	0.012	0.037
66.4 V - 5 A - Cos φ=0.5 ind (R)	0.006	0.037

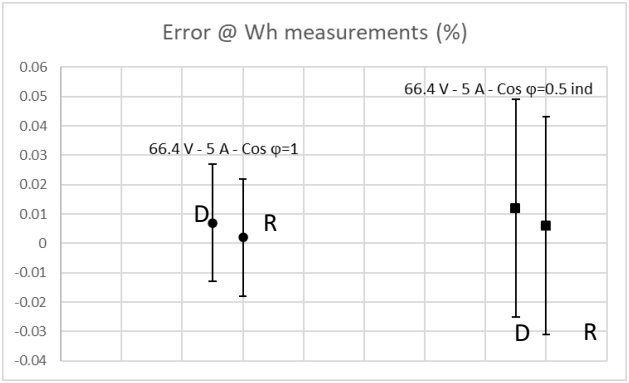

Fig. 8. 0,5S and C accuracy class electricity meter calibration results (Wh).

Table 6 and Figure 9 show the calibration results for reactive energy (varh) of the INMETRO C accuracy class electricity meter. Maximum permissible error is 1.0 % for Sin φ = 1 ind and 1.2 % for Sin φ = 0.5 ind. Absolute error difference is 0.003% for sin φ = 1 ind and sin φ = 0.5 ind, while the ratio (absolute error diference) / (measurement uncertainty) is 0.15 and about 0.08.

Table 6. C accuracy class electricity meter calibration results (varh).

Calibration point	e (%)	U (%)
66.4 V - 5 A – Sin φ=1 (D)	-0.034	0.020
66.4 V - 5 A - Sin φ=1 (R)	-0.037	0.020
66.4 V - 5 A - Sin φ=0.5 ind (D)	-0.035	0.037
66.4 V - 5 A - Sin φ=0.5 ind (R)	-0.032	0.037

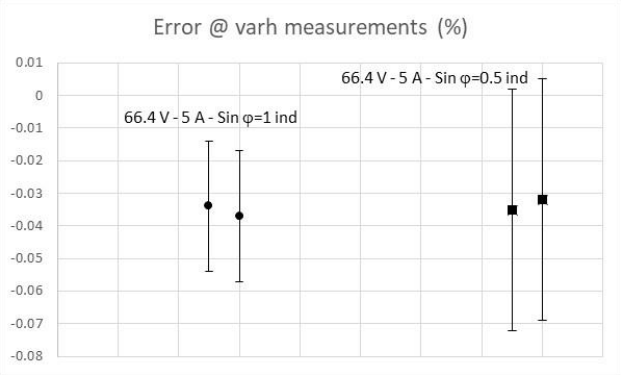

Fig. 9. C accuracy class electricity meter calibration results (varh).

V. ANALYSIS

The tests presented in Section IV shown that, for the four electricity meters tested, calibration results at each point were statistically the same for both direct and reverse power flow directions, since the difference between calibration values were much smaller than associated measurement uncertainty. The highest ratio of (calibration result difference) / (measurement uncertainty) was about 0.55, but most of these ratios were close to 0.1. Measurement uncertainty was appropriate for all calibration points, as it was always smaller than 1/5 of the maximum permissible error. These results were very satisfactory considering meter's maximum permissible error required by IEC and INMETRO standards, so these meters can be reliably used in bidirectional electric energy metering.

As the tests were performed only under sinusoidal voltage and current conditions, it is possible that under different conditions, for example, when voltage and current waveforms are distorted by harmonic components, the results are not so satisfactory. This condition can be found where renewable power generation systems, as photovoltaic, are connected to the grid.

VI. CONCLUSION

This paper presented metrological evaluation of bidirectional electricity meters when measuring electrical energy in direct and reverse power flows. The calibration results shown that the difference of direct and reverse calibration values is not significant, much smaller than measurement uncertainty and maximum permissible errors, so they can be reliably used in bidirectional electric energy metering. As only 0,2S and 0,5S accuracy classes electricity meters were evaluated this time, for further work, it is planned to test less accurate electricity meters, as classes 1 and 2 meters. It is also planned to test the meters under non-sinusoidal conditions, as voltage and current waveforms distorted by harmonic components.

REFERENCES

[1] Z.Li, B. Lianping, "Research about bi-directional electronic energy meter and power quality analyzers", hird International Conference on Instrumentation, Measurement, Computer, Communication and Control, 2013, pp. 1323-1327.

[2] B. Paul, S. Mondal, D. Ghosh and D. K. Mohanta, "Reactive Power Pricing Through Phasor Measurement Based Bi-Directional Energy Meter," 2nd Int. Conf. on Power, Energy and Environment: Towards Smart Technology (ICEPE), 2018, pp. 1-6, doi: 10.1109/EPETSG.2018.8658500.

[3] IEC 62052-11, "Electricity metering equipment – General Requirements, tests and test conditions," 2020.

[4] IEC 62053-22, "Electricity metering equipment – Particular requirements – Static meters for AC active energy (classes 0,1 S, 0,2 S and 0,5 S)", 2020.

[5] Brazilian Electrical Energy Agency (ANEEL) Grid Procedure 6.16, "Electrical Energy Billing System Maintenance", 2021.

[6] INMETRO Document 587/2012, "Metrological technical regulation for electronic meters of active/reactive electric energy, single phase and polyphase, including refurbished ones", 2012.

[7] M. Bearden, "Understanding Power Flow and Naming Conventions In Bi-directional Metering Applications", avaliable on https://www.landisgyr.com/webfoo/wp-content/uploads/2012/09/Power_Flow_2.pdf.

[8] R.H.Stevens, "Power Flow Direction Definitions For Metering Of Bidirectional Power", IEEE Trans. on Power App. and Syst., vol. PAS-102, no. 9, pp. 3018-3022, 1983, doi: 10.1109/TPAS.1983.318107.

[9] IEC 60027-1, "Letter symbols to be used in electrical technology – Part 1: General", 2005;

[10] BIPM JCGM 2008, "Evaluation of measurement data — Guide to the expression of uncertainty in measurement", 2008.

25th IMEKO TC4 International Symposium
23rd International Workshop on ADC and DAC Modelling and Testing
IMEKO TC-4 2020
Brescia, Italy / September 12-14, 2022

Application Scenarios for Gait Analysis with Wearable Sensors and Machine Learning

Mauro D'Arco[1], Martina Guerritore[1], Annarita Tedesco[2]

[1]*University Federico II of Naples (DIETI), via Claudio 21, 80125 Napoli ITALY*
[2]*IMS Lab., University of Bordeaux, Cours de la liberation, 33405 Talence cedex, FRANCE*

***Abstract* – The digital revolution that characterizes the beginning of the 4.0 Era has already prompted out a variety of smart living technologies, which rely on the pervasive connectivity granted by the Internet of Things. These technologies are having a relevant impact on health systems, working and domestic environments, sports and rehabilitation, by enabling new promising practices for human body kinematic studies. This paper provides a specific discussion on how kinematic studies in clinical diagnosis, rehabilitation and sport, take benefit from the use of the recent smart living technologies. More specifically, in exploring the latest trends in the application of gait analysis using wearable sensors and Machine Learning techniques.**

I. INTRODUCTION

As well known, smart sensors are about designing systems people can and will use, regardless of the contexts they are living or working in. Their innovation is pervasive and impacts a variety of fields, such as Home, Workplace, Governance, Manufacturing, Commerce, Health, Infrastructure, Agriculture, Mobility, Energy and many others.

Internet of things (IoT) technologies are the recognized tools to operate on these playgrounds and transform the traditional solutions into innovative schemes, capable of enabling the smart services that are expected to watermark the 4.0 Era.

A number of novel sensors with built-in IoT solutions for (wireless) data transfer to the cloud are receiving more and more attention. Among the others, the compact inertial measurement units (IMU), which embed tri-axial accelerometers, gyroscopes, and magnetic field sensors, are widely integrated into smartphones, smartwatches, or sold as nice wearable accessories, that are aimed at monitoring biological and bio-mechanical parameters, and are perhaps the most promising; the compact inertial measurement units (IMU), are in general widely used to measure kinematic parameters[1, 2].

The gait analysis deals with the scientific evaluation of the human locomotion, which requires the measurement of the kinetic and kinematic parameters characterizing the stride as the basic constituent of the walk. The traditional practice used video camera systems [3] to perform qualitative monitoring approaches. But, the analysis of video recordings obtained from multi-camera systems required laboratories, expensive equipment and extended times for system calibration and subject preparation. Nonetheless, the tests carried out in the laboratory did not perfectly reflect the natural movements because of the patient's behavior in a laboratory, could be different from that in everyday life [4].

At present, the gait analysis is taking benefits from the use of wearable sensors, which are quite inexpensive, suitable for tests outside the laboratory environment, and capable of recording physiological conditions and movement activities in unspoiled conditions.

Hereinafter, the attention is mainly paid to the gait analysis, which is receiving more and more credit as a viable tool for ergonomics, training program evaluation for athletes, and clinical assessment in orthopedics, neurology, and several other fields focused on musculoskeletal disorders [5, 6] . For example, gait analysis provides useful indicators for the early diagnosis of Parkinson's disease. Specifically, the affected patients exhibit poor movement of the facial, upper and lower limb muscles, and flexed-forward trunk, that implies difficulty with stop and turn movements. Consequently, the space and time parameters of the gait cycle, such as gait velocity, cadence, stride time, and length are different with respect to those measured for healthy subjects [7].

Gait analyses are useful for objectively evaluating the functionality after arthroplasty and identifying joint overloads with possible gait deficits. For example, the presence of persistent walking abnormalities after knee arthroplasty surgery is sometimes detected in clinically asymptomatic patients, and significant alterations of kinematic parameters, such as reduction in walking speed, increase in the stance phase duration, decrease in a joint excursion, can be detected even a long time after surgery [8]. The walking speed is commonly lower than in normal subjects, even in the presence of good clinical conditions and absence of pain [9]. To give an example, gait analysis plays a role in rehabilitation treatment planning, choice/adaptation of an orthosis, functional surgery proposal, pre- and post-operative comparison in the rehabilitation of stroke victims. It is at the bases of rehabilitation programs for patients with lower limb prostheses, or patients that have suf-

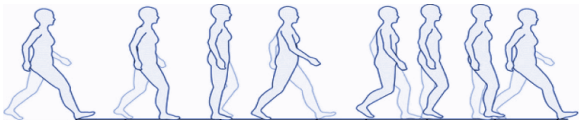

Fig. 1. Gait phases of a normal gait cycle: stance phase and swing phase

fered bone lesions or fractures. The outcomes of the analysis allow suitable refinements of the rehabilitation program and reduce any abnormal stresses on the prosthetic or injured limb. The remote control offers many advantages, such as allowing continuous monitoring of the patient, which is not available in classic monitoring. During rehabilitation, the caregiver can remotely guide the patient in carrying out exercises and eventually modifying the rehabilitation program. The clinical history of the patient is easily available, and large savings related to the monitoring costs of hospital structures are possible [10, 11].

The purpose of the paper is providing a discussion on the main applications where gait kinematic analysis takes benefits by means of IMU sensors and machine learning. To this end, the possibilities of gait analysis, as a means to perform clinical assessment in orthopedics and neurology, diagnosis of musculoskeletal disorders, as well as to plan training programs for athletes, fall prevention and detection, is first extensively discussed. In particular, more technical details related to gait analysis and examples of signals are given in Section II. In Section III , interesting and very recent applications based on machine learning paradigms for gait analysis are reviewed. Finally, concluding remarks and plans for future studies are summarized in Section IV.

II. FUNDAMENTALS OF GAIT ANALYSIS

A. *Gait phases and parameters*

The gait analysis pays attention to the gait or stride cycle, which consists in a series of basic movements that are continuously repeated by an individual. A single stride is performed in the time interval delimited by two successive initial ground contacts for the same foot, and it is shown in Figure 1. The time interval of the stride is the reference for all the other time parameters related to muscle activities. The stride is divided into stance and swing, and the time intervals corresponding to them are in turn divided each one into three sub-intervals. Specifically, the stance includes the initial double support, single support, and double terminal support; these movements are performed in the related time intervals that are defined in the following.

- Initial double support: the time interval in which both feet have contact with the ground.
- Single support: the time interval during which the opposite foot comes off and swings.
- Double terminal support: the time interval delimited by the initial contact of the contra-lateral foot, and the support limb detachment precluding a swing.

The swing includes the initial swing, the intermediate swing or mid swing, and the terminal swing; these constituent movements are performed in the related time intervals that are defined in the following.

- Initial swing: the time interval that starts with lifting the foot from the ground, and ends when the swinging limb is parallel to the supporting foot.
- Intermediate swing: the time interval that begins when the swinging limb is opposite to the supporting limb, and ends when the first shows the tibia in vertical position during its advancing.
- Terminal swing: the time interval that starts with the tibia in vertical position, and ends when the foot makes contact with the ground.

B. *Measurements*

Measurements are related to space and time parameters obtained by processing raw data from acceleration and gyroscope signals. The most common parameters useful in human kinematic studies, and in particular in gait analysis, are given hereinafter.

- evaluated steps: number of steps considered in the analysis;
- gait cycle time (GTC) (seconds): duration of a complete cycle in seconds;
- cadence (steps/min): number of steps per minute;
- swing duration (% GCT): average value of the duration of the right and left swing movements as a percentage of GTC, further divided into right swing duration, expressed as percentage of the gait cycle the right foot is off the ground (% GCT), and left swing duration, expressed as percentage of the gait cycle the left foot is off the ground (% GCT);
- stance duration (% GCT): average value of the duration of the right and left support phases as a percentage of the gait cycle duration, further divided into right stance duration, expressed as percentage of the gait cycle the right foot is on the ground (% GCT), and left stance duration, expressed as percentage of the gait cycle the left foot is on the ground (% GCT);
- double support duration (% GCT): percentage of the gait cycle both feet are on the ground;
- single support duration (% GCT): average value of the single right and left support duration as a percentage of GCT;

- stride length: average value of the distances between each initial contact and the next of the same foot for left and right side;
- normalized stride length (% height): stride length is normalized to the height of the individual body;
- stride velocity: average value of the right and left limb velocity.
- normalized stride velocity (% height): Stride velocity normalized to the height of the body.

Several additional parameters are also defined by combining the aforementioned ones, like the symmetry index, which provides the percentage of symmetry between the acceleration curves of the right and left foot during the gait cycle. The symmetry index provides information on the general balance during the walk; it is dimensionless and its values are up to 100, where the value 100 indicates total balance between both feet. As an example, two typical signals acquired with different protocols and sensors are reported. The first example in Figure 2 shows the acceleration signals of the right and left feet. The signals are acquired with an IMU sensor positioned between the vertebrae S1-S2. By observing each graph in Figure 2, it is possible to distinguish the double support phase and the single support phase. A descending trend characterizes the acceleration signal during the double support phase and an ascending trend during the single support phase, which starts with the detachment of the contra-lateral foot, and ends with the ground contact of the contra-lateral foot. The single support phase is delimited in the upper graphic by the vertical cursors, represented with dashed lines. The tilted line that connects the beginning and endpoints of the single support phase highlights the propulsion, and its inclination quantifies the propulsion index. High values for the propulsion index highlight strong capacities at advancing. The second example in Figure 3 shows a signal produced by a gyroscope monitoring the angular velocity of the shank. The signals are acquired with an IMU sensor positioned on the shanks of the subject. The higher angular velocity values correspond to the swing, the lower to the stance. Estimates of the time parameters can be obtained from the angular velocity signal; the repetitiveness of the movements allows both estimates of individual occurrences and average values.

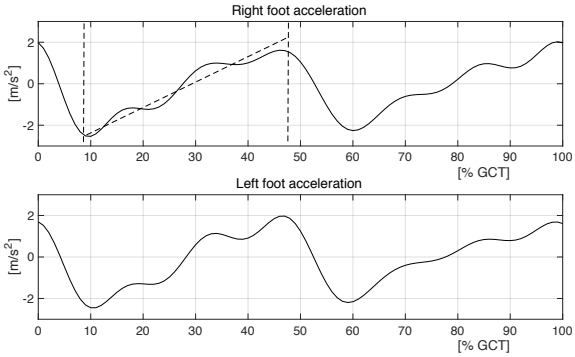

Fig. 2. Acceleration signals of the right and left foot in anterior-posterior component acquired by a typical accelerometer positioned by the Venus dimples aside the S1-S2 vertebrae.

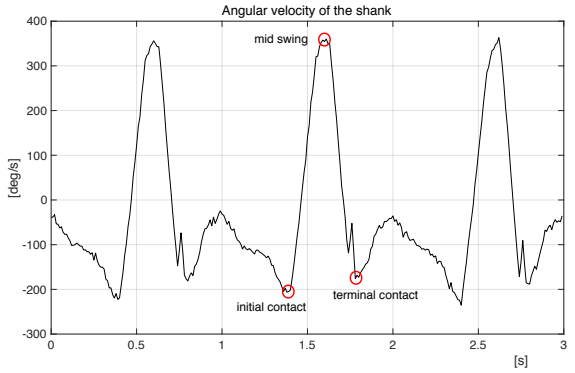

Fig. 3. Portion of the signal related to the angular velocity of the shank, angle in the sagittal plane, acquired by means of a typical wearable gyroscope.

III. APPLICATION SCENARIOS

The practice of gait analysis is at present one among the most promising diagnostic tools in a variety of application scenarios, discussed in the following.

Long-term high-intensity training affects athletes and can even lead to injuries, which in turn prevent them from keeping on training and/or taking part to the scheduled competitions. A prognostic system to predict risks of injuries is discussed in [12], where a machine-learning approach to evaluate the anterior cruciate ligament injury risk is proposed. The anterior cruciate is one of the four main ligaments of the knee and its injury represents the main issue affecting players, especially in contact sports. The study analyzes the stress of the ligament through experiments performed on 39 basketball players, when performing monopodalic jumps or single-leg power squat, the latter executed maintaining the arms with the hands on the hip and extending the resting leg in front of the body. The duration of the basic movements required by each exercise are considered as features of interest. Their values are normalized to the stabilization time, defined as the time between the contact with the ground and the instant in which the active leg is stable, which corresponds to the local minimum of the angular velocity of the shank after ground contact. The study considers data collected by IMU sensors, placed on the shank by means of an elastic belt designed to avoid movement artifacts. Data are processed

using supervised machine learning approaches for injury prediction, either based on support vector machine, or k-nearest neighbor, or decision tree concepts. The results of the study highlight the capability of the linear support vector machine, as the best performant approach, of accomplishing 95% accuracy in the classification. Methods like gait analysis are also exploited to improve the performance of athletes or prevent injuries. The skill in sport is in fact improved also by investing in training tools and systems. Traditional training methods such as coach supervising or video recording have some disadvantages, such as time-consumption and/or limits imposed by the environment. Differently, wearable sensors for gait analysis offer the possibility to non intrusively measuring the performance, and by coding the experience of the trainer, also to automatically providing feedbacks. The study [13] developed a system for recognizing the Baduanjin movements and evaluating their accuracy using wearable devices. The system can be used to help students in learning from their mistakes during use by comparing their movements with teachers' ones. Fifty-four volunteers, among students and teachers, participated in the experiment and several sequence-based techniques were used, such as dynamic time distortion (DTW) combined with different types of classifiers, the hidden Markov model (HMM), and recurrent neural networks (RNN). Three methods, nameley DTW + k-NN, DTW + SVM, and HMM, had the best accuracy, scoring over 99 % in evaluating and recognizing Baduanjin movements.

Instead, the studio [14] developed a system for player evaluation and classification of five prototype tennis strokes in real-time. An imu sensor mounted on the participants' wrists and connected to an Android smartphone via Bluetooth wireless technology, was used. The experiment was attended by 36 participants with average age equal to 25 years. The processing of the IMU data includes the preprocessing, segmentation, feature extraction, dimensionality reduction, and classification phases. The pre-processing phase involves noise reduction and the compilation of missing data cases. Different types of SVM classifiers were used, such as MinMaxScaler, MaxAbsScaler, StandardScaler, MinMaxScaler, MinMaxScaler. The study showed that SVM (StandardScaler), SVM (MinMaxScaler) and SVM (MaxAbsScaler) classifiers achieve, respectively, 90 %, 88 % and 89 % accuracy, while the SVM (RobustScaler) and SVM (Normalizer) provide 85 % and 77 % accuracy, respectively.

Falls are widespread among older people, and responsible of severe physical and/or psychological consequences, that can affect the quality of life. Fall detection systems should be capable of distinguishing falls from routine activities, in order to provide immediate medical assistance in the former case. The study presented in [15] reports a fall detection system enabled by wearable inertial sensors placed on the chest, waist, head, right wrist, right ankle, and right thigh. The system can transmit the data via wireless link to a remote PC. The study considers 14 volunteers that perform 16 daily life activities and 20 fall actions. It uses the PCA method to reduce the features dimensionality, and set up a fall detection system based on a convolutional neural network with 8 layers, that offer 98.27% classification accuracy. An alternative fall detection system, also enabled by the use of inertial sensors, is illustrated in [16]. The proposed system uses the event-triggered approach to acquire the pre-impact, impact and post-impact phases, evidenced by the acceleration signal. The pre-impact is recognized by an acceleration peak greater than an experimental threshold, and it is characterized by subsequent peaks precluding to a highest peak, corresponding to the moment when the subject hits the ground. Further samples are collected for recording the post-impact phase, characterized by an absence of peaks. The study reports about 46 healthy subjects acting 14 falls, and several activities of daily living, for 23 minutes each one. The extracted features are 27 and relates to the pre-impact, impact and post-impact phases. The proposed classifiers, based on k-NN and SVM approaches, reach accuracy equal to 95.6% and 97.2%, respectively.

It has been underlined in the previous Sections that gait analysis has become an interesting research topic due to the widespread availability of inertial sensors in wearable devices, and that activity recognition provides reliable information about the functional abilities and lifestyle of an individual. The study presented in [17] uses data collected by means of inertial sensors in smartphones, and an artificial neural networks to perform human activity recognition and classification. The optimal architecture is implemented with 100 neurons in the input layer, 60 in hidden layer 1, 20 in hidden layer 2, and 12 in the output layer for recognizing 12 classes of activities: standing, sitting, lying down, walking, walking upstairs, walking downstairs, stand-to-sit, sit-to-stand, sit-to-lying, lying-to-sit, stand-to-lying, lying-to-stand. The extracted spatio-temporal features are followed by dimension reduction based on PCA. A total of 7767 and 3162 events are used for training and testing phases, respectively, where each event is made of 561 features. The proposed ANN can achieve 89% accuracy, following by the alternative SVM method that scores 82% in activities classification.

The study [18] classifies six different human-walking styles using kinematic parameters obtained from sensors placed on six joints for twenty-five volunteers. From the IMU signals, space-time parameters were extracted for training neural networks. The neural network with the highest accuracy approximately 90 %, is made of three hidden layers with 100 neurons, 6 inputs neurons, and 6 output neurons corresponding to 6 walking activities. Instead, the study [19] proposes different combinations of deep learn-

ing architectures based on convolution neural network for human walking activities recognition reaching 97 % accuracy.

Gait and balance analysis represent recognized practices in many clinical areas to distinguish between healthy patients from patients affected by diseases such as cerebral palsy, spinal cord injury, hemiplegia, hip dysplasia, geriatric disorder, osteoarthritis, orthopedic and others [20].

Patients with neurodegenerative disorders can undergone freezing of gait (FOG), that consists in a loss of movement, despite their resolute intention to walk; FOG commonly arises in patients with the Parkinson disease. The study presented in [21] describes a reliable FOG prediction system, realized with machine learning algorithms that process data gained by means of inertial sensors. The proposed system is capable of recognizing the degradation of the walking preceding FOG in patients with Parkinson. To this end, it uses the timed-up-and-go (TUG) and exploits inertial sensors placed on the shins to gather measurement information. The clinical TUG test, aims at measuring how long the subject takes to standing up from a chair, walking 7 meters, turning 180 degrees, walking back to the chair and sitting down. The feature extraction is performed analyzing the angular velocity signals in the time and frequency domains. Subsequently, wrapper techniques are deployed to select the features that can optimize the machine learning classifiers for detecting pre-FOG episodes. Classifiers based on SVM and k-NN approaches show an accuracy of 92.1% and 89.8%, respectively.

Osteoarthritis (OA) is a common musculoskeletal disorder affecting the older population, and resulting in chronic pain and disability. Gait retraining is an effective intervention for patients with osteoarthritis of the medial compartment knee, that aims at reducing knee adduction moment (KAM). The study presented in [22], shows how estimating KAM during walking by using machine learning techniques applied to data collected from low-cost IMU sensors placed on the malleoli. Participants, both with knee OA and healthy, are invited to walk along a 20 meter path. It is shown that a neural network with 10 fully connected layers, composed by 256 neurons in layers 1-6, 128 neurons in layers 7-8, and 64 neurons in layers 9-10 allows accurate KAM evaluations.

Brain stroke is a widespread cause of disability, and rehabilitation exercises represent essential steps for post stroke recovery, as discussed in Section 2.1. The physical exercises performed in the laboratory under the supervision of a specialist represent, however, a poor recovery program, that needs to be complemented with home exercise programs. Making conclusions about the correctness of rehabilitation exercises in both clinical settings requires reliable methods. The study presented in [23] proposes an approach based on machine learning techniques for the remote rehabilitation of lower limbs in post stroke patients. In detail, the study analyzes the data related to 2 volunteers with stroke, during the rehabilitation sessions performed along 4 days; the data are collected by means of inertial sensors placed on triceps and ankles. Using PCA method, 36 features are distinguished and analyzed by means of machine learning techniques based on SVM, RF, and ANN, which show typical accuracy equal to 72.5%, 76.5%, and 79%, respectively, in assessing the success of the exercise.

IV. CONCLUSIONS AND FUTURE RESEARCH

Smart sensors are playing an essential role in enabling novel services and applications aimed at improving the quality of life. Wearable sensors have been revolutionary for some systems and practices, for instance, in gait analysis, where they offer quantitative and repeatable results for long periods at a low cost. The integration of multiple wearable sensors with low size and data transfer capabilities allows the automation of processes that relied on empirical bases in the past. The most significant applications concern: (i) clinical practice, where gait analysis permits the diagnosis of neurodegenerative diseases and the implementation of rehabilitation programs for injured subjects; (ii) sport, where the smart systems can be applied to prevent injuries and improve the performance of athletes; (iii) fall prevention and detection. Special attention has been paid to the gait analysis and the measurement of the human gait parameters, which include walking speed, stride and step length, swing and stance times. The key role of the novel technologies, and in particular of the wearable sensors, that allow measuring the parameters of interest over long periods of time during daily activities, has been evidenced. Examples of typical signals acquired with different acquisition protocols have also been given. Secondly, an overview on interesting and very recent applications based on machine learning paradigms and IMU sensors for gait analysis, have been shown.

Future research is going to pay attention to the following issues, namely: sensor improvement, power consumption, data processing, and management. Concerning sensor improvement, it is necessary to develop new wearable sensors that provide new space-time parameters. More specifically, new sensors need to provide more accurate measurements such as segment position, orientation, velocity, and joint angles; it is also interesting recognizing optimal sensor positions. Power consumption is a crucial issue of the current wearable systems for gait analysis since it affects the capacity of the system to measure and monitor over long periods. Future research should develop new systems characterized by reduced energy consumption, and batteries with extended battery life duration. Finally, new signal processing algorithms to both improve the reliability of the results and produce additional insight are also expected.

REFERENCES

[1] Weizman, Yehuda, et al. "Recent State of Wearable IMU Sensors Use in People Living with Spasticity: A Systematic Review", Vol.22, No.5, Sensors, 2022, 1791.

[2] H. Geng, Z. Huan, J. Liang, Z. Hou, S. Lv and Y. Wang, "Segmentation and Recognition Model for Complex Action Sequences," in IEEE Sensors Journal, vol. 22, no. 5, pp. 4347-4358, 1 March1, 2022, doi: 10.1109/JSEN.2022.3144157

[3] Y. Wang et al., "SAIL: A Deep-Learning-Based System for Automatic Gait Assessment From TUG Videos," in IEEE Transactions on Human-Machine Systems, vol. 52, no. 1, Feb. 2022, pp. 110-122, doi: 10.1109/THMS.2021.3123232.

[4] X. Chen, X. Luo, J. Weng, W. Luo, H. Li and Q. Tian, "Multi-View Gait Image Generation for Cross-View Gait Recognition," in IEEE Transactions on Image Processing, vol. 30, 2021, pp. 3041-3055, doi:10.1109/TIP.2021.3055936.

[5] Celik, Yunus, et al. "Gait analysis in neurological populations: Progression in the use of wearables." Medical Engineering & Physics, vol.87,2021, 9-29.

[6] Desai, Radhika, et al. "Postural control and gait measures derived from wearable inertial measurement unit devices in Huntington's disease: Recommendations for clinical outcomes." Clinical Biomechanics, 2022, 105658.

[7] Lin, Chin-Hsien, et al. "Early Detection of Parkinson s Disease by Neural Network Models", IEEE Access, vol.10, 2022, 19033-19044.

[8] Kim, Jeong-Kyun, et al. "Explainable Artificial Intelligence and Wearable Sensor-Based Gait Analysis to Identify Patients with Osteopenia and Sarcopenia in Daily Life." Biosensors 12.3, 2022, 167.

[9] Prill, Robert, et al. "A Systematic Review of Diagnostic Accuracy and Clinical Applications of Wearable Movement Sensors for Knee Joint Rehabilitation." Sensors, vol.21, No.24, 2021, 8221.

[10] Bolam, Scott M., et al. "Remote Patient Monitoring with Wearable Sensors Following Knee Arthroplasty." Sensors, Vol.21, No.15, 2021, 5143.

[11] Zhao, Wenbing, Shunkun Yang, and Xiong Luo. "Towards rehabilitation at home after total knee replacement." Tsinghua Science and Technology, vol.26,No.6 , 2021, 791-799.

[12] Taborri, Juri; Molinaro, Luca; Santospagnuolo, Adriano; Vetrano, Mario; Vulpiani, Maria Chiara; Rossi, Stefano. "A Machine-Learning Approach to Measure the Anterior Cruciate Ligament Injury Risk in Female Basketball Players",Sensors, vol.21, No.9,2021.

[13] Li, H.; Khoo, S.; Yap, H.J. "Implementation of Sequence-Based Classification Methods for Motion Assessment and Recognition in a Traditional Chinese Sport (Baduanjin)", Int. J. Environ. Res. Public Health, vol.19, 2022, 1744. https://doi.org/10.3390/ijerph19031744

[14] Wu, Mingyue, et al. "A Real-Time Tennis Level Evaluation and Strokes Classification System Based on the Internet of Things." Internet of Things 2022, 100494.

[15] Alarifi, A.; Alwadain, A. Killer heuristic optimized convolution neural network-based fall detection with wearable IoT sensor devices. Measurement , vol.167, 2021, 108258.

[16] I. Putra; J. Brusey; E. Gaura; R. Vesilo, An event-triggered machine learning approach for accelerometer-based fall detection. Sensors , vol.18, No.1, 2017,20.

[17] Hassan, M. M.; Uddin, M. Z.; Mohamed, A.; Almogren, A. "Robust human activity recognition system using smartphone sensors and deep learning", Future Generation Computer Systems , vol.81, 2018, 307-313.

[18] Semwal, Vijay Bhaskar, et al. "Pattern identification of different human joints for different human walking styles using inertial measurement unit (IMU) sensor", Artificial Intelligence Review, Vol.55, No2 ,2022, 1149-1169.

[19] Semwal, Vijay Bhaskar, Anjali Gupta, and Praveen Lalwani. "An optimized hybrid deep learning model using ensemble learning approach for human walking activities recognition", The Journal of Supercomputing Vol.77, No.11 ,2021, 12256-12279.

[20] Krutaraniyom, S., Sengchuai, K., Booranawong, A., and Jaruenpunyasak, J. " Pilot Study on Gait Classification Using Machine Learning", In 2022 International Electrical Engineering Congress (iEECON), IEEE, 2022 March, pp. 1-4.

[21] Borzi, L.; Mazzetta, I.; Zampogna, A.; Suppa, A.; Olmo, G.; Irrera, F. "Prediction of freezing of gait in Parkinson's disease using wearables and machine learning" Sensors, 2021 , Vol.21, No.2, 614.

[22] Wang, Chao ; Chan, Peter PK ; Lam, Ben MF; Wang, Sizhong ; Zhang, Janet H ; Chan, Zoe YS ; Chan, Rosa HM ; Ho, Kevin KW ; Cheung, Roy TH "Real time estimation of knee adduction moment for gait retraining in patients with knee osteoarthritis", IEEE Transactions on Neural Systems and Rehabilitation Engineering, vol.28, No.4, 2020, 888-894.

[23] Espinoza Bernal VC; Hiremath SV; Wolf B, Riley B; Mendonca RJ; Johnson MJ. "Classifying and tracking rehabilitation interventions through machine-learning algorithms in individuals with stroke", Journal of Rehabilitation and Assistive Technologies Engineering, 2021.

25th IMEKO TC4 International Symposium
23rd International Workshop on ADC and DAC Modelling and Testing
IMEKO TC-4 2022
Brescia, Italy /September 12-14, 2022

Human exposure in a 5G cellular base station environment in residential districts of Iasi city

Marius-Vasile Ursachianu[1], Catalin Lazarescu[1], Ovidiu Bejenaru[1], Alexandru Salceanu[2]

[1]*"National Authority for Management and Regulation in Communications" (ANCOM), Romania,marius.ursachianu@ancom.ro, catalin.lazarescu@ancom.ro, ovidiu.bejenaru@ancom.ro*
[2] *Gheorghe Asachi" Technical University of Iasi, Romania, alexandru.salceanu@academic.tuiasi.ro*

***Abstract* – The paper presents a pilot study over human exposure to radiofrequency (RF) electromagnetic field (EMFs) levels generated by the 5G cellular base stations installed in different residential district in city of Iasi, Romania.Also, a comparison with different EMFs levels generated by different mobile phonetechnologies, from our national operators, have been done. Measurement of electromagnetic field levels (instantaneous exposure) expressed in terms of power density levels has been performed in city of Iasi, fom March to November 2021, in nine locations with a high density of cellular base stations. The EMF exposure levels for different mobile communications standards have been measured with an up to date calibrated NARDA SRM 3006 field strength analyser system connected to an isotropic electric field probe.The methodology for measuring the non-ionising electromagnetic radiation levels described by ECC RECOMMENDATION (02)04have been respected.**

I. INTRODUCTION

As the world continues to embrace new technology in various aspect of our lives, from phones to smart devices, there is growing attention and concerns around the world over the effects of EMFs on human health.Without EMF, the everyday life as we know it would not exist.

We are surrounded by a complex mixture of a large number of RF EMF sources and questions and public discussions about the exposure have been raised more and more in the last decade, especially with the development of the new 5G mobile network. The rollout of the new 5G cellular base stations in the sub-6 GHz band is already in progress in many countries.

For human protection against electromagnetic radiation, different organizations like ICNIRP (International Commission on Non-ionizing Radation Protection, FCC (Federal Communication Commission) and IARC (International Agency on Research on Cancer) are recognized by WHO forvarious studies over EMF biological effects over the human body.

EMF exposure regulation according the ICNIRP have been adopted in many contries all over Europe. But there are some countries in Europe not follow exactly the ICNIRP guidelines and they defined and adopted own national legislations with restrictiv values of limits for the protection of general public against exposure at EMF levels.Countries like Poland, Bulgaria, Lithuania and Italy, because of theri national legislation have already problems in past with migration from 3G to 4G. This restrictive limitation could have now in 2022 a real negative impact over the future deploy of 5G network infrastructure in theses countries.. This problem raise the question of whether it is not necessary for these restrictive limits imposed by these countries to be relaxed and possibly harmonized with the other countries from Europe.

ICNIRP guidelines identify basic limits and reference levels.

In Romania, the exposure of the population to electromagnetic fields (also including the range of frequencies used for nw 5G NR technology) is regulated by the Order of the Minister of Public Health no. 1193 from 29.09.2006, [1]. Romania approved norms regarding the limitation of the exposure of the general population to electromagnetic fields from 0 Hz to 300 GHz, described by the Romanian National Ministry Order 1193/2006 integral transposition for 519/1999 Recommendation of the Council of the European Union, [2].The EU Council Recommendation 1999/519/EC, which is the reference document in the Europe Union, is based on the emission limits set out by the new ICNIRP's 2020 guidelines, [3], who is an updated version of ICNIRP 1998 guidelines. The 5G NR mobile communication technology was take into account when the new version of ICNIRP guidelines was developed.

In addition to determining the maximum exposure for verifying the compliance with the exposure limits using different extrapolation methods, [4], [5],could be also of interest to determine the instantaneous exposure, [6].

The instantaneous exposure can reflect the actual exposure of a person and depend over the actual traffic demand in a cellular base station, demand who can varying over time.

The present paper is focused mainly on the 5G human exposure, EMF levels monitoring beeing investigated with a mobile equipment in the vicinity of such cellular base stations.

We here present the measurement of electromagnetic

field levels (in terms of power density values) performed in 2021 form March to November in Iasi city. For the assessment of human exposure to RF EMF generated by cellular base stations was take into consideration nine residentialareas in the city with high density of mobile phone base stations sites, covering a wide range of mobile phone communications standards– 2G, 3G, 4G and the new 5G. For each location we investigated the EMF exposure level from all mobile services taking in consideration for the 5G mobile telephony service two situations – without or with generated data traffic.

In the final a comparison between instantanoeusmeasured fields values data and limits imposed by international organizations and national regulatory bodies has been performed. Also, a compliance check was performed and a set of preliminary conclusions have been taken.

II. MATERIAL AND METHODS

According to ICNIRP guidelines, the reference levels for public exposure in frequency range of mobile phone communications standards, included also the new 5G are presented in Table 1, where f is the frequency expressed in MHz.

Table 1. ICNIRP reference levels for public exposure

Frequency f [Mhz]	E [V/m]	S [W/m^2]
400 – 2000 MHz	$1.375 \times \sqrt{f}$	f/200
2000 – 300 000	61	10

All measurements have been performed indaytime during the peak hours of a working day and the total measurement time was6 minutes.

For determining the EMF levels, we used a mobile equipment from Narda, Narda SRM 3006 spectrum analyzer. The device is set to work in Safety Evaluation mode. This mode was developby Narda for a fast overview of the exposure levelsdue to individually definable frequency ranges (for a single or multi frequency environment), services and providers as absolute values or automatically evaluated according to common human safety standards, [7].

Using the SRM-3006 Tools software associated with device, we have created a special service table called Mobile Phone Operators. The service table contain six individual frequency bands used for different telephony services of our national operators between 790 MHz and 3.8 GHz. The all six frequency bands range assigned for Mobile Phone Operators service table is presented in Table 2.

In theory to avoid underestimation of the immission, it is important that the resolution bandwidth (RBW) to not be set less than the bandwidth of the signal to be measured. For example, for GSM service, GSM frequency spacing / signal channel width is 200 kHz, this value can be set for RBW for this service, [8].

Table 2. Mobile Phone Operators service table

Index	Cellular Service Name	F start [Mhz]	F stop [Mhz]	RBW
1	MOBIL 800 DL	791	821	200 kHz
2	MOBIL 900 DL	925	960	200 kHz
3	MOBIL 1800 DL	1805	1880	200 kHz
4	MOBIL 2100 DL	2110	2170	5 MHz
5	MOBIL 2600 DL	2570	2690	5 MHz
6	MOBIL 3500-3700	3400	3800	20 MHz

As a part of measurement procedure descbribed in ECC (02)04, for spectrum analysers it is recommended for 300 MHz – 3 GHz frequency band a value of 100 kHz for bandwidth, [9].

Also, NARDA SRM 3006 automatically sets the RBW if the user don't set an individual RBW, so that four spectral lines cand still be detected in the narrowest band.

As a particularity,wedon't use the automatically setting of the RBWby Narda,and individual values for RBW has been assignedby user for every cellular service created.We set the RBW value as the lowest value based on the presence of a specific mobile communication standard in the frequency band corresponding toeverycellular service defined.

The measurement points of EMF exposure levels generated by cellular base stations in city of Iasi are presented in Table 3. Each location have a 5G-enable mobile base station.

Table 3. EMF measurement point locations

Measurement Location	Adress	Cellular base station ground level height (m)	Distance to cellular base station (m)
MP1	Metalurgiei street	~70	~300
MP2	Ciornei street	~55	~100
MP3	Tudor Vladimirescu Boulevard	~45	~200/110
MP4	Socola Boulevard	~55	~95
MP5	Graniceri street	~30	~80
MP6	Ciric street	~40	~210
MP7	Prof. Dimitrie Mangeron Boulevard	~55	~300
MP8	Titu Maiorescu street	~57	~120
MP9	Anastasie Panu street (Palace of Culture Square)	~60	~190/190

Fig.1 Location of EMF measurement points

On a detailed Iasi city map, all three locations can be visualized in Figure 1.

The EMF exposure levels generated by investigated cellular base stations in all selected location have been measured using a calibrated up to date Narda SRM 3006 field strength analyzer connected to an isotropic probe as presented in Figure 2, for MP9 EMF measurement point location.The electric field probe [10] is designed to measure to electric field in frequency range domain from 420 MHz to 6 GHz. This frequency domainwill cover very well all of the frequency bands for all mobile communications standards used for cellular base stations transmissions.

According to the manufacturer's specifications, the measurement uncertainty of the level measured by the Narda SRM 3006 is + 2.7 / -3.8 dB.

The measurements were performed with a good visibility to the cellular base station with no obstacles between measurement system and antennas.

The measurements have been performed in accordance with by integrating signals into specified frequency bands corresponding to the cellular services createdover a 6 (six) minute time frame (averaged value), with an electrical probe rising to a ground height of 1,5 m, [9].

Fig.2 Narda SRM 3006 field strenght analyzer

Using an isotropic probe denote the fact that the measurement results is not affected by the direction of the arrived signal. The result is not also affected by the polarization of the measured field.

The value of the total resultant electric field measured in one location is given by the equation (1):

$$E_{tot} = \sqrt{E_x^2 + E_y^2 + E_z^2} \quad (1)$$

where Ex, Ey and Ez are the electric field components measured on the perpendicular axes of the 3D coordinate system.

Before starting the evaluation of EMF levels using Safety Evaluation mode, we take a short and rapid view over the presence or not of cellular telephony services in all measurement point locations, setting the Narda to work in Spectrum Analyzer mode.A synthetic and suggestive image acquired by Narda software, regarding the presence of cellular telephony services (Actual values) in the spectrum in MP9 location is represented by Figure 3.

The sensitivity of anequipment in signal detection depends on the input attenuator setting. In Narda SRM 3006 spectrum analyzer this setting is determined by the Measurement Range (MR) parameter, [10].

In case of measuring signals with different power from a cellular telephone base station it is important to not overload the device. Also choosing a correct MR the situation of having false measured results is prevented.

After some preliminary tests, for each EMF measurement point location, the MR value was setting manually depending on the strength of the signals in the area.

In each from all nine measurement points, a 5G cellular base stations were present in the area. Because we assumed that the presence of 5G terminals with 5G services active in the area will be very reduce, we force the appearance of a traffic beam in the measurement point for 5G telephony service. With a 5G mobile phone terminal placed next to the measurement device we simulate a downlink using the Netograf application developed internaly by ANCOM, [11]. This could be called a**single user exposure scenario**.

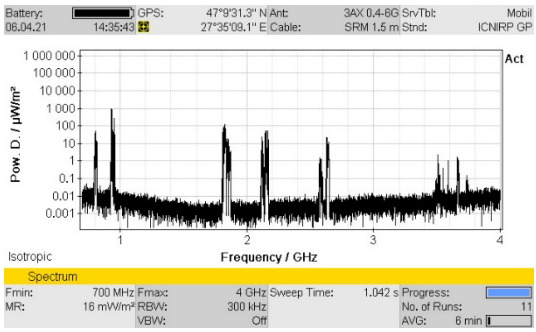

Fig.3 Spectral distribution of cellular telephony services

For each location where the assessment of human exposure to cellular base stations was performed, we measured the instantaneous (Avg values) and maximal (Max values) possible exposure for a perioad of time of 6 minutes.

In a multi frequency exposure scenario, the contribution of all individual frequencies can be express by the total EMF immission level across all bands measured in terms of total power densitity, [8]its value being given by the equation (2):

$$S_{tot} = \sum_{i=1}^{N} S_i \quad (2)$$

where:

S_{tot} is the total immission level expressed in terms of total power densityfor all cellular services

S_i is the immission level expreesed in term of power density corresponding to a specific cellular service from service table created.

On the spectrum analyzer display exposure levels are reported in real time both for a single cellular service and the sum of all services,as presented in Figure 4.

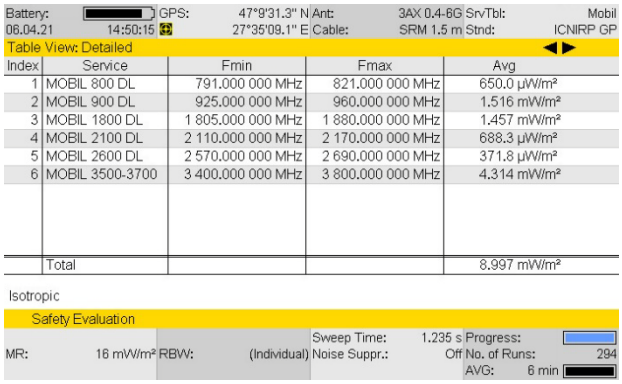

Fig.4Avg values of EMF level strength in MP9 location with 5G cellular service activated

III. RESULTS AND DISCUSSION

The instantaneous exposure can reflect the actual exposure of a person and depend over the actual traffic demand in a cellular base station, demand who can varying over time.

The instantaneous and maximal possible exposure in terms of field strength values, expressed by power density (S) values, maximum (Max) and averaged (Avg) values over a 6-minute time interval are presented in Table 4 for all nine EMF measurement points.

The values of interest for the assessment of human exposure to electromagnetic fields generated by mobile base stations according to ICNIRP guidelines isAvg value of power density which must be compared with the limit value imposed by ICNIRP guidelines.

From the results presented in Table 4 we can observe that for each locationwhere the assessment of exposure was investigated, the S Avg values are very well below with those limit values imposed by ICNIRP guidelines, especially for the case when data traffic was generated for 5G telephony services.

The highest values of S Avg was recorded in MP3 and MP9 measurement point locations. Both locations are representative for the city of Iasi in terms of urban agglomeration and cellular base stations density. This locations could be marked like being a hot spot areas.

Graphically, a comparison between instantaneous S Avg and maximum S Max values for all telephony services identified in MP3 location, for a 5G single user exposure scenario, is presented in Figure 5.

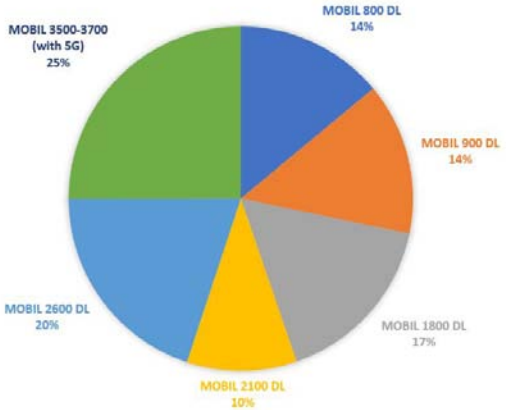

Fig.5 Quantitative and comparative S Avg values, for the identified cellular services in MP3 location

A comparison between maximum values of power density (S Max)field strength levels for all telephony services identified in MP3 location, for a forecd 5G traffic beam, is presented in Figure 6.

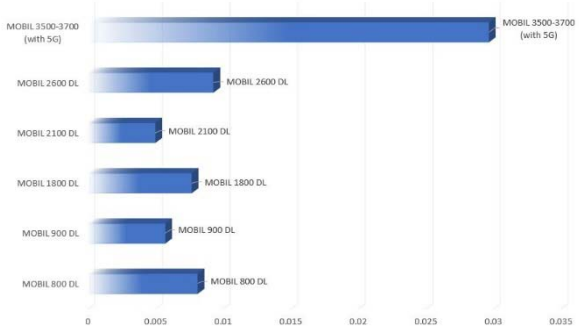

Fig.6 S Max values comparison, for the identified cellular services in MP3 location

The highest S Avg and S Max values for 5G cellular service with forced traffic beam have been measured in MP5 location.This fact correspond to the fact that the measurements were performed at the smallest distance from the site compared to the rest of the measurements performed.

Table 4. Electromagnetic field power density measured values in MP1 – MP9 locations

Location	Cellular Service Name	F start [MHz]	F stop [MHz]	S Max [W/m^2]	S Avg [W/m^2]	S Std [W/m^2]
MP1 - no 5G *(Metalurgiei street)*	MOBIL 800 DL	791	821	0.0002122	0.0000811	3.95
	MOBIL 900 DL	925	960	0.0007103	0.0003492	4.62
	MOBIL 1800 DL	1805	1880	0.0006903	0.0002996	9.02
	MOBIL 2100 DL	2110	2170	0.0003991	0.0002116	10
	MOBIL 2600 DL	2570	2690	0.0007978	0.0003124	10
	MOBIL 3500-3700	3400	3800	0.0001118	0.0000192	10
MP1 - with 5G	MOBIL 3500-3700	3400	3800	**0.0195500**	**0.0017400**	10
MP2 - no 5G *(Ciornei street)*	MOBIL 800 DL	791	821	0.0003178	0.0001973	3.95
	MOBIL 900 DL	925	960	0.0006241	0.0002991	4.62
	MOBIL 1800 DL	1805	1880	0.0000817	0.0000267	9.02
	MOBIL 2100 DL	2110	2170	0.0007138	0.0002911	10
	MOBIL 2600 DL	2570	2690	0.0008813	0.0001967	10
	MOBIL 3500-3700	3400	3800	0.0003180	0.0000333	10
MP2 - with 5G	MOBIL 3500-3700	3400	3800	**0.0227200**	**0.0046100**	10
MP3 - no 5G *(Tudor Vladimirescu Boulevard)*	MOBIL 800 DL	791	821	0.0081100	0.0028880	3.95
	MOBIL 900 DL	925	960	0.0057170	0.0029560	4.62
	MOBIL 1800 DL	1805	1880	0.0076700	0.0034070	9.02
	MOBIL 2100 DL	2110	2170	0.0049880	0.0021340	10
	MOBIL 2600 DL	2570	2690	0.0092800	0.0041110	10
	MOBIL 3500-3700	3400	3800	0.0002192	0.0000303	10
MP3 - with 5G	MOBIL 3500-3700	3400	3800	**0.0296500**	**0.0051760**	10
MP4 - no 5G (*Socola Boulevard)*	MOBIL 800 DL	791	821	0.0009110	0.0003710	3.95
	MOBIL 900 DL	925	960	0.0027170	0.0009330	4.62
	MOBIL 1800 DL	1805	1880	0.0008230	0.0003170	9.02
	MOBIL 2100 DL	2110	2170	0.0019880	0.0009340	10
	MOBIL 2600 DL	2570	2690	0.0062800	0.0023210	10
	MOBIL 3500-3700	3400	3800	0.0003112	0.0000701	10
MP4 - with 5G	MOBIL 3500-3700	3400	3800	**0.0336500**	**0.0057130**	10
MP5 - no 5G (*Graniceri street)*	MOBIL 800 DL	791	821	0.0003338	0.0002113	3.95
	MOBIL 900 DL	925	960	0.0008141	0.0003751	4.62
	MOBIL 1800 DL	1805	1880	0.0001915	0.0003667	9.02
	MOBIL 2100 DL	2110	2170	0.0005134	0.0001131	10
	MOBIL 2600 DL	2570	2690	0.0003813	0.0011354	10
	MOBIL 3500-3700	3400	3800	0.0001170	0.0000491	10
MP5 - with 5G	MOBIL 3500-3700	3400	3800	**0.0516500**	**0.0074960**	10
MP6 - no 5G (*Ciric street)*	MOBIL 800 DL	791	821	0.0003719	0.0000957	3.95
	MOBIL 900 DL	925	960	0.0006129	0.0002976	4.62
	MOBIL 1800 DL	1805	1880	0.0027120	0.0009918	9.02
	MOBIL 2100 DL	2110	2170	0.0008204	0.0003860	10
	MOBIL 2600 DL	2570	2690	0.0005641	0.0001731	10
	MOBIL 3500-3700	3400	3800	0.0000991	0.0000381	10
MP6 - with 5G	MOBIL 3500-3700	3400	3800	**0.0217100**	**0.0019220**	10
MP7 - no 5G *(Prof. Dimitrie Mangeron Boulevard)*	MOBIL 800 DL	791	821	0.0003953	0.0000891	3.95
	MOBIL 900 DL	925	960	0.0005941	0.0004010	4.62
	MOBIL 1800 DL	1805	1880	0.0000584	0.0000211	9.02
	MOBIL 2100 DL	2110	2170	0.0031179	0.0009870	10
	MOBIL 2600 DL	2570	2690	0.0002013	0.0001172	10
	MOBIL 3500-3700	3400	3800	0.0003180	0.0000981	10
MP7 - with 5G	MOBIL 3500-3700	3400	3800	**0.0198600**	**0.0025710**	10
MP8 - no 5G (*Titu Maiorescu street)*	MOBIL 800 DL	791	821	0.0021490	0.0008201	3.95
	MOBIL 900 DL	925	960	0.0004117	0.0001140	4.62
	MOBIL 1800 DL	1805	1880	0.0007210	0.0005250	9.02
	MOBIL 2100 DL	2110	2170	0.0048520	0.0017540	10
	MOBIL 2600 DL	2570	2690	0.0002130	0.0001150	10
	MOBIL 3500-3700	3400	3800	0.0002100	0.0000980	10
MP8 - with 5G	MOBIL 3500-3700	3400	3800	**0.0161100**	**0.0037450**	10
MP9- no 5G (*Anastasie Panu street)*	MOBIL 800 DL	791	821	0.0014840	0.0007437	3.95
	MOBIL 900 DL	925	960	0.0031660	0.0026000	4.62
	MOBIL 1800 DL	1805	1880	0.0093880	0.0029000	9.02
	MOBIL 2100 DL	2110	2170	0.0036170	0.0015900	10
	MOBIL 2600 DL	2570	2690	0.0024850	0.0008950	10
	MOBIL 3500-3700	3400	3800	0.0003668	0.0001132	10
MP9 - with 5G	MOBIL 3500-3700	3400	3800	**0.0244900**	**0.0043140**	10

IV. CONCLUSIONS

This paper provides an overview on the assessment of human exposure to RF EMF generated by different types of cellular base stations in nine residential district locations from city of Iasi, Romania. The selected locations are public with a high density of cellular base stations sites, covering a wide range of mobile phone communications standards, from 2G to 5G NR.

This is the first major public study from Romania over the assessment of human exposure to EMF fields generated by the 5G cellular base station, even the 5G traffic beam was forced to be generated in a so called 5G single user exposure scenario.

The assessment was realized from the point of view of the instantaneous and maximal possible exposure in term of field values, expressed in maximum and averaged values of power density (S) over a 6-minute measurement time interval.

The instantaneous exposure can reflect the actual exposure of a person and depend over the actual traffic demand in a cellular base station, demand who can varying over time.

For each frequency band associated with defined cellular services the measurement equipment was set accordingly in accordance with actul standard and recommended guidelines.

All power density averaged values measured, were very well below with those limit values imposed by international organizations and national regulatory bodies, even for a 5G single user exposure scenario when traffic beam was forced to be generated.

The highest S Avg values was measured in MP5 location for forced 5G cellular service, this value representing0,07 %from standard value.

For every location investigated, will notice that the measurements values for forced 5G cellular service show some variations between the exposure levels measured at each location. This is likely to be due, by the difference in the position of the measurement electric field probe against the position of cellular base station.This behaviorcan be checked in detail in a future study.

The measurement method proposed in this study can be used successfully when the instantaneous field strength values (averaged values over a 6-minutes period of time) would be enough for an assessment of human exposure to electromagnetic fields generated by various telephony services at an aleatory moment of time. If the measured averaged field values are well below those impose by limits, then the maximum field strength values can be used for a better accurate assessment of the reality of exposure.Without exception, the measured values of the electric field strength must be extrapolated to the maximum load of the cellular networkfor an accurate and precise assessment of human exposure.

Also, as a future research, the assessmenet of human exposure needs to be extendedin a 5G multi-exposure scenario to be more relevant for everyday life.

ACKNOWLEDGMENT

This paper has been developed in the framework of the collaboration agreement settled between "Gheorghe Asachi" Technical University of Iasi, Faculty of Electrical Engineering and ANCOM, Romania.

REFERENCES

[1] O.M. 1193/2006 https://www.ancom.ro/uploads/links_files/Odinul_1193_2006_norme.pdf

[2] EU Council Recommendation 1999/519/EC https://op.europa.eu/en/publication-detail/-/publication/9509b04f-1df0-4221-bfa2-c7af77975556/language-en

[3] International Commission on Non-Ionizing Radiation Protection, "Guidelines for Limiting Exposure to Electromagnetic Fields (100 kHz to 300 GHz)", Health Physics, vol. 118 - Issue 5, p 483-524, 2020.

[4] O. Bejenaru, E. Lunca, V. David, “Simulation and Measurement of the Radiofrequency Electromagnetic Field Generated by a LTE Base Station”, 2019 International Conference on Electromechanical and Energy Systems (SIELMEN), Chisinau, October 2019.

[5] H. Keller, “On the Assessment of Human Exposure to Electromagnetic Fields Transmitted by 5G NR Base Stations”, Health Physics, vol. 117, No 5, November 2019, pp 541-545.

[6] C. Bornkessel, T. Kopacz; A. M. Schiffarth, D. Heberling, M. A. Hein, “Determination of Instantaneous and Maximal Human Exposure to 5G Massive-MIMO Base Stations”, 15th European Conference on Antennas and Propagation (EuCAP), Dusseldorf, Germany, 2021.

[7] Matthias Wuschek, “Measuring RF Electromagneti Fieldds at Mobile Communications Base Station and Broadcast Transmitter Sites” Narda Safety Test Solution GmbH,Germany, 2019.

[8] IEC 62232:2017, Determination of RF field strength, power density and SAR in the vicinity of radiocommunication base stations for the purpose of evaluating human exposure.

[9] ECC RECOMMENDATION (02)04, Measuring non-ionising electromagnetic radiation (9 kHz – 300 GHz, evised Bratislava 2003, Helsinki 2007.

[10] https://www.narda-sts.com/en/selective-emf/srm-3006-field-strength-analyzer/.

[11] https://www.netograf.ro

25th IMEKO TC4 International Symposium
23rd International Workshop on ADC and DAC Modelling and Testing
IMEKO TC-4 2020
Brescia, Italy / September 12-14, 2022

Gaussian-based analysis for accurate compressed ECG trace streaming

Alessandra Galli[1], Giada Giorgi[1], Claudio Narduzzi[1]

[1]*Department of Information Engineering, University of Padua, via G. Gradenigo, 6/b, I-35131, Padova, Italy, e-mail:* {alessandra.galli, giada.giorgi, claudio.narduzzi}@unipd.it

***Abstract* – Wearable cardiac monitors can usefully contribute to early detection of potential cardiovascular pathologies, however ECG trace data streaming over wireless links creates some significant challenges. We propose a signal analysis approach based on a Gaussian dictionary to model and compress ECG traces. The algorithm operates on fixed-length segments, and achieves effective compression for wireless data transmission, associating just 10 bytes to each Gaussian feature. At the same time it enables accurate reconstruction of ECG traces from the reduced data set. We tested our method on a set of 46 ECG recordings taken from the Physionet MIT-BIH Arrythmia Database, obtaining 90% data compression rates, while percent relative deviation of reconstructed traces is always below 5%.**

I. INTRODUCTION

Recent years have witnessed an explosive growth in the availability of wearable cardiac monitoring devices, from fitness trackers to medical grade monitors analysing multiple-lead electrocardiogram (ECG) signals [1]. On account of their reduced impact on patient quality of life and mobility, these devices can contribute to heart profile evaluation and enhance diagnostics. In particular, continuous heart monitoring plays an important role in early detection of potential cardiovascular pathologies, that are a major cause of death worldwide.

In a mobile context, data acquisition and processing devices are tasked with delivering healthcare measurement information to a data collection and analysis centre, most likely a cloud-based one [2]. For instance, Bluetooth low-energy (BLE) is often employed for short-range data transmission from sensing units to a smartphone, the latter then providing the link to a cloud-based application [3]. The combination provides good throughput, while range is dependent on wireless network coverage and transmission endurance can be limited by energy consumption.

Unobtrusive long-term cardiac monitoring requires *guaranteed throughput* to reliably transfer an accurate continuous flow of measured data [4], hence endurance and transmission range need to be emphasized. It is also useful to remember, as a reference, that one ECG channel sampled at 500 Hz with 12-bit resolution produces 6000 bits per second. This yields over 500 Mb per lead in a single day [5], creating some significant challenges to mobile applications streaming data over wireless links.

Several papers have presented effective data compression algorithms for wireless applications [6, 7]. The focus is on the use of simple, low complexity algorithms to reduce the amount of transmitted data and prolong sensor battery life, while minimizing information loss [8]. However, compression is often treated as an independent problem, rather than by ECG-specific feature analysis [9].

Signals recorded during largely unrestricted daily life activities can be affected by acquisition noise, motion and electrode artifacts [10], placing greater emphasis on denoising. In this regard, compressive sensing (CS) exploits to advantage the underlying sparse-signal assumptions [11], [12]. Besides achieving useful compression ratios, CS allows detection of significant ECG features directly from compressed data, dispensing with the need to reconstruct waveforms first [5], [13]. On the contrary, traditional Holter recorders *preserve* information about whole traces, enabling trained clinicians to carry out detailed analyses of waveforms where the need arises. It might be impossible to do this from compressed data, unless full waveforms can be accurately reconstructed from them.

With these requirements in mind, we present a signal analysis approach that provides an effective compression scheme for wireless data transmission, at the same time enabling accurate reconstruction of ECG traces from the reduced data set. For this purpose we rely on signal modelling by Gaussian kernels and exploit the fact that a low number of suitable components suffices to accurately represent each cardiac cycle. This allows to meet different challenges at the same time:

1. achieve greater robustness against noise and artifacts in recorded traces;
2. support accurate and reliable trace interpretation for analysis and diagnosis;
3. provide compact representations of trace data for archiving, transmission and efficient analysis.

Advanced cardiac monitors can often run rather sophisticated signal analysis algorithms, suggesting that computing power is generally available within edge devices to support the monitoring framework we propose.

II. WAVEFORM MODEL

A cardiac cycle corresponds to a sequence of elementary waves representing different stages of activity (P wave, QRS complex formed by Q, R and S waves, and T wave). Each wave can be modelled by at least one Gaussian kernel, that is, a function $g_\sigma(t)$ defined as:

$$g_\sigma(t) = \frac{1}{\sqrt{2\pi}\sigma} e^{-\frac{t^2}{2\sigma^2}}. \quad (1)$$

To help describe asymmetries in P and T waves, the addition of a second kernel is suggested in the literature [14]. Therefore, in principle a QRS complex is modeled by three Gaussian kernels, P and T waves by two kernels each, totalling *seven*.

The ECG trace is usually partitioned into segments containing only a single heart beat, which requires preliminary detection of peaks associated with the R waves. Single-beat segmentation is critically dependent on the R-peak detection algorithm running on the monitoring device. In our approach we adopt instead *fixed* segmentation, that allows to dispense with R-peak detection. ECG traces are partitioned into segments represented by a sample vector $\underline{\mathbf{x}} = [x(n_1T_s), \ldots, x(n_2T_s)]^T$, where T_s is the sampling interval, $n_1T_s < 0 < n_2T_s$ with $n_2 - n_1 + 1 = N$, and superscript 'T' denotes transposition. Segment length is NT_s *regardless* of the number of heart beats within.

The location and number of ECG wave complexes can vary and is, in general, unpredictable, although an upper bound based on physiological limits can be set. The model then takes the form:

$$x(nT_s) = \sum_{i=1}^{I} a_i g_{\sigma_i}(nT_s - \tau_i), \quad (2)$$

where a_i is the magnitude of the i-th Gaussian component, σ_i is its shape (dispersion) parameter and τ_i the time position relative to the start of the segment. For greater flexibility, we just set a generic upper bound I on the total number of kernels within a segment.

The use of Gaussian mixture models was proposed in [15] for the generation of realistic synthetic ECG traces and in [14] for ECG compression and classification. Several authors have since considered Gaussian models in ECG-related works and adapted them to different purposes, but identification of model parameters in (2) is a non-linear estimation problem that is often associated with computationally-intensive algorithms, ill-suited to a wearable context [16], [17].

An effective alternative is represented by dictionary-based analysis. The basic idea is to provide a predefined pool of Gaussian kernels, called a *dictionary*, where each kernel is characterized by a different combination of parameters τ and σ. The analysis algorithm picks the ones that best match model (2) for the given segment $\underline{\mathbf{x}}$. The use

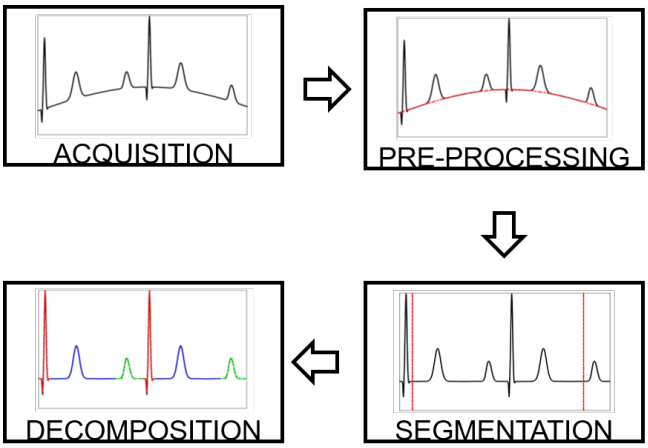

Fig. 1. Main steps of the proposed framework.

of a Gaussian dictionary was shown to provide promising results in the analysis of ECG traces [18].

Each dictionary element (*atom*) can be described as a column vector of N sampled values of a Gaussian kernel:

$$\underline{\mathbf{g}}_{(\tau_h,\sigma_k)} = [g_{\sigma_k}(n_1T_s - \tau_h), \ldots, g_{\sigma_k}(n_2T_s - \tau_h)]^T. \quad (3)$$

where τ_h is a specific time position in a set of H allowable values and σ_k is a specific dispersion taken from a set of K possible choices. As a dictionary only allows discrete sets of values for parameters σ and τ, correct design and a suitable trade-off between the size of the dictionary and waveform approximation accuracy are essential.

The generic dictionary matrix $\mathbf{D}$ has the form:

$$\mathbf{D} = [\mathbf{D}_{\sigma_1}\ \mathbf{D}_{\sigma_2}\ \ldots\ \mathbf{D}_{\sigma_K}] \quad (4)$$

where each $N \times H$ matrix block contains H column vectors $\underline{\mathbf{g}}_{(\tau_h,\sigma_k)}$ characterised by different time shifts, but with a common value of parameter σ_k. The size of the full dictionary $\mathbf{D}$ is $N \times M$, with $M = HK$. Because of the way $\mathbf{D}$ is built, the indication of column index m suffices to determine values of *both* τ and σ, that is: $\underline{\mathbf{g}}_{(\tau_h,\sigma_k)} = \underline{\mathbf{d}}_m$ for some m.

To find all the components of model (2) we apply an *orthogonal matching pursuit* (OMP) recursive greedy algorithm [19].

III. SEGMENTATION AND PROCESSING

Processing steps in the proposed approach follow the straightforward sequence shown in Fig. 1.

A. *Pre-processing*

The acquired ECG trace is first pre-processed to remove low frequency noise and baseline wander due to respiration and motion artifacts. These components are first extracted by applying two cascaded median filters. The first filter of

200-ms width removes QRS complexes and P waves, the resulting signal is then processed by a median filter of 600-ms width to remove T waves [20]. The resulting output contains baseline wander, that is then subtracted from the original ECG signal.

B. *Segmentation*

Although fixed segmentation may appear straightforward, it calls for great care in dealing with edge effects. In fact, it may happen that larger elementary waves are found close to either end of the analyzed segment, resulting in significant truncation of the relevant waveform.

Gaussian model (2) can adapt to a variety of waveforms which, unfortunately, means that it is easily affected by edge effects. The analysis algorithm attempts to replicate truncation by concentrating as many Gaussian kernels as needed close to the edge of the analyzed segment, resulting in local overfitting. Since a limited number of kernels is allotted for each segment, this may cause sub-optimal allocation and underfitting elsewhere in the segment.

The problem has been addressed as follows:

- head and tail edge extensions of the segment are introduced to minimize truncation in Gaussian kernel vectors within the dictionary;
- overlap is introduced between consecutive segments. As a consequence, elementary waveforms subjected to truncation are considered for both segments, but only the better fitting is kept;
- the upper bound I is increased to account for overlaps and discarded estimates.

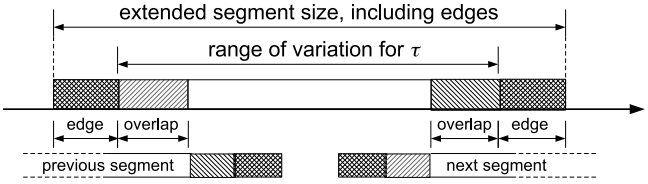

Fig. 2. Segment structure, with edges and overlap areas.

The segment structure assumed for the algorithm is shown in Fig. 2, where the cross-hatched parts at the two ends represent the edge allowance for Gaussian atoms. Edge width is equal to the maximum value assigned to the dispersion parameter σ within the dictionary. Single-hatched rectangles represent the overlap areas, that are the same width as the edges.

Figure 3 refers to one of the ECG traces analyzed for this work. For a 30-minute recording time, a trace is partitioned into 1042 segments, that are all superposed in this figure. Estimated Gaussian kernel amplitudes α_i are plotted versus time position τ_i. This parameter was allowed to

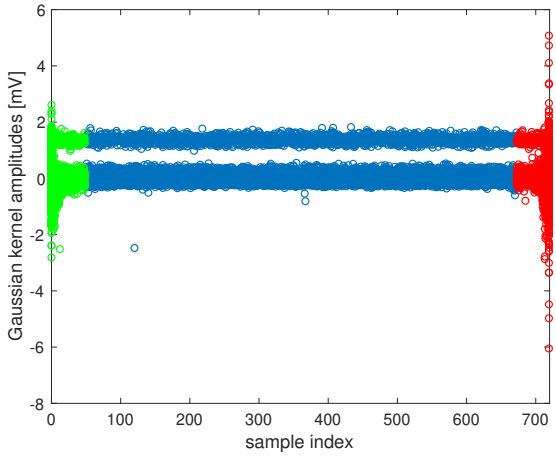

Fig. 3. Plot of Gaussian kernel amplitudes versus delays. All segments of a single ECG trace are overlapped. Green and red show overlap areas where estimated coefficients are discarded.

vary over a range of 2 s, that is the full segment length, corresponding to 720 samples as shown, since the sampling rate is 360 Hz. Edges are 48 samples long (approximately 130 ms), which is the same length as the overlap areas.

Analyzed segment length is actually 624 samples (1.73 s), that is, the blue part of the plot in Fig. 3. Estimates from this part of the segment can be streamed out for wireless transmission. The halves of the leading and trailing overlap areas, where coefficient estimates are discarded, are shown respectively in green and red. Some coefficients in those areas are significantly larger, as a result of the algorithm attempt to overfit truncated waveforms.

For the trace of Fig. 3 overlap areas where estimates are discarded are little more than 14% of the range of delay variation. On the other hand, discarded estimates are about 25% of the total provided by the algorithm. This confirms the clustering effect caused by overfitting at the segment ends and suggests that the overlap-and-discard approach described above can deal with edge effects effectively.

C. *Decomposition*

Dictionary-based signal analysis centers on finding a sparse solution to a matrix-vector equation, formally:

$$\hat{\underline{\mathbf{a}}} = \arg\min_{\underline{\mathbf{a}}} ||\underline{\mathbf{a}}||_0 \quad \text{subject to:} \quad ||\underline{\mathbf{x}} - \mathbf{D}\underline{\mathbf{a}}||_2 < \epsilon \qquad (5)$$

where $\underline{\mathbf{a}}$ is the vector of Gaussian kernel coefficients a_i and ϵ is a threshold value associated to the energy of the residual $\underline{\mathbf{r}} = \underline{\mathbf{x}} - \mathbf{D}\hat{\underline{\mathbf{a}}}$.

The OMP iterative approximation algorithm can be summarized as follows. After initializing the set of selected dictionary column indexes to the empty set, $\mathcal{S} = \varnothing$ and the signal estimate to $\hat{\underline{\mathbf{x}}} = \underline{\mathbf{0}}$, the algorithm is the itera-

tive application of the following steps:

1. compute $\underline{\mathbf{r}} = \underline{\mathbf{x}} - \underline{\hat{\mathbf{x}}}$, then select dictionary index: $m^* = \arg\max_m |\underline{\mathbf{d}}_m^T \underline{\mathbf{r}}|^2$
2. accordingly update the selected index set: $\mathcal{S} = \mathcal{S} \cup m^*$ and the dictionary submatrix $\mathbf{D}_\mathcal{S}$;
3. compute a new amplitude estimate: $\underline{\hat{\mathbf{a}}}_\mathcal{S} = \left(\mathbf{D}_\mathcal{S}^T \mathbf{D}_\mathcal{S}\right)^{-1} \mathbf{D}_\mathcal{S}^T \underline{\mathbf{x}}$;
4. calculate the new signal estimate: $\underline{\hat{\mathbf{x}}} = \mathbf{D}_\mathcal{S} \underline{\hat{\mathbf{a}}}_\mathcal{S}$.

Iterations are stopped either when the maximum allocated number of Gaussian kernels I_{max} has been reached, or when percent relative deviation (PRD) of $\underline{\hat{\mathbf{x}}}$ from the analyzed segment $\underline{\mathbf{x}}$ drops to 1% or lower.

Each OMP iteration step involves matrix-vector products, the computation of a pseudo-inverse of progressively larger size and, above all, the search for a peak value over a vector the same size as the dictionary column. Computational cost increases with the number of components modelled by (2). Shorter segments can be processed faster, but the number of segments gets larger and, with fixed overlap length, efficiency decreases. The selected 2-s segment length appears to be a reasonably effective compromise.

For our trials MatLab running on a 2,6 GHz Intel Core i7 quad-core processor took about 240 ms for the analysis of a 2-s segment, which suggests real-time analysis is achievable also with less-performing processors.

IV. MAIN RESULTS

To characterise the proposed approach we considered the set of 30-minute ECG recordings provided by the MIT-BIH Arrythmia Database, hosted at *https://physionet.org* [21]. Specifically, we selected only traces from modified limb lead II, as they were available for 46 records. Results thus refer to the analysis of nearly 48,000 segments and over 100,000 heart beats, some of which are labelled as anomalies.

A. Compression

For each Gaussian kernel modelling the trace, the algorithm provides amplitude, dictionary column index and absolute position index within the trace. The latter is the sum of the segment start index and relative position τ_i within the segment. Since amplitude accuracy is important we use for this a 32-bit floating point format. Dictionary column indexes are represented by unsigned 16-bit values, while 32 bits are needed for the position index. This means exactly 10 bytes are needed for each Gaussian component.

Since heart rate and ECG trace shape can vary, it is easier to assess compression by comparing the size of acquired traces with the corresponding sequence of parameter estimates. This shows that a 30-minute ECG trace taking about 1 Mbyte is converted into a data sequence of approximately 100 kbytes. The resulting compression ratio is around 90% and corresponds to less than 500 bits per second, which is compatible with typical low-power wide-area network data rates.

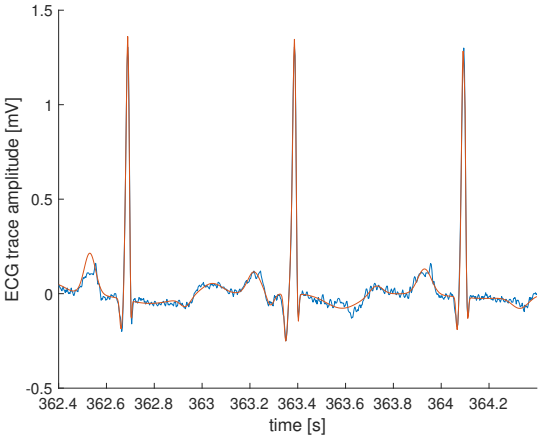

Fig. 4. Comparison between original (blue) and reconstructed (red) trace for a representative ECG segment.

B. Waveform reconstruction accuracy

If the Gaussian model that describes the ECG signal is accurate enough, the proposed algorithm enables to reconstruct a trace without introducing artifacts. An example of reconstruction for one of the ECG trace segments is shown in Fig. 4, where it can be seen that some mild smoothing has been introduced in the reconstructed trace.

Percent Root mean square Difference (PRD) is an index of distortion caused by model approximation, defined as:

$$\mathrm{PRD} = 100 \cdot \sqrt{\frac{\sum \left[\hat{x}(nT_s) - x(nT_s)\right]^2}{\sum x^2(nT_s)}} \qquad (6)$$

where $\hat{x}(nT_s)$ is the signal reconstructed by the proposed Gaussian model and summations extend over a whole trace.

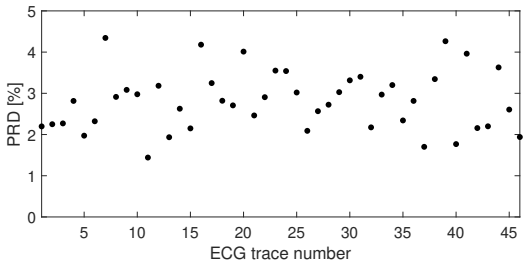

Fig. 5. Percent relative deviation (PRD) for 46 analysed traces from MIT-BIH Arrythmia Database (for trace interpretation, usually 0-2% = very good, 2-9% = good) [22].

PRD values are plotted in Fig. 5 for each of the reconstructed traces. Even for the pathological traces contained in the database they are always below 5%, which is considered to correspond to good trace quality [22].

V. CONCLUSIONS

Our model-based approach makes use of an algorithm where accuracy and computational complexity can be tuned to meet the needs of long-term ECG monitoring, overcoming issues about acquisition and wireless transmission of signals by wearable devices.

The proposed signal analysis approach achieves significant data compression, allowing to send ECG trace data as a stream at around 500 bit/s, which is sustainable by low-power wide-area network devices in mobile applications. Gaussian kernels achieve accurate morphological modelling of ECG traces, allowing accurate waveform reconstruction.

REFERENCES

[1] Yin, S. *et al.* "Wearable Physiological Multi-Vital Sign Monitoring System With Medical Standard." *IEEE Sensors Journal*, vol. 21, no. 23, pp. 27157-27167, 2021.

[2] Villanueva-Miranda, I., Nazeran, H., and Martinek, R. "CardiaQloud: A Remote ECG Monitoring System Using Cloud Services for eHealth and mHealth Applications." *In 2018 IEEE 20th Int. Conf. on e-Health Net., App. and Services (Healthcom)*, pp. 1-6, 2018.

[3] Giorgi, G., Galli, A. and Narduzzi, C. "Smartphone-based IOT systems for personal health monitoring." *IEEE Instrum. & Meas. Magazine*, vol. 23, no. 4, pp. 41-47, 2020.

[4] Ali, H., Naing, H. H. and Yaqub, R. "An IoT assisted real-time high CMRR wireless ambulatory ECG monitoring system with arrhythmia detection." *Electronics*, vol. 10, no. 16, pp. 1871, 2021.

[5] Abdelazez, M., Rajan, S. and Chan, A. D. "Detection of Abnormal Heartbeats in Compressed Electrocardiograms" *In 2018 IEEE Int. Sym. on Medical Measurements and Applications (MeMeA)*, pp. 1-6, 2018.

[6] Jambek, A. B. and Khairi, N. A."Performance comparison of Huffman and Lempel-Ziv Welch data compression for wireless sensor node application." *American Journal of Applied Sciences*, vol. 11, no. 1, pp. 119-126, 2014.

[7] Jha, C. K., and Kolekar, M. H. "Electrocardiogram data compression techniques for cardiac healthcare systems: A methodological review", *IRBM*, 2021.

[8] Giorgi, G. "A Combined Approach for Real-Time Data Compression in Wireless Body Sensor Networks." *IEEE Sensors Journal*, vol. 17, no. 18, pp. 6129-6135, 2017.

[9] Elgendi, M., Mohamed, A. and Ward, R. "Efficient ECG Compression and QRS Detection for E-Health Applications." *Scientific Reports*, vol. 7, no. 1, pp. 1-16, 2017.

[10] Servati, A. *et al.* "Novel flexible wearable sensor materials and signal processing for vital sign and human activity monitoring." *Sensors*, vol. 17, no. 7, pp. 1622, 2017.

[11] Galli A., Frigo, G. and Giorgi, G. "Robust ECG Denoising for eHealth Applications." *In 2018 IEEE Int. Sym. on Medical Measurements and Applications (MeMeA)*, pp. 1-6, 2018.

[12] Galli A. *et al.* "Denoising ECG Signal by CSTFM Algorithm: Monitoring During Motorbike and Car Races." *IEEE Trans. Instrum. Meas.*, vol. 68, no. 7, pp. 2433-2441, 2019.

[13] Galli, A., Narduzzi, C., and Giorgi, G. "ECG monitoring and anomaly detection based on compressed measurements." *In Proc. of the 2018 3rd Int. Conf. on Biomed. Imag., Sig. Proc.*, pp. 10-17, 2018.

[14] Clifford, G. D. *et al. "Model-based filtering, compression and classification of the ECG."*, *Int. Journal of Bioelectromagnetism*, vol. 7, no. 1, pp. 158-161, 2005

[15] McSharry, P. E. *et al.* "A dynamical model for generating synthetic electrocardiogram signals." *IEEE Trans. Biomed. Eng.*, vol. 50, no. 3, pp. 289-294, 2003.

[16] Sayadi, O. and Shamsollahi, M. B. "A model-based Bayesian framework for ECG beat segmentation." *Physiol. Meas.*, vol. 30, no. 3, pp. 335-352, 2009.

[17] Kheirati Roonizi, E., and Sassi, R. "A signal decomposition model-based Bayesian framework for ECG components separation." *IEEE Trans. Signal Proc.*, vol. 64, no. 3, pp. 665-674, 2016.

[18] Da Poian, G., Bernardini, R. and Rinaldo, R. "Gaussian dictionary for compressive sensing of the ECG signal." *In Proc. of 2014 IEEE Workshop on Biometric Measurements and Systems for Security and Medical Applications (BIOMS)*, pp. 80-85, 2014.

[19] Tropp, J. A. and Gilbert, A. C. "Signal recovery from random measurements via orthogonal matching pursuit." *IEEE Trans. Inf. Theory*, vol. 53, no. 12, pp. 4655-4666, 2007.

[20] De Chazal, P. *et al.* "Automated processing of the single-lead electrocardiogram for the detection of obstructive sleep apnoea." *IEEE Transactions on Biomedical Engineering*, vol. 50, no. 6, pp.686-696, 2003.

[21] Moody, G. B. and Mark, R. G. "The impact of the MIT-BIH Arrhythmia Database." *IEEE Eng in Med and Biol* vol. 20, no. 3, pp. 45-50, May-June 2001.

[22] Zigel, Y., Cohen, A., and Katz, A. (2000). The Weighted Diagnostic Distortion (WDD) Measure for ECG Signal Compression. IEEE Transactions on Biomedical Engineering, 47(11), 1422-1430.

25th IMEKO TC4 International Symposium
23rd International Workshop on ADC and DAC Modelling and Testing
IMEKO TC-4 2022
Brescia, Italy / September 12-14, 2022

Multiwavelet-based ECG compressed sensing with samples difference thresholding

Jozef Kromka, Ondrej Kovac, Jan Saliga, Linus Michaeli

Technical University of Kosice, Letna 9, 04200 Kosice, Slovakia
e-mail addresses: {jozef.kromka, ondrej.kovac, jan.saliga, linus.michaeli}@tuke.sk

***Abstract* – This paper introduces a novel Multiwavelet-based hybrid method of Compressed sensing (CS). A case study of CS and reconstruction of Electro Cardio Diagram (ECG) signals with the presented method was performed. For ECG signals the proposed method does not require a wave position detector and can reconstruct the signal with minimal DC offset error. The method is completely patient-agnostic and does not require prior patient-specific information as well. The proposed method was evaluated using the MIT-BIT database. The obtained results show a good reconstruction quality while keeping a high compression ratio.**

I. INTRODUCTION

Remote health monitoring systems are becoming more important for doctors to perform long-term patient monitoring [1], [2]. They can help diagnose various health issues the patient may suffer with. One of the signals often measured by the remote health monitoring system is ECG. There are also others signals measured by the remote health monitoring systems [2], but the focus throughout this article will be on ECG signals.

Remote health monitoring systems are usually composed of nodes. Nowadays, the most significant specification which poses the challenge is power consumption. Since nodes often use wireless transmission to communicate and transmit data, this step is the most power-demanding [3]. By utilizing signal compression, the number of transmissions can be reduced, which would save energy. Used compression should not be computationally difficult because that would significantly increase power consumption [4]. Standard compressions are performed by sampling the signal according to Shannon's theory. This signal is often processed to remove redundancy by decorrelation. Then only a few coefficients from the transformed signal need to be transmitted. This approach showed a good compression efficiency with a low error after reconstruction. But the standard compressions also have several drawbacks. For example, matrix multiplication which is used to perform transformation is power-demanding [5]. The compression which utilizes transformation works by prioritizing low-frequency components of the signal over high-frequency components [6]. Compressed sensing [7] is a novel method of compression, which is not power-demanding as the standard compression methods [8]. It performs the compression directly while acquiring the signal. CS utilizes the signal sparsity to achieve sufficient compression and signal reconstruction at the sub-Shannon sampling rate. These properties of CS can be used to lower power consumption in remote health monitoring systems.

In recent years, various methods for the application of CS directly to ECG signals were proposed. A hybrid encoding algorithm for real-time CS acquisition of ECG signals was introduced in [9]. The algorithm can be used for efficient ECG acquisition with a reduced computational load on the compressor. Dictionary-based CS reconstruction method was introduced in [10]. A novel approach for the optimization of a dictionary, which is used in ECG signal reconstruction was proposed. The results showed this dictionary can increase performance, over the standard trained dictionaries, due to lower redundancy. But these methods use the R peak detector which requires additional logic and computational power. In [11] a new greedy algorithm was proposed. This algorithm requires the support information about the signal to improve reconstruction quality. ECG CS method with high compression ratio and dynamic model reconstruction was proposed in [12], [13]. This method uses a QRS detector to detect the exact R wave position for signal segmentation before compression. The drawback of this method is that it requires the R peak detector and that it introduces a DC offset error to the signal between the frames.

The proposed algorithm is based on Multiwavelets and a novel approach of CS sampling. The method was evaluated on ECG signals. For ECG signals this approach of CS does not require a wave position detector and can reconstruct the signal with minimal DC offset error. The method is completely patient-agnostic and does not require prior patient-specific information as well.

The article is organized as follows: The second section introduces the theoretical background of CS and Discrete Multiwavelet transform (DMWT). The third section describes proposed CS sampling, and signal reconstruction algorithms. In the fourth section, the performance of the new algorithm was assessed using the MIT-BIH arrhythmia database. Finally, the conclusion and direction of future works are presented in the last section.

II. THEORETICAL BACKGROUND

In this section, the theoretical background of CS is explained. The basic theory of DMWT, used as the basis for sparse signal recovery, is presented in the latter part of this section.

A. Compressed sensing theory

CS assumes that the signal can be represented by only K nonzero coefficients with a suitable basis, where K is much smaller than the signal length. This signal is called a sparse signal. Usually, the signals are sparse on some orthogonal basis [11]. Some signals do not show sparsity with an orthogonal basis. In that case, a dictionary basis [10] can be used to sparsify the signals. In both cases, the sparse representation of a signal can be obtained according to (1)

$$f = \psi x, \tag{1}$$

where f is a signal with length N, ψ is a N × N basis matrix, and x is the sparse representation of the signal. The sparse representation of the signal has length N, but only K coefficients are nonzero values.

In CS, the signal is sampled not uniformly like in common signal acquisition methods. The signal is sampled according to the measurement matrix. The sampling can be defined by the following equation (2)

$$y = \phi f, \tag{2}$$

where y is a compressed measurement with length M, ϕ is the M × N measurement matrix, and f is the signal with length N.

If the signal f is sparse on some basis, and K < M << N, then the compressed measurement y contains enough information to reconstruct the signal f. The signal is reconstructed according to (1). The sparse representation of the signal can be obtained by substituting the signal f in (2) by expression (1) forming the following equation (3)

$$y = \phi\psi x. \tag{3}$$

One of the requirements to be able to obtain the sparse solution to (3) is that the measurement matrix must be incoherent with the basis matrix. In other words, rows of measurement matrix can not sparsely represent the columns of the basis matrix [15]. Incoherency can be achieved by constructing the measurement matrix in a way that the signal is sampled at random places.

Usually, in (3) the measurement and the basis matrix are substituted with the reconstruction matrix A. The reconstruction matrix can be obtained according to (4)

$$A = \phi\psi. \tag{4}$$

The size of the reconstruction matrix is M × N. By substituting the basis and the measurement matrix by (4) in (3) following equation (5) is obtained

$$y = Ax. \tag{5}$$

The equation (5) is used to find the sparse representation of the signal for the compressed measurement. Since there are N unknowns and M equations, and N > M, this system of equations is an undetermined system of linear equations.

The solution to the undetermined system of linear equations is usually based on minimalization according to (6)

$$\min_{x\in\mathbb{R}^n} \|x\|_p, \qquad subject\ to\ y = Ax, \tag{6}$$

where $\|-\|_p$ indicates l_p norm. Initially, an l_0 norm was proposed in [7]. But among all possible norms, the l_0 norm is polynomial-time hard, highly unstable and the solution can be found only by brute force methods [13]. Thus using the l_1 norm was proposed in [16]. The l_1 norm problems can be solved by convex optimization algorithms, or by greedy algorithms. One difference between the algorithms is that greedy algorithms are suboptimal. Another difference is that they can reach an almost optimal solution with a lower number of computations compared to convex optimization algorithms [17]. The greedy algorithms usually require prior knowledge of how much the signal is sparse. The convex optimization algorithms do not require this prior information. The most used convex optimization algorithm is the basis pursuit algorithm [15]. The most used greedy algorithms are Orthogonal Matching Pursuit (OMP), Compressive sampling matching pursuit (CoSaMP), and Iterative Hard Thresholding (IHT) [15].

B. Discrete Multiwavelet transform

DMWT was developed as the result of the advancement in the development of Discrete Wavelet transform (DWT) and Wavelet theory. The main difference between DMWT and DWT is that DWT uses only one scaling and one wavelet function to approximate the signal, while DMWT can use up to r scaling and r wavelet functions. In the DMWT case, these functions are called multiscaling and multiwavelet functions. The advantage of DMWT over DWT is that the multiscaling and multiwavelet function has compact support, high smoothness, and high approximation order. Multiscaling and multiwavelet functions are symmetric as well as orthogonal [18]. They are represented as vectors according to (7)

$$\begin{aligned} \varphi &= (\varphi_1, \dots, \varphi_r)^T \\ \psi &= (\psi_1, \dots, \psi_r)^T, \end{aligned} \tag{7}$$

where φ is the multiscaling function, ψ is the multiwavelet function, r is the multiplicity of multiscaling and multiwavelet function, and T means transpose. As in the DWT case, these functions are not defined as shown in (7), but rather in the form of an impulse response. In the DMWT case, these impulse responses are defined as matrices with the size $r \times r$. In general $g_0(0) \dots g_0(n)$ are the matrix impulse responses of multiscaling functions and $g_1(0) \dots g_1(n)$ are the matrix impulse responses of wavelet functions.

Multiwavelets used in the presented method are Donovan-Geronimo-Hardin-Massopust (DGHM), BAT,

Chui – Lian (CL), Daubechies (DB), Symmetric Asymmetric of order 4 (SA4), and Haar Multiwavelet. These Multiwavelets were selected because they can be easily found in literature as well as they are implemented and ready to use in the following Multiwavelet toolbox [19]. The matrix impulse responses of these Multiwavelets with the corresponding literature can be found in [18].

To use DMWT as a basis for CS, the basis matrix needs to be constructed. The Multiwavelet basis matrix can be constructed similarly to the Wavelet basis matrix [20]. The Wavelet scalar impulse responses are replaced by the matrix impulse responses of Multiwavelets. The basis matrix then can be constructed according to (8). It is also important to keep in mind, that the constructed matrix will be r times bigger after substituting the coefficients of matrix impulse responses, into the designed basis matrix

$$U=\begin{bmatrix} g_0(n) & g_0(n-1) & \dots & g_0(0) & \dots & 0 \\ g_1(n) & g_1(n-1) & \dots & g_1(0) & \dots & 0 \\ 0 & 0 & g_0(n) & g_0(n-1) & \dots & g_0(0) \\ 0 & 0 & g_1(n) & g_1(n-1) & \dots & g_1(0) \end{bmatrix}. \quad (8)$$

The basis matrix can be constructed in another way by using the DMWT on the columns of the identity matrix and rearranging the coefficients. With this approach, it is also possible to construct a multilevel Multiwavelet basis matrix. For the multilevel Multiwavelet basis matrix, multilevel DMWT should be applied to the columns of the identity matrix. The implementation of the DMWT and multilevel DMWT can be found in [19].

III. THE PROPOSED CS ALGORITHM

This section presents a novel hybrid method of CS. The section is split into two parts. The proposed method of CS on the transmitter side is introduced, in the first part. Subsequently, the reconstruction algorithm is explained in the following subsection. To perform DMWT and to construct the basis, a Multiwavelet toolbox for MATLAB was used [19]. To find the sparse solution according to equation (5) in the proposed signal reconstruction method, the CVX package for specifying and solving convex programs was used [21].

A. CS performing

The block diagram of the proposed ECG compression algorithm is outlined in Fig. 1. The ECG signal is acquired at the sampling frequency f_S and split into frames with constant length N. From the frame, DC offset is removed and saved to the data block. The frame $f[n]$ is then filtered with the multiscaling impulse responses of chosen Multiwavelet. This filtration is performed L times, achieving L^{th} level of DMWT transform for only multiscaling coefficients. These multiscaling coefficients $c_{1,2}$ with respective length $N/2^L$ are stored for quantization and encoding as well as filtered with the inverse multiscaling impulse responses of chosen Multiwavelet. This filtration is also performed L times, achieving L^{th} level of inverse DMWT transform. The resulting signal will present the low-frequency component of the ECG signal. Low-frequency component ECG signal is then removed from the original ECG signal. After removal, a high-frequency component ECG signal is obtained.

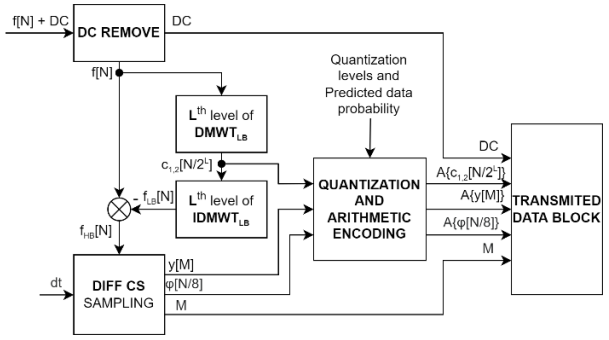

Fig. 1. Block diagram of CS ECG signal acquisition

The high-frequency component of ECG will be input to the block which performs the Samples Difference Thresholding. (SDT). SDT block performs the CS sampling and constructs the sensing matrix, used for the signal reconstruction. The SDT block computes the difference between the two samples, and if the difference is higher than the defined constant dt then the latter sample is stored in a compressed measurement signal, and the position is stored in the sensing matrix. If the difference is less than dt then only zero is stored in the sensing matrix. The SDT block also keeps track of the size of the compressed measurement signal. The SDT would never sample the first sample of the frame as well as it cannot evaluate the difference between the last sample and the first sample of the following frame. That is why the first and the last sample are stored automatically. The size of the compressed measurement signal is then directly stored in the data block. Compressed measurement signal y, together with the sensing matrix ϕ and the multiscaling coefficients $c_{1,2}$ are then quantized and encoded with the arithmetic encoding. A linear quantization with a defined number of quantization levels was used. While evaluating the method, it was found that the histogram of the Compressed measurement signal and multiscaling coefficients is resembling the Gauss function. This information is used while performing the arithmetic encoding. The sensing matrix is stored in a form of a binary number with N bits. The binary number is then divided into the binary array with a length of 8 forming 8-bit numbers. These 8-bit numbers are also encoded with the arithmetic encoder because they have big redundancy. DC offset, compressed measurement signal, length of the compressed measurement signal, multiscaling coefficients, and sensing matrix are then stored in the data block.

B. CS reconstruction

The reconstruction method is outlined in Fig. 2. The

method is slightly different from the basic CS signal reconstruction. All data from the transmitted data block are decoded and then dequantized.

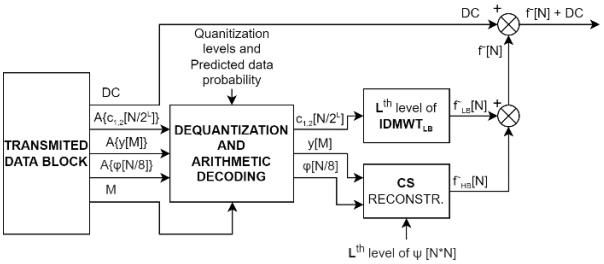

Fig. 2. Block diagram of ECG signal reconstruction

The compressed measurement signal, with the signal length and measurement matrix are used to reconstruct the high-frequency component of the ECG signal. The multiscaling coefficients are used to restore the low-frequency component of the ECG signal. The low-frequency and the reconstructed high-frequency component are then combined. In the end, the DC offset is restored and the final reconstructed ECG frame is obtained.

IV. EXPERIMENTAL RESULTS

The proposed method was evaluated in the MATLAB environment using the MIT-BIH arrhythmia database [14] as a set of test ECG signals. The database contains 48 ECG records sampled at 360 Hz with 11-bit resolution. To evaluate the compression ratio (CR) of the proposed method following equation (9) was used

$$CR = \frac{N\mathrm{B}_0}{D}. \qquad (9)$$

In equation (9), N is the frame length, B_0 is the bit resolution of the original signal, which is 11 in the case of the MIT-BIH database. The D represents the number of bits in the transmitted data block. The number of transmitted bits is calculated by adding the length of respective data according to (10)

$$D = len\left(A\{c_{L,(1,2)}\}\right) + len\{A\{y\}\} + len\{A\{\phi\}\} + 2B_0, \qquad (10)$$

where $c_{L,(1,2)}$ are multiscaling coefficients, y is a compressed measurement signal, ϕ is a sensing matrix, $A\{arg\}$ means arithmetic encoding, and $len\{arg\}$ is an operation that will return the length of the code. 2 times B_0 represents the DC offset information and the length of the compressed measurement signal. Another parameter used to evaluate the proposed method is the reconstruction error. Reconstruction error is evaluated with percentage root mean squared difference (PRD) given by (11)

$$PRD = 100\sum_{n=1}^{N}\frac{\|x_n - \hat{x}_n\|_2}{\|x_n\|_2}, \qquad (11)$$

where x_n represents an original signal sample and $\hat{x}_n$ represents the reconstructed signal sample. The obtained error is a result of several factors. The first is the noise included in the MIT-BIH database. This noise is not present in the reconstructed signal, which influences the obtained error. The second factor is a quantization noise after quantization of the compressed measurement signal and multiscaling coefficients. And last is the error caused by the CS compression method.

All the tests to evaluate the proposed method were performed on the first channel of all MIT-BIH database records. The parameters used during the test are listed in Table 1.

Table 1. Parameters used during the evaluation

Parameter	Value	Parameter	Value
N	2048	$\max Q_{LB}\ level$	2
L	3	$\min Q_{LB}\ level$	-2
dt	0.03	$\max Q_{HB}\ level$	0.5
B_{LB}	6; 7 (64; 128 levels)	$\min Q_{HB}\ level$	-0.5
B_{HB}	6; 7 (64; 128 levels)		

where B_{LB} is the number of bits used to quantize the low-frequency component of the ECG signal. Similarly B_{HB} is the number of bits used to quantize the high-frequency component of the ECG signal. The max and min Q_{LB} and Q_{HB} levels represent the maximal and the minimal quantization level for respective ECG signal components. The evaluation was performed for seven Multiwavelets. For each Multiwavelet the evaluation was performed while using 6 and then 7 bits for quantization. The results are shown in Fig. 3.

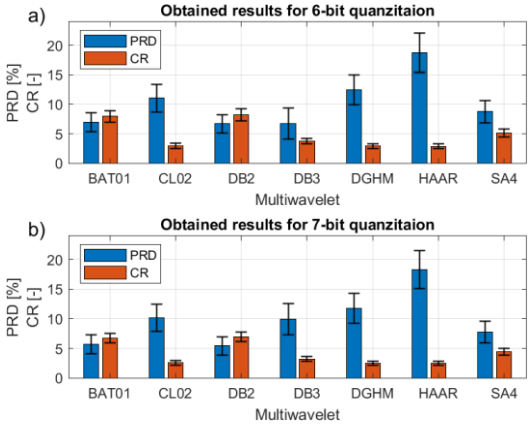

Fig. 3. PRD and CR results for a) 6-bit quantization, b) 7-bit quantization

As expected, the results for 7-bit quantization have lower CR and lower PRD than the results for 6-bit quantization. Lower PRD is the result of a smaller quantization error. From all Multiwavelets evaluated, DB2 and BAT01 Multiwavelets performed the best. Since DB2 Multiwavelet performed slightly better than BAT01 Multiwavelet, the next section will be focused on experiments performed with DB2 Multiwavelet.

The next experiment was focused on the influence of the quantization on the PRD and CR after reconstruction. This experiment was performed similarly to the previous

experiment but only with the use of DB2 Multiwavelet. The experiment was performed for 7 different numbers of quantization bits. The results are shown in Fig. 4.

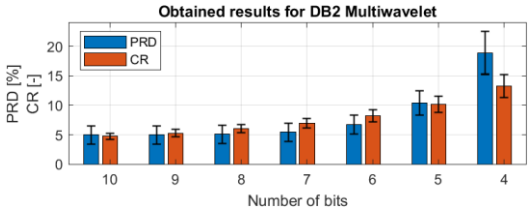

Fig. 4. PRD and CR results for DB2 Multiwavelet

Both PRD and CR were rising with the use of fewer bits for quantization. For the 10 to 8 bits used for quantization, the PRD change was less than 0.1 %. From 7 bits, the PRD started to exponentially increase. The CR was steadily increasing throughout the whole experiment. The best CR to PRD ratio was achieved by using 8-6 bits for quantization. For ECG signals the proposed method could operate at 8-6 quantization bits depending on the required PRD and CR. In the next section, a case study for chosen ECG record will be performed.

The visual comparison of the original ECG signal and reconstructed ECG signal for 6-bit and 7-bit quantization, with the use of DB2 Multiwavelet, is shown in Fig. 5.

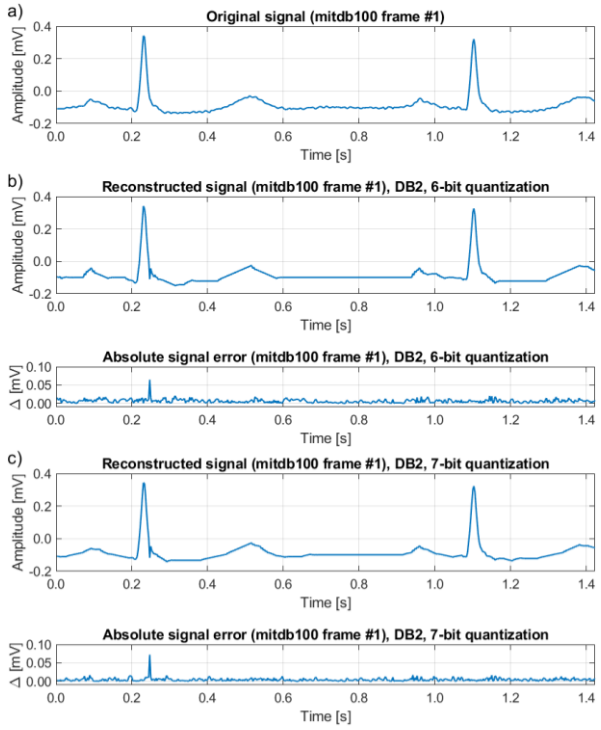

Fig. 5. Case study of ECG frame #1 a) Original ECG signal, b) Reconstructed ECG signal with 6-bit quantization and absolute error, c) Reconstructed ECG signal with 7-bit quantization and absolute error

In Fig. 5, the detail of two heartbeats from the first frame is shown. The reconstruction error is shown as well. The obtained results for the first frame with 6-bit quantization, shown in Fig. 5 b), were as follows. The calculated PRD after the signal reconstruction was 6.982 % and CR was 11.384. The obtained results for the first frame with 7-bit quantization, shown in Fig. 5 c), were as follows. The calculated PRD after the signal reconstruction was 4.966 % and CR was 9.422. The exact position of R waves of the heartbeat in Fig. 5 was in both cases included. The reconstruction error was mostly influenced by the quantization and by the noise which is present in the MIT-BIH database. The error after sparse signal reconstruction is present as well. The reconstructed signals in Fig. 5 are noiseless because the sparse signal recovery algorithms do not reconstruct the signal noise. The ECG signal in Fig. 5. c) is smoother than in Fig. 5. b). It is directly influenced by quantization. In both cases, there is an error around the 0.25-second mark. This error was caused by the signal reconstruction. But the error peak is lower than 80 µV which represents roughly 15 % error compared to peak to peak value of the ECG wave. Visually for the diagnostic, the error peak does not represent a significant error because it is a single value error. That peak error may be minimized by using more optimized method parameters.

The last experiment was focused on the frame transition and R wave amplitude change. The algorithm removes DC offset from the frame and then after reconstruction DC offset is restored. This can distort the transition between frames.

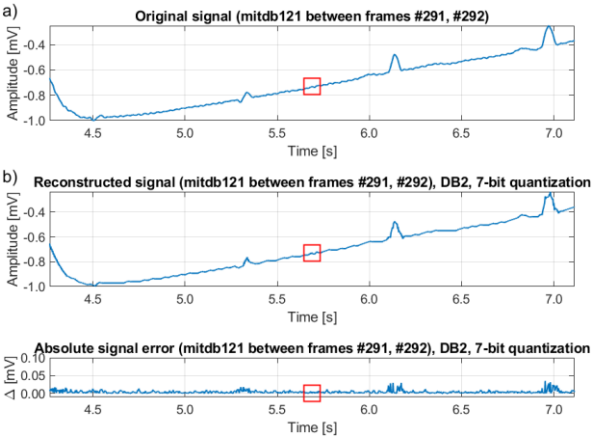

Fig. 6. DC offset error case study a) Original ECG signal b) Reconstructed ECG signal with absolute error

The distortion between the frames was present in the previously proposed method [13]. The method proposed in this article does not remove only the DC offset but removes the low-frequency component of ECG as well. Thus the distortion between the frames is minimal. This can be shown in the transition between the 291 and 292 frames of the mitdb121 record. The difference in DC offset is the biggest for this record. The detail of the transition between frames is shown in Fig. 6. The distortion is lower than 10 µV which is much less than in the previous method proposed in [13] where the DC offset error was more than 100 µV for the same record.

V. CONCLUSION AND FUTURE WORKS

In this paper, a novel method of CS usable for ECG signals was introduced. The proposed method can reconstruct the ECG signal with sufficient quality to perform patient diagnostics while keeping high CR. The main advantage of the novel method is that it does not acquire prior information, patient-specific information, or any detector for ECG signal compression.

Future work is directed to: (i) evaluation of the method for different signals, (ii) evaluation of other Multiwavelets, (iii) evaluation of nonlinear quantization, (iv) searching for optimal configuration for the proposed method, (v) implementation of hardware prototype.

ACKNOWLEDGMENT

The work is a part of the project supported by the Science Grant Agency of the Slovak Republic (No. 1/0413/22).

REFERENCES

[1] S. Majumder, T. Mondal, and M. J. Deen, "Wearable Sensors for Remote Health Monitoring," *Sensors*, vol. 17, no. 1, Art. no. 1, Jan. 2017.

[2] N. El-Rashidy, S. El-Sappagh, S. M. R. Islam, H. M. El-Bakry, and S. Abdelrazek, "Mobile Health in Remote Patient Monitoring for Chronic Diseases: Principles, Trends, and Challenges," *Diagnostics*, vol. 11, no. 4, p. 607, Mar. 2021.

[3] S. C. Mukhopadhyay, "Wearable Sensors for Human Activity Monitoring: A Review," *IEEE Sens. J.*, vol. 15, no. 3, pp. 1321–1330, Mar. 2015.

[4] P. Klavík, A. C. I. Malossi, C. Bekas, and A. Curioni, "Changing computing paradigms towards power efficiency," *Philos. Transact. A Math. Phys. Eng. Sci.*, vol. 372, no. 2018, p. 20130278, Jun. 2014.

[5] M. Kumm, M. Hardieck, and P. Zipf, "Optimization of Constant Matrix Multiplication with Low Power and High Throughput," *IEEE Trans. Comput.*, vol. 66, no. 12, pp. 2072–2080, Dec. 2017.

[6] K. Sayood, *Introduction to Data Compression*. Morgan Kaufmann, 2017.

[7] D. L. Donoho, "Compressed sensing," *IEEE Trans. Inf. Theory*, vol. 52, no. 4, pp. 1289–1306, Apr. 2006.

[8] D. Craven, B. McGinley, L. Kilmartin, M. Glavin, and E. Jones, "Compressed Sensing for Bioelectric Signals: A Review," *IEEE J. Biomed. Health Inform.*, vol. 19, no. 2, pp. 529–540, Mar. 2015.

[9] P. Bera and R. Gupta, "Hybrid encoding algorithm for real time compressed electrocardiogram acquisition," *Measurement*, vol. 91, pp. 651–660, z 2016.

[10] L. De Vito, E. Picariello, F. Picariello, S. Rapuano, and I. Tudosa, "A dictionary optimization method for reconstruction of ECG signals after compressed sensing," *Sensors*, vol. 21, no. 16, 2021.

[11] M. Melek and A. Khattab, "ECG compression using wavelet-based compressed sensing with prior support information," *Biomed. Signal Process. Control*, vol. 68, 2021.

[12] J. Saliga, P. Dolinsky, I. Andras, and L. Michaeli, "A new CS method for ECG signal," in *24th IMEKO TC4 International Symposium and 22nd International Workshop on ADC and DAC Modelling and Testing (IMEKO TC-4 2020)*, Palermo, Italy, 2020, pp. 6–11.

[13] J. Šaliga, I. Andráš, P. Dolinský, L. Michaeli, O. Kováč, and J. Kromka, "ECG compressed sensing method with high compression ratio and dynamic model reconstruction," *Measurement*, vol. 183, p. 109803, Oct. 2021.

[14] G. B. Moody and R. G. Mark, "The impact of the MIT-BIH Arrhythmia Database," *IEEE Eng. Med. Biol. Mag.*, vol. 20, no. 3, pp. 45–50, May 2001.

[15] Y. C. Eldar and G. Kutyniok, Eds., *Compressed sensing: theory and applications*. Cambridge ; New York: Cambridge University Press, 2012.

[16] G. M. Fung and O. L. Mangasarian, "Equivalence of Minimal ℓ0- and ℓp-Norm Solutions of Linear Equalities, Inequalities and Linear Programs for Sufficiently Small p," *J. Optim. Theory Appl.*, vol. 151, no. 1, pp. 1–10, Oct. 2011.

[17] L. De Vito, F. Picariello, S. Rapuano, I. Tudosa, and L. Barford, "A Compressive Sampling-Based Channel Estimation Method for Network Visibility Instrumentation," *IEEE Trans. Instrum. Meas.*, vol. 69, no. 5, pp. 2335–2344, May 2020.

[18] F. Keinert, *Wavelets and Multiwavelets*, 1st edition. Boca Raton, FL: Chapman and Hall/CRC, 2003.

[19] J. Kromka, O. Kováč, and J. Šaliga, "Multiwavelet toolbox for MATLAB," in *2022 32nd International Conference Radioelektronika (RADIOELEKTRONIKA)*, Apr. 2022, pp. 01–05.

[20] A. Jensen and A. la Cour-Harbo, *Ripples in Mathematics*. Berlin, Heidelberg: Springer Berlin Heidelberg, 2001.

[21] "CVX: Matlab Software for Disciplined Convex Programming | CVX Research, Inc." http://cvxr.com/cvx/ (accessed Mar. 18, 2022).

25th IMEKO TC4 International Symposium
23rd International Workshop on ADC and DAC Modelling and Testing
IMEKO TC-4 2022
Brescia, Italy / September 12-14, 2022

Numerical Modelling of the Magnetic Fields Generated by Underground Power Cables with Two-point Bonded Shields

Eduard Lunca[1], Silviu Vornicu[2], Alexandru Salceanu[3]

[1]*Faculty of Electrical Engineering, 23 Prof. Dimitrie Mangeron Blvd., 700050 Iasi, Romania, elunca@tuiasi.ro, +40 232701246*
[2]*Faculty of Electrical Engineering, 23 Prof. Dimitrie Mangeron Blvd., 700050 Iasi, Romania, silviusieca@gmail.com, +40 232701246*
[3]*Faculty of Electrical Engineering, 23 Prof. Dimitrie Mangeron Blvd., 700050 Iasi, Romania, asalcean@tuiasi.ro, +40 232701157*

***Abstract* – In this study we present a 2D finite element model for computing magnetic fields generated by underground power cables with two-point bonded shields. The model is developed in ANSYS Maxwell 2D low-frequency electromagnetic field simulation software for a typical 12/20 kV three-phase underground power cable system in flat formation, but it can be adapted to any line. The model validation is achieved by analytical computations conducted with a software tool based on the Biot-Savart law and superposition principle. RMS magnetic flux density profiles calculated at various heights above the ground with these two methods correlate very well. This is also true for induced shield currents.**

I. INTRODUCTION

The continuous development of urban centers leads to an increase in the demand for electricity, hence underground power cables (UPCs) are becoming more frequent in these places. It is well known that, similar to overhead power lines, UPCs generate low-frequency electric and magnetic fields. The electric fields are nearly completely eliminated by the surrounding metallic sheath(s) and the conducting soil. In contrast, the magnetic fields are not shielded and reduce only by distance. In fact, the magnetic fields from an UPC sometimes can be stronger than those generated by a corresponding overhead power line because these lines are located farther away from ground [1,2].

Calculating magnetic fields from UPCs is very important in several research areas, including human exposure evaluation studies [3-8]. A common 2D approach is based on the Biot-Savart law and superposition principle, assuming that the conductors are straight, horizontal, infinitely long and parallel to each other and the effect of the induced shield currents on the magnetic field is negligible. However, when dealing with solid bonding (i.e., the underground cables operate with their metallic shields bonded and grounded at both ends), the circulating currents induced in shields may achieve the same order as the wire-core currents, which leads to a weakening of the total magnetic field. In some references, e.g. [9] and [10], analytical expressions for the induced shield currents have been obtained under balanced three-phase conditions. It has also been considered the magnetic field reduction.

Some finite element models have also been developed for computing magnetic fields from UPCs with two-point bonded shields. An extensive study is presented in [11], which uses COMSOL Multiphysics to investigate the magnetic field reduction rate for a three-phase flat cable system as a function of the distance between cables, the shield diameter, as well as the cross-sectional area of the cable shields. In [12], QuickField was mainly used for predicting underground cable ampacity (for both flat and trefoil formations), while the developed 2D model also allows investigating the magnetic field distribution at the ground surface. Another study to be mentioned is [13], in which ANSYS Maxwell 2D was used for studying loss reduction in cable sheathing and, in much lesser extent, magnetic field distribution close to the ground surface.

In our study, the problem of the magnetic field from underground power cables with two-point bonded shields is also solved using ANSYS Maxwell 2D. The proposed model is developed for a typical 12/20 kV three-phase underground power cable system in flat formation, but it can be adapted to any line. For validation, calculated magnetic fields are checked against analytical results obtained with a software tool based on the Biot-Savart law and superposition principle, which represents an updated version of a previously developed program [2].

The rest of the paper is structured as follows: Section II presents the geometry and simulation conditions for the

UPC system considered for analysis; Section III describes the proposed finite element model; Section IV deals with model validation; Section V discusses numerical simulation results; Section V draws conclusions.

II. UNDERGROUND POWER CABLE SYSTEM SELECTED FOR ANALYSIS

The basic geometry of the three-phase cable system selected for analysis is presented in Fig. 1a. It consists of three NA2XS(FL)2Y 12/20 kV single-core medium voltage cables in flat formation, separated by a distance between centers of 0.1 m and buried in the ground at a depth of 0.8 m. Each cable has an aluminum (Al) core conductor with the cross-sectional area of 150 mm^2 and a copper (Cu) wire shield with the cross-sectional area of 25 mm^2. The copper shields are grounded at the ends of the cables as depicted in Fig. 1b. For computation, it is assumed that the three-phase UPC system has balanced currents, as follows: $\underline{I}_1$ = 100 A ∠ -120°, $\underline{I}_2$ = 100 A ∠ 0° and $\underline{I}_3$ = 100 A ∠ 120°. The simulation temperature is set to 22 °C, which is default in ANSYS Maxwell 2D.

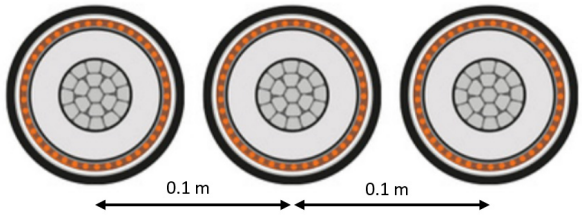

a)

b)

Fig. 1. Three-phase UPC system: a) basic geometry; b) two-point bonding scheme

III. FINITE ELEMENT MODEL

ANSYS Maxwell 2D is a software package that uses finite element method (FEM) to solve 2D low-frequency electromagnetic problems, by specifying the appropriate geometry, material properties and excitations for a device or system of devices – in our case, a three-phase underground power cable system. The proposed problem is solved using the "eddy current solver", which allows computing steady state, time-varying (AC) magnetic fields at a given frequency, here 50 Hz.

The global FEM model is illustrated in Fig. 2a, where the computational domain is a square of side a = 40 m, sufficiently large to determine the behavior of the magnetic field well outside from the centerline. The three-phase UPC system is buried – at the mentioned depth – in a ground with the electrical conductivity σ = 0.05 S/m and the relative magnetic permeability μ_r = 1. Each power cable is modeled as presented in Fig. 2.b, using a simplified 4-layer cable model consisting of Al core conductor ($\sigma = 34.45 \cdot 10^6$ S/m and $\mu_r = 1$), XLPE insulation ($\sigma = 1 \cdot 10^{-15}$ S/m and $\mu_r = 1$), Cu shield ($\sigma = 58 \cdot 10^6$ S/m and $\mu_r = 1$) and HDPE cover ($\sigma = 1 \cdot 10^{-14}$ S/m and $\mu_r = 1$). The thickness (th) of the Cu shield layer is chosen so that it matches the specified 25 mm^2 cross-sectional area.

The values of the wire-core currents (amplitude and phase) are assigned using the software functionality "Current Excitation", whereas the shield bonding is encoded in the model by the coupled electrical circuit in Fig. 2c, where external windings are used for controlling the induced shield currents. This electrical circuit was defined with Maxwell Circuit Editor.

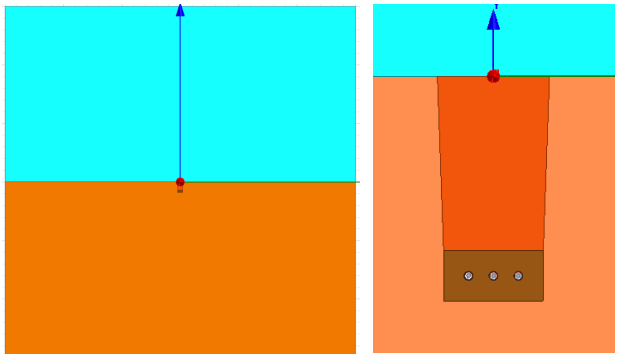

a)

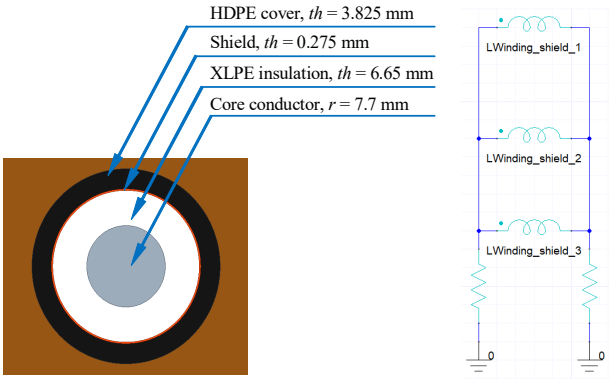

b) c)

Fig. 2. ANSYS Maxwell 2D model for computing magnetic fields from power cables with two-point bonded shields: a) global geometric model; b) simplified cable model; c) coupled circuit for shield bonding

The applied boundary conditions are of Balloon type, which models the region outside the defined space as extending to infinity. In this case, the magnetic vector

potential, $\vec{A}$, goes to zero at infinity; the magnetic flux lines are neither tangential nor normal to the Balloon boundary [14].

A fine mesh was defined for analysis, totalizing a number of triangle elements in the order of 710000. The adaptive setup was configured with a maximum number of passes of 10 and a percent error of 0.1. The convergence was set as 30% refinement per pass, minimum number of passes of 2 and minimum converged passes of 1. The adaptive frequency was 50 Hz.

With this approach, ANSYS Maxwell 2D allowed us generating instantaneous magnetic flux density distributions in the cross section of the cable system (over a period of 20 ms), as presented in Fig. 3a. The RMS magnetic flux density at any desired height h above the ground is determined by importing a sufficiently large number of instantaneous magnetic flux density profiles (Fig. 3b) in Microsoft Excel, where they are summed together with the formula [15, 16]:

$$B_{RMS}(i) = \sqrt{\frac{1}{N}\sum_{n=1}^{N} B_n^2(i)}, \quad (1)$$

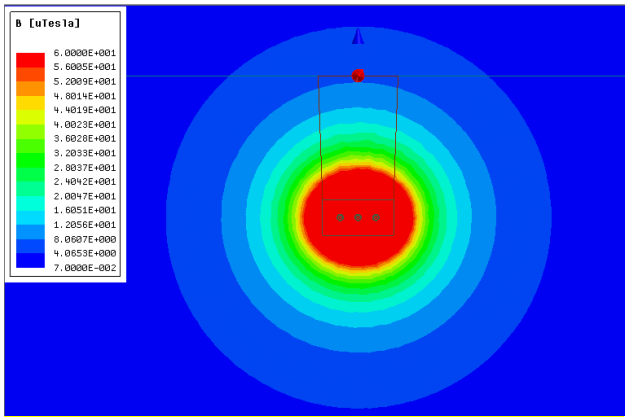

a)

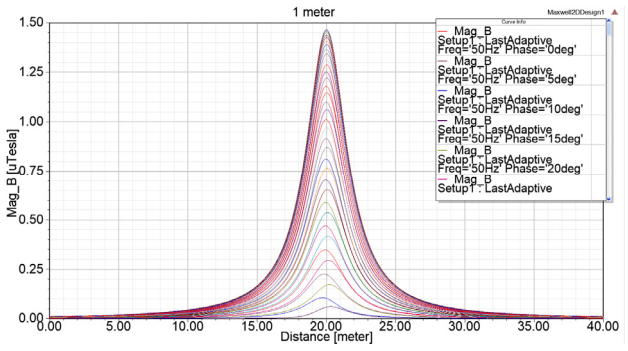

b)

Fig. 3. Example of simulation results: a) momentary magnetic field distribution in the cross section of the cable system (t = 15.55 ms); b) instantaneous magnetic flux density profiles at h = 1 m above the ground

where $B_1(i)$, …, $B_N(i)$ are the instantaneous values of the magnetic flux density corresponding to the point i of the profile and $N = 73$ is the total number of values. These results will be discussed in Section V.

IV. MODEL VALIDATION

In order to verify the numerical results obtained with the proposed FEM model, an interactive software tool based on the Biot-Savart law and superposition principle has been developed. Based on the assumptions in Section I, the total magnetic flux density at any measuring point (x, y) in the vicinity of the cable system can be calculated as:

$$\underline{B}_x = \sum_{i=1}^{3} \frac{-\mu_0}{2\pi}\left(\underline{I}_i + \underline{I}_{shi}\right)\left[\frac{y-y_i}{r_i^2}\right]; \quad (2)$$

$$\underline{B}_y = \sum_{i=1}^{3} \frac{\mu_0}{2\pi}\left(\underline{I}_i + \underline{I}_{shi}\right)\left[\frac{x-x_i}{r_i^2}\right]; \quad (3)$$

$$B = \sqrt{\left|\underline{B}_x\right|^2 + \left|\underline{B}_y\right|^2}, \quad (4)$$

where $\underline{I}_i$ is the phase current carried by the conductor located at (x_i, y_i), $\underline{I}_{shi}$ is the circulating current in the shield located at (x_i, y_i), $r_i = \sqrt{(x-x_i)^2 + (y-y_i)^2}$ represents the distance between the conductor/shield and the measurement point (x, y) and $\mu_0 = 4\pi \cdot 10^{-7}$ H/m is the magnetic permeability of the free space.

If assuming the same phase sequence ($\underline{I}_1 = I \angle -120°$, $\underline{I}_2 = I \angle 0°$ and $\underline{I}_3 = I \angle 120°$), it can be shown that the currents induced in the shields of a three-phase underground cable system in flat formation have the following expressions [17]:

$$\underline{I}_{sh1} = \frac{\underline{I}_2}{2}\left[\frac{Q^2}{R_{sh}^2+Q^2} - \frac{\sqrt{3}R_{sh}P}{R_{sh}^2+P^2} + j\left(\frac{R_{sh}Q}{R_{sh}^2+Q^2} + \frac{\sqrt{3}P^2}{R_{sh}^2+P^2}\right)\right]; \quad (5)$$

$$\underline{I}_{sh2} = -\underline{I}_2\left(\frac{Q^2}{R_{sh}^2+Q^2} + j\frac{R_{sh}Q}{R_{sh}^2+Q^2}\right); \quad (6)$$

$$\underline{I}_{sh3} = \frac{\underline{I}_2}{2}\left[\frac{Q^2}{R_{sh}^2+Q^2} + \frac{\sqrt{3}R_{sh}P}{R_{sh}^2+P^2} + j\left(\frac{R_{sh}Q}{R_{sh}^2+Q^2} - \frac{\sqrt{3}P^2}{R_{sh}^2+P^2}\right)\right], \quad (7)$$

where:

- R_{sh} is the shield resistance at the considered temperature, in Ω/m;
- $Q = X - \frac{X_m}{3} = \omega\left(M - \frac{M_m}{3}\right)$;
- $P = X + X_m = \omega(M + M_m)$;
- $M = 2 \cdot 10^{-7} \ln\left(\frac{s}{r_{sh}}\right)$, in H/m;
- $M_m = 2 \cdot 10^{-7} \ln 2$, in H/m.

In the expression of M above, s is the spacing between the centers of the adjacent conductors, in m, and r_{sh} is the mean of the outer and inner radii of the shield, also in m.

Finally, the shield resistance R_{sh} (at a shield temperature t_{sh}) is calculated with the formula:

$$R_{sh} = \frac{\rho_{sh20}}{A_{sh}}[1 + \alpha_{sh20}(t_{sh} - 20)], \qquad (8)$$

where ρ_{sh20} is the electrical resistivity of the shield material at 20 °C, A_{sh} is the shield cross-sectional area and α_{sh20} is the temperature coefficient of resistance at 20 °C. In our case, at t_{sh} = 22 °C, R_{sh} = 0.695 mΩ/m.

All these mathematical equations, together with a field mapping algorithm, have been implemented into a LabVIEW program that generates lateral profiles of the total RMS magnetic flux density, B, as well as of its transversal components, B_x and B_y, at any user-defined height above the ground. The program also displays the induced shield currents (RMS value and phase). Examples of magnetic flux density profiles generated with this simulation tool are presented in Fig. 4.

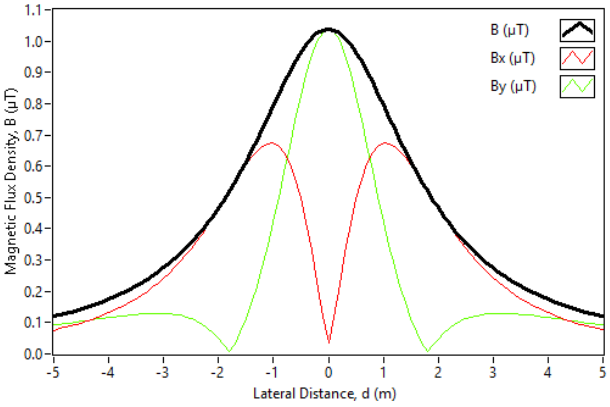

Fig. 4. The total RMS magnetic flux density and its transversal components at the height of 1 m above the ground (analytical computation)

V. RESULTS AND DISCUSSION

A comparison between numerical simulation results and analytical computation results (lateral profiles of the total RMS magnetic flux density at the height of 1 m above the ground, which is generally preferred in health-related exposure studies when dealing with power-frequency systems) is given in Fig. 5. Induced shield currents calculated by both methods are given in Table 1 and Table 2, respectively. As we can see, the results obtained by the two methods correlate very well.

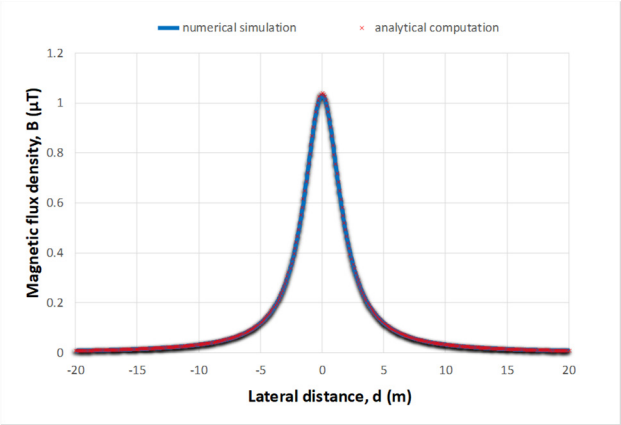

Fig. 5. Comparison between numerical and analytical results (RMS magnetic flux density profiles at the height of 1 m above the ground)

Table 1. Induced shield currents obtained by numerical simulation.

Current No.	$\underline{I}_{sh}$ (A)	RMS value (A)	Phase (°)
1	-18.40+j12.26	22.11	146.32
2	-2.35-j15.13	15.31	-98.83
3	20.75+j2.86	20.95	7.85

Table 2. Induced shield currents obtained by analytical computation.

Current No.	$\underline{I}_{sh}$ (A)	RMS value (A)	Phase (°)
1	-18.30+j12.13	21.96	146.46
2	-2.31-j15.02	15.21	-98.75
3	20.61+j2.89	20.82	7.99

Lateral profiles of the total RMS magnetic flux density at several heights above the ground, obtained by numerical simulation, are presented in Fig. 6. As it can be observed, the magnetic field at the centerline varies strongly, from 5.18 μT at 0 m to 0.63 μT at 1.5 m. Modifying the grounding resistance (see Fig. 2c) between 0.1 Ω and 50 Ω has virtually no effect on the magnetic field distribution.

Fig. 7 compares lateral profiles of the total RMS magnetic flux density computed with two-point bonded shields and non-bonded shields, respectively (h = 1 m). As shown in this figure, the underground cable system with two-point bonded shields produces a magnetic field that is 2.64% (2.63%, analytically) lower than the magnetic field created by the non-bonded cable system.

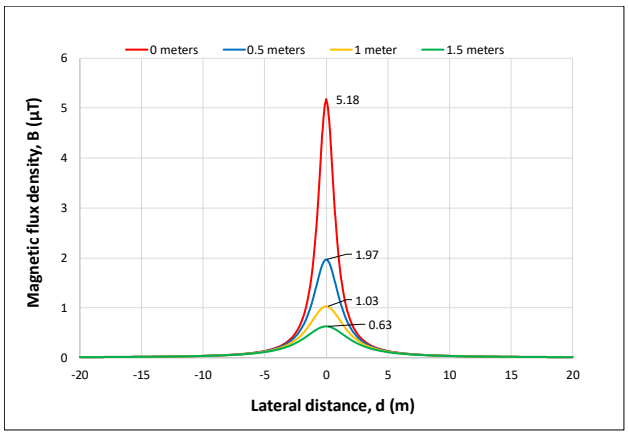

Fig. 6. Magnetic field from the three-phase underground cable system at several heights above the ground (numerical simulation)

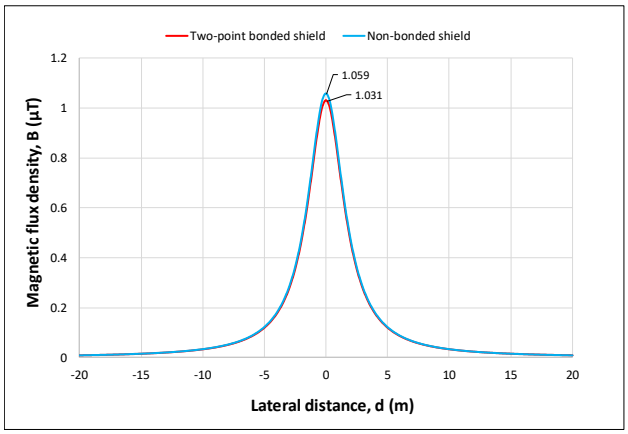

Fig. 7. Magnetic field from the three-phase phase under-ground cable system with two-point bonded shields and non-bonded shields, h = 1 m (numerical simulation)

Vertical profiles of the total RMS magnetic flux density at the centerline, obtained by numerical simulation, are presented in Fig. 8 (top dashed line – non-bonded cable system; bottom solid line – bonded cable system).

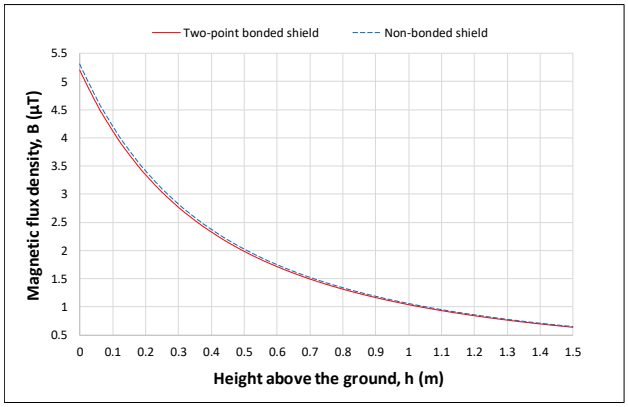

Fig. 8. Magnetic field at the centerline for two-point bonded shields and non-bonded shields (numerical simulation)

As it can be observed from the results presented above, the magnetic field reduction rate for the analyzed three-phase cable system is very low. However, for other cable systems, depending on their geometry and the cable characteristics, it may significantly increase.

VI. CONCLUSIONS

The main achievement of this study consists in the development and validation of a simple and effective ANSYS Maxwell 2D model for computing and analyzing magnetic fields generated by underground cable systems with two-point bonded shields. Comparisons to analytical computations based on the Biot-Savart law and superposition principle revealed a very good agreement between results. The proposed FEM model can be adapted to calculate magnetic field distributions for any three-phase cable layout, as well as for various cable groups, taking into account influencing factors such as cable spacing, burial depth, phase sequence, magnetic permeability of soil, etc.

REFERENCES

[1] EMFs.info, “Underground power cables”, online at https://www.emfs.info/sources/underground/ (Accessed April 2022).

[2] S. Vornicu, E. Lunca, A. Salceanu, “Computation of the Low Frequency Magnetic Fields Generated by a 12/20 kV Underground Power Line”, 2018 International Conference and Exposition on Electrical and Power Engineering (EPE), 2018, pp. 0630-0633.

[3] E. Fernandez, J. Patrick, “Magnetic Fields from High Voltage Power Cables”, online at https://elek.com.au/articles/magnetic-fields-from-high-voltage-power-cables/ (Accessed April 2022).

[4] V.J. Hernández Jiménez, E.D. Castronuovo, I. Sánchez Rodríguez-Morcillo, “Optimal statistical calculation of underground cable bundles positions for time-varying currents”, International Journal of Electrical Power & Energy Systems, Vol. 95, 2018, pp. 26-35.

[5] R. Djekidel, D. Mahi, S.A. Bessedik, C. Hadjaj, “Analysis of magnetic flux density generated by a three-phase underground power cable”, 10th National Conference on High Voltage (CNHT), 2016, pp. 1-6.

[6] K. Ates, H.F. Carlak, S. Ozen, “Magnetic Field Exposures due to Underground Power Cables: A Simulation Study”, 2nd World Congress on Electrical Engineering and Computer Systems and Science (EECSS’16), 2016, pp. 1-7.

[7] Z.A. Abu Zarim, T.M. Anthony, “Magnetic field simulation & measurement of underground cable system inside duct bank,” 22nd International Conference on Electricity Distribution, Stockholm, 2013, pp. 1-3.

[8] A.S. Farag, A.A. Hossam-Eldin, H.M. Karawia,

"Magnetic fields management for underground cables structures" 21st International Conference on Electricity Distribution Frankfurt (CIRED2011), 2011, pp 1-4.

[9] V. Rozov, V. Grinchenko, O. Tkachenko, A. Yerisov, "Analytical Calculation of Magnetic Field Shielding Factor for Cable Line with Two-Point Bonded Shields" IEEE 17th International Conference on Mathematical Methods in Electromagnetic Theory (MMET), 2018, pp. 358-361.

[10] J.R. Riba Ruiz, X. Alabern Morera, "Effects of the circulating sheath currents in the magnetic field generated by an underground power line", International Conference on Renewable Energy and Power Quality, 2006, pp. 1-5.

[11] V. Grinchenko, O. Tkachenko, K. Chunikhin, "Magnetic field calculation of cable line with two-point bonded shields", IEEE Int. Young Scientists Forum on Applied Physics and Engineering, 2017, pp. 211-214.

[12] S. Dubitsky, G. Greshnyakov, N. Korovkin, "Refinement of underground power cable ampacity by multiphysics FEA simulation", International Journal of Energy, Vol. 9, 2015, pp. 12-19.

[13] B. Novák, L. Koller, I. Berta, "Loss reduction in cable sheathing", International Conference on Renewable Energies and Power Quality (ICREPQ'10), 2010, pp. 293-297.

[14] S. Fericean, "Inductive Sensors for Industrial Applications", Artech House, Norwood, 2019.

[15] E. Lunca, B.C. Neagu, S. Vornicu, "Finite Element Analysis of Electromagnetic Fields Emitted by Overhead High-Voltage Power Lines", in *Numerical Methods for Energy Applications*, Springer, Cham, 2021.

[16] S. Vornicu, E. Lunca, A. Salceanu, "ANSYS Maxwell Finite Element Model for 2D Computation of the Magnetic Field Generated by Overhead High-Voltage Power Lines," 2019 International Conference on Electromechanical and Energy Systems (SIELMEN), 2019, pp. 1-4.

[17] O.E. Gouda, "Environmental Impacts on Underground Power Distribution", 1st edition, IGI Global, 2016.

25th IMEKO TC4 International Symposium
23rd International Workshop on ADC and DAC Modelling and Testing
IMEKO TC-4 2022
Brescia, Italy / September 12-14, 2022

Interlaboratory Comparison of Low Impedance for Impedance Spectroscopy

Stanislav Mašláň[1], Hans He[2], Tobias Bergsten[2], Steffen Seitz[3], Tom Patrick Heins[3]

[1]*Czech metrology institute, Okružní 31, 638 00 Brno, Czech Republic, smaslan@cmi.cz*
[2]*Research Institutes of Sweden, Lindholmspiren 7 A, 417 56 Göteborg, Sweden*
[3]*Physikalisch-Technische Bundesanstalt, Bundesallee 100, 38116 Braunschweig, Germany*

***Abstract* – The paper reports an interlaboratory comparison of low impedance measurements at frequencies relevant for electrochemical impedance spectroscopy (EIS) of commercial lithium-ion cells. The comparisons cover an impedance range from 50 µΩ to 100 mΩ across the full complex plane in a frequency range 0.01 Hz up to 5 kHz. A first comparison covered calibration of low impedance standards by reference digital sampling impedance setups in 4-terminal and 4 terminal-pair connections. A second comparison used commercial 4-terminal EIS meters to measure the low impedance standards characterised in the first comparison.**

I. INTRODUCTION

Electrochemical impedance spectroscopy (EIS) is one of the most common laboratory methods used to investigate internal electrochemical processes of lithium-ion batteries in a non-destructive way. Typical impedances of Li-ion cells may vary from sub-milliohm values for large cells with capacity of tens of ampere-hours up to over 100 mΩ for smaller aged cells. The characteristic features in the frequency spectrum are semicircles in the Nyquist plane, which are associated with processes at the electrode/electrolyte interfaces and lie typically in a frequency range from tens of millihertz up to kilohertz range. The measured impedance has arbitrary phase angle, so a full complex plane measurement capability is needed. Traceability of impedances and frequencies in this range is not well established, even in the primary impedance laboratories of national metrology institutes (NMI) and less so in electrochemistry laboratories. The measurements performed in particular laboratories are often not repeatable or comparable. This situation was identified as a major problem by the consortium of the EMPIR [1] project "LiBforSecUse - Quality assessment of electric vehicle Li-ion batteries for second use applications" [2]. Thus, one of the basic goals of this project was to improve metrology of low impedances down to very low frequencies and values.

The plan of the LiBforSecUse project was to: (i) Develop low-impedance standards; (ii) Develop a reference impedance bridge; (iii) Characterise the impedance standards; (iv) Use the impedance standards for an interlaboratory comparison of EIS meter measurements. On top of the original plan, one more bilateral comparison was conducted between ČMI and RISE to validate the characterisation of standards in step (iii).

II. SELECTION OF IMPEDANCE STANDARDS

Several types of impedance standards were developed within the scope of the LiBforSecUse project. The standards covered a wide range of impedance in the full complex plane, and covered an impedance range from submilliohm to over 1 Ω. Apart from the new standards, several commercially available standards were used in the project. The following standards were included in the comparisons:

- **4TP/4T resistors**: Commercial low impedance standards manufactured by Hioki with values 0 - 1 - 3 - 10 - 100 mΩ. The standards are equipped with four BNCs with split-ground topology and banana terminals for a 4-wire measurement with return current loop. Thus, the standards have a minimal difference of impedance between 4TP and 4T measurement (below ± 0.5 nH), so they are suitable for both 4TP measurements and 4T measurements using EIS analysers.
- **4TP reactance**: ČMI developed a reactance standard with a controllable DC bias source [3] having four ranges: ± 340 nH and ± 3.4 µH. The difference between 4TP and 4T measurement is below 1 nH.
- **4T simulators with arbitrary phase angle**: PTB developed two simulators based on the combination of a current shunt and an active modifying circuit producing semicircles in complex impedance space. The simulators provided 13 different simulated impedance values (ranges) covering an impedance range from 0.5 to 10 mΩ.
- **Analogue impedance multiplier**: RISE designed an impedance multiplier simulating a capacitance of 1 F.

III. BILATERAL COMPARISON ČMI - RISE

The first phase of comparisons conducted in the project was a bilateral comparison between ČMI and RISE of low impedance measurements using digital sampling setups.

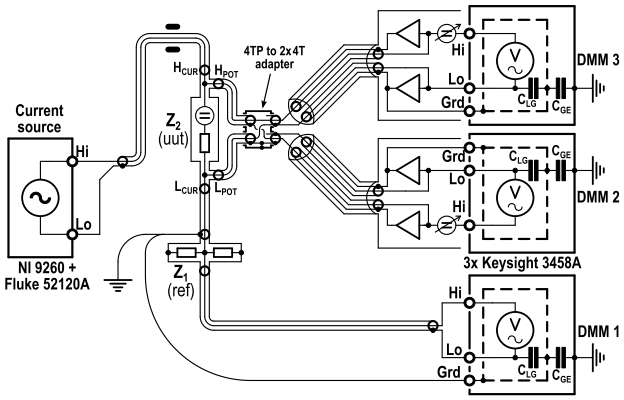

Fig. 1. ČMI digital sampling impedance bridge for mΩ-range EIS measurements.

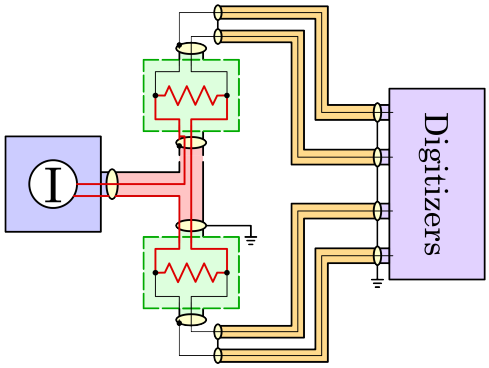

Fig. 2. RISE digital sampling impedance bridge for current shunts calibration.

All measurements were performed without DC bias voltage or current at rms current of 1 A. The frequency range was 10 mHz to 5 kHz with frequency step 1 - 2 - 5.

ČMI used two measurement setups. The first setup was a new impedance bridge setup specialised for EIS based on low the cost digitizer National Instruments NI 9238 with four floating inputs. The setup shown in Fig. 1 was described in detail in [4]. The source of a measurement current was a DDS synthesizer based on the NI 9260 DAC with transconductance amplifier Fluke 52120A to deliver required current. Current output was connected via coaxial cable via measured impedance standard (UUT) and then to the reference coaxial current shunt. The current returns back via the coxial shield of the same cable. This simple arrangement ensured well balanced current in the current cable, so the electromagnetic interference to the potential sensing cables was minimized. Voltage on the reference shunt was digitized in a single ended connection using first digitizer channel DMM 1. The voltage of the UUT was digitized using channel DMM 3 connected between the live potential terminals of UUT. This is sufficient for 4T measurements. For a 4TP measurement, the potential between UUT potential ports shields was digitized by DMM 2 channel of NI 9238. Voltages of both high-side digitizers DMM 2 and DMM 3 were combined to obtain an effective 4TP voltage drop. Connection to the high-side digitizers was via active guarded twin-axial cables to minimize leakage currents. The guarding unit also contained DC bias compensators, but those were not used in this comparison as the measurement was performed without DC bias voltage. Sampling was coherent, so a simple FFT analysis was used to obtain complex voltages which were used for calculation of impedance ratio. This setup covered a measurement range of 0.01 Hz to 5 kHz with expanded uncertainties starting at about 20 µΩ/Ω at low frequencies and up to order of 100 µΩ/Ω at 5 kHz.

The second ČMI setup was a traditional 4TP digital sampling impedance bridge [5] with balancing circuits containing injection transformers. Therefore, its frequency range starts from 20 Hz. Thus, it was used only to validate the measurement using EIS bridge in the higher frequency range from 20 Hz to 5 kHz. The second setup enabled uncertainties below 20 µΩ/Ω across the full frequency range. The reference impedances for both ČMI setups were coaxial current shunts with impedances from 30 to 600 mΩ traceable to calculable resistors. The linearity of both bridge setups was also traceable to the ratio of the calculable resistors.

RISE used a 2 terminal-pair impedance bridge developed for low impedance current shunts [6], [7]. A schematic is shown in Fig. 2. The measured impedances were compared to the impedance of a calibrated wideband coaxial current shunt of 8 mΩ. The normal procedure with this bridge is to reverse the high and low potential of the impedances in order to eliminate loading effects. However, since the impedances were very low, the input impedance of the digitizers and connecting cables had no influence on the results, and the reversing procedure was not needed. The digitizers used were National Instruments NI-PXI 5922 dual channel 24-bit digitizers, and the current source was a Clarke-Hess 8100 transconductance amplifier controlled by an Agilent 33522 waveform generator. The uncertainty was approximately 300 µΩ/Ω for all measurements.

A few tens of comparison measurements were performed in total. The following paragraphs will cover just a selection of them. The first selected result, a comparison of the PTB cell impedance simulator, is shown in Fig. 4. The object of comparison (UUT) had an equivalent impedance of $\hat{Z} = 1\,\mathrm{m\Omega} + 2\,\mathrm{m\Omega} \parallel 4\,\mathrm{F}$. The PTB standard contains also a 0 Ω-range which was used as a short correction for all measurements. This eliminated most of the mutual couplings between current and potential leads that would otherwise worsen the reactance match by several or-

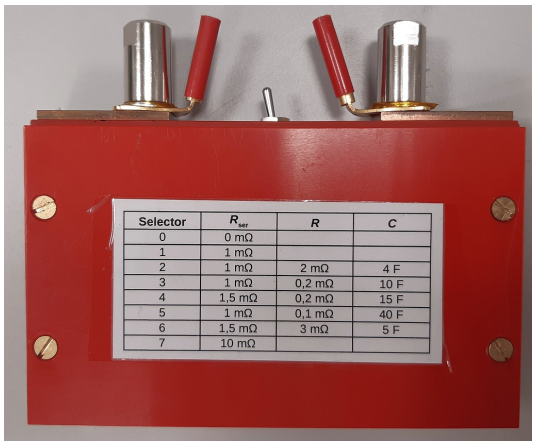

Fig. 3. PTB designed multi range Lithium cell impedance simulator with 4T connection terminals.

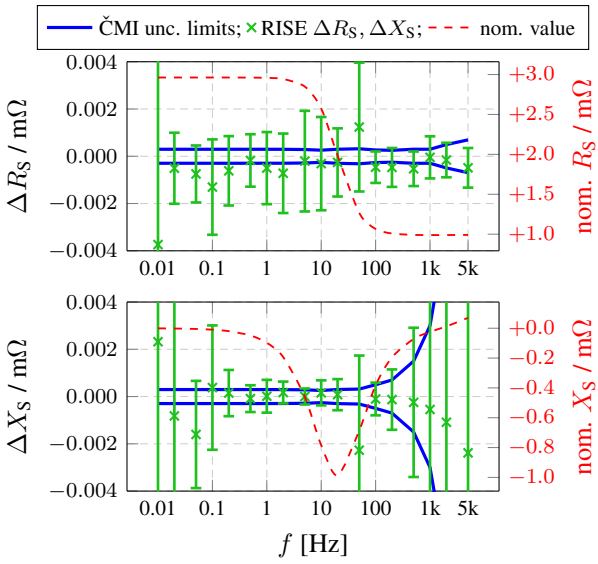

Fig. 4. ČMI - RISE comparison on PTB standard, range no. 2 ($\hat{Z}$ = 1 mΩ + 2 mΩ ‖ 4 F). The blue lines are ČMI expanded uncertainties, the green marks are RISE absolute deviations from ČMI, the green error bars are RISE expanded uncertainties and the red trace is nominal value of R_S and X_S parameter, respectively.

ders of magnitude. Deviations were mostly below ±1 µΩ, with most of the error being standard deviation of the RISE measurements. The increasing uncertainty of reactance at higher frequencies was caused by the mutual couplings between the potential and current leads which was conservatively estimated to ±1 nH. The deviations on about half of the 7 impedance ranges provided by the first PTB standard were of a similar order. The other half showed deviations on a real component up to a few microohms, sometimes even outside assigned uncertainties. The most likely explanation is the limited stability of the active modifying circuit of the standard, which was observed during characterisation at ČMI.

The next comparison was performed with another PTB cell impedance simulator with an impedance of $\hat{Z} = 0.5\,\text{m}\Omega + 1\,\text{m}\Omega \,\|\, 4\,\text{F}$. The results are shown in Fig. 5. In contrast to the previous comparison, the standard contains no 0 Ω-range, so no short correction was performed in this case. This was possible due to good geometrical separation between the current input and potential sensing terminals and thus very little mutual coupling between the potential and current leads. The stability of the standard was also superior to the previous case. The deviations between ČMI and RISE were of the order of ±100 nΩ for both the real and imaginary components. A similar order of errors was obtained on all other ranges of the PTB simulator, covering an impedance range 0.5 to 10 mΩ. These measurements confirm the assumption that the failure to match the real component of the first PTB standard was caused by its instability, as the measured impedances here were of the same order.

A further comparison was performed with the ČMI reactance simulator. The exemplar results shown in Fig. 6 are for the low, positive range, i.e. roughly +340 nH with negligible series resistance. Deviations were up to few microohms on both real and imaginary axes, except at high frequencies. The deviations were most likely caused by different terminal configurations. ČMI measured in 4TP, whereas RISE measured in 4T with the return current via a shorted L_{CUR} BNC port of UUT. The characterisation performed within the scope of [3] showed that there is a reactance difference of roughly 1 nH, and of a few microohms in the real component, between 4TP and 4T connection, so small deviations were expected. Similar results were obtained in the other three ranges of the ČMI reactance standard.

Several comparison measurements between RISE and ČMI failed completely. Some failed due to limited stability of the travel standard (the RISE capacitance multiplier) and some failed due to incompatible wiring. One example for all is attempt to compare the Hioki resistance standards. In theory, it should have been the easiest measurement of all. However, yet unidentified mistake in the wiring caused a massive deviation of the measured reactance roughly equal to 26 nH for all measured values, which is almost 1 mΩ at 5 kHz. That is already comparable to reactance of larger li-ion cells. Most likely explanation of this fail is effect of unwanted mutual coupling due to different wiring among the participants.

IV. COMPARISON OF EIS MEASUREMENTS

A second phase of comparisons focused on calibration and use of commercial EIS meters. The procedure for the comparison was following: (i) Use calibrated refer-

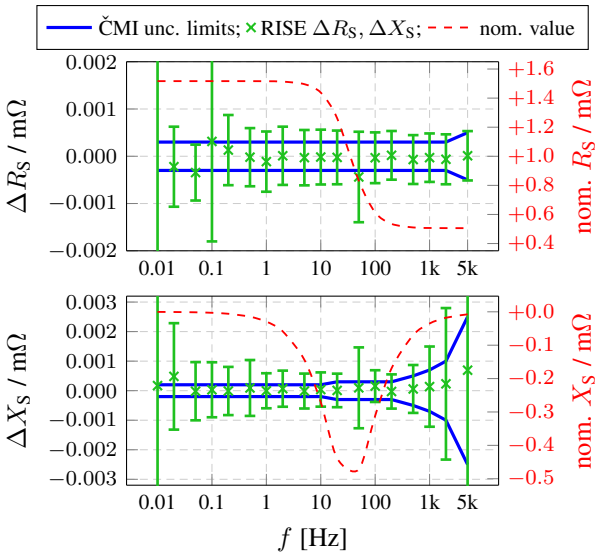

Fig. 5. ČMI - RISE comparison on PTB standard, range no. 1 ($\hat{Z}$ = 0.5 mΩ + 1 mΩ || 4 F). See Fig. 4 caption for details.

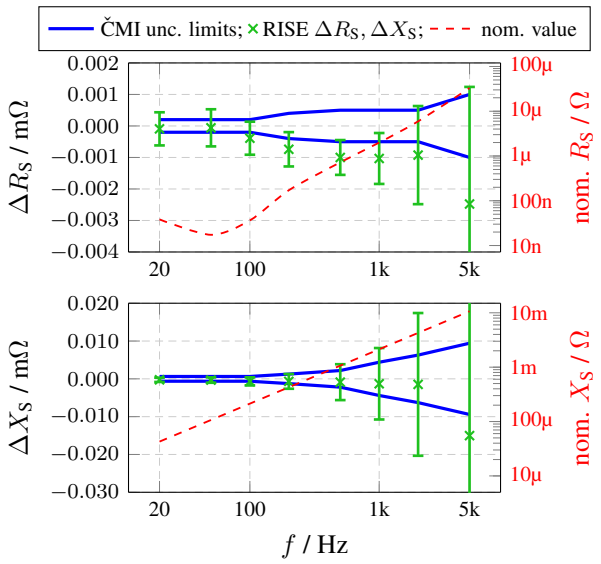

Fig. 6. ČMI - RISE comparison on ČMI reactance standard, at positive reactance range of approx. 340 nH. See Fig. 4 caption for details.

ence impedance standards to calibrate the EIS meter; (ii) Use the EIS meter to measure another impedance standard characterised by reference laboratory ČMI; (iii) Compare to the ČMI reference measurement of the standards.

There were three participants apart from ČMI: The National Physical Laboratory (NPL, Teddington, UK), Physikalisch-Technische Bundesanstalt (PTB, Germany) and Institute for Applied Materials - Electrochemical Technologies, Karlsruhe Institute of Technology (KIT, Karlsruhe, Germany). The comparisons were performed using EIS meters from three different manufacturers: Biologic VMP3 with VM3B-10 10 A booster (used by NPL), Zahner Zenium (used by KIT) and Gamry Ref 3000 (used by PTB).

The calibration and measurement procedure of the EIS meter was as follows:

- **Short correction**: Connect the test leads to a short arrangement, twisting current and potential leads separately to minimise mutual coupling between the pairs. Measure the residual "short" impedance $\hat{Z}_S$ for each frequency. Subtract measured short impedance $\hat{Z}_S$ from all subsequent measurements.
- **Range error calibration**: Measure the error of the EIS meter using two impedance standards with known values, one having impedance below and one above the value of the UUT (Unit Under Test) to be measured. Calculate complex correction factors for the EIS errors for each frequency.
- **Error correction**: Use the correction factors to correct all subsequent measurements (so called load correction).

The first step had to be performed manually in postprocessing of the measured data as most of the EIS meters studied do not implement short correction. Problems arose from the load correction attempt. The last two steps in the procedure work well for traditional RLC meters such as Keysight E4980A; the method is able to reduce the error of the RLC meter, especially in phase angle, by orders of magnitude. However, for EIS meters, two major problems were identified. First, the EIS meters mostly do not have a manual range lock function. Thus, when the error evaluation is performed e.g. with resistor of 10 mΩ and the UUT has impedance of e.g. 6 mΩ, there is no guarantee that EIS meter is using the same internal range. It may switch some internal amplifier gain or reference impedance and thus its error may differ. Therefore, trying to apply such corrections may actually increase the error. The second identified problem was that the EIS meters exhibit considerable noise (standard deviation of measurements), which mostly exceeded observed EIS meter errors. Therefore, to make the corrections work, it would be necessary to use extensive averaging; this would not be practical for actual lithium-ion cell measurements, nor even possible due to changes in cell state between discrete measurements. Despite these obvious challenges to the correction method, it was decided to perform the comparison with all three steps of calibration procedure.

The objects of the comparison were a "pure" resistance of 3 mΩ (Hioki resistor) and the PTB cell simulator at two different ranges. Calibration impedances were chosen to be "pure" resistances of 1 and 10 mΩ (Hioki resistors). The short correction for Hioki resistors was made using

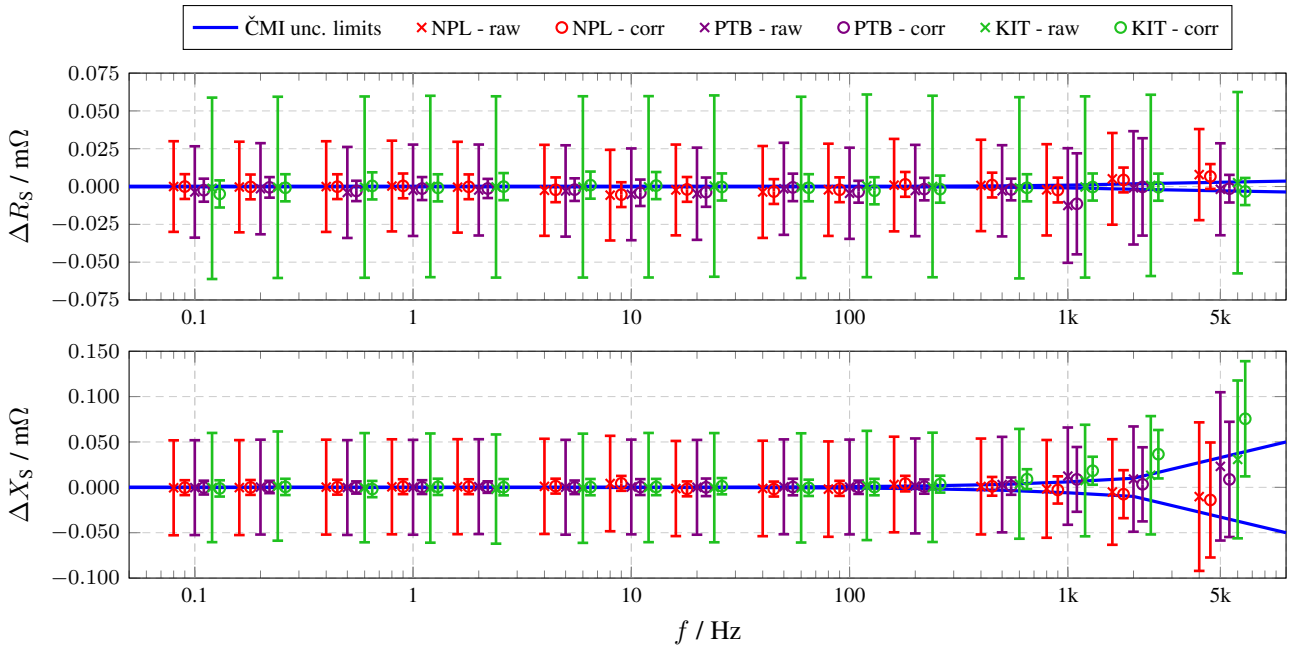

Fig. 7. Comparison of EIS meter measurement of 4-wire resistor 3 mΩ. Blue lines are ČMI reference expanded uncertainties, colored measurements with error bars are participants' absolute deviations from ČMI measurement with expanded uncertainties. "raw" are measurements with just short correction, "corr" are measurement after short and LOAD corrections.

the Hioki 0 Ω resistor and using PTB simulator's internal 0 Ω range for the PTB simulator measurements. This minimised the effect of variable mutual couplings of the test leads.

An exemplar result from the UUT Hioki 3 Ω comparison is shown in Fig. 7. Each participating institution provided two results to the graph. The result marked "raw" is measurement with just a short correction, whereas the result marked "corr" is with the load correction applied. The expanded uncertainty bars for the "raw" measurement are given directly by the specification of the EIS meter expanded in reactance by a mutual coupling uncertainty of ±2 nH. This is a conservative estimate that should cover variations in the mutual couplings when short is performed correctly. The uncertainty bars for the "corr" measurement are an estimated expecting EIS meter range linearity of 0.05 % and are also expanded by mutual coupling uncertainty. As expected, the difference between the results with and without correction is negligible for all of the participants. On the other hand, it must be mentioned that the short correction reduced errors by more than 10 times for both real and imaginary components. The spread of reactances without short correction was up to ±400 µΩ, which would correspond to no match above 1 kHz.

V. CONCLUSION

Two interlaboratory comparisons of impedance in the milliohm range in a full complex plane were conducted. The first comparison was undertaken between ČMI and RISE. It mostly showed agreement in the range from a few microohms down to the order of 100 nΩ, when the compared impedance standards were sufficiently stable. However, in some cases high deviation on reactance were observed, most likely due to different wiring among the participants. These failed results showed utmost importance of clearly defining wiring arrangement as even small differences may lead to the large offsets especially on reactance.

The second comparison was focused on measurements using commercial EIS meters calibrated by reference impedances. The comparison showed good match between the participants on various impedances from 1.5 to 4.5 mΩ across the full complex plane. Short correction was identified as a critical procedure for the reduction of measurement errors at frequencies above 1 kHz despite EIS meters control SW usually implements no such feature internally, thus it had to be performed in postprocessing. Further results will be presented at the conference.

VI. ACKNOWLEDGMENT

The National Physical Laboratory (NPL, Teddington, UK) and Institute for Applied Materials - Electrochemical Technologies, Karlsruhe Institute of Technology (KIT), Karlsruhe, Germany contributed to experiments reported in EIS meters comparison in section iv.

The comparison was carried out in scope of the EMPIR

project LiBforSecUse (17IND10). The project received funding from the EMPIR programme co-financed by the Participating States and from the European Union's Horizon 2020 research and innovation programme.

REFERENCES

[1] MSU EURAMET. *European Metrology Programme for Innovation and Research (EMPIR)*. [online]. URL: http://msu.euramet.org/calls.html.

[2] MSU EURAMET. *EMPIR project - Lithium Batteries for Second Use*. [online]. URL: https://www.ptb.de/empir2018/libforsecuse/home/.

[3] Stanislav Mašláň. "High capacitance simulation using mutual inductors". In: *24th IMEKO TC4 International Symposium, Palermo, Italy, September 14-16*. 2020, pp. 168–173. URL: https://www.imeko.org/publications/tc4-2020/IMEKO-TC4-2020-32.pdf.

[4] Stanislav Mašláň. "Design of digital sampling impedance bridge for battery impedance spectroscopy". In: *24th IMEKO TC4 International Symposium, Palermo, Italy, September 14-16*. 2020, pp. 151–156. URL: https://www.imeko.org/publications/tc4-2020/IMEKO-TC4-2020-29.pdf.

[5] S. Mašláň et al. "Four-Terminal Pair Digital Sampling Impedance Bridge up to 1MHz". In: *IEEE Transactions on Instrumentation and Measurement* 68.6 (June 2019), pp. 1860–1869. DOI: 10.1109/TIM.2019.2908649.

[6] Karl-Erik Rydler, Tobias Bergsten, and Valter Tarasso. "Determination of phase angle errors of current shunts for wideband power measurement". In: *2012 Conference on Precision electromagnetic Measurements*. 2012, pp. 284–285. DOI: 10.1109/CPEM.2012.6250913.

[7] Tobias Bergsten and Karl-Erik Rydler. "Realization of Absolute Phase and AC Resistance of Current Shunts by Ratio Measurements". In: *IEEE Transactions on Instrumentation and Measurement* 68.6 (2019), pp. 2041–2046. DOI: 10.1109/TIM.2018.2882927.

25th IMEKO TC4 International Symposium
23rd International Workshop on ADC and DAC Modelling and Testing
IMEKO TC-4 2020
Brescia, Italy / September 12-14, 2022

Comparison of DC current comparator bridges for resistance metrology

Martina Marzano[1], Pier Paolo Capra[1], Cristina Cassiago[1], Vincenzo D'Elia[1], Enrico Gasparotto[1], Luca Callegaro[1]

[1]*INRIM Istituto Nazionale di Ricerca Metrologica, Strada delle Cacce 91, m.marzano@inrim.it*

***Abstract* – Direct-current comparator bridges (DCC) are the working horse of primary resistance metrology in the intermediate resistance range. Having a ratio accuracy reaching 10^{-7} or better, they allow the realisation of resistance scales and the calibration of artifact standard resistors for customers. In this paper we compare the performances of three commercial DCC bridges, by performing measurements on decadal resistors ($1\,\Omega$ to $10\,\mathrm{k}\Omega$) of very high stability in a thermostated environment. The results show that the three bridges give mutually compatible results within the manufacturer specifications, therefore mutually validating the bridges; nevertheless, the readings time series show quite different statistical behavior, with internal correlations, making an evaluation of the Type A measurement uncertainty not trivial.**

I. INTRODUCTION

Direct-current comparator bridges (DCC) [1] are instruments which can measure the resistance ratio between two four-terminal resistance standards R_1 and R_2 with a base relative accuracy of 1×10^{-7} or better for the intermediate resistance range ($1\,\Omega$ to $10\,\mathrm{k}\Omega$), and are therefore suitable for the realisation of a primary resistance scale and to sustain a calibration service in National Metrology Institutes and calibration laboratories. Commercial, fully-automated bridges are on the market since more than 40 years.

Research is ongoing in INRIM to simplify and automate the traceability chain for the maintained resistance standard and to perform calibration for customers, and commercial DCCs are employed as a check of the scaling in the intermediate resistance range, and as a direct calibration instrument for the low resistance scale ($10\,\mu\Omega$ to $1\,\Omega$). Checking the measurement accuracy of the different DCCs employed is therefore a basic metrology verification requirement.

In this paper, we compare the performance of three different commercial DCCs in performing measurements on the maintained national standard of dc resistance, in the intermediate range.

II. DIRECT-CURRENT COMPARATORS

The direct-current comparator bridges (DCC) [2] measure resistance ratio between two four terminal-pair resistors R_1 and R_2. The resistors are energized by two current sources; the resulting currents I_1 and I_2 flow through two windings, having turns N_1 and N_2, wound on a ferromagnetic core. The magnetic flux in the core is given by $\mathcal{R}\Phi = N_1 I_1 - N_2 I_2$, where $\mathcal{R}$ is the reluctance of the core. Φ is measured by a fluxgate detector [1, 3, 4], whose output constitutes the error signal of a feedback control. The output of such control drives one of the two current sources (e.g., I_2) to keep $\Phi = 0$ and therefore the condition $N_1 I_1 = N_2 I_2$. The voltage difference $\Delta V = R_1 I_1 - R_2 I_2$ between the two resistors is measured, and the turns of one of the two windings (say, N_2) are also adjusted to set ΔV to a minimum. This second adjustment was manual in early bridges [1] and is presently also automated [5]. The readings of the bridge are the two values N_1/N_2 and ΔV, which give the measurement equation

$$\frac{R_1}{R_2} = \frac{N_1}{N_2}\left(1 - \frac{\Delta V}{R_2 I_2}\right). \qquad (1)$$

During the measurement the currents I_1 and I_2 are periodically reversed to reduce the influence of voltage offsets.

The DCC bridge measurement accuracy [6] is limited by the sensitivities of the flux detector and of the voltage detector which sense ΔV, and by flux leakage in the magnetic circuit. Bridges measuring resistors in the $\mu\Omega$ to the $\mathrm{M}\Omega$ range are available; best accuracy is achieved for medium-ranged resistors ($1\,\Omega$ to $10\,\mathrm{k}\Omega$) and ratios within the $1:10$ range.

The DCCs under comparison are three different models from the Measurement International that acquired at different times. In the following, the measurements are labelled as follows:

6010B Measurement International model 6010B, serial 1020904, acquired in 2006.

6010D Measurement International model 6010D, serial 1104668, acquired in 2021.

6010Q Measurement International model 6010Q, serial 1100670, acquired in 2008.

Table 1. Measurements settings employed in the measurements of the 10/1, 100/10, 1k/100 and 10k/1kratios with the 6010B, 6010D and 6010Q DCC bridges.

	I/ mA	t_{set}/s	$Filter$	6010Q $\#ADC$
10/1	10	6	3	6
100/10	3	8	3	8
1k/100	1	8	3	8
10k/1k	0.1	12	3	12

III. THE MAINTAINED NATIONAL STANDARD OF DC RESISTANCE

The comparison of the three bridges required equipment consisting of a series of high stability standard resistors, a Guildline VT9732 oil bath, a Kambic TK-105 US air bath and a low noise switching system. The resistors used have nominal values in the $1\,\Omega$ to $10\,\mathrm{k}\Omega$ range, manufactured by Leeds & Northrup and Tinsley, all kept inside a constant temperature oil bath at a level of of $23\,^{\circ}\mathrm{C}$ with a stability of $0.001\,^{\circ}\mathrm{C}$. The measurements also involved two ESI SR104 resistors maintained at a temperature of $23\,^{\circ}\mathrm{C}$ inside a Kambic air bath with a stability of $0.005\,^{\circ}\mathrm{C}$. The bridges and the resistors are connected by means of an automatic Leeds & Northrup type rotary switch system with low thermo-electromotive forces (less than $5\,\mathrm{nV}$). The comparison of the bridges, whose measurements could not be made at the same time, was possible due to the high stability of the standards used both in short and medium term (about 1×10^{-7} per year), and of the influence parameters.

IV. MEASUREMENT PROCEDURE

We define the ratios between $10\,\Omega$ and $1\,\Omega$, $100\,\Omega$ and $10\,\Omega$, $1\,\mathrm{k}\Omega$ and $100\,\Omega$, $10\,\mathrm{k}\Omega$ and $1\,\mathrm{k}\Omega$ as 10/1, 100/10, 1k/100 and 10k/1k, respectively. All the ratios were measured with the 6010B, 6010D and 6010Q DCC bridges in sequence by employing the same resistance standards, described in Section III., and the same measurement configurations, reported in Table 1. For all the bridges it is possible to set the desired current I for the highest resistor under test, the settle time $t_{\mathrm{set}}/$ between the current reversal during the measurement and the filter size $Filter$ corresponding to the number of averaged values ($Filter \times 10$) before each value is displayed. For only the 6010Q DCC bridge, it is possible to set the parameter $\#ADC$ representing the number of conversions of the analog-to-digital converters.

The three bridges were automatically controlled by the same software developed specifically for the comparison that ensures the same procedure and execution of the measurements with the same integration times.

V. RESULTS

Table 2 shows the results of an example measurement of each ratio performed with the 6010B, 6010D and 6010Q DCC bridges on 2 March 2022. For each measurement, the nominal ratio, the measured ratio (the mean of repeated measurements), the standard deviation, the applied current, the number of repeated measurements and the measurement time are reported.

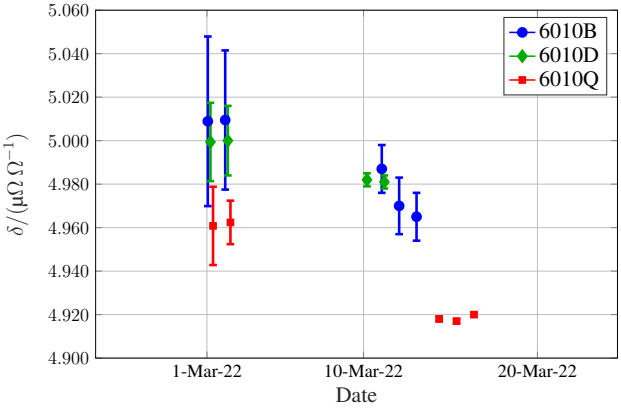

Fig. 1. ***10/1 ratio****. Relative deviations from the nominal ratio 10/1 for different measurements performed in about 20 days with the 6010B (blue), the 6010D (green) and 6010Q (red).*

Figures 1, 2, 3 and 4 show the comparison among the results obtained with the 6010B, 6010D and 6010Q DCC bridges in the measurements of the 10/1, 100/1, 1k/100 and 10k/1k, respectively. Each plot reports the relative deviation δ of the measured ratio from the nominal ratio obtained from several measurements performed in about 20 days. In all figuresbefore the 10 March 2022 the results are obtained from 100 repeated measurements, while after the 10 March 2022 the results are obtained from 800 repeated measurements. The uncertainty is calculated by applying the multiplying factor 2 to the standard deviation of the mean, as proposed in [7] for a similar experiment.

In fact, the expression of the type A uncertainty is non-trivial, since for all measurements the readings' time series display internal correlations, and therefore the standard deviation of the mean underestimates the real uncertainty. To support this, Figures 5, 6 and 7 show examples of a measurement acquisition of the 10k/1k ratio performed with the 6010B, 6010D and 6010Q bridges, respectively, in the same measurements conditions.

VI. DISCUSSION

Despite that the three bridges come from the same manufacturer and are realised with different technologies, the three time series of Figures 5, 6 and 7 have a different behaviour and show a different amount of internal correlations. This might be due to different raw data processing inside the bridge firmwares.

Table 2. Results of an example measurement of each ratio performed with the 6010B, 6010D and 6010Q DCC bridges on 2 March 2022. For each measurement, the nominal ratio, the measured ratio (the mean of repeated measurements), the standard deviation of the mean, the applied current, the number of repeated measurements n and the measurement time are reported.

6010B					
Nom. Ratio $/\Omega\,\Omega^{-1}$	Meas. Ratio $/\Omega\,\Omega^{-1}$	St. Dev. $/\mu\Omega\,\Omega^{-1}$	I/mA	n	Meas. Time
10/1	10.00005010	0.016	10	100	15 min 44 s
100/10	9.99999868	0.008	3	100	18 min 13 s
1k/100	10.00008113	0.009	1	100	18 min 12 s
10k/1k	9.99995057	0.053	0.1	100	23 min 58 s
6010D					
Nom. Ratio $/\Omega\,\Omega^{-1}$	Meas. Ratio $/\Omega\,\Omega^{-1}$	St. Dev. $/\mu\Omega\,\Omega^{-1}$	I/mA	n	Meas. Time
10/1	10.00005000	0.008	10	100	12 min 31 s
100/10	9.99999867	0.004	3	100	12 min 30 s
1k/100	10.00008102	0.003	1	100	15 min 49 s
10k/1k	9.99995190	0.060	0.1	100	22 min 19 s
6010Q					
Nom. Ratio $/\Omega\,\Omega^{-1}$	Meas. Ratio $/\Omega\,\Omega^{-1}$	St. Dev. $/\mu\Omega\,\Omega^{-1}$	I/mA	n	Meas. Time
10/1	10.00004962	0.005	10	100	21 min 4 s
100/10	9.99999821	0.003	3	100	20 min 45 s
1k/100	10.00008150	0.001	1	100	20 min 59 s
10k/1k	9.99995003	0.010	0.1	100	40 min 39 s

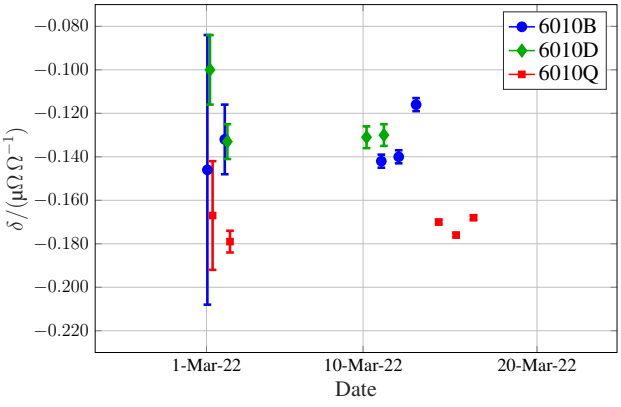

Fig. 2. ***100/10 ratio****. Relative deviations from the nominal ratio 100/10 for different measurements performed in about 20 days with the 6010B (blue), the 6010D (green) and 6010Q (red).*

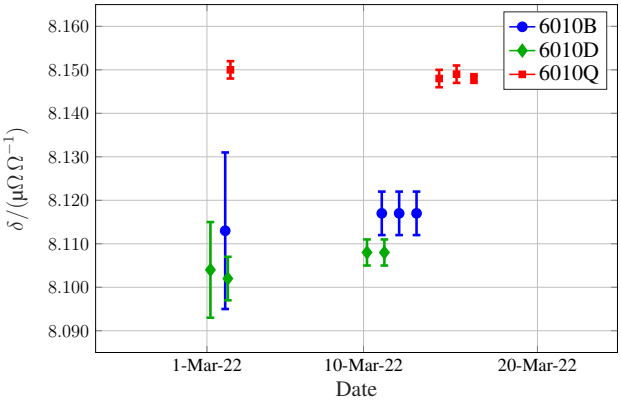

Fig. 3. ***1k/100 ratio****. Relative deviations from the nominal ratio 1k/100 for different measurements performed in about 20 days with the 6010B (blue), the 6010D (green) and 6010Q (red).*

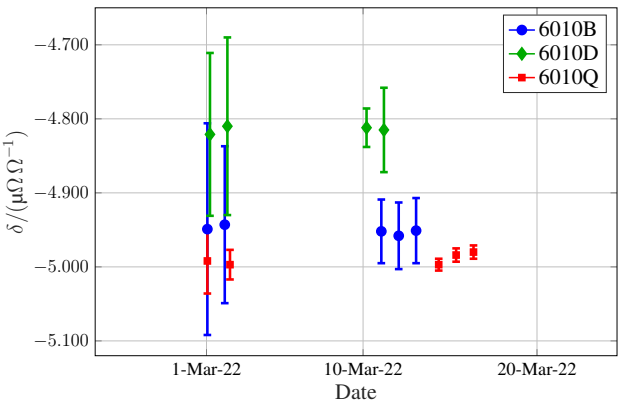

Fig. 4. ***10k/1k ratio****. Relative deviations from the nominal ratio 10k/1k for different measurements performed in about 20 days with the 6010B (blue), the 6010D (green) and 6010Q (red).*

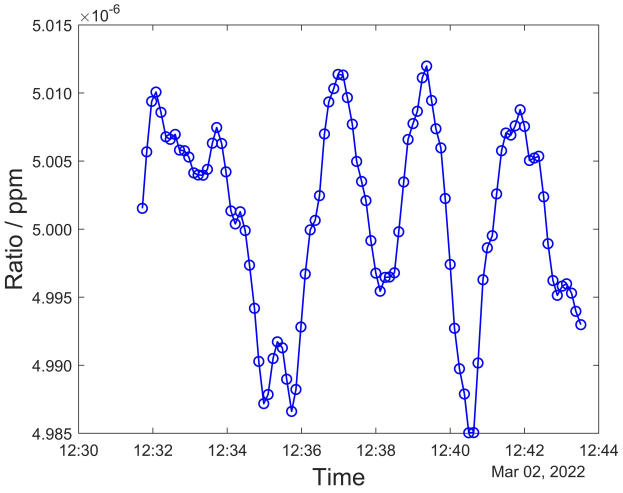

Fig. 6. Example of a measurement acquisition of the 10/1 ratio with the 6010D DCC bridge (100 repeated measurements).

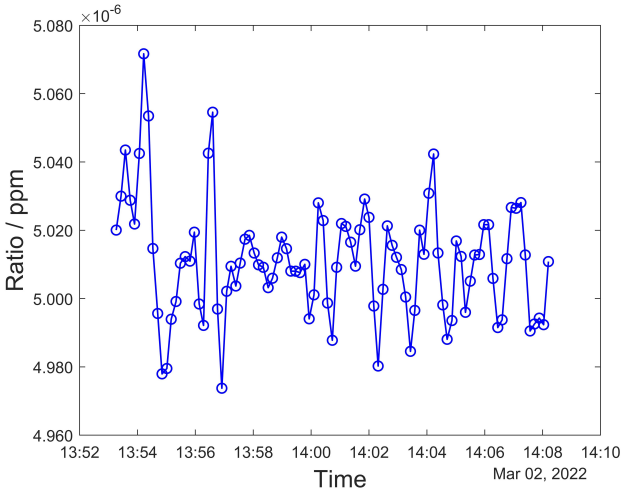

Fig. 5. Example of a measurement acquisition of the 10/1 ratio with the 6010B DCC bridge (100 repeated measurements).

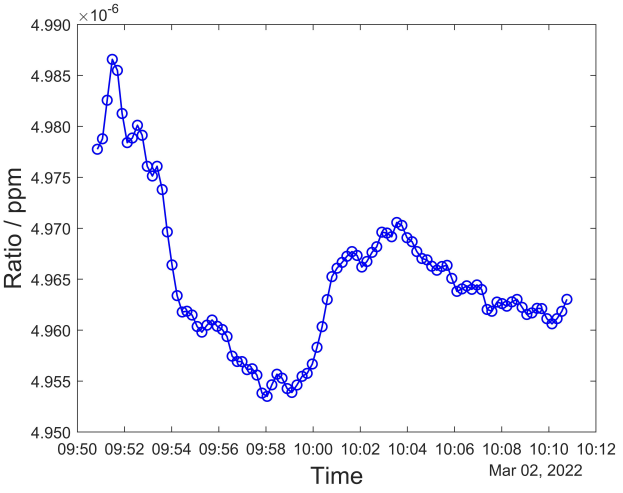

Fig. 7. Example of a measurement acquisition of the 10/1 ratio with the 6010Q DCC bridge (100 repeated measurements).

The short-term stability of the resistors due to drift and temperature variations can be estimated to be better than 3×10^{-10} over a day, hence the deviations between the readings of the three bridges are related only to the reading noise and bridge ratio errors.

It must be stressed that the error bars reported in the Figures 1, 2, 3 and 4 correspond to a (rough, to be improved) evaluation of the sole statistical uncertainty, and do not consider any Type B uncertainty. The visual effect is an apparent incompatibility of the results. The reported differences between the different estimates, however, match the manufacturer specifications of the relative errors of the bridges (of several parts in 10^8 for each bridge); the measurements, therefore, provide a mutual validation of the three bridges.

A better evaluation of the type A uncertainty can be approached by considering the Allan deviation [8] or the autocorrelation function [9, 8] or the series. For the moment, we performed a rough estimation by applying a multiplying factor to the standard deviation of the mean, as proposed in [7] for a similar experiment. A proper evaluation is ongoing and will be presented at the Conference.

The bridge ratio errors can be determined in an absolute way by comparing their readings with those of a cyrogenic current comparator [10], which allows measurements accuracies of parts in 10^9 and thus in this sense can be considered a perfect reference. A comparison experiment is under planning.

VII. ACKNOWLEDGEMENTS

This work is supported by the project MIUR PRIN 2020A2M33J CAPSTAN Quantum electrical Italian national capacitance standard.

VIII. *

References

[1] M. P. MacMartin and N. L. Kusters, "A direct-current-comparator ratio bridge for four-terminal resistance measurements," *IEEE Trans. Instr. Meas.*, vol. 15, no. 4, pp. 212–220, 1966.

[2] W. J. M. Moore and P. N. Miljanic, *The current comparator*, ser. IEE electrical measurement series. London, UK: Peter Peregrinus Ltd, 1988, vol. 4, iSBN 0863411126.

[3] P. Odier, "DCCT technology review," in *Proc. of Workshop on DC current transformers and beam-lifetime evaluations*, A. Peters, H. Schmickler, and K. Wittenburg, Eds. Lyon, France: CARE-HHH-ABI Networking, 1-2 Dec 2004, pp. 3–5.

[4] P. Ripka, "Electric current sensors: a review," *Meas. Sci. Technol.*, vol. 21, p. 112001, 2010, 23 pp.

[5] D. Brown, A. Wachowicz, and S. Huang, "The enhanced performance of the DCC current comparator using AccuBridge technology," in *2016 Conference on Precision Electromagnetic Measurements (CPEM 2016)*, 2016, pp. 1–2.

[6] S. Haiming, "The uncertainty evaluation of automatic direct current comparator bridge," in *Conference Digest Conference on Precision Electromagnetic Measurements*, 2002, pp. 58–59.

[7] A. F. Rigosi, A. R. Panna, S. U. Payagala, M. Kruskopf, M. E. Kraft, G. R. Jones, B.-Y. Wu, H.-Y. Lee, Y. Yang, J. Hu, D. G. Jarrett, D. B. Newell, and R. E. Elmquist, "Graphene devices for tabletop and high-current quantized Hall resistance standards," *IEEE Trans. Instr. Meas.*, vol. 68, no. 6, pp. 1870–1878, 2019.

[8] T. J. Witt, "Practical methods for treating serial correlations in experimental observations," *Eur. Phys. J.: Spec. Top.*, vol. 172, pp. 137–152.

[9] N. F. Zhang, "Calculation of the uncertainty of the mean of autocorrelated measurements," *Metrologia*, vol. 43, no. 4, pp. S276–S281, aug 2006.

[10] J. Williams, "Cryogenic current comparators and their application to electrical metrology," *IET Science, Measurement & Technology*, vol. 5, pp. 211–224, Nov. 2011.

25th IMEKO TC4 International Symposium
23rd International Workshop on ADC and DAC Modelling and Testing
IMEKO TC-4 2020
Brescia, Italy / September 12-14, 2022

Mutual validation of PTB's Josephson and INRIM-POLITO's electronic impedance bridges for the realization of the farad from graphene quantum standards

Martina Marzano[1], Yaowaret Pimsut[2,3], Mattias Kruskopf[2], Yefei Yin[2], Marco Kraus[2], Massimo Ortolano[4,1], Stephan Bauer[2], Ralf Behr[2], Luca Callegaro[1]

[1]*INRIM Istituto Nazionale di Ricerca Metrologica, Torino, Italy, m.marzano@inrim.it*
[2]*Physikalisch-Technische Bundesanstalt, Braunschweig, Germany*
[3]*National Institute of Metrology (Thailand), Pathum Thani, Thailand*
[4]*Politecnico di Torino, Torino, Italy*

***Abstract* – In the International System of Units, the impedance units can be realized from the quantum Hall effect, a macroscopic quantum phenomenon producing quantized resistance values. Established experiments employ individual GaAs devices [1], but novel materials such as graphene can be exploited to realize the units with relaxed experimental conditions. Furthermore, simple traceability chains can be implemented with novel digital impedance bridges. By combining novel digital impedance bridges and graphene quantum standards, an easy-to-operate and affordable impedance standard has been developed in the framework of the European EMPIR project 18SIB07 GIQS (Graphene Impedance Quantum Standards). An onsite comparison of an electronic and a Josephson impedance bridge developed at INRIM (Istituto Nazionale di Ricerca Metrologica, Italy) together with POLITO (Politecnico di Torino, Italy) and at PTB (Physikalisch-Technische Bundesanstalt, Germany), respectively, were organized for their mutual validation in the realization of the farad from graphene quantum standards. The result of the comparison and the last progresses of the GIQS project are here presented.**

I. INTRODUCTION

In the International System of Units (SI), a possible realization of the unit of electrical capacitance can be obtained directly from the quantized Hall resistance (QHR) $R_\mathrm{H} = R_\mathrm{K}/i$, where $R_\mathrm{K} = h/e^2 = 25\,812.807\,459\,304\,5\,\Omega$ is the exactly defined von Klitzing constant [2]. The resistance R_H depends only on the Planck constant h, the elementary charge e and by the small integer i. The traditionally employed GaAs/AlGaAs QHR devices require extreme experimental conditions, as very high magnetic field (of about 10 T) and very low temperatures (of about 1 K), to show the QHR $R_\mathrm{H} = 12\,906.403\,729\,652\,25\,\Omega$, corresponding to $i = 2$ and typically exploited for metrological applications.

In the AC regime, the farad can be obtained from the QHR by means of suitable impedance bridges. With the traditional transformer-ratio impedance bridges this was only possible implementing the quadrature bridge, which is a double product impedance bridge [3] comparing two resistors and two capacitors at a properly chosen fixed angular frequency. The implementation of the quadrature bridge principle [4] is a very complex electrical network with many electromagnetic components. Digitally-assisted implementations [5] reduce the network complexity to some extent and allow a partial automation. With two resistances calibrated against a QHR standard or that are QHR standards themselves, measured in the AC regime (ACQHR standards), the quadrature bridge can be used to realize the farad from the QHR. To date, only one laboratory worldwide operates a permanent quadrature bridge with two quantum Hall effect devices in a single cryostat [1], a massive and complex experiment filling an entire laboratory.

A valid alternative to quadrature bridges to directly realize the farad from the QHR can be digital impedance bridges, which allow the comparison of impedances with arbitrary phase angles. This is possible with recently developed impedance bridges based on adjustable digital signal synthesizers that provide much more flexibility with respect to older analog generators. These bridges can compare a single resistance standard and a single capacitance standard. The digital approach allows the design and implementation of much simpler bridges [6, 7]. A further alternative can be a special type of digital impedance bridge, which exploits two pulse-driven Josephson junction arrays (also called Josephson Arbitrary Waveform Synthesizer, JAWS) to provide arbitrary voltage ratios with an arbitrary phase angle. By providing quantum based AC signals with high accuracy and extremely low harmonic content [8], the JAWS can efficiently be adopted for impedance metrol-

ogy [9].

The aim of the European EMPIR project 18SIB07 GIQS [10] is to enable an economically efficient traceability of impedance quantities to the defining constants of the SI that can be adopted by national metrology institutes, calibration centers and industry. In this project, graphene QHR devices were adopted for the realization of electrical units. This because they display the quantum Hall effect at lower magnetic field (e.g., at 5 T) and higher temperature (e.g., at 4.2 K) than those of the well-established GaAs devices [11], allowing relaxed operating conditions achievable with simpler and less expensive cryogenic systems. Graphene QHR standards can be thus exploited as affordable and easy-to-operate impedance standards that can be perfectly combined with all types of impedance bridges.

In this framework, an electronic and a Josephson impedance bridge were developed by INRIM [12], together with POLITO, and by PTB [13], respectively. An onsite comparison of the bridges was organized for their mutual validation and to assess their performance in the realization of the farad. The INRIM-POLITO's travelling electronic impedance bridge was moved to PTB to perform measurements with both bridges on the same graphene ACQHR standard, developed at PTB. The developed digital impedance bridges and their comparison are described in sections II and III, respectively. The results are discussed in section IV.

II. DIGITAL IMPEDANCE BRIDGES

A digital impedance bridge is a measuring system operating in the AC regime that allows to determine an impedance ratio by the ratio of two signals generated by an adjustable digital signal source. Figure 1 shows the principle schematic of a four-terminal-pair digital impedance bridge. In a four-terminal-pair digital impedance bridge the impedances Z_1 and Z_2 are four-terminal-pair impedances defined as $Z_k^{4\mathrm{TP}} = V_{\mathrm{HP}k}/I_{\mathrm{LC}k}$, where $V_{\mathrm{HP}k}$ is the voltage at the high potential terminal-pair of the kth impedance and $I_{\mathrm{LC}k}$ is the current at the low current terminal-pair of the kth impedance, with the boundary conditions $I_{\mathrm{HP}k} = 0$, $V_{\mathrm{LP}k} = 0$ and $I_{\mathrm{LP}k} = 0$, where $I_{\mathrm{HP}k}$ and $I_{\mathrm{LP}k}$ are the currents at the high and low potential terminal-pair of the kth impedance, and $V_{\mathrm{LP}k}$ is the voltage at its low potential terminal-pair. The four-terminal-pair definition of the impedances is obtained by means of auxiliary circuits (I_1, I_2 and E_{L} in Figure 1). When the bridge is balanced, that is, when the reading of the detector D is zero at the same time at all the detection points (dashed lines in Figure 1), the equation $W = Z_1/Z_2 = -E_1/E_2$ holds. Both the INRIM's and PTB's impedance bridges are four-terminal-pair digital impedance bridges.

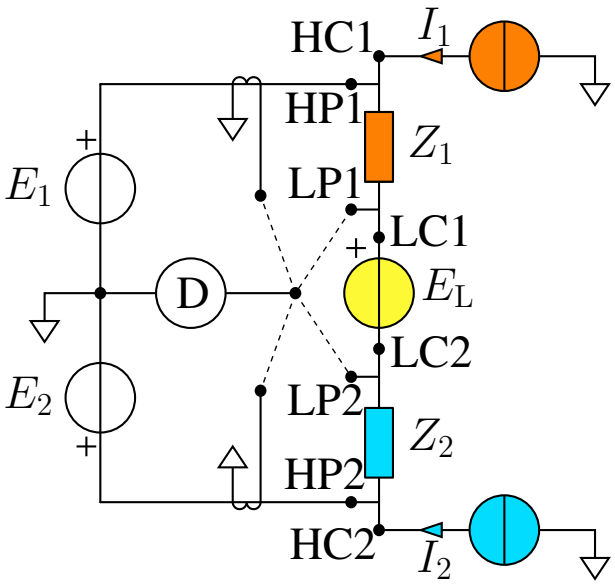

Fig. 1. Principle schematic (only inner conductors) of a four-terminal-pair digital impedance bridge.

A. *INRIM-POLITO's electronic impedance bridge*

The INRIM-POLITO's electronic impedance bridge [12] is a four-terminal-pair impedance bridge that determines an impedance ratio by the voltage ratio generated by an electronic polyphase generator. With an auxiliary injection added to the schematic of Figure 1, the uncertainty is minimized when the impedance magnitude ratio $|W| = 1$. The bridge is thus optimized for the direct comparison of a standard capacitor with an ACQHR standard when the nominal value of the standard capacitor and the frequency are chosen to obtain the $1:1$ ratio condition. The bridge is based on a 7-channel polyphase digital sine wave generator developed by the University of Zielona Góra, Poland: two channels produce the reference voltage ratio against which the impedance ratio is compared; three other channels drive the auxiliary circuits realizing the four terminal-pair impedance definition; and a further channel is the auxiliary injection. The bridge balance is detected by a phase-sensitive detector and the bridge balance procedure is automated. The bridge balancing time is about 20 min. The target uncertainty of the bridge is at the level of 10^{-7} or less.

B. *PTB's Josephson impedance bridge*

The PTB's Josephson impedance bridge [13] is a four-terminal-pair impedance bridge that determines an impedance ratio by the voltage ratio generated by two JAWS [8]. Two independent arrays are operated in liquid helium. The required rf pulses are generated with a pulse pattern generator with two independent memories sharing the same clock. The phase angle is set by shifting the

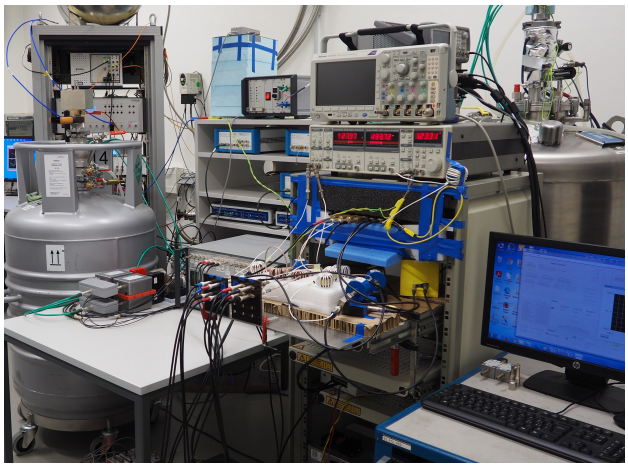

Fig. 2. Implementation of the INRIM-POLITO's (right) and PTB's (left) impedance bridges at PTB. The cryogenic systems hosting the graphene ACQHR and the JAWS device are shown on the right and left of the picture, respectively.

start bit of the pulse pattern in the second memory with respect to that in the first memory. In the PTB's Josephson impedance bridge, the ratio between the waveforms synthesized by the JAWS at arbitrary frequencies is equal to the ratio between the impedances under comparison when the bridge is balanced. The target uncertainty of the bridge is at the level of parts in 10^{-8} or less.

III. COMPARISON OF THE DIGITAL IMPEDANCE BRIDGES

The mutual validation of the PTB's Josephson and the INRIM-POLITO's electronic impedance bridge was performed by moving the INRIM-POLITO's bridge to PTB and reassembling it in the laboratory of PTB's bridge, as shown in Figure 2, where also the cryogenic systems hosting the graphene ACQHR and the JAWS device are located.

The temperature controlled calibrated impedance standards employed in the technical assessment of the bridges are a $12.9\,\mathrm{k\Omega}$ resistance standard and a $10\,\mathrm{nF}$ capacitance standard. Both the standards have small time-dependent drifts, a few $\mathrm{n\Omega/\Omega}$ per day and a few $\mathrm{nF/F}$ per day, respectively, which do not need to be considered for the comparison since the measurements of the same standards are typically performed with both the impedance bridges within one working day. All standards are located in the same two-stage thermostat with a stability in the mK range.

The graphene ACQHR device employed in the comparison is a graphene device fabricated in the cleanroom facility of the PTB as described in the literature [14]. The number of contacts is minimized to 6 to reduce the stray capacitances by allowing at the same time the required triple series connection [15]. The holder of the device was specifically designed for AC measurements with two electrodes above and below the device splitted in its center in two parts [16], the high-side and low-side shields, thus allowing the double-shield technique [17]. In the following study, this technique is not implemented: the high-side shields are kept floating, while the low-side shields are shorted to the low potential side of the device. The ACQHR device was preliminary characterized in both the DC and AC regimes, and resulted to be well quantized at a magnetic flux density of $5\,\mathrm{T}$ at a temperature of $4.2\,\mathrm{K}$. In these conditions, the graphene ACQHR device was measured with both bridges against the temperature-controlled impedance standards.

The combined uncertainties are estimated separately for each bridge. For the INRIM-POLITO's electronic impedance bridge, the main uncertainty sources are:

- Bridge reading.
- Phase error of the auxiliary injection.
- Crosstalk between the channels of the generator.
- Cable correction in the measurements involving the ACQHR device (this component is zero for temperature-controlled impedances).
- Asymmetry error due to a not perfect equalization of the currents.

For the PTB's Josephson impedance bridge, the main uncertainty sources are:

- Bridge reading.
- Crosstalk between the Josephson arrays and the inductance of the arrays.
- Cable corrections.
- Bridge deviation error from an improper balance of currents in the high potential arms.

The bridges were assessed by performing the triangle measurements shown in Figure 3 at the working frequency $f = 1233.15\,\mathrm{Hz}$ with both bridges and comparing the results. The $C_1 = 10\,\mathrm{nF}$ capacitance standard was first calibrated directly against the graphene ACQHR standard R_{QHR} and then against the $R_1 = 12.9\,\mathrm{k\Omega}$ resistance standard in turn calibrated against the graphene ACQHR standard R_{QHR}. For each bridge, the result of the triangle measurement is thus the comparison between the results obtained with the two calibrations of the capacitance standard, given by $(R_{\mathrm{QHR}}/R_1)(R_1C_2)/(R_{\mathrm{QHR}}C_2) - 1$, and evaluate the self-consistency of each bridge.

The results of the triangle measurements with the PTB's Josephson and the INRIM-POLITO's electronic impedance bridges are 0.036 ± 0.032 and 0.024 ± 0.388,

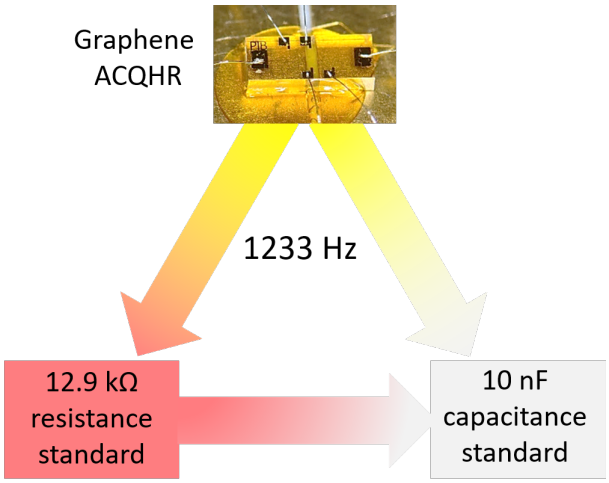

Fig. 3. Schematic of the triangle measurements performed in the technical assessment of the INRIM-POLITO's and PTB's bridges at 1233 Hz. At top of the picture there is a photo of the graphene ACQHR device fabricated by PTB.

respectively. The mutual validation of the bridges was then obtained from the discrepancies between the calibrations of the standards obtained with the two bridges, that is, 0.012 ± 0.390. All the reported uncertainties are combined uncertainties with a coverage factor $k = 2$. The measurements are thus compatible within the expanded uncertainties ($k = 2$).

IV. DISCUSSION

Thanks to the onsite comparison between the INRIM-POLITO's and PTB's impedance bridges it was possible to exchange our knowledge and experiences, and thus solve some issues that affected the bridges. For example, the behaviour of the digital source employed in the INRIM-POLITO's bridge was dependent on the room temperature, which was not controlled, and was also affected by the switches involved in the balance automatization. The current equalization in the circuit was also improved. Finally, the comparison of the bridges resulted in a very good agreement of a few parts in 10^8 within the expanded uncertainty. The Josephson impedance bridge has indeed an uncertainty that is lower than that of the electronic bridge, and is able to operate over a wide range of impedance ratios and frequencies. The electronic impedance bridge is an affordable impedance bridge able to calibrate like and quadrature impedance standards, including ACQHR standards, in the $1:1$ magnitude ratio with an uncertainty of about one part in 10^7 ($k = 1$), suitable for primary impedance metrology.

More details about the results and the methods adopted in the comparison will be presented at the conference.

V. ACKNOWLEDGEMENTS

This work is supported by the Joint Research Project GIQS (18SIB07). This project received funding from the European Metrology Programme for Innovation and Research (EMPIR) co-financed by the Participating States and from the European Unions' Horizon 2020 research and innovation programme. Martina Marzano received fundings from the EMPIR Research Mobility Grant 18SIB07-RMG1 related to the Joint Research Project GIQS.

The authors thank J. Schurr for calibrating the 10 nF capacitance standards.

REFERENCES

[1] J. Schurr, V. Buerkel, and B. P. Kibble, "Realizing the farad from two ac quantum Hall resistances," *Metrologia*, vol. 46, no. 6, pp. 619–628, oct 2009.

[2] Consultative Committee for Electricity and Magnetism, "*Mise en pratique* for the definition of the ampere and other electric units in the SI," 20 May 2019, Appendix 2 of the SI Brochure. [Online]. Available: www.bipm.org

[3] L. Callegaro, "Electrical Impedance: Principles, Measurement and Applications," Series in *Sensors*, Boca Raton, FL: CRC Press, 2013.

[4] S. Awan, B. P. Kibble and J. Schurr, "Coaxial Electrical Circuits for Interference-Free Measurements," *Electrical Measurement Series*, London: The Institution of Engineering and Technology, 2011.

[5] L. Callegaro, V. D'Elia and B. Trinchera, "Realization of the farad from the dc quantum Hall effect with digitally assisted impedance bridges," *Metrologia*, vol. 47, 464, 2010.

[6] L. Callegaro, V. D'Elia, M. Kampik, D. B. Kim, M. Ortolano and F. Pourdanesh, "Experiences with a two-terminal-pair digital impedance bridge," *IEEE Transactions on Instrumentation and Measurements*, 64 1460–5, 2015.

[7] J. Kučera and J. Kováč, "A reconfigurable four terminal-pair digitally assisted and fully digital impedance ratio bridge," *IEEE Transactions on Instrumentation and Measurements*, 67, 1199–206, 2018.

[8] S. P. Benz and C. A. Hamilton, "A pulse-driven programmable Josephson voltage standard," *Applied Physics Letters*, vol. 68, no. 22, pp. 3171–3173, may 1996.

[9] F. Overney, N. Flowers-Jacobs, B. Jeanneret, A. Rüfenacht, A. Fox, P. Dresselhaus and S. Benz, "Dual Josephson impedance bridge: towards a universal bridge for impedance metrology", *Metrologia*, 57, 065014, 2020.

[10] E. Joint Research Project 18SIB07 GIQS, "Graphene Impedance Quantum Standard." [Online]. Available: www.ptb.de/empir2019/giqs/

[11] R. Ribeiro-Palau, F. Lafont, J. Brun-Picard,

D. Kazazis, A. Michon, F. Cheynis, O. Couturaud, C. Consejo, B. Jouault, W. Poirier, and F. Schopfer, “Quantum Hall resistance standard in graphene devices under relaxed experimental conditions,” *Nature Nanotechnology*, vol. 10, no. 11, pp. 965–971, sep 2015.

[12] M. Marzano, M. Ortolano, V. D’Elia, A. Müller, and L. Callegaro, “A fully digital bridge towards the realization of the farad from the quantum Hall effect,” *Metrologia*, vol. 58, no. 1, p. 015002, dec 2020.

[13] S. Bauer, R. Behr, R. E. Elmquist, M. Götz, J. Herick, O. Kieler, M. Kruskopf, J. Lee, L. Palafox, Y. Pimsut, and J. Schurr, “A four-terminal-pair Josephson impedance bridge combined with a graphene-quantized Hall resistance,” *Measurement Science and Technology*, vol. 32, no. 6, p. 065007, mar 2021.

[14] D.-H. Chae, M. Kruskopf, J. Kučera, J. Park, N. T. M. Tran, D. B. Kim, K. Pierz, M. Götz, Y. Yin, P. Svoboda, P. Chrobok, F. Couëdo, and F. Schopfer, "Investigation of the stability of graphene devices for quantum resistance metrology at direct and alternating current,” *Measurement Science and Technology*, vol. 33, no. 6, p. 065012, mar 2022.

[15] F. Delahaye, "Series and parallel connection of multiterminal quantum Hall effect devices," *Journal of Applyed Physics*, vol. 73, no. 11, pp. 7914-7920, 1993.

[16] M. Kruskopf, S. Bauer, Y. Pimsut, A. Chatterjee, D. K. Patel, A. F. Rigosi, R. E. Elmquist, K. Pierz, E. Pesel, M. Götz, and J. Schurr, "Graphene quantum Hall effect devices for AC and DC electrical metrology," *IEEE Transactions on Electron Devices*, vol. 68, n. 7, pp. 3672-3677, jul 2021.

[17] J. Schurr, B. P. Kibble, G. Hein, and K. Pierz, "Controlling losses with gates and shields to perfect a quantum Hall impedance standard," *IEEE Transactions on Instrumentation and Measurements*, vol. 58, pp. 973-979, 2009.

25th IMEKO TC4 International Symposium
23rd International Workshop on ADC and DAC Modelling and Testing
IMEKO TC-4 2022
Brescia, Italy / September 12-14, 2022

A New Impedance Metrology Infrastructure at GUM

Krzysztof Musioł[1], Maciej Koszarny[2], Marian Kampik[1], Krzysztof Kubiczek[1], Adam Ziółek[2], Jolanta Jursza[2]

[1] *Silesian University of Technology (SUT), ul. Akademicka 2a, 44-100 Gliwice, Poland, krzysztof.musiol@polsl.pl; marian.kampik@polsl.pl; krzysztof.kubiczek@polsl.pl*
[2] *Central Office of Measures (GUM), ul. Elektoralna 2, 00-139 Warsaw, Poland, maciej.koszarny@gum.gov.pl; adam.ziolek@gum.gov.pl; jolanta.jursza@gum.gov.pl*

***Abstract* – Collaboration of the Polish National Metrology Institute (GUM, Warsaw) with the Silesian University of Technology (SUT, Gliwice) and joint participation in international projects focused on the development of digital sources and digital impedance bridges contributed to the development of the impedance metrology infrastructure at GUM. The article presents current work related to expanding the current infrastructure with a new 4TP, mostly thermostated impedance standards terminated with MUSA connectors. Design solutions, results of thermal stability measurements and results of the comparison of new impedance standards made with the currently implemented digital impedance bridge are presented in the paper.**

I. INTRODUCTION

For almost 60 years, it has been known that a four-terminal pair (4TP) definition achieves the highest accuracy in impedance measurement [1]. The 4TP definition requires more complex measurement setups than simpler impedance definitions, but on the other hand, it reduces to a minimum the dependence of the measurement outcome on the effects of electrical connections and circuit layout details [2-6]. Consequently, a 4TP definition allows the best accuracy in impedance measurement to be achieved. Unfortunately, although some commercial LCR measuring instruments like HP 4284, GenRad 1693, or Agilent E4980A are designed for 4TP measurements, manufacturers of impedance standards rarely equip them with four coaxial connectors. This prompts national metrology institutions (NMIs) to develop and construct their own solutions or modify the present standards to fit them to the 4TP definition. With the beginning of the present century, many NMIs started to replace their impedance standards with BPO MUSA connectors or construct new ones [7-11]. At the NMI level, the accuracy and frequency range are steadily increasing; hence, the role of the 4TP definition will be very important.

The newly available technology of digital impedance bridges, developed in the framework of recent joint research projects (in particular SIB53 AimQuTE [12] and 17RPT04 VersICaL [13]), has shown the potential to realize SI impedance units and scales at GUM at a reduced cost, and thus provide new primary-level electrical impedance calibration services for industry and calibration centres. Due to the implementation at GUM of a new 4TP sampling-based digital impedance bridge, it was necessary to adapt the current infrastructure to the new measuring system. This is especially important in terms of impedance standards. Therefore, thermostated sets of RLC standards were designed and constructed, which are described in detail in Section 2. When designing the standards, it was considered that such standards usually work in a laboratory with a temperature variable within the limits of 23±1ºC. The target impedance comparison uncertainty is at the level of few ppm, therefore, taking into account the temperature coefficients of the available *R* and *C* components of the standards (the maximum values are up to 30 ppm/ºC), thermoregulation of these objects is necessary. In such a case, thermoregulation at the level of hundredths of a degree causes that the influence of the standard value fluctuations caused by the temperature change may be neglected in the final uncertainty calculation. The assumed operating frequency of the standards covers the range from 20 Hz to 20 kHz.

II. 4TP IMPEDANCE STANDARDS

A. Capacitors

In 2018-2021, three sets of thermostated capacitance standards were built successively at GUM: 1) KC0G-10nF, 2) KC0G-1XF L52-1/20; and 3) KC0G-1XF L52-2/21 (see Fig. 1). KC0G-1XF L52-1 and L52-2 consist of five capacitance standards: 1 nF, 10 nF, 100 nF, 1 μF and 10 μF. All standards use SMD 1206 GMR31 series C0G

capacitors from Murata, Japan [14]. The C0G (NP0) dielectric is the most popular formulation of the "temperature-compensating," EIA Class I ceramic materials. Modern C0G formulations contain neodymium, samarium, and other rare earth oxides. C0G ceramics offer one of the most stable capacitor dielectrics available. The change in capacitance with temperature is 0 ± 30ppm/°C. Capacitance drift or hysteresis for C0G (NP0) ceramics is less than ± 0.05% versus up to ± 2% for films. The typical capacitance change with life is less than ± 0.1% for C0G (NP0), one-fifth that shown by most other dielectrics. Moreover, C0G (NP0) formulations show no aging characteristics.

Stages of the construction of the capacitance standards are presented in Fig. 2. The SMD capacitors are first embedded in natural pure wax, which has a positive effect on the long-term stability of the parameters of the standard. Then each single capacitor is inserted into the shielded housing visible in the upper left photo in Fig.2. After that, the capacitors are placed in an enclosure with heating foil and insulated with an aerogel mat. The aerogel used has low density and extremely low thermal conductivity 0.014 W/(m·K). Aerogels are usually made based on silica, although recently carbon nanotubes and graphene have also been utilized. There are also aerogels based on zeolites and aluminoxanes, but silica is by far the most widely used.

The temperature controller stabilizing temperature of the capacitors uses an NTC temperature sensor. An additional Pt100 sensor serves as temperature monitor. Both sensors are mounted inside the case. The controller is a simple and rugged on/off electronic controller, mounted within the thermal insulation (see Fig. 1), and adjusted to operate at approximately 26.5ºC with 0.01ºC hysteresis. This temperature results from the fact that, according to the specifications of the manufacturers of multilayer ceramic capacitors (MLCC) [14], the smallest changes in capacitance along with temperature changes can be expected around 26-27ºC. The temperature controller of the set of standards is supplied from a +12 V DC power supply through a 4-pin socket. It is recommended to use a battery during calibration. However, a power supply can be used to charge the battery. The internal temperature of the enclosure is measured using resistance thermometer Pt100 that can be accessed through two BNC connectors indicated with Pt100. The standards are equipped with MUSA Metrology Grade silver-plated connectors manufactured by Canford, UK. The connectors are indicated with H_{CUR} and L_{CUR} for the current high and current low, respectively, and H_{POT} and L_{POT} for the potential high and potential low, respectively.

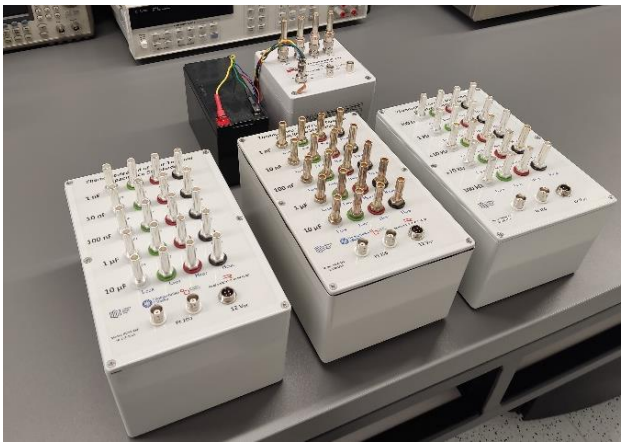

Fig. 1. 4TP resistance and capacitance standards used at GUM and SUT (two sets of thermostated capacitors and one set of thermostated Vishay resistors – at the bottom from the left, and 10 nF thermostated capacitors with battery – at the top.

Fig. 2. Stages of construction of the thermostated set of standard capacitors (shielded housing with a single capacitor – top left, enclosure with heating foil – top right, set of five capacitors mounted in the heating enclosure and insulated with aerogel – bottom left, complete set without cover – bottom right)

B. *Resistors*

A set of five 4TP resistance standards was manufactured at SUT in 2021 (Fig. 3). The standards have nominal values of: 10 Ω, 100 Ω, 1 kΩ, 10 kΩ, and 100 kΩ. Ultra-high precision Vishay HZ-series (Z-foil) resistors were used to fabricate these standards [15]. Since the temperature coefficient of resistance is ± 0.2 ppm/°C there is no need to mount them in the thermostat.

Another set of resistance standards was manufactured at GUM (see the rightmost standard in Fig. 1). High precision Vishay H-series bulk metal foil resistors were used to fabricate these standards [16]. Since the resistance temperature coefficient for this type of resistor is ± 2 ppm/°C, the temperature of the standards is controlled in the same way as described for the capacitance standards in Chapter II.A. The standard was indicated as Vishay-1XΩ, Nr L52-1/21.

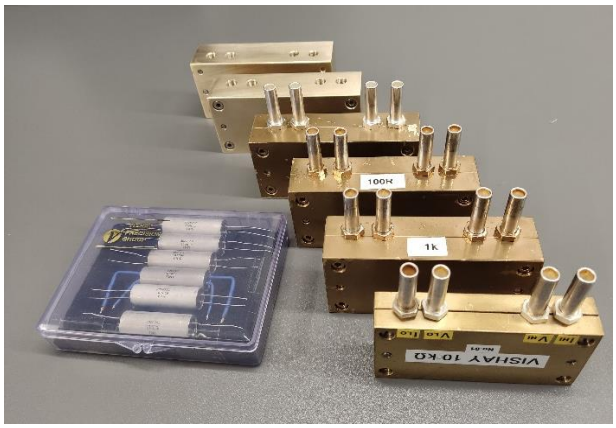

Fig. 3. 4TP resistance standards manufactured at SUT (Vishay HZ resistors with brass body, terminated with MUSA connectors)

C. *Inductors*

Calibration laboratories maintain traceability to national standards using 2T or 3T inductance standards. When such standards are used to calibrate a 4TP impedance meter, the standard must be reconverted from 2T or 3T to 4TP with suitable adapters [9] that are not commercially available, what reduces the calibration accuracy. It is therefore advisable to replace the three original binding post terminals with a 4TP coaxial connectors (e.g. BPO MUSA [7, 8]). Currently at GUM all inductance standards are 3T. Some of them were modified to be thermostated (see Fig. 4). The thermostat stabilizes the internal temperature within 0.01°C for ambient temperature within 18-25°C. However, it was decided to manufacture custom MUSA adapters and tees (see the lower right corner of Fig. 4) that enable one to meet the 4TP definition.

Fig. 4. Thermostated standard inductor 1482-L. Modified by Ukrainian NMI. The MUSA adapter and the MUSA tees are visible in the small window at the bottom right

D. *Temperature stability of the standards*

Temperature stability of the capacitance and resistance standards presented in Fig. 1 was examined at ambient temperature of 23.5±1.0ºC using a four-wire resistance measurement of the Pt100 sensor built into the standards. Measurements were made using an Agilent 3458A precision multimeter and software made in the LabView environment. The temperature of each of the standards was monitored in two seconds intervals from the moment the power was turned on (that correspond to the ambient temperature) until the steady state temperature was reached. The measurement results are presented in the Fig. 5 and Fig. 6 for capacitance standards and for resistance standard, respectively.

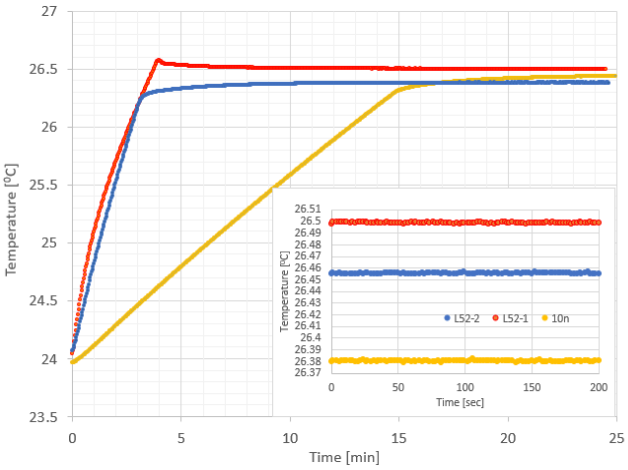

Fig. 5. Temperature stability of capacitance standards KC0G-10nF, KC0G-1XF L52-1/20 and KC0G-1XF L52-2/21

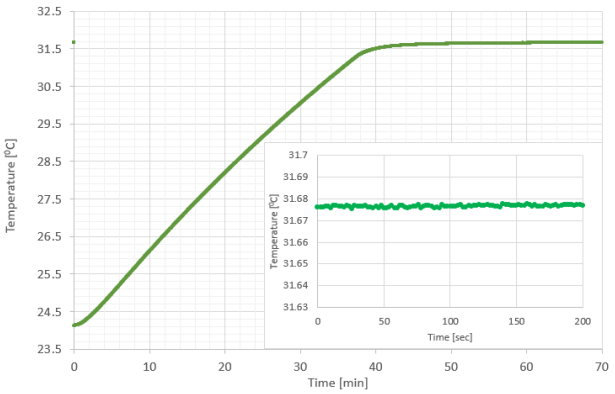

Fig. 6. Temperature stability of resistance standard Vishay-1XΩ, No. L52-1/21.

The last 100 measurement results obtained in the steady state are shown in the small windows inside the graphs. It is visible that temperature changes in the steady state do not exceed 0.01°C.

III. 4TP BRIDGE

A 4TP sampling-based digital impedance bridge developed at SUT is currently being implemented at GUM. Fig. 7 shows the schematic of the sampling-based GUM bridge and Fig. 8 shows the photograph of the bridge. Detailed description of the bridge and the high-performance source used to supply the bridge are given in [15] and [16], respectively.

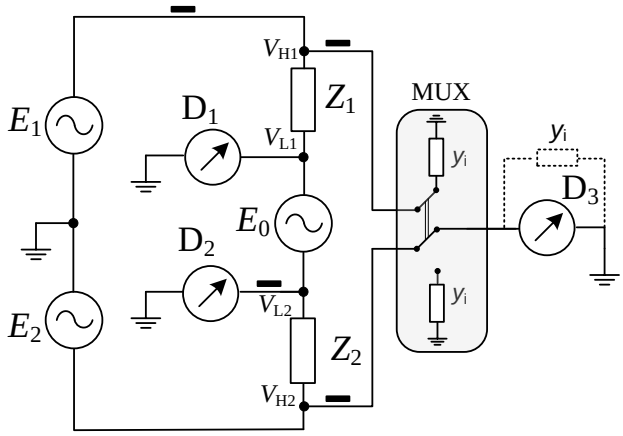

Fig. 7. Basic schematic of the GUM 4TP bridge. Solid black rectangles represent coaxial current equalizers (chokes) and y_i represents input admittance of the digitizer D_3

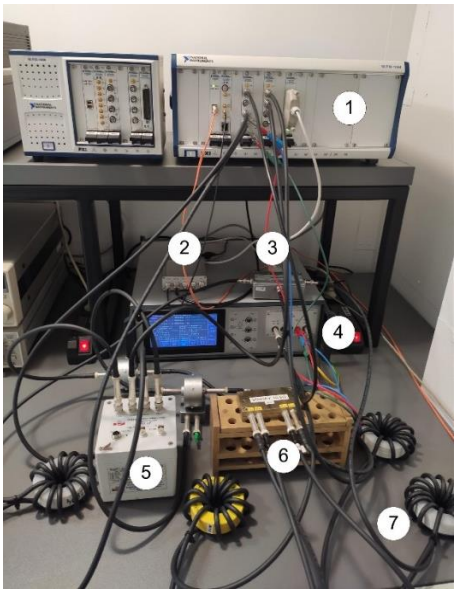

Fig. 8. Photograph of the bridge: 1- NI PXI sampling system, 2-opto/TTL converter, 3- multiplexer, 4- DSS_2CH two-channel AC voltage source, 5- thermostated 4TP capacitance standard KC0G-10nF , 6- 4TP standard Vishay resistor, 7-current equalizer.

IV. COMPARISONS

The construction of appropriately stable impedance standards encouraged us to perform further validation tests of the implemented bridge. Initially, two new sets of capacitance standards (KC0G-1XF L52-1 and L52-2) were calibrated at GUM using the ultra-precision capacitance bridge Andeen-Hagerling AH2700A to determine their reference values. In turn, the third new capacitor KC0G-10nF was calibrated at INRiM using the three-voltmeter method. Next, four 4TP Vishay standard resistors (100 Ω, 1 kΩ, 10 kΩ, and 100 kΩ) presented in Fig. 3 were calibrated through R-C comparison using the new 4TP sampling-based bridge developed at SUT.

V. CONCLUSIONS

The article presents new design solutions of impedance standards, which have been recently implemented at GUM. Only initial tests have been presented for some newly developed standards. No disturbing behavior was observed during the comparison for any of the thermostated capacity standards. The monitoring of the standards temperature with the use of the built-in Pt100 sensor indicates a relatively quick (less than 30 minutes) achievement of the steady state of the capacitance standards and shown that the temperature fluctuations are within 0.01 K. Thus, the component of the uncertainty of comparison related to the instability of the standard can be ignored in this case. The *R-C* comparison performed with the use of the 4TP sampling-based bridge has shown

Table. 1. R-C Comparison results (the value of the unknown standard resistors was calculated from the R-C ratio measured by the new 4TP digital impedance bridge at GUM)

Standards compared	Reference value			DUT		Difference
	C, nF	$u_{rel}(C)$, μF/F	tgδ, $\times 10^{-5}$	R, kΩ	τ, $\times 10^{-5}$	ΔR, μΩ/Ω
100 Ω vs. 1 μF (L52-1/20)	1000.035	70	65	0.09999938	11	
100 Ω vs. 1 μF (L52-2/21)	1000.020	70	75	0.10000004	10	6.6
1 kΩ vs. 100 nF (L52-1/20)	99.99634	35	8.6	1.0000170	0.93	
1 kΩ vs. 100 nF (L52-2/21)	100.00397	35	8.6	1.0000193	0.75	2.3
10 kΩ vs. 10 nF (L52-1/20)	10.000157	2	1.9	10.000153	0.67	
10 kΩ vs. 10 nF (L52-2/21)	10.000531	2	5.7	10.000106	0.95	4.7
10 kΩ vs. 10 nF (L52-1/20) *	10.000115	2	2.4	9.9999898	0.66	
10 kΩ vs. 10 nF (KC0G-10n) *	9.9999453	2	4.3	9.9998810	0.7	1.0

high consistency of the results obtained for a standard resistor compared with two different capacitors. In addition to the high consistency of the active components, a good agreement of the reactive components (τ) was also observed. The results of the comparison presented in the article, which are only a part of the tests performed to validate the new 4TP digital bridge, demonstrate the high accuracy and usefulness of the bridge for standard comparison at GUM. Currently, GUM and SUT are working on the inclusion of the new bridge in the national system of measures, which is associated with the development of an uncertainty budget for all new comparisons and the declaration of a new CMC.

REFERENCES

[1] R. D. Cutkosky, “Four-terminal-pair networks as precision admittance and impedance standards,” Commun. Electron., vol. 70, pp. 19–22, Jan. 1964.

[2] S. Awan, B. Kibble, and J. Schurr, Coaxial Electrical Circuits for Interference-Free measurements (Electrical Measurement). Edison, NJ, USA: IET, 2010.

[3] L. Callegaro, “Electrical Impedance: Principles, Measurement, and Applications”, CRC Press, 1st edition, 2012.

[4] AR. Calhoun, “Four terminal pair concepts,” Cal Lab, pp. 38–41, Nov./Dec. 1996.

[5] B. P. Kibble, “Four terminal-pair to anything else!” in Proc. IEE Colloq. Interconnections From DC Microw. (Ref. No. 1999/019), London, U.K., Feb. 18, 1999, pp. 6/1–6/6.

[6] B.P. Kibble, “Proposals for Extanding Traceable Impedance Measurements to Higher Frequencies”, Metrologia, vol. 35, No. 1, pp. 17-20, 1998.

[7] L. Callegaro, V. D’Elia, F. Francone, and D. Serazio, “100 mH travelling standard for the EUROMET 607 pilot intercomparison,” in CPEM Tech. Dig., Ottawa, ON, Canada, Jun. 16–21, 2002, pp. 352–353.

[8] L. Callegaro, V.D’Elia and D. Serazio, “10-nF Capacitance Transfer Standard”, IEEE Trans. Instr. Meas., Vol. 54, No. 5, pp. 1869-1872, 2005.

[9] E. Dierikx, J. Melcher, L. Callegaro, “Final report on the supplementary comparison EURAMET.EMS26: inductance measurements of 100 mH at 1 kHz” (EURAMET project 816), Metrologia 49 (1A), January 2012.

[10] L. Callegaro, V. D'Elia and J. Bohacek, "Four-Terminal-Pair Inductance Comparison Between INRIM and CTU," in IEEE Transactions on Instrumentation and Measurement, vol. 58, no. 1, pp. 87-93, Jan. 2009

[11] L. Callegaro, V. D'Elia, F. Francone and D. Serazio, "100 mH travelling standard for the EUROMET 607 pilot intercomparison," Conference Digest Conference on Precision Electromagnetic Measurements, 2002, pp. 352-353.

[12] SIB 53 AIM QuTE final publishable JRP Report “Automated Impedance Metrology extending the quantum toolbox for electricity”, Euramet, June 2017

[13] 17RPT04 VersICaL final publishable JRP Report “A versatile electrical impedance calibration laboratory based on digital impedance bridges”, Euramet, 2020

[14] https://www.murata.com, specification of Murata GRM31C5C1H104JA01#

[15] www.foilresistors.com, Specification of Vishay HZ Series, Document Number: 63120, March 2010

[16] www.foilresistors.com, Specification of Vishay H Series, Document Number: 63006, March 2010

[17] K. Musioł, “A new sampling-based four-terminal-pair digital impedance bridge”, Measurement-Sensors, Volume 18, December 2021.

[18] M. Kampik, K. Musioł, “Investigations of the high-performance source of digitally synthesized sinusoidal voltage for primary impedance metrology”, Measurement, Volume 168, 2021.

25th IMEKO TC4 International Symposium
23rd International Workshop on ADC and DAC Modelling and Testing
IMEKO TC-4 2022
Brescia, Italy / September 12-14, 2022

Bias-induced Impedance of Current-carrying Conductors: Measurements Simulation Using FRA

Sioma Baltianski [1]

[1] *Wolfson Dept. of Chemical Engineering, Technion – Israel Institute of Technology, Haifa, Israel,* cesema@technion.ac.il

***Abstract* – The paper presents mainly the simulation of impedance measurements utilizing a frequency response analyzer (FRA) for the study of the current-carrying conductors under the influence of bias. It is vital to have confidence in the results of impedance spectroscopy because one of the informative quantities has very little impact on the resulting impedance. During the passage of an electric current, the studied objects have an additional low-frequency impedance called the bias-induced impedance effect (*Z_{BI}-effect*) [1]. An emphasis was placed on explaining how the *Z_{BI}-effect* acts as an amplifier for temperature modulation of a resistance caused by the test signal. A description of the investigated object is based on electrical models whose parameters provide useful information for further research. Several studies have been done to assess the consistency of electrical parameters. A silver wire was used in research as an object under study and as a representative of pure metals.**

***Keywords* – current-carrying conductors, bias-induced impedance, impedance spectroscopy, FRA**

I. INTRODUCTION

In previous work [1], the bias induced impedance effect (*Z_{BI}-effect*) was described. Experimental results related to the study of current-carrying conductors under bias using impedance spectroscopy were mainly presented.

In this study, we provide a more detailed overview and modeling of the measurement process. First, it is worth making a few remarks. The interpretation of the measurement results in [1] was restricted to electrical models - equivalent circuits. A possibility was expressed, but a thermophysical interpretation was not made since the author lacks the necessary knowledge, and such a task was not outlined. The following introduction will highlight the main works associated with this interpretation.

The first mention of the analysis of the response of a conductor with DC and AC currents was found in [2]. A platinum resistance heater/thermometer (PRT) is fabricated on two membranes. One membrane can be Joule heated to cause heat conduction through the sample to the other membrane. An SR830 lock-in amplifier is used to measure the first harmonic component of the voltage drop across the heating PRT, yielding the differential resistance.

It is worth paying attention to the work [3]. This paper illustrates the reaction of a conductor with current to various combinations of electrical influences known in the literature as the 1ω, 2ω, and 3ω methods. It has established a theoretical basis that links the parameters of the transfer function to the parameters of the object under study and the electrical impact on it. Note that what is referred to as the electrical transfer function (see, for example, Table 1 in the paper cited above) is actually a thermal transfer function denoted by K/W units of measurement - the same units as the thermal resistance R_{th} that is a parameter in the following equations in this paper. An undeniable advantage of the article is the possibility to interpret electrical measurements directly into thermophysical parameters of the objects under study - a specific thermal conductivity and a heat capacity.

An important article [4] deals with the practical aspects of developing resistive thermal probes for scanning thermal microscopy. It is based mainly on the theoretical contributions of [3]. Yet, some analytical expressions are more transparent and, in some respects, differ from the one stated in [3]. The expressions in this work also link the thermal characteristics and electrical parameters of the research object, which is an undoubted advantage.

We emphasize here that all of our work in [1] and here focuses on electrical parameters. The measuring method will be followed without considering the thermophysical properties of the studied objects. Our research has produced "output products" in the form of electrical parameters that can be effectively applied by specialists within the framework of thermophysical theories.

In the papers [2] - [4] and the works following them, the Lock-in Amplifier class devices are used as meters for measuring electrical parameters. These devices do not directly measure the impedance of the objects under investigation (especially using bias), but with some additions, they can implement this function.

Our research employs commercially available instruments that directly measure the impedance of objects under bias conditions. Potentiostat and Galvanostat are commonly used terms to describe these devices. Initially, they were designed to operate in the time domain, but in recent decades, they have begun to be equipped with impedance modules with decent metrological properties. The Potentiostat/Galvanostat Biologic SP-240 (BioLogic Sciences Instruments) was used as the measuring instrument [5]. In our earlier paper [1], we considered the nature of the Z_{BI}-*effect* in sufficient detail, using various materials to evaluate it in a broad context. A promising result associated with the dynamic nature of the temperature coefficient of resistance (TCR) has been revealed. This result may explain the behavior of the alloys. In this work, we will simulate the measurement process using one of the representatives of pure metals as an object under test.

Fig. 1 shows the impedance characteristics of a silver wire (Aldrich Chem. Co. 99.99+%) 500 mm long and 0.25 mm in diameter in two modes of current exposure: without bias I_{dc} = 0 A and with bias I_{dc} = 3 A. The amplitude of the test signal I_{ac} was 100 mA, which met the small-signal requirements.

The measurements were conducted by operating the Biologic SP-240 in galvanostatic mode. Data were verified in some cases using the Gamry Reference 3000 potentiostat/galvanostat (Gamry Instruments). We used a 4-wire sample holder [1] inside the Faraday cage. The experiment was conducted at a temperature of about 20 °C in a room environment.

Without bias, the impedance of the investigated conductor is well described by the three-element model, Fig. 2 (a). The R_p parameter in this model is responsible for the skin effect in the high-frequency region. The remaining two parameters, L_p and R_s, relate to the size and material of the object. In the low-frequency region, imaginary part noise is natural (in this region, ReZ/ImZ > 10^3) and depends, in particular, on the sensitivity of the measuring device. The use of a Faraday cage can reduce the level of this noise significantly.

In the low-frequency part of the spectrum, it is immediately observed that the nature of the reactance changes dramatically with presenting bias: from inductive to capacitive. To deal with experimental data in the case of bias, it is necessary to incorporate in the previous model other elements which are responsible for the Z_{BI}-*effect*: parallel R_{BI} and C_{BI}, Fig. 2 (b).

As you can see from the fitting results, bias has a very small effect on the high-frequency part of the impedance spectrum (R_p and L_p). Throughout the entire frequency range, there is a noticeable change in the R_s – one of the real components of the impedance. Bias causes a shift in the temperature of the conductor, resulting in this change. The effect is common. Generally, model (b) well approximates the impedance of the object under study over

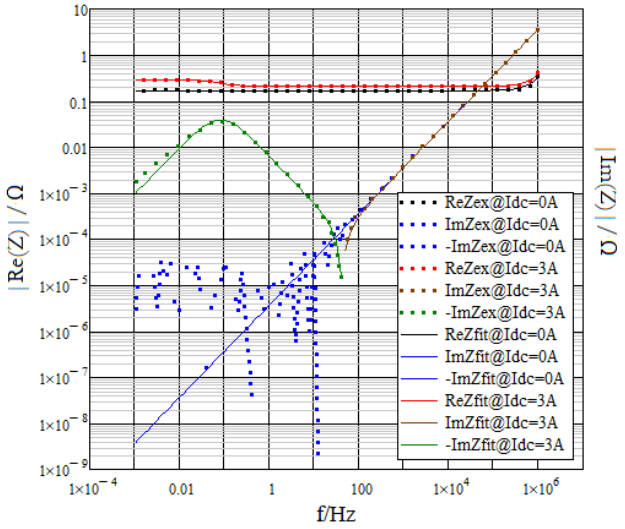

Fig. 1. Experimental Re*(Z),* Im*(Z) and fitted results; silver wire; bias:* I_{dc} *= 0* A *and* I_{dc} *= 3* A*; length 500* mm *and diameter 0.25* mm*; frequency range 1* MHz *... 0.001* Hz*.*

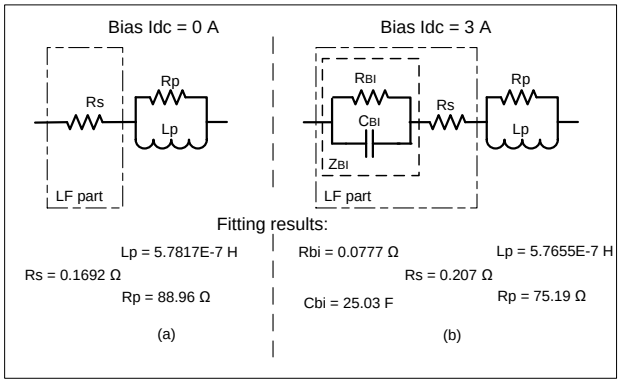

Fig 2. Electrical models and their parameters used to fit experimental data presented in Fig.1; (a) - results at zero bias (I_{dc} *= 0* A*); (b) - results at* I_{dc} *= 3* A.

the entire experimental frequency range. The effect of bias on the high-frequency part of the spectrum is not significant, and we are not concerned with it. We will further study the low-frequency part of the spectrum - approximately frequencies below 10 Hz.

In the following section, the simulation of the measurement process will be examined to confirm the validity of the results obtained using our instruments.

II. IMPEDANCE MEASUREMENTS SIMULATION UTILIZING FRA

The modern impedance measuring instruments have several basic structures [6]. We will simulate a structure called a Frequency Response Analyzer (FRA). An impedance part of the instruments used in this work is centered around the FRA.

To understand the measurement process, we must first build a model of the object under study – the current-carrying conductor under the influence of the superposition of the test signal and bias. Here, we will examine how the blocks act upon the object in the process of considering the operation of the blocks. These blocks are included in the FRA structure.

The work [6] presents a simplified block diagram of FRA and explains how such a structure operates. Here are some details of this block to simulate and verify the measurement results. Fig. 3 illustrates the FRA that underlies the measurement procedure. Let us choose the galvanostatic mode as the option of operating for definiteness. It means that the sample under test will receive a sum of the bias current I_{dc} and a sinusoidal test signal with an amplitude I_{ac} having a circular frequency $\omega = 2\pi f$:

$$I_{act}(t) = I_{dc} + I_{ac}\sin(\omega t) \tag{1}$$

The total current causes Joule heating $Q = I^2R$ and therefore leads to a change in the resistance of the conductor due to its weak but existing nonlinearity. The square of the current will have three components:

$$I_{act}^2(t) = I_{dc}^2 + 2I_{dc}I_{ac}\sin(\omega t) + {I_{ac}}^2\sin(\omega t)^2 \tag{2}$$

The last term of expression (2) will generate the 2nd harmonic in the heating of the conductor and, accordingly, this component will modulate the second harmonic of the conductor's resistance. In this work, we are considering the small-signal condition ($I_{ac} << I_{dc}$) and a weak nonlinearity of the object under study. Thus, ignoring the second and higher harmonics, the expression for the resistance of the conductor under the influence of the bias and test signal can be approximately described as

$$R_{rsp}(t) \approx R_{wp} + R_{ac}(\omega)\sin(\omega t + \psi(\omega)) \tag{3}$$

where: $R_{wp} \propto I_{dc}^2$ - static resistance at working point; $R_{ac} \propto I_{dc}I_{ac}$ - amplitude of modulation part of the resistance. The value of R_{ac} at the operating point depends on the circular frequency ω due to inertia. The phase shift ψ is also related to the test signal frequency due to inertia. Ignoring the second and higher harmonics in expression (3) is also justified by the FRA functional, which will be discussed below.

With an increase in the frequency of the test signal, the modulation value of resistance due to the test signal tends to zero, and the phase angle tends to 90 degrees. With decreasing frequency, the modulation value will tend to be maximum, and the phase angle will tend to zero. All this is due to the inertia of the object under study.

Thus, we have formed a model of the object under study (3) – the current-carrying conductor under the influence of the superposition of the test signal and bias.

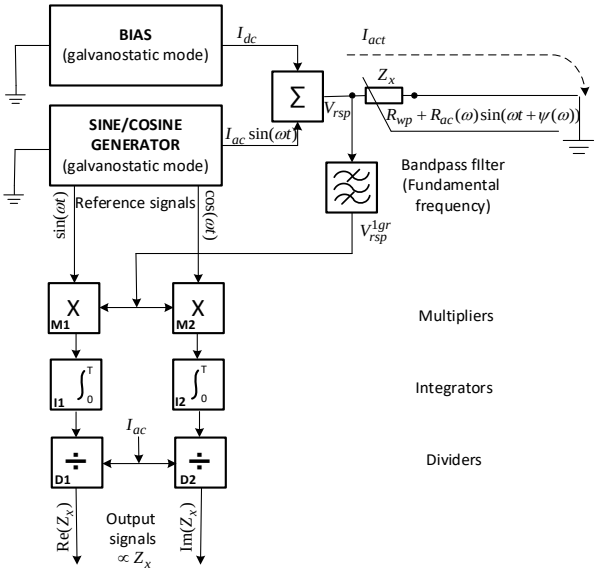

Fig. 3. Functional diagram of a frequency response analyzer.

According to Ohm's law, the voltage drops $V_{rsp}(t)$ across the object under study will be equal to the product of expression (1) and (3):

$$\begin{aligned} V_{rsp}(t) &= [I_{dc} + I_{ac}\sin(\omega t)]\times \\ &\times[R_{wp} + R_{ac}(\omega)\sin(\omega t + \psi(\omega))] \end{aligned} \tag{4}$$

Corresponding to the functionality of the FRA [6], [7], harmonics that are multiples of the fundamental will be suppressed. This also applies to the appearance of the DC component in the signal. We designate this function by introducing a bandpass filter into the circuit (Fig. 3), which only passes the fundamental frequency. Therefore, following the bandpass filter, higher harmonics and DC components are removed. In this case, the output signal will only contain the fundamental frequency (1gr):

$$V_{rsp}^{1gr}(t) = I_{ac}\sin(\omega t)R_{wp} + I_{dc}R_{ac}(\omega)\sin(\omega t + \psi(\omega)) \tag{5}$$

The expression (5) contains two components. The first term of this expression determines the static component of the investigated object. The second term defines the dynamic component generated by resistance modulation and bias. The signal (5) is fed into one of the inputs of two multipliers M1 and M2 (see Fig. 3).

Other inputs received the sinusoidal and cosine signals with unit amplitude transmitted from the generator (reference signals). As a result, the quadrature components of the output signal of the multipliers are respectively equal:

$$V_{\sin}(t) = \sin(\omega t)[I_{ac}\sin(\omega t)R_{wp} + \\ + I_{dc}R_{ac}(\omega)\sin(\omega t + \psi)] \quad (6)$$

$$V_{\cos}(t) = \cos(\omega t)[I_{ac}\sin(\omega t)R_{wp} + \\ + I_{dc}R_{ac}(\omega)\sin(\omega t + \psi)] \quad (7)$$

The outputs of the multipliers are fed into the inputs of integrators I1 (which extracts a real component of the signal) and I2 (which extracts an imaginary component of the signal). After the integrators, the signals will have the following form:

$$\mathrm{Re}V = I_{ac}R_{wp}\frac{2}{T}\int_0^T[\sin(\omega t)\sin(\omega t)]dt + \\ + I_{dc}R_{ac}(\omega)\frac{2}{T}\int_0^{T`}[\sin(\omega t)\sin(\omega t + \psi(\omega))]dt \quad (8)$$

$$\mathrm{Im}V = I_{ac}R_{wp}\frac{2}{T}\int_0^T[\cos(\omega t)\sin(\omega t)]dt + \\ + I_{dc}R_{ac}(\omega)\frac{2}{T}\int_0^{T`}[\cos(\omega t)\sin(\omega t + \psi(\omega))]dt \quad (9)$$

Further, we will use the equalities (10) and (11):

$$\frac{2}{T}\int_0^T[\sin(\omega t + \psi(\omega))\sin(\omega t)]dt \equiv \cos(\psi(\omega)) \quad (10)$$

$$\frac{2}{T}\int_0^T[\sin(\omega t + \psi(\omega))\cos(\omega t)]dt \equiv \sin(\psi(\omega)) \quad (11)$$

taken from [6] to form the final expression. The first parts of expressions (8) and (9) do not depend on the phase angle and only give the real component of the signal. Dividing (8) and (9) by the known amplitude of the test signal I_{ac} (D1 and D2, see Fig. 3) and considering expressions (10) and (11) noted above, we finally get:

$$Z_x = R_{wp} + \frac{I_{dc}}{I_{ac}}R_{ac}(\omega)\{\cos[\psi(\omega)] + j\sin[\psi(\omega)]\} \quad (12)$$

According to the electrical model for the low-frequency part of the impedance (see LF part in Fig.2b), we can write

$$Z_x = R_s + Z_{BI} \quad (13)$$

where $R_s \equiv R_{wp}$ and

$$Z_{BI} \equiv \frac{I_{dc}}{I_{ac}}R_{ac}(\omega)\{\cos[\psi(\omega)] + j\sin[\psi(\omega)]\} \quad (14)$$

The analysis (14) shows that the effect of R_{ac} modulation in the resulting impedance will increase with an increase in the ratio of the bias I_{dc} to the test signal I_{ac}. It is worth reminding that the R_{ac} modulation will also depend on the amplitude of the test signal (Joule heating), but their ratio (R_{ac}/I_{ac}) remains almost the same at the low signal approach. For example, it has been experimentally confirmed that at a bias I_{dc} = 3 A, a 10-fold increase in the test signal from 10 mA to 100 mA leads to an increase in this ratio by only 0.1%.

Because the inertia will be absent at extremely low frequencies, we can assume that the angle ψ will tend to zero. Therefore, the imaginary part in (14) will be disappeared. In addition, the modulation amplitude caused by the test signal will be maximized: $R_{ac}(\omega) \to R_{ac}^{\max}$. In this case, the expression (14) takes the form:

$$R_{BI} = \frac{I_{dc}}{I_{ac}}R_{ac}^{\max} \quad (15)$$

Let us estimate the value of the $R_{ac}^{\max}$ modulation. After fitting with a bias I_{dc} = 3 A and a test signal I_{ac} = 100 mA, R_{BI} = 0.0777 Ω is found (Fig. 2b). As a result of the expression (15), we arrive at the value of the amplitude of the maximum modulation $R_{ac}^{\max}$ = 0.0026 Ω. This value provides valuable information about the thermophysical properties of the object under study [3], [4]. A further useful parameter for assessing the thermophysical properties is the time constant $\tau_{BI} = R_{BI}\,C_{BI}$ obtained from the model in Fig. 2b.

From the value of $R_{ac}^{\max}$ above, let us estimate the temperature modulation. The well-known formula for finding resistance at a given temperature is:

$$\rho_2 = \rho_1 \cdot [1 + \alpha \cdot (T_2 - T_1)] \quad (16)$$

where $\alpha = 3.8 \cdot 10^{-3}\,\Omega/\Delta°\mathrm{C}$ is a temperature coefficient of resistance at room temperature; ρ_1 is a silver resistivity at T_1; ρ_2 is a required value of resistivity at temperature T_2. Based on (16), considering the geometric dimensions of the conductor, to solve the inverse problem - finding the temperature from the resistance at the operating point R_s, the corresponding expression will be written as follows:

$$T_{wp} = \frac{R_S^{3A} + R_S^{0A} \cdot (T_{Room} \cdot \alpha - 1)}{\alpha \cdot R_S^{0A}} \quad (17)$$

where values are: $R_S^{3A} = 0.207\ \Omega$ and $R_S^{0A} = 0.1692\ \Omega$ (see Fig 2b and Fig2a accordingly). The ambient temperature T_{Room} used in the calculation according to formula (17) was approximately 20 °C. Calculation by formula (17) gave the result T_{wp} = 78.79 °C.

To find the temperature variation from the variation in resistance $R_{ac}{}^{\max}$ caused by the test signal, formula (17) is modified as follows:

$$T_{wp}^{ac} = \frac{\left(R_s^{3A} + R_{ac}^{\max}\right) + R_s^{0A} \cdot \left(T_{Room} \cdot \alpha - 1\right)}{\alpha \cdot R_s^{0A}} \qquad (18)$$

A calculation using formula (18) gave the result $T_{wp}^{ac} = 82.83$. Thus, the difference between the temperature values obtained by formulas (18) and (17) is 4.04 °C. This temperature increase should be observed at extremely low frequencies when the thermal inertia of the system is close to zero.

It can be seen that the temperature modulation is small in comparison with the high temperature additive component at the operating point. Nonetheless, this value is available for direct and not very complicated measurements (without pretensions to accuracy, but only to assess the order). In the following section, we demonstrate the effectiveness of direct temperature measurement in evaluating this temperature modulation. Thus, it will be possible to confirm the value of temperature modulation of the resistance $R_{ac}{}^{\max}$, found above, caused by the test signal, by an independent method.

III. CHECK OF DATA CONSISTANCY USING DIRECT TEMPERATURE MEASUREMENTS

Direct measurements of the temperature of the sample under test (SUT) are conducted as follows. A small piece of investigated conductor - about 5 mm (1% of the full length) was wrapped around the thermocouple. Using repeat impedance measurements in the same frequency range, we examined the thermocouple effect on the SUT's impedance and found no noticeable difference with or without the thermocouple. We estimated the thermocouple's time constant experimentally, and it was less than 3 s. Considering this value, a measurement range of up to 1 mHz was chosen to ignore the effect of thermocouple inertia on temperature measurements. Data were collected using a thermocouple type K and a Eurotherm 2416 controller.

For each of the measurement frequencies, three periods of the test signal were carried out. Fig. 4 shows the results of direct temperature measurements.

The initial stage of the experiment included a delay of 15 minutes at a given bias value without applying a test signal.

A temperature response was noticeable from a frequency of 0.25 Hz down to lower frequencies. The initial section of the apparent temperature response of the system is affected by both the inertial properties of the object under study and the inertia of the thermocouple. In this regard, we do not study this frequency fragment. The measurement time from the start frequency (1 MHz) to the visible response of the system to the test signal (0.25 Hz) takes approximately 3 minutes.

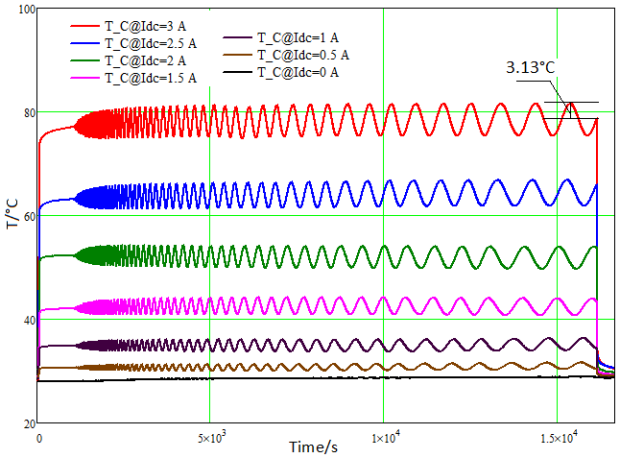

Fig. 4. Temperature of silver wire as a function of time during impedance measurement. The test signals are 100 mA *at different biases: 0 ... 3* A*; frequency range is 1* MHz *... 1* mHz*; length 500* mm *and diameter 0.25* mm*. The initial wait before starting impedance measurements was 15 minutes at fixed bias.*

The subsequent measurement from 0.25 Hz to 1 mHz takes about four hours (ten points per decade with the uniform step at a logarithmic scale and three periods for each frequency).

The experiment reveals that at an extremely low frequency of 1 mHz and a bias value of 3 A, the temperature variation has an amplitude of 3.13 °C at an average temperature of 78.47 °C (see Fig. 4). The test signal was 100mA as before. The measured temperature variation by the thermocouple is relatively close to the temperature estimated by previous indirect measurements and calculations. A difference of about 20% is found between the values obtained by direct and indirect methods of measuring temperature variations. This difference can be attributed to several factors, the analysis of which is not the subject of this study. We have only estimated the order of magnitude here. The measurement of temperature variation with a thermocouple has only an assessment role.

IV. DISCUSSIONS

The current-carrying conductors are nonlinear inertial objects. Non-linearity and inertia are related to the temperature properties of the research object and its environment. In essence, these properties determine the *Z_{BI}-effect.*

Previous studies [1] mainly dealt with experiments demonstrating the *Z_{BI}-effect* of various material types. This article focuses on the measurement procedure - what is actually measured and what the measurement results can

tell us about further research on examined objects. The answer to this question is as follows. The mathematical modeling of the measurement process using FRA showed that the impedance modulation caused by the test signal on fundamental frequency is amplified by the ratio of the bias to the signal amplitude when a bias is applied. This phenomenon is worthy of its name: bias induced impedance effect (Z_{BI}-*effect*).

We can say allegorically that this is an "honest cheating" of the measuring devices. The measuring device captures two components of the reaction at the fundamental frequency. One of them is caused by a test signal at the working point. The second reaction is an additional response caused indirectly. In this response, an ac-signal is generated from the applied bias because of the temperature modulation of the wire initiated by the same test signal. No matter where the fundamental frequency signal comes from, it will be perceived by the measuring device as "native" and evaluated in comparison with the excitation signal.

The estimate of the modulation component of the impedance caused by the test signal, obtained using the FRA, is credible. The measurement error of this modulation will be determined by the metrological characteristics of the instruments used for measuring the impedance.

It is important to emphasize that the higher the bias level (all other things being equal), the stronger the Z_{BI}-*effect* manifests itself. In the absence of bias, the Z_{BI}-*effect* disappears (Fig. 1). Using the results of impedance spectroscopy in the form of electrical models and calculating the modulation parameter R_{ac} can provide useful information for determining thermophysical parameters [2,3] and [4].

V. CONCLUSIONS

This work describes in detail the operation of the Frequency Response Analyzer underlying the impedance meters employed for the study of the current-carrying conductors under the influence of bias.

The electrical model of the object under study has been constructed. One of the informative parameters of this model is the temperature modulation of the resistance caused by the test signal. At low frequencies, FRA output signals provide information about the bias-induced impedance Z_{BI}. With bias applied, the Z_{BI}-*effect* acts as an amplifier for the temperature modulation of the resistance caused by the test signal. An amplifying gain is determined by the bias-to-test signal ratio.

Using impedance measurement devices, you can determine the modulation component of the resistance of the current-carrying conductor R_{ac} by knowing the levels of the test signal and bias. Together with the parameters of the electrical model (especially the Z_{BI} time constant), the R_{ac} can serve as an informative parameter for finding the thermophysical parameters of the objects being studied.

REFERENCES

[1] S. Baltianski, “Bias-induced impedance effect of the current-carrying conductors”, ACTA IMEKO 10(2), 2021, pp. 88-97. http://dx.doi.org/10.21014/acta_imeko.v10i2.1044

[2] L. Shi, D. Li, C. Yu, W. Jang, D. Kim, Z. Yao, P. Kim, A. Majumdar, “Measuring thermal and thermoelectric properties of one-dimensional nanostructures using a microfabricated device”, Journal of Heat Transfer. 125, 2003, pp. 881–888. https://doi.org/10.1115/1.1597619

[3] C. Dames, G. Chen, “1ω, 2ω, and 3ω methods for measurements of thermal properties”, Review of Scientific Instruments. 76, 2005, pp. 1–14. https://doi.org/10.1063/1.2130718.

[4] J. Bodzenta, J. Juszczyk, M. Chirtoc, “Quantitative scanning thermal microscopy based on determination of thermal probe dynamic resistance”, Review of Scientific Instruments. 84, 2013, pp. 1-9. https://doi.org/10.1063/1.4819738.

[5] N. Murer, “Installation and configuration manual for VMP-300-based instruments and boosters”. Online [Accessed 05 June 2021]. https://www.biologic.net/documents/vmp300-based-manuals/

[6] E. Barsoukov, J. R. Macdonald (Eds.), “Impedance Spectroscopy, Theory, Experiment, and Applications”, 2nd Ed., New Jersey, John Wiley & Sons. Inc., 2005.

[7] Cogger, N. D., & Webb Btech, M. R. v. (n.d.). “*Frequency Response Analysis”*. http://www.solartron.com

Increasing of Sampling Rate of Internal ADC in Microcontrollers by Equivalent-Time Sampling

Jakub Svatos[1], Jan Fischer[1], Jan Holub[1]

[1] *Czech Technical University in Prague, Faculty of Electrical Engineering, Department of Measurement, Technicka 2, 166 27, Prague 6, Czechia, svatoja1@fel.cvut.cz*

***Abstract* – The paper describes the Equivalent-Time Sampling (ETS) in Software-Defined Instruments (SDI) - typically oscilloscopes. It introduces a possible solution of the microcontrollers drawback caused by the maximal sampling frequency and its limitations in digitizing quick transient responses. The principle of ETS used in microcontrollers is explained, and the jitter effect is taken into account. Analog-to-digital converter input model and real properties of software-defined oscilloscope from ETS point of view are introduced and explained. In the system for circuit behavior analysis as a step response, where a microcontroller with internal peripherals (pulse-width modulation and analog-to-digital converter) is used for a test signal generation and data digitization, the use of ETS may increase the equivalent sampling rate of the internal analog-to-digital converter up to tens of MSa/s.**

I. INTRODUCTION

Most current microcontrollers (MCU) are equipped with internal analog-to-digital converters (ADC). The used type of ADC is usually the Successive Approximation Register (SAR) architecture [1]. MCU with SAR ADC is very often used in measuring applications, where they are used for digitization of DC or quasi-static voltages. Another area is the digitization of AC voltages, e.g., measurement in the power line, power measurement, effective values of voltage and current measurement, or motor control where the digitization of controlling signals may require the sampling with a sufficiently high frequency. Notwithstanding, in signal digitization, the sampling frequency is chosen to fulfill the sampling theorem ($f_s > 2 \cdot f_m$, where f_s is the sampling frequency, and f_m is the maximal frequency of the sampled signal). This sampling is referred to as Real-Time Sampling (RTS).

Thanks to the growing power of MCUs, which are also equipped with a number of peripherals to process analog signals (ADC, Operational Amplifier, Analog Comparators, Digital-to-Analogue Converter - DAC), it is possible to use them for software-defined instruments (SDI) [2]. All instrument functions are implemented only by programming and using the internal peripherals of the microcontroller without the need for external circuits. This was the situation at Czech Technical University in Prague (CTU), Faculty of Electrical Engineering (FEE), Department of Measurement, where several SDIs were developed and are used as a replacement for standard measuring instruments (typically digital oscilloscopes) in individual projects or as part of a Home Lab in distance learning [2] – [3]. However, the limitation of such an SDI is given by the maximal sampling frequency, which, in the case of internal ADCs in microcontrollers, is commonly from hundreds of kSa/s to a maximum of few units MSa/s. The corresponding bandwidth of an oscilloscope implemented by SDI is tens to hundreds of kHz. Thus, the measurement tasks are limited. For example, measurement of frequency characteristics of the circuit, determination of the circuit bandwidth – a cut-off frequency etc. If the SDI includes a functional signal generator, an internal DAC connected to the internal output buffer is used. This combination makes it possible to generate harmonic signal approximations, but typically, at frequencies up to tens of kHz, which is insufficient to evaluate the system's behavior (amplifiers, operational amplifiers - OA, etc.) on a broader scale frequency range. System response to a unit step function also describes the system's dynamic behavior in the tasks such as determining the time constant of a system, a slew rate of the OA, etc. Even in simple SDIs, there is a periodic pulse signal PWM, which has sufficiently steep edges. The classical method of determining the system response would be using a real-time oscilloscope with a sufficiently high sampling rate f_s. However, in the case of SDI, the limitation is given by the conversion time of the internal ADC. Therefore, it is necessary to find another way to solve the limitation. This article presents the solution using the Equivalent-Time Sampling (ETS) principle, which may increase the equivalent sampling rate of the internal analog-to-digital converter of the microcontroller up to tens of MSa/s.

II. EQUIVALENT-TIME SAMPLING IN MCU

The ETS principle is used for digitizing the periodic signal in many areas, for example, in oscilloscopes or radio applications [4] – [10]. In SDI oscilloscopes, the simplest form of ETS is used at the Department of Measurement. The idea is that the periodic signal is digitized at a precisely defined speed to the fundamental frequency. The only requirement of ETS is that the analog input bandwidth of the ADC is sufficient and does not limit the spectrum of

the digitized signal. ETS used in the internal ADC of the MCU can be implemented as stroboscopic sampling. The digitized signal is strictly periodic with the fundamental frequency $f_{PWM,}$ and its digitization takes place at a speed of f_{SAMP} very close to the f_{PWM}. Only one sample is taken in each period. This results in aliasing.

The ETS model can also be implemented by skipping one or more signal periods and taking a sample after k_s periods (where k is an integer). Thanks to this, it is possible to digitize a signal whose frequency is significantly higher than the f_{SAMP}. However, a sufficient analog input bandwidth of the ADC is necessary for this ETS mode.

To verify the analog input bandwidth of the internal ADCs in the MCUs, experiments were performed according to the connection in Fig. 1 [11].

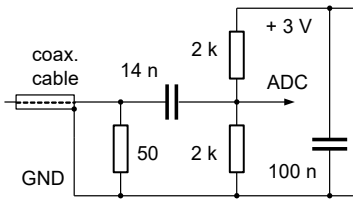

Fig. 1. Connection for ADC bandwidth verification.

The HP 8647A harmonic signal generator is connected to the ADC input via a set of capacitors connected in parallel. The resistance divider sets the DC signal offset to a level suitable for ADC input. The generated signal was digitized with an internal ADC with f_{SAMP} in order of hundreds of kSa/s. The generated frequencies were chosen very close to a multiple ADC f_{SAMP} to obtain the aliased signal with a sufficiently high number of samples per period. STM32 series MCU was used for the measurements (F051, F303, F407), each of them with slightly different internal ADC.

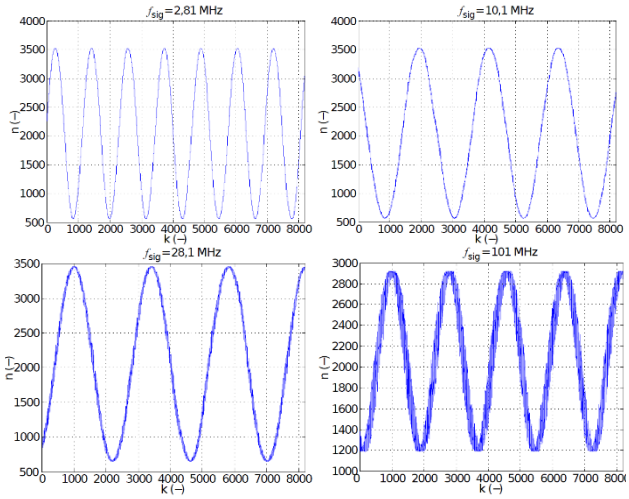

Fig. 2. Signals digitized by the F303s ADC

The analog input bandwidth of the ADC could be estimated from the decrease in the amplitude of the aliased signal. An example of the signal digitized by the ADC in F303 is shown in Fig. 2.

With the increasing frequency of the signal, the jitter caused by a random relative shift of the generated harmonic signal f_{SIG} and the f_{SAMP} becomes more and more apparent. At high signal frequencies, the effect of the input signal crosstalk via parasitic capacitances to the SAR ADC block could also occur and affect the SAR process by the charge transfer. The MCU internal ADCs analog input bandwidth characteristics are shown in Fig. 3.

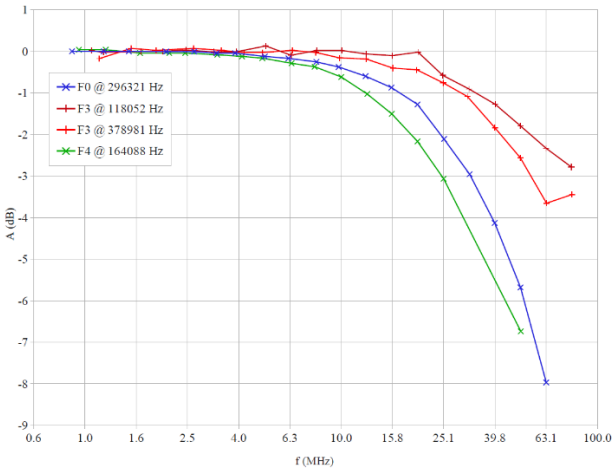

Fig. 3. Frequency characteristics of internal ADC inputs of selected MCU

The characteristics show that all tested MCUs have an ADC analog input bandwidth in the order of tens MHz, sufficient for laboratory teaching experiments with SDI oscilloscopes operating in ETS mode.

Effect of Jitter at ETS

As mentioned above, the presented method assumes a strictly periodic input signal with a constant frequency. Any changes in frequency or random shifts in sampling acquiring times cause a degradation of the aliased signal [12]. This is also evident from the measurement presented in Fig. 2. At higher input signal frequencies, the resulting digitized signal appears to be noisy in the presented records, which, however, is caused by jitter [13] or [14]. To determine the jitter, further measurements were performed with the STM32F303VC [11]. The detail of the measured signal at the f_{SIG} = 217.7062 MHz is in Fig. 4.

Inspecting the record in the range k = 0 to 600, it can be seen that the minima approximately follow the value n = 1800. In addition, the local changes in the n position between samples in this area are lower. Thus, it can be stated that this is primarily the effect of jitter. To estimate the jitter, two adjacent samples in the part of the digitized signal with the high steepness were selected; k = 1081 and corresponding n = 2191 and following k = 1082 and corresponding n = 1884, which have the largest difference in the value of n. To determine the size of the jitter, the corresponding points on the idealized sinewave signal are

found to have the same n value. These were the positions corresponding to α_1 = -0.68 rad and α_2 = 0.55 rad. This is a phase difference $\Delta\alpha$ = 1.23 rad, that is 0.195 periods, which at 217.7 MHz represents a time of 0.9 ns. The same analysis was performed for a frequency f_{SIG} = 101 MHz when the detected jitter value was 0.86 ns.

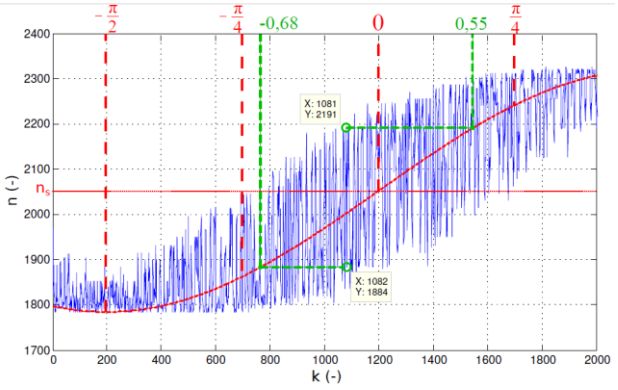

Fig. 4. The detail of the measured signal

The measurement results indicate high requirements for the precise relative sampling timing for the input signal during stroboscopic sampling.

In the case of MCU that use PWM, which frequency is derived from a stable generator of the system clock with frequency f_{SYS} and the sampling times are derived from timers and f_{SYS}, this requirement may be met. The situation is different for simpler MCUs such as the ATmega 328, part of the widely used Arduino module. In this case, the sampling times of ADC are not controlled by a timer but by software, which raises problems with accurate timing.

III. USE OF ETS IN SDI IMPLEMENTED BY MCU

Simple SDI oscilloscopes implemented with STM32F042 or STM32G030 and used as a Home Lab have a maximum sampling rate of 500 kSa/s. If it is necessary to evaluate the response of faster circuits, stroboscopic sampling, which is the ETS method, can be used to increase the sampling rate. The PWM signal generated by the respective peripheral is used to excite the tested circuit. Usually, where it is only necessary to determine the circuit's response to a unit step function signal, the frequency of the PWM signal in the order of units of kHz and the corresponding T_{PWM} period in the order of tens of ms are used. The output signal of the tested circuit is sampled in a way that only one sample is taken in each of its periods. The sampling period T_{SAMP} is chosen to be very close but slightly larger than the PWM signal period T_{PWM}. As a result, the sampling time shifts by ΔT relative to the PWM signal by every sample. If the T_{PWM} and the T_{SAMP} were the same, then ΔT = 0, and a sample would be taken approx. The same signal position. This principle can be used to check the stability of the T_{SAMP}.

If $T_{PWM} < T_{SAMP}$ applies, then the moment of signal sampling at each equivalent time period shifts relative to the PWM signal by a time T_{SEQ}.

$$\Delta T = T_{SAMP} - T_{PWM} = T_{SEQ} \qquad T_{PWM} \le T_{SAMP} \qquad (1)$$

There are several samples per T_{PWM}, which corresponds to the situation as the PWM signal was sampled with a T_{SEQ}, (2) and corresponding $f_{SEQ} = 1/T_{SEQ}$.

$$T_{SEQ} = T_{SAMP} - T_{PWM} = \frac{1}{f_{SAMP}} - \frac{1}{f_{PWM}} = \frac{f_{PWM} - f_{SAMP}}{f_{PWM}} \cdot T_{SAMP} \qquad (2)$$

The situation is shown in Fig. 5, where S_{IN} is the input signal of the ADC, S_{DIG} represents the digitized signal in real-time, and S_{RECON} is the reconstructed signal by ETS.

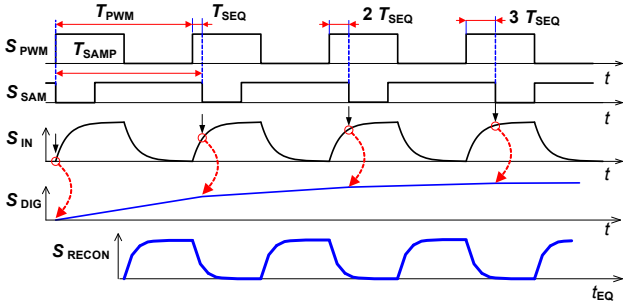

Fig. 5. Signal digitization timing in ETS

If the frequency difference Δf is positive, the f_{SEQ} will also be positive, and the relative sampling points in the time will be shifted to the right in a positive time.

$$f_{SEQ} = \frac{f_{PWM}}{f_{PWM} - f_{SAMP}} \cdot f_{SAMP} = \frac{f_{PWM}}{\Delta f} \cdot f_{SAMP}$$
$$\Delta f = f_{PWM} - f_{SAMP} \qquad (3)$$

However, if Δf is negative, the f_{SEQ} will also be negative, and the sampling points will shift to the left on the equivalent time axis. The obtained reconstructed signal will be mirrored. It also follows from (3), the smaller the difference Δf, the more significant the increase in the equivalent sampling frequency. Thus, an acceleration coefficient of equivalent sampling can be defined as $k_{AEQ} = f_{PWM}/\Delta f$.

The situation where only one sample is taken per PWM signal period is suitable for equivalent sampling. It is necessary to have a detailed record of the response to the input change - typically a unit step function.

However, sometimes it is useful to use equivalent sampling to inspect the circuit's response to a periodic signal with a higher frequency than the sampling frequency. In this case, the situation changes slightly compared to the situation described above. The sample will be taken only once per k_s period, where k_s is a natural number. The equivalent sampling frequency will be defined by (4)

$$f_{SEQ} = \frac{f_{PWM}}{f_{PWM} - k_S \cdot f_{SAMP}} \cdot f_{SAMP} \qquad k_S \approx \frac{f_{PWM}}{f_{SAMP}} \tag{4}$$

The acceleration coefficient k_{AEQ} of the equivalent sampling frequency compared to the real sampling frequency f_{SAMP} is according to (5)

$$k_{AEQ} = \frac{f_{PWM}}{f_{PWM} - k_S \cdot f_{SAMP}} \tag{5}$$

In MCUs, all periodic events are usually derived from the system clock f_{SYS}. The f_{SAMP} and f_{PWM} are also derived by dividing by the coefficient M and N, respectively, using timers.

$$f_{SAMP} = \frac{f_{SYS}}{M} \qquad f_{PWM} = \frac{f_{SYS}}{N} \tag{6}$$

Then, f_{SEQ} is defined by

$$f_{SEQ} = \frac{f_{PWM}}{f_{PWM} - k_S \cdot f_{SAMP}} \cdot f_{SAMP} = \frac{f_{SYS}}{N} \cdot \frac{1}{\frac{f_{SYS}}{N} - k_S \cdot \frac{f_{SYS}}{M}} \cdot \frac{f_{SYS}}{M} \tag{7}$$

And after simplification

$$f_{SEQ} = \frac{f_{SYS}}{M - k_S \cdot N} \tag{8}$$

It follows from (8), the maximum ETS frequency in the MCU can be $f_{SEQ} = f_{SYS}$ for $M - k_sN = 1$. Theoretically, the ETS frequencies in the MCU can take be values where n in (8) is a natural number (1, 2 …).

$$f_{SEQ} = \frac{f_{SYS}}{n} \tag{9}$$

For example, in an oscilloscope with ETS by a MCU STM32G03J6 with f_{sys} = 64 MHz, ETS frequencies can be used f_{SEQ} = 64.0; 32,0; 21,3; 16.0; 12,8; 8,0; … MSa/s.

If the $M - k_sN = 0$, then f_{SEQ} would equal infinity, and the PWM signal would still be sampled in one spot. If the $M - k_sN$ will be negative (-1, -2 …), f_{SEQ} will also be negative, and the signal will be mirrored, but this may not be a problem for some experiments.

When using SDI with an MCU in the form of an oscilloscope, there are tasks such as inspecting the circuit's response to signals with different frequencies. A standard measurement would use a harmonic signal, which is impossible when using a PWM MCU. However, evaluating the system's behavior in response to rectangular signals at different frequencies can provide the necessary information.

IV. ADC INPUT MODEL AND PROPERTIES OF SDI SCOPE FROM ETS POINT OF VIEW

A typical MCU often contains only one ADC to whose inputs the signal can be fed from different input pins using a multiplexer. The simplified equivalent scheme in Fig. 6. Circuit on the left assumes one input channel selected by the multiplexer contains only the basic parts and does not include other parasitic capacitances.

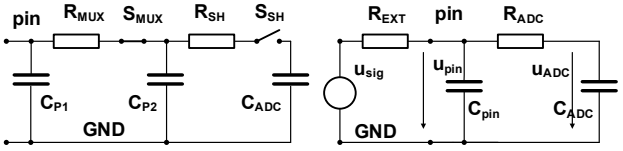

Fig. 6. ADC input equivalent scheme(left) and according to catalog data (right)

There are at least two switches in the signal path. The first is implemented by a multiplexer S_{MUX}; the second is by a switch S_{SH} of the sampling circuit. Each of them can be represented by a resistance R_{MUX} and R_{SH}. The size of the parasitic capacitances is also crucial for evaluating dynamic behavior, where CP1 represents the parasitic capacitance of the pin, CP2 corresponds to the internal parasitic capacitances of the multiplexer C_{ADC} represents the capacity of the SAR ADC itself. For the estimation of the ADC input behavior, the parameters C_{ADC} = 5 pF, C_{P1} = 8 pF and C_{P2} = 2 pF, R_{MUX} = 250 Ω, R_{SH} = 250 Ω for F303 and C_{ADC} = 8 pF, C_{P1} = 8 pF and C_{P2} = 2 pF, R_{MUX} = 300 Ω, R_{SH} = 300 Ω for F051, were used for the model according to Fig. 5. Performed simulations confirmed the results presented in Fig. 3.

In the catalog of MCUs, the parameters can be found corresponding to the model in Fig. 5 (right), where the ADC input is excited by an external signal source u_{sing} an internal resistance R_{EXT}. R_{ADC} includes resistances R_{MUX} and R_{SH}. For F051 MCU, the ADC input equivalent scheme parameters are given as C_{ADC} = 8 pF and R_{ADC} = 1 kΩ. The minimum bandwidth of the ADC input is determined as

$$f_B = \frac{1}{2 \cdot \pi \cdot R_{ADC} \cdot C_{ADC}} = \frac{1}{2 \cdot \pi \cdot 1000 \cdot 8 \cdot 10^{-12}} = 20 \text{ MHz} \tag{10}$$

The analog bandwidth of the ADC input, according to Fig. 3, is valid only for the small R_{EXT} of the signal source, which will be negligible to R_{ADC}. With large R_{EXT} values, a very simplified equivalent model corresponding to the RC circuit according to Fig. 7 can be used.

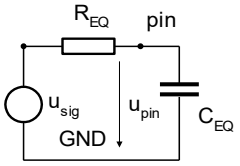

Fig. 7. ADC input scheme for a large value of R_{EXT}

Where the C_{EQ} includes C_{ADC} and other parasitic capacitances, the R_{EQ} resistor includes R_{EXT} and R_{ADC}.

The ADC behaves differently in the ETS mode in terms of sampling. The sampling time when the S_{SH} is switched on can be significantly longer than the period of the digitized signal. It can be a track and hold mode. The moment of sampling is determined by the moment of opening the S_{SH}. At the tracking time, the measured circuit is loaded with the total capacity determined as the

$C_{P1} + C_{P2} + C_{ADC}$. In the end, the S_{SH} opens, and the C_{ADC} is disconnected from the circuit. During the subsequent AD conversion in the ADC with charge redistribution, the voltage u_{ADC} changes to the default value, which can be marked as the residual voltage U_{RES}.

Even if the constant voltage U_{IN} is sampled repeatedly, the measured circuit must supply a charge (positive or negative) to the ADC input, which magnitude depends on the $\Delta U = U_{IN} - U_{RES}$. This causes a transient at the input, causing a short-term change (negative or even positive) of the u_{PIN}. The advantage of ETS over Real-Time Sampling (RTS) is that even a large sampling time value can be used when the ADC is in track mode, that the transient can finish in advance before the actual u_{ADC} value is sampled.

V. PRACTICAL REALIZATION OF SDI WITH ETS

The ETS method has been successfully used in SDI oscilloscopes with various STM32 MCUs (developed software is available at *https://leo.fel.cvut.cz/*). These were either ready-made modules Nucleo, Blue Pill or Black Pill, or standalone MCUs on developed PCB adaptor. Only modules or MCUs without any specialized accessories were used in all cases. This allows SDI to be implemented only by uploading the firmware and running a PC application. In the RTS, maximum sampling rates are in the order of hundreds of kSa/s to a few units MSa/s, but if the ETS is used, the limitation is given practically only by the f_{SYS} according to (9).

The experiment with the SDI [3] based on STM32G030J6M3 MCU has been performed. The sampling rate in RTS is only 3x 200 kSa/s (T_{SAMP} = 5 µs), but using ETS, it is extended to 1x 64 MSa/s (T_{SEQ} = 0.0156 µs), which is presented as an application example of the described method. The experiment aims to demonstrate the effectiveness of ETS by determining the slew rate of the MCP601 OA as a step response. Fig. 8 shows an experiment with the SDI implemented in MCU and the tested MCP601 OA.

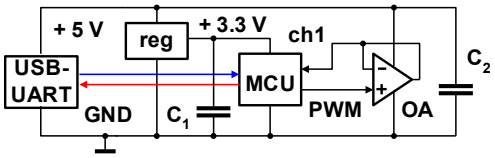

Fig. 8. Experiment connection

The parameters of the experiments are; f_{PWM} = 10 kHz, f_{SAMP} = 9998,437 Hz, f_{SEQ} = 64 MSa/s, k_{AEQ} = 6401. Fig. 9 shows measured step response of the OA.

The measured interval 6.403 ms corresponds to an equivalent time of 1 µs, and the slew rate of the tested OA is measured to SR = 2.2 V/µs, which roughly corresponds to the catalog data of 2.3 V/µs. The same OA has been measured by the HP54622D oscilloscope (RTS = 200 MSa/s), and the measured SR = 2.18 V/µs confirmed the accuracy of the SDI. Looking at Fig. 9, it is clear that in RTS, where T_{SAMP} = 5 µs, the slew rate of approx. Two µs ends faster, and no information would be obtained. However, thanks to ETS with T_{SEQ} = 0.0156 µs, the time resolution for determining the SR is sufficient.

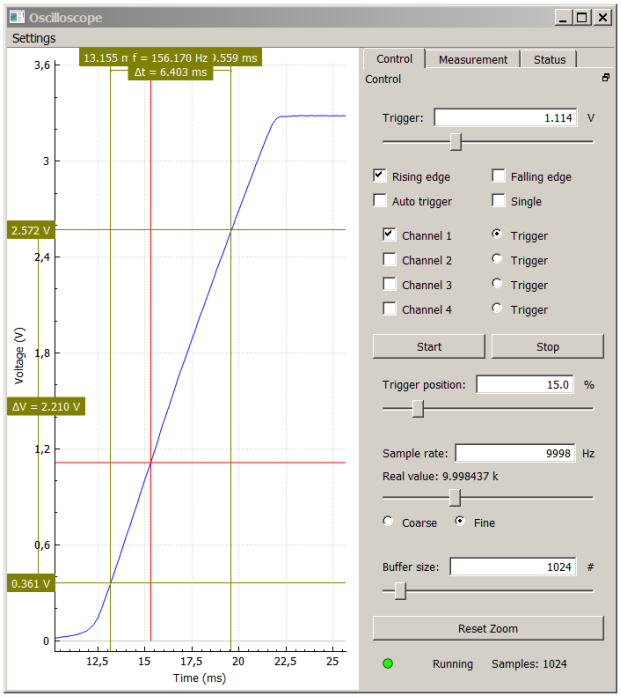

Fig. 9. The measured step response of MCP601

This experiment confirmed the applicability of even very simple SDI oscilloscopes for similar dynamic measurements.

VI. CONCLUSION

The paper presented the principle of equivalent time sampling, where the microcontroller's internal peripheries are used for test signal generation and data digitization. The ETS method has proven very useful in simple oscilloscope-type devices implemented using microcontrollers. ETS, an equivalent sampling rate can be increased up to 100 MSa/s and can be used, for example, for inspecting the step response of the circuit.

During the experiments, the focus was on selected types of MCUs of the STM32 series, which were used at the CTU, FEE, Department of the Measurement as SDI in standard, and distance teaching as the Home Lab. The described principle of ETS and the method of implementation of SDI can be successfully used in the broader range of microcontrollers, such as Arduino. They can find use in other areas of measurement.

VII. ACKNOWLEDGMENTS

Authors would like to thanks to STMicroelectronics for the direct support and for providing the necessary STM32 processors for SDI free of charge.

REFERENCES

[1] K. Y. Leung, K. Leung and D. R. Holberg, "A Dual Low Power 1/2 LSB NL 16b/1Msample/s SAR A/D Converter with on-chip Microcontroller," 2006 IEEE Asian Solid-State Circuits Conference, 2006, pp. 51-54, doi: 10.1109/ASSCC.2006.35784

[2] J. Svatos, J. Holub, J. Fischer, J. Sobotka, "Online teaching at CTU in Prague aka university under COVID restrictions," Measurement: Sensors, vol. 18, 2021.

[3] A. Berlinger, "Implementation of instrument functions using STM32 microcontrollers," Diploma thesis, CTU FEE, 2016.

[4] J. Yang, S. Liu, Ch. Zhu, F. Hao, J. Ma, "Equivalent Sampling Oscilloscope with External Delay Embedded System," IEEE International Conference on High Performance Computing and Communications, 2011.

[5] Y. Sasaki, Y. Zhao, A. Kuwana and H. Kobayashi, "Highly Efficient Waveform Acquisition Condition in Equivalent-Time Sampling System," 2018 IEEE 27th Asian Test Symposium (ATS), 2018, pp. 197-202.

[6] Ch. Nader, W. Moer, N. Björsell, P. Händel, "Wideband radio frequency measurements: From instrumentation to sampling theory," Microwave Magazine, vol.14, 2013, pp. 85-98.

[7] D. Zhijian, W. Qi, Y. Xi, Y. Zhao, "The application of random equivalent sampling in acquisition system with 5Gsps real-time sampling," 2017 13th IEEE International Conference on Electronic Measurement & Instruments, 2017.

[8] D. Williams, P. Hale and K. A. Remley, "The Sampling Oscilloscope as a Microwave Instrument," in IEEE Microwave Magazine, vol. 8, no. 4, pp. 59-68, Aug. 2007, doi: 10.1109/MMW.2007.383954.

[9] J. Qiaodan, An ARM-based sequential sampling oscilloscope, Diploma Thesis, Massachusetts Institute of Technology, Department of Electrical Engineering and Computer Science, 2014.

[10] M. Krauss, H. Thieme, H.-G. Schniek and E. Wittig, "Fully-integrated 5 V CMOS system for a 20 M sample/s sampling oscilloscope," 1996 IEEE International Solid-State Circuits Conference. Digest of TEchnical Papers, ISSCC, 1996, pp. 384-385, doi: 10.1109/ISSCC.1996.488727.

[11] M. Pribil, Three-channel measuring unit with STM32 microcontroller, Diploma thesis, CTU FEE, 2013.

[12] S. Goyal, A. Chatterjee and M. Atia, "Reducing Sampling Clock Jitter to Improve SNR Measurement of A/D Converters in Production Test," Eleventh IEEE European Test Symposium (ETS'06), 2006, pp. 165-172, doi: 10.1109/ETS.2006.39.

[13] A. Goldstein, G. Frigo, "Determination of Digitizer Absolute Phase Using Equivalent Time Sampling," IEEE Transactions on Instrumentation and Measurement, 2019, pp. 1-8.

[14] M. Haney, "Maximizing the measurement accuracy of digitized signals," 2010 IEEE AUTOTESTCON, 2010, pp. 1-6, doi: 10.1109/AUTEST.2010.5613600.

25th IMEKO TC4 International Symposium
23rd International Workshop on ADC and DAC Modelling and Testing
IMEKO TC-4 2020
Brescia, Italy / September 12-14, 2022

Antennas Comparison Applied to Detect Partial Discharges Coupled via Dielectric Window and Oil Valve in Power Transformers

Arthur Silva Souza[1], Raimundo Carlos Silveiro Freire[1], Luiz Augusto M. M. Nobrega[1], Felipe Alexandre Da Silva Bento[1], George Victor Rocha Xavier[2], Marlo Andrade[1,3,4]

[1]*Federal University of Campina Grande, Aprígio Veloso, 882, Campina Grande - 58428-830, Brazil, arthur.souza@ee.ufcg.edu.br, freire@dee.ufcg.edu.br, luiz.nobrega@dee.ufcg.edu.br, felipe.bento@ee.ufcg.edu.br*

[2]*Federal University of Sergipe, Av. Marechal Rondon, S/N, São Cristóvão - 49100-000, Brazil, george.xavier@academico.ufs.br*

[3]*Federal Institute of Pernambuco, Av. Professor Luiz Freire, 500, Recife - 50740540, Brazil, marlo.santos@ee.ufcg.edu.br*

[4]*Univ. Bordeaux, 351 Cours de la Libération, 33405 Talence, France*

***Abstract* – Considering increasing the reliability of electrical systems, continuous equipment maintenance is essential, thus ensuring longevity and avoiding failures that can cause irreparable damage to the equipment. Partial discharges are physical phenomena that cause short circuits in power equipment. There are techniques that use the detection of partial discharges as a condition monitoring techniques for electrical equipment. One of these techniques is the detection of partial discharges in power transformers by means of antennas. Thus, different antennas were analyzed for different coupling to the sensor into the high voltage equipment, either via dielectric window or oil valve. In comparison, the L-probe antenna obtained the best result, at -10 dB, while at -5 dB the log spiral performed better, for insertion via the dielectric window. For coupling via oil valve, the monopole obtained the best result, at -10 dB, considering the bandwidth at -5 dB the conical 70 mm did better.**

I. INTRODUCTION

Power transformers are one of the most important and most expensive equipment for the electrical power system. Therefore, identifying defects, through continuous monitoring techniques, becomes indispensable in order to avoid failures that could damage the equipment in a partial or complete way. Partial discharges (PD) are physical phenomena that generate electrical discharges of low intensity, thus generating short circuits in a partial way, in specific regions of the insulating material that are subjected to intense electric fields[1]. The continuous process of partial discharges can cause degradation and deterioration of the insulating material, which in the medium to long term generates partial or complete rupture of the dielectric, with failure of the equipment. Generally, high voltage equipment has a high market value and plays an essential role in the proper functioning of the electrical system, especially power transformers, whose function is to increase and decrease voltage, load supply, among others. Therefore, transformers directly interfere with the system reliability. Based on the above, several researchers have been studying numerous methods and methodologies that can be applied to the detection of partial discharges, seeking the most efficient and least invasive way. One of these methods is based on the verification of electromagnetic waves that are emitted by current pulses in the event of partial discharge. The frequency range that this phenomenon can be observed is from 300 MHz to 3 GHz [2].

For partial discharges, the frequency spectrum from 300 MHz to 1.5 GHz is the most relevant to be analyzed, as it is in this range that the highest concentrations of energy for pulses of partial discharges in various dielectric materials are reported [3]. Furthermore, as the UHF method is based on a system that works in a high frequency range, the detection system is theoretically immune to common interferences in substations, such as: switching of power electronics equipment and corona discharge, which have components of significant energy signals up to the range of 200 MHz and 300 MHz [4]. To apply the UHF method, it is necessary to use a device to detect partial discharges, in this case, an antenna [5, 6, 7, 8]. A new microstrip antenna was developed in [5], it is designed to detect UHF partial discharge signals for field GIS, it was concluded that the UHF measurement system is suitable for partial discharge detection and diagnosis in GIS field. In [6] microstrip antennas were developed and compared to detect partial discharges. The

models developed proved capable of detecting PD. In [7] optimization methods were applied with the aim of increasing the bandwidth of microstrip antennas. It was possible to observe that the antennas developed had a significant increase in bandwidth. In [8] a bio-inspired sensor was developed to apply insertion via dielectric window in power transformers.

That way, this work aims to carry out a comparative study between antennas applied to detect partial discharges in a continuous way in power transformers, distributed in the environment through dielectric windows or coupled via oil valve. Therefore, simulations were carried out in a computational environment in order to validate which antenna has the best result in detecting partial discharges. This paper is composed of four parts including this introduction. Section II present the materials and methods used, section III the results, and the conclusions in section IV.

II. MATERIALS AND METHODS

In order to choose the antennas that would be simulated, the most appropriate antenna shapes for the type of coupling (via dielectric window or oil valve) and the techniques for bandwidth optimization were analyzed, making it possible to select which one is more efficient in comparison to the application. From the researched references, it was possible to reach the result that, in the case of coupling via dielectric window, most of the works use planar antennas with different formats and optimizations. Thus, the U-slot, L-probe and U-slot with L-probe antennas were based on the work of [7] and can be seen in Fig. 1. Dimensions were modified to obtain the optimizations, at that moment aluminum was used as a radiating element and ground plane, obtaining results closer to reality. The log spiral antenna was based on the equations contained in [9, 10] and can be observed in works such as [11]. The same methodology as the previous antenna was used for the design of this, shown in the Fig. 2.

For the case of insertion via oil valve, the simulated antennas were monopolar and conical antennas, considering a DN80 type valve, with size restrictions of 80 mm in diameter. The monopole and conical antennas were based on the equations contained in [9, 10] and can be observed in works such as [12, 13], as show in Fig. 3. For the case of the conical antenna, a length value was fixed in 300 mm (because commercial sensors use this value) and the cone radius varied, to verify the behavior of the bandwidth.

After choosing the antennas, it was possible to move on to the simulation stage. The simulation of the antenna design was performed using the commercial software $Ansys^{TM}$. For the construction of the simulation environment the following steps were followed:

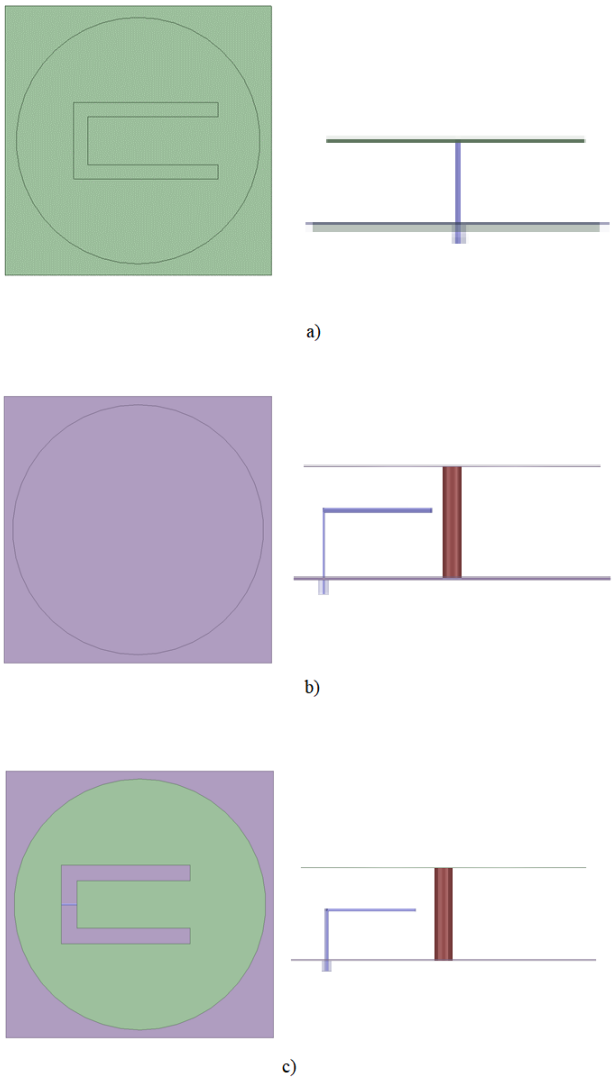

Fig. 1. Computational model of the antenna with a) U-slot, b) L-probe and c) U-slot with L-probe to 0.9 GHz.

1. **Dimensioning of structural parameters of the model:** The physical dimensions of the structure (in this case the antennas) are defined, such as width, thickness, length and positioning of the elements.

2. **Material specification:** The characteristics of each material used in the elements built in the previous step will be assigned. The materials used can come from the software itself, such as copper or epoxy, for example, or they can be created by the user, with the insertion of data such as the dielectric constant, tangent of losses and others. In this paper, copper was considered as the radiating element and ground plane, and as the dielectric substrate, FR4 was used. For the case of the antennas in Fig. 1, air was used as substrate and aluminum as radiating element and ground plane.

Fig. 2. Computer model of planar log spiral antenna to 0.9 GHz.

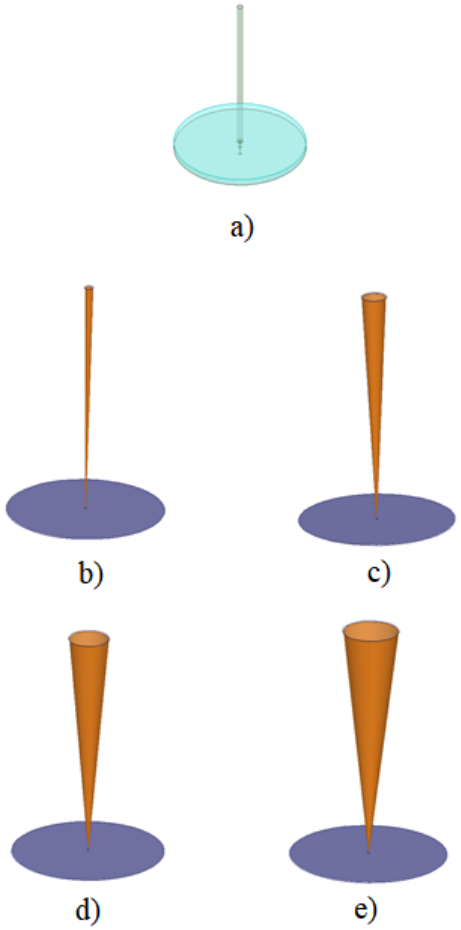

Fig. 3. Computational model of the a) monopole, b) conical (10 mm), c) conical (30 mm), d) conical (50 mm) and e) conical (70 mm) antennas to 0.9 GHz.

3. **Boundary Conditions:** The radiation box is defined, which corresponds to the limits of the simulated space for which the incident radiation on the antenna is absorbed and does not generate return reflections. Thus, the dimensions of the radiation box should be $\frac{\lambda}{4}$ of the central frequency of the antenna and filled with air.

4. **Structure excitation:** The waveport was chosen as excitation source. In order for the result obtained to be accurate, it is necessary to properly define both impedance values and dimensional values. Therefore, the impedance value of 50 Ω was considered for the project, which is the dimension equivalent to the external diameter of the simulated coaxial cable (5 mm).

5. **Analysis settings:** The frequency for solving the problem was determined, as well as the number of steps performed to solve the matrices implemented by the finite element method. For the work, 20 execution steps will be considered and the value 900 MHz as the central frequency.

After the simulations, the results were compared considering some aspects, namely, the bandwidth, physical dimensions, radiation pattern and gain. For the calculation of the bandwidth of the antennas, values below -10 dB and -5 dB were considered for the S_{11}.

III. SIMULATION RESULTS

In this section, the results obtained in this work are presented and discussed. The first section refers to the results related to the antenna coupled via dielectric window, presenting analyzes regarding the simulations and comparisons. For the second section, there are the results related to the antenna coupled via the oil valve.

A. Antennas with dielectric window coupling

After the simulations with the results obtained, it was possible to build Table 1 and Fig. 4, in which the antennas intended for dielectric window coupling in power transformers will be compared.

Table 1. Comparative table between the simulated antennas intended for dielectric window coupling.

Antennas	BW (%)		Size (mm)	Gain (dBi)
	-5 dB	-10 dB		
U-slot	30.77	22.22	87	9.33
L-probe	43.81	28.89	75	9.61
U-slot with L-probe	48.69	5.56	80	9.51
Planar log spiral	95.75	–	100	6.09

The analysis of Table 1 and Fig. 4 allows us to observe some interesting aspects. The antenna that has the highest bandwidth in the comparison is the L-probe, with a result of 28.89%, important in applications for detecting partial discharges. The antenna that has the highest bandwidth,

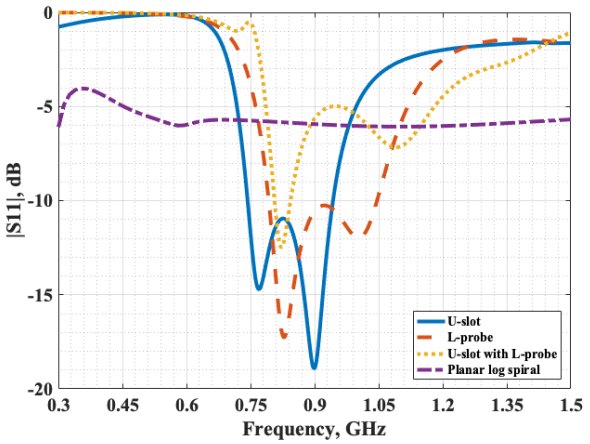

Fig. 4. Comparison between the magnitude of reflection coefficient of antennas inserted into the dielectric window.

gain and smaller size in the comparison is the L-probe, with 9.61 dBi and 75 mm radius. Thus, for the application of via dielectric window, the most suitable antenna would be the antenna with L-probe, because in the comparison it was the one that obtained the best results, in terms of bandwidth, gain and physical dimensions. It is also worth considering that a limit of -5 dB in the magnitude of reflection coefficient for the definition of the antenna bandwidth is possible for PD detection, as it allows the transmission of approximately 70% of the power signal. As can be seen in studies [14, 15], in which the results were satisfactory for the values of the order of -3.5 dB. There are also studies that prove that with a gain of 2 dB it is possible to detect PD [16]. Considering the bandwidth at -5 dB, the spiral log antenna obtains better results compared to the others for bandwidth.

B. Antennas with coupling via oil valve

The first simulated antenna model was the monopole antenna. Then, the conical antenna model was built that would fit the physical limitations imposed by the oil valve, varying the cone diameter to observe the bandwidth behavior. After the simulations with the results obtained, it was possible to construct Table 2, Table 3 and Fig. 5, in which the antennas intended for insertion via oil valve in power transformers will be compared. In Table 2, the bandwidth results in -10 dB are presented, considering different operating bands, the size and gain of the antennas. In Table 3, the bandwidth results are presented in -5 dB considering different operating bands and the total bandwidth value in megahertz.

The monopole antenna has a bandwidth of about 12.22%, being characterized as a broadband antenna, its dimensions would be ideal for the application, due to its diameter being less than 80 mm. Analyzing the graph

Table 2. Comparative table between the simulated antennas intended for oil valve insertion, with bandwidth (operating band) at -10 dB.

Antennas	BW (%)		Size (mm)	Gain (dBi)
	1°	2°		
Monopole	12.22	–	38 x 98	2.19
Con. (10 mm)	5.00	3.42	10 x 300	2.59
Con. (30 mm)	3.35	1.74	30 x 300	2.22
Con. (50 mm)	–	–	50 x 300	3.47
Con. (70 mm)	–	–	70 x 300	2.53

Table 3. Bandwidth comparison table (operating band and total) of simulated antennas inserted via oil valve at -5 dB.

Antennas	BW (%)				BW (MHz)
	1°	2°	3°	4°	
Monopole	54.13	–	–	–	419.00
Con. (10 mm)	16.46	10.26	–	–	235.20
Con. (30 mm)	6.67	20.91	12.17	–	304.30
Con. (50 mm)	13.33	26.47	15.04	2.13	422.00
Con. (70 mm)	20.00	32.84	17.86	4.67	550.00

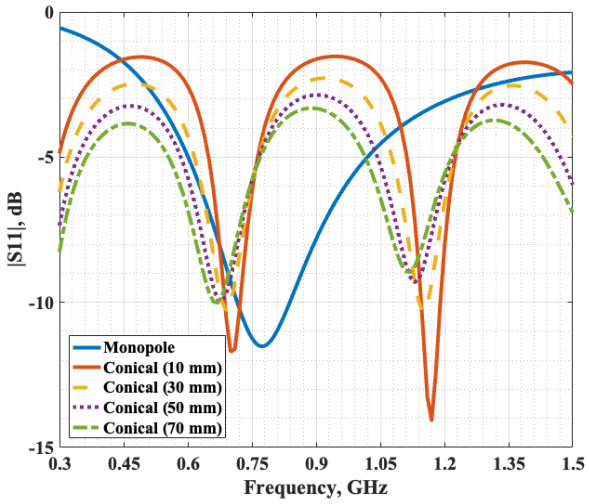

Fig. 5. Comparison between the magnitude of reflection coefficient of antennas inserted into the oil valve.

and the tables, it is possible to observe that when the radius of the conical antenna is increased, the bandwidth

decreases. However, if the same analysis is performed for -5 dB, the path is the opposite, that is, there is a significant improvement.

Comparing the conical antennas, the one with the best gain result was the antenna with 50 mm diameter, however the bandwidth at -10 dB for it is narrow. Observing the bandwidth, the antenna with a diameter of 10 mm obtained the best result. For -5 dB, the result is different, in this case the conical antenna with 70 mm of diameter is the one that obtained the best bandwidth.

When looking at the physical dimensions of the antennas, it is important to highlight some aspects, the first of which is that as the antennas are intended for different forms of insertion (via dielectric window or oil valve) the diameter x height ratio will vary greatly. For example, for antennas for oil valves, it is possible to verify that the height is in most cases much greater than the radius. On the other hand, for antennas coupled via the dielectric window, the relationship is opposite. The radiation patterns will depend on the constructive model applied to the antenna, it is possible to see that for the case of planars, there are generally unidirectional patterns. In the case of monopolar antennas, the characteristic is omnidirectional.

IV. CONCLUSION

In this paper, a comparative analysis was performed between antennas for continuous measurements applied to detect partial discharges coupled via dielectric window or oil valve in power transformers. It was found that for the coupling via the dielectric window, the L-probe antenna obtained the best results, since it was the most compact, had a bandwidth of 28.89% (at -10 dB) and a gain of 9.61 dBi. For -5 dB the spiral log antenna obtained the best result with bandwidth of 95.75% and gain of 6.09 dBi. In the case of coupling via oil valve, the most suitable antenna, considering -10 dB, would be the monopole, with bandwidth of 12.22% and a gain of 2.19 dBi, at -5 dB the conical 70 mm achieved the best results with 550 MHz of bandwidth and gain of 2.53 dBi. As a next step, tests will be carried out at high voltage to verify if the antennas can detect partial discharges in practice.

ACKNOWLEDGMENT

The authors want to acknowledge the Postgraduate Program in Electrical Engineering (PPgEE) of the Federal University of Campina Grande (UFCG), the Coordination for the Improvement of Higher Level Education Personnel (CAPES), the National Council for Technological and Scientific Development (CNPq) and Support Program for Centers of Excellence (PRONEX).

REFERENCES

[1] D.A.Natrass, "Partial discharge measurement and interpretation", IEEE Electrical Insulation Magazine, No. 4, 1988, pp. 10–23.

[2] B.F.Hampton, R.J.Meats, "Diagnostic measurements at UHF in gas insulated substations", IEEE Proceedings, IEEE, vol. 135, No. 2, 1988, pp. 137 - 144.

[3] M.D.Judd, B.M.Pryor, S.C.Kelly, B.F.Hampton, "Transformer monitoring using the UHF technique", Iet. High Voltage Engineering,Eleventh International Symposium On, 1999.

[4] S.Tenbohlen, D.Denissov, S.M.Hoek, S.M.Markalous, "Partial discharge measurement in the ultra high frequency (UHF) Range", IEEE Transactions On Dielectrical And Electrical Insulation, Ieee, vol. 15, No. 6, 2008, pp. 1544 - 1552.

[5] T.Ju, X.Zhongrong, Z.Xiaoxing, S.Caixin, "GIS partial discharge quantitative measurements using UHF microstrip antenna sensors", Annual Report Conference on Electrical Insulation and Dielectric Phenomena, 2007, pp. 116–119

[6] G.V.R.Xavier, E.G.Da Costa, A.J.R.Serres, H.F.S.Sousa, A.C.De Oliveira, L.A.M.M.Nobrega, "Design and application of an UHF microstrip circular antenna for partial discharges detection in power transformers", In: 2018 IEEE International Conference on High Voltage Engineering and Application (ICHVE), IEEE, 2018, pp. 1-4.

[7] G.V.Xavier, E.G.Da Costa, A.J.Serres, C.C.Albuquerque, "L-Probe and U-Slot microstrip circular antenna for application in the detection of partial discharges in power transformers", IEEE International Symposium on Antennas and Propagation and USNC-URSI Radio Science Meeting, 2019, pp. 251-252.

[8] L.A.M.M.Nobrega, G.V.R.Xavier, M.V.D.Aquino, A.J.R.Serres, C.C.R.Albuquerque, E.G.Costa, "Design and development of a bio–inspired UHF sensor for partial discharge detection in Power transformers", Sensors, vol. 19, No. 3, 2019, pp. 653.

[9] C.A.Balanis, "Antenna theory: analysis and design", 4rd edition, John wiley & sons, New Jersey, 2015.

[10] W.L.Stutzman and G.A.Thiele, "Antenna theory and design", 3rd edition, John Wiley & Sons, 2012.

[11] L.Morbidel, L.A.B.Rossini, P.A.C.Caso, "Design of high return loss logarithmic spiral antenna", Microwave And Optical Technology Letters, vol. 59, No. 10, 2017, pp. 2532-2538.

[12] H.H.Sinaga, B.T.Phung, A.P.Ao, T.R.Blackburn, "UHF Sensors sensitivity in detecting partial discharge sources in a transformer", International Symposium on High Voltage Engineering, 2011.

[13] J.Lopez-Roldan, T.Tang, M.Gaskin, "Optimisation of a sensor for onsite detection of partial discharges

in power transformers by the UHF method", IEEE Transactions on Dielectrics and Electrical Insulation, vol. 15, No. 6, 2008, pp. 1634-1639.

[14] B.Sarkar, D.K.Mishra, C.Koley, N.K.Roy, "Microstrip patch antenna based uhf sensor for detection of partial discharge in high voltage electrical equipments", In Proceedings of the Annual IEEE India Conference (INDICON), Pune, India, 2014; pp. 1–6.

[15] J.Li, T.Jiang, C.Cheng, C.Wang," Hilbert fractal antenna for UHF detection of partial discharges in transformers", IEEE Trans. Dielectr. Electr. Insul, vol. 20, No. 6, 2013, pp. 2017–2025.

[16] H.Luo, P.Cheng, H.Liu, K.Kang, F.Yang, K.Liu, "Research on the UHF microstrip antenna for partial discharge detection in high voltage switchgear", In Proceedings of the 2016 IEEE 11th Conference on Industrial Electronics and Applications (ICIEA), Hefei, China, 2016; pp. 2273–2276

25th IMEKO TC4 International Symposium
23rd International Workshop on ADC and DAC Modelling and Testing
IMEKO TC-4 2022
Brescia, Italy / September 12-14, 2022

Iterative Interpolated DFT-based Frequency Estimator for Electrical Waveform Affected by Decaying DC Offset

Daniel Belega[1], Dario Petri[2], Dominique Dallet[3]

[1]*Department of Measurements and Optical Electronics, University Politehnica Timisoara, Bv. V. Parvan, Nr. 2, 300223, Timisoara, Romania, email: daniel.belega@upt.ro*
[2]*Department of Industrial Engineering, University of Trento, Via Sommarive, 9, 38123, Trento, Italy, email: dario.petri@unitn.it*
[3]*IMS Laboratory, Bordeaux INP, University of Bordeaux, CNRS UMR5218, 351 Cours de la Libération, Bâtiment A31, 33405, Talence Cedex, France, email: dominique.dallet@ims-bordeaux.fr*

***Abstract* – An iterative Interpolated Discrete Fourier Transform (IpDFT)-based frequency estimator of a sinewave affected by decaying dc offset is proposed in this paper. The accuracies of the proposed procedure and the classical IpDFT algorithm are compared with each other under different steady-state and dynamic testing conditions suggested in the IEC/IEEE 60255-118.1:2018 - Synchrophasors for power systems – Measurements. A decaying dc offset is added to the test signals suggested in the Standard and off-nominal frequency is considered. Procedure accuracy is analyzed through simulations by considering the maximum of the absolute value of the frequency error. Comparison with the frequency error thresholds proposed in the Standard is also performed.**

I. INTRODUCTION

When a fault occurs in power systems, current relaying signals often contain a decaying dc component. Since the spectrum of that component covers all frequencies, it may heavily affect the accuracy of phasor measurements returned by frequency-domain based algorithms. Various approaches have been proposed to overcome this issue [1]-[5]. Usually, the parameters of the decaying dc offset are firstly estimated and then used to remove that component from the analyzed electrical waveform. The proposed algorithms require only half or a full nominal cycle for decaying dc offset parameter estimation. Their main drawback is that they assume nominal waveform frequency, while this is often not the case when faults occur. Consequently, the estimated parameters are affected by the so-called picket-fence errors [6].

The Interpolated Discrete Fourier Transform (IpDFT) algorithm is capable to ensure accurate sinewave parameter estimates under off-nominal frequency condition [7]-[10]. Indeed, it compensates the picket-fence errors by estimating the inter-bin location of sinewave frequency. Classically, the estimation is performed by interpolating the two largest Discrete Fourier Transform (DFT) samples. Then sinewave amplitude and phase are estimated exploiting the knowledge of the estimated frequency. In addition, to reduce errors due to the spectral leakage from interfering tones, before performing frequency-domain interpolation, the acquired signal is weighted by means of a suitable window [11]. Unfortunately, frequency estimation accuracy of IpDFT algorithms can be heavily affected by a decaying dc offset due to its broad spectrum. In this paper an iterative IpDFT-based procedure that takes into account the contribution of that component is proposed. It is called iIpDFT-dc procedure and it exploits the decaying dc offset parameters estimation algorithm proposed in [12].

The accuracies of the iIpDFT-dc and the IpDFT procedures are then compared with each other under different steady-state and dynamic conditions considered in the Standard IEC/IEEE 60255-118.1:2018 – Synchrophasors for power systems – Measurements [13], called simply Standard in the following for the sake of brevity. Unlike the Standard, the test signals contain a decaying dc offset and off-nominal frequency occurs. The investigation is performed through computer simulations and the maximum of the Frequency Error (FE_{max}) absolute value is assumed to compare the algorithm accuracies.

II. THE iIPDFT-DC PROCEDURE

The acquired discrete-time electrical waveform is expressed as:

$$x(m+r) = x_s(m+r) + x_{dc}(m+r) = a\cos\left(2\pi\frac{f}{f_s}(m-M_h+\mathrm{r})+\phi\right) + a_0 e^{-\frac{m-M_h+\mathrm{r}}{\tau\cdot f_s}},$$
$$m = 0,1,\ldots,M-1,\ r = m_0+M_h, m_0+M_h+1,\ldots. \quad (1)$$

where f_s is the sampling rate, a, f, and ϕ are the

amplitude, frequency, and phase of the sinewave $x_s(\cdot)$, a_0 and τ are the amplitude and the time constant of the decaying dc offset $x_{dc}(\cdot)$, and $M = 2M_h + 1$ is the acquisition length, which is assumed an odd number without loss of generality. It is worth noticing that the sample of index M_h corresponds to the middle of the observation interval. The fault causing the decaying dc offset is assumed to occur at the sampling instant m_0. The subsequent analyzed records of length M are updated sample by sample. They are identified by the index r.

The ratio between the nominal frequency f_n and the sampling rate f_s is chosen in such a way that:

$$\frac{f_n}{f_s} = \frac{J}{M-1}, \tag{2}$$

where J *is* the number of analyzed cycles of a sinewave at nominal frequency. Due to possible off-nominal frequency, the ratio between the waveform frequency f and the sampling rate f_s can be written as in the following expression:

$$\frac{f}{f_s} = \frac{\nu}{M} = \frac{l+\delta}{M}, \tag{3}$$

where $\nu = l + \delta$ is the number of acquired sinewave cycles, expressed as the summation of an integer part l and a fractional part δ representing the inter-bin frequency location.

The time constant τ is expressed as a fraction k of the waveform period $T = 1/f$, that is $\tau = T/k$.

The proposed iIpDFT-dc procedure weights the acquired signal (1) by using a suitable window $w(\cdot)$. Then the Discrete-Time Fourier Transform (DTFT) of the windowed signal $x_{ws}(m + r) = x_s(m + r)\cdot w(m)$ is evaluated:

$$X_{sw}(\lambda) \triangleq \sum_{m=0}^{M-1} x_{sw}(m+r)e^{-j2\pi\frac{\lambda}{M}(m-M_h+r)} \tag{4}$$

The parameters of the sinewave are estimated by the classical IpDFT algorithm based on the Hann window [7]-[10], defined as:

$$w(m) = 0.5 + 0.5cos\left(\frac{2\pi}{M}(m - M_h)\right), \tag{5}$$

$$m = 0, 1, \dots M-1$$

The parameter estimators are given by the following expressions:

$$\hat{\nu} = l + \hat{\delta} = l + \frac{(1+i)\alpha-2+i}{\alpha+1}, \tag{6}$$

in which $\alpha = \frac{|X_{sw}(l+i)|}{|X_{sw}(l+i-1)|}$ with $i = 0$ if $|X_{sw}(l-1)| > |X_{sw}(l+1)|$ or $i = 1$ if $|X_{sw}(l-1)| < |X_{sw}(l+1)|$

$$\hat{a} = \frac{2|X_{sw}(l)|}{|W(-\hat{\delta})|}, \tag{7}$$

where $W(\lambda) \cong \frac{M\cdot sin(\pi\lambda)}{2\pi\lambda\left(1-\lambda^2\right)}$ is the DTFT of the Hann window, and

$$\hat{\phi} = arg\{X_{sw}(l)\}. \tag{8}$$

The DTFT of the decaying dc offset is equal to:

$$X_{dc}(\lambda) \triangleq \sum_{m=0}^{M-1} x_{dc}(m+r)e^{-j2\pi\frac{\lambda}{M}(m-M_h+r)} \tag{9}$$

After some algebraic calculations, it results:

$$X_{dc}(\lambda) = a_0 e^{-k\frac{r-M_h}{M}\nu}\frac{1-e^{-j2\pi\lambda}\beta^M}{1-e^{-j\frac{2\pi}{M}\lambda}\beta}e^{-j\pi\frac{\lambda}{M}(r-M_h)}, \tag{10}$$

where $\beta \triangleq e^{-\frac{k\nu}{M}}$.

From (10) the parameters of the decaying dc offset can be determined as follows [12]:

$$\beta = \frac{|X_{dc}(0)-X_{dc}(1)|}{\left|X_{dc}(0)-e^{-j\frac{2\pi}{M}}X_{dc}(1)\right|}, \tag{11}$$

and

$$a_0 = \frac{1-\beta}{1-\beta^M}\beta^{-(r-M_h)}|X_{dc}(0)|. \tag{12}$$

The proposed iIpDFT-dc procedure is based on the following steps:

step 1: initialize $\hat{x}_s(m+r) = x(m+r)$, $m = 0, 1, \dots, M-1$, $r = m_0 + M_h, m_0 + M_h + 1, \dots$

step 2: estimate the parameters of the sinewave $\hat{x}_s(\cdot)$ by means of the IpDFT algorithm based on the Hann window, using (6) – (8);

step 3: estimate the decaying dc offset contribution:

$$\hat{x}_{dc}(m+r) = x(m+r) - \hat{a}cos\left(2\pi\frac{\hat{\nu}}{M}(m-M_h+r)+\hat{\phi}\right)$$

step 4: calculate the parameters $\hat{\beta}$ and $\hat{a}_0$ of the estimated decaying dc offset $\hat{x}_{dc}(\cdot)$, using (11) and (12)

step 5: estimate the sinewave contribution:

$$\hat{x}_s(m+r) = x(m+r) - \hat{a}_0\hat{\beta}^{(m+r-M_h)}$$

repeat steps 2-5 Q times

step 6: estimate the sinewave frequency $\hat{\nu}$ by applying the IpDFT algorithm based on the Hann window to the last estimated sinewave $\hat{x}_s(\cdot)$.

III. COMPUTER SIMULATIONS

In this Section the accuracies of the proposed iIpDFT-dc procedure and the IpDFT algorithm based on the Hann window are compared with each other considering the off-nominal frequency, harmonics, and modulation testing conditions suggested in the Standard. A decaying dc offset is added to the analyzed signal and off-nominal frequency is considered also in harmonics and modulation testing. The testing signals correspond to either *P-class* or *M-class* performance. The amplitudes of both sinewave and decaying dc offset are equal to 1 p.u. The nominal frequency is f_n = 50 Hz, and the sampling rate is f_s = 6 kHz. According to (2), 120 samples/nominal cycle are acquired. The reporting rate is RR = 50 readings/s. The fault occurs at m_0 = 0, *i.e.,* at the beginning of the $r = M_h$ analyzed record. J = 4 or 5 nominal cycles are observed, so that the record length is M = 481 or M = 601 samples, respectively. Q = 2 iterations are performed since no significant frequency estimation accuracy improvement was observed using a higher number of iterations. The related FE_{max} Standard thresholds are also shown in the presented figures.

A. Off-nominal frequency testing condition

Fig. 1 shows FE_{max} of both the IpDFT algorithm and the iIpDFT-dc procedure as a function of the waveform frequency for J = 4 and 5 nominal cycles when $\tau = T$. In addition, Fig. 2 shows the frequency errors of the considered methods when r = 1000 waveforms with f = 48 Hz and J = 4 nominal cycles are considered.

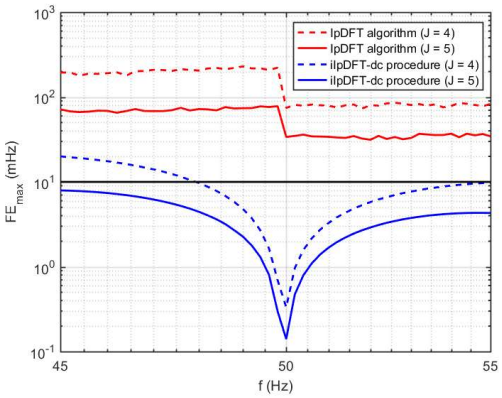

Fig. 1. Off-nominal frequency condition: FE_{max} of the IpDFT algorithm and the iIpDFT-dc procedure versus the waveform frequency when J = 4 and 5 nominal cycles and τ equal to the sinewave period T.

The proposed iIpDFT-dc procedure clearly outperforms the IpDFT algorithm since it is capable to significantly compensate the contribution of the decaying dc offset on the estimated frequency. Moreover, the results returned by the iIpDFT-dc procedure comply with the *P-class* or the *M-class* performance when J = 4 or J = 5 nominal cycles, respectively.

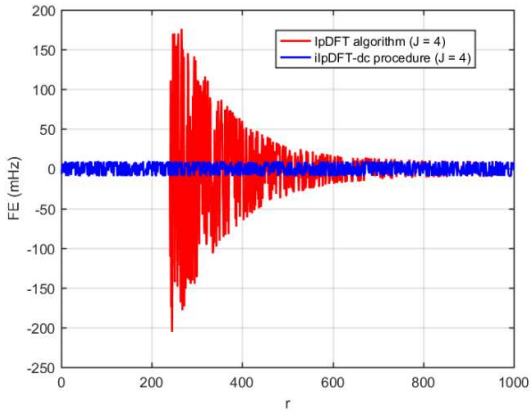

Fig. 2. Off-nominal frequency condition: frequency errors of the IpDFT algorithm and the iIpDFT-dc procedure versus the analyzed record index r when f = 48 Hz, J = 4 nominal cycles, and τ equal to the sinewave period T.

Fig. 3 shows the FE_{max} obtained with both the IpDFT algorithm and the iIpDFT-dc procedure as a function of the ratio τ/T when f = 48 Hz. As it can be seen, the accuracy of the estimates provided by the proposed iIpDFT-dc procedure are almost independent of the time constant τ, unlike the accuracy of the IpDFT algorithm.

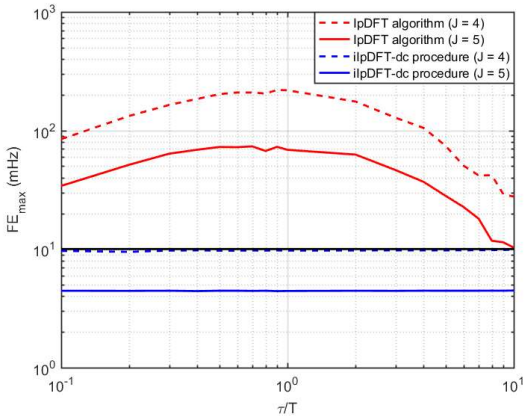

Fig. 3. Off-nominal frequency condition: FE_{max} of the IpDFT algorithm and the iIpDFT-dc procedure versus the ratio τ/T when f = 48 Hz and J = 4 and 5 nominal cycles.

B. Harmonics testing condition

When frequency-domain based estimation algorithms are used, the lower order harmonics, and in particular the 2nd order harmonic, are responsible for

the most detrimental contributions to the estimated frequency [7], [10]. Thus, the effect of a 2nd harmonic on the results returned by the iIPDFT-dc procedure is analyzed in the following.

Fig. 4 shows the FE_{max} of both the IpDFT and the iIpDFT-dc procedures as a function of the waveform frequency for both considered values of the number of observed nominal cycles J when the electrical waveform is affected by a 2nd harmonic and $\tau = T$.

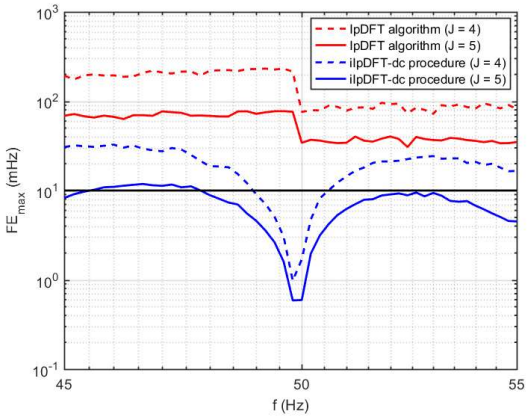

Fig. 4. Harmonics condition: FE_{max} of the IpDFT algorithm and the iIpDFT-dc procedure versus the waveform frequency when the electrical waveform is affected by a 2nd harmonic, $J = 4$ and 5 nominal cycles, and τ equal to the sinewave period T.

As it can be seen, the proposed iIpDFT-dc procedure provides more accurate frequency estimates than the IpDFT algorithm for both the considered values of J. When $J = 4$ nominal cycles, FE_{max} smaller than the 10 mHz Standard threshold is achieved when $f \in [49, 50.5]$ Hz. Conversely, when $J = 5$ nominal cycles, the Standard requirements are fulfilled in almost the whole considered frequency range. Conversely, the FE_{max} of the IpDFT algorithm is always worse than the Standard threshold.
Moreover, simulations showed that in this testing condition the FE_{max} values obtained by the iIpDFT-dc procedure are almost independent of the time constant τ when it takes values between 0.1 and 10 times the sinewave period.

C. Modulation testing condition

Simulations with electrical waveforms affected by either amplitude or phase modulations have been also performed. The amplitude and phase modulation indices were $k_a = 0.1$ and $k_p = 0.1$. Fig. 5 shows the FE_{max} of both the IpDFT algorithm and iIpDFT-dc procedure as a function of the waveform frequency when the waveforms are affected by both amplitude and phase modulation with frequency f_m equal to 2 Hz (Fig. 5(a)) and 5 Hz (Fig. 5(b)). The time constant of the decaying dc component τ is equal to the sinewave period T. Moreover, Fig. 6 shows the frequency errors returned by the considered procedures when $r = 1000$ waveforms with $f = 50$ Hz and $J = 4$ nominal cycles are considered.

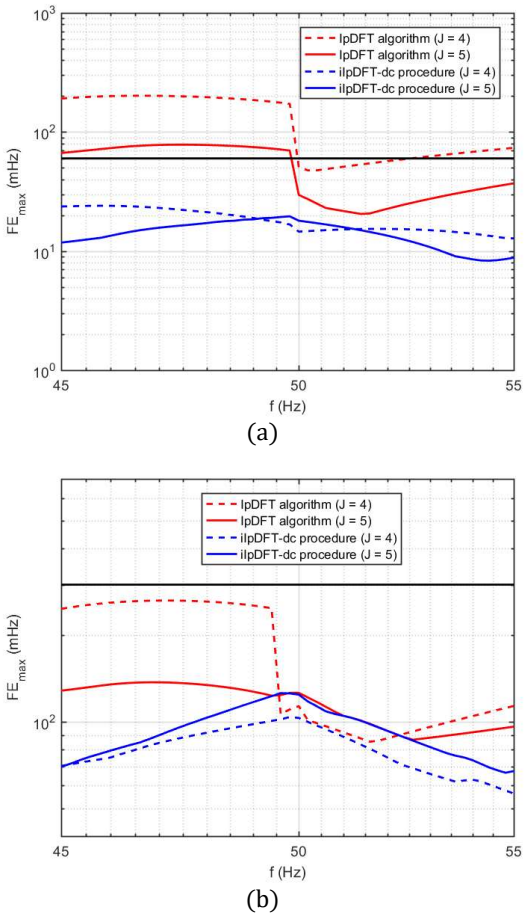

Fig. 5. Modulation condition: FE_{max} of the IpDFT algorithm and the iIpDFT-dc procedure versus the waveform frequency when the modulation frequency is $f_m = 2$ Hz (a) or $f_m = 5$ Hz (b), $J = 4$ and 5 nominal cycles, and τ equal to the sinewave period T. Results obtained by considerring both amplitude and phase modulation are presented.

Fig. 5 shows that the proposed iIpDFT-dc procedure outperforms the IpDFT algorithm in most of the considered conditions. Moreover, it provides FE_{max} values smaller than the related thresholds (i.e., 60 mHz for the *P-class* performance and 300 mHz for the *M-class* performance) in the whole considered frequency range, even if only nominal frequency is considered in the Standard. In addition, for a given modulation frequency, the FE_{max} values of the iIpDFT-dc procedure

obtained by observing $J = 4$ or 5 nominal cycles are quite close to each other. Observe also that, the classical IpDFT algorithm complies only with the *M*-class Standard requirements when the whole frequency range is considered.

As in the previous testing conditions, the FE_{max} values obtained by the iIpDFT-dc procedure are almost independent of the time constant τ when it takes values between 0.1 and 10 times the sinewave period.

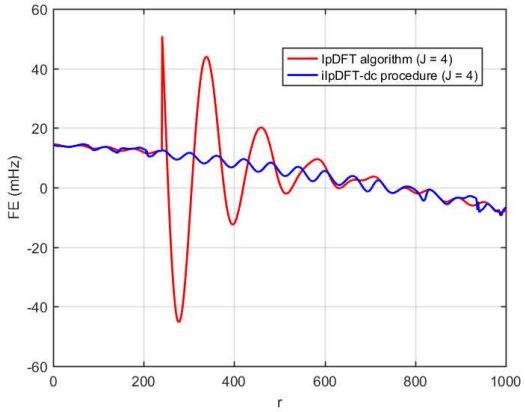

Fig. 6. Modulation condition: frequency errors of the IpDFT algorithm and the iIpDFT-dc procedure versus *r*. Modulation frequency $f_m = 2$ Hz, sinewave frequency $f = 50$ Hz, $J = 4$ nominal cycles, and τ equal to the sinewave period *T*.

Finally, Fig. 6 shows that, in the considered testing conditions, the contribution of the decaying dc component on the frequency estimates returned by the iIpDFT-dc procedure is almost negligible.

IV. CONCLUSIONS

The iIpDFT-dc procedure for frequency estimation of sinewave affected by a decaying dc offset has been proposed. It is based on the classical IpDFT algorithm, and it can be simply implemented. The accuracy of iIpDFT-dc procedure is almost independent of the decaying dc offset time constant. Under off-nominal frequency, harmonics, and modulation conditions the iIpDFT-dc frequency estimator complies with the Standard requirements for *P-class* or *M-class* performance when four or five nominal cycles are analyzed, respectively. The proposed procedure outperforms the classical IpDFT algorithm in all considered testing conditions.

REFERENCES

[1] J-C. Gu, S-L. Yu, "Removal of dc offset in current and voltage signals using a novel Fourier filter algorithm", IEEE Trans. on Power Del., vol. 15, no. 1, Jan. 2000, pp. 73-79.

[2] S-L. Yu, J-C. Gu, "Removal of decaying dc in current and voltage signals using a modified filter algorithm", IEEE Trans. on Power Del., vol. 16, no. 3, July 2001, pp. 372-379.

[3] G. Benmouyal, "Removal of dc-offset in current waveforms using mimic filtering", IEEE Trans. on Power Del., vol. 10, no. 2, Apr. 1995, pp. 621-628.

[4] T.S. Sidhu, X. Zhang, F. Albasri, M.S. Sachdev, "Discrete-Fourier-transform-based technique for removal of decaying DC offset from phasor estimates", IEE Proc.-Gen Transm. Distrib., vol. 150, no. 6, Nov. 2003, pp. 745-752.

[5] S-H. Kang, D-G. Lee, S-R. Nam, P.A. Crossley, Y-C. Kang, "Fourier transform-based modified phasor estimation method immune to the effect of the dc offsets", IEEE Trans. on Power Del., vol. 24, no. 3, July 2009, pp. 1104-1111.

[6] C. Offelli, D. Petri, "Interpolation techniques for real-time multifrequency waveform analysis", IEEE Trans. on Instrum. Meas., vol. 39, no. 1, Feb. 1990, pp. 106-111.

[7] D. Belega, D. Petri, "Accuracy analysis of the muticycle synchrophasor estimator provided by the interpolated DFT algorithm", IEEE Trans. on Instrum. Meas., vol. 62, no. 5, May 2013, pp. 942-953.

[8] D. Belega, D. Petri, "Effect of noise and harmonics on sine-wave frequency estimation by interpolated DFT algorithms based on few observed cycles", Signal Processing, vol. 140, 2017, pp. 207-218.

[9] D.C. Rife, G.A. Vincent, "Use of the discrete Fourier transform in the measurement of frequencies and levels of tones", Bell Syst. Tech. J, vol. 49, 1970, pp. 197-228.

[10] D. Belega, D. Dallet, "Multifrequency signal analysis by interpolated DFT method with maximum sidelobe decay windows", Measurement, vol. 42, no. 3, Apr. 2009, pp. 420-426.

[11] F.J. Harris, "On the use of windows for harmonic analysis with the discrete Fourier transform", Proc. IEEE, vol. 66, no. 1, Jan. 1978, pp. 51–83.

[12] M. Bertocco, C. Offelli, D. Petri, "Analysis of damped sinusoidal signals via a frequency-domain interpolation algorithm", IEEE Trans. on Instrum. Meas., vol. 43, no. 2, Apr. 1994, pp. 245-250.

[13] IEC/IEEE 60255-118-1:2018, IEEE/IEC International Standard - Measuring relays and protection equipment - Part 118-1: Synchrophasor for power systems - Measurements, pp. 1-78, Dec. 2018.

25th IMEKO TC4 International Symposium
23rd International Workshop on ADC and DAC Modelling and Testing
IMEKO TC-4 2022
Brescia, Italy / September 12-14, 2022

Cascaded H-Bridges Multilevel Inverter Drive: Active Power Analysis in Frequency Domain

A.O. Di Tommaso[1], R. Miceli, C. Nevoloso, G. Scaglione, G. Schettino, C. Spataro

[1]*Department of Engineering, University of Palermo, Viale Delle Scienze, Building nr. 9, 90128 Palermo, claudio.nevoloso@unipa.it*

***Abstract* –The international standard IEC 61800-9-2 introduces energy efficiency classification for frequency converters or complete drive module (CDM) and provides instrumentation minimum requirements for accurate measurement of CDM input and output power valid for conventional pulse-width-modulated (PWM) voltage source inverter (VSI). This paper highlights the necessary improvements to update the standard with more detailed prescriptions according to the converter topologies and the modulation techniques adopted. In this framework, this paper address the power analysis in the frequency domain of a cascaded H-bridges-multilevel inverter (CHBMI) in an interior permanent magnet synchronous motor (IPMSM) drive for the identification of the minimum measurement bandwidth. The power spectrums are analyzed for different modulation strategies, different switching frequency values and IPMSM working conditions.**

I. INTRODUCTION

In recent years, a significant increase in global electrical energy consumption by electrical drives has been detected, with more than 47% of world electricity demand [1]-[2]. At present, most commercial electrical drives employ conventional two-level VSI for motor speed and torque control purposes. The desired output voltage is modulated by the PWM strategy, allowing motor operation at partial speed with energy-saving benefits. However, the VSI presents power losses that affect the drive overall efficiency and introduce motor additional harmonic losses [3]-[4]. Therefore, the efforts of the scientific community focused on the adoption of new solutions to optimize the electric drive performance in terms of power losses. A possible solution is the adoption of multilevel power inverters (MPIs) [5]. This technology is widely employed in traction electrical drives [6]. In automotive applications, recent studies highlight that to address long charging time and low maximum driving range issues, it is necessary to move toward higher-voltage DC links with consequent adoption of MPIs [7]. The main benefits derived by MPIs adoption can be summarized in output voltage reduced harmonic content, lower voltage stress, lower power losses and reduced electromagnetic interference (EMI) [8]-[9].

The international standards IEC 61800-9-1 [10] and IEC 61800-9-2 [11] provide the prescriptions for power losses measurement and energy efficiency classification of the power drive system (PDS), CDM and motor. The prescriptions regarding the CDM power losses measurement are defined for a conventional VSI that employs PWM or space vector modulation (SVM) strategy. No specific prescriptions are reported for other inverter topology structures. Although instrumentation minimum requirements prescriptions are general and can be applied for different inverter topologies and modulation strategies, they may be overestimated for MPIs.

This paper deals with the analysis of CHBMI input and output powers in the frequency domain. The goal is to identify the minimum instrumentation bandwidth for accurate power losses identification. Experimental analyses are performed according to IEC 61800-9-2 prescriptions on IPMSM drive fed by CHBMI. The paper is organized as follows: Section II summaries IEC 61800-9-2 main prescriptions for accurate power losses detection; Section III described the test bench, IPMSM drive fed by CHBMI and modulation strategies considered; Section IV presents the experimental results and their analysis.

II. IEC 61800-9-2 PRESCRIPTIONS

In the last decades, different regulatory bodies introduced energy efficiency classification for electrical equipment. The newest IEC 61800-9-2 introduce energy efficiency indicators IE for PDS, motor starter and power electronics systems. The standard defines three different efficiency classes IE0-IE2 for frequency converters or CDMs. The standard defines a reference CDM (RCDM) composed of a line choke, diode rectifier, DC link and output VSI for IE classification as shown in Fig. 1 [11].

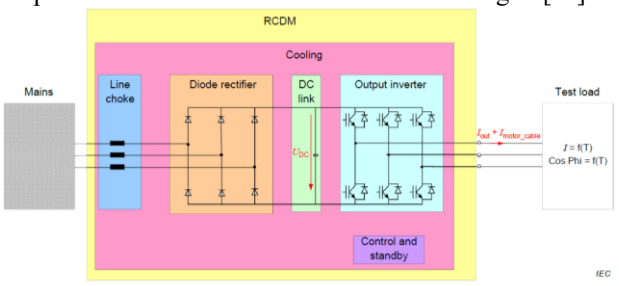

Fig. 1 RDCM and test load.

The standard can be applied for CDMs that present a

power rating range of 0.12-1000 kW, voltage range of 100-1000 V and also for CDM used in low voltage power drive systems. Three different types of testing for CDM loss determination are reported: analytical method, calorimetric method and input-output measurement method. The last method requires the measurement of electrical input and output CDM powers by employing only electrical measurement equipment and it is low time-consuming. Various power loss measurement techniques for power electronics systems, including the above described, are accurately discussed in [12]. To provide extensive loss results applicable for common electric drive applications, IEC 61800-9-2 prescribes the CDM loss measurement at partial loads as shown in Fig. 2.

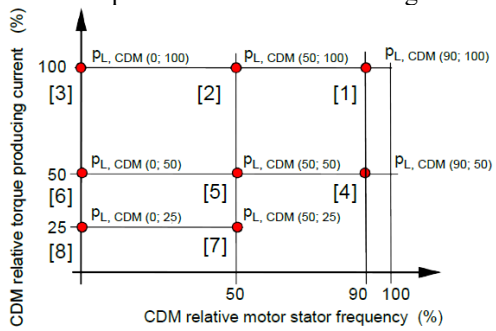

Fig. 2 CDM test point according to IEC 61800-9-2.

The standard does not specify the test load type, thus an electronic load or electric motor can be used. The CDM relative torque producing currents reported represent the minimum values and slightly higher values can be used. The torque producing current values are reported in [11] as a function of motor-rated powers. Moreover, since the VSI is responsible for most of the power losses which are a function of phase displacement between the output voltage and current fundamental components, the standard provides displacement power factor (DPF) reference values for the load as a function of motor-rated power [11]. The tests shall be conducted by the use of a power analyzer or data acquisition systems able to perform harmonic analysis. For CDM testing, a tolerance of ± 0.08 is allowed in DPF reference values. The standard also reports the reference switching frequency that is 4 kHz for CDM range power up to 90 kW and 2 kHz for CDM range power above 90 kW. On the base of the above prescriptions described, the standard provides the minimum accuracy specifications for measurement instruments used for efficiency classification. The instrumentation used for measuring power and CDM electrical quantities shall meet the requirements reported in the standard IEC 60034-2-1 [13]. The standard suggests a bandwidth at least of 10 times of VSI switching frequency.

Although the standard prescriptions are valid for traditional two-level VSI, they are not defined considering other inverter topology structures, modulation strategies and operations at higher switching frequencies. Paying attention to MPIs case, usually, the typical switching frequency adopted ranges from 5 kHz to 20 kHz with typical Multi-carrier PWM (MC-PWM) strategies [9]. Furthermore, the MPIs output voltages present reduced harmonic content with respect to traditional two-level VSIs, resulting in lower harmonic content in motor currents and consequently output power spectrum limited at lower bandwidth values. The modulation strategies adopted for motor control purpose and their control features are a function of the application and motor-rated power [6]. Therefore, traditional PWM or SVM modulations are not always adopted. The analysis related to the accurate measurement of power losses in CHBMI converters is described below.

III. IPMSM DRIVE UNDER TEST AND TEST BENCH

To perform an adequate power analysis, an IPMSM electrical drive fed by CHBMI has been set up. It is composed of a three-phase five-level CHBMI prototype (Fig. 3) whose main parameters are reported in [9] and 6 poles, three-phase IPMSM with interior SmCo magnets, whose rated mechanical speed and torque are 4000 rpm and 1.8 N·m, respectively. A Magtrol hysteresis brake (Model HD-715-8NA), connected to the shaft of the motor is used as a mechanical load. The electrical quantities are acquired by Teledyne LeCroy MDA 8028HD oscilloscope equipped with three high voltage differential probes Teledyne Lecroy HVD3106A 1 kV, 120 MHz, and three high sensitivity current probe Teledyne Lecroy CP030A AC/DC, 30 A rms, 50 MHz. The CHBMI is supplied with six DC RSP-2400 sources with 48 V of rated voltage [9].

A traditional field-oriented control (FOC) strategy, shown schematically in Fig. 4, has been implemented in PED Board FPGA control unit programmable in the Labview environment. This control strategy presents a closed-loop control of speed and currents performed by the use of PI controller. The peculiar feature of this control consists in the possibility to vary the modulation strategy adopted and its main parameter features such as the switching frequency f_{sw}. In this work, Phase Shifted (PS) and Phase Disposition (PD) modulation strategies have been considered with Sinusoidal (S) and Switching Frequency Optimal (SFO) modulating signals (Fig. 5). A detailed description of MC-PWM considered is reported in [9]. The test bench set-up is shown in Fig. 6.

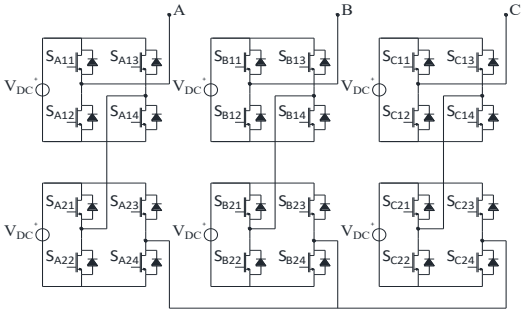

Fig. 3 Three-phase five-level CHBMI.

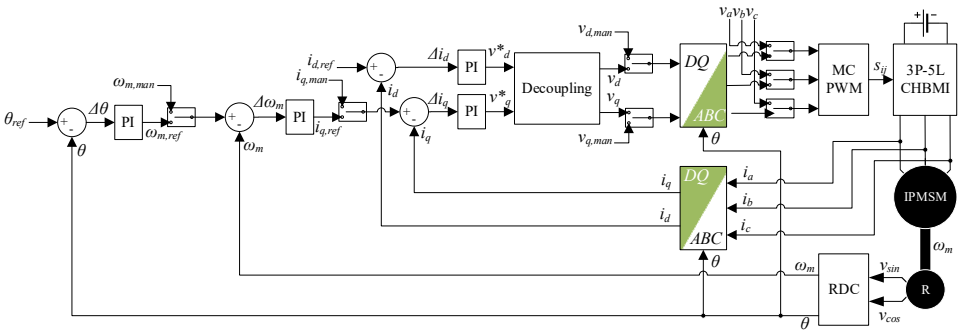

Fig. 4 FOC block diagram.

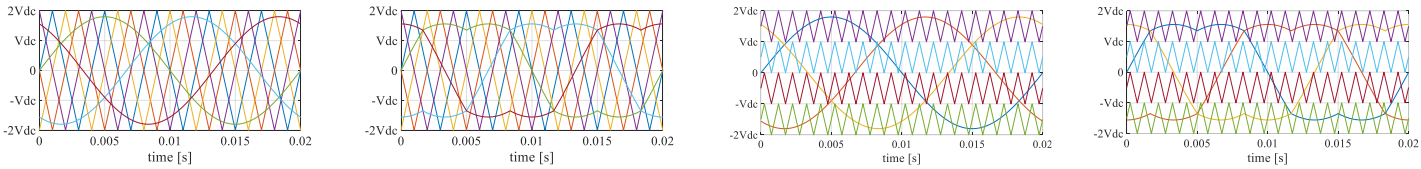

(a) (b) (c) (d)

Fig. 5 MC-PWM strategies: (a) SPSPWM, (b) SFOPWM, (c) SPDPWM, (d) SFOPDPWM.

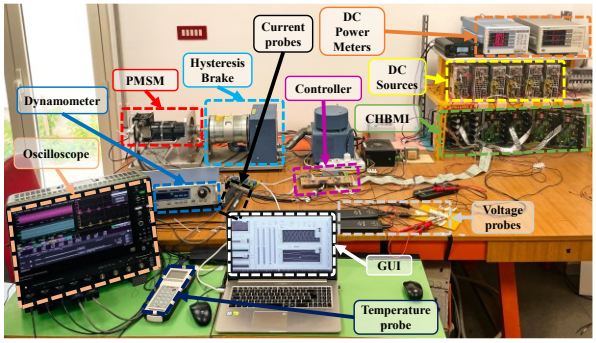

Fig. 6 Test bench.

IV. EXPERIMENTAL RESULTS

The CDM working points defined by the standard IEC 61800-9-2 (Fig. 3) plus an additional measurement point, defined at 90% of motor stator frequency and 25% of motor torque producing current, for a total of 9 measurement points, have been considered. Three different CHBMI switching frequency f_{sw} values equal to 5, 10 and 15 kHz have been considered. The sampling frequency *fs* and acquisition window have been fixed equal to 1 MS/s and 1 s, respectively. Input and output CHBMI electrical quantities have been acquired by MDA 8028HD scope and used for the determination of instantaneous power, active power and its frequency spectrum. These quantities are determined by the computational approach described in [14]. Since similar results have been obtained for all switching frequencies considered, the analysis carried out at 10 kHz is described below. The input voltage and current waveforms of CHBMI single-phase H-bridges, operating at the measurement point 1, are reported in Fig. 7 obtained with SFOPS and SFOPD strategies where the currents present double ripple frequency with respect to the fundamental CHBMI output current. Similar trends have been obtained with SPS and SPD modulation strategies. As expected, almost all of the active power is generated by the DC voltage and current components, and current harmonics generate a very small amount of active power as shown in Fig. 8 (a). The CHBMI input cumulative active power trend, expressed in percent as a function of the frequency, is reported in Fig. 8 (b).

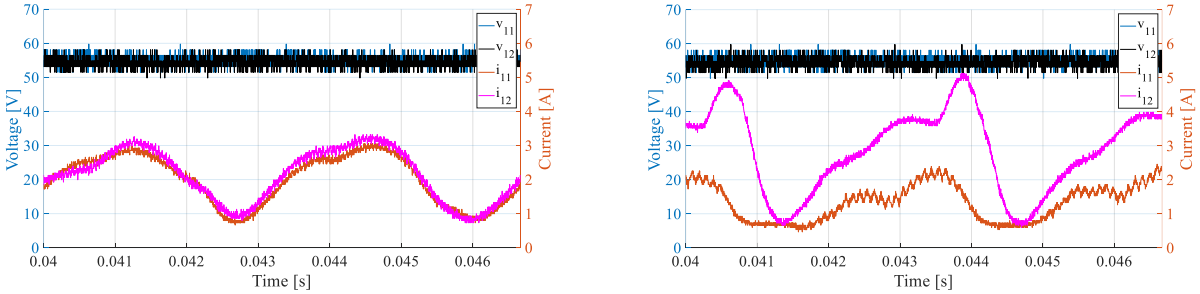

(a) SFOPS (b) SFOPD

Fig. 7 CHBMI input voltage and current waveforms of single-phase H-bridges.

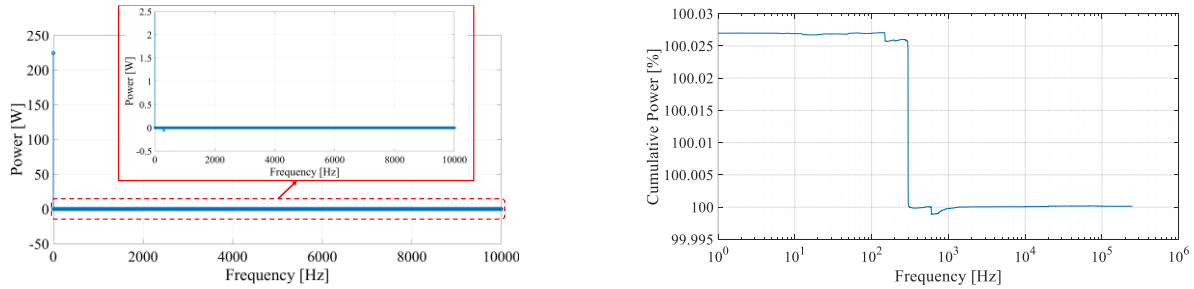

Fig. 8 CHBMI input active power spectrum (a) and cumulative power trend (b) of a single phase

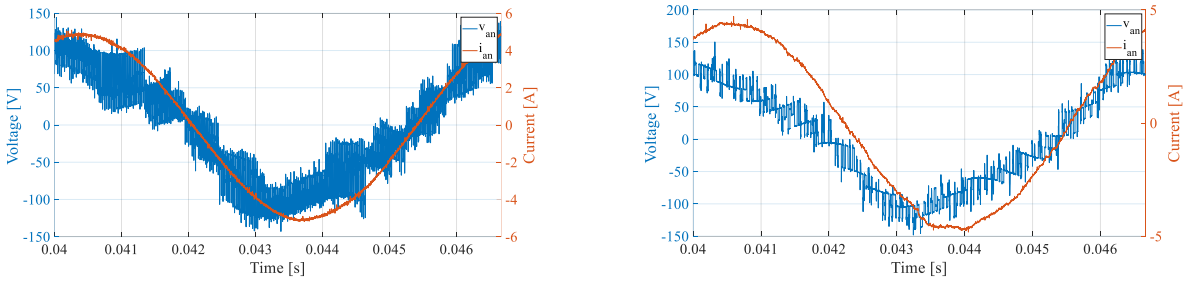

(a) SPS *(b) SPD*

Fig. 9 CHBMI output voltage and current waveforms of a single phase.

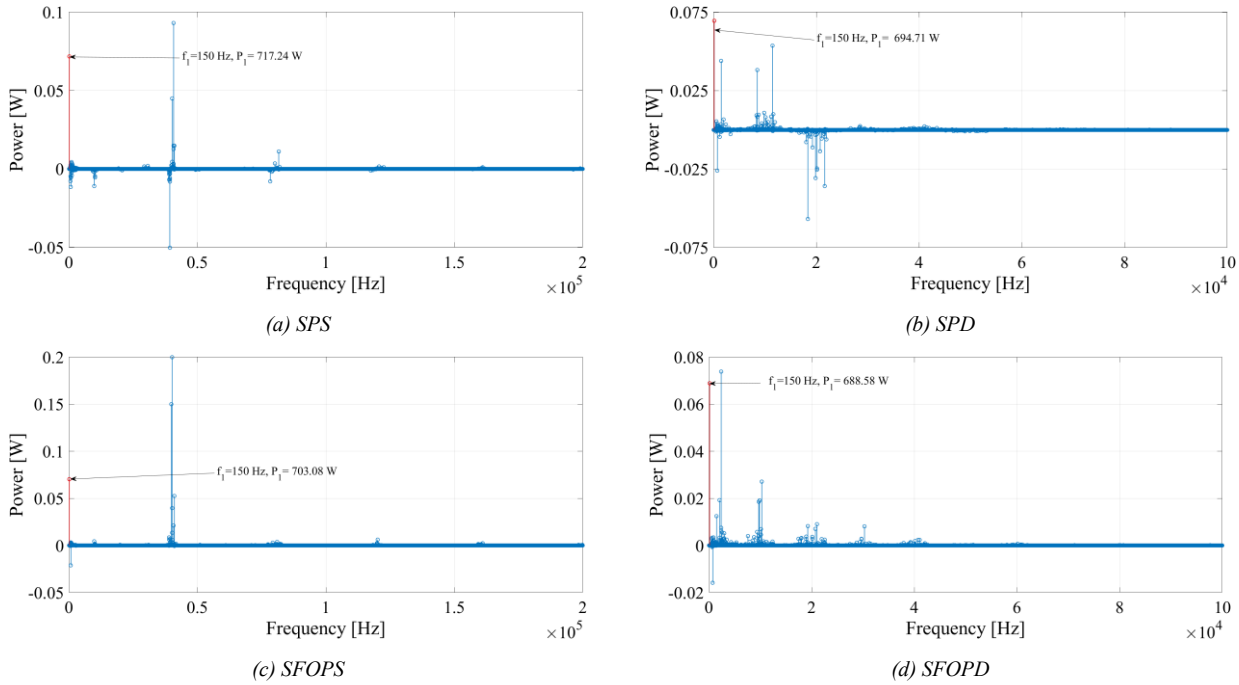

(a) SPS *(b) SPD*

(c) SFOPS *(d) SFOPD*

Fig. 10 CHBMI output active power spectrum.

In detail, the even current harmonics result in a small contribution of active power from the load to the power supply. This analysis highlights that it is not necessary to employ a power analyzer or transducers with a wide bandwidth for adequate active power measurement. A similar analysis has been carried out for CHBMI output section by measuring all phase voltage and current quantities. CHBMI single-phase output voltage and current waveforms, obtained for SPS and SPD strategies in correspondence to point 1, are shown in Fig. 9. In this case, CHBMI output electrical quantities have a much more significant harmonic content than CHBMI input electrical quantities. The CHBMI output voltage is affected by harmonic components that are integer

multiples of the switching frequency f_{sw} for SPD and SFOPD strategies and integer multiples of 4 f_{sw} for SPS and SFOPS [15]. To highlight the impact of voltage and current harmonics on CHBMI output active power, by way of example, the active power spectrum for CHBMI operating at measurement point 1 is reported in Fig. 10. The figure shows a zoomed view of the active power spectrum and the active power value generated by the voltage and current fundamental harmonics. It is possible to observe that the active power generated by the voltage and current harmonics presents significantly reduced amplitude compared to the fundamental one. These results are more appreciable in the cumulative active power trends as a function of the frequency reported in Fig. 11. The zoomed views show that, above the fundamental frequency, the current and voltage harmonics generate an active power contribution of less than 0.5% of total active power. Similar results have been obtained for all measurement points considered. Fig. 12 reports the percent cumulative active power trends obtained by decomposing the frequency range into three different frequency ranges: the first ranges from 0 to f_1, the second ranges from f_1 to f_{sw}-1000 Hz and the third ranges from f_{sw}-1000 to $f_s/2$. In this way, it is possible to highlight the active power contribution of fundamental quantities, the active power contribution of harmonics quantities working at a frequency lower than f_{sw} and the active power contribution of harmonics quantities working in a frequency band including f_{sw} and higher values. The results obtained with SPS and SFOPS strategies show that the fundamental quantities contribute to more than 98.5% of total active power and, below the f_{sw}, the cumulative active power presents a value higher than 99.5 % in all measurement points. Similar results have been obtained with SPD and SFOPD strategies. In some measurement points, the harmonics quantities operating at the third frequency band present an active power contribution higher than 0.6%. The analysis carried out is of considerable importance because it highlights that, to measure almost all of the active power generated by a CHBMI, it is necessary to consider the frequency bandwidth range from 0 to f_{sw}.

V. CONCLUSIONS

This paper presents an experimental active power analysis of an IPMSM drive fed by CHBMI controlled with four different modulation strategies and by considering three different switching frequencies. As expected, the analysis carried out showed that the CHBMI input power is generated by the voltage and current DC components and, therefore, it is not necessary to use power analyzers or transducers with wide bandwidth. The CHBMI output section presents more complex behaviour due to modulation strategies effects that result in not negligible voltage and current harmonic components. The analysis carried out showed that voltage and current harmonics, operating at switching frequency and higher value, contribute to the generation of active power in almost all cases below 0,6%. These results highlight that for CHBMIs, it is not necessary to choose a sampling frequency at least equal to 10 times the switching frequency as described by the standard IEC 618009-2.

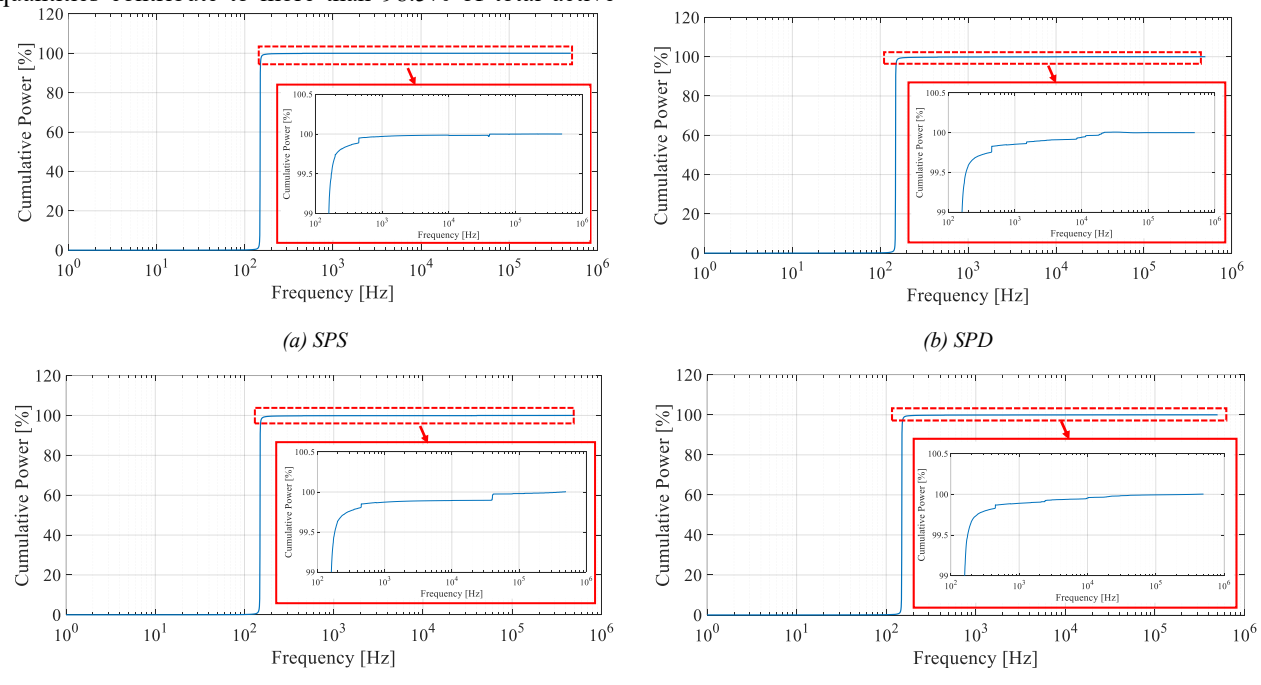

(a) SPS *(b) SPD*

(c) SFOPS *(d) SFOPD*

Fig. 11 CHBMI output active cumulative power trend.

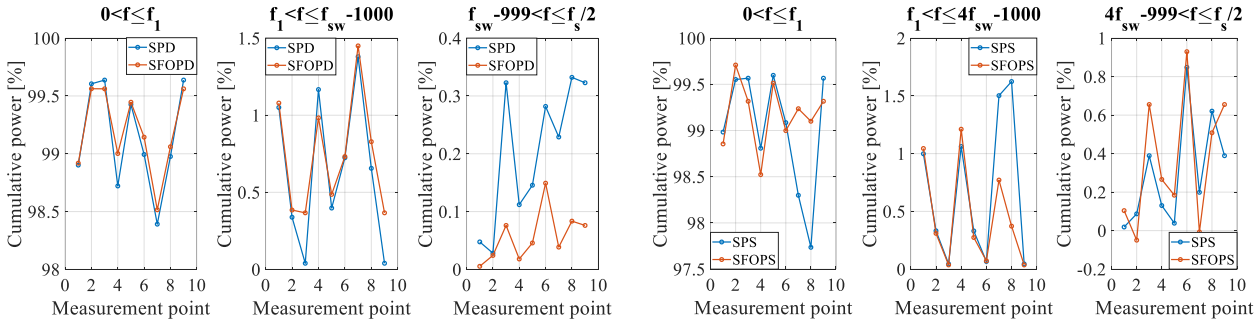

Fig. 12 CHBMI output active cumulative power values for each working point.

REFERENCES

[1] L. Aarniovuori, H. Kärkkäinen, A. Anuchin, J. J. Pyrhönen, P. Lindh and W. Cao, "Voltage-Source Converter Energy Efficiency Classification in Accordance With IEC 61800-9-2," in *IEEE Transactions on Industrial Electronics*, vol. 67, no. 10, pp. 8242-8251, Oct. 2020.

[2] V. Cecconi, V. Di Dio, A. O. Di Tommaso, S. Di Tommaso, D. La Cascia and R. Miceli, "Active power maximizing for Wind Electrical Energy Generating Systems moved by a Modular Multiple Blade Fixed Pitch Wind Turbine," *2008 International Symposium on Power Electronics, Electrical Drives, Automation and Motion*, 2008, pp. 1460-1465.

[3] Caruso, M., Di Tommaso, A.O., Miceli, R., Nevoloso, C. & Spataro, C. 2021, "Uncertainty evaluation in the differential measurements of power losses in a power drive system", *Measurement: Journal of the International Measurement Confederation*, vol. 183, 109795, ISSN 0263-2241.

[4] H. Karkkainen, L. Aarniovuori, M. Niemela and J. Pyrhonen, "Converter-Fed Induction Motor Efficiency: Practical Applicability of IEC Methods," in *IEEE Industrial Electronics Magazine*, vol. 11, no. 2, pp. 45-57, June 2017.

[5] D. Ronanki and S. S. Williamson, "Modular Multilevel Converters for Transportation Electrification: Challenges and Opportunities," in *IEEE Transactions on Transportation Electrification*, vol. 4, no. 2, pp. 399-407, June 2018.

[6] A. Poorfakhraei, M. Narimani and A. Emadi, "A Review of Modulation and Control Techniques for Multilevel Inverters in Traction Applications," in *IEEE Access*, vol. 9, pp. 24187-24204, 2021.

[7] H. Tu, H. Feng, S. Srdic and S. Lukic, "Extreme Fast Charging of Electric Vehicles: A Technology Overview," in *IEEE Transactions on Transportation Electrification*, vol. 5, no. 4, pp. 861-878, Dec. 2019.

[8] A. Poorfakhraei, M. Narimani and A. Emadi, "A Review of Multilevel Inverter Topologies in Electric Vehicles: Current Status and Future Trends," in *IEEE Open Journal of Power Electronics*, vol. 2, pp. 155-170, 2021.

[9] Busacca, A.; Di Tommaso, A.O.; Miceli, R.; Nevoloso, C.; Schettino, G.; Scaglione, G.; Viola, F.; Colak, I. Switching Frequency Effects on the Efficiency and Harmonic Distortion in a Three-Phase Five-Level CHBMI Prototype with Multicarrier PWM Schemes: Experimental Analysis. *Energies* 2022, *15*, 586.

[10] IEC 61800-9-1. Adjustable speed electrical power drive systems - Part 9-1: Ecodesign for power drive systems, motor starters, power electronics and their driven applications - General requirements for setting energy efficiency standards for power driven equipment using the extended product approach (EPA) and semi analytic model (SAM), 2017.

[11] IEC 61800-9-2. Adjustable Speed Electrical Power Drive Systems—Part 9-2: Ecodesign for Power Drive Systems, Motor Starters, Power Electronics & Their Driven Applications—Energy Efficiency Indicators for Power Drive Systems and Motor Starters, 2017.

[12] C. Xiao, G. Chen and W. G. H. Odendaal, "Overview of Power Loss Measurement Techniques in Power Electronics Systems," in *IEEE Transactions on Industry Applications*, vol. 43, no. 3, pp. 657-664, May-june 2007.

[13] IEC 60034-2-1. Rotating electrical machines - Part 2-1: Standard methods for determining losses and efficiency from test, 2014.

[14] A. Anttila, L. Aarniovuori, M. Niemelä, M. Zaheer, P. Lindh and J. Pyrhönen, "Active Power Analysis of PWM-driven Induction Motor in Frequency Domain," *2021 XVIII International Scientific Technical Conference Alternating Current Electric Drives (ACED)*, 2021, pp. 1-6.

[15]S. Benanti *et al.*, "Experimental analysis with FPGA controller-based of MC PWM techniques for three-phase five level cascaded H-bridge for PV applications," *2016 IEEE International Conference on Renewable Energy Research and Applications (ICRERA)*, 2016, pp. 1173-1178.

25th IMEKO TC4 International Symposium
23rd International Workshop on ADC and DAC Modelling and Testing
IMEKO TC-4 2022
Brescia, Italy / September 12-14, 2022

A Preliminary Study on Flexible Temperature Sensors for Eskin Medical Devices

Fapanni Tiziano[1], Emilio Sardini[1], Mauro Serpelloni[1]

[1]*University of Brescia, Brescia, Italy, {t.fapanni, emilio.sardini, mauro.serpelloni}@unibs.it*

***Abstract* – In the latest years, the need of a renewed paradigm for healthcare arose promoting the research towards the idea of remote diagnosis, care and monitoring of physiological parameters. Thus, the wearable and eskin devices arose to be embedded in the standard medical equipment. In this work, a preliminary study on flexible AJP-printed temperature sensors is reported in order to propose a novel approach to evaluate infection sites, monitor the body temperature and compensate the effects of temperature on other on-body sensors. Two different geometries are proposed, designed, produced, evaluated and compared. The results shown a similar dependance on temperature (average TCR = $2.5 \cdot 10^{-3}$ °C^{-1}) and the dependance on substrate deformation was enquired as well as the geometrical features of the sensors.**

I. INTRODUCTION

In the latest years, the need of a renewed paradigm for healthcare arose. The idea of remote diagnosis, care and in general of physiological parameters monitoring is appealing [1]. To address this arising need, new technology arose in the latest years trying to miniaturize the standard medical equipment to fit it in a wearable device [2]. Wearable devices are now widespread both for selfcare monitoring, sports medicine, diagnostics, prosthetics and feedback treatment for rehabilitation [3]–[5]. At the state of art, most wearable devices are wrist watches or bands that provide lower-quality signal collection than the ones that could be collected by skin-like devices [6]. Those devices can be called eskins devices and can be defined as large area and flexible devices that can cover part of the human body mimicking the skin. Those embeds different sensors to collect information both from the environment end from the body itself [7]–[11]. To produce those devices different techniques have been explored in the literature including both classical techniques of microfabrication (e.g. chemical vapor deposition, sputtering, photolithography, etc.) and printed techniques. The latter provide a quicker prototyping process, offers a wide set of different materials and can be adapted to work even on non-planar surfaces. Among the possible printed techniques, aerosol jet printing (AJP) was selected for this preliminary study thanks to its flexibility in terms of available viscosity of the inks and its fully digital and maskless production process. Thus, this technique allows a quick and cheap prototyping that is ideal in the research frame. AJP basic principles are already described in literature [12]. Briefly, three flows of gases are used to atomize the ink (atomizer flow), control the dimension of the particles (exhaust flow) and to focus the aerosol on the nozzle (sheath flow). The eskin sensors cover a plethora of applications such as force sensing, humidity detection, temperature, strain/twist, limb bending, biopotentials and biomarkers. Temperature sensors are of particular interest in the medical field such as for infective diseases and illness control [13]–[15]. Moreover, temperature is a common influence variable for other sensors such as strain gauges and electrochemical sensors [16], [17]. Thus, monitoring the temperature on site and real time can help to compensate its effects on other sensors to obtain reliable information. In the literature different kind of temperature sensors are reported, each featuring its pros and cons. Positive and Negative temperature coefficient thermistors (PTC and NTC respectively) as well as integrated temperature sensors are rigid and usually employ non-printable materials. Thermocouples require to know the temperature at the reference junction and therefore this is not feasible in many wearable applications. On the other hand, resistive temperature sensors (RTD) use the thermoresistive effect of metals allowing simple geometry designs and a production process compatible with printed electronics. Thus, among the different typologies of temperature sensors, RTDs are the most suitable for a fully printed, compact and flexible design. Flexibility, however, may vary the resistance of the sensor due to the effects of deformation of the substrate. Thus, the aim of this work is to propose a preliminary study on flexible AJP-printed temperature sensors. The proposed printed sensors will be characterized analyzing their geometry and the effects of substrate deformation.

II. MATERIALS AND METHODS

The design process of the sensor started analyzing different possible geometries. Among the possible the ones in Fig. 1 where selected. A standard strain gauge-like geometry (Fig. 1a) was selected as state of art and designed following commercial strain gauges. On the other hand, a double helix geometry was further proposed to reduce the area of the sensor and uniform the dependance on strain in

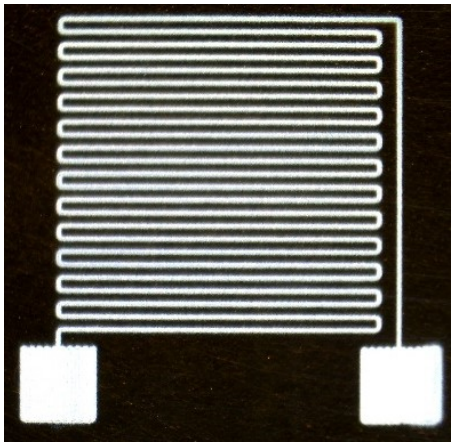

(a)

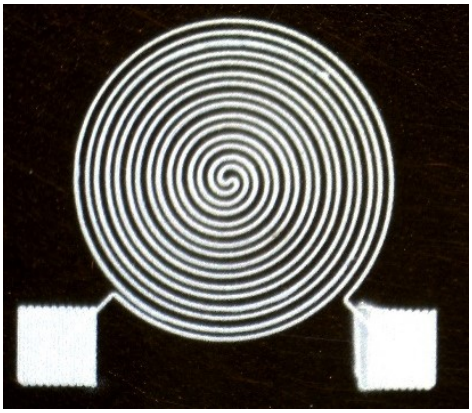

(b)

Fig. 1. Microscope images of the different geometries evaluated in this work. A standard strain gauge geometry (a) and the proposed double helix (b)

each direction. Both the geometries were designed with similar length and with target linewidth of 150 µm.

The devices were printed on a flexible polimide foil (Kapton, DuPont de Nemours, Luxembourg, Grand Duchy of Luxembourg) using an Aerosol Jet Printer (AJ300, Optomec, Albuquerque, NM, USA). The substrate was selected considering the most common substrates used for eskins as well as the mechanical and electrical proprieties of the available materials [18]. Among the possible inks, a silver ink (Smart Aero, Genesink, Rousset, France) was selected and deposed after cleaning the substrate with ethanol to increase the ink-substrate adhesion. The selected process parameters were 1240 SCCM for the sheath flow, 850 SCCM for the atomizer flow and 800 SCCM for the exhaust flow with a process speed of 3 mm/s. The ink was thermally cured in an oven at 150 °C for 60 minutes according to the producers' specifications to achieve proper electrical conductivity.

A. Process Evaluation

In order to evaluate the outcome of the production process two sets of evaluations were carried on. At first, the sensors were inspected using an optical microscope NB50T (Orma Scientific, Sesto San Giovanni, Milan, Italy) equipped with a trinocular zoom 0.8x–5x–LED and a camera. In this evaluation step the lines were analyzed and measured. Then a Filmetrics Profilm 3D optical profilometer (Filmetrics Inc., 10655 Roselle St., San Diego, CA, USA) was used to evaluate the thickness of the printed features.

B. Resistivity Evaluation

In order to calculate the average resistivity (ρ), a set of three straight, 2 cm-long lines were printed. The resistivity (ρ) was then calculated using equation 1 where l is the length (known by design), R is the measured resistance and S is the average cross-section area of the conductor. This was evaluated through the optical profilometer, measuring the profile in three different positions for each sample.

$$\rho = R \cdot \frac{S}{l} \tag{1}$$

The resistance was evaluated using a digital bench-top multimeter Hewlett–Packard 34401a (HP, Palo Alto, CA, USA) and a 4-wire technique.

C. Sensitivity to Substrate Bending

To evaluate the differences between the two geometries different features were evaluated. The behavior of the two geometries under deformation was evaluated. Briefly, the sensors were placed on a planar substrate, then they were bended onto a cylinder with radius 30 mm. The selected deformation axis was the one that maximized the sensibility of the devices. The variation in resistance is measured by a multimeter Hewlett–Packard 34401a with a 4-wire technique. One sample for each geometry was analyzed in bending.

D. Sensitivity to Temperature Variations

In order to evaluate the behavior of the sensors in relation with the temperature they were placed on top of an hotplate and covered with a beaker to avoid airflows. A pt100 was mounted nearby to provide a reliable measurement of the temperature applied to the sensors. All the measurements of resistance were performed using a 4-wire technique with a set of the aforementioned Hewlett–Packard 34401a multimeters connected with a computer through a GPIB interface and controlled by a LabVIEW interface that samples the signals at 1 Hz.

At first a set of increasing temperature setpoints

ranging from room temperature up to 80°C were imposed each for 20 minutes. Then the hotplate was switched off and left to cool down back to room temperature. The collected data were then analyzed in MATLAB to obtain the temperature coefficient of resistance (TCR, α in the equation) and the resistance at 0°C (R_0) to be used in the calibration relation shown in equation 2.

$$R = R_0 \cdot (1 + \alpha T) \quad (2)$$

III. RESULTS AND DISCUSSION

A. Process Evaluation

The microscope evaluation aimed to measure the average line width and its variations in the production process. On the double helix geometry, the width was evaluated as (137 ±19) µm, while it resulted (157 ±16) µm for the strain gauge geometry. In the latter a smaller standard deviation was achieved due to the use of straight lines. In fact, straight lines are a simple trajectory that is easier to produce with linear stepper motors employed by the AJP. The analysis at the optical profilometer provided a set of clear images on the thickness of the printed traces revealing an uneven deposition of the functional material and an average thickness of 0.6 µm for the double helix and 0.4 µm for the classical strain gauge geometry.

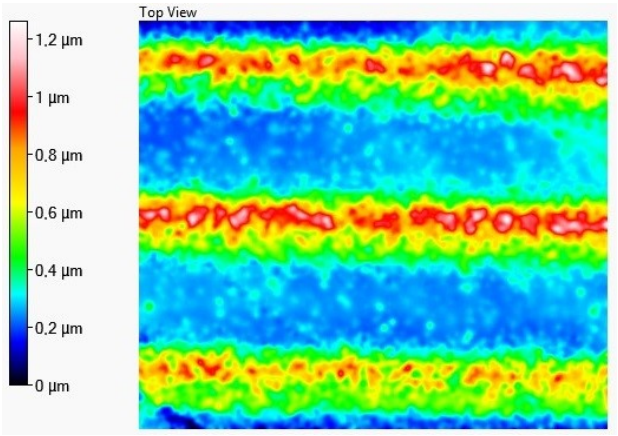

(a)

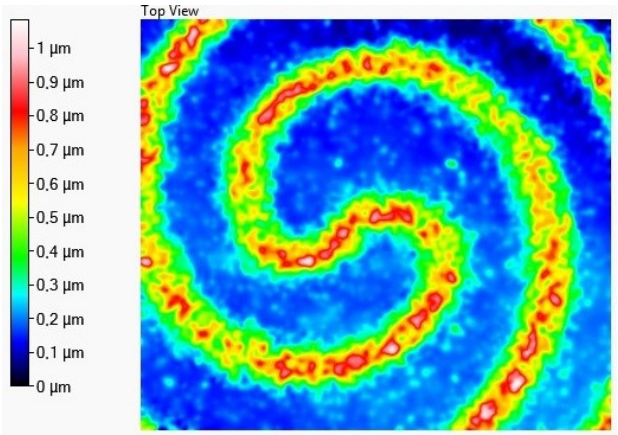

(b)

Fig. 2. Thickness of the printed lines obtained for the standard strain gauge geometry (a) and for the proposed double helix (b)

B. Resistivity Evaluation

The average line width for the straight lines used for the resistivity evaluation resulted (52.3±4.5) µm. The average cross-section area was evaluated by integrating the data collected with the optical profilometer through a MATLAB program. An average of (150.3±30.0) µm^2 was obtained. The measured line-resistance resulted on average (10.90±4.85) Ω. The obtained average resistivity resulted (8.2±4.0) Ωcm that resulted comparable with the one presented in the ink datasheet.

C. Sensitivity to Substrate Bending

The resistance variation due to substrate deformation is shown in Fig. 3. The two geometries presented a slightly different behavior when subjected to the same stimulus. The double helix geometry (in blue in the image) presented a fast-rising spike that settled then to a lover value and has equally fast rising and falling times. On the other hand, the strain gauge geometry (in red in the image) presented a slower rising and falling times similar to a first order system behavior. Both the geometries however presented a small variation of the resistance evaluated in the rest position.

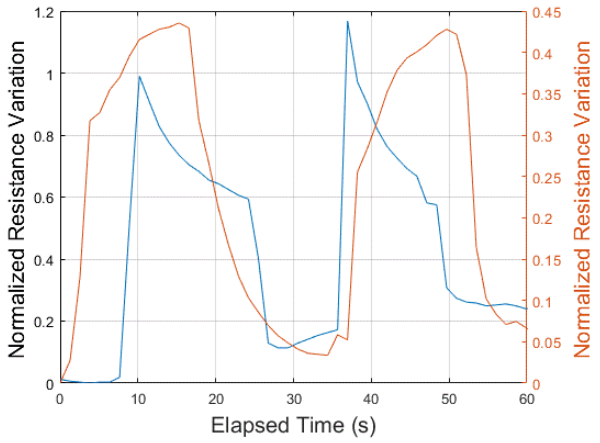

Fig. 3. Stress-induced resistance variation in the sensors for double helix (blue) and strain gauge (red) geometries

D. Sensitivity to Temperature Variations

The relative variations of sensors resistance to temperature are shown in Fig. 4. The printed devices present similar behavior perfectly comparable to the one of the Pt100 used as reference sensor. Moreover, the collected data was used to obtain a resistance-temperature

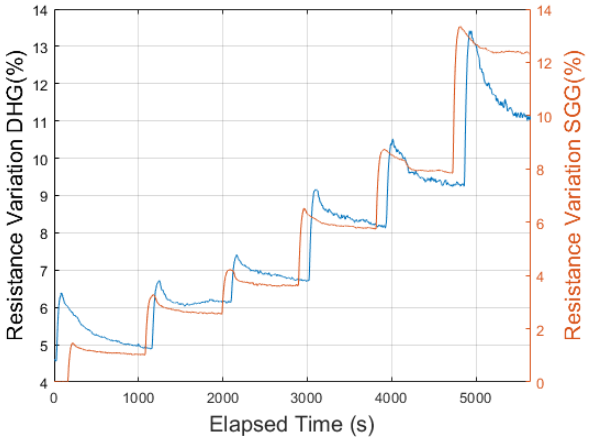

Fig. 4. Temperature dependance of the sensors shown in time. The resistance variation for the double helix geometry is reported in blue, while the one of the strain gauge geometry is reported in red

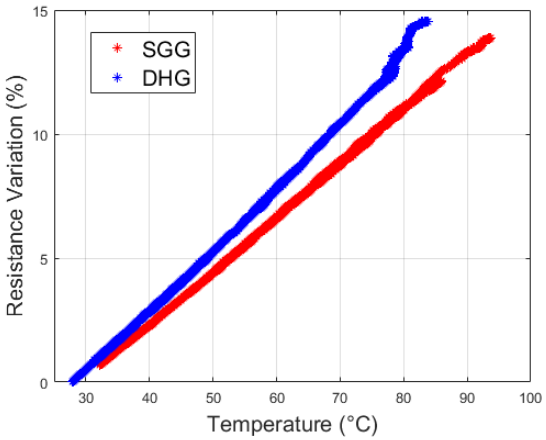

Fig. 5. Resistance-Temperature plot for the strain gauge geometry (in red) and the double helix geometry (in blue)

characteristics for each sensor (Fig. 5). Both resulted linear, with reduced hysteresis. As regards the sensibility, the double helix geometry performed slightly better with a TCR of $2.7\pm0.3\cdot10^{-3}$ °C^{-1} than the strain gauge geometry (TCR=$2.3\pm0.1\cdot10^{-3}$ °C^{-1}).

IV. CONCLUSIONS

In this work, two different geometries were preliminary analyzed in order to propose a fully AJP printed and flexible temperature sensor that can be used in the eskin application field. The sensors were designed and produced. Then the production process, the design idea and the materials were evaluated. The average resistivity of the conductive ink was evaluated to be 8.2 Ωcm and comparable with the one presented in the material datasheet. Microscope analysis provided an average line width of 137 µm for the double helix geometry and 157 µm for the strain gauge one. A preliminary evaluation of the resistance variation under deformation was performed and revealed that the two geometries perform in different way, but the double helix presented lower variations. Considering on the other hand the effects of temperature, the two geometries performed similarly and resulted linear, with reduced hysteresis and similar sensibility. Even though, those results are promising, different future research topics are still open, such as exploring different materials and new geometries, as well as designing a whole system whose metrological characteristics can meet application requirements, such as a temperature resolution of 0.1°C.

REFERENCES

[1] S. Zhang, S. Li, Z. Xia, and K. Cai, "A review of electronic skin: Soft electronics and sensors for human health," *J. Mater. Chem. B*, vol. 8, no. 5, pp. 852–862, 2020, doi: 10.1039/c9tb02531f.

[2] K. K. Yeung, T. Huang, Y. Hua, K. Zhang, M. M. F. Yuen, and Z. Gao, "Recent Advances in Electrochemical Sensors for Wearable Sweat Monitoring: A Review," *IEEE Sens. J.*, vol. 21, no. 13, pp. 14522–14539, 2021, doi: 10.1109/JSEN.2021.3074311.

[3] A. C. Bunea *et al.*, "E-skin: The dawn of a new era of on-body monitoring systems," *Micromachines*, vol. 12, no. 9, 2021, doi: 10.3390/mi12091091.

[4] E. Cantu *et al.*, "Printed Multi-EMG Electrodes on the 3D Surface of an Orthosis for Rehabilitation: A Feasibility Study," *IEEE Sens. J.*, vol. 21, no. 13, pp. 14407–14417, 2021, doi: 10.1109/JSEN.2021.3059308.

[5] S. Tonello *et al.*, "Preliminary study of a flexible printed multi-sensing platform for electromyography and lactate measuring during rehabilitation," *2021 IEEE Int. Symp. Med. Meas. Appl. MeMeA 2021 - Conf. Proc.*, 2021, doi: 10.1109/MeMeA52024.2021.9478729.

[6] H. S. Oh, C. H. Lee, N. K. Kim, T. An, and G. H. Kim, "Review: Sensors for biosignal/health monitoring in electronic skin," *Polymers (Basel).*, vol. 13, no. 15, 2021, doi: 10.3390/polym13152478.

[7] J. Huang *et al.*, "Editors' Choice—Review—Impedance Response of Porous Electrodes: Theoretical Framework, Physical Models and Applications," *J. Electrochem. Soc.*, vol. 167, no.

16, p. 166503, 2020, doi: 10.1149/1945-7111/abc655.

[8] G. Wolterink, R. Sanders, F. Muijzer, B. van Beijnum, and G. Krijnen, “3D-printing soft sEMG sensing structures,” in *2017 IEEE SENSORS*, 2017, pp. 1–3, doi: 10.1109/ICSENS.2017.8233935.

[9] K. Kim *et al.*, “Low-voltage, high-sensitivity and high-reliability bimodal sensor array with fully inkjet-printed flexible conducting electrode for low power consumption electronic skin,” *Nano Energy*, vol. 41, no. June, pp. 301–307, 2017, doi: 10.1016/j.nanoen.2017.09.024.

[10] P. S. Das and J. Y. Park, “A flexible touch sensor based on conductive elastomer for biopotential monitoring applications,” *Biomed. Signal Process. Control*, vol. 33, pp. 72–82, 2017, doi: 10.1016/j.bspc.2016.11.008.

[11] M. Chung, G. Fortunato, and N. Radacsi, “Wearable flexible sweat sensors for healthcare monitoring: A review,” *J. R. Soc. Interface*, vol. 16, no. 159, 2019, doi: 10.1098/rsif.2019.0217.

[12] M. Borghetti, E. Cantù, E. Sardini, and M. Serpelloni, “Future sensors for smart objects by printing technologies in Industry 4.0 scenario,” *Energies*, vol. 13, no. 22, 2020, doi: 10.3390/en13225916.

[13] H. S. Jeon, J. H. Kim, M. B. G. Jun, and Y. H. Jeong, “Fabrication of thermochromic membrane and its characteristics for fever detection,” *Materials (Basel).*, vol. 14, no. 13, 2021, doi: 10.3390/ma14133460.

[14] Y. Zhang *et al.*, “Flexible integrated sensing platform for monitoring wound temperature and predicting infection,” *Microb. Biotechnol.*, vol. 14, no. 4, pp. 1566–1579, 2021, doi: 10.1111/1751-7915.13821.

[15] A. Al-Halhouli, A. Albagdady, J. Alawadi, and M. A. Abeeleh, “Monitoring symptoms of infectious diseases: Perspectives for printed wearable sensors,” *Micromachines*, vol. 12, no. 6, pp. 1–35, 2021, doi: 10.3390/mi12060620.

[16] S. Yoon, H. Yoon, M. A. Zahed, C. Park, D. Kim, and J. Y. Park, “Multifunctional hybrid skin patch for wearable smart healthcare applications,” *Biosens. Bioelectron.*, vol. 196, no. October 2021, p. 113685, 2022, doi: 10.1016/j.bios.2021.113685.

[17] Y. Zhao, Y. Liu, Y. Li, and Q. Hao, “Development and application of resistance strain force sensors,” *Sensors (Switzerland)*, vol. 20, no. 20, pp. 1–18, 2020, doi: 10.3390/s20205826.

[18] Z. Yuan, S. T. Han, W. Gao, and C. Pan, “Flexible and Stretchable Strategies for Electronic Skins: Materials, Structure, and Integration,” *ACS Appl. Electron. Mater.*, vol. 4, no. 1, pp. 1–26, 2022, doi: 10.1021/acsaelm.1c00025.

25th IMEKO TC4 International Symposium
23rd International Workshop on ADC and DAC Modelling and Testing
IMEKO TC-4 2022
Brescia, Italy / September 12-14, 2022

A novel CS-based measurement method for radial artery pulse wave estimation

Jozef Kromka[1], Jan Saliga[1], Ondrej Kovac[1], Luca De Vito[2], Francesco Picariello[2], Ioan Tudosa[2]

[1]*Technical University of Kosice, Letna 9, 04200 Kosice, Slovakia*
[1]*e-mail addresses: {jozef.kromka, jan.saliga, ondrej.kovac}@tuke.sk*
[2]*University of Sannio, Department of Engineering, 82100 Benevento, Italy*
[2]*e-mail addresses: {devito, fpicariello, ioan.tudosa}@unisannio.it*

***Abstract* – This paper presents a compressive sampling (CS) based measurement method for estimation of radial artery pulse wave from bio-impedance (Bio-Z) variation. The mathematical steps of the method, the 3D electrical model of the wrist used for simulations as well as the preliminary simulation investigations are presented. The reported result shows that the proposed method could be used to estimate radial artery pulse wave, which could be further used in blood pressure (BP) computation.**

I. INTRODUCTION

Measurement of hemodynamic parameters such as BP, heart rate (HR), and pulse transit time (PTT) plays a vital role in the prevention of cardiovascular diseases (CVD), which are the leading cause of death worldwide [1]. Continuous monitoring of hemodynamic parameters could improve the diagnosis and help in the early prevention of CVD [2], [3]. The methods for hemodynamic parameters measurement are relying on bulky and uncomfortable specific instruments, thus they are not suitable to carry out continuous monitoring [4]. Therefore, long-term monitoring of a patient should be carried out by means of a non-invasive method based on wearable instrumentation.

In literature, several non-invasive methods for hemodynamic parameters measurement have been proposed [5]. The methods relying on Bio-Z [6, 7] measurement appears to be the most promising for hemodynamic parameter measurement by wearables. In [8], the pulsation of blood inside the artery is measured by means of Bio-Z sensors. Therefore, by measuring arterial pulse on two points along the artery, PTT can be obtained and this could be used to estimate BP [9]. Bio-Z measurement system used for continuous BP monitoring was developed also in [10], where a single-channel impedance plethysmography measurement device was implemented. This device injects current with a frequency of 100 kHz to perform the measurement. Another recent published Bio-Z measurement system was presented in [7]. To perform the measurement, the developed device injects current with a frequency of 50 kHz. From literature survey, Bio-Z based measurement systems use as excitation signal a sine-wave at different frequencies [5]. This suggests that the optimal excitation frequency may change and depend on the patient. A broadband signal can be used instead of a sine-wave for estimating the radial artery pulse wave. In this case, a pulsed signal needs to be injected into the patient and then the obtained response acquired by an analog-to-digital converter (ADC). As broader is the frequency spectrum of the injected signal as higher should be the sampling frequency of the ADC. This limits the use of this technique for wearable device implementations, where low sampling frequency ADC are utilized to keep low the energy consumption and the amount of acquired data. In this paper, a CS method is proposed with the aim of reducing the sampling frequency of the ADC under the required Nyquist rate, thus overcoming the above mentioned limit. As a result, the radial artery pulse wave estimation from Bio-Z variation is obtained and afterwards it could be used for BP estimation.

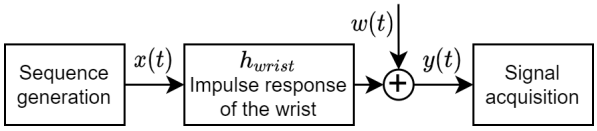

Fig. 1. The proposed measurement method.

The paper is organized as follows. In Section II, the mathematical formulation of the proposed method is presented. The preliminary experimental results obtained by means of simulation are reported in Section III. The main conclusion and some future work directions are drawn in Section IV.

II. THE PROPOSED METHOD

In this paper, the proposed measurement method is based on the determination of the impulse response of the radial artery on the wrist by exploiting a CS-based technique, followed by the estimation of the pulse wave propagation signal from the maximum values of the obtained impulse responses for each frame (i.e., time stamp).

The simplified block diagram of the proposed measurement method is shown in Fig. 1. This CS technique has its roots based on the DAC frequency response characterization method introduced in [11, 12]. Herein, in order to obtain the impulse response estimation of the wrist (i.e.,

$h_{wrist}(t)$), a pseudo-random binary sequence (PRBS) is used as an excitation signal. A finite number of input $x(n)$, with $n = 0, \ldots, N+L-1$ are considered for PRBS signal, where N and L are defined as follows: (i) $N \cdot T_u$ represents the duration of the acquisition window, and (ii) $L \cdot T_u$ is the maximum duration of the system impulse response, while T_u is the update interval of $x(n)$ samples. Let us model the $y(t)$ signal (see Fig. 1) as:

$$y(t) = x(t) * h_{wrist}(t) + w(t), \tag{1}$$

where $x(t)$ is defined as follows:

$$x(t) = \sum_{n=-L}^{N-1} x(n) \cdot \delta(t - nT_u). \tag{2}$$

In eq.(1), $w(t)$ is the additive white Gaussian noise (AWGN), which affects the $y(t)$, and in eq.(2), $\delta(t)$ is the Dirac's impulse function. Thus, the resulting $y(t)$ is further processed by an anti-aliasing filter and sampled by an ADC with sampling frequency f_{ADC}.

By defining $h_c(t) = h_{wrist}(t) * h_s(t)$, where $h_s(t)$ is the impulse response of the sampling system, the final impulse response $y_f(t)$ can be rewritten (i.e., cascade) as [12]:

$$\begin{aligned} y_f(t) &= x(t) * h_c(t) + w_f(t) = \\ &= \int_{-\infty}^{\infty} x(t-\tau) h_c(\tau) d\tau + w_f(t), \end{aligned} \tag{3}$$

where, $w_f(t) = w(t) * h_s(t)$. By taking into account eq.(2), while considering $h_c(t)$ as time invariant during the $x(n)$ generation, eq.(3) can be expressed as follows:

$$y_f(t) = \sum_{n=-L}^{N-1} x(n) \cdot h_c(t - nT_u) + w_f(t). \tag{4}$$

Eq.(4) can be discretized with a sampling period T_u, [12]:

$$\begin{aligned} &y_f(mT_u) = \\ &\sum_{n=-L}^{N-1} x(n) \cdot h_c[(m-n)T_u] + w_f(mT_u). \end{aligned} \tag{5}$$

In matrix form, it can be expressed as:

$$\mathbf{z} = \mathbf{X} \cdot \mathbf{h_c} + \mathbf{w_f}, \tag{6}$$

where $\mathbf{X}$ is represented as follows:

$$\mathbf{X} = \begin{bmatrix} x(0) & x(-1) & \cdots & x(-L+1) \\ x(1) & x(0) & \cdots & x(-L) \\ \vdots & \vdots & \ddots & \vdots \\ x(N-1) & x(N-2) & \cdots & x(N-L-2) \end{bmatrix}, \tag{7}$$

and $\mathbf{z}$, $\mathbf{w_f}$ and $\mathbf{h_c}$ are written as:

$$\begin{aligned} \mathbf{z} &= [y_f(0), y_f(T_u), \ldots, y_f((N-1)T_u)]^T \\ \mathbf{w_f} &= [w_f(0), w_f(T_u), \ldots, w_f((N-1)T_u)]^T. \\ \mathbf{h_c} &= [h_c(0), h_c(T_u), \ldots, h_c((N-1)T_u)]^T \end{aligned} \tag{8}$$

The sampled version of the system impulse response is considered K-sparse in the time domain, considering that it contains K non-zero coefficients, where $K < L$. To exploit the sparsity of the system impulse response in the time domain, the ADC can work at a sampling frequency lower than the Nyquist frequency $f_u = 1/T_u$. By using a much lower sampling frequency, during the time window $N \cdot T_u$, the ADC will acquire only M samples, $m = 0, ...M-1$, expressed as $y(m) = [y(1), y(2), \ldots, y(M-1)]^T$. Here, the downsampling factor represents the compression ratio, $CR = f_u/f_{ADC}$. This operation can be modeled as follows:

$$\mathbf{y} = \mathbf{R} \cdot \mathbf{X} \cdot \mathbf{h_c} + \mathbf{w_f}. \tag{9}$$

In eq.(9), $\mathbf{R}$ is a $M \times N$ matrix, which represents the downsampling process by CR factor. If $M < L$ in the time domain, then $\mathbf{h_c}$ can be estimated by solving the following minimization problem:

$$\begin{aligned} \widehat{\mathbf{h_c}} &= arg \min_{\mathbf{h_c}} ||\mathbf{h_c}||_1 \\ subject\ to &: \mathbf{y} = \mathbf{R}\mathbf{X}\mathbf{h_c}, \end{aligned} \tag{10}$$

where $|| \cdot ||_1$ represents the l_1 norm operator. A solution to the problem in eq.(10) can be obtained by using various algorithms [13]. However, in this study, the orthogonal matching pursuit (OMP) algorithm was used [14].

According to [7], the impedance of the radial artery changes with the the radial artery area. Therefore, in present study, the impedance change that would cause a proportional change in the impulse response was assumed. In consequence, the pulse wave propagation signal $x_t[n]$ is obtained from the maximum values of the obtained impulse responses for each frame duration.Thus, $\widehat{x}_t[n]$ is obtained from maximum values of $\widehat{h}_{wrist}(t)$.

III. SIMULATION ANALYSIS

A. *The 3D electrical model of the wrist*

In this work, a modified version of the wrist 3D electrical model described in [15] was considered. To this aim, two different datasets were considered. The first dataset [16] was used to define the electrical impedance of tissues. This dataset contains dielectric properties of several biological tissues from frequency $f = [10\,\text{Hz} - 100\,\text{GHz}]$. The second dataset [17] was used to model blood flow inside the radial artery. This dataset contains blood pressure, blood flow speed, and artery area values for different arteries.

The developed model consists of 3D impedance voxels as shown in Fig. 2. This impedance voxel is a cube made of

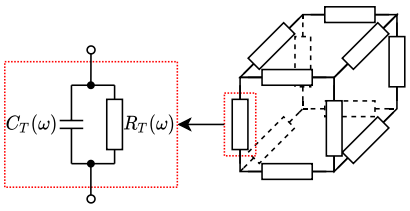

Fig. 2. The equivalent electrical circuit of the voxel.

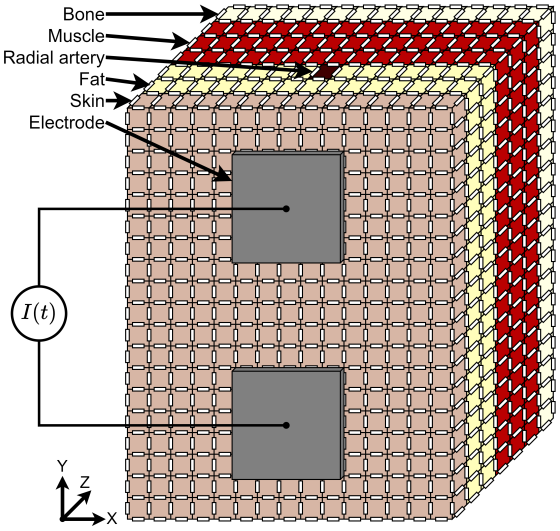

Fig. 3. The developed 3D wrist model.

parallel combinations of resistance and capacitance values. The resistance $R_T(\omega)$ and capacitance $C_T(\omega)$ are calculated as follows. First, the complex permittivity is obtained for the required frequency from the dataset in [16]. Then impedance is calculated by the following formula [18]:

$$Z_T(\omega) = \frac{1}{j\omega C_0 \varepsilon_T^*(\omega)}, \tag{11}$$

where $\omega = 2\pi f$, $\varepsilon_T^*(\omega)$ is the complex permittivity of tissue and $C_0 = \frac{A\varepsilon_0}{d}$, with A is the area of the tissue, d is the depth, and ε_0 is the permittivity of vacuum. Since the model is created by cube voxels, thus $A = d \cdot d$, then the eq.(11) can be simplified as:

$$Z_T(\omega) = \frac{1}{j\omega d \varepsilon_0 \varepsilon_T^*(\omega)}. \tag{12}$$

$R_T(\omega)$ and $C_T(\omega)$ are calculated from $Z_T(\omega)$ as follows:

$$R_T(\omega) = \frac{1}{\mathbf{Re}\left(\frac{1}{Z_T(\omega)}\right)}, \; C_T(\omega) = \frac{\mathbf{Im}\left(\frac{1}{Z_T(\omega)}\right)}{\omega}. \tag{13}$$

The impedance voxels with their respective values are then connected in a 3D configuration, thus forming the 3D wrist electrical model (see Fig. 3). The size of the voxel edge (i.e., d) was set to 2 mm, and the used type of tissues are skin, fat, blood, muscles, and bone. The total size of the 3D wrist model is 30×38×14 mm, where: (i) the first layer is the skin layer, (ii) the second and third layers are fat, (iii) a radial artery which is located around 2 mm inside the fat layer under the skin [19], (iv) three layers are the muscle layer, and (v) the bottom layer which is modeled as a bone. The Bio-Z sensing electrodes have size of 10×10 mm and are placed on top of the skin, positioned 10 mm from each other, with radial artery in the middle, below the electrodes.

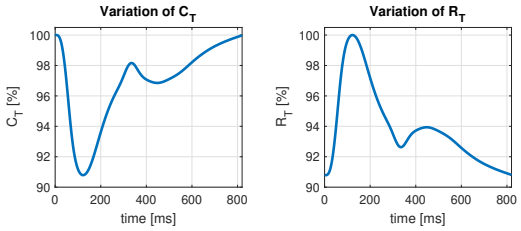

Fig. 4. Percentage variation of R_T and C_T in time.

In order to simulate the blood flow inside the radial artery, the dataset of the first subject (which consists of 411 points sampled at 500 Hz) in [17] was used to evaluate how the capacitance and resistance were changing (i.e., the area data were used in eqs.(11) and (13)). From the simulation results, a variation about 10 % for capacitance and resistance of the radial artery was obtained (e.g., proportionally to the area of the radial artery R_T was increasing while C_T was decreasing).

Thus, the obtained time variations shown in Fig. 4 were used to model radial artery voxels during blood flow. In these voxels, the values of capacitance and resistance were changed according to their variation at an imposed time stamp of 2 ms. For example, the next voxel along the y-axis, has its own variation for the successively time stamp that is considered, and so on.

The netlist of the 3D wrist electrical model was generated by using MATLAB, while the simulation was performed by means of LTspice. Since there are different values of resistance and capacitance with the frequency variation, the model was made in a way that for each frequency, a new netlist is generated and then it is simulated by using AC analysis. In order to obtain the impedance value, a current source of 500 μA was used as shown in Fig. 3, while the voltage on the electrodes was read and the complex impedance was calculated.

In order to simulate the proposed CS-based measurement method, a local dataset was generated using the previously described 3D wrist electrical model, consisting of 411 frequency responses of the wrist impedance. Each frequency response represents the state of the wrist at 411 time stamps (i.e., each of 2 ms) according to blood flow inside the radial artery. The frequency responses are recorded for over 500 different frequency points linearly distributed from 10 Hz to 1 GHz.

B. Simulation setup

In Fig. 5, a simplified circuit model describing the adopted simulation setup is depicted. Herein, R_i is a resistor used to reduce the injected current into the body and to measure the output signal $y(t)$, $Z_{wrist}(\omega)$ is the impedance of the wrist generated by the 3D wrist electrical model. The output signal $y(t)$ is obtained by calculating the current flow according to the Ohm's law, by obtaining the

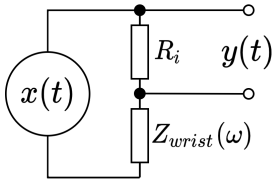

Fig. 5. Simplified simulation circuit.

impedance change of the wrist $Z_{wrist}(\omega)$ depending on the $x(t)$ frequency, and by applying the fast Fourier transform (FFT) of the voltage-frequency spectrum of $x(t)$. Furthermore, by using inverse FFT, the current flow in the time domain is evaluated. This current is then multiplied by the resistance R_i and thus, the output signal $y(t)$ is obtained. Since the developed dataset contains a discretized version of the frequency response different from the simulated one, the dataset was interpolated to estimate the missing frequencies components needed for the simulations.

In particular, the discrete time processing steps are summarized in the following. The $x[n]$ signal (e.g., PRBS sequence) is generated having a length of $N + L$ samples. Then the sequence is used to generate $x(t)$ by simulating the output of a digital-to-analog converter (DAC) working at a simulation frequency f_{sim}. The DAC's output is modelled to update the samples of $x[n]$ at T_u with n_{DAC} resolution, FS_{DAC} full-scale and SNR_{DAC} as signal to noise ratio (SNR). In the simulation, the low-pass filtering of $x(n)$ with the order of filter $Nord_{DAC}$ and with the cut-off frequency fl_{DAC} was also considered. Then $x(t)$ was used to stimulate the $h_{wrist}(t)$ thus to obtain $y(t)$ according to the proposed method (see Fig. 5).

The acquisition of $y(t)$ was realized by simulating: (i) an ADC having $f_{ADC} = f_u/CR$ sampling frequency, n_{ADC} bit resolution, and FS_{ADC} full scale input voltage, and (ii) an anti-aliasing filter having $Nord_{ADC}$ the order and fl_{ADC} cutoff frequency. In Table 1, all the values of the above listed parameters are given.

The proposed CS-based method was then evaluated for different CR in terms of root mean square error $RMSE$ as main figure of merit. The $RMSE$ was calculated from the magnitude of the CS-based estimated impulse response $\widehat{H}(k/T_u)$, respect to the actual impulse response, $H(k/T_u)$ as:

$$RMSE\big|_{dB} = \sqrt{\frac{1}{L}\sum_{k=0}^{L-1}\left[|\widehat{H}(k)|_{dB} - |H(k)|_{dB}\right]^2}. \quad (14)$$

Furthermore, Monte Carlo analyses have been performed on 100 trials, always with a different $x[n]$, and the resulting $RMSE$ values were averaged and expressed as $RMSE_m$.

The reconstruction quality of the pulse wave propagation signal inside the radial artery was evaluated in terms of

Table 1. Parameters used for simulation.

f_{sim}	8 MHz
f_{update}	1 MHz
n_{DAC}	12 bit
FS_{DAC}	2 V
SNR_{DAC}	70 dB
$Nord_{DAC}$	100
fl_{DAC}	1.2 MHz
R_i	500 Ω
CR	2, 4, 8, 16
N	1024
L	1024, 512, 256, 128
n_{ADC}	16 bit
FS_{ADC}	2 V
$Nord_{ADC}$	2000
fl_{ADC}	0.45 MHz

percentage root mean squared difference PRD [13]:

$$PRD = \sum_{n=1}^{N} \frac{||x_t[n] - \widehat{x}_t[n]||_2}{||x_t[n]||_2} \cdot 100[\%], \quad (15)$$

where, $x_t[n]$ is ideal pulse wave propagation signal, $\widehat{x}_t[n]$ is reconstructed pulse wave propagation signal, and $||\cdot||_2$ represents the l_2 norm operator.

C. Preliminary results

The first performed simulation test was focused to observe how CR affects on the reconstruction quality of each $\widehat{h}_{wrist}(t)$. The results for the considered CR and L values reported in Table 1 are shown in Fig. 6, where the $RMSE_m$ values were plotted as red dots, and the maximum and the minimum values as blue bars.

The next evaluated simulation test was concentrated to observe the influence of L length on the reconstruction quality of each $\widehat{h}_{wrist}(t)$, by considering three different CR values and various L lengths. In Fig. 7, the $RMSEm$ variation for $CR = 2$ is shown, for values of L changing from 576 to 1024 with step of 64, where it can be observed that there is no significant changes in $RMSEm$ variation up to $L = 768$.

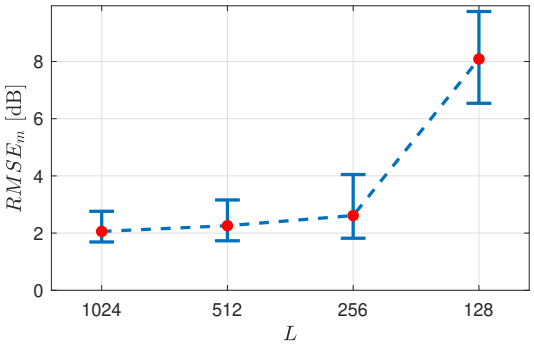

Fig. 6. $RMSE_m$ variation against CR and L.

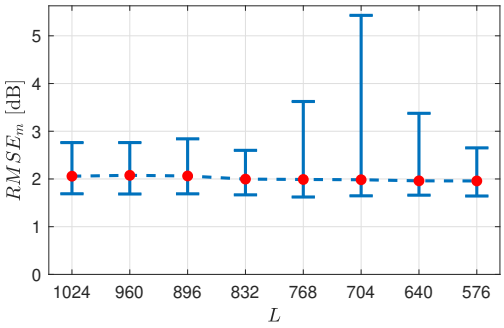

Fig. 7. $RMSE_m$ variation with $CR = 2$ against L.

In Fig. 8, the obtained $RMSEm$ variations for $CR = 4$ are shown, by considering L changing from 320 to 1024 with step of 64. Similarly, as in the previous case, there is no significant changes in $RMSEm$ variation up to $L = 320$.

At the end of the second experiment, $RMSEm$ results for $CR = 8$ were evaluated. The results are shown in Fig. 9. The simulation was performed for L from 192 to 1024 with step of 64.

In this case, $RMSEm$ changes against the number of the adopted L. In particular, the $RMSE$ averages slightly decrease with the increasing of L. From 320 the average started to rise again, but the minimum values were still declining. The best $RMSE$ was obtained for $L = 192$. The results below 192 are not shown because the method could not reconstruct the impulse response with a lower number of L.

The last performed simulation analysis was carried out with the aim to observe the variation of the $\widehat{x}_t[n]$ respect to $x_t[n]$. Because of the reconstruction error, the blood propagation wave contains a high amount of high-frequency noise. Therefore the obtained results were filtered with a filter with cutoff frequency of 10 Hz. Three different simulations were performed for $CR = 2, 4, 8$. The results are shown in Fig. 10.

The value of PRD was calculated for the reconstructed $\widehat{x}_t[n]$ according to the reference pulse wave $x_t[n]$ signal (i.e., actual, obtained without using CS) shown in Fig. 10 a). Thus, for the case b) where $CR = 8$, $PRD = 11.668\%$ was obtained, for case c) with $CR = 4$, $PRD = 10.720\%$,

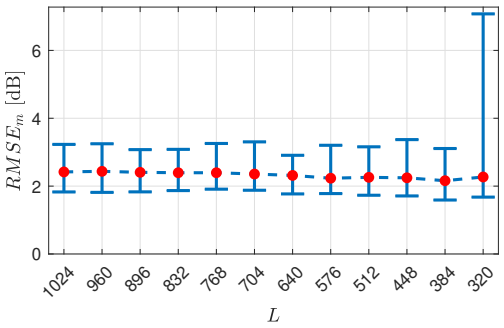

Fig. 8. $RMSE_m$ variation with $CR = 4$ against L.

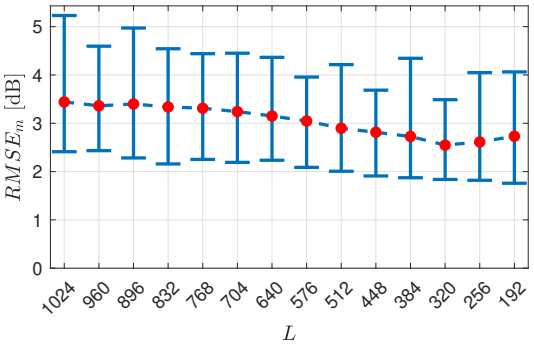

Fig. 9. $RMSE_m$ variation with $CR = 8$ against the L.

while for case d) where the $CR = 2$ the $PRD = 7.954\%$ was obtained. In all cases, the estimated and reconstructed pulse wave propagation signal can be utilized to calculate PTT in a further processing step. Consequently, in order to compute PTT, data coming from two pulse wave propagation signals of the blood circulating for radial artery are needed together with their known distance. In this case, the same proposed measurement method could be used with two additional Bio-Z electrodes placed to a known distance.

IV. CONCLUSION AND FUTURE WORK

In this paper, a novel measurement method using CS for estimating the pulse wave propagation which can be used as a non-invasive technique for BP assessment was presented. The method exploits the time domain sparsity of the impulse response of the wrist. As it was expected, the proposed measurement method based on CS could be utilized to develop a BP sensing system. The obtained simulation results confirmed that the impulse response of the

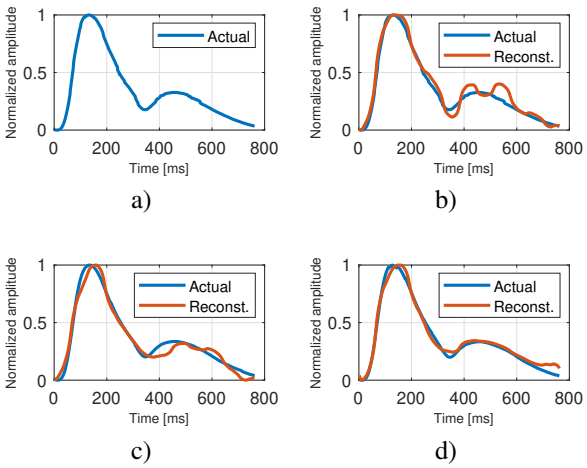

Fig. 10. a) actual pulse wave propagation, b) reconstruction of pulse wave propagation with $CR = 8, L = 320$, $PRD = 11.668\%$, c) reconstruction of pulse wave propagation with $CR = 4, L = 384$, $PRD = 10.720\%$, d) reconstruction of pulse wave propagation with $CR = 2, L = 640$, $PRD = 7.954\%$.

wrist is changing according to the change in blood flow area inside the radial artery. The simulations also proved that the proposed CS-based measurement method is able to sense this change in the impulse response.

Further work is directed to: (i) implement a hardware prototype, (ii) improve the simulation model, (iii) search for optimal configuration parameters for the proposed measurement method in order to maximize the reconstruction quality of the pulse wave, and (iv) assess the comparison of the experimental results with the results obtained in simulations.

ACKNOWLEDGMENT

The work is a part of the project supported by the Science Grant Agency of the Slovak Republic (No. 1/0413/22).

REFERENCES

[1] R. Jagannathan, S. A. Patel, M. K. Ali, and K. Narayan, "Global updates on cardiovascular disease mortality trends and attribution of traditional risk factors," *Current diabetes reports*, vol. 19, no. 7, pp. 1–12, 2019.

[2] G. Parati, G. S. Stergiou, E. Dolan, and G. Bilo, "Blood pressure variability: clinical relevance and application," *The Journal of Clinical Hypertension*, vol. 20, no. 7, pp. 1133–1137, 2018.

[3] M. H. Mehlum, K. Liestøl, S. E. Kjeldsen, S. Julius, T. A. Hua, P. M. Rothwell, G. Mancia, G. Parati, M. A. Weber, and E. Berge, "Blood pressure variability and risk of cardiovascular events and death in patients with hypertension and different baseline risks," *European heart journal*, vol. 39, no. 24, pp. 2243–2251, 2018.

[4] A. Barszczyk and K. Lee, "Measuring blood pressure: from cuff to smartphone," *Current Hypertension Reports*, vol. 21, no. 11, pp. 1–4, 2019.

[5] T. Panula, J.-P. Sirkia, D. Wong, and M. Kaisti, "Advances in non-invasive blood pressure measurement techniques," *IEEE Reviews in Biomedical Engineering*, pp. 1–1, 2022.

[6] S. Grimnes and O. G. Martinsen, *Bioimpedance and bioelectricity basics*. Academic press, 2011.

[7] T.-W. Wang, W.-X. Chen, H.-W. Chu, and S.-F. Lin, "Single-channel bioimpedance measurement for wearable continuous blood pressure monitoring," *IEEE Transactions on Instrumentation and Measurement*, vol. 70, pp. 1–9, 2021.

[8] R. Mukkamala, J.-O. Hahn, O. T. Inan, L. K. Mestha, C.-S. Kim, H. Töreyin, and S. Kyal, "Toward ubiquitous blood pressure monitoring via pulse transit time: Theory and practice," *IEEE Transactions on Biomedical Engineering*, vol. 62, no. 8, pp. 1879–1901, 2015.

[9] C. Poon and Y. Zhang, "Cuff-less and noninvasive measurements of arterial blood pressure by pulse transit time," in *2005 IEEE Engineering in Medicine and Biology 27th Annual Conference*, pp. 5877–5880, 2005.

[10] T. H. Huynh, R. Jafari, and W.-Y. Chung, "Noninvasive cuffless blood pressure estimation using pulse transit time and impedance plethysmography," *IEEE Transactions on Biomedical Engineering*, vol. 66, no. 4, pp. 967–976, 2018.

[11] L. De Vito, F. Picariello, and I. Tudosa, "A novel measurement method for dac frequency response characterization," in *24th IMEKO TC4 International Symposium and 22nd International Workshop on ADC and DAC Modelling and Testing, IWADC 2020*, pp. 395–400, International Measurement Confederation (IMEKO), 2020.

[12] L. De Vito, F. Picariello, S. Rapuano, and I. Tudosa, "A new built-in loopback test method for digital-to-analog converter frequency response characterization," *Measurement*, vol. 182, p. 109712, 2021.

[13] J. Šaliga, I. Andráš, P. Dolinskỳ, L. Michaeli, O. Kováč, and J. Kromka, "Ecg compressed sensing method with high compression ratio and dynamic model reconstruction," *Measurement*, vol. 183, p. 109803, 2021.

[14] J. A. Tropp and A. C. Gilbert, "Signal recovery from random measurements via orthogonal matching pursuit," *IEEE Transactions on information theory*, vol. 53, no. 12, pp. 4655–4666, 2007.

[15] B. Ibrahim, D. A. Hall, and R. Jafari, "Pulse wave modeling using bio-impedance simulation platform based on a 3d time-varying circuit model," *IEEE Transactions on Biomedical Circuits and Systems*, vol. 15, no. 1, pp. 143–158, 2021.

[16] S. Gabriel, R. W. Lau, and C. Gabriel, "The dielectric properties of biological tissues: III. parametric models for the dielectric spectrum of tissues," *Physics in Medicine and Biology*, vol. 41, pp. 2271–2293, nov 1996.

[17] P. H. Charlton, J. Mariscal Harana, S. Vennin, Y. Li, P. Chowienczyk, and J. Alastruey, "Modeling arterial pulse waves in healthy aging: a database for in silico evaluation of hemodynamics and pulse wave indexes," *American Journal of Physiology-Heart and Circulatory Physiology*, vol. 317, no. 5, pp. H1062–H1085, 2019. PMID: 31442381.

[18] J. R. Macdonald and E. Barsoukov, *Impedance spectroscopy: theory, experiment, and applications*. John Wiley & Sons, 2018.

[19] J. U. Kim, Y. J. Lee, J. Lee, and J. Y. Kim, "Differences in the properties of the radial artery between cun, guan, chi, and nearby segments using ultrasonographic imaging: a pilot study on arterial depth, diameter, and blood flow," *Evidence-Based Complementary and Alternative Medicine*, vol. 2015, 2015.

25th IMEKO TC4 International Symposium
23rd International Workshop on ADC and DAC Modelling and Testing
IMEKO TC-4 2022
Brescia, Italy / September 12-14, 2022

Comparison between a PPG Wearable Device and an AFE4403-Based Pulse Oximeter

Erika Pittella[1], Alice Bologni[2], Roberta Cervoni[1], Vincenzo Fortunato[2], Emanuele Piuzzi[1]

[1] *Department of Information Engineering, Electronics and Telecommunications, Sapienza - University of Rome, Rome, Italy, erika.pittella@uniroma1.it, cervoni.1714470@studenti.uniroma1.it, emanuele.piuzzi@uniroma1.it*
[2]*EsseDH S.r.l., Rome, Italy, alice.bologni@essedh.com, vincenzo.fortunato@essedh.com*

***Abstract* – The paper shows a comparison between a photoplethysmography wearable device and a bare pulse-oximeter based on an analog front-end for optical bio-sensing applications. In particular, a specific experimental set-up was implemented, simulating an artery, which allows to compare and acquire signals from both proposed devices on a repeatable system. Results both on the artery model and on a healthy volunteer are shown.**

I. INTRODUCTION

National Health System is based on fundamental principles, such as universality, equality and equity; currently, especially after the Covid-19 pandemic, it aims towards the frontiers of Digital Health [1]. The term Digital Health refers to the application of digital technologies to support innovation in the health system, including telemedicine or home automation. In this context, the concept of continuous and remote monitoring is introduced: this type of service allows facilities and doctors to communicate easily both with patients and with other experts, without being physically present, optimizing time and resources [2].

In this way, an invisible connection is established between the doctor and the patient which, through a remote monitoring, allows the acquisition of numerous data relating to his state of health, continuously and in diversified psychophysical conditions. The acquisition of this type of health data takes place mainly through the use of wearable medical devices, i.e. electronic devices that can be easily worn in peripheral areas of the patient's body (such as watches, earphones, glasses) [3].

Some of the wearable medical devices currently on the market base their operating principle on the photoplethysmographic technique. Photoplethysmography (PPG) is a non-invasive method based on optical properties, such as absorption, scattering, and transmission properties of human body composition under a specific light wavelength, that allows the measurement of blood volume changes in a microvascular bed of the skin [4].

The purpose of this paper consists in the comparison of different devices based on the photoplethysmographic technique: first of all, an experimental setup was created, simulating an artery model, from which to acquire detectable and repeatable signals via an analog pulse-oximeter sensor (AFE4403 from Texas Instruments) [5] and the cosinuss° Two headset [6]. Subsequently, the PPG signals from the two different sensors were acquired on the simulated model of an artery. Finally, measurements on a healthy subject were performed.

II. METHODS AND MODELS

A. Artery model

One of the main objectives was to create an experimental setup, which allows to compare and acquire signals from both proposed devices, on a single elementary reference system. The idea was to prepare an apparatus, which was equipped with both a hydraulic system capable of reproducing the pulsating motion of the blood, and an element that simulated peripheral blood perfusion, namely an artery. In this regard, it was decided to modify a model already developed and available within the Microwaves and Electromagnetic Compatibility Laboratory of the Sapienza University of Rome [7, 8]. The Arduino-Controlled Common Artery (ACCA) model features a centrifugal pump (HPR6/8 by Totton Pumps) which draws from a parallelepipedal tank containing water, to bring it into the hydraulic circuit at constant pressure. To simulate the pulsating motion of blood, the following are used: a proportional solenoid valve (PVQ-13-5L-08-M5-A, SMC), three “needle” valves (i.e. flow control) and a T junction valve.

The ACCA system is also equipped with a pressure sensor (Drucksensor RS). The signal sent to the solenoid valve is generated starting from the characteristic points relating to the motion of the blood [9]. All the details of the model are described in [7] and [8].

On the basis of the ACCA model, some additions were made to the set-up in order to make it suitable for PPG device testing. In particular, to simulate the artery perfused from the blood, a transparent tube in flexible rubber and silicone was added, inside which the fluid pumped by the

hydraulic system of the ACCA model flows; the dimensions of the tube are respectively 14.5 mm (width) × 4.5 mm (thickness).

The insertion of the transparent tube in the hydraulic circuit took place by connecting both ends of the transparent tube with the drain valve and with the filling valve of the hydraulic system. The connection was made through the use of two pairs of elements for each end, created with the 3D printer (Creality 3D model) present in the EsseDH S.r.l laboratories:

- main connector designed to fit both the transparent tube, with a rectangular section, and the drain and hydraulic fill tube;
- flow reducers, of different sections.
-

The 3D-prints, on the other hand, were made in gray PLA, using filaments with a diameter of 1.75 mm, produced by Basicfil Filament. The additional elements listed above were designed in SolidWorks.

The main connector structure consists of:

- a rectangular section parallelepiped, slightly "bulging" on the larger sections, to avoid the collapse of the rectangular section tube when the fluid flows;
- a cylinder with a section of 4 mm;
- a parallelepipedal connection section with a rectangular section.
-

The projects were created in STL format (STereo Lithography interface format or acronym for "Standard Triangulation Language" or alternatively "Standard Tassellation Language"), a binary or ASCII file format, created for CAD stereolithography software. The files were then uploaded to the Ultimaker Cura software (a view of the software interface is shown in Fig. 1), for the conversion of project files for 3D printing. A basic elliptical section (in light blue) has also been added through Ultimaker Cura to ensure the absence of displacement of the connector during the printing process (see Fig. 1).

The same procedure took place for the construction of the reducer; in particular, three reducers with different sections were created to experiment which section favored the optimal motion of the fluid inside the transparent rubber tube, which was correctly detectable from the sensors.

The assembly of the main connector and the reducer on each end of the tube was then carried out (see Fig. 2), thus creating a prototype that can be implemented in the ACCA system. As shown in the figure, the designed prototype envisages a flexible rubber and silicone hose, to which a main connector-reducer pair is assembled for each end.

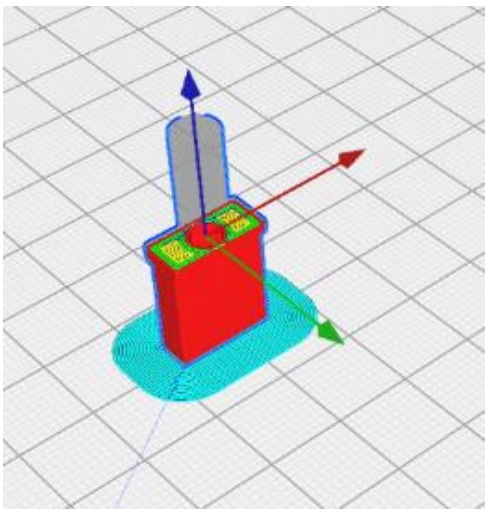

Fig. 1. View of the Ultimaker Cura software interface: representation of the main connector.

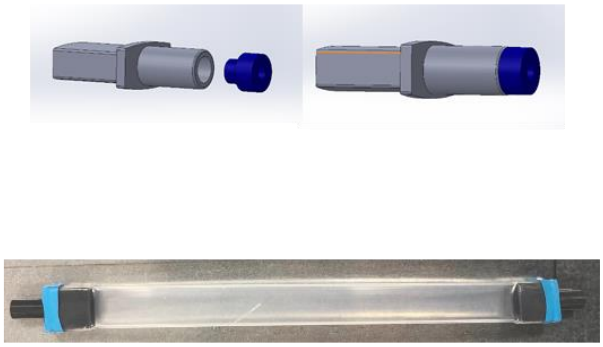

Fig. 2. Main connector and interlocking reducer (top-view); sensor prototype (bottom-view).

B. AFE4403EVM sensor

The AFE4403EVM device is a sensor for monitoring heart rate and oxygen saturation (SpO2). The instrument consists of a low-noise receive channel, the LED transmission section, and diagnostics for sensor and LED fault detection. Its operating principle is based on the use of the photoplethysmographic technique by reflection: the sensor is able to illuminate the area of interest and record, through a specific interface, the reflected signal. Inside the sensor there is a highly configurable timing controller, which allows the user to have complete control of the timing characteristics of the device. The device also has a built-in oscillator that works from two clock sources: an external crystal or the clock from an external host processor to facilitate clock requirements and provide a low jitter clock to the AFE4403. The device communicates with an external host processor using the serial peripheral

interface (SPI). The purpose of the AFE4403EVM is to accelerate system evaluation and development activities related to the AFE4403 device [5]. The demonstration kit (Fig. 3) includes:

- an USB cable for connection to the PC;
- an NJRC NJL5310R sensor with green or infrared LED;
- an OSRAM SFH7050 sensor with red or infrared LED;
- a data acquisition and storage board;
- a cable with 8 connection pins for the sensor, to be connected to the acquisition board.

The AFE4403EVM settings and its configurations can be controlled through a Graphical User Interface (GUI) downloadable from the official Texas Instruments website.

Fig. 3. AFE4403 demonstration kit.

C. cosinuss° Two

Cosinuss° Two [6] was born from the idea of wanting to introduce remote monitoring of patients in domestic isolation, affected by Covid-19 in a medium-low progress of the infection. The cosinuss° Two wearable sensor (Fig. 4) is designed to detect, analyze and transmit information regarding the physiological signals of the body such as vital signs and environmental data that allow immediate biofeedback to the wearer and/or remote healthcare workers, collecting the following raw data:

- the optical signal, which is the PPG signal;
- internal body temperature;
- 3D acceleration of the head.

From which it is possible to extract the following physiological parameters:

- body temperature;
- heart rate;
- blood oxygen saturation;
- R-R or intra-beat interval;
- blood perfusion index;
- signal quality;
- movements.

The wearable sensor measures vital signs from inside the ear canal and transmits the data via Bluetooth to cosinuss° LabGateway.

Fig. 4. cosinuss° Two wearable sensor

The Gateway forwards the data to a telecommunications network which sends it to cosinuss° LabServer. Through the WebInterface, healthcare professionals are able to view and access the vital information of each patient.

III. RESULTS

A. Measurements on the Artery Model

In the case of the ACCA model, the signals acquired by the two sensors are periodic and morphologically similar.

The dynamics of the signals show the same order of magnitude; however, the intensity of the signal acquired with the AFE4403 sensor is higher than the intensity of the signal acquired with the cosinuss° Two headset. From the graphic superimposition of the two signals (Fig. 5), the following can be deduced:

1. in both traces, approximately 3 peaks can be observed every 10 seconds: this data is physically linked to the frequency with which the device sends the pulses to the artery prototype; corresponding to each impulse, the formation of a belly on the prototype can be observed, due to the perfusion of the water inside the rubber tube, site of the measurement;
2. the dynamics of the signal acquired with the AFE4403 sensor is about 5 times higher than the dynamics of the signal acquired with the cosinuss° Two headset; this is due to the greater sensitivity of the AFE4403 sensor, also in terms of noise, compared to the cosinuss° Two headset.

Fig. 6 shows a normalized graph, in order to better compare the two signals.

It is important to highlight that the ACCA model can be easily reconfigured to produce a pulsating signal that is not exactly periodic, but shows a pre-defined variability. This would allow not only to test the optical response of the devices, but also to assess their functionality in terms of heart rate measurement and possible detection of pathological conditions related to heart activity. The measurement results are repeatable for both devices.

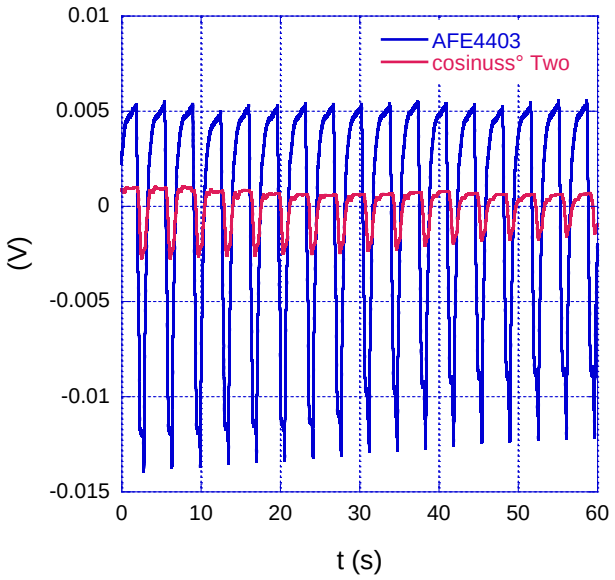

Fig. 5. Comparison between the two sensor signals.

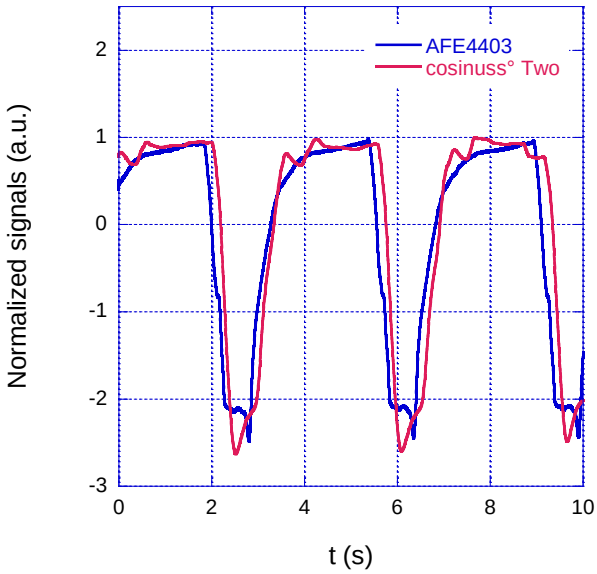

Fig. 6. Comparison between the two normalized sensor signals.

B. Measurements on a healthy subject

In the case of measurement on subjects, the cosinuss° Two was placed on the ear of the volunteer and the AFE4430 on the wrist. The two signals were aligned creating a simultaneous artifact on the two recorded signals. Results on a 20 s time window are shown in Fig. 7.

The obtained results highlight that the two sensors record two very similar signals, also considering the different acquisition location (i.e. ear vs. wrist).

Altogether, the signal acquired with the bare pulse-oximeter exhibits a larger peak-to-peak amplitude (higher sensitivity), even though a higher noise level is present. From the performed tests, the cosinuss° Two represents a reliable and comfortable solution for long term non-obtrusive patient monitoring at home, despite the slightly worse sensitivity as compared to a finger-clamp pulse oximeter.

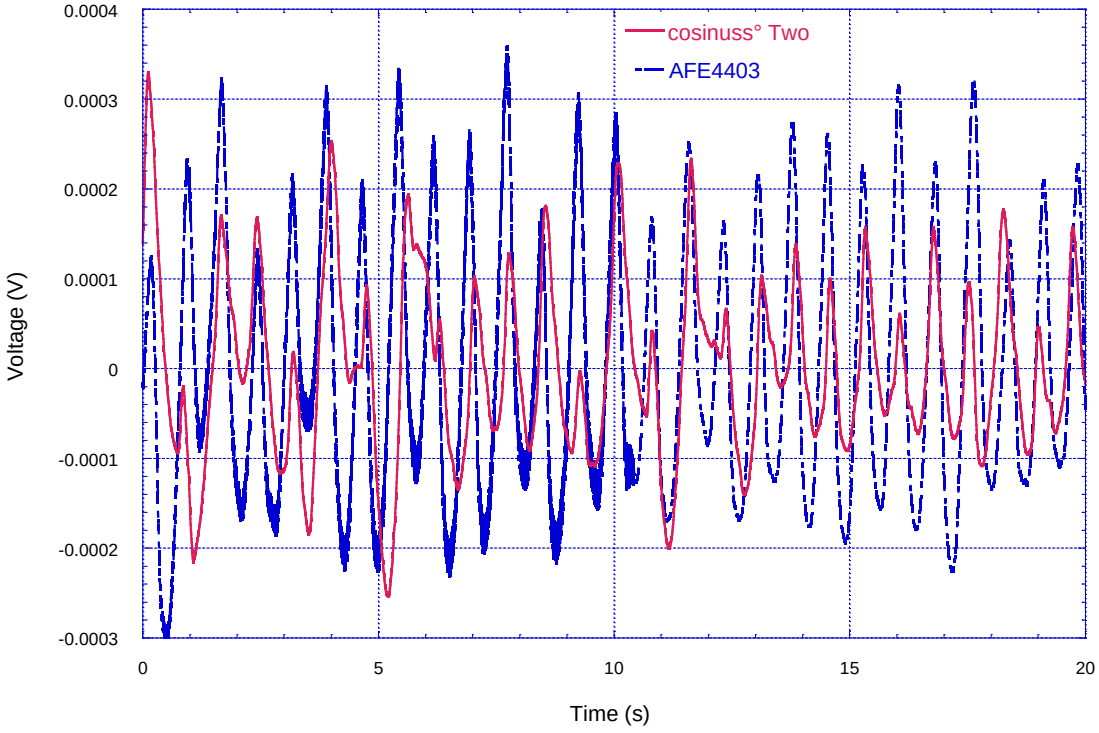

Fig. 7. Comparison between the two sensor signals on a subject.

IV. CONCLUSIONS

The implementation of an experimental setup that uses the prototype of an artery model to compare in a repeatable and controlled way the acquisitions of two different devices opens up the possibility of comparing and analyzing signals from other wearable technologies. Results on volunteers show a good agreement between the two tested devices, proving the feasibility of long-term monitoring with comfortable wearable solutions.

REFERENCES

[1] S.R.N. Kalhori, K. Bahaadinbeigy, K. Deldar, M. Gholamzadeh, S. Hajesmaeel-Gohari, S.M. Ayyoubzadeh, "Digital Health Solutions to Control the COVID-19 Pandemic in Countries with High Disease Prevalence: Literature Review", J. Med. Internet Res. 2021, 23, e19473.

[2] M. Umair, M.A. Cheema, O. Cheema, H. Li, H. Lu, "Impact of COVID-19 on IoT Adoption in Healthcare, Smart Homes, Smart Buildings, Smart Cities", Transportation and Industrial IoT. Sensors 2021, 21, 3838. https://doi.org/10.3390/s21113838.

[3] D. Verma, K.RB. Singh, A.K. Yadav, V. Nayak, J. Singh, P.R. Solanki, R.P. Singh, "Internet of things (IoT) in nano-integrated wearable biosensor devices for healthcare applications, Biosensors and Bioelectronics: X, 2022, 100153, ISSN 2590-1370.

[4] J. Park Junyung, H.S. Seok, S.-S. Kim, H. Shin "Photoplethysmogram Analysis and Applications: An Integrative Review", Frontiers in Physiology, vol. 12 2022, 10.3389/fphys.2021.808451, 1664-042X.

[5] https://www.ti.com/product/AFE4403 (available online: 11/05/2022)

[6] https://www.cosinuss.com/en/products/data-acquisition/in-ear-sensors/#_two (available online: 11/05/2022)

[7] S. Pisa, S. Chicarella, E. Pittella, E. Piuzzi, O. Testa and R. Cicchetti, "A Double-Sideband Continuous-Wave Radar Sensor for Carotid Wall Movement Detection," in IEEE Sensors Journal, vol. 18, no. 19, pp. 8162-8171, 1 Oct.1, 2018, doi: 10.1109/JSEN.2018.2862430.

[8] S. Pisa, E. Pittella, E. Piuzzi, O. Testa and R. Cicchetti, "A double sideband continuous wave radar for monitoring carotid artery wall movements," 2017 IEEE MTT-S International Microwave Symposium (IMS), 2017, pp. 1007-1010, doi: 10.1109/MWSYM.2017.8058761.

[9] D.W. Holdsworth, C.J. Norley, R. Frayne, D.A. Steinman, B.K. Rutt, "Characterization of common carotid artery blood-flow waveforms in normal human subjects", Physiological measurement, 20(3), 219–240, 1999. https://doi.org/10.1088/0967-3334/20/3/301.

25th IMEKO TC4 International Symposium
23rd International Workshop on ADC and DAC Modelling and Testing
IMEKO TC-4 2022
Brescia, Italy /September 12-14, 2022

Design, metrological analysis and optimization of solenoid for homogenization of electromagnetic fields in biomedical experiments

Slavica Gajić[1], Platon Sovilj[2]

[1] *University of Banja Luka, Faculty of Electrical Engineering, Banja Luka, Bosnia and Herzegovina, slavica.gajic@etf.unibl.org*
[2] *Faculty of Technical Science, University of Novi Sad, Novi Sad, Serbia. e-mail: platon@uns.ac.rs*

***Abstract* – In recent years, usage of electromagnetic field of static magnets in biomedical experiments is increased. It has been shown that extremely low-frequency (ELF) magnetic fields improve the impact of oncological therapy on cancer cells. Therefore, there is a huge need for ELF magnetic fields usage in biomedical experiments. In this paper, different designs and optimizations of solenoid for electromagnetic field homogenization along its axis, as well as in experimental volume, is compared. Using metrological analysis, the best design based on achieved homogenization of electromagnetic field and design complexity is selected. Also, a number of series expansions in 1st and 2nd kind of Elliptical integrals calculations is analysed in order to emphasize computer resources necessary for numerical modelling process.**

I. INTRODUCTION

In recent years, there is a great interest for the extremely low frequency (ELF) electromagnetic field in the scientific community, because of its influence on human life through different applications in the diagnosis and treatment of various diseases. Therefore, ELF fields are the subject of many researches, and there are many experiments performed *in vitro* on human and animal tissues, as well as *in vivo* on volunteers or with animals. In addition, the results of the experiments performed in a magnetic resonance (MR) scanner, and in a cyclotron magnet, indicate that strong static magnetic fields (SMFs) cause significant effects on the exposed body. It is well known that use of homogeneous, as well as inhomogeneous static magnetic fields initiate biomedical changes. There are evidences suggesting that SMFs have an effect on gene expression, calcium signaling, growth factor receptors, and cell cycle regulators [1]. Usage of those fields in therapy directly increases cytotoxic effects of the drugs in an *in vitro* cell growth assay. In the past two decades, analysis results suggest that SMFs can enhance the killing effect of antineoplastic drugs on cancer cells, indicating that SMFs may act synergistically with pharmacological treatment. Previous experiments have shown that combined treatment of 8.8 mT SMF with 10 mg/ml cisplatin (DDP) resulted in the inhibition of metabolic activity, a change in cell cycle distribution and serious damage to deoxyribonucleic acid (DNA) [2]. The application of SMF to human leukemia cells, combined with a mixture of chemotherapy drugs (5-fluorouracil, cisplatin, doxorubicin, and vincristine), enhanced the cytotoxic effects of the drugs in an in vitro cell growth assay1. Also, there is shown that SMF at 3.0 mT is able to sensitize cancer cells to Tumor necrosis factor a (TNF) -related apoptosis-inducing ligand (TRAIL) mediated apoptosis via the repression of Cdc2 and the subsequent downregulation of surviving (such as breast cancer cells), an anti-apoptotic protein demonstrating cell cycle-regulated expression. Effects of low strength SMF on Vascular Smooth Muscle Cells (VSMCs) biological performances, including proliferation, migration and adhesion are also described [3].

The state-of the-art technology where industrial electronics are called upon to play a key role in cancer treatment is described in [4]. Because of rapidly increasing use of ELFs fields in biomedical experiments, there are inevitable questions on the threshold levels of that fields, on the reversibility of arose effects, on how the effects depend on the field level, directions and homogeneity. To find answers on these all questions, researches require further experimenting. Preferably, that will be an exposure system designed for the purpose, which can provide scalable homogeneous ELF magnetic field with relatively strong peak value inside an experimental volume large enough to accommodate in vivo as well as in vitro experiments.

There are various methods in the literature that result in an increase in field uniformity inner the solenoid volume. One of them is a method [5] that uses copper plates and rings to obtain a modified solenoid with an experimental volume of 125 m, while the dimensions of the Helmholtz coil are adjusted for the homogenization of the magnetic field [6]. For the purpose of homogenizing relatively weak fields, a set of four circular coils arranged around the same axis with a larger number of coils on the inner

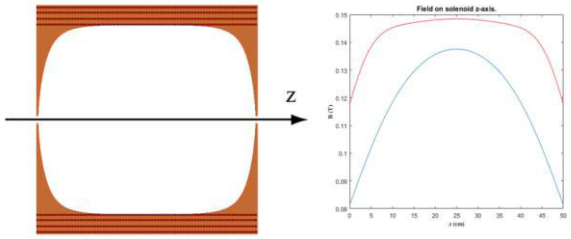

Fig. 1. Field flattening along solenoid axis. (a) The darker pattern emphasizes cross-section of a 50 cm long and 5 cm thick base solenoid. For ideal field flattening the additional wire windings form the shaped lid on each end of the solenoid [12]. (b) The magnetic induction along the solenoid axis for the base solenoid and solenoid with the additions (dimensions d = 6.5 cm and l = 5.5 cm), respectively.

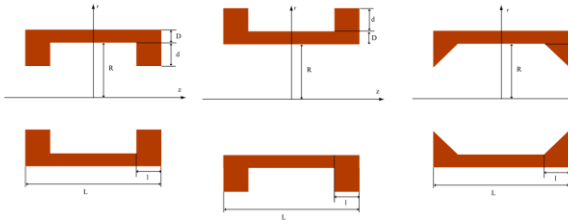

Fig. 2. Modified solenoid dimensions. The length and thickness of the basic solenoid are taken to be L and D, whereas the corresponding measures of the additional solenoids are l and d, respectively.

segments and a smaller radius of the outer segments is used [7]. Also, for this purpose square coils with sets of three, four and five further coils are proposed [8]. Design and optimization of a ring-pair permanent magnet array are proposed in [9] and compared with other proposed designs such as H-shaped magnet, C-shaped magnet, Halbach cylinder [10] and Aubert ring pair [11]. All of those designs are complex and difficult for hardware realization, so a simpler solution is required.

Main goal of this research is design and optimization of basic solenoid configuration to provide better homogeneity of electromagnetic field above solenoid axis, as well as in complete experimental volume. On this way, new solenoid design will be easier to realize and will be applicable in *in vitro* and *in vivo* biomedical experiments. Also, in this paper precision of numerical modeling process is tested. Obtained results are analyzed in order for provide information about dependency between used number of series expansion in 1st and 2nd kind of Elliptical integrals and calculation precision.

II. METHODS

A. Calculations

Magnetic induction along the axis B_z of a solenoid is derived using the Biot-Savart law by decomposing a solenoid into a set of very thin, i.e., single layer solenoids, and further into circular current loops, where R is inner radius, L is length, and D is thickness of solenoid, such as proposed in [12]. However, calculation of magnetic induction besides of solenoid axis is based on magnetic vector potential calculation in any point of 3D space and therefore is more complicated [13]. Because of the solenoid symmetry, cylindrical coordinate system is usually used for calculation process, where z, r and φ are its coordinates. Therefore, magnetic vector potential intensity doesn't depend of cylindrical coordinate φ, and calculation can be implemented in $\{r\text{-}O\text{-}z\}$ plane, for $\varphi = 0$. Then, the same concept of decomposing the solenoid into individual circular current loops proposed in [12] can be used. So, r-component and z-component of magnetic induction in any point in the 3D space inside the solenoid arises as the influence of only one winding is calculated as:

$$B_r = \frac{\mu_0 I}{2\pi} \frac{z}{r\sqrt{(R+r)^2+z^2}} \left[-K + \frac{R^2+r^2+z^2}{(R-r)^2+z^2} E\right], \quad (1)$$

$$B_z = \frac{\mu_0 I}{2\pi} \frac{1}{\sqrt{(R+r)^2+z^2}} \left[K + \frac{R^2-r^2-z^2}{(R-r)^2+z^2} E\right], \quad (2)$$

where R is radius of one current loop in solenoid corresponding to a wire segment, i.e. winding, with current I, and r and z are cylindrical coordinates of point in 3D space in which the magnetic induction is calculated ($\varphi = 0$). K and E are 1st and 2nd kind of Elliptic integrals:

$$K = \int_0^{\pi/2} \frac{dR}{\sqrt{1-k^2\sin^2 R}}, \quad (3)$$

$$E = \int_0^{\pi/2} \sqrt{1-k^2\sin^2 R}\, dR, \quad (4)$$

where k is:

$$k^2 = \frac{4Rr}{(R+r)^2+z^2}. \quad (5)$$

Integrals (3) and (4) expressed through series are:

$$K = \frac{\pi}{2}\left[1 + \left(\frac{1}{2}\right)^2 k^2 + \left(\frac{1\cdot 3}{2\cdot 4}\right)^2 k^4 + \cdots\right], \quad (6)$$

$$E = \frac{\pi}{2}\left[1 - \left(\frac{1}{2}\right)^2 k^2 - \left(\frac{1\cdot 3}{2\cdot 4}\right)^2 \frac{k^4}{3} - \cdots\right]. \quad (7)$$

It is easy to check that in points along solenoid axis ($r = 0$) equations (1) and (2) are reduced to:

$$B_r = 0, \quad B_z = \frac{\mu_0 I R^2}{2(R^2+z^2)^{3/2}}, \quad (8)$$

which represents an well-known term for the magnetic induction vector along the solenoid axis.

The derived formula quantitatively expresses the fact that magnetic induction along the axis of a solenoid is maximal in the solenoid's center and that it decreases towards each of solenoid's ends, for both of coordinates r and z. For example, the darker pattern in Fig. 1a emphasizes the cross-section of a 50 cm long and 5 cm thick solenoid with the inner radius of 17 cm (intended for testing in mice), whereas the corresponding magnetic field induction calculated using (1) - (2) and the current density of J = 2.7 A/mm^2 is given as the blue curve in Fig. 1b. In general, the described field can be flattened if the thickness of the solenoid is increased at its ends. Ideally, the additional windings shape of a modified solenoid which provides a constant value of magnetic induction along the axis, as well as inside 3D solenoid space [12] is illustrated witha brighter pattern in Fig. 1a. Additional rectangular shape wirewindings on each end of the solenoid, with dimensions d = 6.5 cm and l = 5.5 cm, results that field along the solenoid axis becomes more flat than forbasic solenoidandit is shown asred curve on Fig. 2b. Blue curve on Fig. 1.b corresponds of magnetic induction along the axis of basic solenoid.

The shape of a modified solenoid which provides ideal flattening inside 3D solenoid space would be quite difficult to wind. In addition, the volume that is required for biomedical experiments can be shorter than the solenoid length. Consequently, although it is desirable that the flat section of the field is as long as possible, it is not necessary that it covers complete length of the solenoid. Therefore, three simplified modifications of basic solenoid are provided for experimental tests and analysis of obtained results is presented.

The ideal additions with elaborate shape (see Fig. 1a) were replaced in three different ways in order to achieve the approximate elaborated design, i.e. by two simple rectangular shape solenoids in the following manner, at the inner ends of the base solenoid, at the external ends of the base solenoid and with two triangle shape solenoids inner base solenoid ends, as shown in Fig. 2. The length and thickness of the basic solenoid are defined with L and D, whereas the corresponding measures of the additional solenoids are l and d, respectively. In the case of triangle shape additions solenoids l and d arecathetus of triangle (see Fig 2).

In order to enable comparison of experimental test results obtained using different modified solenoids the same induction current density of 2.72 A/mm^2 is used in all cases. This value corresponds to the maximal current density of 3 A/mm^2 and the wire winding fill factor of 0.907. Therefore the fields obtained in all solenoids examples are the strongest available; for weaker fields, induction current should be adequately scaled. Besides, for purpose of testing process, inner radius of base solenoid R = 17 cm is chosen which suits to biomedical experimental volume intended for testing in mice.

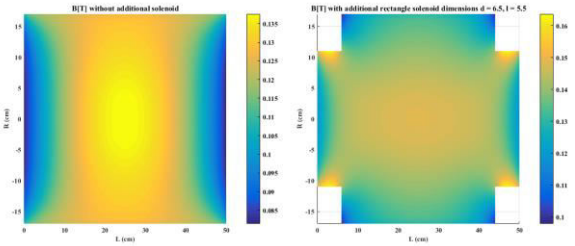

Fig. 3. Magnetic induction in 2D solenoid space for base solenoid and modified solenoid with additional dimensions d = 6.5 cm and l = 5.5 cm.

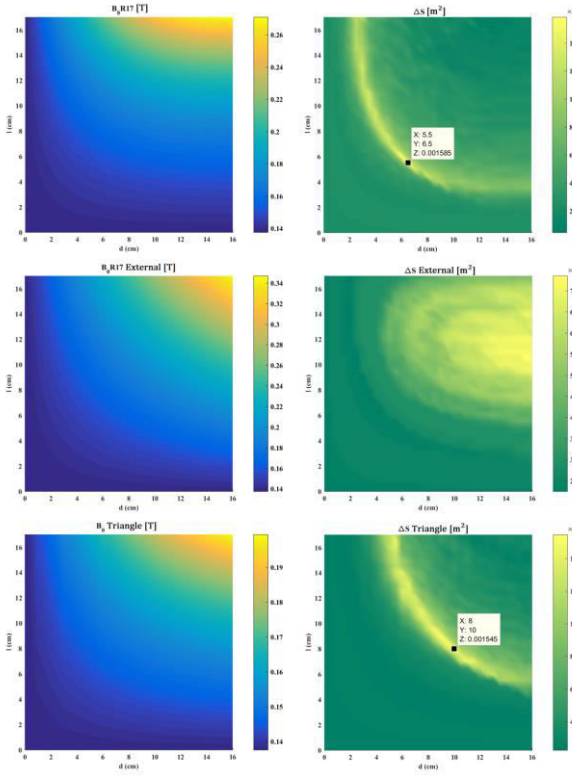

Fig. 4. Dependence of field level and flatness on size of additional solenoids(ΔB/B0 < 0.5 %).

III. RESULTS AND DISCUSSION

A. Analytical modeling

Proposed three simplified solenoid modifications of base solenoid are tested and (2) - (3) equations are used to study the influence of the modified solenoid dimensions on the strength and flatness of its field in 3D space. Because of solenoid symmetry, calculation is implemented in $\{r\text{-}O\text{-}z\}$ plane, for $\varphi = 0$.

With the increase of the additional solenoids' size, the shape of the field in inner solenoid space transforms from a surface with a maximum at $z = 0$, $r = 0$ to a surface with four local maximums. This transition is illustrated in Fig. 3 where first graph is without and second is with inner rectangle shape additions on solenoid ends with

dimensions d = 6.5 cm and l = 5.5 cm. Base solenoid is defined with L = 50 cm, D = 5 *cm*, R = 17 cm, as well as the similar results with others inner radius was obtained.

The two parameters chosen to quantitatively describe the strength and flatness of the field are B_0, the magnetic induction at z = 0, r = 0, and ΔS, the surface of the *{r-O-z}* plane segment along which the magnetic induction deviation is smaller than 0.5 % of B_0, i.e., along which $\Delta B/B_0$ < 0.5%. Field quality, described by these two parameters, depends on all five (*R, L, D, l, d*) dimensions that define the size of a modified solenoid. The influence of the additional solenoid size is investigated firstly, and the results for all of proposed additional solenoids are given in Fig. 4.

The field level, B_0, increases with the increase in d as well as in l, as can be seen in the left graphs in Fig. 4. The field flatness, ΔS, depends strongly on l as well as on d, and its large values are restricted to the narrow set of (*d, l*) pairs depicted with the bright area in the top and downright graphs in Fig. 4. As can be seen, the external additional solenoid doesn't provide good field flatness and value is 2 times lower compared to other additional solenoids. For additional rectangle shape solenoid dimensions pairs d = 6.5 cm, l = 5.5 cm there is maximum field flatness ΔS = 15.45 cm^2, as well as for triangle solenoid dimensions pairs d = 10 cm, l = 8 cm with ΔS = 15.85 cm^2. Due to symmetry, those values are valid for every angle φ, so these surfaces correspond to 97.07 cm^3 and 99.59 cm^3 volumes, respectively. Difference between those additional solenoids is in 0.4 cm^2 surface, i.e. 2.52 cm^3 volumes. Obtained result shows that the triangular additional solenoids ensure better field homogenization than additional solenoids rectangle shape. On the other hand, rectangle additional solenoid is much easier to wind. So, the solution should be chosen according to the required ratio of achieved performance and system complexity. The obtained qualitative dependence of B_0 and ΔS on the additional solenoid's length l as well as thickness d, is valid in general, regardless of the basic solenoid size, L and D.

For a biomedical experiment, it is preferred that conditions in the experimental volume are equal and that the ranges of available values of input parameters are as broad as possible. Based on the fact that additional solenoid rectangle shape is much easier to wind than triangle shape additional solenoid, those differences in surface/volume flatness can be disregard. So, other tests just on rectangle shape additional solenoid are evaluated. One more confirmation of field flatness is evaluated using standard deviation and variance of field without additional solenoids (base solenoid) and with additional solenoids rectangle shape with the best d = 6.5 cm and l = 5.5 cm parameters. Obtained results are given in Table 1 and it can be seen that modification of the solenoid provides better electromagnetic field homogenization.

B. Numerical modeling

In numerical modeling process, for integral calculation parameters K and E described with (6) and (7) are used. These parameters represent series of 1st and 2nd kind of Elliptic integrals, so calculation precision directly depends of used number of series expansion (n) in calculation process. Testing influence of the series expansion is evaluated in MATLAB, where n = 3, 4, 5, which is equivalent that K and E takes 3, 4, 5 members of the series, respectively. For testing of required execution time in those scenarios, Intel Core i7-3820 3.60 GHz processor with 64 GB of RAM and MATLAB function *cputime.m* are used. The results are given in Table 2. As can be seen, in case of basic solenoid, for n = 4 processor takes about 3.1 times more time for execution and for n = 5 it takes about 3.7 times more that time than for n = 3. For modified solenoid with rectangle shape additional solenoid with dimensions that provide the best field flatness, those times are about 3.3 and 4 times higher, respectively. Execution time extremely increases when n increases.

On the other hand, precision of numerical calculations in MATLAB doesn't so much degraded using just 3 series expansion n. This parameter doesn't influence on calculation precision of field intensity in solenoid center (z = 0, r = 0), there isminor influence on solenoid axis (r = 0), but withincreasing radius r the calculation error is also increased. Illustration of thosecalculation deviations is given on Fig. 5 and it represent differences between calculations with n = 3 and n = 4, i.e. n = 4 and n = 5, and n = 3 and n = 5, respectively, in all of *{r-O-z}* plane points, for φ = 0. Because of symmetry, those results are the same for all of $\varphi \in [0, 2\pi]$. Maximum difference values are 10^{-3} [mT] and 10^{-4} [mT] order, as shown in Table 3, where R = 17 cm, L = 50 cm and D = 5 cm. This speaks in favor that n = 3 is a sufficient number of series expansion used in the numerical calculation process based on eq. (6) and (7).

Table 1. Comparison of standard deviation and variance through {r-O-z} plane for basic and proposed solenoid.

Solenoid type	Stand. deviation	Variance
d = 0 cm and l = 0 cm	0.0036773	8.1998e-09
d = 6.5 cm and l = 5.5 cm	0.0021959	6.5419e-10

Table 2. Execution time for tested number of series expansions in 1st and 2nd kind of Elliptic integrals K and E that are used for integral calculation.

Execution time [s]	Number of series expansions (n)		
Solenoid type	3	4	5
d = 0 cm and l = 0 cm	125.33	391.47	467.58
d = 6.5 cm and l = 5.5 cm	15207	50004	60742

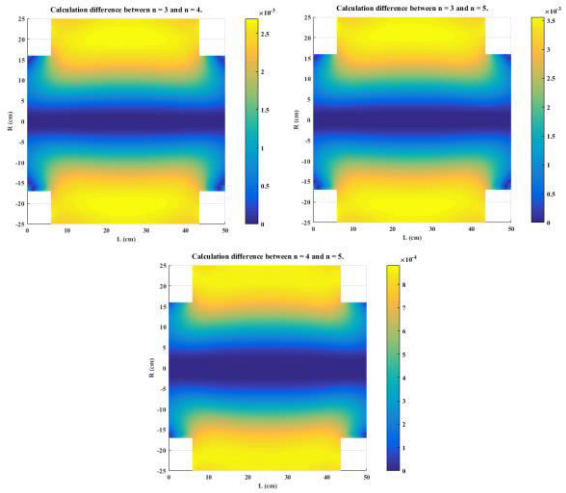

Fig. 5. Dependence of field level between different number of series expansions that are used for 1st and 2nd kind of Elliptic integrals calculation.

Table 3. Differences between calculations for different number of seriesexpansions in 1st and 2nd kind of Elliptic integrals K and E that are used for integral calculation.

Difference between:	n = 3 or 4	n = 4 or 5	n = 3 or 5
ΔB [mT]	$2.7 \cdot 10^{-3}$	$8.81 \cdot 10^{-4}$	$3.6 \cdot 10^{-3}$

IV. CONCLUSION

In this paper, solenoid modifications for purpose of its usage in biomedical experiments are proposed. Solenoid electromagnetic field homogenization along its axis, as well as in experimental volume is required. Three new solenoid designs are performed and their complexity and achieved performance are compared. It was concluded that triangle additional solenoids gives better field homogenization, while rectangle shape additional solenoids gives little weaker electromagnetic field homogenization, but this modification is easier to wind. Further, selected modified solenoid design for estimation of performed numerical calculations precision is used. It is obtained that number of series expansion, $n = 3$, has enough precision for numerical modeling. Experimental results show that solenoid modification designs provides more homogeneous field along its axis, as well as in all experimental volume compared with base solenoid.

REFERENCES

[1] T. Lin, et all, “A moderate static magnetic field enhances trail-induced apoptosis by the inhibition of cdc2 and subsequent downregulation of survivin in human breast carcinoma cells,” *Bioelectromagnetics*, vol. 35, no. 5, pp. 337–346, 2014.

[2] K. Zhang, et all, “Decreased p-glycoprotein is associated with the inhibitory effects of static magnetic fields and cisplatin on k562 cells,” *Bioelectromagnetics*, vol. 35, no. 6, pp. 437–443, 2014.

[3] Y. Li, L.-Q. Song, et al., “Low strength static magnetic field inhibits the proliferation, migration, and adhesion of human vascular smooth muscle cells in a restenosis model through mediating integrins β1-fak, ca 2+ signaling pathway,” *Annals of biomedical engineering*, vol. 40, no. 12, pp. 2611–2618, 2012.

[4] O. Lucia, H. Sarnago, et all, "Industrial Electronics for Biomedicine: A New Cancer Treatment Using Electroporation," in *IEEE Industrial Electronics Magazine*, vol. 13, no. 4, pp. 6-18, Dec. 2019.

[5] D. Bordelon, R. Goldstein, et all, “Modified solenoid coil that effciently produces high amplitude ac magnetic fields with enhanced uniformity for biomedical applications,” *IEEE transactions on magnetics,* vol. 48, no. 1, pp. 47–52, 2011.

[6] R. Beiranvand, “Effects of the winding cross-section shape on the magnetic field uniformity of the high field circular helmholtz coil systems,” *IEEE Transactions on Industrial Electronics*, vol. 64, no. 9, pp. 7120–7131, 2017.

[7] G. Gottardi, P. Mesirca, C. Agostini, D. Remondini, and F. Bersani, “A four coil exposure system (tetracoil) producing a highly uniform magnetic field,” Bioelectromagnetics: *Journal of the Bioelectromagnetics* Society, The Society for Physical Regulation in Biology and Medicine, The European Bioelectromagnetics Association, vol. 24, no. 2, pp. 125–133, 2003.

[8] R. Merritt, C. Purcell, and G. Stroink, “Uniform magnetic field produced by three, four, and five square coils,” *Review of Scientific Instruments,* vol. 54, no. 7, pp. 879–882, 1983.

[9] Z. H. Ren, W. C. Mu and S. Y. Huang, "Design and Optimization of a Ring-Pair Permanent Magnet Array for Head Imaging in a Low-Field Portable MRI System," in *IEEE Transactions on Magnetics,* vol. 55, no. 1, pp. 1-8, Jan. 2019, Art no. 5100108.

[10] K. Halbach, “Design of permanent multipole magnets with oriented rare Earth cobalt material,” *Nucl. Instrum. Methods*, vol. 169, no. 1, pp. 1–10, 1980.

[11] G. Aubert, “Permanent magnet for nuclear magnetic resonance imaging equipment,” U.S. Patent 5332971, Jul. 26, 1994.

[12] Jasna Ristic-Djurovic, et all, „Desing and Optimization of electromagnets for Biomedical Experiments With Static Magnetic and ELF Electromagnetic Fields”, *IEEE Trans. on Industrial Electronics*, ISSN: 0278-0046, vol. 65, no. 6, pp. 4991-5000, June 2018, (doi: 10.1109/TIE.2017.2772158)

[13] A. Djordjevic, Osnovielektrotehnike, 3. deo, Elektromagnetizam. Akademska Misao, 2007.

25th IMEKO TC4 International Symposium
23rd International Workshop on ADC and DAC Modelling and Testing
IMEKO TC-4 2022
Brescia, Italy / September 12-14, 2022

Material Characterization at Millimeter Wave Frequencies in TUBITAK UME

Erkan DANACI[1], Emre CETIN[2]

[1] *TUBITAK National Metrology Institute (UME), Kocaeli, TURKIYE, erkan.danaci@tubitak.gov.tr*
[2] *Spark Ölçüm Teknolojileri A.Ş., Ankara, TURKIYE, emre_cetin@sparkmeasure.com*

***Abstract* – The frequency response of the materials which are used in milimetre wave communication system has gained increasing importance nowadays. Frequency response measurement of materials in laboratory environments do not contain sufficient information about real working environment conditions. Free space, known as one of the most frequently used material characterization method at high frequencies, is used to give more accurate results under real operating conditions. In this study, using the TUBITAK UME's infrastructure, the measurement results in free space and the uncertainty calculations of the measurements are given for some materials such as teflon, fr4, air, komacel. Measurements were performed at 67 GHz to 115 GHz and 110 GHz to 170 GHz frequency bands by using KMMS software which is known run up to 50 GHz frequency . Measurement results of materials were compared with known low frequency response of the materials in this study.**

I. INTRODUCTION

Many insulators and semiconductor materials are used in circuits and systems that are designed in high frequency regions. While the designed electronic circuits are being realized, copper-clad fibre reinforced bases are used for standing platform. Moreover teflon insulators are used for the coating or protection of the circuits, and teflon-derived radoms are also used for the housing of the antennas. Information on the frequency responses of these type of materials at the operating frequencies helps to ensure reliable designs by having prior knowledge of the situations that will be encountered in the realization of the designed circuits with simulations.

In order to determine the frequency response of a material, it will be sufficient to measure the dielectric permitivity (ε) and magnetic permeability (μ) coefficients.

Relative permittivity (ε_r) of a material is defined in (1) [1].

$$\kappa = \varepsilon_r = \frac{\varepsilon}{\varepsilon_0} = \varepsilon_r' + j\varepsilon_r'' \quad (1)$$

Where, ε_o is vacuum permittivity, and ε is the complex frequency-dependent permittivity of the material. Relative permittivity is a dimensionless number that is in general complex-valued; its real (ε_r') and imaginary (ε_r'') parts are denoted in (1).

Relative permittivity of a medium is related to its electrical susceptibility. There are so many publications and studies on the relative permittivity measurements in literature [2-12].

By the development of vector measuring devices such as Vector Network Analysers (VNA), vector measurements of the relative dielectric coefficient have been made possible.

The real component (ε_r') of the relative dielectric coefficient of the material gives information about the energy it can store at the operating frequency, while the imaginary component (ε_r'') gives information about the energy it will absorb.

Relative dielectric coefficients measurement methods such as open-ended coaxial probes, transmission lines, resonator cavities, free space method (for lower and higher frequencies), parallel plates and inductance (up to 1 GHz) are commonly used at high frequencies.

Transmission line [2] and free space measurement systems [3, 4] are used to measure the complex dielectric permittivity and magnetic permeability coefficients of materials, whereas open-ended coaxial probe kits [5] are used to measure the complex dielectric permittivity only. Although the reflection coefficients of materials are generally measured with arch measurement systems, studies are continuing for its use in electromagnetic material characterization [6].

The transmission line method is a useful technique for determining the dielectric and magnetic properties of the rectangular prism-shaped material, sized in the waveguide cross-section, in the frequency range of the waveguide used [7].

All other methods are operated under laboratory conditions and under special ambient conditions, except for the free space method [8].

The free space method also allows for measurements using special heating or cooling systems or special ambient conditioning systems such as clamshell furnace.

We can list the advantages and disadvantages of the free space measurement system as follows.

Advantages;

- Preferred for high frequency measurement.
- Allows non-destructive measurement.

- Measure material under test (MUT) in harsh environment.
- The magnetic and electric properties can be evaluated.

Disadvantages;

- As the frequency decreases, a wide and flat material surface is needed.
- Multiple reflections between antenna and surface of material.
- Diffraction effects at the edge of material.

In recent years, many studies can be seen in the scientific literature on the measurements of dielectric coefficients when millimeter wave frequencies are achievable [9, 10, 11]. In addition, these measurements can be made by using some special measurement kits (SWISSto12) [12] and some special software (Keysight Material Measurement Suits – KMMS etc.).

In this study, the KMMS software in the TUBITAK UME infrastructure was operated for free space method at millimeter frequencies and the dielectric coefficients of materials (MUT) such as Teflon, Fr4, Komacel, and Air were measured. Measured values were compared with low frequency values of materials. Type A uncertainties of relative permittivity measurement of MUT was given in this study either.

II. FREE SPACE MEASUREMENT TECHNIQUES

Free space measurement method uses the S-Parameters to determine relative permittivity. A basic free space measurement setup is given in Fig. 1 by VNA at millimetre wave frequencies.

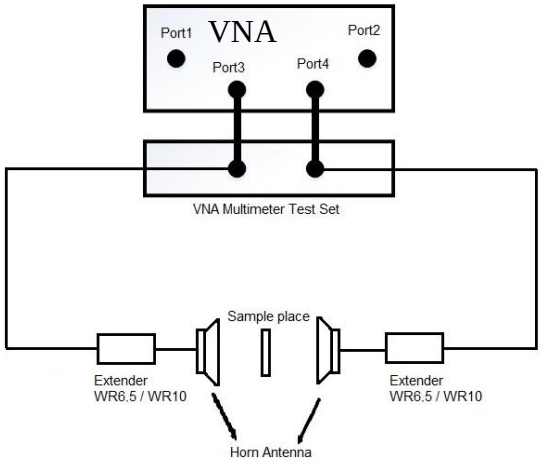

Fig. 1. Basic free space measurement setup.

MUT is fixed between the antennas with a proper distance in this method. This distance should be more than the far field region of antennas. Far-field (Fraunhofer) region is defined as that region of the field of an antenna where the angular field distribution is essentially independent of the distance from the antenna. Far-field region is commonly taken to exist at distances greater than $2D^2/\lambda$ from the antenna, where λ is wavelength and D is maximum aperture of antenna [13, 14]. The far-field patterns of some antennas, such as multibeam reflector antennas, are sensivite to variations in phase over their apertures. For these antennas far field distance might be inadequate.

Before starting the permittivity measurement, VNA should be calibrated first. At the VNA calibration, through-reflect-line (TRL), the through-reflect-match (TRM) and the line-reflect-line (LRL) can be preferred.

In free space measurement process, TRL calibration is firstly performed done at frequency extender's waveguide ports. Then S-parameters of an empty sample holder are measured by placing the sample holder in the middle between the two antennas. As a reflect standard, a metal plate is also placed at sample holder. The MUT is then placed on the sample holder and the S-parameter measurement is performed again. The influence of the sample holder can be cancelled out by using the de-embedding function of the VNA. So only the S-parameter of the MUT can be obtained.

In order to get correct S-parameters in free space method, MUT surface should be larger than the antennas beam pattern. Also time domain gating should be applied to prevent multiple reflection from material. Time domain gating also eliminates the diffraction of energy from the edge of the antennas. The dielectric properties can be determined by post processing in a dedicated software.

There are various approaches for obtaining the permittivity and permeability from S-parameters. Commonly used permittivity measurement method which uses the S-parameters are listed in Table 1 [15].

Table 1. Permittivity measurement method by using S-parameters

Method Name	Used parameters	Properties
Nicholson-Ross-Weir	S_{11}, S_{21}, S_{12}, S_{22} or S_{11}, S_{21}	ε_r, μ_r
NIST Iterative	S_{11}, S_{21}, S_{12}, S_{22} or S_{11}, S_{21}	ε_r, μ_r=1
New non-iterative	S_{11}, S_{21}, S_{12}, S_{22} or S_{11}, S_{21}	ε_r, μ_r=1
Short circuit line (SCL)	S_{11}	ε_r

Nicholson-Ross-Weir (NRW) is the most commonly used method for performing direct calculation of both the permittivity and permeability from the S-parameters [16]. This method requires all reflection coefficients and transmission coefficients (S_{11}, S_{21}, S_{12}, S_{22}) or a pair (S_{11}, S_{21}) of S-parameters of the material under test to be measured.

However, material thickness is important for this measurement method. This method diverges for low loss materials at frequencies corresponding to integer multiples of one-half wavelength in the sample which is due to the phase ambiguity. So, optimum sample thickness should be times of $\lambda/4$.

Nicholson-Ross-Weir (NRW) method uses the following formula for determining the relative permittivity.

$$S_{11} = \frac{\Gamma(1-T^2)}{(1-\Gamma^2 T^2)} \quad (2)$$

$$S_{21} = \frac{T(1-\Gamma^2)}{(1-\Gamma^2 T^2)} \quad (3)$$

Where;

$$\Gamma = X \pm \sqrt{X^2 - 1} \quad (4)$$

And by solving of (4), (5) can be obtained.

$$X = \frac{S_{11}^2 - S_{21}^2 + 1}{2S_{11}} \quad (5)$$

$$T = \frac{S_{11}^2 + S_{21}^2 - \Gamma}{1-(S_{11}+S_{21})\Gamma} \quad (6)$$

Relative permittivity and relative permeability can be calculated in (7) and (8).

$$\varepsilon_r = \frac{\lambda_0^2}{\mu_r}\left(\frac{1}{\lambda^2} - \left[\frac{1}{2\pi L} ln\left(\frac{1}{T}\right)\right]^2\right) \quad (7)$$

Where;

$$\mu_r = \frac{1+\Gamma}{\Lambda(1-\Gamma)\sqrt{\frac{1}{\lambda_0^2} - \frac{1}{\lambda_c^2}}} \quad (8)$$

$$\frac{1}{\Lambda^2} = \left(\frac{\varepsilon_r.\mu_r}{\lambda_0^2} - \frac{1}{\lambda_C^2}\right) = -\left(\frac{1}{2\pi L} ln\left(\frac{1}{T}\right)\right) \quad (9)$$

III. KMMS APPLICATION AND CAPABILITIES

Keysight Material Measurement Suite (KMMS) is a commercial software [17, 18]. It has so many special tools for permittivity and permeability measurement. By using KMMS, measurements can be performed from 200 MHz to 50 GHz frequency ranges and from -40 ºC to 200 ºC temperature ranges with the different probes such as high temperature and different type of open-ended coaxial probes. With KMMS tools, paramagnetic materials, flat, isotropic and homogeny materials can be measured. KMMS has also NRW calculation method for permittivity and permeability.

KMMS can run with multiport VNA also and it calculates permittivity and permeability coefficients by using the S-parameter measurement with VNA. The permittivity and permeability model obtained with KMMS is valid for higher frequencies.

In this study, KMMS software was also used at millimeter wave frequencies with NRW method, assuming with the dielectric calculation model would be the same at millimeter wave frequencies. During the measurements discontinuties appered where thickness is not an integer multiplier of λ/4. For that reason, "Reflection/Transmission Epsilon Fast Model" was choosen in KMMS software. All measurement were performed using "Reflection/Transmission Epsilon Fast Model".

IV. MEASUREMENT RESULTS WITH FREE SPACE METHOD AT MILLIMETER WAVE FREQUENCIES

Relative dielectric coefficient measurements were performed in TUBITAK UME RF and Microwave laboratory at two different millimeter wave frequencies. These frequency ranges were selected as 67 GHz to 115 GHz and from 110 GHz to170 GHz. VNA calibration for error term calculation was performed with two different calibration kits (WR 10 and WR6.5). Measurements and calculated uncertainties are given in this study at two different frequency ranges.

TUBITAK UME free space dielectric measurement setup functional block diagram is similar as Fig. 1 and setup picture is given in Fig. 2.

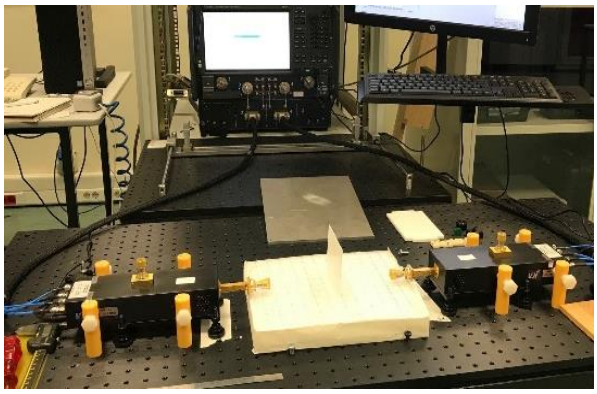

Fig. 2. Free Space measurement setup at TUBITAK UME.

In order to reach the millimeter wave frequencies with VNA, some suitable special frequency extenders were used for these frequency ranges. In this study, two compatible frequency extenders were used to reach for each millimeter wave frequency bands.

List of the equipment used at the measurement setup is given as below;

- Keysight N5247B PNA-X Network Analyser
- Keysight N5292A VNA Multimeter Test Set
- VDI Extender WR6.5 110-170 GHz Model VNAX
- VDI Extender WR10 67-115 GHz Model VNAX
- VDI 6.5 VNAX Calibration Kit N5262AC06
- VDI 10.0 VNAX Calibration Kit N5262AC10
- Horn antennas for 65-115 GHz frequency band
- Horn antennas for 110-170 GHz frequency band

Below parameters were applied before measurements.

- Thickness of the reflector metal which is used for KMMS calibration is 5.0 mm at 67-115 GHz frequency band and 1.0 mm at 110-170 GHz frequency band.
- 10 measurements for each frequency step with 2 second wait.

- Number of points were selected 1201 at 110-170 GHz band and 961 at 67-115 GHz band.
- Nominal power was arranged less than 10 dBm for both frequency bands.
- Distances between antennas were arranged as 76.6 mm for 67-115 GHz frequency band.
- Distances between antennas were arranged as 35 mm for 110-170 GHz frequency band.
- Teflon thickness was 1 mm and 6 mm, Fr4 thickness was 1.2 mm, Komacel thickness was 19 mm.

Measurement results were given in Table 2 as magnitude, real and imaginary components of relative dielectric coefficient for Air, Fr4, Teflon, and Komacel in two different millimeter frequency bands. At the measurements, relative permittivity were measured. Permeability were not measured.

From the measurement results, we can list the parameters that affect the measurement accuracy as follows;

- Antennas alignment (faced each other in mm)
- Perpendicular of the measured material to the antennas
- The roughness of the surface of MUT
- The accuracy of the VNA calibration for calculating the error terms
- Determining the distance of the material to be measured from the antenna with the time domain.

Table 2. Relative dielectric constant values for Air, FR4, Teflon and Komacel from 67 to 115 GHz and 115 to 170 GHz frequency bands

Freq.	Air				Fr4				Teflon				Komacel			
(GHz)	e_r'	e_r"	Mag	u_A	e_r'	e_r"	Mag.	u_F	e_r'	e_r"	Mag.	u_T	e_r'	e_r"	Mag.	u_K
67	1.00	0.00	1.00	4E-05	4.02	0.38	4.50	6E-03	2.05	0.00	2.10	6E-05	1.22	0.01	1.20	6E-05
70	1.00	0.00	1.00	2E-05	4.03	0.30	4.51	7E-03	2.07	-0.01	2.09	2E-04	1.24	0.00	1.24	6E-05
75	1.00	0.00	1.00	2E-05	3.88	-0.06	4.38	2E-03	2.04	0.00	2.09	3E-04	1.29	0.00	1.29	7E-05
80	1.00	0.00	1.00	8E-06	3.86	0.09	4.33	2E-03	2.10	0.00	2.07	3E-04	1.31	0.01	1.31	5E-05
85	1.00	0.00	1.00	2E-05	3.94	0.07	4.42	1E-03	2.08	0.00	2.06	2E-04	1.34	0.01	1.34	5E-05
90	1.00	0.00	1.00	1E-05	4.02	0.22	4.50	1E-03	2.07	-0.01	2.09	6E-04	1.37	0.01	1.37	6E-05
95	1.00	0.00	1.00	1E-05	3.90	0.13	4.37	1E-03	2.08	-0.01	2.08	3E-04	1.39	0.01	1.39	6E-05
100	1.00	0.00	1.00	9E-06	3.90	0.13	4.38	1E-03	2.08	0.01	2.08	2E-04	1.41	0.01	1.41	6E-05
105	1.00	0.00	1.00	9E-06	3.83	0.21	4.29	2E-03	2.08	-0.01	2.08	1E-04	1.43	0.01	1.43	6E-05
110	1.00	0.00	1.00	8E-06	3.76	0.09	4.22	3E-03	2.07	0.01	2.09	2E-04	1.44	0.01	1.45	6E-05
115	1.00	0.00	1.00	1E-05	3.75	0.13	4.20	4E-03	2.08	-0.01	2.09	3E-04	1.15	0.01	1.15	2E-04
120	1.00	0.00	1.00	1E-05	4.56	0.15	4.56	2E-03	2.07	-0.01	2.07	2E-04	1.17	0.01	1.17	2E-05
125	1.00	0.00	1.00	9E-06	4.56	-0.11	4.56	4E-03	2.07	-0.01	2.07	2E-04	1.19	0.01	1.19	2E-05
130	1.00	0.00	1.00	8E-06	4.66	0.13	4.66	3E-03	2.06	0.00	2.06	8E-05	1.21	0.02	1.21	2E-05
135	1.00	0.00	1.00	8E-06	4.73	-0.02	4.73	1E-03	2.07	0.00	2.07	1E-04	1.23	0.02	1.23	2E-05
140	1.00	0.00	1.00	9E-06	4.77	0.06	4.77	7E-04	2.07	0.00	2.07	7E-05	1.25	0.02	1.25	2E-05
145	1.00	0.00	1.00	8E-06	4.68	0.10	4.69	4E-04	2.06	-0.01	2.06	1E-04	1.27	0.02	1.27	1E-05
150	1.00	0.00	1.00	7E-06	4.76	0.11	4.76	2E-04	2.07	-0.01	2.06	7E-05	1.29	0.02	1.29	2E-05
155	1.00	0.00	1.00	6E-06	4.74	0.14	4.74	1E-03	2.07	0.00	2.07	2E-04	1.30	0.02	1.30	1E-05
160	1.00	0.00	1.00	7E-06	4.63	0.18	4.63	2E-03	2.07	0.00	2.07	1E-04	1.32	0.02	1.32	9E-06
165	1.00	0.00	1.00	4E-06	4.76	0.11	4.76	2E-03	2.06	0.00	2.06	1E-04	1.33	0.02	1.33	2E-05
170	1.00	0.00	1.00	8E-06	4.65	0.24	4.65	7E-03	2.07	-0.03	2.07	8E-05	1.34	0.02	1.34	2E-05

Relative dielectric coefficient was calculated from real and imaginary component of the measurements for each materials in this study. Relative dielectric coefficient were given in Fig. 4 in two frequency bands with reference magnitude values. Ref_A is air, Ref_F is Fr4, Ref_T is Teflon, Ref_K is Komacel reference values in Fig. 4. These reference values were obtained out from older studies performed at lower frequencies.

Imaginary component values of relative permittivity of the material are less than zero in some frequencies in Table 2. Values below zero are assumed as numerical calculation error of the calculation of the model.

Due to the measurements performed using two different cal kits, differences in the relative permittivities were observed at the adjacent frequencies of the two different frequency bands.

V. TYPE A UNCERTAINTY CALCULATION OF RELATIVE DIELECTRIC MEASUREMENTS AT MILLIMETER WAVE FREQUENCIES

While calibration services are provided, the calculated value from repeated measurements made with reference devices during the devices are in the laboratory is one of the inputs of the measurement uncertainty calculation. The uncertainty component (u_x), called Type A, from the repeatable measurements, is calculated as in (10) [19].

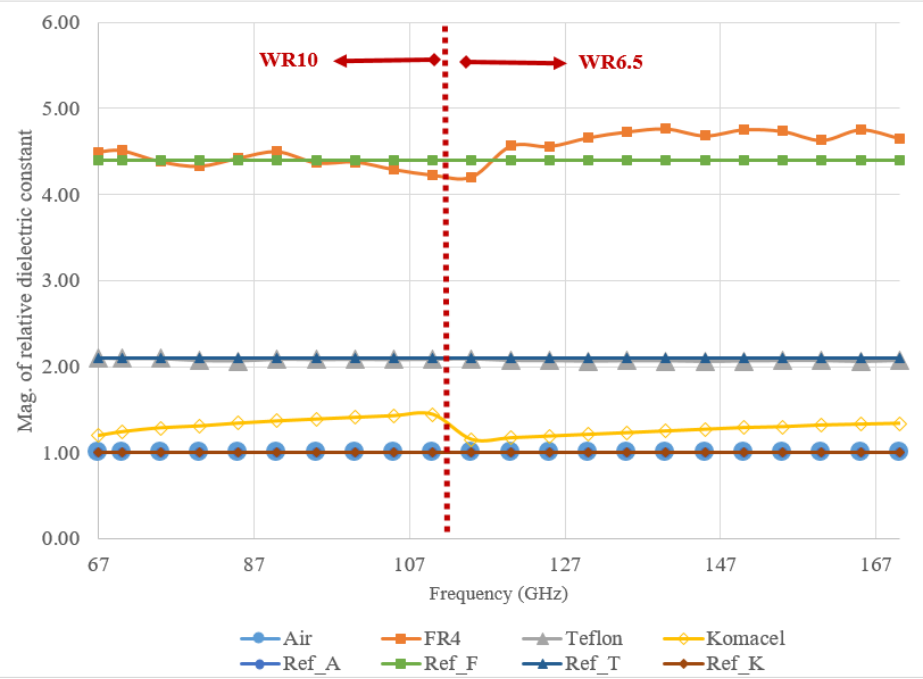

Fig. 4. Relative dielectric contants of Air, Fr4, Teflon and Komacel with known lower frequency reference values at 67 to 115 GHz frequency band and 110 to 170 GHz frequency band

$$u_X = \sqrt{\frac{\frac{1}{(N-1)}\sum_1^N (x_i - x_{Aveg})^2}{N}} \qquad (10)$$

Where x_i is the instant measurement data, x_{Aveg} is the mean of the repeated measurements, and N is the number of measurements.

Uncertainty calculated from repeatable measurements over 10 metrological is assumed to have a normal distribution.

In this study, for each material measurement, 10 repetitive measurement had been performed. Calculated Type A uncertainty of magnitude values of permittivities were given in Table 2 for two millimeter wave frequency bands as Air (u_A), Fr4 (u_F), Teflon (u_T) and Komacel (u_K).

Type A uncertainty of magnitude permittivity of Fr4 is higher than the other uncertainties. Standard deviation of Fr4 measurements were also higher than the other materials'.

VI. CONCLUSION

In this study, repeatable relative dielectric coefficient measurements were performed at millimeter wave frequencies (from 67 to 115 GHz and from 110 to 170 GHz) with KMMS software by using the infrastructure of TUBITAK UME RF and Microwave Laboratory. Although, KMMS was known a software that run up to 50 GHz with its own special probes, it is also proved with this study that KMMS can be able to use at millimeter wave frequencies.

From the measurement results, the parameters that affect the relative permittivity measurement accuracy were determined such as antennas alignment, material position in the setup, accuracy of VNA calibration, thickness of the material. Imaginary component values of relative permittivity of the material were measured less than zero in some frequencies. This kind of values were assumed as numerical calculation error of the calculation of the model.

The uncertainty component from repeatable measurements was calculated and the results of the measurements were shared in the study. Type A uncertainty were less than the compared measured values.

With performed measurements, it has been shown that the calculation model in KMMS (Reflection/Transmission Epsilon Fast Model) can also be used at millimeter wave frequencies. With this study, it has been demonstrated that dielectric coefficient measurements can be performed at millimeter wave frequencies with the free space method in future studies in the environment where the materials are used.

ACKNOWLEDMENT

This study was carried out within the scope of the project (2018-2020) named "Expanding the Microwave Power and S Parameter Measurement Infrastructure up to 170 GHz" supported by TUBITAK UME internal resources. I would like to thank laboratory technician Murat Arslan, internship senior students Aslıhan Ersamut Muhammed Işık, B. Elif Cirik and H. Ibrahim Battal for their contribution to the measurements and the creation of the graphics.

REFERENCES

[1] Paris, D.T, Hurd, F.K., (1969) "Basic Electromagnetic Theory" *Reflection and Refraction of Plane Waves*, pp. 346–397, McGraw Hill, USA.

[2] Paula, A.L. de, Rezende, M.C., Barroso, J.J., (2011) "Experimental Measurements and Numerical Simulation of Permittivity and Permeability of Teflon in X band" *J. Aerosp. Technol. Manag.*, 3-1, 59-64.

[3] Zivkovic, I, Murk, A., (2012) "Free-Space Transmission Method for the Characterization of Dielectric and Magnetic Materials at Microwave Frequencies" *Microwave Materials Characterization*, pp. 1–18, Ch. 5, Eds. Costanzo, S., Intech Publications.

[4] Ghodgaonkar, D. K., Varadan, V. V., Varadan, V. K., (1989) "A Free-Space Method for Measurement of Dielectric Constants and Loss Tangents at Microwave Frequencies", *IEEE Trans. Inst. And Meas*., 37-3, 789-793.

[5] Agilent Technologies, (2012) "Printed Version of Agilent 85070E/85071E Dielectric Probe Kit Software's Help File".

[6] Dvurechenskaya, N., Zielinski, R.J., (2011) "Advantages and disadvantages of the free-space arch method used for investigation of shielding materials at low gigahertz frequencies" *Proceedings of the 10th Int. Symposium on Electromagnetic Compatibility*, 790– 795, York, UK.

[7] Ünal, İ., Türetken, B., (2013) "Electromagnetic Methods in Radar Absorber Material Development", *Project Report*, MİLTAL, Material Institute, TÜBİTAK MAM, Gebze-Kocaeli (in Turkish).

[8] Deepak K. G., Vasundara V.V., Vijay K.V., (1989) "A Free Space Method for Measurement of Dielectric Constant and Loss Tangents at Microwave Frequencies", *IEEE Trans. On Instrumentation and Measuremen*t, Vol 37, No 3.

[9] Ridler N., et all, (2019) "Publishable Summary for 18SIB09 TEMMT Traceability for electrical measurements at millimeter-wave and terahertz frequencies for communications and electronics Technologies", *https://www.euramet.org/research-innovation/search-research-projects/details/project/temmt*.

[10] Kazemipour A., Wollnsack M., Hoffman J., Hudlicka M., Yee S.K, et all, (2020) "Analytical Uncertainty Evaluation of Material Parameter Measurements at THz Frequencies", *International Journal of Infrared and Millimeter Waves*, 41:1199-1217.

[11] Kazemipour A., Hudlicka M., et all, (2015) "Design and Calibration of a Compact Quasi-Optical System for Material Characterization in Millimeter / Submillimeter Wave Domain", *IEEE Trans. On Instrumentation and Measuremen*t, Vol 64, No 6.

[12] K. B. Khadhra, A. Olk, O. Gomez and A. Fox, (2019) "Permittivity estimation of rough dielectric surfaces by means of polarimetric bistatic measurements at millimeter wave frequencies", *2019 16th European Radar Conference (EuRAD)*, pp. 369-372.

[13] Balanis C. A., "Antenna Theory", *John Wiley & Sons*, 2016.

[14] Pozar D. M., "Microwave Engineering", *John Wiley & Sons*, 2011.

[15] Yaw K.C., (2012) "Measurement of Dielectric Material Properties", *R&S Application Note*, RAC0607-0019_1_4E.

[16] Nicolson A.M., Ross G.F., (1970) "Measurement of the Intricsic Properties of Materials by Time Domain Techniques", *IEEE Trans. On Instrumentation and Measuremen*t, Vol IM-19, No 4.

[17] "Agilent Basic of Measuring the Dielectric Properties of Materials", *Agilent Application Note 5989-2589EN*, Agilent Technologies Inc., USA, April 2013.

[18] "Keysight N1500A Material Measurement Suite", *Technical Overview Document 5992-0263EN*, Agilent Technologies Inc., USA, 2021.

[19] JCGM 100:2008, "Evaluation of measurement data – Guide to the expression of the uncertainty in measurement", 1st ed., *Bureau Int. des Poids et Measures*, Sep. 2008.

25th IMEKO TC4 International Symposium
23rd International Workshop on ADC and DAC Modelling and Testing
IMEKO TC-4 2022
Brescia, Italy / September 12-14, 2022

An electro-optic system implementing an accurate phase measurement method for sinewave signals

Luca De Vito, Francesco Picariello, Sergio Rapuano, Ioan Tudosa

Department of Engineering, University of Sannio, 82100 Benevento, ITALY
e-mail: {devito, fpicariello, rapuano, ioan.tudosa}@unisannio.it

***Abstract* – This paper deals with a preliminary design of an electro-optic system for accurately measuring the phase of sinewave signals output by generators up to 100MHz. In particular, a short description of the measurement method and an envisioned application, namely the characterization of waveform recorders, is provided. In the paper, an initial selection of the commercially-available instruments, which are suitable for implementing the proposed electro-optic system and the chosen specifications, are shown. To estimate the repeatability of the phase measurements according to the main characteristics of the chosen equipment, a simulator was implemented and its description is available in the paper. According to the simulation, a maximum standard deviation of 0.028° can be achieved at 100 MHz.**

I. INTRODUCTION

The calibration of waveform recorders (e.g., oscilloscopes) requires the utilization of well characterized (i.e., reference) signals at their input in order to obtain an accurate estimation of their frequency response [1]. According to the chosen type of reference signal, the utilized techniques, which are available in the literature, can be classified as [2]: (i) pulse-based and (ii) swept-frequency based. The former one takes the advantage of frequency combs and multisine signals, however, it exhibits low accuracy in the estimation of the phase response at high frequencies (e.g., GHz range). The latter technique exhibits very good accuracy in estimating the magnitude response, while cannot be adopted for phase response because the knowledge of the input phase of the test sinusoidal signal is extremely difficult to be obtain with the methods described in the literature and with the currently available instrumentation [3]. Furthermore, due to the increasing analog bandwidth of the waveform recorders available on the market, as stated in [3], it is not possible to find a measurement method that is capable of covering a wide range of frequencies while also maintaining a low value of the phase measurement uncertainty.

In [4], a method for measuring the phase spectrum of the output of a sinusoidal frequency source is described for the calibration of an electroshock weapon characterization system. An electroshock weapon characterization system consists of a long-epoch (e.g., 12s) and 200 MHz analog bandwidth for the waveform recorder to acquire both high voltage and current waveforms, simultaneously [4]. Preliminary hardware implementations of the phase measurement method [4] were described in [1] and [5]. In particular, a proof of concept was proposed in [1] with an arbitrary waveform generator, an oscilloscope and an universal digital counter.
An experimental assessment of the phase measurement repeatability in terms of standard deviation for sinewave frequencies ranging from 100 Hz to 10 MHz was published in [1]. The reported results exhibit maximum standard deviations of 0.009° for both 100 Hz and 10 MHz, [1]. However, this implementation is limited to characterize only arbitrary waveform generators with two output channels synchronized to each other and to a maximum sinewave frequency of 10 MHz.

In this paper, a preliminary design of an electro-optic system that implements the method proposed in [4] is described. This implementation aims to increase the maximum sinewave frequency (i.e., to 100 MHz) that can be analyzed respect to the electrical hardware implementations, which were demonstrated in literature as achieving a maximum working frequency range of 10 MHz, [1], [5]. In particular, the proposed implementation has been simulated by means of the OptiSystem [10] software and MATLAB tools and the assessment of the phase standard deviation is provided for 100 MHz.

The paper is structured as follows. Section ii. describes the phase measurement method. A description of the electro-optic phase measurement system for implementing the adopted phase measurement method is provided in Section iii.. In Section iv., a simulator of the system implemented with OptiSystem and MATLAB tools is described and the obtained simulation results in terms of standard deviation of the phase estimates are discussed. The last Section concludes the paper.

II. PHASE MEASUREMENT METHOD

In the following, the phase measurement method from [1] is shortly described. As depicted in Fig. 1, in order to measure the phase of a sinewave signal with the method described in [1], the following functional blocks are utilized: (i) pulse source, (ii) pulse delay, (iii) pulse selector,

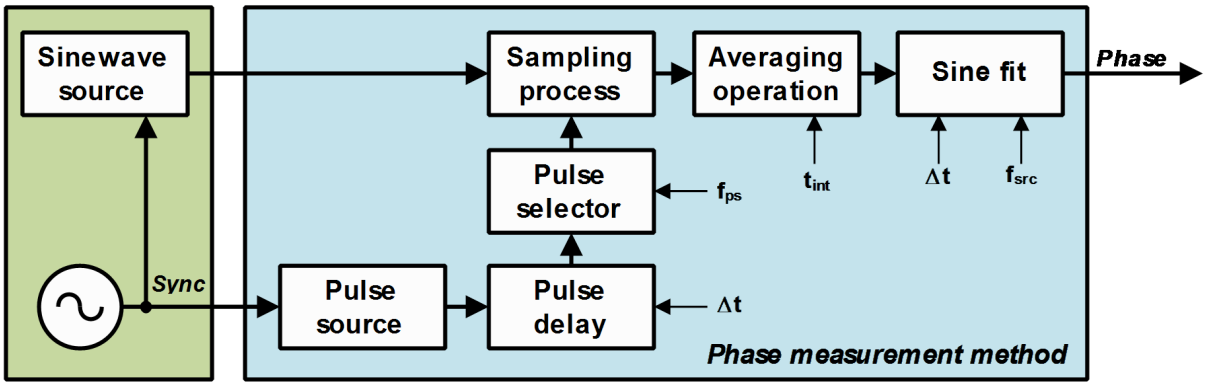

Fig. 1. General overview of the phase measurement method [1].

(iv) sampling process, (v) averaging operation, and (vi) the sine fit.

The sinewave source under test provides a signal synchronized with an external clock (i.e., Sync). This synchronization signal is also utilized by the pulse source to provide a pulse train signal working at the same frequency of the Sync signal. The pulse train signal is then delayed according to an imposed Δt by the pulse delay block. The delayed pulse train signal drives a pulse selector that allows to reduce the frequency of the pulse train signal according to the desired f_{ps} value. In particular, the pulse train signal must have a frequency that is an integer sub-multiple of the sinewave frequency (i.e., f_{src}). The sampling process provides a measurement of the sinewave amplitude at the instant defined by the pulse train signal. Because the frequency of the pulse train signal is an integer sub-multiple of f_{src}, the amplitude measurements are provided at the desired pulse train rate and, therefore, it refers to the same sinewave phase. An averaging operation is performed on the amplitude measurements obtained at Δt. The averaging operation is performed to reduce the effect of noise on the variability of the amplitude measurements. When at least three amplitude measurements at three different Δt delays along the sinewave period are obtained, the 3-parameter sine fit interpolating algorithm is applied for estimating the sinewave phase according to its frequency f_{src}.

The main uncertainty sources affecting the phase measurement method are: (i) the jitter on the pulse train signal defining the sampling instants, (ii) the noise affecting the amplitude measurements, and (iii) the synchronization error between the pulse train and the sinewave. An influence quantity of the phase measurement is the clock drift of the external clock that directly affects the synchronization between the pulse train and the sinewave under test. The effect of the random jitter and noise on the phase measurement accuracy can be reduced by increasing the number of amplitude measurements utilized in the averaging operation (i.e., both random variables are assumed to be Gaussian distributed with zero mean). However, the required time for a single measurement of a phase increases with the number of samples applied to the averaging operation. As a consequence, the effect of the synchronization error increases too, with an effect of reducing the measurement repeatability.

III. THE ELECTRO-OPTIC PHASE MEASUREMENT SYSTEM

An implementation of the phase measurement method based on electro-optic components is depicted in Fig. 2. The synchronization signal (i.e., Sync) provided by the sinewave generator is used for generating an optical pulse train. This optical train is produced by means of an electrical pulse generator that provides to a Mach Zehnder Modulator (MZM) driver a pulse train synchronous with the Sync signal and having its repetition rate at an integer sub-multiple of f_{src}. Furthermore, the pulse generator is controlled by a control unit for introducing a delay on the electrical pulse train signal to sample the sinewave in different instants of its period. The MZM provides as output an optical pulse train at the wavelength of 1550nm (wavelength of the continuous wave laser) with a pulse located at the instants defined by the electrical pulse train.

The optical pulse train is then utilized as an optical input to a second MZM (i.e., included in the sampler processing block, see Fig. 2). This second MZM acts as an optical sampler for the optical signal output by the first MZM. The resulting optical signal at the sampler's output is again an optical pulse train having the amplitude modulated by the sinewave. Because the electrical pulse train signal is synchronized with the sinewave, the resulting optical pulse train at the sampler's output will present an optical energy proportional to the sinewave amplitude at the set delay values. Finally, the sampler's output is then converted in an electrical signal by means of a high-bandwidth photodiode (PD).

The electrical signal from the PD is acquired by a data acquisition (DAQ) system that performs a coherent sam-

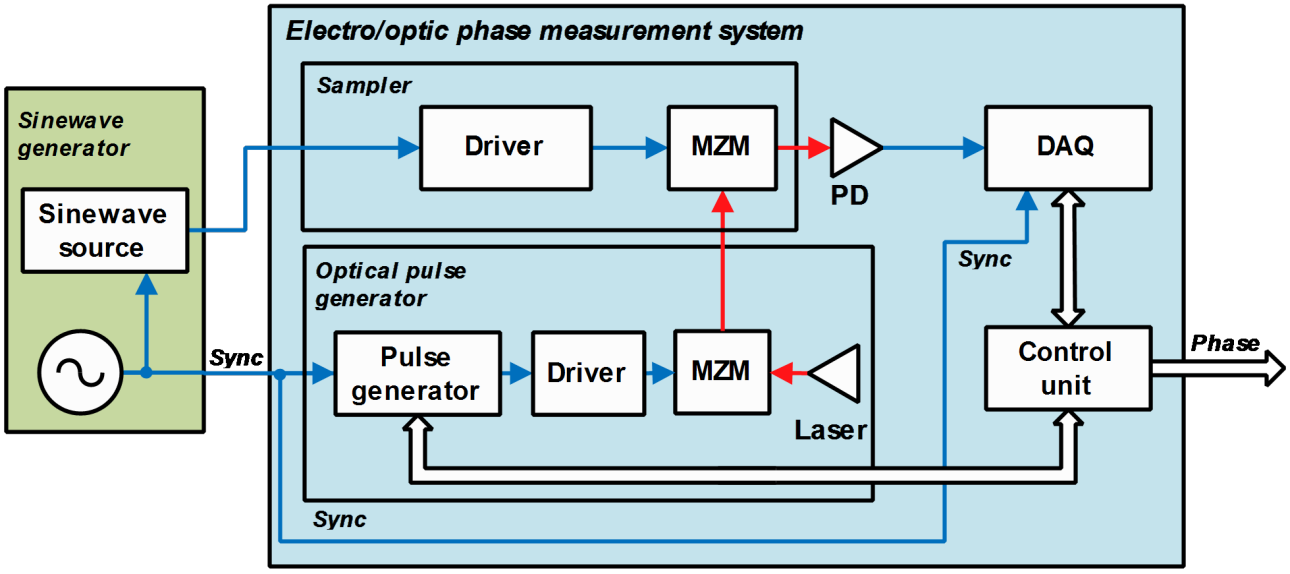

Fig. 2. The proposed electro/optic PMS.

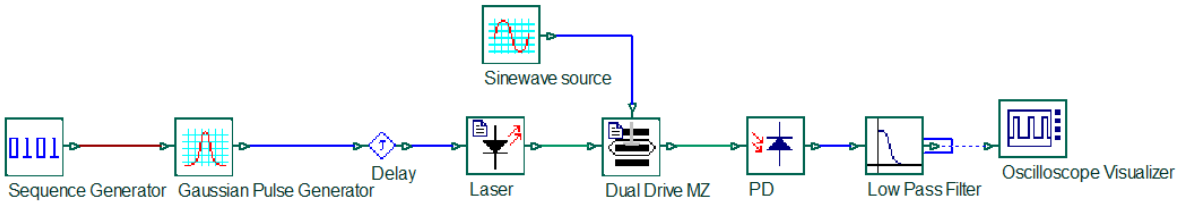

Fig. 3. The simulated OptiSystem diagram.

pling over several periods. From the acquired samples, a signal value is extracted and stored for further processing. The control unit imposes several delays to the pulse train signal to obtain measurements at several instants along the sinewave period. From the obtained measurements, by knowing the imposed delay and the sinewave frequency, the 3-parameter sine fit is applied to estimate the phase.

An initial analysis of the equipment available on the market that can be suitable for the implementation of the proposed system is described. As an optical pulse generator, the ModBox C-Band pulse by iXblue [6] could be a valid solution. It can be driven externally by an electrical trigger signal for generating an optical pulse train with a pulse repetition rate adjustable up to 20 MHz. The pulse duration (see [6]) can be controlled within the range of 100 ps to 25 ns and, furthermore, it is possible to introduce on the pulse train a delay respect to the trigger of up to 2.5 ns, guaranteeing a root-mean-square jitter of 10 ps. The nominal optical wavelength of the continuous wave laser is 1550 nm and the Relative Intensity Noise (RIN) is -140 dB/Hz, [6]. As a sampler, the MXLER-LN-20 MZM [7] embedding a specific driver for bias control by iXblue controller has been selected as a possible solution for this implementation. This MZM exhibits a nominal working bandwidth of 20 GHz, having an extinction ratio of 40 dB and a nominal insertion loss of 3.5 dB. At the output of the sampler block, the O2E-1201-MTRQ optical to electrical converter [8] has been chosen as a detector. It exhibits a conversion gain of 100 V/W at 1550 nm with a typical noise equivalent power of 39.7 pW/$\sqrt{Hz}$. For implementing the coherent sampling of the converted signal, the PicoScope 9302-25 [9] has been selected as a possible device. In particular, it exhibits an electrical working bandwidth of 25 GHz with a time-base ranging from 5 ps/div to 3.2 ms/div.

IV. SIMULATION TESTS

The proposed electro-optic system implementation has been simulated by means of the OptiSystem tool [10] (see Fig. 3). The assessment of its performance in terms of standard deviation of the phase measurements has been done in MATLAB. In particular, the optical pulse generator has been simulated by considering the Gaussian pulse generator library that provides an electrical output, which

Table 1. The polynomial equation coefficients.

Coefficient	Value	95% confidence bounds
p1	5.32×10^9	$[-2.61, 13.26] \times 10^9$
p2	-5.13×10^9	$[-12.29, 2.03] \times 10^9$
p3	2.11×10^9	$[-0.63, 4.86] \times 10^9$
p4	-0.49×10^9	$[-1.07, 0.01] \times 10^9$
p5	6.86×10^7	$[-0.65, 14.37] \times 10^7$
p6	-6.09×10^6	$[-12.10, -0.01] \times 10^6$
p7	3.38×10^5	$[0.42, 6.34] \times 10^5$
p8	-1.12×10^4	$[-1.97, -0.27] \times 10^4$
p9	211.3	[83.38, 393.30]
p10	2.46	$[-3.21, -1.71]$

is delayed through the electrical signal time Delay block. The delayed Gaussian pulse drives a laser block working at the wavelength of 1550 nm with a power of 20 mW. A dual drive MZM modulator was used to simulate the sampler block. In particular, the laser output is connected to its optical input, while the electrical input is driven by a sinewave signal having an amplitude of 1 V. The MZM is polarized with bias voltages of -2.8 V and -1.1 V, respectively. These two values of bias voltage have been demonstrated to guarantee the best linearity and sensitivity performance according to the absorption/phase MZM characteristic available in the simulator.

The output of MZM modulator is connected to a PD working at the nominal wavelength of 1550 nm and exhibiting an electrical bandwidth of 25 GHz. The PD current is converted into a voltage signal, therefore providing a conversion gain of 100 V/W. The voltage signal is connected to an oscilloscope visualizer block available in the OptiSystem libraries that is configured by means of a developed MATLAB script. In particular, this MATLAB script reads the acquired samples and finds the maximum in the record. A record contains a single optical pulse period. Furthermore, this MATLAB script allows imposing a delay to the electrical signal time delay block to perform the sampling operation of the sinewave signal in different instants. The 3-parameter sine fit algorithm was implemented in MATLAB and applied on the obtained maximum values according to the imposed delays and the sinewave frequency.

By considering the equipment analysis described in the previous section, in the simulations, the following non-idealities have been considered: (i) a random jitter of 10 ps impacting the delay stability of the optical pulse train, (ii) a RIN of -140 dB/Hz for the laser, and (iii) a noise equivalent power of 39.7 pW/$\sqrt{Hz}$ for the voltage signal at the output of the PD.

The simulations have been performed by considering a sinewave working at 100MHz. Future work will be intended to perform the analysis at 1 GHzand more, too.

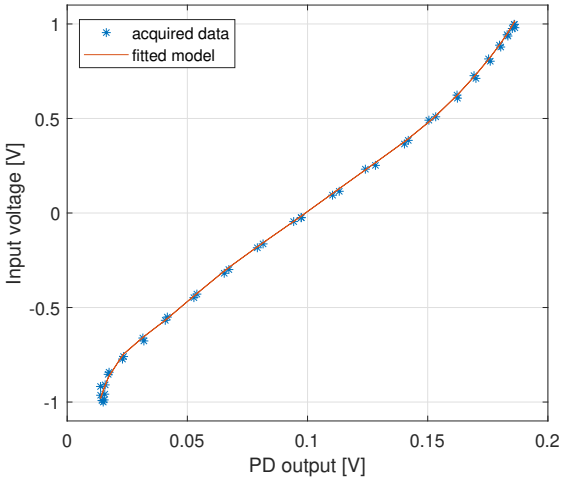

Fig. 4. MZM characteristic at sine-wave frequency of 100 MHz.

A. *The MZM-based sampler*

By considering as inputs the sinewave signal and the optical pulse train, and as output the maximum voltage provided by the PD, the MZM characteristic is nonlinear. This limits the utilization of this MZM as a sampler for the desired phase measurement system implementation. Thus, the theoretical nonlinear characteristic of the MZM needs to be firstly characterized by means of simulation analysis and then compensated before applying the 3-parameter sine fit to the signal data. To this aim, a MATLAB script has been implemented with the goal of measuring the maximum amplitude at the PD's output for several MZM input voltages. In particular, the MZM electrical input has been driven by a sinewave of 1 V as amplitude and having a phase ranging from 0 ° up to 360 °. The optical pulse train delay was set to 0 s and the maximum PD's output voltages for several imposed phases were evaluated.

In Fig. 4, the sinewave amplitude at 0 s for the different applied voltages is plotted against the maximum PD's output voltage. A polynomial equation has been estimated with the aim of compensating this nonlinear behavior. In Tab. 1, the obtained coefficients of the polynomial equation with the relative ranges at 95% of confidence level are reported. The obtained fitted equation exhibits a root mean square error of 0.018 V.

B. *Monte Carlo analyses*

For assessing the repeatability of the phase measurement against non-idealities (e.g., random jitter, RIN and noise equivalent power affecting the PD's output voltage), two Monte Carlo analyses have been conducted with 40 trials considering a sine fit applied on: (i) a single maximum PD voltage measurement at each imposed delay, and (ii) the average of 100 maximum PD measurements at each delay.

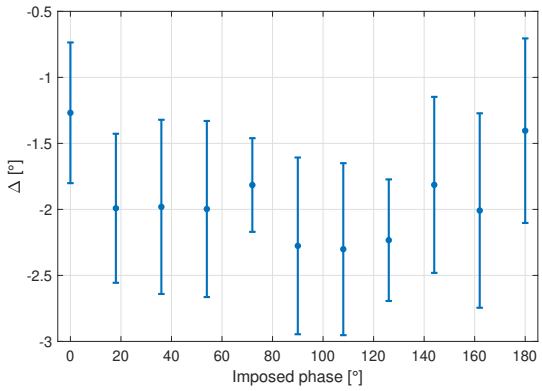

Fig. 5. Phase estimate error for imposed phases ranging from 0° to 180 °, with bars representing $3 \cdot \sigma$, considering a single PD measurements for each delay.

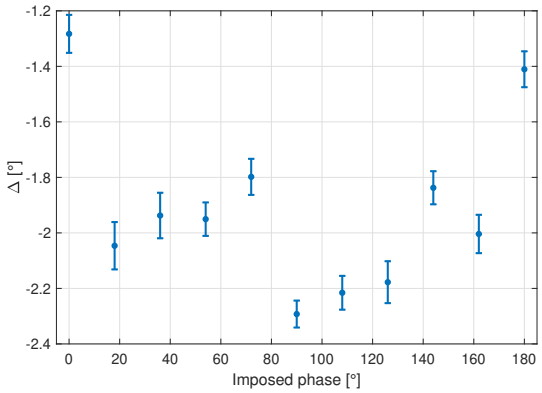

Fig. 6. Phase estimate error for imposed phases ranging from 0° to 180 °, with bars representing $3 \cdot \sigma$, considering the average of 100 PD measurements for each delay.

In this way, the fact that the averaging operation reduces the variability of the phase measurements is expected.

The obtained results by considering a single maximum PD voltage measurement are depicted in Fig. 5, as in terms of error between the provided phase estimate and the imposed one (i.e., $\Delta = \hat{\phi} - \phi$). For each imposed phase, 40 estimates are calculated and the error average together with the standard deviation σ are evaluated. In the graph, the bars represent $3 \cdot \sigma$. Among the imposed phases, the maximum obtained standard deviation is 0.25 °. As shown in Fig. 5, the phase estimates have an offset of around -2 ° and, being covered by their variability, a trend on the error averages is not clearly visible.

In Fig. 6, the obtained results by considering the average of 100 maximum voltage measurements for each time delay, before to perform sine fit, are shown. In this case, the maximum standard deviation is 0.028 °, i.e., as it was expected, about one order less than the one obtained by considering a single measurement. As in the previous case, the error offset is around -2 °, while an error trend is more visible. This trend can be minimized by considering a further compensation step.

V. CONCLUSION AND FUTURE WORK

In this paper, the architecture of an electro-optic system implementing an accurate measurement of the phase of sinewave signals up to 100 MHz was described. In particular, a first selection of the suitable instruments for its implementation was provided. According to the major uncertainty sources that may affect the accuracy of phase measurements, several Monte Carlo analyses were performed with the aim of assessing the standard deviation of the phase estimates. Furthermore, the compensation of the non-linearity of the chosen MZM was performed by means of simulations. This allowed correcting the sampling results from the sinewave signal with the optical pulse train. The obtained results expressed a maximum standard deviation of 0.028 ° at 100 MHz.

Future works will be focused on: (i) the assessment of the performance of the electro-optic system at 1 GHz and more, (ii) considering the clock drifts and synchronization error in the simulator, (iii) adopting in the simulator as absorption/phase characteristic a model closer to the real characteristic of the selected MZM, and (iv) a first implementation of the proposed system by means of hardware.

ACKNOWLEDGEMENT

The research presented in this paper has been supported from grant 70NANB19H074 "An electro/optical phase measurement system for the characterization of electroshock weapon electrical sources" awarded by the National Institute of Standards and Technology (NIST), USA. The Authors thank Nicholas G. Paulter for his assistance with methodology and comments that greatly improved the manuscript.

REFERENCES

[1] S. Rapuano, P. Daponte, L. De Vito, F. Picariello, I. Tudosa and N. Paulter, "A phase measurement method to guarantee the traceability of the calibration systems", Conference on Precision Electromagnetic Measurements (CPEM), 2020, pp. 1-2, 24-28 Aug. 2020, Denver, CO, USA.

[2] C.A. Remley, P.D. Hale and D.F. Williams, "Absolute magnitude and phase calibrations", RF and microwave circuits, measurements, and modeling, Taylor and Francis, Boca Raton, FL, 2007.

[3] E. Balestrieri, L. De Vito, F. Picariello, S. Rapuano and I. Tudosa, "A review of accurate phase measurement methods and instruments for sinewave signals", ACTA IMEKO, vol. 9, No. 2, 2020.

[4] N.G. Paulter, Jr., "Method for measuring the phase

spectrum of the output of a frequency source used in the calibration of an electroshock weapon characterization system", Journal of research of the National Institute of Standards and Technology, vol. 122, no. 35, pp. 1-14, Sept. 2017.

[5] F. Picariello, I. Tudosa, L. De Vito, S. Rapuano and N.G. Paulter, "An initial hardware implementation of a new method for phase measurement of sinewave signals," 11th International Symposium on Advanced Topics in Electrical Engineering (ATEE), 2019, pp. 1-6, 28-30 March 2019, Bucharest, Romania.

[6] ModBox C-Band pulse by iXblue, datasheet available online: https://www.ixblue.com/photonics-space/optical-pulse-shaper-laser-front-end/

[7] MXER-LN-20 by iXblue, datasheet available online: https://www.ixblue.com/photonics-space/intensity-modulators/

[8] O2E-1201-MTRQ by Quantifi Photonics, datasheet available online: https://www.quantifiphotonics.com/products/optical-electrical-converters/matriq-optical-electrical-converter/

[9] PicoScope 9302-25 by pico Technology, datasheet available online: https://www.picotech.com/oscilloscope/9300/picoscope-9300-features

[10] OptiSystem tool by Optiwave photonic software, software description available online: https://optiwave.com/optisystem-overview/

25th IMEKO TC4 International Symposium
23rd International Workshop on ADC and DAC Modelling and Testing
IMEKO TC-4 2020
Brescia, Italy / September 12-14, 2022

Compact Monopole Antenna for Smart Meter Applications in ISM Band 900 MHz

Marlo Andrade[1,2,4], Raimundo C.S. Freire[4], Paulo Fernandes da Silva Júnior[3], Ewaldo E.C. Santana[3], Eduarda Froes dos Santos[3], Maria G.A. de Souza[4], Arthur S. Souza[4], Alexandre J.R. Serres[4]

[1]*Univ. Bordeaux, 351 Cours de la Libération, 33405 Talence, France, marlo.santos@ee.ufcg.edu.br*
[2]*Federal Institute of Pernambuco, Av. Professor Luiz Freire, 500, Recife - 50740540, Brazil, marlo.santos@ee.ufcg.edu.br*
[3]*State University of Maranhão, Avenida Sarney Filho, Sao Luís - 65081-400, Brazil, pfs1224@gmail.com, ewaldoeder@gmail.com, eduardamtm2013@hotmail.com*
[4]*Federal University of Campina Grande, Aprígio Veloso, 882, Campina Grande - 58428-830, Brazil, freire@dee.ufcg.edu.br, maria.souza@ee.ufcg.edu.br, arthur.souza@ee.ufcg.edu.br, alexandreserres@dee.ufcg.edu.br*

***Abstract* – A compact monopole antenna for smart meters in Industrial Scientific and Medical (ISM) band 900 MHz is developed in this paper. The antenna was built in low-cost material (FR4), with spirals in P-Shape, and a total area of 4.32 cm^2. The monopole antenna has broadband characteristics, however, the use of a spiral in P-Shape provides a reduction of the bandwidth, making it operate in narrowband. The P monopole antenna presents good relation between simulated and measured results, a difference of 0.32 %, measured bandwidth of 32 MHz (896 - 928 MHz), covering the ISM band 900 MHz (902 - 918 MHz), omnidirectional radiation pattern, without secondary lobes, with simulated HPBW of 107 degrees, the maximum gain of 2.29 dBi, and current density of 387.19 A/m^2.**

I. INTRODUCTION

In the recent years researches in smart grids has been intensive, a difficult is the long distances management of electrical systems distributed in real-time. The smart grids require an intelligent energy management system, an efficient communication infrastructure to estimate and control of distributed energy resources systems demands smart devices controller [1]. The wireless commercial networks, as cellular communications (2G, 3G, 4G), industrial, science and medical applications (ISM), IEEE 802 and your families (Wi-Fi, Wi-Max), and others, with compatibility of machine-to-machine (M2M) technologies are used possibilities for application in smart grids [2, 3]. Machine to machine communications has characterized by automated connectivity among machines or devices without any human intervention, and relationship with Internet of Things (IoT), and others systems [4]. The ISM band ((910 - 928) MHz have intensive use in several communications systems, being a good candidate of use in M2M application for smart grids, thus the antenna operating in this band provide implementation of low cost.

The smart meters are M2M devices used in automatic meter reading systems (AMR), with the function of collecting and transmitting information automatically to a meter data, and management system, for further processing and storage. The project of a smart meters antenna requires some characteristics like compact structure, omnidirectional radiation pattern, low cost, easy reproduction, and operation in the commercial band [5, 6, 7]. The project of antenna for smart meters presented application in various frequencies, such as cellular communications technologies, wireless local area network, Global Positioning System (GPS) and ultra-high frequencies (UHF) [8, 9, 10].

The printed monopole antenna is generally used in ultra-wideband antenna, with interesting characteristics for use in smart meters as, compact structure, low cost, a facility built, the possibility of circular polarization, omnidirectional radiation pattern, wideband, and low effective isotropic radiated power. However, it presents limitations as susceptibility to interference by metallic plates and other electromagnetic devices near to the ground plane, and the possibility of group delay, i.e., the signal sent may be delayed by the receiver, depending on its position relative to the antenna [11, 12]. The use of the spiral in a monopole antenna provides a reduction of the bandwidth, making the narrow band antenna. A spiral antenna has the following attributes: lightness, quick assembly and compatibility with microwave circuit. Thus, it has essential features in many wireless communication applications. The spiral structure makes the antenna lighter and provides broadband action [13].

This paper presents the design of the compact spiral monopole antenna, the total area of 4.32 cm^2, with P-Shape, operating in ISM band 900 MHz, low cost, and

omnidirectional radiation pattern, with a comparison of simulated and measured results. This paper is composed of three parts before this introduction. Section II present the materials and methods used, section III the results, and the conclusions in section IV.

II. MATERIALS AND METHODS

The design method for the P antenna, was developed by steps:

1. The definition of the application and determination of operating frequencies, choice of the antenna characteristics suitable for the application;
2. The selection of the conductor and dielectric materials, with a characterization of the properties of the material;
3. Simulation and optimization of the antenna, where some adjustments are done targeting the desired resonant frequency, with the construction of the antenna, and comparison of the measured and simulated results.

The electrical characterization, was performed with the measurement of the permittivity, loss tangent, and thickness of the dielectric, were performed in the laboratory of the Federal Institute of Paraiba, the campus of João Pessoa, Paraiba, by probe process with the software Dielectric Probe 85070, using the Vector Network Analyzer (VNA) of Agilent Technology model E5071C (300 kHz - 20 GHz). The results of the dielectric characterization are shown in Fig. 1.

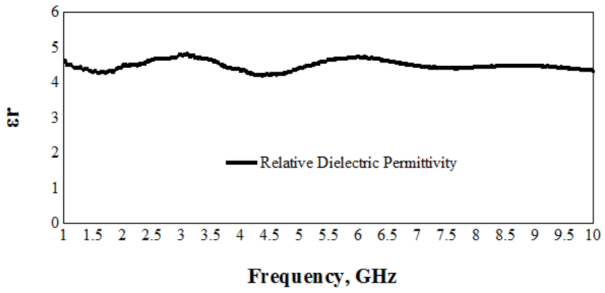

Fig. 1. Fiberglass permittivity of dielectric characterization.

In this project, we used the printed monopole antenna structure, feeding by a transmission line, and spiral patch element. Fig. 2 shows the antenna design with dimensions (mm), Fig. 3 show the prototype. The simulations were performed in the Radiometry laboratory, Federal University of Campina Grande, in Vector Network Analyzer (VNA) Agilent Technologies, model E5071C (9 kHz - 8 GHz). The antennas was built in FR4, dielectric thickness h = 1.55 mm, dielectric permittivity ϵ_r = 4.34, and loss tangent of δ = 0.002. The transmission line used presented width of 0.5 mm, and length 16.2 mm. The monopole antenna has shaped of "P" with three concentrically spirals, calculated by multiple of guided wavelength (λ_g), thus the width of greater spiral dimension has approximately λ_g/7, length λ_g/15, width spiral core of λ_g/10, and length of λ_g/39, provides total area of 4.32 cm^2. The effective wavelength can be calculated by equation (1),

$$\lambda_g = \frac{c}{f_0\sqrt{\epsilon_r}}, \tag{1}$$

were ϵ_r is the relative dielectric constant, and f_0 is resonance frequency of antenna. The spacing of spirals used was 1 mm. The matching impedance has obtained by the proximity of spiral terminals. Simulation and adjusts of antenna design were performed by commercial software $Ansys^{TM}$. The Fig.2 and Fig. 3 shows simulated P monopole antenna dimensions (mm) and prototype.

The experimental setup used to measure the antenna response can be seen in Fig. 4: An antenna (1) connected by SMA connector, receiving signals from a coaxial cable 30 cm RG-174 (2) from the VNA (3) , connected by a UBS cable (4) to the computer (5), avoiding movements during measurements. For each measurement, SOL (short-open-load) calibrations were performed.

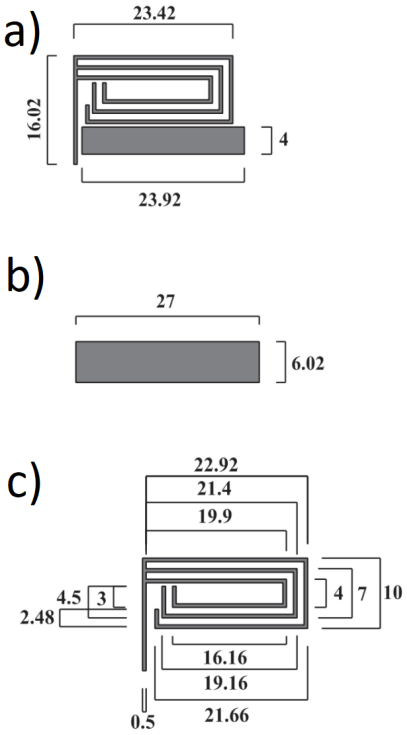

Fig. 2. P monopole antenna: (a) top vision of antenna with dimensions, (b) bottom vision of antenna with dimensions and (c) patch element with dimensions.

Fig. 3. P monopole antenna: prototype top and bottom vision.

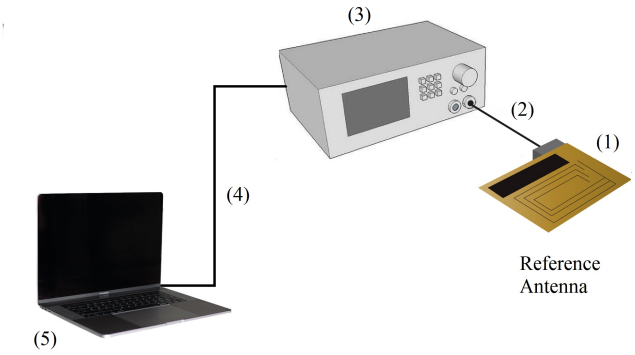

Fig. 4. Schematic of the experimental setup for measurement.

III. EXPERIMENTAL RESULTS AND DISCUSSION

This paper presents the use of spiral P-Shape in a monopole antenna for smart meters operating in ISM band 900 MHz. The use of spiral P-shape in an antenna with broadband characteristics provides a reduction in the bandwidth, making it operate in narrowband. The antenna presented good relation between measured and simulated resonance frequency, difference Δ_f = 0.32 %, measured bandwidth of 32 MHz, compact structure, 4.32 cm^2, omnidirectional radiation pattern, simulated Half Power Beam Width (HPBW) of 107°, the maximum gain of 2.29 dBi, and high current density of 387.19 A/m^2.

Fig.5 shows comparison of return loss ($|S_{11}|$) parameter simulated and measured of P monopole antenna for smart meters. Values has been observe in the Tab. 1 and Tab.

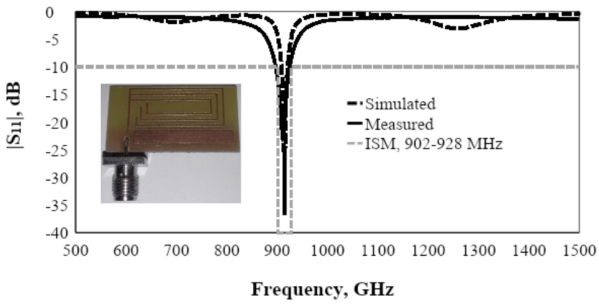

Fig. 5. Result values of P antenna simulated and measured.

2. The antenna presented good concordance of simulated and measured results, with difference in the resonance frequencies of 0.32 %, return loss S_{11} = -23 dB and bandwidth covering the ISM band.

Table 1. Result values of P antenna simulated and measured - Frequency

P(antenna)	f_0 (MHz)	f_1 (MHz)	f_2 (MHz)
Simulated	915	909	922
Measured	912	896	928

Table 2. Result values of P antenna simulated and measured - Bandwidth and Return Loss

P(antenna)	Bandwidth (MHz)	Return Loss (dB)
Simulated	13	-36.8
Measured	32	-23

Measured impedance on Smith chart can be observed in Fig. 6. The point 1 indicating the impedance in resonance frequency (912 MHz), with result closed to the input impedance (50 Ω), with Voltage Standing Wave Ratio (VSWR) close to the 1 (one), demonstrating the narrowband operation.

Fig. 7 shows simulated 3D and 2D radiation patterns of the P monopole antenna in resonance frequency, with gain, HPBW, and current density indicated. The antenna presented an omnidirectional radiation pattern, with the maximum gain in broadside direction of 2.29 dBi, the current density of 387.19 A/m^2, HPBW in the patch direction of 97°, and ground plane direction of 107°. The lack of secondary lobes observed in the radiation pattern indicates low group delay, so the signal sent arrives at all points illuminated by the antenna without delay. The high current density is due to the width of the spirals used in the antenna. Current tends to traverse the structure more in the

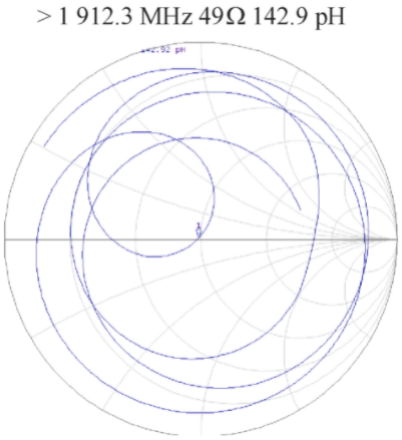

Fig. 6. Smith chart of P monopole antenna with resonance frequency indicating.

edges than in the center of the radiant element [12], thus, the thinner the element, the less difficulty in the passage, and the stronger will be the current on the surface of the antenna.

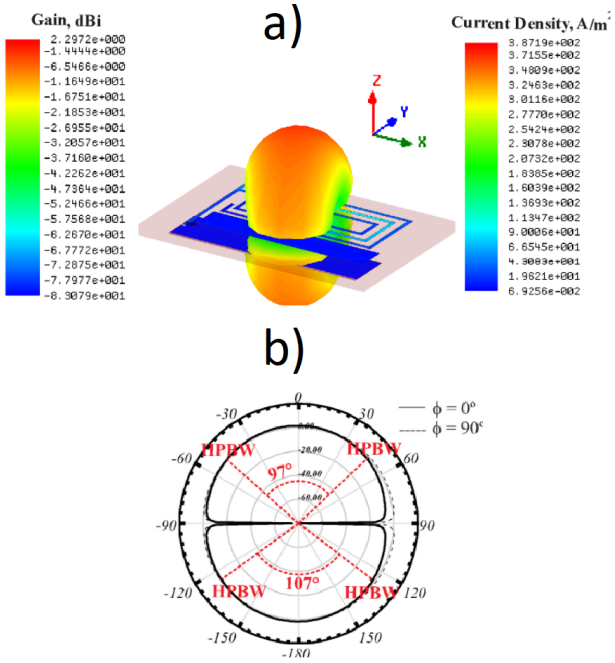

Fig. 7. Radiation pattern of P monopole antenna: (a) 3D with gain and current density, (b) 2D with HPBW.

IV. CONCLUSION

This paper presents the use of spiral P-Shape in a monopole antenna for smart meters operating in ISM band 900 MHz. The use of spiral P-shape in an antenna with broadband characteristics provides a reduction in the bandwidth, making it operate in narrowband. The antenna presented good relation between measured and simulated resonance frequency, difference Δ_f = 0.32 % measured bandwidth of 32 MHz, compact structure, 4.32 cm^2, omnidirectional radiation pattern, simulated HPBW of 107°, the maximum gain of 2.29 dBi, and high current density of 387.19 A/m^2.

ACKNOWLEDGMENT

We greatly appreciate the FAPEMA, UEMA, COPELE and UFCG by supporting and funding this project, without which this work would not be possible.

REFERENCES

[1] M.Rana and L.Li, "Microgrid state estimation and control for smart grid and Internet of Things communication network", Electronics Letters, vol.51, No.2, 2015, pp.149-151.

[2] Y.Cao, T.Jiang, and Z.Han, "A survey of emerging M2M systems: Context, task, and objective", IEEE Internet of Things Journal, vol.3, No.6, 2016, pp.1246-1258.

[3] R.Lu, X.Li, X.Liang, X.Shen, and X.Lin, "GRS: The green, reliability, and security of emerging machine to machine communications", IEEE communications magazine, vol.49, No.4, 2011, pp.28-35.

[4] F.Ghavimi and H.H.Chen, "M2M communications in 3GPP LTE/LTE- A networks: Architectures, service requirements, challenges, and applications", IEEE Communications Surveys Tutorials, vol.17, No.2, 2014, pp.525-549.

[5] M.Moghavemi, S.Tan, and S.Wong, "A reliable and economically feasible automatic meter reading system using power line distribution network", 2005, pp.301-318.

[6] J.Zheng, D.W.Gao, and L.Lin, "Smart meters in smart grid: An overview", IEEE Green Technologies Conference (GreenTech), 2013, pp.57-64.

[7] P.Zhang, F.Li, and N.Bhatt, "Next-generation monitoring, analysis, and control for the future smart control center", IEEE Transactions on Smart Grid, vol.1, No.2, 2010, pp.186-192.

[8] Z.M.Fadlullah, M.M.Fouda, N.Kato, A.Takeuchi, N.Iwasaki, and Y.Nozaki, "Toward intelligent machine-to-machine communications in smart grid", IEEE Communications Magazine, vol.49, No.4, 2011, pp.60-65.

[9] A.Loutridis, M.John, and M.J.Ammann, "Folded Meandered Monopole for Emerging Smart Metering and M2M Applications in the Lower UHF Band [Wireless Corner]", IEEE Antennas and Propagation Magazine, vol.58, No.2, 2016, pp.60-65.

[10] J.Buckley, D.Gaetano, K.McCarthy, L.Loizou, B.O'Flynn, and C.O'mathuna, "Compact 433 MHz

antenna for wireless smart system applications", Electronics Letters, vol.50, No.8, 2014, pp.572-574.

[11] M.Ghavami, L.Michael, and R.Kohno, "Ultra wideband signals and systems in communication engineering", John Wiley Sons, 2007.

[12] O.Haraz and A.-R.Sebak, "UWB antennas for wireless applications", Advancement in microstrip antennas with recent applications, 2013, pp.125-152.

[13] A.M.Mozi, D.S.A.Damit and Z.Faiza,"Rectangular spiral microstrip antenna for WLAN application", 2012 IEEE Control and System Graduate Research Colloquium. IEEE, 2012, pp. 181-185.

25th IMEKO TC4 International Symposium
23rd International Workshop on ADC and DAC Modelling and Testing
IMEKO TC-4 2022
Brescia, Italy / September 12-14, 2022

Static Characterization of the X-Hall Current Sensor in BCD10 Technology

Gian Piero Gibiino[1], Marco Crescentini[1,2], Marco Marchesi[3], Marco Cogliati[3], Aldo Romani[1,2], Pier Andrea Traverso[1]

[1]*Dept. Electrical, Electronic, and Information Engineering (DEI), University of Bologna, Italy*
[2]*Advanced Research Center on Electronic Systems (ARCES), University of Bologna, Italy*
[3]*STMicroelectronics, Analog and Smart Power Technology R&D, Cornaredo, Italy*

***Abstract* – This work presents on-wafer characterization measurements of the X-Hall current sensor architecture implemented in 90-nm BCD10 silicon process by STMicroelectronics. With respect to a previous implementation, technological improvements in terms of active region, isolation layers, and metal stack configuration result in a substantially improved sensitivity. In addition, it is reported that the sensitivity can be further improved by applying a negative voltage to the depletion layer.**

I. INTRODUCTION

Current sensors are critical components of modern power electronic circuits and systems. They are used in many different applications, e.g., in the control feedback loop of power converters [1, 2], for monitoring and diagnostic purposes in complex power systems [3, 4], or in metering functions for smart grids and smart homes [5, 6]. The target application sets particular specifications on current sensors, which are ideally required to be small, lossless, accurate, broadband, low-power, or display a combination of such features [7, 8]. Recent research works targeting accuracy and broadband behavior have proposed lossless current sensing solutions based on magnetic approaches for silicon chip implementation [9, 10, 11, 12, 13, 14].

Among these, the X-Hall sensor [15, 14] demonstrated wide bandwidth and minimum space occupation, although suffering from limited sensitivity and suboptimal offset reduction. The improvement of these two static parameters can be addressed at a process technology level by employing selected solutions such as an active region with reduced implants, the substitution of field oxide with shallow trench isolation, and the miniaturization of the metal stack.

This article presents the experimental characterization of an X-Hall sensor implemented in Silicon 90-nm BCD10 technology, which is a more advanced process technology with respect to previous implementations [14]. Section I summarizes the main theory behind the X-Hall sensor and it outlines the major technological features of the BCD10 technology. Section II describes the experimental setup, while Section III discusses the experimental results, comparing the performances against the X-Hall sensor implemented in the previous generation of the BCD process.

II. DESCRIPTION OF THE SENSOR

A. X-Hall sensor topology

The device-under-test (DUT) is a current sensor based on the X-Hall topology, which was firstly proposed in [16]. As shown in Fig. 1, the active region is realized by adopting a lowly-doped n-type well (Fig. 1b), typically used in the BCD process technology as body region for high-voltage devices. Such an active region is shaped as an octagon (Fig. 1a) and it features eight contacts, namely four large contacts (T, B, L, R) for biasing the probe, and four small contacts (1, 2, 3, 4) for the readout of the Hall voltage (Fig. 1c).

The X-Hall probe is DC-biased to overcome the methodological limit of current-spun Hall sensors [11, 17] and thus to maximize the bandwidth. The biasing is applied by feeding two bias currents through two opposite bias contacts (i.e., B and T), while the other two bias contacts (i.e., L and R) are connected to a low-impedance node, typically a ground node. This configuration creates a uniform current distribution in the active region, while polarizing the probe in four orthogonal directions [14]. The application of two opposite bias currents leads to the generation of two output voltages V_A and V_B showing an opposite Hall effect:

$$V_A = V_H + V_{OS,plate}^{(A)}; \tag{1}$$

$$V_B = -V_H + V_{OS,plate}^{(B)}; \tag{2}$$

where $V_{OS,plate}^{(A)}$ and $V_{OS,plate}^{(B)}$ are additive offset voltages. Since there is a unique active region, it is reasonable to assume that these two offset voltages will have the same sign.

The cross-like short-circuit of the sense contacts (Fig. 1d) imposes specific boundary conditions to the charge distribution, implying:

$$V_A = V_B = V_{probe}; \tag{3}$$

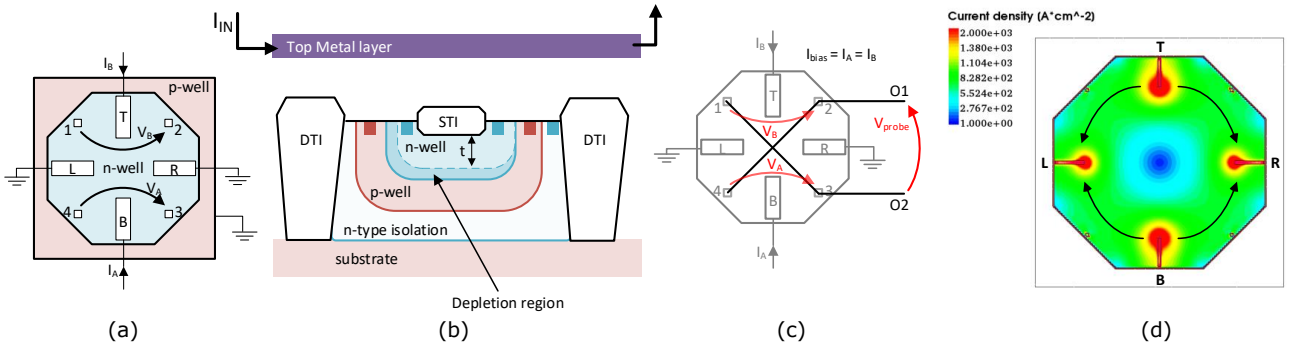

Fig. 1. (a) Top-view of the X-Hall probe displaying the connections of the contacts. (b) Cross-section of the X-Hall probe implemented in BCD10 technology. (c) Cross-like short-circuit of the sense contacts for static offset cancellation. (d) Current density distribution inside the X-Hall sensor obtained by TCAD simulation.

which results in the minimization of the offset voltage. Indeed, the only value for $V_{OS,plate}^{(A)}$ and $V_{OS,plate}^{(B)}$ theoretically satisfying the relationships in (1), (2), and (3) is zero. In practice, there will always be local defects asymmetrically affecting V_A and V_B, so that a residual additive offset ΔV_{OS} will likely be present in the actual sensor device.

Therefore, the output voltage V_{probe} can be written as

$$V_{probe} = V_H + \Delta V_{OS}; \tag{4}$$

where the Hall voltage V_H is related to the bias current I_{bias} and the incident magnetic field B_z by the current-related sensitivity S_I [8]:

$$V_H = S_I I_{bias} B_z. \tag{5}$$

The general expression for the current-related sensitivity is

$$S_I = G_H \frac{r_H}{nqt}; \tag{6}$$

where G_H is the geometrical correction factor, r_H is the Hall factor, t is the effective thickness of the active region, and q is the electron charge [8, 18]. The current-related sensitivity expresses the gain factor of the Hall probe to the magnetic input, while the the overall sensitivity S of the sensor is defined as

$$S = G_{IB} S_I I_{bias}; \tag{7}$$

where G_{IB} is the current-to-magnetic field gain [8].

As usually done in BCD technologies, the active region is isolated from the p-type substrate by a surrounding p-type well (Fig. 1b). This configuration creates a depletion layer involving the junction-field effect, eventually causing nonlinearity due to the modulation of the effective thickness of the active region [18, 8]. In this context, the application of negative voltages on the p-type layer allows to further shrink the effective thickness t and achieve higher sensitivity values.

B. *Prototype in BCD10 technology*

The DUT is implemented in the STMicroelectronics 90-nm BCD10 technology using the 60-V tolerant n-type diffusion as active layer. With respect to the previous implementation in BCD8 [14], the active layer is covered by a shallow trench isolation (STI) instead of field oxide. This solution reduces the effective thickness, which should lead to higher sensitivity. Moreover, the sensor is laterally isolated using deep-trench isolation (DTI) regions allowing to place the probe closer to high-voltage devices. Finally, the metal stack has smaller dimensions, reducing the distance between the top metal layer and the active region.

This configuration enhances the incident magnetic field on the X-Hall probe for the input current flowing through the 260-μm-wide copper trace realized on the top metal layer [8], eventually improving the overall sensitivity. The active region was designed as an octagon shape inscribed into a circle of 40-μm radius, leading to an active area that is 10% bigger than in the previous version in [14]. This should further increase the sensitivity [19], while also reducing the mean value of the incident magnetic field.

III. MEASUREMENT SET-UP

The block diagram of the on-wafer measurement set-up is reported in Fig. 2a, while a photo of the X-Hall die is reported in Fig. 2b. The die features 22 pads contacted by a custom 22-needle DC probe system. Two slots of a modular DC supply (Agilent N6705B) are used to provide the global device supply (V_{DD}) and to bias the p-ring layer (V_p). The X-Hall device is biased by means of a Source-Measure Unit (Keithley 2450 SMU with accuracy 0.012% and 6.5-digit resolution), allowing to directly impose the bias current (I_{bias}) in the mA range, and sense the bias voltage (V_{bias}) in the V range.

The measurand current (I_{in}) flowing through the metal strip is generated by applying a DC voltage (V_{in}) on a 10-Ω power resistor by means of an additional slot of the modular DC supply. A digital multimeter (Agilent 34401A fea-

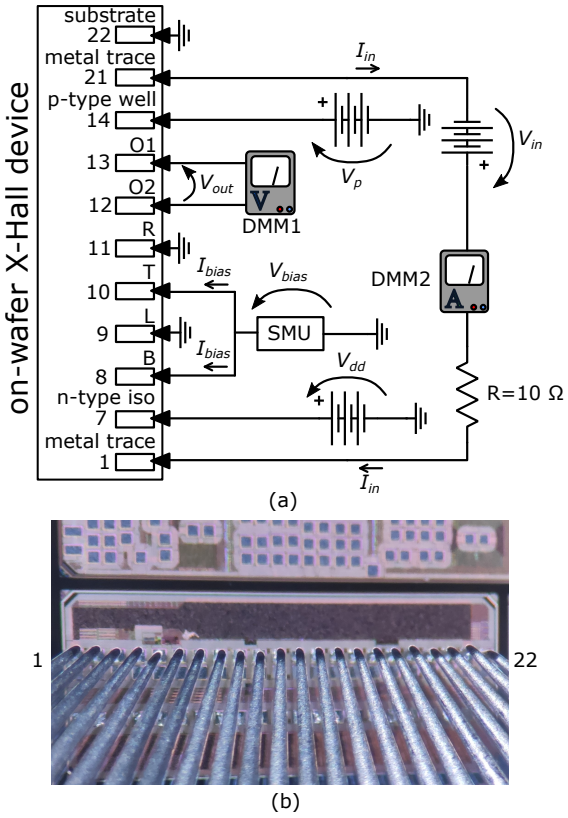

Fig. 2. (a) On-Wafer measurement set-up. (b) Photo of the X-Hall sensor die contacted with a 22-needle DC probe system.

turing 6.5-digit resolution) in ampermeter mode (DMM2 in Fig. 2) is used to retrieve the value of I_{in}, which should be precisely known to accurately characterize the sensitivity of the sensor. The output voltage (V_{out}) is acquired by another digital multimeter (Agilent 34401A, DMM1 in Fig. 2) in voltmeter mode.

IV. EXPERIMENTAL RESULTS

A. *Sensitivity and offset*

The static characteristics for the DUT biased at $I_{bias} = 1.5$ mA, estimated over the input range of ± 0.5 A for one DUT sample, is reported in Fig. 3a. Ten acquisitions for each input current value have been performed, resulting in an estimated overall sensitivity $\hat{S} = 487$ μV/A with expanded uncertainty $U(\hat{S}) = 3$ μV/A (95% confidence level), and an estimated output-referred residual offset $\Delta\hat{V}_{OS} = 116$ μV with expanded uncertainty $U(\Delta\hat{V}_{OS}) = 1$ μV (95% confidence level). The static characteristic is substantially linear over the entire input range, with a maximum deviation from the linear relationship of 15 μV. The estimated input resistance is 2.24 kΩ, in agreement with the nominal value of 2.5 kΩ.

The measurement procedure over a reduced input range

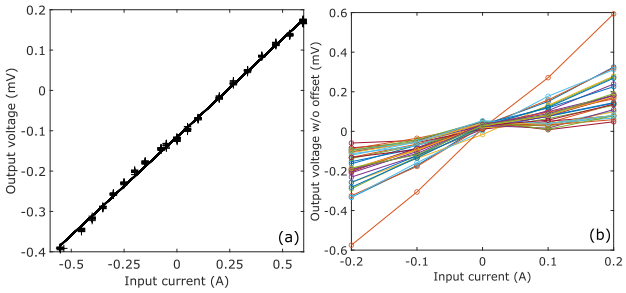

Fig. 3. (a) Static characteristics of a single sample of the DUT biased with I_{bias} = 1.5 mA. (b) Normalized static characteristics of 36 samples of the DUT (different colours for the different samples).

was repeated over a population of 36 DUTs placed on the same wafer, resulting in the static characteristics shown in Fig. 3b, while the process dispersion of sensitivity, offset, and Hall resistance are reported in Fig. 4. The average sensitivity over the entire test population is 0.9 mV/A, whereas the average offset is 384 μV with a standard deviation of 700 μV.

Table 1 compares the above results with those of the same device realized in BCD8 technology as retrieved from [14]. In particular, considering that in [14] the X-Hall sensor was biased at 500 μA, the values reported in Table 1 are the result of an extrapolation to I_{bias} = 1.5 mA. The BCD10 device demonstrated an average improvement of the overall sensitivity by a factor of 28%, which can be attributed to the combination of the larger active area, reduced thickness, and the closeness of the metal trace. To better assess the actual source of sensitivity improvement and identify the G_{IB} factor and Hall sensitivity S_I, it would be necessary to package the devices and provide a controlled magnetic input. However, this is out of the scope of the present work and will be investigated in the future.

The output-referred offset of the X-Hall device in BCD8 technology reported in Table 1 was extrapolated for $I_{bias} = 1.5$ mA multiplying by a factor 3 the value in [14]. The novel DUT in BCD10 technology demonstrated an higher mean residual offset but a similar process spread. This result suggests the possible presence of a systematic error in the silicon process that should be further investigated and likely be tackled in future realizations. Whereas state-of-the-art spun Hall sensors report a sensitivity up to 964 V/AT and offset as low as 15 μV [20], these cannot typically feature MHz-range bandwidths and, anyway, differ from this prototype in terms of technology, sensing methodology, biasing, and layout, which do not allow for a fair comparison.

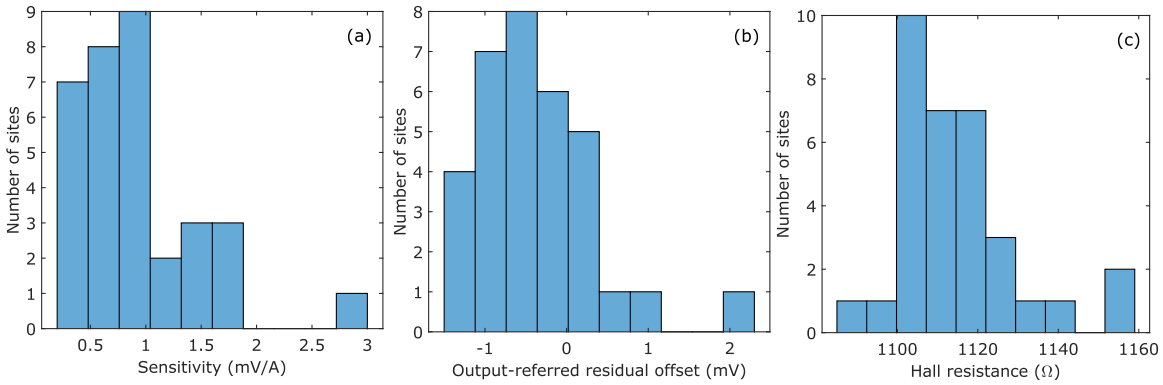

Fig. 4. Distribution of (a) sensitivity, (b) output-referred offset, and (c) input resistance for the DUT in BCD10 technology.

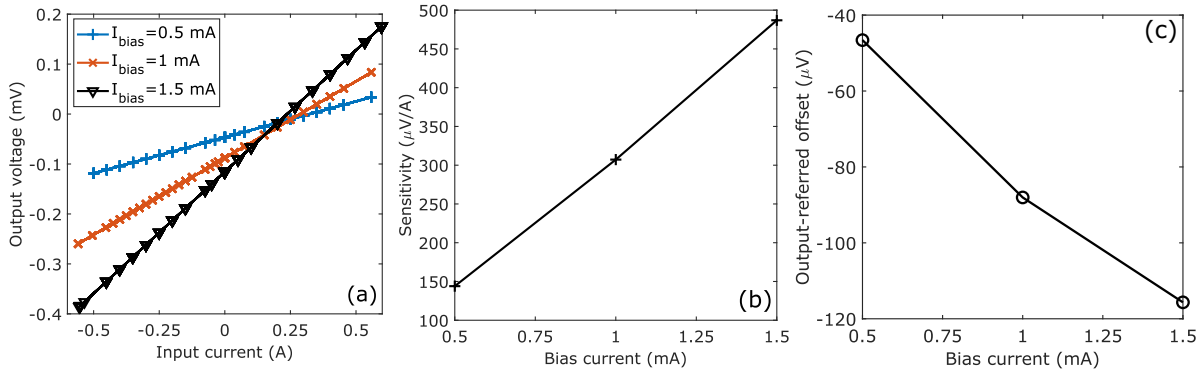

Fig. 5. Effect of the bias current on (a) output voltage, (b) sensitivity, and (c) offset for the DUT in BCD10 technology.

	$\hat{S}$ (mV/A)	$\hat{V}_{OS}$ (μV)	$\sigma(V_{OS})$ (μV)	R_{IN} (kΩ)
BCD8	0.7	195	700	2.5
BCD10	0.9	384	700	2.2

Table 1. Performance comparison between BCD8 and BCD10 technologies.

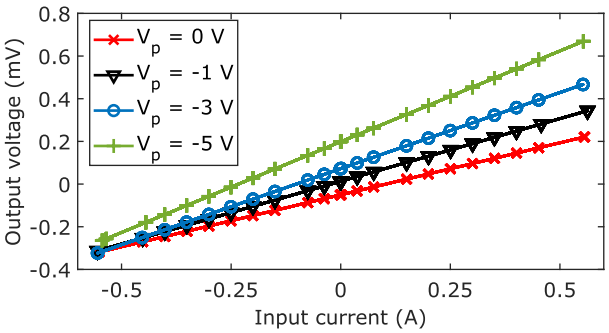

Fig. 6. Static characteristic of a single sample of the DUT in BCD10 technology for different polarization voltages of the p-type encapsulation well.

B. *Effect of polarization*

To prove the linear extrapolation procedure, the static characteristic of a single sample in BCD10 technology was estimated for three values of I_{bias}, namely 500 μA, 1 mA, and 1.5 mA. Sensitivity and residual offset are estimated from the characteristic and reported in Fig. 5, demonstrating a substantially linear relationship. As can be clearly seen, higher values of I_{bias} improve the sensitivity, but they also increase the residual offset, hindering the accuracy.

Finally, the effect of the depletion region on the effective thickness t was investigated by repeating the measurement procedure with different negative voltages applied to the p-type well. The measured static characteristics and the estimated sensitivity and offset performance are reported in Figs. 6 and 7, respectively. The application of negative voltages nearly doubles the sensitivity for an applied voltage of $V_p = -6$ V. However, as expected, the thinner active region also causes an higher offset, limiting the effectiveness of the methodology.

Future work will involve the evaluation of the long-term drifts of the residual offset as well as the temperature dependency, which typically are the most critical aspects.

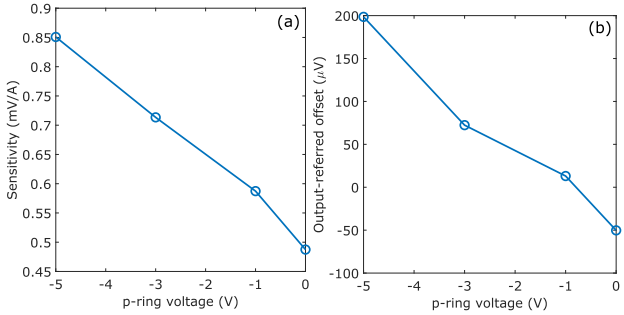

Fig. 7. Effect of the polarization voltage of the p-type well on (a) sensitivity and (b) residual output-referred offset.

ACKNOWLEDGMENT

This work was jointly supported by the European Union's Horizon 2020 research and innovation program, under the Electronic Components and Systems for European Leadership (ECSEL) Joint Undertaking, and from Germany, Slovakia, Netherlands, Spain, and Italy under grant agreement No. 876868.

REFERENCES

[1] H. Wang, X. Hu, Q. Liu, G. Zhao, D. Luo, An On-Chip High-Speed Current Sensor Applied in the Current-Mode DC–DC Converter, IEEE Transactions on Power Electronics 29 (9) (2014) 4479–4484.

[2] A. B. Jorgensen, S. Beczkowski, C. Uhrenfeldt, N. H. Petersen, S. Jorgensen, S. Munk-Nielsen, A Fast-Switching Integrated Full-Bridge Power Module Based on GaN eHEMT Devices, IEEE Transactions on Power Electronics 34 (3) (2019) 2494–2504.

[3] S. Zhao, F. Blaabjerg, H. Wang, An overview of artificial intelligence applications for power electronics, IEEE Transactions on Power Electronics 36 (4) (2021) 4633–4658.

[4] M. Pizzotti, M. Crescentini, A. N. Tallarico, A. Romani, An Integrated DC/DC Converter with Online Monitoring of Hot-Carrier Degradation, Institute of Electrical and Electronics Engineers (IEEE), 2020, pp. 562–565.

[5] L. Peretto, The role of measurements in the smart grid era, IEEE Instrumentation and Measurement Magazine 52 (10) (2010) 22–25.

[6] D. Bellasi, M. Crescentini, D. Cristaudo, A. Romani, M. Tartagni, L. Benini, A Broadband Multi-Mode Compressive Sensing Current Sensor SoC in 0.16um CMOS, IEEE Transactions on Circuits and Systems I: Regular Papers 66 (1) (2019) 105–118.

[7] P. Ripka, Electric current sensors: a review, Measurement Science and Technology 21 (11) (2010) 112001.

[8] M. Crescentini, S. F. Syeda, G. P. Gibiino, Hall-effect current sensors: Principles of operation and implementation techniques, IEEE Sensors Journal 22 (11) (2022) 10137–10151.

[9] V. Mosser, N. Matringe, Y. Haddab, A Spinning Current Circuit for Hall Measurements Down to the Nanotesla Range, IEEE Transactions on Instrumentation and Measurement 66 (4) (2017) 637–650.

[10] T. Funk, B. Wicht, A fully integrated DC to 75 MHz current sensing circuit with on-chip Rogowski coil, in: Proc. IEEE Custom Integrated Circuits Conference (CICC), IEEE, San Diego, 2018, pp. 1–4.

[11] M. Crescentini, M. Marchesi, A. Romani, M. Tartagni, P. A. Traverso, A broadband, on-chip sensor based on hall effect for current measurements in smart power circuits, IEEE Transactions on Instrumentation and Measurement 67 (6) (2018) 1470–1485.

[12] Y. Li, M. Motz, L. Raghavan, A Fast T&H Overcurrent Detector for a Spinning Hall Current Sensor With Ping-Pong and Chopping Techniques, IEEE Journal of Solid-State Circuits 54 (7) (2019) 1852–1861.

[13] A. Jouyaeian, Q. Fan, M. Motz, U. Ausserlechner, K. A. A. Makinwa, A 25A Hybrid Magnetic Current Sensor with 64mA Resolution, 1.8MHz Bandwidth, and a Gain Drift Compensation Scheme, in: 2021 IEEE International Solid- State Circuits Conference (ISSCC), Vol. 64, IEEE, 2021, pp. 82–84.

[14] M. Crescentini, et al., The x-hall sensor: Toward integrated broadband current sensing, IEEE Transactions on Instrumentation and Measurement 70 (2020) 1–12.

[15] M. Crescentini, et al., A broadband current sensor based on the x-hall architecture, in: IEEE Int. Conf. on Electronics, Circuits and Systems (ICECS), 2019, pp. 807–810.

[16] M. Crescentini, M. Biondi, M. Marchesi, A. Romani, M. Tartagni, P. A. Traverso, Bandwidth enhancement in hall probe by x-hall DC biasing, Journal of Physics: Conference Series 1065 (2018) 052031.

[17] M. Crescentini, M. Marchesi, A. Romani, M. Tartagni, P. A. Traverso, Bandwidth Limits in Hall Effect-based Current Sensors, ACTA IMEKO 6 (4) (2017) 17.

[18] R. Popovic, Hall Effect Devices, CRC Press, U.S.A, 2003.

[19] M. Crescentini, M. Biondi, A. Romani, M. Tartagni, E. Sangiorgi, Optimum Design Rules for CMOS Hall Sensors, Sensors 17 (4) (2017) 765.

[20] Z. Zhang, F. Lyu, S. He, L. Li, J. Sha, H. Pan, Z. Zhang, Y. Pan, High Sensitivity Horizontal Hall Sensors in 0.35 um BCD Technology, in: 2015 Fifth International Conference on Instrumentation and Measurement, Computer, Communication and Control (IMCCC), IEEE, 2015, pp. 510–514.

25th IMEKO TC4 International Symposium
23rd International Workshop on ADC and DAC Modelling and Testing
IMEKO TC-4 2022
Brescia, Italy / September 12-14, 2022

Image quality comparison of two different experimental setups for MEMS actuators functional evaluation: a preliminary study

Gabriele Bocchetta[1], Giorgia Fiori[2], Andrea Scorza[3], Salvatore Andrea Sciuto[4]

Dep. of Industrial, Electronic and Mechanical Engineering, Roma TRE University, Rome, Italy
[1] gabriele.bocchetta@uniroma3.it, [2] giorgia.fiori@uniroma3.it,
[3] andrea.scorza@uniroma3.it, [4] salvatore.sciuto@uniroma3.it

***Abstract* – The high interest of scientists and industries in the application of MEMS micro-actuators to several fields requires effective and robust measurement methods and systems for their quality assessment, focusing on their functional characterization, usually carried out through image analysis-based methods. In this study, a comparison of two experimental setups for image acquisition is proposed, aiming at establishing which setup collects images with higher quality for MEMS microgripper functional evaluation. The proposed work describes an experimental approach based on the evaluation of five parameters, i.e., brightness, saturation, contrast, sharpness, and signal-to-noise ratio, applied to 24 regions of interest in two sets of images of a same micro-actuator acquired from different optical setups at three magnification levels. Measurement results have been assessed following an objective approach by processing the acquired data through an in-house algorithm and a subjective approach by showing the acquired images to six observers and collecting their preferences.**

I. INTRODUCTION

Microgrippers (MGs) are devices based on MEMS (Micro Electro-Mechanical System) technology, able to grasp and manipulate objects of microscopic size, suitable for a wide range of applications, especially in the biomedical field and in particular, the manipulation of cells and tissues where they can contribute to the development of minimally invasive surgery techniques and the characterization of biological samples [1-3]. In this regard, the present study is part of a research aimed at developing image analysis-based measurement methods and systems for the characterization of electrostatic actuated MGs [4-9]. The Device Under Test (DUT) is the MG prototype in Fig. 1, fabricated by Deep Reactive Ion Etching (DRIE) process, using an aluminum hard mask on a silicon-on-insulator wafer [4-5]. Previous studies from the Authors [5-8] focused on measuring the displacement as a function of the supply voltage. Due to the small displacement values obtained for low supply voltage values and the small size of some parts of the device (e.g., the fingers thickness in the comb-drives is 4 µm only), the optical setup should be able to acquire images whose quality guarantee the measurement of a few microns and therefore the performance of a digital imaging system for this type of analysis in optical microscopy strongly depends also on the camera used for image digitalization. In this study, a comparison between two different digital cameras (modified GoPro HERO 10 Black and OrmaEurotek MD6iS) for acquiring images of the microgripper prototype useful for its functional characterization has been carried out.

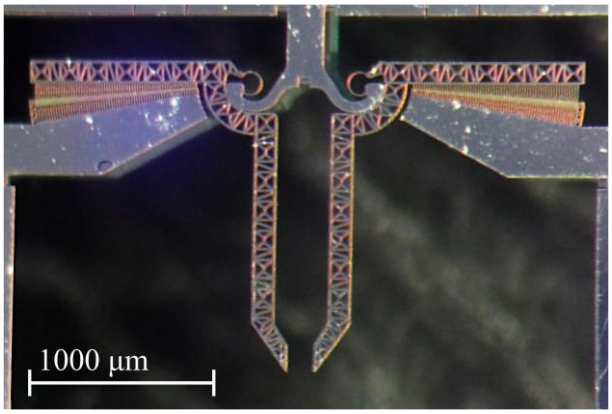

Fig. 1. Front view of the microgripper prototype.

II. MATERIALS AND METHODS

To compare the outcomes from two different optical setups depending on their digital cameras, two sets of images have been acquired under the same operating conditions: illuminance, DUT position, trinocular microscope, lens mount and default camera settings. Three different levels of magnifications have been used on the microscope (16×, 40×, 100×) and from each image, four different square Regions Of Interest (ROIs) have been selected, thus obtaining a total of 24 different ROIs to compare in pairs. In the present work a method for comparing digital cameras in MEMS testing setups is proposed, based on two

different approaches: an objective evaluation, through the use of an in-house software developed in MATLAB, and a subjective approach, showing the different ROIs of the collected images to independent observers. Five representative parameters [9] for the characterization of MEMS micro-actuators have been chosen to carry out the image quality evaluation:

- Brightness – it refers to pixels' intensity and to a visual perception that allows the observer to see an image as lighter or darker. It depends on the energy carried by the electromagnetic waves through the camera sensor and depends on the sensor sensitivity.
- Saturation – it describes the intensity of colors. A high-saturated image is characterized by vivid colors, while a low-saturated one is closer to the grayscale. Saturation, together with brightness, is influenced by the interaction between the DUT and the light source.
- Contrast – it is defined by the difference in luminance between light and dark areas of an image. High contrast makes an object in an image more distinguishable, as for the fingers in the comb-drives.
- Sharpness – it determines the amount of detail a digital camera can reproduce and depends on the acuity between the edges of an object in an image. In a sharp the edges of the DUT are better preserved, e.g., the comb-drive moving part edges, characterized by a triangle-shaped etch-holes pattern, which allow the micro-actuator angular displacement evaluation.
- Signal-to-noise ratio (SNR) – it compares the amount of desired signal to the level of background noise. High SNR values allow appreciating thin parts of the DUT, as in the case of the Conjugate Surfaces Flexural Hinges (CSFH).

Table 1. Experimental Setup

Device	Characteristics
Device Under Test (DUT)	Silicon microgripper prototype equipped with electrostatic rotary comb-drives.
Light Microscope	Zoom Range: 16×, 20×, 40×, 60×, 80×, 100×
Light source	LED Light, Color temperature: 5600 °K
Image Processing Software	In-house algorithm implemented in MATLAB (2021b, MathWorks)
PC	Intel core i7-4790, 32 GB RAM, Nvidia GeForce GTX 960

A. Experimental setup

The DUT is a MG prototype with two electrostatic comb-drive with radial geometry and with two CSFHs. The images of the DUT have been acquired through a trinocular light microscope, equipped with C-mount for the digital camera connection. Furthermore, the microgripper prototype has been placed on an *ad hoc* 3D printed stand to ensure the correct positioning under the microscope. In Table 1, the main components of the experimental setup have been reported.

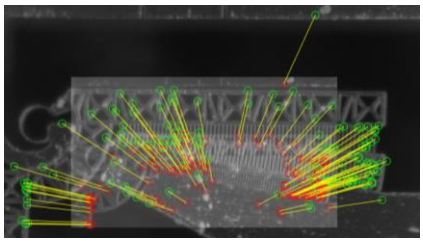

Fig. 2. Matched Kaze Points of Camera A (red) and B (green) images for ROIs transformation evaluation.

B. Comparison among images with different resolution

The acquired images have different sizes, 6.0 MP and 23.3 MP for Camera A and Camera B, respectively and their main specifications have been reported in Table 2, together with the pixel resolution at both minimum and maximum magnification levels, which has been estimated using a micrometric slide. This means that also ROIs have different dimensions for carrying out a comparison [10]. From each image, the Kaze Features [11] have been detected and matched (Fig. 2) in order to find those key points that allow the ROI a transformation [12-13], i.e., a similarity transformation, which is an isometry composed with an isotropic scaling. The algorithm used for the transformation matrix evaluation has been performed for 10^3 cycles for each image pair and the average transformation matrices have been determined.

Table 2. Digital cameras specifications

Specification	Camera A	Camera B
Lens mount	C-mount	C-mount
Number of pixels	6.0 MP	23.3 MP
Sensor model	Sony IMX236	Sony IMX677
Sensor type	CMOS	CMOS
Sensor size	½.8 inch	½.3 inch
Pixel size	2.8 µm	2.0 µm
Image size [pixel]	3264×1840	5568×4176
Pixel resolution at min zoom level (16×) [µm/px]	0.713 ± 0.015	1.060 ± 0.022
Pixel resolution at max zoom level (100×) [µm/px]	0.114 ± 0.004	0.172 ± 0.007

C. Objective image quality assessment

The selected ROIs have been processed and compared in pairs (Fig. 3) and the five parameters have been evaluated using an in-house algorithm implemented in MATLAB. Brightness (*V*) has been assessed as the highest value of a color among the red (*R*), green (*G*), and blue (*B*) components, while saturation (*S*) describes the measure of the departure of a hue from achromatic and both have been evaluated following the approach proposed in the HSV hexcone model [14]:

$$V = \max(R,G,B) \qquad S = \frac{V - \min(R,G,B)}{V} \qquad (1,2)$$

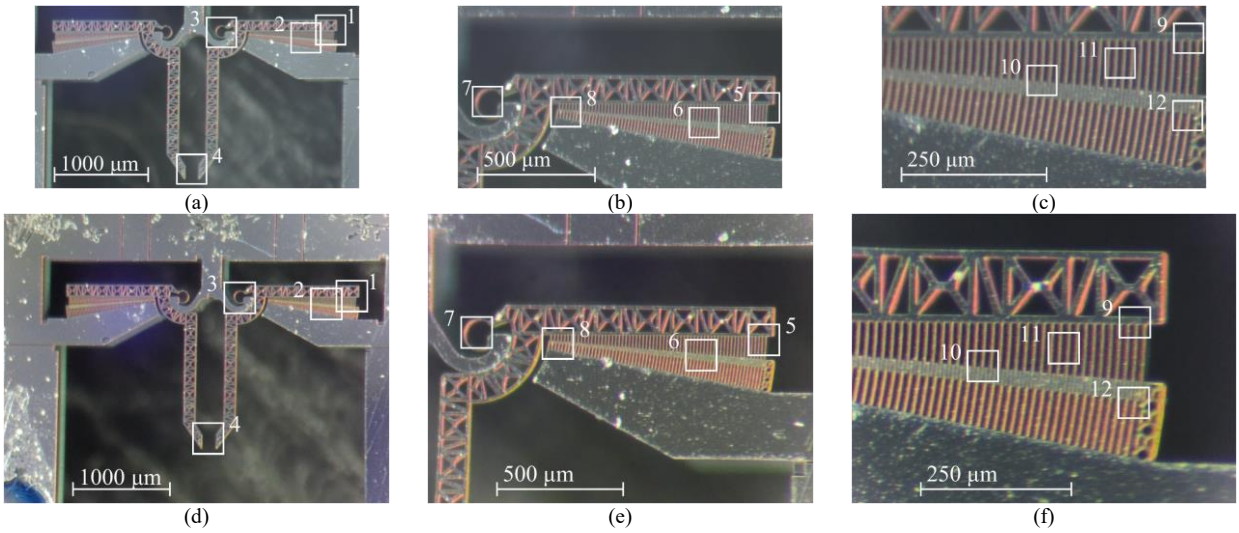

Fig. 3. ROIs in the processed images. Camera A: (a) 16×, (b) 40×, (c) 100×. Camera B: (d) 16×, (e) 40×, (f) 100×.

Contrast (*C*), also defined as the visibility by Michelson in [15], has been calculated following:

$$C = \frac{I_{max} - I_{min}}{I_{max} + I_{min}} \quad (3)$$

where I_{max} and I_{min} represent the highest and lowest luminance, as intensity of the pixels in the grayscale image. Sharpness is a fundamental parameter for evaluating the quality of an image and is an indispensable parameter for measuring small length values in the case of optical microscopy. In scientific literature, several No-Reference methods for sharpness evaluation have been proposed [16-18], most of them based on the maximum gradients and gradients variability, the calculation of the width of edges, modulation transfer function (MTF) and Spatial Frequency Response (SFR). This is due to the fact that although the human eye is easily able to distinguish sharp from blurred areas in an image, to present day, it is yet laborious for numeric computing environments. In the present work, sharpness evaluation algorithm is based on Local Phase Coherence (LPC) analysis. This parameter has been proposed in [19-20], in which it has been shown that a local phase variation is a more important factor than high-frequency energy for sharpness perception. Specifically, defined edges cause a solid coherence in local phase in the complex wavelet transform domain. For the SNR evaluation, the acquired images of the microgripper prototype have been compared with two sets of images by keeping the microscope in the same position, but without the DUT (considered as the desired signal) positioned on the 3D printed stand. Following [21], the SNR has been evaluated pixel by pixel as:

$$SNR = I / I_B \quad (4)$$

where I_B represents the background image, considered as noise. Finally, the proportion between the number of pixels characterized by a SNR greater than a threshold value to the number of ROI total pixels has been calculated.

D. Subjective image quality assessment

A subjective score is of utmost importance in imaging system quality evaluation, particularly in the case of biomedical imaging systems [18,21-24]. In literature comparisons of different methods for subjective images quality assessment have been presented, and among them, the forced-choice pairwise comparison has been found to be the most accurate [25], and besides, it has also been reported as the easiest for observers, as it requires a direct comparison between two images shown simultaneously and only one choice. Therefore, the proposed subjective approach is based on the forced-choice pairwise comparison method, showing all selected ROIs in pairs, in random order, to six independent observers, who have been asked to choose which of the two ROIs presented the higher value of each of the five parameters.

Table 3. Variable settings in MCS

Parameter	Distribution	Camera A		Camera B	
		μ_A	σ_A	μ_B	σ_B
ROI size [px]	Uniform	300	15	446	23
ROI shift [px]	Uniform	0	15	0	23

III. RESULTS AND DISCUSSION

In this section, the preliminary results obtained by means of the two different setups have been reported and commented. Before discussing the results, a Monte Carlo Simulation (MCS) with 10^4 iterations has been carried out to evaluate the software uncertainty, since the ROIs position depends directly on the operator's decision and because of pixel approximations in the transformation matrix evaluation. The following uniform distributions, shown in Table 3, have been assigned to the variables influencing the present study: ROI size and ROI shift, expressed as number of pixels. Moreover, for Camera A and B images, the standard deviation values (σ_A and σ_B)

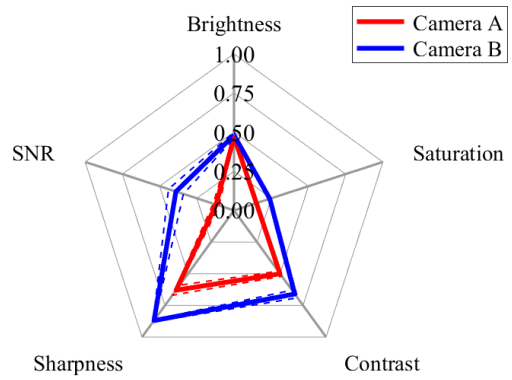

Fig. 4. Example of the Kiviat diagram applied to the objective image quality assessment results.

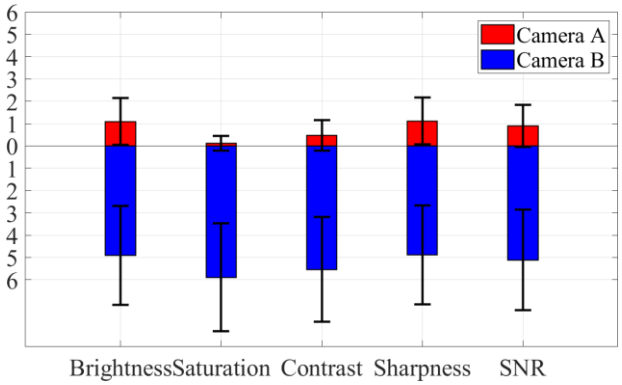

Fig. 5. Subjective image quality assessment results.

have been assumed as 5% of the corresponding ROIs average size (μ_A and μ_B respectively). The uncertainty has been expressed following Chebyshev's inequality [26], as three times the value of the calculated standard deviation. In order to express an overall score describing the two digital cameras, ROIs enclosing the same MG part for every image at each level of magnification have been considered, and in particular those ROIs representing the comb-drive fingers that are the useful elements for the displacement evaluation. The obtained parameters have been plotted on a Kiviat diagram, shown in Fig. 4, and the polygon with the largest area represents the digital camera with the highest total score and consequently the digital camera that is able to acquire microgripper images with higher quality. Table 4 shows the results obtained by the objective and the subjective method, with their relative uncertainties. The total scores evaluated by the image quality assessment algorithm are 0.28 ± 0.04 and 0.65 ± 0.07 for Camera A and Camera B respectively. As regards the subjective method, each one of the six observers repeated the test six times and the obtained results have been computed as the average of all individual tests and they have been expressed with a maximum score of 6, while the uncertainty has been evaluated with the Square-Root Rule for Counting Experiments, following the approach in [27]. Finally, the subjective image quality assessment scores have been evaluated by combining the results obtained from all the observers and as shown in Fig. 5 Camera B scored higher values for each considered parameter, thus supporting the objective image quality assessment results, and demonstrating that for both methods it is able to capture images with higher quality for MEMS actuators functional assessment.

Table 4. Experimental results

Parameter	**Camera A**	**Camera B**
	Objective image quality assessment	
Brightness	0.47 ± 0.01	0.48 ± 0.02
Saturation	0.15 ± 0.01	0.24 ± 0.01
Contrast	0.50 ± 0.02	0.66 ± 0.03
Sharpness	0.63 ± 0.04	0.87 ± 0.01
SNR	0.12 ± 0.02	0.39 ± 0.05
Total score	**0.28 ± 0.04**	**0.65 ± 0.07**
	Subjective image quality assessment	
Brightness	1.1 ± 1.0	4.9 ± 2.2
Saturation	0.1 ± 0.3	5.9 ± 2.4
Contrast	0.5 ± 0.7	5.5 ± 2.4
Sharpness	1.1 ± 1.1	4.9 ± 2.2
SNR	0.9 ± 0.9	5.1 ± 2.3

IV. CONCLUSIONS

The present preliminary study aims at comparing 24 different ROIs to determine the higher image quality to identify which of two different cameras is most suitable to be integrated into an optical setup for the analysis of the MEMS micro-actuators characteristics. Five parameters (brightness, saturation, contrast, sharpness and SNR) have been evaluated for every region of interest, following both an objective and a subjective approach. Two sets of images of a MG prototype for three different levels of magnification have been acquired through a trinocular optical microscope equipped with two different digital cameras. The acquired images have been processed through an image quality assessment algorithm implemented by the Authors. The uncertainty analysis of the method has been carried out through a Monte Carlo Simulation with 10^4 iterations. The obtained results of this preliminary study confirm that Camera B images are characterized by higher quality: higher values of contrast, sharpness and SNR allow a better determination of the parts that compose the micro-actuator, useful for the functional characterization. Moreover, Camera B is equipped with a larger sensor and a higher resolution that ensure the acquisition of a larger area and a higher micron/pixel ratio, respectively. In the near future, it will be important to improve the experimental setup and the image processing algorithm, to perform further tests and comparisons between the two digital cameras focusing on other aspects for the MG prototype characterization, such as the video quality assessment, especially if the prototype behavior over time is going to be studied, e.g., if the MG is supplied with a periodic signal.

REFERENCES

[1] K.R.Oldham, “Applications of MEMS technologies for minimally invasive medical procedures”, in “MEMS for Biomedical Applications”, Woodhead Publishing, 2012, pp. 269–290.

[2] S.Byun, J.-M.Lim, S.-J.Paik, A.Lee, S.Park, J.Park, “Barbed micro-spikes for micro-scale biopsy”, J. Micromech. Microeng., vol.15, No.6, May 2005, pp. 1279–1284.

[3] M.Verotti, P.Di Giamberardino, N.P.Belfiore, O.Giannini, “A genetic algorithm-based method for the mechanical characterization of biosamples using a MEMS microgripper: numerical simulations”, J. Mech. Behav. Biomed. Mater., vol.96, August 2018, pp. 88–95.

[4] A.Bagolini, S.Ronchin, P.Bellutti, M.Chistè, M.Verotti, N.P.Belfiore, “Fabrication of Novel MEMS Microgrippers by Deep Reactive Ion Etching with Metal Hard Mask”, J. Microelectromechanical Syst., vol.26, No.4, May 2017, pp. 926–934.

[5] N.P.Belfiore, A.Bagolini, A.Rossi, G.Bocchetta, F.Vurchio, R.Crescenzi, A.Scorza, P.Bellutti, S.A.Sciuto, “Design, Fabrication, Testing and Simulation of a Rotary Double Comb Drives Actuated Microgripper”, Micromachines, vol.12, No.10, October 2021, p. 1263.

[6] F.Vurchio, G.Bocchetta, G.Fiori, A.Scorza, N.P.Belfiore, S.A.Sciuto, “A preliminary study on the dynamic characterization of a MEMS microgripper for biomedical applications,” Proc. of 2021 IEEE International Symposium on Medical Measurements and Applications (MeMeA), 2021.

[7] F.Vurchio, G.Fiori, A.Scorza, S.A.Sciuto, “A comparison among three different image analysis methods for the displacement measurement in a novel MEMS device,” Proc. of 24th IMEKO TC4 International Symposium and 22nd International Workshop on ADC and DAC Modelling and Testing, 2020, pp. 327–331.

[8] F.Vurchio, P.Ursi, F.Orsini, A.Scorza, R.Crescenzi, S.A.Sciuto, N.P.Belfiore, “Toward operations in a surgical scenario: Characterization of a microgripper via light microscopy approach”, Appl. Sci., vol.9, No.9, May 2019.

[9] R.C.Gonzalez, R.E.Woods, “Digital Image Processing”, 4th Edition, Pearson, 2018.

[10] Y.Dufournaud, C.Schmid, R.Horaud, “Image matching with scale adjustment”, Comput. Vis. Image Underst., vol.93, No. 2, February 2004, pp. 175–194.

[11] P.F.Alcantarilla, A.Bartoli, A.J.Davison, “KAZE Features,” Proc. of ECCV 2012, pp. 214–227.

[12] M.Muja, D.G.Lowe, “Fast Matching of Binary Features,” Proc. of Conference on Computer and Robot Vision. CRV, 2012.

[13] R.Hartley, A.Zisserman, “Multiple View Geometry in Computer Vision”, 2nd ed. Cambridge, UK; New York: Cambridge University Press, 2003.

[14] A.R.Smith, “Color gamut transform pairs,” Proc. of 5th Annual Conference on Computer Graphics and Interactive Techniques (SIGGRAPH ‘78), 1978, pp. 12–19.

[15] A.Michelson, “Studies in Optics”, University of Chicago Press, 1927.

[16] Y.Zhan, R.Zhang, “No-Reference Image Sharpness Assessment Based on Maximum Gradient and Variability of Gradients”, IEEE Trans. Multimed., Vol.20, No.7, July 2018, pp. 1796–1808.

[17] K.Bahrami, A.C.Kot, “A fast approach for no-reference image sharpness assessment based on maximum local variation”, IEEE Signal Process. Lett., vol.21, No.6, June 2014, pp. 751–755.

[18] M.Ukishima, T.Nakaguchi, K.Kato, Y.Fukuchi, N.Tsumura, et al., “Sharpness comparison method for various medical imaging systems”, IEICE Trans. Inf. Syst., Vol.J89-A, No.11, 2006, pp.914–921.

[19] R.Hassen, Z.Wang, M.M.A.Salama, “Image sharpness assessment based on local phase coherence”, IEEE Trans. Image Process., vol.22, No.7 , July 2013, pp. 2798–2810.

[20] S.Ryu, K.Sohn, “No-reference sharpness metric based on inherent sharpness”, Electron. Lett., Vol.47, No.21, November 2011, pp. 1178–1180.

[21] G.Fiori, F.Fuiano, A.Scorza, J.Galo, S.Conforto, S.A.Sciuto, “A Preliminary Study on the Adaptive SNR Threshold Method for Depth of Penetration Measurements in Diagnostic Ultrasounds”, Appl. Sci., vol.10, No.18, September 2020, 6533.

[22] G.Fiori, F.Fuiano, A.Scorza, J.Galo, S.Conforto, S.A.Sciuto, “A preliminary study on an image analysis based method for lowest detectable signal measurements in PW Doppler ultrasounds”, ACTA IMEKO, vol.10, No.2, June 2021, pp.126–132.

[23] S.Koho, E.Fazeli, J.E.Eriksson, P.E.Hänninen, “Image Quality Ranking Method for Microscopy”, Sci. Rep., vol.6, August 2016, pp. 1–15.

[24] C.Otero, N.García-Porta, et al., “Comparison of different smartphone cameras to evaluate conjunctival hyperaemia in normal subjects”, Sci. Rep., vol.9, No.1, February 2019, pp. 1–8.

[25] R.K.Mantiuk, A.Tomaszewska, R.Mantiuk, “Comparison of Four Subjective Methods for Image Quality Assessment”, Comput. Graph. Forum, vol.31, No.8, December 2012, pp. 2478–2491.

[26] W.C.Navidi, “Statistics for Engineers and Scientists”, 5th edition, McGraw-Hill Education, New York, USA, 2020.

[27] J.R.Taylor, “An introduction to Error Analysis: The study of Uncertainties in Physical Measurements”, 2nd edition, University Science Books, New York, USA, 1997.

25th IMEKO TC4 International Symposium
23rd International Workshop on ADC and DAC Modelling and Testing
IMEKO TC-4 2022
Brescia, Italy / September 12-14, 2022

A preliminary study on the blind angle estimation for Quality Assessment of Color Doppler ultrasound diagnostic systems

Giorgia Fiori[1], Andrea Scorza[1], Maurizio Schmid[1], Jan Galo[2], Silvia Conforto[1], Salvatore A. Sciuto[1]

[1] *Dep. of Industrial, Electronic and Mechanical Engineering, Roma TRE University, Rome, Italy*
[2] *Clinical Engineering Service, IRCCS Children Hospital Bambino Gesù, Rome, Italy*

***Abstract* – Quality Controls (QCs) for the evaluation of Color Doppler (CD) performance play a pivotal role since CD is one of the most widely used Doppler techniques in medical imaging. Among the recommended test parameters, directional accuracy at 90° is included, even if its assessment is carried out visually. Therefore, in this study, a novel CD test parameter, called blind angle, has been proposed and defined as it allows testing the Doppler frequency shift dependency on the insonation angle. Moreover, a novel automatic method for the estimation of this parameter through the post-processing of CD videos has been proposed. Data have been collected from a single ultrasound diagnostic system equipped with a phased array probe. Tests have been carried out for two probe frequencies and three constant flow rate regimes set on a flow phantom. Based on the preliminary promising outcomes, further studies are going to be carried out.**

I. INTRODUCTION

In diagnostics, Color Doppler (CD) is one of the most widely used Doppler techniques, as it allows the 2D real-time representation of blood flow superimposed on the anatomical image [1,2]. A color map codifies and quantifies the velocity of blood flow inside a region of interest (or color box) adjusted by the operator on the B-mode grayscale ultrasound (US) image depending on the clinical question. Since CD measurement uncertainties reach up to 50% or more [3,4], such technique is often assumed to provide qualitative diagnostic data [5,6], although the scientific community has not reached a definitive consensus on this issue. The low measurement accuracy could be overcome by monitoring a clinical parameter of interest through a series of exams carried out over time. In this way, measurement repeatability can help the clinician prevent diagnostic errors. However, variations in measurement outcomes may be also due to the worsening of the US system performance, resulting in misleading diagnostic information. In this regard, periodic Quality Controls (QCs) for the evaluation of Doppler mode performance are needed and play a key role despite a commonly accepted reference standard on US equipment testing is still lacking [7-9]. Among the performance tests for Color Doppler QC recommended by the American Institute for Ultrasound in Medicine (AIUM), directional accuracy at 90° is included. The latter is qualitatively defined by the professional agency that recommends performing a visual assessment directly on the US system monitor [5]. This test parameter takes into account the Doppler frequency shift dependency on the insonation angle ϑ, i.e., the angle between the US beam path and the flow direction [1].

The angle can change because of variations in the orientation of the probe or the vessel, and consequently, the detected Doppler shift varies according to the cosine function: it is maximum for $\vartheta = 0°$, while it is minimum for $\vartheta = 90°$. The latter condition can be avoided by combining the probe angulation and the beam steering to keep the insonation angle in the range between 40° and 70° at which an adequate CD flow and B-mode display of the vessel walls can be obtained [1]. Since the flow detection depends on the insonation angle, as well as on the flow velocity, and it is strictly related to the sensitivity of the US probe, a novel QC parameter can be defined as the range of beam angles around 90° for which the US system is not able to detect moving reflectors, and it can be denoted as blind angle. In this regard, the present study is a preliminary attempt to propose a novel automatic method for the estimation of the blind angle parameter through the post-processing of CD videos. Data have been acquired from a single US diagnostic system equipped with a phased array probe. Moreover, because of the Doppler shift dependency on both the transmitted frequency and the flow velocity, tests have been repeated for two different probe Doppler frequencies and three constant flow rate regimes set on a flow phantom model available on the market.

II. BLIND ANGLE ESTIMATION

The estimation of the blind angle can be carried out through Doppler flow phantoms that allow displaying a portion of the vessel perpendicularly to the US propagation

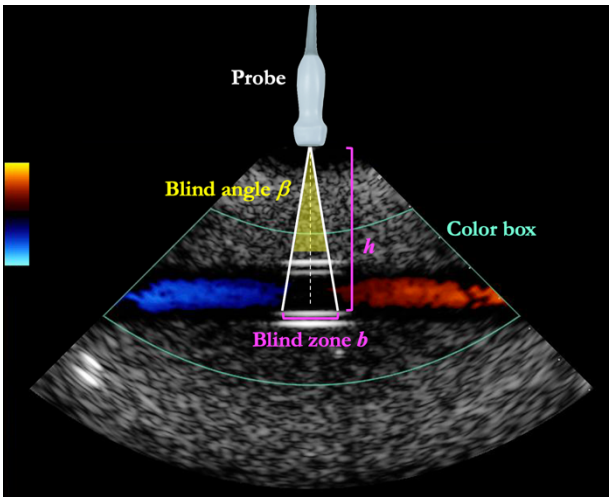

Fig. 1. Color Doppler blind angle in a straight tube parallel to the scanning surface.

axis. In particular, when the insonation angle approaches 90° the Doppler shift is almost zero, therefore in the corresponding area inside the color box, no color-coded flow is shown [1,2]. For a sector scanner, preferred for echocardiography, the displayed velocity inside a straight tube parallel to the scanning surface decreases by approaching the center of the image, and then it rises again. This effect is due to the variation of ϑ, and it is shown in the color box as a change in the flow color.

From this consideration, the blind angle can be defined as the range of beam angles at which a flow area in the image is black due to the incapacity of the probe to detect flow velocities at around $\vartheta = 90°$. By considering the US image shown in Fig. 1, the blind angle β can be estimated as follows:

$$\beta = 2\arctan\left(\frac{b}{2h}\right) \tag{1}$$

where b is the blind zone in which no Doppler shifts are detected, while h is the tube depth from the scanning surface. Since the distribution of the moving reflectors determines the Doppler signal power, the blind zone can narrow or widen in different temporal instants. Therefore, the evaluation of the blind angle in the present study has been carried out through the post-processing of a video rather than a single image. In the following, the main steps of the proposed automatic method are reported.

Firstly, the text boxes surrounding the diagnostic box are excluded through automatic masking [10,11], and a saturation filter based on a threshold th_{CD} is applied to extract the color-coded information only, removing the gray-scale coded B-mode information [12]. After that, an average image A_i is obtained from the CD video by averaging K consecutive frames at a time, for a total of N average images ($i = 1, \ldots, N$). The latter are filtered through a median filter with a n_{px}-by-n_{px} kernel to remove the color noise that can be shown as isolated color pixels within the black zone and the normalized square sum of the RGB components is computed. At this point, the flow central axis is automatically assessed on A_1, as in [13], and its coordinates are used to determine the endpoints of M parallel flow axes placed at a fixed distance Δd, above and below the central one, therefore obtaining a total of M+1 axes. The coordinates retrieved for the M+1 axes are kept fixed for all the N average images.

In the next step, the intensity I_{px} of the pixels that intersect the M+1 axis in the area at around $\vartheta = 90°$ is compared with a color threshold th_{blind} to determine the length of the blind zone b_j ($j = 1, \ldots, M+1$) on each axis. If $I_{px} \leq th_{blind}$, the corresponding pixel is assumed to be a blind pixel and b_j is computed as the distance between the first and the last blind pixel. Finally, the blind angle β_j is calculated for each flow axis by applying Eq. (1), assuming h_j as the mean depth from the scanning surface of the j-th axis. Afterwards, the blind angle β_i for each average image can be computed as follows:

$$\beta_i = \frac{1}{M+1}\sum_{j=1}^{M+1}\beta_{ij} \tag{2}$$

The procedure as described until now allows the estimation of the blind angle value on the i-th average image, therefore, the overall blind angle $\bar{\beta}$ is computed as:

$$\bar{\beta} = \frac{1}{N}\sum_{i=1}^{N}\beta_i \tag{3}$$

while the corresponding standard deviation $\sigma_{\bar{\beta}}$ can be estimated as follows:

$$\sigma_{\bar{\beta}} = \frac{1}{N}\sqrt{\sum_{i=1}^{N}\sigma_i^2} \tag{4}$$

where σ_i is the equivalent standard deviation (SD) assessed on each average image.

III. MATERIALS AND METHODS

Color Doppler videos have been collected by means of Doppler 403™ flow phantom [14], a self-contained reference test device (Table 1) able to provide repeatable flows from 1.7 to 12.5 ml·s^{-1} in constant or pulsatile mode. It consists of a Tissue-Mimicking Material (TMM) and a hydraulic circuit to simulate the acoustic properties of the biological tissues and blood vessels, respectively. In particular, the hydraulic circuit is constituted by a horizontal and a diagonal tube segment of 5 mm inner diameter filled with a Blood Mimicking Fluid (BMF).

Data have been collected through a phased array probe on a portion of the horizontal tube segment that simulates a carotid artery at a depth of 2 cm from the phantom

Table 1. Doppler 403^{TM} flow phantom specifications.

Parameter	Characteristics
TMM	Patented High Equivalence (HE) Gel^{TM}
Scanning surface	Patented composite film
TMM sound speed	1540 ± 10 m·s^{-1}
BMF sound speed	1550 ± 10 m·s^{-1}
Flow measurement range	(1.7 – 12.5) ± 0.4 ml·s^{-1}
Tube inner diameter	5.0 ± 0.2 mm
Attenuation coefficient	0.70 ± 0.05 dB·cm^{-1}·MHz^{-1}
Dimensions	28.0 × 30.5 × 22.0 cm

scanning surface. The US diagnostic system used has been set in raw CD working conditions, reported in Table 2. A single video clip lasting 12 s has been acquired for two Doppler frequencies and three constant flow rates (i.e., Q_1 = 6.0 ml·s^{-1}, Q_2 = 8.5 ml·s^{-1} and Q_3 = 11.0 ml·s^{-1}) set on the flow phantom in order to guarantee at least 110 frames per video.

Table 2. B-mode and Color Doppler settings.

Parameter	Setting
Nominal B-mode frequency (MHz)	H4.0$^{(*)}$
Field of view (cm)	6
TGC$^{(**)}$ – slide controls	Medium position
Nominal Doppler frequency (MHz)	f_1 = 2.0 , f_2 = 2.5
Wall filter	Minimum
Persistence	Minimum
Line density	Medium
Video clip duration (s)	12

$^{(*)}$ H = harmonic frequency; $^{(**)}$ TGC = Time Gain Compensation.

The proposed automatic method for blind angle estimation has been implemented through a custom-written algorithm using MATLAB routines. Each acquired video has been processed by applying the steps described in the previous section with the following specifications. The color-coded information has been extracted through the saturation filter with th_{CD} = 0.35 [12], and N = 15 images have been obtained from each video by averaging K = 6 consecutive frames. Color noise has been removed through a median filter with a 4-by-4 px kernel. Afterwards, M = 2 parallel flow axes have been placed above and below the central one at a fixed distance Δd = 7 px (corresponding to about 1 mm). In this study, the color threshold used to detect the blind pixels on each axis has been chosen as th_{blind} = 10, i.e., about the minimum gray level difference the human eye may distinguish [10,11,15]. Finally, the results obtained from each average image have been used to estimate the overall blind angle $\bar{\beta}$ and corresponding SD value by applying Eq. (3) and (4), respectively.

IV. MONTE CARLO SIMULATION

Monte Carlo Simulation (MCS) is a proper tool for both measurement uncertainty estimation and software-based method robustness assessment, as already experienced in several fields [16-21]. Therefore, a MCS with 10^4 iterations has been carried out for each Doppler frequency and flow rate acquired. Uniform distributions, whose characteristics are reported in Table 3, have been assigned to the main parameters influencing the blind angle assessment.

Table 3. Monte Carlo Simulations settings.

Parameter	Symbol	Distrib.	Mean ± SD
Threshold on color saturation	$th_{CD} \pm \sigma_{CD}$	Uniform	0.35 ± 0.01
Number of averaged frames	$K \pm \sigma_K$	Uniform	6 ± 1
Median filter kernel	$n_{px} \pm \sigma_{px}$	Uniform	4 ± 1 px
Distance from the central flow axis	$\Delta d \pm \sigma_d$	Uniform	7 ± 1 px
Blind pixel threshold	$th_{blind} \pm \sigma_{blind}$	Uniform	10 ± 1

Distrib. = distribution.

V. RESULTS AND DISCUSSION

The blind angle outcomes retrieved at different flow rates (Q_1, Q_2 and Q_3) and Doppler frequencies (f_1 and f_2) are reported in Table 4 and shown in Fig. 2. Standard

Table 4. Blind angle outcomes (mean ± SD) for each flow rate and Doppler frequency.

Flow rate	Doppler frequency	Blind angle $\bar{\beta}$ (°)
Q_1	f_1	15.9 ± 1.9
	f_2	13.1 ± 1.6
Q_2	f_1	5.4 ± 1.2
	f_2	5.8 ± 1.6
Q_3	f_1	2.6 ± 0.7
	f_2	1.4 ± 0.5

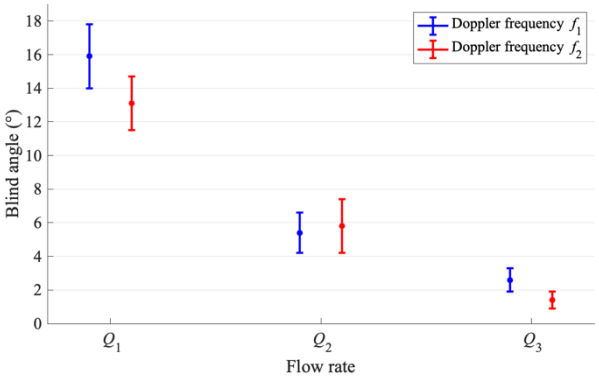

Fig. 2. Blind angle outcomes for f_1 and f_2 Doppler frequencies at Q_1, Q_2 and Q_3 flow rates.

deviation values have been computed by combining the SD obtained by applying Eq. (4) with the corresponding one estimated through the MCS.

The outcomes obtained are always compatible at the same flow regime and, as expected, they show a decreasing trend for increasing flow rate values, almost independently of the probe frequency.

VI. CONCLUSIONS

The present study aims at giving a contribution to Color Doppler QC tests by investigating a novel parameter, called blind angle, derived from a performance test recommended by the AIUM, i.e., directional accuracy at 90°. The latter has been defined only qualitatively by the professional agency that recommends a visual assessment directly on the monitor. The blind angle parameter, defined as the range of beam angles around 90° at which moving reflectors cannot be detected, has been retrieved to test the Doppler frequency shift dependency on the insonation angle. In fact, such parameter is strictly related to the US probe sensitivity and to the performance of the diagnostic system. Moreover, to overcome the limitations of the subjective procedure, a novel automatic method for the estimation of the blind angle parameter through the post-processing of CD videos has been proposed. In this preliminary attempt, data have been collected from a single US diagnostic system equipped with a phased array probe. Because of the further dependence of the detected Doppler shift on the transmitted frequency and the flow velocity, tests have been repeated for two probe frequencies and three constant flow rate regimes (i.e., 6.0, 8.5 and 11.0 $ml \cdot s^{-1}$) set on a flow phantom. The promising results obtained provide the basis for further studies to be carried out on a higher number of (a) ultrasound diagnostic systems, (b) phased array probes, (c) probe models, and (d) phantom settings.

REFERENCES

[1] P.R.Hoskins, K.Martin, A.Thrush, "Diagnostic Ultrasound. Physics and Equipment", 3rd edition, CRC Press, Boca Raton, FL, USA, 2019.

[2] D.Maulik, "Doppler Ultrasound in Obstetrics and Gynecology", 2nd edition, Springer, Germany, 2005.

[3] A.H.Steinman, J.Tavakkoli, J.G.Myers Jr, R.S.Cobbold, K.W.Johnston, "Sources of error in maximum velocity estimation using linear phased-array Doppler systems with steady flow", Ultrasound Med. Biol., vol.27, No.5, May 2001, pp.655-664.

[4] P.Hoskins, "Accuracy of maximum velocity estimates made using Doppler ultrasound systems", Br. J. Radiol., vol.69, No.818, February 1996, pp.172-177.

[5] AIUM Technical Standards Committee, "Performance Criteria and Measurements for Doppler Ultrasound Devices", 2nd edition, USA, 2002.

[6] S.F.Stewart, "Effects of transducer, velocity, Doppler angle, and instrument settings on the accuracy of color Doppler ultrasound", Ultrasound Med. Biol., vol.27, No.4, April 2001, pp.551-564.

[7] E.Samei, D.E.Pfeiffer, "Clinical Imaging Physics: Current and Emerging Practice", 1st edition, Wiley Blackwell, Hoboken, NJ, USA, 2020.

[8] J.E.Browne, "A review of Ultrasound quality assurance protocols and test devices", Phys. Med., vol.30, No.7, September 2014, pp.742-751.

[9] J.M.Thijssen, M.C.van Wijk, M.H.M.Cuypers, "Performance testing of medical echo/Doppler equipment", Eur. J. Ultrasound, vol.15, No.3, October 2002, pp. 151-164.

[10] G.Fiori, F.Fuiano, A.Scorza, J.Galo, S.Conforto, S.A.Sciuto, "A Preliminary Study on the Adaptive SNR Threshold Method for Depth of Penetration Measurements in Diagnostic Ultrasounds", Appl. Sci., vol.10, No.18, September 2020.

[11] G.Fiori, F.Fuiano, F.Vurchio, A.Scorza, M.Schmid, S.Conforto, S.A.Sciuto, "A preliminary study on a novel method for Depth of Penetration measurement in Ultrasound Quality Assessment," Proc. of 24th IMEKO TC4 International Symposium & 22nd International Workshop on ADC Modelling and DAC Modelling and Testing, 2020, pp. 332–336.

[12] A.Scorza, D.Pietrobon, F.Orsini, S.A.Sciuto, "A preliminary study on a novel phantom based method for performance evaluation of clinical colour Doppler systems," Proc. of 22nd IMEKO TC4 International Symposium & 20th International Workshop on ADC Modelling and Testing, 2017, pp. 175–179.

[13] G.Fiori, A.Scorza, M.Schmid, J.Galo, S.Conforto, S.A.Sciuto, "A preliminary study on the Average Maximum Velocity Sensitivity index from flow velocity variation in quality control for Color Doppler", Measurement: Sensors, vol.18, No.100245, December 2021.

[14] Sun Nuclear Corporation, "Doppler 403™ & Mini-Doppler 1430™ Flow Phantoms,"

https://www.sunnuclear.com/uploads/documents/datasheets/Diagnostic/DopplerFlow_Phantoms_113020.pdf (accessed July 2022).

[15] A.Scorza, G.Lupi, S.A.Sciuto, F.Bini, F.Marinozzi, "A novel approach to a phantom based method for maximum depth of penetration measurement in diagnostic ultrasound: a preliminary study," Proc. of 2015 IEEE International Symposium on Medical Measurements and Applications (MeMeA), 2015.

[16] G.Fiori, F.Fuiano, A.Scorza, J.Galo, S.Conforto, S.A.Sciuto, "A preliminary study on an image analysis based method for lowest detectable signal measurements in PW Doppler ultrasounds", ACTA IMEKO, vol.10, No.2, June 2021, pp.126-132.

[17] F.Fuiano, G.Fiori, A.Scorza, M.Schmid, S.Conforto, S.A.Sciuto, "A preliminary approach based on numerical simulations for the design of a PWV-varying arterial simulator", Measurement: Sensors, vol.18, No.100240, December 2021.

[18] F.Vurchio, G.Fiori, A.Scorza, S.A.Sciuto, "Comparative evaluation of three image analysis methods for angular displacement measurement in a MEMS microgripper prototype: a preliminary study", ACTA IMEKO, vol.10, No.2, June 2021, pp.119-125.

[19] F.Vurchio, G.Bocchetta, G.Fiori, A.Scorza, N.P.Belfiore, S.A.Sciuto, "A preliminary study on the dynamic characterization of a MEMS microgripper for biomedical applications," Proc. of 2021 IEEE International Symposium on Medical Measurements and Applications (MeMeA), 2021.

[20] F.Vurchio, G.Fiori, A.Scorza, S.A.Sciuto, "A comparison among three different image analysis methods for the displacement measurement in a novel MEMS device," Proc. of 24th IMEKO TC4 International Symposium & 22nd International Workshop on ADC Modelling and DAC Modelling and Testing, 2020, pp. 327–331.

[21] F.Fuiano, G.Fiori, A.Scorza, S.A.Sciuto, "A novel experimental set-up for Young Modulus Assessment through Transit Time measurements in Biomedical applications," Proc. of 2021 IEEE International Workshop on Metrology for Industry 4.0 and IoT (MetroInd4.0&IoT), 2021, pp. 117–121.

25th IMEKO TC4 International Symposium
23rd International Workshop on ADC and DAC Modelling and Testing
IMEKO TC-4 2022
Brescia, Italy / September 12-14, 2022

Development and Prototyping of a Capacitive Oil Level Sensor for Aeronautical Applications

Francesco Adamo, Filippo Attivissimo, Sergio de Gioia, Attilio Di Nisio, Daniel Lotano, Mario Savino

Department of Electrical and Information Engineering, Polytechnic University of Bari, Via E. Orabona 4, Bari

***Abstract* – Capacitive Level Sensors (CLSs) are one of the most used level-sensing technologies in the industry as they are cheap, reliable and show high sensitivity. A typical capacitive level sensor with concentric and closed cylindrical armatures has slow dynamical response when used for high viscosity liquids such as lubricating oil for aeronautic applications. This work investigates a conditioning circuit that uses a capacitance to frequency converter and that could provide fast and accurate measurements when paired with cylindrical sensor using an LC tank-based oscillator as the exciting source. The preliminary experimental results show a linear response with small error and standard deviation.**

I. INTRODUCTION

Capacitive sensors are widely used in the industry for measuring several parameters in different applications, such as displacements, forces, ECG (Electrocardiogram) Signals, liquid level, and sound pressure [1]-[6]. Aircrafts require reliable level monitoring for lubricant liquids. One method for level sensing is using time domain reflectometry or microwaves [7]-[12], but this is a very complex approach that requires high-end costly hardware. Other typical level sensing methods are floating, ultrasonic or radar and hydrostatic [13]-[14]. These methods have proven to be reliable for industry sensing or automotive applications but cannot be applied to aerospace because of EMI (Electromagnetic interferences) phenomena or vibrations.

Another challenge for aeronautical application is the develop of autonomous sensor nodes for aircraft monitoring systems exploiting energy harvesters such those based on thermoelectric generators [15] or photovoltaic modules. Indeed, aircraft pass through huge outside temperature variations providing heated cabin environments too. To make use of these temperature gradients most efficiently, additional effort to characterize such systems is required [16] –[18].

This paper investigates motor oil level monitoring using a novel capacitive sensor geometry [19], focusing on obtaining a reduced settling time with a customized conditioning circuit. A typical capacitive level sensor is made of two concentric cylinders of conductive materials with the monitored fluid filling the intermediate gap. However, due to high lubricant oil viscosity this could result in a slow settling time of capacitance vs. time. For this reason, a different type of sensor is proposed, such as a cylindrical sensor with helical cuts on both internal and external cylinders.

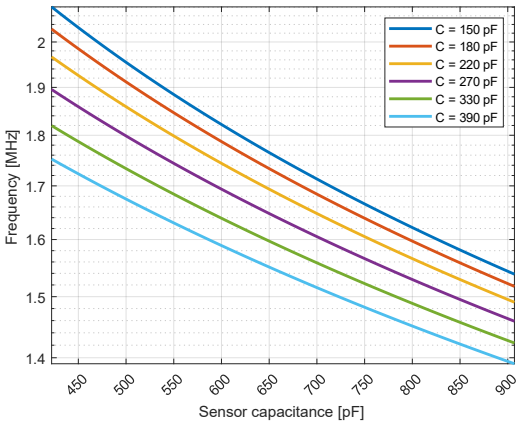

Fig. 1. Simulation of the resonant frequency of an LC tank with L = 10 uH and C = 150-390 pF vs the sensor capacitance in parallel with C

Each of the cylinders is an armature of the capacitor and it is simple to calculate its capacitance when the gap between armatures is filled by the sensed medium using:

$$C_m = \frac{2\pi \cdot \varepsilon_0 \cdot \varepsilon_m \cdot l_m}{\ln\left(d_e/D_i\right)} \quad (1)$$

where $\varepsilon_0 = 8.85 \cdot 10^{-12}$ F/m is the vacuum dielectric constant, ε_m is the relative dielectric constant of the sensed liquid, l_m is its level measured from the bottom of the cylindrical sensor, d_e is the inner diameter of the external cylinder and D_i is the outer diameter of the internal cylinder.

Starting from (1) it is then possible to calculate the total capacitance of the cylindrical sensor with respect to air as

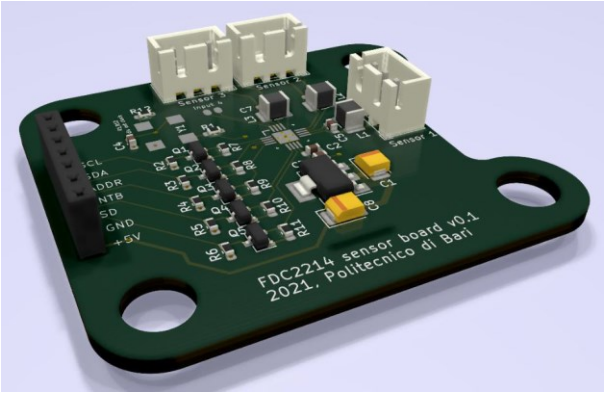

Fig. 2. Prototype rendering.

$$C_{cyl} = \frac{C_{air}}{l}(\varepsilon_{air} \cdot (l - x) + \varepsilon_m \cdot x) \quad (2)$$

with l being the total length of the sensor and x being the level of the sensed liquid.

Differentiating (2) with respect to x, we can obtain the sensitivity of the sensor as:

$$S = \frac{dC(x)}{dx} = \frac{C_{air}}{l}(\varepsilon_m - 1). \quad (3)$$

It can be shown that the sensitivity of the cylindrical sensor is high.

As previously said, the dynamic response of the "classic" cylindrical armatures level sensor is slow. This is since there are no apertures in the cylindrical armatures, so the oil must diffuse into the gap between the armatures which is of the order of 1 mm or less. Helical cuts provide a way for the liquid to diffuse between the armatures more rapidly, making the settling time faster. The negative aspect of making helical cuts is that the mechanical structure is weaker, making the sensor more exposed to vibrations that can result in increased errors in the measure; it is then important to read the sensor with a conditioning circuit that provides high sample rates and high precision.

One of the most common, easy and cheap ways to condition a capacitive sensor is to calculate the time constant of a RC circuit [20], where the capacitance is the sensor itself or a parallel or series combination of the sensor with a fixed, reference capacitance. In fact, applying a constant voltage V to an RC circuit, the current will be given by

$$i(t) = \frac{V}{R}e^{-\frac{t}{\tau}} \quad (4)$$

where $\tau = RC$ is the time constant. Using (4) the capacitance can be calculated measuring the Δt needed to charge the capacitor to a known voltage value; the most common way to do this is using an ADC (Analog to Digital Converter) integrated in a microcontroller.

Although the above method is easy to implement, it is highly dependent on the ADC resolution, typically limited to 12 bits or less.

For this reason, in this paper a different approach is investigated.

II. CONDITIONING CIRCUIT

A. Capacitive sensor

The conditioning circuit had to be designed to fit the initial helical capacitive sensor design, having a capacitance ranging from 422 pF to 907 pF when sensing avionic motor oil ($\varepsilon_{oil} \approx 2.15$).

B. LC oscillator

A method to calculate the capacitance of a capacitive sensor is to measure the oscillating frequency of a resonant LC circuit which is a function of the capacitance. A LC tank oscillator [21] will have a well-known resonant frequency where the capacitor reactance matches the inductor reactance:

$$X_C = \frac{1}{2\pi fC} = 2\pi fL = X_L \quad (5)$$

This results in the resonant frequency

$$f = \frac{1}{2\pi\sqrt{LC_{tot}}}. \quad (6)$$

In (6), C_{tot} is the total capacitance of the LC tank i.e., the sum of a fixed reference capacitor in parallel with the sensor and the parasitic capacitances (C_x and C_{par} respectively), so it can be rewritten as

$$f(C_X) = \frac{1}{2\pi\sqrt{L(C + C_{par} + C_x)}}. \quad (7)$$

A variation in the sensor capacitance will result in a shift of the resonant frequency. It is easy to verify that the sensor's capacitance can be obtained as

$$C_x(f) = \frac{1}{L(2\pi f)^2} - (C + C_{par}). \quad (8)$$

C. Conditioning circuit design

The LC tank oscillator circuit was implemented using standard commercial capacitors and inductors, and the shift in the frequency was simulated in MATLAB.

The simulation was performed using a value of 10 µH for the inductor and assuming 10 pF of parasitic capacitance. Capacitance values ranging from 150 pF to 390 pf were tested for C (Fig. 1). The chosen capacitance value was then C = 270 pF which would give a total frequency shift of 436.54 kHz on the full-scale range of the sensor.

The oscillation frequency is measured using a FDC2214,

that is an integrated capacitance to frequency converter IC by Texas Instruments. The FDC2214 was chosen because it has a nominal full-scale range up to 250 nF, has 4 input channels, a nominal resolution of 28 bits, an RMS noise of 0.3 fF and an output rate up to 4.08 ksamples/s. It is also easy to interface to a microcontroller thanks to its I^2C (Inter Integrated Circuit) interface.

D. Prototype

Fig. 2 shows the render of the conditioning circuit prototype; the PCB (Printed Circuit Board) was designed using the KiCad® EDA (Electronic Design Automation) software. The prototype board includes the power supply regulation circuitry to power the FDC2214 with 3.3 V starting from a 2.7-6 V input voltage, and level shift converters to permit its use with different microcontrollers (with 3.3 V or 5 V logic levels).

E. Firmware

The control firmware was written for an Arduino Uno microcontroller development system. A C++ library contains the definition of the class FDC with all the properties and methods needed for the setup and the data sampling. Speaking about the sampling methods, the user can choose to get a single sample raw data for the post processing using another software, or to get frequency or capacitance conversions directly from the library.
Several measurements routines have been implemented in a FSM (Finite State Machine) taking advantage of hardware peripherals of the Atmega328P microcontroller on the Arduino Uno (e.g. low level timer control for driving the stepper without blocking measurement routines).

III. TEST RESULTS

Tests were performed using avionic kerosene ($\varepsilon_{ker} \approx 1.95$) and a sensor made of carbon fiber pipes ($D_i = 20.0$ mm, $d_e = 22.0$ mm) shown in Fig. 4. For every step of level measurements, 1000 data samples were taken for the post-processing.
A first calibration process was performed with no sensor connected to the circuit. Such value was assumed as the parasitic capacitance on the PCB ($C_{par} = 12.387\ pF$) that is close to the estimated value of 10 pF. This value is used in (8) to get the sensor's capacitance.
The increase of the liquid level was simulated using a stepper motor driving a T6 lead screw with 1 mm pitch, such that for every 250 steps of the motor a container full of kerosene would move upwards exactly 1.25 mm for a total of 75 mm during the whole experiment. The sensor was held in position by a tripod in order to avoid any sensor's motion. A total of 61 sampling steps were made. Every sample acquisition requires 20 ms, so a single step of 1000 samples lasted 20 s.
Fig. 3 shows in red the sampled data. The first sample

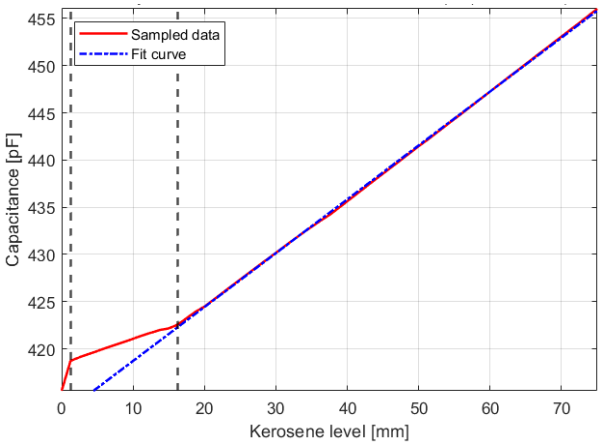

Fig. 3. Linear fitting of the sampled data; fit only considers levels above 16.25 mm

reports the sensor barely touching the liquid (415.6 pF). The second sample, when the fuel tank moves 1.25 mm upwards, has the sensor touching the liquid (418.7 pF). It is necessary to notice that the two concentric pipes are held in fixed relative position by 3 spacers made of electrical adhesive tape, thus having less air gap for the oil. For this reason, the samples up to 16.25 mm show a lower sensitivity. It is still noticeable that the lower part of the sensor is still linear.
Samples obtained for kerosene levels > 16.25 mm show a linear distribution. Data fitting was done using a first-grade polynomial expressed as

$$C_{fit} = p_1 \cdot h + p_2 \tag{9}$$

with $p_1 = 0.5707$ pF/mm and $p_2 = 413$ pF.
The residuals are calculated as

$$r_i = C_{sampled} - C_{fit}. \tag{10}$$

The residuals have been plotted in Fig. 5. The root mean square error is $RMSE = 0.1229$ pF and the mean standard deviation of the steps is $\sigma = 124.2$ fF to provide uncertainty estimation and evaluate repeatability of the measurement method [22].
To evaluate the effect of the number of samples of each step, data were decimated: using the first 10 samples of the same dataset resulted in a new $RMSE = 0.1240$ pF (that is $\Delta RMSE = 0.0011$ pF) and $\sigma = 125.3$ fF (that is $\Delta\sigma = 1.1287$ fF). Hence, a difference of less than 1% was observed.
The results show a high precision and repeatability of the measurement system and the model in (9) proves that there is a sensitivity of 570.7 fF/mm.
The difference in standard deviations shows that 10 samples are enough for an accurate measure, that requires 200 ms.
Further improvements can be done on the system if a trade-off with the precision is acceptable.

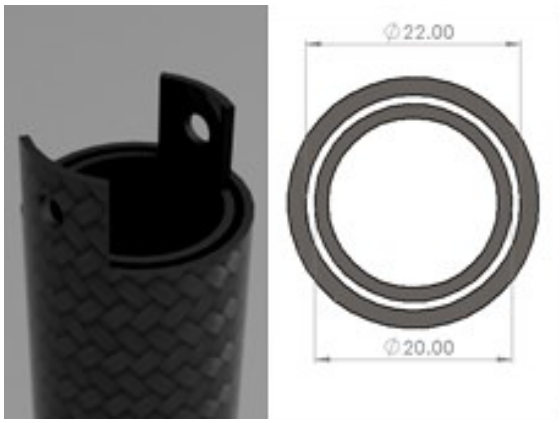

Fig. 4. Carbon fiber sensor rendering (left) and dimensions (right)

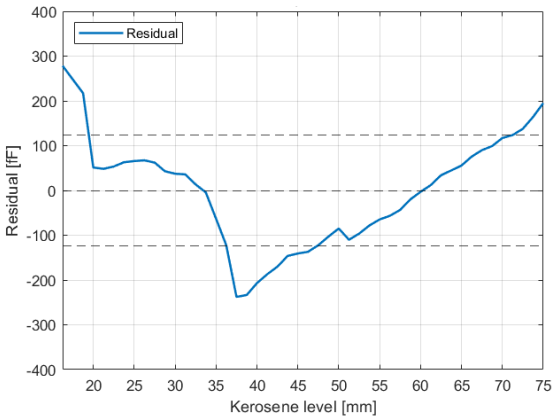

Fig. 5. Residual errors in the linear fitting of experimental data

CONCLUSIONS

In this paper the authors have presented a linear and high sensitivity capacitive level sensor able to measure oil level for aerospace industry. The preliminary test results obtained by the presented experimental setup has produced results in good agreement with theoretical analysis. Further investigation will be done to validate the proposed prototype and to verify repeatability and reproducibility of the system.

IV. APPENDIX: RELATIVE ERROR TO PERMITTIVITY CHANGES

A change in permittivity causes a variation in the value of the liquid level corresponding to a given measured capacitance which can be calculated with first order approximation as follows. Starting from the formula of the capacitance C as a function of the level x relative to the bottom end of the sensor:

$$C(x) = C_0[(\varepsilon_{l,r} - 1)\frac{x}{L} + 1] \qquad (11)$$

where C_0 is the capacitance of the empty sensor and L is its length, the functional dependence of x from the relative permittivity $\varepsilon_{l,r}$ is obtained by inversion of (11):

$$x(\varepsilon_{l,r}) = \frac{C/C_0 - 1}{\varepsilon_{l,r} - 1} L \qquad (12)$$

Then, if the relative permittivity of the liquid is changed from $\varepsilon_{l,r}$ to $\varepsilon'_{l,r} = \varepsilon_{l,r} + \Delta\varepsilon_{l,r}$ the level at which a given capacitance value C is measured can be obtained expanding (12) with a Taylor series:

$$x(\varepsilon'_{l,r}) = x(\varepsilon_{l,r}) - \frac{C/C_0 - 1}{(\varepsilon_{l,r} - 1)^2} L(\varepsilon'_{l,r} - \varepsilon_{l,r}) + higher\ order\ terms \qquad (13)$$

Then putting (12) into (13), the relative variation of the level with respect to the relative variation of the relative permittivity at any value of the measured capacitance is:

$$\frac{\Delta x}{x} \cong -\frac{\varepsilon_{l,r}}{\varepsilon_{l,r} - 1}\frac{\Delta\varepsilon_{l,r}}{\varepsilon_{l,r}} \cong -2.05\frac{\Delta\varepsilon_{l,r}}{\varepsilon_{l,r}} \qquad (14)$$

where in the right-hand side coefficient 2.05 has been calculated for the nominal value $\varepsilon_{l,r}$ of kerosene equal to 1.95. That is, in relative terms, an increase in $\varepsilon_{l,r}$ is almost doubled to give the decrease in liquid level at any fixed value of the measured capacitance.

On the contrary, a sensor calibrated for a liquid with relative permittivity $\varepsilon_{l,r}$, if used with a liquid of a different permittivity, gives rise to a level relative error of +1.9 the relative variation of $\varepsilon_{l,r}$.

Funding: This research was funded by the MUR on the "PON R&I 2014-2020 – Area di specializzazione "Aerospazio", Project "FURTHER" with Avio Aero SpA.

ACKNOWLEDGMENTS

The authors would like to thank Dr. Giuseppe Giliberti for his valuable cooperation and consistent support.

REFERENCES

[1] X. X. Liu, K. Peng, Z. Chen, H. Pu and Z. Yu, "A New Capacitive Displacement Sensor with Nanometer Accuracy and Long Range", IEEE Sensors Journal, vol. 16, no. 8, pp. 2306-2316, Apr. 2016.

[2] M.-Y. Cheng, C.-L. Lin, Y.-T. Lai and Y. J. Yang, "A Polymer-Based Capacitive Sensing Array for Normal and Shear Force Measurement", Sensors, vol. 10, no. 11, pp. 10211-10225, 2010.

[3] A. Ueno, Y. Akabane, T. Kato, H. Hoshino, S. Kataoka and Y. Ishiyama, "Capacitive Sensing of Electrocardiographic Potential Through Cloth from the Dorsal Surface of the Body in a Supine Position: A Preliminary Study", IEEE Transactions on Biomedical Engineering, vol. 54, no. 4, pp. 759-766, Apr. 2007.

[4] Ragolia, M.A.; Lanzolla, A.M.L.; Percoco, G.;

Stano, G.; Di Nisio, A. Thermal Characterization of New 3D-Printed Bendable, Coplanar Capacitive Sensors. *Sensors* 2021, *21*, 6324. doi: 10.3390/s21196324

[5] Yang, Q.; Yu, A.J.; Simonton, J.; Yang, G.; Dohrmann, Y.; Kang, Z.; Li, Y.; Mo, J.; Zhang, F.-Y. An inkjet-printed capacitive sensor for water level or quality monitoring: Investigated theoretically and experimentally. J. Mater. Chem. A 2017, 5, 17841–17847

[6] R. N. Miles, W. Cui, Q. T. Su and D. Homentcovschi, "A MEMS Low-Noise Sound Pressure Gradient Microphone with Capacitive Sensing", Journal of Microelectromechanical Systems, vol. 24, no. 1, pp. 241-248, Feb. 2015.

[7] M. Scarpetta, M. Spadavecchia, F. Adamo, M.A. Ragolia and N. Giaquinto, "Detection and Characterization of Multiple Discontinuities in Cables with Time-Domain Reflectometry and Convolutional Neural Networks." Sensors 2021, 21, 8032. https://doi.org/10.3390/s21238032

[8] M. Scarpetta, M. Spadavecchia, G. Andria, M. A. Ragolia and N. Giaquinto, "Analysis of TDR Signals with Convolutional Neural Networks," 2021 IEEE International Instrumentation and Measurement Technology Conference (I2MTC), 2021, p.1-6, doi: 10.1109/I2MTC50364.2021.9460009.

[9] M. Vogt, C. Schulz, C. Dahl, I. Rolfes and M. Gerding, "An 80 GHz radar level measurement system with dielectric lens antenna," 2015 16th International Radar Symposium (IRS), 2015, pp. 712-717, doi: 10.1109/IRS.2015.7226222.

[10] Kunde Santhosh Kumar, A. Bavithra, M. Ganesh Madhan, "A cavity model microwave patch antenna for lubricating oil sensor applications," Materials Today: Proceedings, 2022, doi: 10.1016/j.matpr.2022.06.136.

[11] A.M. Loconsole, V.V. Francione, V. Portosi, O. Losito, M. Catalano, A. Di Nisio, F. Attivissimo, F. Prudenzano, "Substrate-Integrated Waveguide Microwave Sensor for Water-in-Diesel Fuel Applications," Appl. Sci. 2021, vol. 11, no. 21, art. no. 10454, Nov. 2021, doi: 10.3390/app112110454

[12] G. Andria, F. Filippo Attivissimo, S.M. Camporeale, A, Di Nisio, P. Pappalardi, A. Trotta , "Design of a Microwave Sensor for Measurement of Water in Fuel Contamination," Measurement, vol. 136, Mar. 2019, pp. 74-81, doi: 10.1016/j.measurement.2018.12.076.

[13] J. Kredba and M. Holanda, «Precision ultrasonic range sensor using one piezoelectric transducer with impedance matching and digital signal processing,» 2017 IEEE International Workshop of Electronics, Control, Measurement, Signals and their Application to Mechatronics (ECMSM), pp. 1-6.

[14] J. Huang, Z. Zhou, X. Wen and D. Zhang, «A diaphragm-type fiber Bragg grating pressure sensor with temperature compensation,» Measurement, p. 1041–1046, 2013.

[15] D. Samson, T. Otterpohl, M. Kluge, U. Schmid, e Th. Becker, "Aircraft-Specific Thermoelectric Generator Module", Journal of Electronic Materials, vol. 39, n. 9, p. 2092–2095, set. 2010, doi: 10.1007/s11664-009-0997-7

[16] F. Attivissimo, C. Guarnieri Calò Carducci, A.M.L. Lanzolla, M Spadavecchia ."An extensive unified thermo-electric module characterization method", Sensors, vol. 16, no. 12, pp. 1-20

[17] C. Guarnieri Calò Carducci, M. Spadavecchia, e F. Attivissimo, «High accuracy testbed for thermoelectric module characterization», Energy Conversion and Management, vol. 223, 2020, doi: 10.1016/j.enconman.2020.113325.

[18] F. Adamo, F. Attivissimo, A. Di Nisio, e M. Spadavecchia, "Analysis of the Uncertainty of the Double-diode Model of a Photovoltaic Panel", in 2011 IEEE International Instumentation & Measurement Technology Conference Proceedings, 2011, p.616–620. doi: 10.1109/IMTC.2011.5944253.

[19] L. De Palma, F. Adamo, F. Attivissimo, S. de Gioia, A. Di Nisio, A. M. L. Lanzolla and M. Scarpetta, "Low-cost capacitive sensor for oil-level monitoring in aircraft," 2022 IEEE International Instrumentation and Measurement Technology Conference (I2MTC), 2022, pp. 1-4, doi: 10.1109/I2MTC48687.2022.9806667.

[20] W. Djatmiko, "Capacitance Measurements System Using RC Circuit", Social Sciences, vol. 3, no. 12, pp. 603-610, Mar. 2019.

[21] B. V. Rao, "Electronic Circuit Analysis", Pearson Education India, 2011.

[22] F. Attivissimo, A. Cataldo, L. Fabbiano, N. Giaquinto, "Systematic errors and measurement uncertainty: An experimental approach", Measurement, vol. 44, no. 9, pp. 1781-1789, Nov. 2011

25th IMEKO TC4 International Symposium
23rd International Workshop on ADC and DAC Modelling and Testing
IMEKO TC-4 2022
Brescia, Italy / September 12-14, 2022

EMC Case Study: Using Resistors Instead of Ferrite Ring to Reduce Emission of Battery Powered Equipment

Tamás Bodolai[1], Gábor Hegyi[2], Angéla Váradiné Szarka[3]

[1] *Department of Energy and Electronic Systems, Bay Zoltán Nonprofit Ltd. for Applied Research, Miskolc, Hungary, tamas.bodolai@bayzoltan.hu*
[2] *Department of Energy and Electronic Systems, Bay Zoltán Nonprofit Ltd. for Applied Research, Miskolc, Hungary, gabor.hegyi@bayzoltan.hu*
[3] *Department of Energy and Electronic Systems, Bay Zoltán Nonprofit Ltd. for Applied Research, Miskolc, Hungary, angela.szarka@bayzoltan.hu*

***Abstract* – Electromagnetic compatibility levels of the electrical and electronic equipment limited by relevant standards has more and more importance with increasing number of device density. EMC basic concept states that the conformity of a product must be ensured at the design stage. Retrospective solutions are usually much more expensive. Nonetheless, numerous post-modification methods are used in many products. A typical example of these is the separately built-in mains interference filter, ferrite rings placed on wires, clamp on ferrites. This type of modifications incurs significant additional costs in mass production including not only the cost of the additional materials, parts or equipment but also the related services. Although several proven retrospective methods exist for reducing emissions afterwards, these are far not the optimal solutions in terms of the costs. This article describes a cost-effective solution for the retrospective EMC level reduction.**

I. INTRODUCTION

In 2021, we have performed a radiated emission measurement on a commercially available, battery-powered household appliance. The product met the requirements of the standard using ferrite rings placed on the most critical point of the wire [1]. The original aim of the measurements was comparing emission level reduction efficiency of ferrite rings from different suppliers and defining the cost reduction capability of different ferrite rings. We have to state, that exact technical and material specification of the ferrite rings were not available, but this information did not affect the evaluation of the original measurements or the evaluation of the measurements for further scientific research, and this information was not required to achieve the result. As the manufacturers are not public, the article refers only to the various ferrite rings in the numbering.

Results of the first set of measurements performed according to the original requirements, we have stated that there are no significant differences between the emission reduction levels of the three different ferrite rings. After performing the original tests we have received permission to perform further measurements with aim of scientific research and competence development.

We performed various measurements to determine and analyze effects of the incorporated ferrites, learned about the product, and then began systematic solution determination resulting neglection of the relatively expensive ferrites.

II. HARDWARE SITE OF THE MEASUREMENT

The measurement of the EMC emission of the battery household appliance was limited to the measurement “Radiated emission - 30 MHz to 1,000 MHz” according to the standard [1].

Measurements were performed in a SAC-3 type semi anechoic chamber with a measuring distance of 3 m (Fig. 1.).

The measuring antenna is an HL562E ultralog, to which a BBV 9744 preamplifier is connected. The end of the measuring chain is accompanied by ESR26 measuring receiver with K53 "Time domain scan" option, and an automated positioning system served the moving of the antenna and rotating of the product.

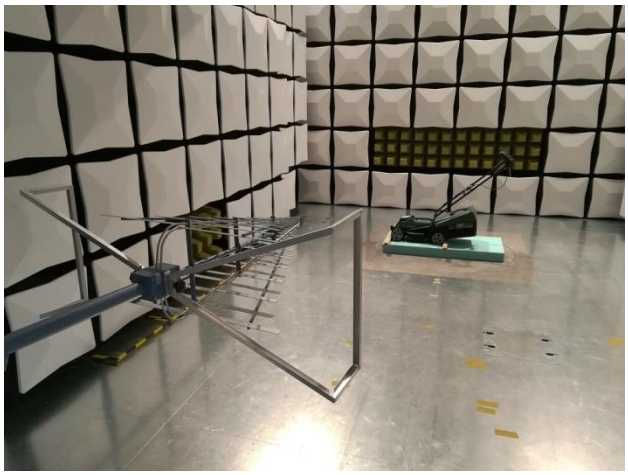

Fig. 1. Measurement setup of radiated emission measurement

III. SOFTWARE SITE OF THE MEASUREMENT

We have started the measurement planning with definition of our test procedure in the measurement control software. Radiated emission measurement for commercial equipment consists of several steps. The overview of this process can be seen in Figure 2. The purpose of multi-stage measurement is to find the most critical frequencies for EMC emissions and their most critical positions. Final measurements must be performed at these frequencies and positions. Otherwise, the standard does not provide an accurate description for determining the most critical points, leaving this responsibility to the person planning and performing the measurement. Accordingly, measurement settings not defined in the standard are usually determined jointly by the design engineer and test engineer.

A. Preview Measurement

Preliminary measurements were performed similarly to the final measurement with a quasi-peak detector, but with a much shorter measurement time. While 1 sec is used in final measurement, in preview measurement 50 ms was used. The standard allows the use of "Fast scan" or time domain-based measurement, which greatly reduces the time required to perform measurements. This is especially important for cordless machines, as the measurement time is limited by the accumulator capacity. The resolution bandwidth (RBW) is 120 kHz.

Preliminary measurements were performed with an antenna height of 1.5 m, in the 0 °, 45 °, 90 ° position of the turntable, in both horizontal and vertical polarization for the entire frequency range. The results of the total of 6 measured curves are combined into separate vertical and horizontal views.

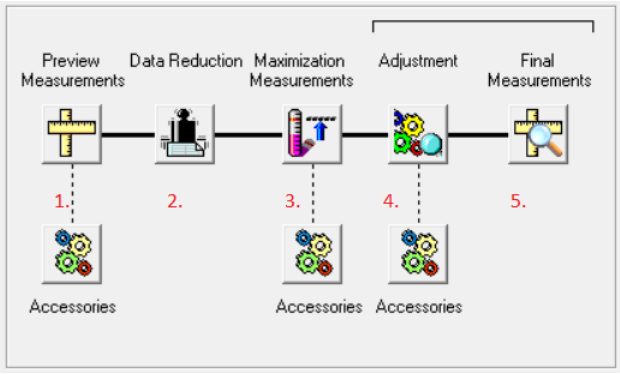

Fig. 2. Simplified measurement process in EMC32

B. Data Reduction

The software offers several automated options for selecting the points to be measured in detail, i.e. a given antenna height and position with a given product position pairs results a test setting for final measurement. In our setting definition we only used the "Peak Search" function with a relative threshold level of 6 dB. It should be noted, however, that "Interactive data reduction" is always active, meaning that after automated evaluation, we have the option to manually delete the suggested points and add points that we find interesting. According to our experiences, we typically pass on 6 points, unless the pre-measurement justifies clarifying additional points. Number of test point passed to final measurement highly increases the testing time, therefore six points proved to be a good compromise for cordless machines.

C. Maximization Measurement

The purpose of this test step is to determine direction in which the emission of the product is the highest. The standard [1] gives several recommendations for positioning of the turntable. We decided to position the table in every 15 degrees and to perform the measurement at rest, which means tests are performed in 24 positions. Measurements were performed in both vertical and horizontal positions. This means 48 positions were tested and analyzed. At each position, the critical frequencies determined in the previous step are measured with a measurement time of 50 ms. It means that the clear measurement time is much less, then the positioning of the turn table. The net measuring time is about 300 ms at each position while the time of the turning is about 3 sec. In this test step, the height of the antenna is not changed, mainly because this would mean an unacceptably long measurement time for a battery-powered machine. For some types of battery-powered machines, it is still necessary to replace the battery several times during the test process.

D. Adjustment and Final Measurements

In the flowchart, the adjustment and the final measurement are shown as two separate steps, in reality they take place directly one after the other at each critical point.

Each critical measurement point has an antenna height (which in this case is 1.5 meters), a polarization state, and a rotary table angle from the previous step. The "Adjustment" step is used to refine this worst case. First, the rotary table is turned slowly in the range of ± 15 ° from its pre-existing position, while the interference emission is continuously measured using the polarization inherited from the previous step. This process provides detailed environment checking of each critical point which was defined in the previous step. From this we get the worst-case scenario of the turntable position.

Next step is the changing the height of the antenna from 1 m to 4 m to find the worst-case height. After defining the worst-case antenna position and worst-case product position on the turntable, the positioning system adjusts these positions and the "Final Measurement" is performed.

IV. UNCERTAINTY, LIMIT AND MARGIN

In the field of EMC, several sources [2][3][4] deal with the professional determination of the measurement uncertainty of different measurements. The measurement uncertainty of emission measurements performed with antennas is relatively high, the standard also estimates a value of around 6 dB. The research team has calculated the measurement uncertainty of their own system, and the result was slightly below 6 dB.

The calculations are very complicated and not scope of this paper, however we would like to give an overview which type of uncertainty should be taken into account. First we need to know the parameters of receiver. These data mostly come from datasheet of the unit and in some cases from the calibration certificate. Parameters of the receiver include the receiver reading, sine wave accuracy, pulse amplitude response, pulse repetition rate response, noise floor proximity, and frequency step. Other group of parameters concerns the uncertainty of the measurement path. The focus is on the transmissions and reflections caused by mismatches but also need to deal with antenna factor, frequency interpolation and cross polarization parameters. Finally, we need to calculate with stability of measurement system in other words measurement system repeatability. This item describes what happens when the measurement system is disassembled and reassembled. Value between 1 and 1.5 dB of the stability is relatively high in most of laboratories.

It means that the highest permitted emission level defined by the standard as limit is minus 6 dB if one piece of sample is tested. Approach to the limit and margin at the automotive and commercial assets is surprisingly different. While the automotive standard [5] always defines values for one product, the standard for hand tools [1] allows statistical determination. For example, if one piece of lawn mower is measured, the margin should be at least 6 dB, but if 3 or 6 pieces are measured, 3.8 dB and 0.7 dB margins are sufficient for each piece. Products of this type are typically tested in numbers of 3 to 6. For the results reported below, the 3.8 dB margin is relevant.

V. RESULTS OF MEASUREMENTS

A. Measurement of the product with original ferrite ring

The product with original ferrite ring (hereinafter "Ferrite 1.") fully met the expectations, with the value closest to the limit of 136 MHz, where the margin was 7.03 dB (Fig. 3). The other two test pieces gave very similar results. One showed a margin of 5.64 dB at 147 MHz and the other a margin of 6.64 dB at 142 MHz.

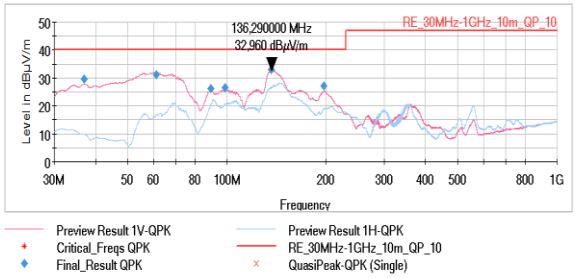

Fig. 3. Emission diagram of testing the product with Ferrite 1.

B. Other ferrite rings

After measuring the product with Ferrite 1, we have tested the product with two other types of ferrite rings (hereinafter "Ferrite 2" and "Ferrite 3. "). The measuring system was not modified or reassembled, all measurements were performed with the same measurement set-up. This is important when comparing the results because the mounting error can be neglected in the measurement uncertainty. Measurements of products using Ferrite 2. and Ferrite 3. produced slightly worse results, with a margin of 3.9 dB at 156.2 MHz in the worst case (Fig. 4). Summarizing the results appropriateness of all tested ferrites can be stated, if the statistical principle of 3 samples is considered. This point is the end of the official tests, however, the partner company approved further studies for research purposes.

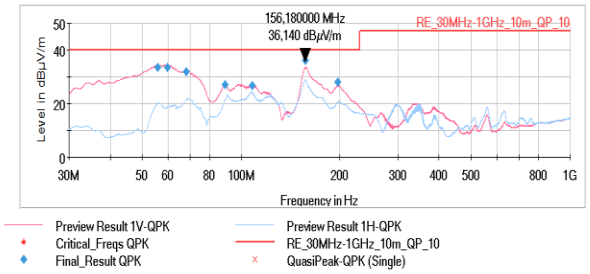

Fig. 4. Emission diagram of testing the product with Ferrite 2.

C. Study of the emission levels without ferrite

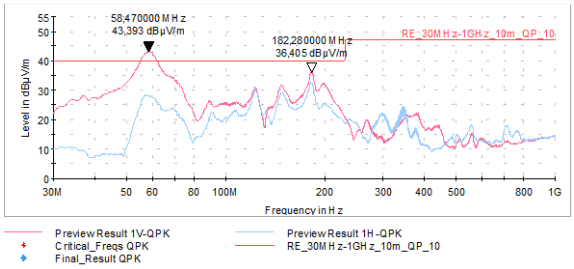

Fig. 5. Emission diagram without ferrite

The first step in the study was to determine exact effect of the use of ferrite on the product, so the ferrite was removed from one of the products. The result is shown in Figure 5. It can be stated that the use of ferrite is mainly necessary due to the emission in range of 50-60 MHz. A value of 36.405 dB (~ 3.6 dB margin) measured at 180.28 MHz with an even larger sample size would be acceptable without the use of ferrite.

D. Study of emission without antenna

The subject of the research is a battery-powered garden machine, in the construction of which the main components, the electronics, the battery, the motor are essentially integrated in one place, in the body of the device. However, due to safety features and convenient switch-on, a circuit loop must be built into the handle. In most cases, this circuit loop is just a wire with switches, which during operation forms a closed loop, i.e. an antenna. The aim of the following experiment is to determine the emission level added by this "antenna" to the complex interference emission of the product. Therefore, while meeting the safety conditions, the equipment was operated without a wire loop. The machine was started directly at the connector on the control panel.

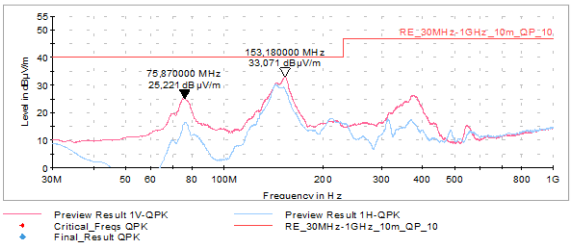

Fig. 6. Emission diagram without wire loop

The results show that the interference emissions are significantly reduced in both the 50-80 MHz and 100-200 MHz bands. However, it can also be stated that the device would meet the requirements without the wiring loop. Of course, it cannot be a solution because of security concerns. However, the use of a mechanical signal transmission, such as a Bowden cable, could also be a solution. It is also true that today's manufacturing industry prefers to avoid such elements and of course they are not advantageous in terms of design either. However, there are a few household appliances exist on the market where the control signals are transmitted via wireless communication from the handle to the device central unit and motor. At this point of the research the engineering team conducting the measurement attempted to come up with a different and cheaper solution if the original wire loop concept must be used, but the use a ferrite ring should be avoided.

The wiring diagram of the tested machine is not known for the research group, but the measurement results show that the battery voltage is applied to one endpoint of the switch line. Presumably, the other end activates a switching element, such as a MOSFET, when it is turned on. Ideally, this wire is at a constant potential, meaning it should not act as an antenna at all.

Because the motor drive circuit is constantly switching, it causes a fluctuating supply voltage, which means that it causes a constantly changing battery voltage. This fluctuating voltage is applied to the switching line, which thus becomes the transmitter of the electromagnetic waves. In essence, the ferrite ring placed on the wire is also designed to reduce this fluctuation. The question for researchers to answer is whether this fluctuation can be reduced by any other cheap, passive element. Since the total length of the built-in switching line is approximately 2.5 meters, based on the wavelength-frequency relationship, this corresponds to approximately 120 MHz, while the half-wavelength corresponds to 60 MHz.

E. Study of using additional resistors

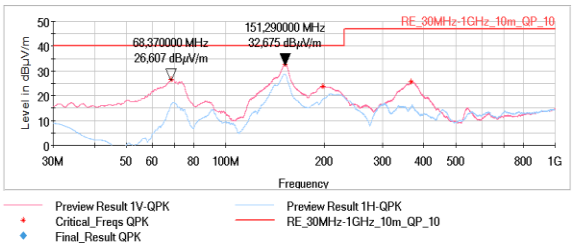

Fig. 7. Emission diagram with two resistors

The basic idea was to modify the impedance of the "antenna" effect caused by the wire to some extent. It has been assumed that the supply voltage must be in a certain range to turn on the device, so increasing the resistance of the wire presumably should not cause any problem. According to calculations, 1.2 kΩ resistors were built at both ends of the switch wire. The result is shown in Figure 7.

Based on the 13.4 dB margins obtained at 68.4 MHz and the 7.32 dB margins obtained at 151.3 MHz, it can be concluded that better results were obtained with the two resistors than with any of the ferrite rings. It is important to mention that both resistors are required to achieve the result. Leaving it at either end of the wire gives a result substantially free of the ferrite ring.

F. Method of antenna splitting

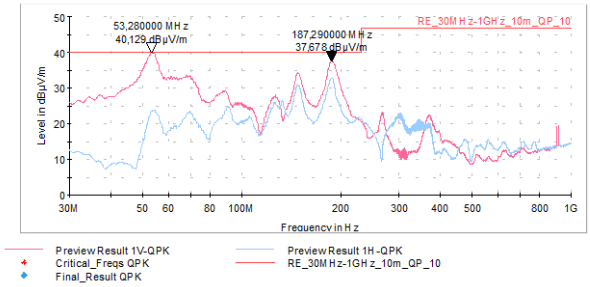

Fig. 8. Emission diagram with one resistor at switch

In one step of the systematic scientific test design, analyzing the length of the switch wire, a resistor was installed in the center of the antenna, which point practically is located at the switch of the device.

Analyzing Fig. 8, although the level of interference emission decreased by a few dB compared to that shown in Fig. 5, it did not prove to be as effective as the two resistors used at the ends.

VI. CONCLUSION

In ideal case, the EMC compliance of a product is ensured at the design stage. However, due to the complexity of the topic and possible unexpected situations, the product may fail during the EMC test despite best intentions. As the product is usually already on the verge of production, the well-known quick solutions, ferrites, interference filters and possibly special coatings and absorbers come to the force. These are usually quick procedures, as they can be retrofitted (even into products that have already been manufactured) without major modifications, but these are relatively expensive methods. The costs of retrofitting increase in nearly proportion to the number of pieces of the product. However, with analyzation and accurate understanding of the disturbance phenomenon, application of a specific, low-cost solution may become available, even if cost of test development and performance and cost of analysis procedure are also calculated and added.

The results of research summarized in this paper proved, that using two low-cost resistances ensure higher emission limitation capability, than the originally used and widely accepted methods with ferrite rings. In the industrial practice the retrofitting methods are very often supplemented with additional enhanced power limitation, in order to achieve further emission limitation. The research will be continued in the future to analyze if the enhanced power limitation in the products may be avoided by using the two-resistance method for emission lowering. The use of low-cost, low-conversion solutions can lead to significant savings in industry, which is of paramount importance in mass production.

REFERENCES

[1] CISPR 14-1: Electromagnetic compatibility - Requirements for household appliances, electric tools and similar apparatus - Part 1: Emission, 2016

[2] CISPR 16-4-2: Specification for Radio Disturbance and Immunity Measuring Apparatus and Methods – Part 4-2: Uncertainties, Statistics and Limit Modelling – Uncertainty in EMC Measurements, 2003.

[3] JCGM 100:2008 Evaluation of Measurement Data – GUIDE to theExpression of Uncertainty in Measurement, 2008

[4] M.Bittera, V.Smiesko, K.Kovac, "Modified uncertainty estimation of antenna factor measurement by standard site method", Measurement, February 2012, DOI: 10.1016/j.measurement.2011.07.002

[5] CISPR 25: Vehicles, boats and internal combustion engines - Radio disturbance characteristics - Limits and methods of measurement for the protection of on-board receivers, 2016

25th IMEKO TC4 International Symposium
23rd International Workshop on ADC and DAC Modelling and Testing
IMEKO TC-4 2022
Brescia, Italy / September 12-14, 2022

Using a Simulation of ALSE Long Wire Method to Lower Measurement Uncertainty in EMC Measurements

Gábor Hegyi[1], Tamás Bodolai[2]

[1] *Department of Energy and Electronic Systems, Bay Zoltán Nonprofit Ltd. for Applied Research, Miskolc, Hungary, gabor.hegyi@bayzoltan.hu*
[2] *Department of Energy and Electronic Systems, Bay Zoltán Nonprofit Ltd. for Applied Research, Miskolc, Hungary, tamas.bodolai@bayzoltan.hu*

***Abstract* – Electronic devices have become an essential part of our modern world, and manufacturers are obliged to ensure their safe coexistence and the reliable performance of their tasks. Operating safety means that nearby devices interfere with each other as little as possible. These interferences and immunity to interference signals are addressed in the field of Electromagnetic Compatibility (EMC). EMC has been in the focus of researchers since the mid-20th century, but serious regulations were not introduced until the late 1980s.**
The article describes the basics of EMC and the challenges and uncertainties of this relatively new field of science, despite of the strict standard regulations of numerous measurement procedures. Also a simulated environment is presented to demonstrate examination possibilities and variations of the standard interpretations.

I. INTRODUCTION

Electromagnetic compatibility measurements are based on standards determining test procedures of different types of products. The research was motivated by the fact that in many cases the standards are not clear and gives the laboratories and the test engineers freedom in making decisions. This situation causes differences between the results of two different laboratories performing a theoretically same, completely regular test, but using two different methods. Because of this, a product may fail in one laboratory and pass in the other. The aim of the research is to develop a simulation in which different test conditions can be analyzed under validated conditions, and how the different test definitions can be interpreted and how they affect the measurement uncertainty.

II. FUNDAMENTALS OF EMC

The concept of electromagnetic compatibility is defined in IEC 1000-1-1:1992 standard, which summarizes the fundamental definitions and terms. According to this, EMC is: “The ability of an equipment or system to function satisfactorily in its electromagnetic environment without introducing intolerable electromagnetic disturbances to anything in that environment.” [1] There are two additional definitions in the standard describing essentials of EMC: Electromagnetic environment is “the totality of electromagnetic phenomena existing at a given location” [1] and electromagnetic interference can be “any electromagnetic phenomena which may degrade the performance of a device, equipment or system, or adversely affect living or inert matter” [1].

According to the EMC concept, electrical devices can cause disturbances, which can interfere with other devices or even themselves. These disturbances can occur in several ways. There may be noise from electromagnetic radiation source, noise from the power cord or a communication line, or interference from some other source, such as an electrostatic discharge from a person's hand. These disturbances can have harmful effects, such as if a mobile phone transmits signals to an HDMI cable that distort communication so much that the projector can no longer process it, but it can also have life-threatening consequences if the same phone interferes with the vehicle's electronics. The spread of electronic devices began at the first half of the previous century. More and more commercially available devices have entered the market. Telephones and radios, followed by televisions and computers. This extremely fast increase of equipment number has forced manufacturers to use cheaper and smaller parts which can be manufactured more easily. An important step for EMC was when robustly designed high-immunity electron tubes were continuously replaced by semiconductor-based circuit elements. Their immunity is significantly lower than their predecessor. [2] Furthermore, their size has allowed developers to implement more complex circuits in smaller devices. Over time, researchers have recognized that there is a steady narrowing gap between the decline in immunity caused by new technologies and the increase in emissions caused by the continued spread of electronic devices. This is called the EMC Gap, which

is illustrated in the following figure. [3]

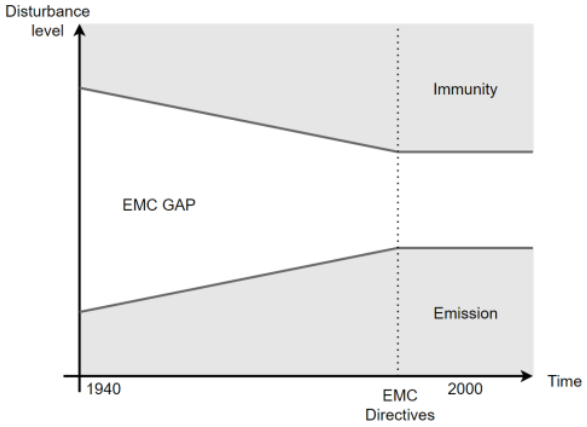

Fig 1. Illustration of EMC Gap

The illustration shows that over time, the general immunity and emission limits of electronic devices have become closer and closer to each other. If these two bands overlap, the devices cannot be operated without disturbance in each other's electromagnetic environment. To avoid this, the IEEE (The Institute of Electrical Engineers) introduced strict regulations in 1982, which came into force in Europe in 1996. [2]

III. EMC STANDARDS

Standards describing electromagnetic compatibility testing are regulated by the CISPR (Comité International Spécial des Perturbations Radioélectriques - International Special Committee on Radio Interference) within the IEC (International Electrotechnical Commission). There are a number of standards for EMC that are product-specific.

There are several product fields defined by different EMC standards, like commercial, automotive, medical, military equipment and others. The basic standard for commercial measurements is CISPR 16. Several other standards that apply to different subtypes of commercial equipment often refer to the specifications set out in CISPR 16. These include for example CISPR 14 for household appliances and hand tools, CISPR 11 for industrial, scientific and medical equipment or CISPR 32 for electromagnetic compatibility testing of multimedia equipment. Similarly, CISPR 25 is the basic standard for automotive measurements, but in many cases, it also refers back to CISPR 16. So we can see that standards also overlap between the different device types, thus creating a very complex system of regulations for the EMC specifications of the devices.

In addition to the tested equipment, the EMC can be further classified according to the measurement of emissions, the electromagnetic interference emitted by a particular device, and the immunity, the ability of a device to perform without degradation in the presence of an electromagnetic disturbance. [1]

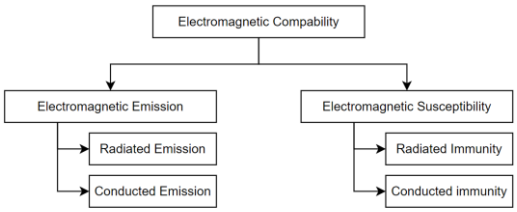

Fig 2. EMC classes

In the simulation created in the framework of the research the aim is to measure emission, so this article will cover that topic. The emission measurements include wide range of measurement methods. The two common test methods that are in the focus of our research are, the radiated emission tests using antenna and the conducted emission test using artificial network. An artificial network according to the CISPR 25 standard is a "network inserted in the supply lead or signal/load lead of an apparatus to be tested which provides, in a given frequency range, a specified load impedance for the measurement of disturbance voltages and which may isolate the apparatus from the supply or signal sources/loads in that frequency range" [4] In these tests, the radiated electromagnetic interference emitted by the product is measured with an antenna from a defined distance and in case of conducted emission measurement, an artificial network is connected between the device and the power supply or on the signal lead, and the interference signals are measured through it.

The test description usually specifies the level of emission limits to be applied for a given frequency range. This is because different electronic devices have higher electromagnetic susceptibility in certain frequency ranges or may have some form of wireless communication, such as Wi-Fi, Bluetooth, GSM and so on. If the product emits more than this limit, the device may not be placed on the market.

In addition, the standards specify the level of measurement uncertainty accepted for each measurement. This is ± 6dB for antenna measurements and ± 3dB for conducted emission measurements. These values are high compared to the limit values for the frequency ranges. For example, according to CISPR 25, the highest value of the radiated emission limits used in automotive applications is 26dB(µV). [4] In theory, it is possible that the measuring instrument results 26dB(µV) radiated emission, but the real value is close to 32dB(µV). Since decibel denotes the ratio of two values as a logarithmic unit, it is worth converting the result to a linear unit for which equation (1) can be used to make the problem easier to understand.[5]

$$[\mathrm{dB\,\mu V}] = 20\log_{10}\left(\frac{[\mu \mathrm{V}]}{1\,\mu \mathrm{V}}\right) \quad (1)$$

Rearranging to voltage, keeping in mind, that 1μV equals to 0dBμV:

$$[\mu V] = 10^{\frac{([dB\,\mu V])}{20}} \quad (2)$$

Using formula (2), 26dB(μV) corresponds to 19.95μV and 32dB(μV) to 39.81μV, which is twice the specified emission limit.

Commercial and automotive standards have developed a different solution to deal with this degree of uncertainty. For automotive measurements, the measured interference signal must not reach the level of uncertainty. So, the measured signal must always be 6 dB below the limit set for the frequency range. In case of the interference still reaches this value, the measurement must be repeated with a lower resolution bandwidth at that frequency. If the value measured by this way is still higher than 6 dB below the limit, the product has failed. [4] Similarly, in commercial devices, the difference between the limit and acceptable level of the interference signal can be determined, but here it is determined on a statistical basis which limit value belongs to a given sample number. Table 1 shows these limits. [6]

Table 1. Commercial measurement limits

Sample size (n)	3	4	5	6
General Margin to the limit (dB)	3.8	2.5	1.5	0.7

As the Table 1. shows, in case of higher number of samples the EMC conformity can be determined using a lower margin.

A very important question is to answer why do standards allow measurements with such high measurement uncertainties in EMC tests? To perform most of electromagnetic compatibility measurements an Absorber Lined Shielded Enclosure (ALSE) or EMC chamber is required. Figure 3 shows the Rejtő Ferenc EMC chamber of the University of Miskolc, Hungary.

Fig 3. EMC chamber

This chamber is a SAC-3 EMC chamber. The SAC is an abbreviation for Semi Anechoic Chamber and means that the inner wall of the enclosure has been partially coated with foam absorbers in addition to the ferrite tiles. The number 3 means that maximum distance of 3 meters can be set between the product and the antenna. Figure 4. shows the inside of the EMC chamber.

The purpose of ferrite tiles and absorbers is to prevent the reflection of electromagnetic interference from the product to ensure measurement of direct radiation only. The difference between the two covers is in the frequency range they are able to absorb. Ferrite tiles are efficient at lower frequencies, up to about 1 GHz, while foam is sized to work properly in the range above, up to 20 GHz. In a SAC chamber only, the internal wall and ceiling are covered with absorbers, on the floor it is not needed (nevertheless in some cases they can be used). [7]

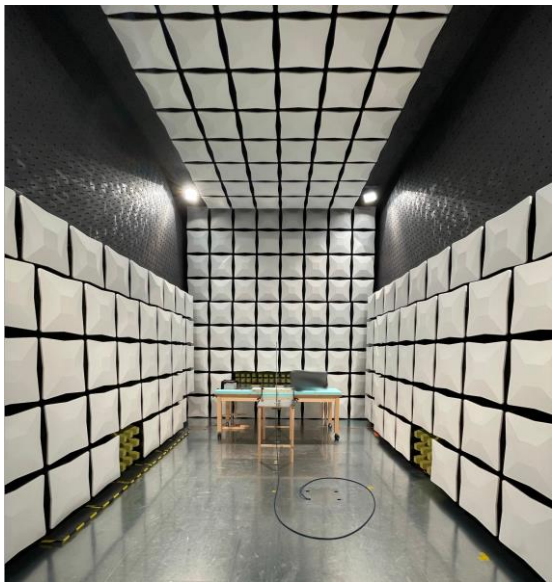

Fig 4 Inside of a SAC-3 EMC chamber.

Building an ALSE is a highly skilled task and even if the right specialists are available, environmental factors cannot be neglected. Proper grounding and power supply is one of the most important tasks. To ensure this, a suitable location should be defined, where the surrounding buildings do not cause disruption to the power grid. One of the other problems is the perfect fitting of the chambers shielding panels. Fitting inaccuracies can degrade the shielding causing noise from outside which can affect the measurement. The goal is to keep the background noise within the ALSE as low as possible.

Quality of such a building depends on many parameters, so there is no enclosure that can be used for comparative measurements to validate newly built chambers. There is no etalon. The CISPR 25 standard contains two validation procedures to determine if valid

measurements can be conducted in an ALSE from 150kHz to 1GHz. These are the reference measurement method and the modelled long wire method.

The two methods are very similar. In the case of a reference measurement, comparative measurements shall be made at the ALSE being tested and at an alternative test site that meets the validation requirements of the standards. In case of the modeled long wire antenna, the measurements are performed only in the ALSE to be validated, the reference data are provided by a simulation described in the standard. The latter method is suitable for the implementation of the research project, as a validated simulation environment can be created based on the CISPR 25 standard. In this simulation different test procedure interpretations and the measurement uncertainties caused by them can be validated. This method is described in the next section of this paper.

IV. ALSE LONG WIRE METHOD

In the process, a long wire antenna is used with parameters specified in the standard. The antenna emits a known interference signal in the EMC chamber in the 150kHz-1GHz frequency range and the amplitude of the interference signal is measured. The advantage of this method is the comparison possibility of the values measured during the validation procedure and to the simulation results described in the standard. In this way, a comparative measurement with ideal parameters can be performed. Validation of a chamber is successful if 90% of the measured values are within ± 6dB of the specified data. [4]

The Long Wire antenna consists of two L-shaped sheet profiles to which a female N-connector is attached. Between them is a 500mm, 4mm diameter copper rod that serves as an antenna. The measurement also requires a 50Ω termination resistor, a 10dB attenuator and an RF cable on which the generated interference signal can be connected to the antenna. The standard highly recommends placing of ferrites with a minimum impedance of 50Ω at 25MHz and 100Ω at 100MHz in every 20cm along the entire length of the RF cable. In addition, recommended type of antenna for different frequency ranges is also determined, which is summarized in Table 2. [4]

Table 2. Antenna types for different frequency ranges

Frequency	Antenna type
0.15MHz to 30MHz	1m vertical monopole antenna
30MHz to 300MHz	biconical antenna
200MHz to 1000MHz	log-periodic antenna

The first step in the validation process is to assemble the test setup by placing the long wire antenna in the center of the edge of the measurement table used in automotive chambers. The measuring antenna shall be positioned so that the reference point of the antenna is 1000mm ±10mm above the reference ground plane of the measuring table and 1000mm ±10mm from the vertical plane of the long wire antenna. The output of the signal generator is set to deliver 1Vrms (120dB(μV)) This can be seen on figure 5. [4]

The test included two measurements. First is a preliminary measurement, when the measurable signal output of the signal generator is determined. In this measurement the interference signal is connected directly to the input of the spectrum analyzer inside the chamber. The test layout must be unchanged during the test. [4]

In the second measurement, the signal generator is connected to the Long Wire antenna via the 10dB attenuator, the other end of which is terminated. Here the input of the spectrum analyzer is connected to the measuring antenna. [4]

Performing the two measurements, two data sets are created, on the basis of which the equivalent field strength at the given frequencies can be calculated using formula (3).

$$E_{eq} = 120\text{dB}(\mu\text{V}) + (M_A - M_0) + k_{AF} \qquad (3)$$

where M_0 is the directly measured value, M_A is the value measured at the antenna output, k_{AF} is the antenna factor and E_{eq} is the equivalent field strength. [4]

The formula shows that if we would have an ideal function generator, this calculation would be not necessary, as its output is a stable 120dB(μV) at all frequencies. But in the reality, the error should be compensated by this method.

Fig 5. Validation of Rejtő Ferenc EMC chamber

V. THE SIMULATION

The ANSYS Electronics desktop was used to perform a finite element simulation for the validation procedure. In this part of the research, the simulation focuses primarily on the frequency range of measurements between 30MHz and 200MHz further ranges will be developed later. The ground plane of the measuring table and the long wire antenna were drawn in the 3-dimensional area. The floor

and a 10cm wide grounding strap were also drawn according to the CISPR25 standard. The excitation of 120dB (µV) was determined on one N-connector of the long wire antenna and the 50Ω termination on the other, thus the test setup was implemented. This is shown in Figure 6.

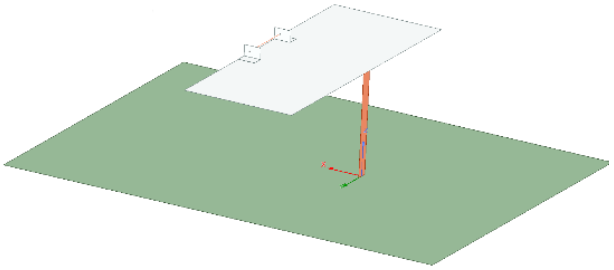

Fig 6. 3D model of the simulation

The excitation is determined at one end of the long wire antenna. The ANSYS software assigns power values to the wave ports, so 120dB (µV) must be converted to dBm (short form of dB (mW)). If the system has constant impedance, a conversion can be done between the two units of measurement. First, the voltage level represented in dB (µV) can be calculated by formula 2.

$$10^{\frac{(120\text{dB}\,\mu\text{V})}{20}} = 1\text{V} \tag{4}$$

To calculate the power of the excitation, formula 5 is used.

$$\text{P} = \frac{V^2}{R} = \frac{1V^2}{50\Omega} = 20mW \tag{5}$$

To understand the calculation, it has to be mentioned that 0dBm corresponds to 1mW. Calculating the dBm level means calculating dBm compared to 0dBm. The dBm of a 120dB (µV) excitation in a 50Ω system is calculated by formula 6. [5]

$$10\log_{10}\left(\frac{20\text{mW}}{1\text{mW}}\right) = 13.01dBm \tag{6}$$

The description of the validation procedure also includes a 10dB attenuator that connects directly to the long wire antenna. This is used to correct signal mismatch. This means that if not all parts of the system are exactly 50Ω, reflection occurs, which can interfere with the incoming signal increasing measurement uncertainty. By using an attenuator, the reflected signals can be attenuated also. Because the simulated excitation is connected directly to the antenna, its power value was lowered by 10dBm and 50Ω renormalization was set on both end of the antenna, which means that the effects of reflection are negligible. The Figure 7 shows the excitation model.

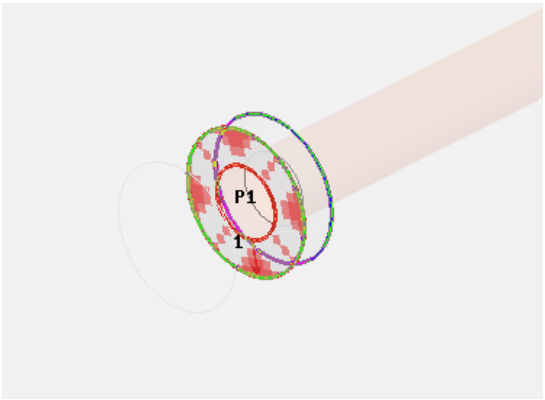

Fig 7 The 3D model of the excitation

The frequency range set in the simulation was determined according to the standard. The figures in the standard shows the model for the 30MHz - 200MHz frequency range, so it was known which parts of the system is represented to implement the simulation.

The standard contains equivalent field strength values in 1MHz increments in this frequency range; so the simulation is set accordingly.

The results of the analysis are shown on the Figure 8.

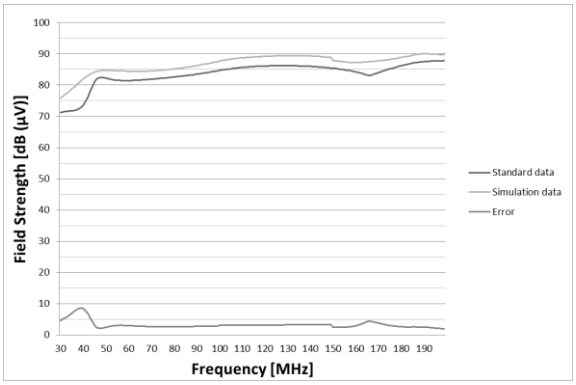

Fig 8 Comparison of data from the CISPR25 Standard and the Simulation results

It can be seen that the values in the standard and the simulation result do not overlap. The highest difference is seen at low frequencies, where a larger slope is included by standard, the error over 50MHz is mostly an offset error.

There can be several reasons for the discrepancies. Firstly, the height of the grounding plane, should be between 90 cm and 100 cm according to the CISPR25 standard, but this is not detailed in the description of the ALSE long wire method. Another source of error can be the size of the floor. ALSE describes the floor as a grounded metal surface, so it can affect the field strength in the test area. Although the floor is shown in the figures

given in the standard, its size is not specified.

Despite the errors, the correlation between the two data sets is 0.81, which means a high connection, so the experiment proved that the desired result can be achieved by further refining the simulation model. This was calculated using the following formula.

$$C(X,Y) = \frac{\Sigma(x-\bar{x})(y-\bar{y})}{\sqrt{\Sigma(x-\bar{x})^2(y-\bar{y})^2}} \quad (5)$$

VI. SUMMARY

The research included a simulation development to examine how different deviations from the test layout specified in the standard affect the measurement uncertainty in a validated virtual environment.

These deviations may include for example a hole in the ground plane of the test bench. When compiling the ALSE Long Wire method, the standard recommends fastening the radiating antenna to the test table with plastic clamps or screws. In theory, screws reduce the contact resistance, which has a beneficial effect on the measurement uncertainty, but the effect of the hole - left in the ground plane of the table - to the subsequent measurements is not known. Another example is placing the artificial network on the test table. The standard specifies where to place it in relation to other equipment and how to ground its enclosure through its feet. However, these artificial networks can vary in size and thus in weight, depending on performance, which can affect the degree of contact resistance created through the feet. The other issue with these devices is the orientation, as the orientation of placing on the test table is not specified in the standard. These networks have a shielded enclosure, but in the GHz range the efficiency of this shielding can be lower and reflections on its surface might happen. This can cause unexpected measurement results and can increase the measurement uncertainty.

The research is continued by development of the simulation environment in order to have minimal deviation from the values reported in the standard. Then, using that virtual environment, development and execution of two phases systematic test procedures can be performed. In the first phase virtual conditions, in the second real conditions will be used.

REFERENCES

[1]IEC 1000-1-1:1992, “Electromagnetic Compatibility (EMC), Part 1 General, Section 1 Application and Interpretation of Fundamental Definitions and Terms” Electromagnetic Compatibility Sectional Committee, 1992

[2]G.Diamant, E.Halahmi, L.Kronik, J.Levy, R.Naaman, J.Roulston, “Integrated circuits based on nanoscale vacuum phototubes”, Applied Physics Letters, vol.92, July 2008

[3]Ferenc Rejtő, “EMC alapok”, Magyar Elektronikai Testület, 2009, ISBN 9639299081

[4]CISPR 25:2016, “Vehicles, boats and internal combustion engines – Radio disturbance characteristics - Limits and methods of measurement for the protection of on-board receivers”, European Committee for Electrotechnical Standardization, 2016

[5]Jeff Beasley, Ph.D, “The dB in Communications”, Technology Interface, 1996

[6]CISPR 14-1:2016, “Electromagnetic compatibility - Requirements for household appliances, electric tools and similar apparatus - Part 1: Emission”, European Committee for Electrotechnical Standardization, 2016

[7]C.L.Holloway, P.M.McKenna, R.A.Dalke, R.A.Perala, C.L.Devor, “Time-Domain Modeling, Characterization, and Measurements of Anechoic and Semi-Anechoic Electromagnetic Test Chambers” IEEE Transactions On Electromagnetic Compatibility, vol.44, No.1, February 2002, pp.102-118.

25th IMEKO TC4 International Symposium
23rd International Workshop on ADC and DAC Modelling and Testing
IMEKO TC-4 2022
Brescia, Italy / September 12-14, 2022

Design and test of an inkjet-printed microwave interdigital capacitor on flexible Kapton substrate

Giovanni Gugliandolo[1], Andrea Alimenti[2], Kostiantyn Torokhtii[2], Nicola Pompeo[2], Giuseppe Campobello[1], Giovanni Crupi[3], Enrico Silva[2], Nicola Donato[1]

[1]*Dept. of Engineering, University of Messina, Contrada Di Dio, 98166 Sant'Agata, Messina, Italy*
[2]*Dept. of Industrial, Electronic and Mechanical Engineering, Roma Tre University, Via Vito Volterra 62, 00146, Roma, Italy*
[3]*Dept. of Biomedical and Dental Sciences and Morphofunctional Imaging, University of Messina, 98125 Messina, Italy*

***Abstract* – The inkjet printing for flexible electronics is an emerging technology that is continuously expanding in different fields, such as healthcare, sports, space science, and, in general, where the traditional rigid electronics is not adequate. In this paper, the design and test of an inkjet-printed device on a flexible substrate are presented. The device is an interdigital capacitor (IDC) fabricated by deposition of conductive ink on a 127 μm-thick polyimide (Kapton®) film. First, the electrical characterization of the substrate material is presented. The obtained results are then used for the IDC design. Finally, the prototype is fabricated by means of an inkjet printer and tested in a frequency range from 1 GHz to 5 GHz.**

I. INTRODUCTION

Recently, growing attention has been paid to inkjet printing (IJP) technology for electronics applications. The prominent factors that are playing a major role in raising the research interest in this technology include cost efficiency, fast prototyping, better optimization in large-scale production, and rapid testing of the products [1]. Moreover, such technology represents an environmentally friendly alternative to the more conventional printed circuit board (PCB) fabrication processes; the pattern is directly printed onto substrates without employing screens or masks, thus generating nearly zero waste [1].

IJP technology has witnessed a remarkable progress by moving from the design and integration of simple electronic elements (e.g., sensors [2]) to the development of more advanced systems [3]. Nevertheless, the use of inkjet printing techniques in the RF and microwave field is still limited because of the limited accuracy and repeatability of the printed patterns [4]. Furthermore, in microwave applications, an accurate control of the ink surface roughness [5] and the final ink conductivity is mandatory [6]. Despite this, the IJP technology is expected to advance significantly, as continuous innovations are being made to address these limitations and make it viable for RF and microwave device fabrication.

In such a context, many typologies of inkjet-printed microwave sensors have been proposed in the literature. In [6], a low-cost and lightweight wireless sensor node has been proposed. It includes a carbon-nanotube-based sensitive element combined with an inkjet-printed patch antenna. The developed prototype has been successfully used for ammonia detection. More recently, in [7] a chipless RFID inkjet printed humidity sensors was proposed. This prototype is composed of three concentric rings that produce three dips in the amplitude of the reflection coefficient of the microwave device. The resonant frequency of such dips was exploited as a tracker for humidity detection.

One of the biggest advantages of the IJP technology relies on the possibility to use thin and flexible/stretchable materials as substrate [8]. This allows the development of wearable devices with a higher level of wearing comfort in comparison to traditional electronics. They can be placed in contact with the human skin or integrated into clothes for different applications aimed at health care, sports, biomonitoring, and human-machine interaction [8, 9]. In such a context, several microwave devices have been proposed [9], such as flexible antennas [1], gas sensors [10], humidity and temperature sensors [11], and even more complex microwave systems have been developed for energy-harvesting [12], smart skin [13], and telecommunication applications [14].

In this paper, a preliminary design of a flexible inkjet printed microwave resonator is presented. The microwave resonator is an interdigital capacitor (IDC). This type of capacitor is used to realize small capacitances in microwave integrated circuits [15] and it is widely employed in sensing applications [16–19]. It can be modeled as a RLC series circuit [20] where R and L are the parasitic resistive and inductive elements, while C is the IDC equivalent capacitance which describes the capacitive contribution of the multi-finger structure. Similarly to RLC circuits, IDCs have a specific resonant frequency [16, 20]. The IDC design is carried out using a computer-aided de-

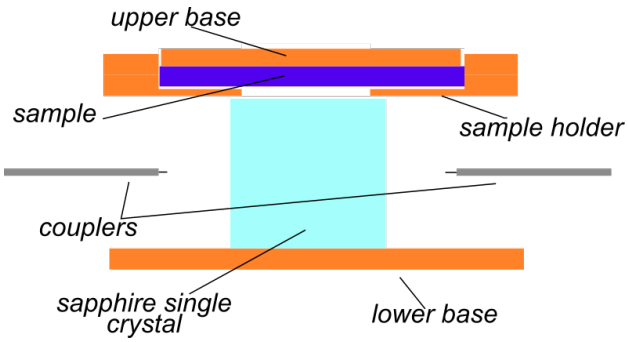

Fig. 1. Sketch of the dielectric loaded resonator used for the ε measurement of the Kapton® film. The lower/upper bases and the sample holder are made of brass. The dielectric crystal is a sapphire cylinder 5 mm high and 8 mm in diameter. The TE_{011} mode is excited through coaxial cables ended with magnetic loops at $\sim$ 12.5 GHz. The dielectric sample is loaded under the upper base and the resonator closed by applying a 500 g weight on it. Further details can be found in [24].

sign (CAD) software and validated through computer simulations. The final prototype is then fabricated on a 127-μm thick Kapton® film substrate using a Voltera V-One PCB printing machine. Tests are carried out in the frequency range spanning from 1 GHz up to 5 GHz.

The paper is organized as follows. In the next section, the electrical characterization of the flexible material used as a substrate for the microwave resonator is presented. In Section III, the design, fabrication and test of the developed prototype are discussed. Finally, conclusions are drawn in Section IV.

II. MATERIAL AND CHARACTERIZATION

The first step of the IDC design process consists in the characterization of the electromagnetic properties of the used substrate material. The values of the dielectric constant of polyimide films are rather different, depending on the source [21, 22]. Thus, a direct measure is appropriate for a suitable simulation of the device. The response of a dielectric material to electromagnetic (e.m.) fields is described through the complex dielectric permittivity $\varepsilon_0\tilde{\varepsilon} = \varepsilon_0(\varepsilon' - \mathrm{i}\varepsilon'')$, where ε_0 is the vacuum dielectric constant, $\varepsilon' = \mathrm{Re}\,\varepsilon$, $\varepsilon'' = -\mathrm{Im}\,\varepsilon$, the ratio $\tan\delta = \varepsilon''/\varepsilon'$ is known as loss tangent and $\mathrm{i} = \sqrt{-1}$ [23]. Thus, $\tilde{\varepsilon}$ of the Kapton® film used for the realization of the IDC substrate must be measured accurately to design the resonator geometry parameters. For the characterization of the Kapton® film we decided to use the dielectric loaded resonator in the configuration shown in [24] (see Fig. 1), due to its high sensitivity and precision.

The measurement method is a volume perturbation technique [25]. Part of the inner volume of an e.m. resonating structure is substituted first by a reference material and then by the material under investigation: from the variation of the quality factor Q and resonance frequency f_0, the e.m. magnetic properties of the unknown material can be estimated [25]. Air is used as reference, considering its $\tilde{\varepsilon} \approx 1 - \mathrm{i}0$. It can be shown [24, 25] that $\Delta f_0 \propto \varepsilon'$ and $\Delta(Q^{-1}) \propto \tan\delta$, where Δx is used to indicate the variation of the x parameter with respect to a reference value (of air, in this case).

Due to the expected large losses of Kapton® , only a small volume of the resonator is substituted with this material to avoid reducing too much Q and therefore losing sensitivity. The optimization of the volume of the sample, with respect to its expected e.m. properties, is discussed in [24]. In this case, to reach the desired sensitivity, ten layers of the Kapton® film are stacked to form a parallelepiped, with dimensions $15.0 \times 15.0 \times 1.27$ mm^3, and loaded into the resonator as shown in Fig. 1. To evaluate the measurement repeatability, the transmission and reflection scattering S-parameters of the resonator are measured 20 times dismounting the sample for each measurement. Q and f_0 are measured through the fit of the acquired S-parameters with the method shown in [26]. For each mounting, only one measurement was performed since it was observed that the type-A uncertainties on Q and f_0 evaluated with a statistical analysis of repeated measurements were equivalent with those provided by the fitting procedure and evaluated starting from the fit residuals of only one measurement [26].

The reference measurement is obtained substituting the same volume of the Kapton® sample with one filled with air. In this configuration the upper base of the resonator is held in position with a ring printed with the same thickness as the sample under investigation and put in the resonator in place of the sample itself. This allows not changing the geometry of the resonator but entering into the resonator a controlled volume of air. With the Kapton® sample we obtained $Q = 3866(3)$ and $f_0 = 12.45930(7)$ GHz, where the numbers in parentheses are the numerical value of the experimental standard deviations, $s(Q)$ and $s(f_0)$ respectively, referred to the corresponding last digits of the quoted results. The repetition of 20 measurements with the air reference sample gave $Q = 5066(3)$ and $f_0 = 12.486000(22)$ GHz.

The obtained Δf_0 is compared with the calibration curves $\varepsilon'(\Delta f_0)$ and $\eta(\Delta f_0)$, with η the sample filling factor [25], shown in Fig. 2, which are obtained with e.m. simulations of the structure [24]. Once ε' and η are determined, $\tan\delta \approx \Delta(Q^{-1})/\eta$ can be obtained [24].

For the analyzed Kapton® film we obtained $\varepsilon' = 4.0 \pm 0.5$ and $\tan\delta = (1.02 \pm 0.16) \times 10^{-2}$, which are in good agreement with literature values [21], and where the uncertainties are expanded uncertainties with 95 % level of probability evaluated propagating the

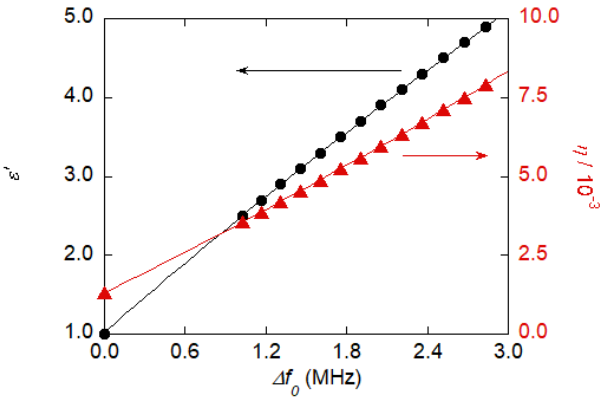

Fig. 2. Calibration curves $\varepsilon'(\Delta f_0)$ (black dots-left scale) and $\eta(\Delta f_0)$ (red triangles-right scale). The continuous curves are obtained by a 2^{nd}-order polynomial fit: $\varepsilon' = -49800(400)\Delta f_0^2 + 1512(2)\Delta f_0 + 1.000(1)$ and $\eta = 78.79(4)\Delta f_0^2 + 2.101(2)\Delta f_0 + 1.1315(2) \times 10^{-3}$, with Δf_0 expressed in MHz. The uncertainty bars are within the symbols dimensions.

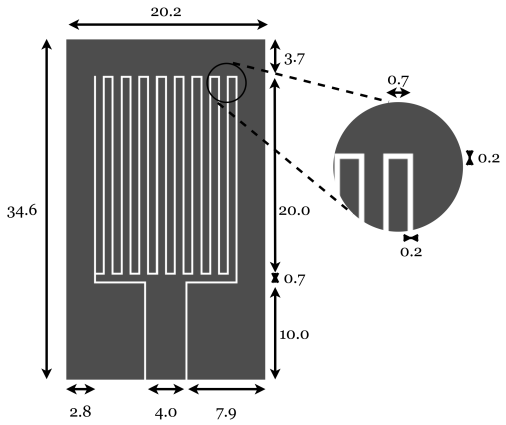

Fig. 3. Sketch of the designed one-port IDC device. All the reported dimensions are in mm.

distribution of simulated and measured quantities using a Monte Carlo method in compliance with [27, 28]. The simulated f_0 and η are assumed to be normally distributed with 1 % relative standard deviation. Thus, for each trial of the Monte Carlo simulation the calibration curves $\varepsilon'(\Delta f_0)$ and $\eta(\Delta f_0)$ are re-evaluated and fitted with a 2^{nd} order polynomial, obtaining the uncertainties on the fitting parameters reported in the caption of Fig. 2. Hence, from the measured Δf_0 and $s(f_0)$, ε' and η (and their uncertainties) are obtained, then $\tan\delta$ (and its uncertainty) is obtained from the measured Q and $s(Q)$. 10^6 trials are performed to deliver the 95 % coverage interval of the derived quantities [27].

III. DESIGN, REALIZATION AND TEST

The proposed prototype is a single-port IDC characterized by a total of 16 fingers in a parallel configuration as depicted in Figure 3. The fingers have been designed with a length, a width, and a spacing of 20 mm, 0.7 mm, and 0.2 mm, respectively. The nominal IDC dimensions are 34.6 mm × 20.2 mm. A complete description of the IDC geometrical parameters is reported in Figure 3.

The IDC geometry has been widely studied in the literature and several lumped-element equivalent circuit models have been proposed [16, 29, 30]. Such circuits accurately describe the device behavior in a relatively wide frequency range. However, at high frequency, additional resonances appear [20] and the equivalent-circuit model becomes less reliable. In this case a full-wave e.m. solver is required for the accurate study of the microwave device. As the IDC equivalent capacitance increases, spurious resonances are moved towards lower frequencies [20].

The proposed IDC is meant to be used for sensing applications and, in this case, spurious resonances are desirable since they may be exploited as trackers [31]. In the literature, IDCs and, in general, planar resonators have been employed for sensing purposes and they exhibited good performance when used in the frequency range between 1 GHz and 5 GHz [32–36]. For this reason, the proposed IDC is designed to operate on this frequency band. Several e.m. simulations are carried out on the IDC geometry. Since the IDC equivalent capacitance is proportional to the number of fingers and to their length, these two parameters are varied to get the desired result, i.e., resonances that occur in the selected frequency range. Moreover, the fingers width is chosen to maximize the quality factor of the resonant dips. The final IDC geometric dimensions are reported in Figure 3. It is worth noting that the feedline is designed with an input impedance of 50 Ω.

Once the IDC geometry is defined, the prototype is fabricated using a Voltera V-One PCB printing machine. The 127 μm-thick Kapton® film is selected as substrate, while a flexible conductive ink is used for the conductive layer printing. In particular, the Voltera Flexible Conductor 2 ink [37] is used. It is characterized by an electrical resistivity of 1.36×10^{-7} Ω·m, and the typical cured film thickness is between 40 μm and 70 μm. The prototype is printed using a 150-μm Voltera nozzle, as suggested by the ink datasheet [37], and, once the printing process is completed, the sample is cured in the oven at about 170 °C for 30 minutes. The curing procedure is essential to trigger the ink chemical reactions, thereby allowing the metal particles to fuse in a conductive layer. The IDC is then cleaned with isopropyl alcohol and burnished. Finally, a 50 Ω straight PCB mount SMA connector is soldered at the end of the feedline as an input port to allow the connection of Vector Network Analyzer (VNA).

An Agilent 8753ES VNA is used for the prototype test. The VNA is calibrated using a one-port short-open-load

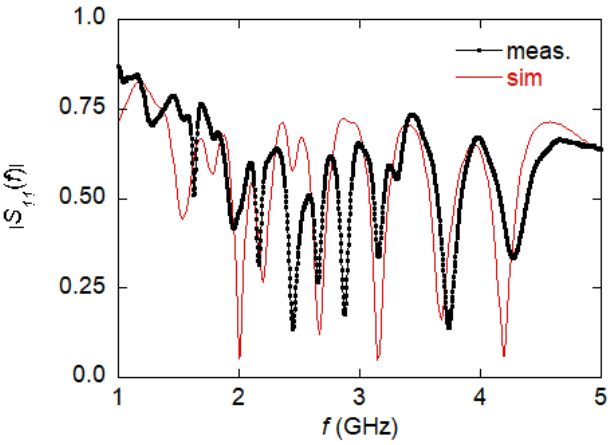

Fig. 4. Comparsion bewteen measurement (black) and COMSOL simulation (red) of the magnitude of the reflection coefficient for the developed IDC. The explored frequency range goes from 1 GHz to 5 GHz.

(SOL) calibration procedure, and the reflection coefficient S_{11} is measured. The VNA is set to acquire 1601 points, the RF power is set to 0 dBm, and the intermediate frequency (IF) is 1 kHz. In Figure 4 a comparison between the simulated and measured $|S_{11}(f)|$ is reported. As expected from simulations, several resonances occur in the considered frequency range. Simulations are carried out using the COMSOL software. A good agreement can be observed between simulation and measurement, although not all resonances are accurately predicted by COMSOL. Such mismatches may be ascribed to tolerances in the fabrication process. In particular, the fabricated prototype exhibits additional resonances in the frequency range from 2 GHz to 3 GHz. However, this should be not taken as a practical limitation for the intended applications, since the additional resonances might be exploited for detection purpose.

IV. CONCLUSIONS

In this work, the design and test of a flexible inkjet-printed IDC are presented. The design process has been supported by the electrical characterization of the dielectric Kapton® film used here as substrate. This allowed a better description of the microwave device behavior through computer simulations. The measured performance of the proposed device is found to be in line with the simulation-based expectations. Further activities are in progress in order to use the developed prototype for practical sensing applications.

REFERENCES

[1] I. I. Labiano and A. Alomainy, "Flexible inkjet-printed graphene antenna on kapton," *Flexible and Printed Electronics*, vol. 6, no. 2, 2021, Art. Id. 025010.

[2] E. Bihar, S. Wustoni, A. M. Pappa, K. N. Salama, D. Baran, and S. Inal, "A fully inkjet-printed disposable glucose sensor on paper," *npj Flexible Electronics*, vol. 2, no. 1, pp. 1–8, 2018.

[3] J. Lemarchand, N. Bridonneau, N. Battaglini, F. Carn, G. Mattana, B. Piro, S. Zrig, and V. Noel, "Challenges and prospects of inkjet printed electronics emerging applications–a chemist point of view," *Angewandte Chemie International Edition*, 2022.

[4] V. Camarchia, A. Chiolerio, M. Cotto, J. Fang, G. Ghione, P. Pandolfi, M. Pirola, R. Quaglia, and C. Ramella, "Assessment of silver nanoparticle inkjet-printed microstrip lines for rf and microwave applications," in *2013 IEEE International Wireless Symposium (IWS)*. IEEE, 2013, pp. 1–4.

[5] A. Alimenti, K. Torokhtii, N. Pompeo, and E. Silva, "Evaluation of the surface roughness detrimental effects on the surface resistance of good conductors," in *Proceedings 25th IMEKO TC4 International Symposium*. IEEE, 2022 (submitted).

[6] H. Lee, G. Shaker, K. Naishadham, X. Song, M. McKinley, B. Wagner, and M. Tentzeris, "Carbon-nanotube loaded antenna-based ammonia gas sensor," *IEEE Transactions on Microwave Theory and Techniques*, vol. 59, no. 10, pp. 2665–2673, 2011.

[7] M. Borgese, F. A. Dicandia, F. Costa, S. Genovesi, and G. Manara, "An inkjet printed chipless rfid sensor for wireless humidity monitoring," *IEEE Sensors Journal*, vol. 17, no. 15, pp. 4699–4707, 2017.

[8] K. Yan, J. Li, L. Pan, and Y. Shi, "Inkjet printing for flexible and wearable electronics," *APL Materials*, vol. 8, no. 12, 2020, Art. Id. 120705.

[9] S. Kim, "Inkjet-printed electronics on paper for rf identification (rfid) and sensing," *Electronics*, vol. 9, no. 10, p. 1636, 2020.

[10] J. George, A. Abdelghani, P. Bahoumina, E. Cloutet, N. Bernardin, K. Frigui, H. Hallil, C. Dejous, S. Bila, and D. Baillargeat, "Inkjet-printed rf gas sensors based on conductive nanomaterials for VOCs monitoring," in *2021 IEEE MTT-S International Microwave Symposium (IMS)*. IEEE, 2021, pp. 93–96.

[11] J. Courbat, Y. Kim, D. Briand, and N. De Rooij, "Inkjet printing on paper for the realization of humidity and temperature sensors," in *2011 16th International Solid-State Sensors, Actuators and Microsystems Conference*. IEEE, 2011, pp. 1356–1359.

[12] H. Saghlatoon, T. Björninen, L. Sydänheimo, M. M. Tentzeris, and L. Ukkonen, "Inkjet-printed wideband planar monopole antenna on cardboard for rf energy-harvesting applications," *IEEE Antennas and Wireless Propagation Letters*, vol. 14, pp. 325–328, 2014.

[13] M. M. Tentzeris, S. Kim, R. Vyas, A. Traille, P. Pons, H. Aubert, A. Georgiadis, and A. Col-

lado, "Inkjet-printed "zero-power" wireless sensor and power management nodes for iot and "smart skin" applications," in *2014 20th International Conference on Microwaves, Radar and Wireless Communications (MIKON)*. IEEE, 2014, pp. 1–7.

[14] L. Yang and M. M. Tentzeris, "Design and characterization of novel paper-based inkjet-printed RFID and microwave structures for telecommunication and sensing applications," in *2007 IEEE/MTT-S International Microwave Symposium*. IEEE, 2007, pp. 1633–1636.

[15] Z. A. Maricevic, "Analysis and measurements of arbitrarily shaped open microstrip structures," Ph.D. dissertation, Syracuse University, 1994.

[16] G. Crupi, X. Bao, O. J. Babarinde, D. M.-P. Schreurs, and B. Nauwelaers, "Biosensor using a one-port interdigital capacitor: A resonance-based investigation of the permittivity sensitivity for microfluidic broadband bioelectronics applications," *Electronics*, vol. 9, no. 2, p. 340, 2020.

[17] G. Gugliandolo, Z. Marinković, A. Quattrocchi, G. Crupi, and N. Donato, "Development of an inkjet-printed interdigitated device: Cad, fabrication, and testing," in *2021 IEEE International Conference on Integrated Circuits, Technologies and Applications (ICTA)*. IEEE, 2021, pp. 153–154.

[18] G. Gugliandolo, K. Naishadham, G. Crupi, and N. Donato, "Design and characterization of a microwave transducer for gas sensing applications," *Chemosensors*, vol. 10, no. 4, p. 127, 2022.

[19] Z. Marinković, G. Gugliandolo, M. Latino, G. Campobello, G. Crupi, and N. Donato, "Characterization and neural modeling of a microwave gas sensor for oxygen detection aimed at healthcare applications," *Sensors*, vol. 20, no. 24, p. 7150, 2020.

[20] F. P. Casares-Miranda, P. Otero, E. Marquez-Segura, and C. Camacho-Penalosa, "Wire bonded interdigital capacitor," *IEEE Microwave and Wireless Components Letters*, vol. 15, no. 10, pp. 700–702, 2005.

[21] S. Sahin, N. K. Nahar, and K. Sertel, "Dielectric properties of low-loss polymers for mmW and THz applications," *Journal of Infrared, Millimeter, and Terahertz Waves*, vol. 40, no. 5, pp. 557–573, 2019.

[22] S. Chisca, I. Sava, V.-E. Musteata, and M. Bruma, "Dielectric and conduction properties of polyimide films," in *CAS 2011 Proceedings (2011 International Semiconductor Conference)*, vol. 2, IEEE, 2011, pp. 253–256.

[23] J. D. Jackson, *Classical electrodynamics*. American Association of Physics Teachers, 1999.

[24] A. Alimenti, K. Torokhtii, N. Pompeo, E. Piuzzi, and E. Silva, "Characterisation of dielectric 3d-printing materials at microwave frequencies," *ACTA IMEKO*, vol. 9, no. 3, pp. 26–32, 2020.

[25] L.-F. Chen, C. Ong, C. Neo, V. Varadan, and V. K. Varadan, *Microwave electronics: measurement and materials characterization*. John Wiley & Sons, 2004.

[26] K. Torokhtii, N. Pompeo, E. Silva, and A. Alimenti, "Optimization of Q-factor and resonance frequency measurements in partially calibrated resonant systems," *Measurement: Sensors*, vol. 18, 2021, Art. Id. 100314.

[27] Joint Committee for Guides in Metrology, "JCGM 101: Evaluation of Measurement Data - Supplement 1 to the Guide to the Expression of Uncertainty in Measurement - Propagation of distributions using a Monte Carlo method," JCGM, Tech. Rep., 2008.

[28] ——, "JCGM 100: Evaluation of Measurement Data - Guide to the Expression of Uncertainty in Measurement," JCGM, Tech. Rep., 2008.

[29] G. Crupi, X. Bao, P. Barmuta, I. Ocket, D. M. M.-P. Schreurs, and B. Nauwelaers, "Microfluidic biosensor for bioengineering: High-frequency equivalent-circuit modeling of interdigital capacitor," in *2019 14th International Conference on Advanced Technologies, Systems and Services in Telecommunications (TELSIKS)*. IEEE, 2019, pp. 315–318.

[30] X. Bao, I. Ocket, J. Bao, Z. Liu, B. Puers, D. M. M.-P. Schreurs, and B. Nauwelaers, "Modeling of coplanar interdigital capacitor for microwave microfluidic application," *IEEE Transactions on Microwave Theory and Techniques*, vol. 67, no. 7, pp. 2674–2683, 2019.

[31] G. Bailly, A. Harrabi, J. Rossignol, D. Stuerga, and P. Pribetich, "Microwave gas sensing with a microstrip interdigital capacitor: Detection of nh3 with tio2 nanoparticles," *Sensors and Actuators B: Chemical*, vol. 236, pp. 554–564, 2016.

[32] L. Ali, C. Wang, F.-Y. Meng, Y.-C. Wei, X. Tan, K. K. Adhikari, and M. Zhao, "Simultaneous measurement of thickness and permittivity using microwave resonator-based planar sensor," *International Journal of RF and Microwave Computer-Aided Engineering*, vol. 31, no. 10, 2021, Art. Id. e22794.

[33] J. Bao, T. Markovic, G. Maenhout, I. Ocket, and B. Nauwelaers, "An impedance matched interdigital capacitor at 1.5 GHz for microfluidic sensing applications," *Sensors and Actuators A: Physical*, vol. 330, 2021, Art. Id. 112867.

[34] C. Wang, L. Ali, F.-Y. Meng, K. K. Adhikari, Z. L. Zhou, Y. C. Wei, D. Q. Zou, and H. Yu, "High-accuracy complex permittivity characterization of solid materials using parallel interdigital capacitor-based planar microwave sensor," *IEEE Sensors Journal*, vol. 21, no. 5, pp. 6083–6093, 2020.

[35] H.-R. Sun, G. Du, G. Liu, X. Sun, T. Tang, W. Liu, and R. Li, "Symmetric coplanar waveguide sensor loaded with interdigital capacitor for permittivity characterization," *International Journal of RF and*

Microwave Computer-Aided Engineering, vol. 30, no. 1, 2020, Art. Id. e22023.

[36] J. Yeo and J.-I. Lee, "High-sensitivity microwave sensor based on an interdigital-capacitor-shaped defected ground structure for permittivity characterization," *Sensors*, vol. 19, no. 3, p. 498, 2019.

[37] *Voltera Flexible Conductor 2 (1000383)*, Voltera, 6 2020, rev. Date 2020-06-09.

25th IMEKO TC4 International Symposium
23rd International Workshop on ADC and DAC Modelling and Testing
IMEKO TC-4 2022
Brescia, Italy / September 12-14, 2022

Microwave dielectric resonator device concept for surface impedance measurement of rotating sample

Kostiantyn Torokhtii[1], Andrea Alimenti[1], Nicola Pompeo[1], Enrico Silva[1]

[1]*Dept. of Industrial, Electronic and Mechanical Engineering, Roma Tre University, Via Vito Volterra 62, 00146, Rome, Italy*

***Abstract* – The surface impedance of superconductors in function of intense ($\sim$ 10 T) static magnetic field at varying orientations with respect to the crystallographic axes is of large interest for both characterization purposes, in view of the material engineering, and from the point of view of devices to be used in fundamental physics experiments. A varying field orientation is customarily obtained with mechanically rotating magnets, whose complexity limits the attainable maximum fields to a few T. Here we propose a special proof of concept design for a measuring cell in which the magnetic field orientation is fixed, while the sample orientation can be changed through its incorporation in a rotating portion of the cell. The main design choices are thus proposed for the measuring cell: a cylindrical dielectric loaded resonator, to be used within the surface perturbation approach for the measurement of the surface impedance of flat samples with typical size $10\times10\,\mathrm{mm}^2$. The main focus in this preliminary work is put on the sensitivity attainable on the surface resistance, i.e. the real part of the surface impedance.**

I. INTRODUCTION

Measurements of the surface impedance Z_s of superconductors in high magnetic fields with varying orientations are of specific but strong interest. Indeed, the most promising superconductors for the realization of next generation high field magnets, in applications such as high definition Nuclear Magnetic Resonance (NMR) [1] and future compact fusion reactors [2], are anisotropic. Hence, angle-dependent surface impedance is a useful characterization tool for the material engineering process. Moreover, large physics experiments, such as the Future Circular Collider [3] and the hunt for Dark Matter [4], require low surface impedance superconductors to be operated in high magnetic fields applied at various orientations with respect to the crystallographic axes. A standard approach in surface impedance measurements is based on the dielectric-loaded resonator (DR) [5]. Indeed, the dielectric loaded resonator method is the most sensitive technique for Z_s measurements in a wide range of temperatures and magnetic fields [5, 6, 7].

Usually, the measurement cell is a simple Hakki-Coleman DR [8], where a cylindrical dielectric puck is coaxially placed within a cylindrical conducting enclosure. In the commonly used surface perturbation technique, the sample replaces one of the conducting flat surfaces of the cavity. By changing an external parameter, such as the dc magnetic field intensity H, the induced variations "Δ" of the real (R_s) and imaginary (X_s) parts of Z_s with respect to a reference value $Z_{s,ref} = Z_s(H = H_{ref})$, can be derived from the measurement of the DR quality factor Q and resonant frequency f_0, respectively [9, 10, 11]:

$$\Delta R_s + \mathrm{i}\Delta X_s = G_s \left(\Delta \frac{1}{Q} - \mathrm{i}2 \frac{\Delta f_0}{f_0} \right) - \mathrm{background} \quad (1)$$

where the geometrical factor of the sample G_s is a constant analytically computed or determined through electromagnetic simulations; the term "background" refers to other DR contributions that can be removed by a proper calibration procedure [10]. Performing simple calculations, the sensitivity on R_s and X_s can be obtained:

$$S_{R_s} = \left| \frac{\partial Q}{\partial R_s} \right| = \frac{Q^2}{G_s}, S_{X_s} = \left| \frac{\partial \Delta f_0}{\partial X_s} \right| \propto \frac{1}{2G_s} \quad (2)$$

In standard configurations the static magnetic field is applied parallel to the resonator axis, and hence normal to the sample surface (see Fig 1a). In order to study the material anisotropic response to the *orientation* of the applied magnetic field, two possible approaches can be used: either rotate the magnet around the measuring cell or rotate the whole measuring cell within a fixed magnet. In the first case, specific magnets must be used, rotating either mechanically or magnetically. The added complexity makes them more expensive and limited in the maximum field attainable. The rotation of the whole cell, on the other hand, is hindered by the connection cables, given mainly by the microwave (mw) lines connecting the resonator to a microwave source and detector, which must be fixed.

Here we present a proof of concept based on a third path: a DR based measuring cell designed with a mobile part hosting the flat sample to be measured in various field orientations. To this purpose, the sample would replace a portion of the lateral (curved) cavity wall. Indeed, the

measurement of Z_s on curved surfaces is more complex and seldom dealt with [12]. Thus, in the proposed design we postpone the optimization for the measurement of both R_s and X_s for future developments.

II. DESIGN

The here presented concept is based on the standard approach for the Z_s measurement by means of DR, whereas several additional constraints are taken into account to pursue the stated goal.

First, the measuring cell with all its components and connectors should be accommodated in the bore of a standard cryomagnet, which in high field magnets has typical radii R_{cr} no larger than 32.5 mm. Second, the DR must be able to operate in the $\leq$30 GHz range, where both the characteristic frequency of the materials to be studied and the operating frequencies of the mentioned applications are located [13, 14].

A. *Definition of the DR geometry*

The small sample space and the necessity to insert moving parts and cables are the main limiting factors for the DR cell size. A small cell size in turn leads to the higher resonant frequencies of DR.

In order to define the design framework, we first choose the DR resonant mode as a Transverse Electric TE_{0m1} mode, where $m = 1, 2....$ Indeed, it is well-known that the TE_{011} mode has one of the lowest resonant frequency with good frequency separation from other modes [6]. Moreover, the TE_{011} modes induce circular currents both on the bases and on lateral wall of the cylindrical cavity. Hence, no current paths cross the base-wall boundary allowing to physically separate the bases from the wall without disrupting the resonance. This feature will prove extremely valuable in the forthcoming design process. Moreover, the TE_{011} mode induces the maximum current density at the middle plane of the dielectric puck.

The draft of the DR cell is shown in Fig. 1b. The main idea is to conceive the the DR cell as composed by two parts. The fixed part consists of the dielectric puck and flat circular bases, while the lateral wall of the resonant cavity becomes a moving, rotating part. The sample is fixed on the moving part, at the dielectric puck's mid-height level, where the induced currents are maximum. This positioning allows obtaining maximum sensitivity on Z_s and, moreover, linear microwave currents on the sample surface. This is opposed to the circular current pattern encountered in the standard DR setup which, once used with tilted fields, determine non-homogeneous angles between field and currents on the sample surface and ultimately hindering an anisotropy investigation [15].

To place the sample in the rotating part, a recessed blind hole, covered by a thin metallic mask with a rectangular

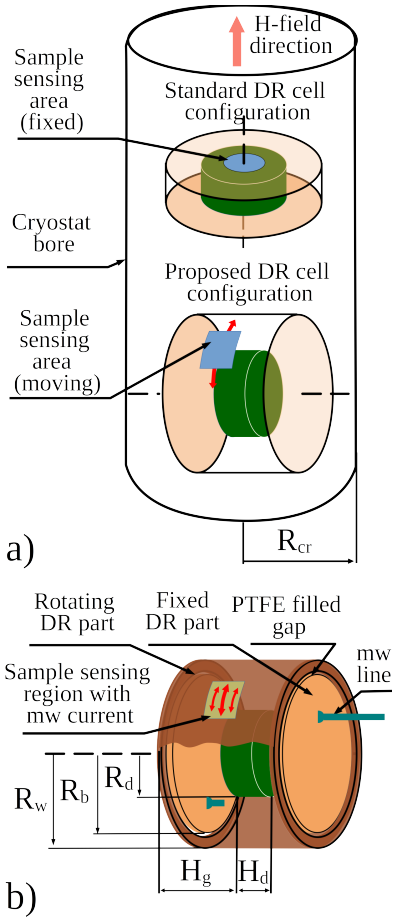

Fig. 1. Draft of the DR cell. a) sketch of the DR cell inside a magnet bore. b) Draft of the DR cell with the two parts, the fixed one with the dielectric puck and the rotating one with the sample holder.

slot, can be made in the lateral wall. In this way, the sample would not protrude in the cavity interior, and only a regular portion of its surface would be exposed to the microwave electromagnetic fields. In this preliminary design, we do not consider the details of mechanical supporting parts. To maintain a constant distance between the fixed resonator bases and the freely rotating lateral wall, we incorporate a thick PTFE layer between the parts. This gap does not affect the TE_{011} mode electromagnetic fields, which are concentrated near the dielectric puck, nor the current pattern induced in the enclosing surfaces, and thus minimally influences the characteristics of the DR cell.

The main components of the DR cell are represented in Fig. 1b: the dielectric puck is placed coaxially to the cavity, between the two flat bases, and has radius R_b smaller than the wall radius R_w.

We put (symmetrical) gaps H_g between the dielectric puck and the bases, so that power dissipation on the bases is reduced. The coupling ports between the DR and mi-

crowave lines are placed on the fixed bases (see Fig. 1b), instead of the more often used lateral wall, since the latter is a moving part in the present design.

B. *Definition of the size ranges*

We performed an optimization of the size of the DR cell focusing on the sensitivity of the resonator response on R_s of the sample. The size starting value is given by the cryomagnet bore: considering the smaller values - encountered in high ($\sim$ 10 T magnets), we set an upper limit for the external size of the whole cell to R_{cr} =22.5 mm. Considering that the main part of the DR cell volume will consist in structural supporting parts, together with semi-rigid cryogenic coaxial cables, basic estimations yield the maximum external size of the cylinder, 31 mm. Indeed, the structural cavity parts should be at least 5 mm thick. Adding the space needed for coaxial cables ($\sim$5 mm), the internal cavity wall radius R_w is $\leq$10 mm, and analogously the corresponding maximum cavity height is $\leq$20 mm.

A first simulation of the simple Hakki-Coleman DR structure [16] allowed determining the optimal ratio 0.98 between the dielectric puck radius R_d and height H_d to yield a TE_{011} mode well isolated in frequency from spurious modes. For the present design, which involves a gapped structure a possible different optimal value for R_d/H_d as been sought in a range centered in 0.98 mm.

The choice of the dielectric puck material is of paramount importance. Dielectrics with high relative (real) permittivity ε_r are preferable, since they concentrate more the electromagnetic field within the dielectric puck and thus minimize the disrupting effects of the DR inhomogeneities and gaps. At cryogenic temperatures, single crystal sapphire is usually chosen due to its relatively high ε_r (11.58 and 9.40 parallel and normal to the crystal main anisotropy axis, respectively) and one of the lowest dielectric loss tangents ($\tan\delta$=2.0 $\times$ 10^{-5} at room temperature [17]), enabling high Q factors. Other higher ε_r materials, such as rutile, could be used to reduce the cavity size and/or resonant frequency, but with the drawback of a decreased Q and corresponding sensitivity. Specific studies in this direction could be considered in future studies.

Since DR operates in the high magnetic field in cryogenic environments all metallic parts of DR should be nonmagnetic and should have a high thermal conductivity. For the following, we considered a medium-quality copper with R_s=42 mΩ for all metallic parts of DR. To investigate the capabilities of the proposed DR cell we performed a full-wave Finite Element Method (FEM) simulation. A 3D simulation of the detailed resonator structure needs large calculating power and thus is inefficient in the initial stages of the design process. Hence, in the following we present the results of a 2D (axisymmetric) model, made possible by the axisymmetry of both the DR structure and of the chosen TE_{011} mode.

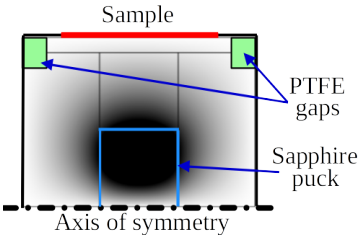

Fig. 2. An example of the simulated TE_{011} mode, in terms of its electric field spatial intensity (darker regions correspond to higher intensity). The red line represents the sample sensing area.

III. DISCUSSION

The FEM simulation performed taking into account the material properties, for both dielectrics and conductors, at room temperature. The extension to cryogenic temperatures will be considered in future works.

In Fig. 2 we illustrate a representative example of electric field distribution corresponding to TE_{011} mode under study. For this 2D axisymmetric model, the sensing area is represented as a 10 mm-wide strip along the whole cavity wall circumference. For future 3D simulation and real DR, samples will be only a portion of this strip as shown in Fig. 1b.

As anticipated in the previous Section, the optimization of the DR cell size is done by taking a fixed ratios R_d/H_d in the range near 0.98 . The symmetrical gap between dielectric puck and bases H_g is varied in the range 0.1 mm–9 mm. Since a small cavity radius is preferable, we studied also the effect of the cavity wall radius R_w by varying it between 6 mm and 12 mm. Given the circular shape of the magnet bore, analogous limits hold also for the longitudinal direction of the DR cell, being $H_d + 2H_g$ its total height (see Fig. 1b). As a result, the investigated parameters space is: R_d/H_d=0.8 –1.2 , H_g=0.1 mm–9 mm, R_w =6 mm–12 mm. Since this multi-variable space of parameters is large, here we focus on selected results.

For each parameters set, the resonant modes were calculated. The TE_{011} mode was identified from other modes using an automatic script which detects the maxima, minima and lobes in the field spatial distributions to identify the mode type and indexes. Upon increasing the dielectric puck size R_d/R_w from 0.2 to 0.8 , the Q factors exhibit a maximum whose position slowly shifts to higher values by increasing the gap H_g (see Fig. 3). Independently from the dielectric puck size R_d/R_w and from the cavity size R_w, even for small gaps H_g above 2 mm, the maxima of $Q(R_d/R_w)$ are in the same R_d/R_w region $R_d/R_w = 0.3 - 0.5$.

Although Q is an important parameter for the sensitivity on R_s, also the geometrical factor of the sensing region (G_s) contributes (see Eq. 2). Analysing the sensitivity,

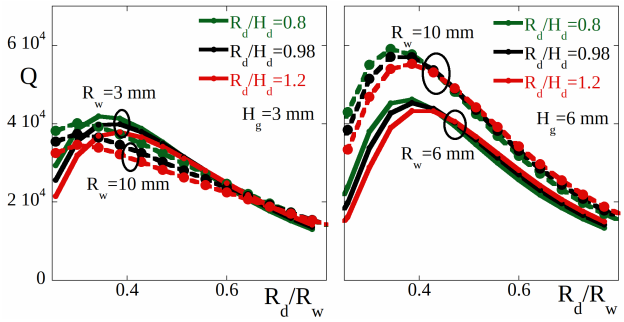

Fig. 3. Q-factor vs the normalized size of dielectric puck R_d/R_w, for TE_{011} mode, different R_d/H_d, R_w and H_g.

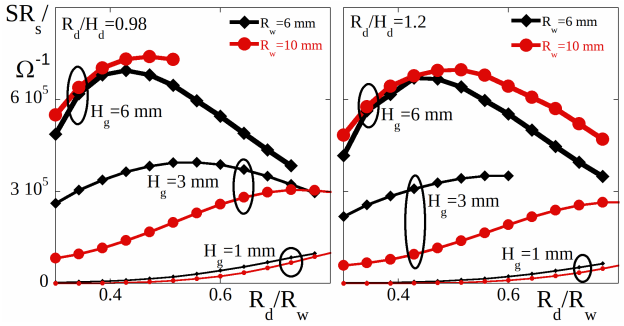

Fig. 4. Sensitivity of the resonator on R_s as a function of dielectric puck size for TE_{011} mode, different R_d/H_d values, varying R_w and H_g. Cavity height is kept below 20 mm.

it can be seen that $S_{R_s}(R_d/R_w)$ is also characterized by a peak (see Fig. 4). As in the case of Q, by increasing the gap, the S_{R_s} maximum moves to lower R_d/R_w values and does not change visibly above H_g=6 mm. Maximum sensitivity at large gap can be obtained for dielectrics with R_d/R_w=0.45 .

Summarising, the DR geometry yielding an optimal sensitivity is: R_d/H_d=0.45 , H_g=6 mm and R_w=6 mm. An estimation of the minimum detectable R_s variation ($\Delta R_s = \min(Q)/S_{R_s}$) can be done considering a minimum detectable $\min(Q)$=40 and a realistic size for the sample. Taking for the latter a rectangle 10 mm wide and ℓ=6 mm long, it would cover a fraction $\ell/(2\pi R_w)$=0.16 of the lateral wall circumference, with a proportional reduction on the sensitivity. Thus, for TE_{011} mode one obtains ΔR_s=0.36 mΩ.

IV. CONCLUSIONS

We have proposed a concept of a DR-based measuring cell for the measurement of the surface impedance of superconducting samples in a magnetic fields with varying orientations. The proposed measuring cell consists in a DR divided in two parts. A fixed one includes the dielectric puck and the bases. The second one, given by the lateral wall, is conceived to accommodate the sample and to be able to rotate within a fixed magnetic field. The main design goals and constraints have been identified and tackled with. A preliminary study, with FEM simulations, allowed to identify the ranges for the resonator dimensions needed to optimize the sensitivity on R_s measurements. A potential minimum detectable ΔR_s for measurements on 10 mm-wide and 6 mm long samples at 16 GHz is expected to be ΔR_s=0.36 mΩ.

REFERENCES

[1] P. Wikus, W. Frantz, R. Kummerle, and P. Vonlanthen,"Commercial gigahertz-class NMR magnets," Supercond. Sci. Technol., vol. 35, Art. Id. 033001, 2022.

[2] A. E. Costley, "Towards a compact spherical tokamak fusion pilot plant," Philosophical Transactions of the Royal Society A: Mathematical, Physical and Engineering Sciences, vol. 377, Art. Id. 20170439, 2019.

[3] S. Calatroni, "HTS Coatings for Impedance Reduction in Particle Accelerators: Case Study for the FCC at CERN," IEEE Trans. Appl. Supercond., vol. 26, Art. Id. 3500204, 2016.

[4] D. Alesini et al., "Galactic axions search with a superconducting resonant cavity," Phys. Rev. D, vol. 99, Art. Id. 101101(R), 2019.

[5] International Electrotechnical Commission, "IEC 61788-7:2020 Superconductivity – Part 7: Electronic characteristic measurements - Surface resistance of high-temperature superconductors at microwave frequencies." p. 87, 2020.

[6] A. Alimenti, K. Torokhtii, E. Silva, and N. Pompeo, "Challenging microwave resonant measurement techniques for conducting material characterization," Meas. Sci. Technol., vol. 30, 2019.

[7] N. Pompeo, K. Torokhtii, A. Alimenti, and E. Silva, "A method based on a dual frequency resonator to estimate physical parameters of superconductors from surface impedance measurements in a magnetic field," Measurement, vol. 184, 2021.

[8] B. W. Hakki and P. D. Coleman, "A Dielectric Resonator Method of Measuring Inductive Capacities in the Millimeter Range," IRE Trans. Microw. Theory Tech., vol. 8, pp. 402-410, 1960.

[9] L. F. Chen, C. K. Ong, C. P. Neo, V. V. Varadan, and V. K. Varadan, "Microwave Electronics: Measurement and Materials Characterization", Wiley, 2004.

[10] N. Pompeo, K. Torokhtii, and E. Silva, "Dielectric resonators for the measurements of the surface impedance of superconducting films," Meas. Sci. Rev., vol. 14, pp. 164–170, 2014.

[11] A. Alimenti, K. Torokhtii, N. Pompeo, E. Piuzzi, and E. Silva, "Microwave characterization of 3D-printer dielectric materials," in Proceedings of the

23rd IMEKO TC4 international symposium electrical & electronic measurements promote industry 4.0, Budapest, 2019, pp. 93-97.

[12] K. Torokhtii, A. Alimenti, N. Pompeo, and E. Silva, "Surface resistance scanner of the irregular pipe structures," in 24th IMEKO TC4 Int. Symp. 22nd Int. Work. ADC DAC Model. Test., 2020, pp. 70–74.

[13] A. Alimenti, N. Pompeo, K. Torokhtii, and E. Silva, "Surface Impedance Measurements in Superconductors in DC Magnetic Fields: Challenges and Relevance to Particle Physics Experiments," IEEE Instrumentation and Measurement Magazine, vol. 24, no. 9, pp. 12–20, Dec. 2021

[14] A. Alimenti, K. Torokhtii, D. Di Gioacchino, C. Gatti, E. Silva, and N. Pompeo, "Impact of Superconductors Properties on the Measurement Sensitivity of Resonant-Based Axion Detectors," Instruments, vol. 6, no. 1, p. 1, 2021.

[15] N. Pompeo and E. Silva, "Analysis of the Measurements of Anisotropic AC Vortex Resistivity in Tilted Magnetic Fields," IEEE Trans. Appl. Supercond., vol. 28, Art. Id. 8201109, 2018.

[16] K. Torokhtii, N. Pompeo, S. Sarti, and E. Silva, "Study of cylindrical dielectric resonators for measurements of the surface resistance of high conducting materials," in 22nd IMEKO TC4 International Symposium, 2017, pp. 131–134.

[17] J. Krupka, K. Derzakowski, M. Tobar, J. Hartnett, and R. G. Geyer, "Complex permittivity of some ultralow loss dielectric crystals at cryogenic temperatures," Meas. Sci. Technol., vol. 10, no. 5, pp. 387–392, May 1999.

25th IMEKO TC4 International Symposium
23rd International Workshop on ADC and DAC Modelling and Testing
IMEKO TC-4 2020
Brescia, Italy / September 12-14, 2022

Traceability routes for magnetic measurements

Marco Coïsson[1], Javier Diaz De Aguilar Rois[2], Yolanda Alvarez Sanmamed[2], Oliver Power[3], Robert Walsh[3]

[1]*INRIM, strada delle Cacce 91, 10135 Torino (TO), Italy, m.coisson@inrim.it*
[2]*CEM, calle Alfar, 2, 28760 Tres Cantos (Madrid), Spain*
[3]*NSAI, 1 Swift Square, Northwood, Santry, Dublin 9, Ireland D09 A0E4*

***Abstract* – Magnetic measurements are vital to support European challenges in areas such as electric vehicles; health; power transformation and harvesting; clean, affordable and secure energy; information and sensor technology. However, only very few European NMIs have the capabilities to perform traceable measurements of all of the most important magnetic quantities. Consequently, the adoption of novel technologies and materials is hindered by the lack of local metrological expertise that research and development activities in academia and industry could exploit. A new European project (TRaMM, 21SCP02), in the framework of the Small Collaborative Projects (SCP) call 2021, aims at transferring the expertise of INRIM (Italy) in the field of magnetic calibration and measurements to CEM (Spain) and NSAI (Ireland), thus addressing market and stakeholder requirements in the European Union and paving the way toward future smart specialisation concepts at the European level.**

I. INTRODUCTION

Magnetic measurements are relatively common in academia and in industrial research and development, as they are widely employed for the measurement of magnetic fields and for the characterisation of the magnetic cores in sensors or electronics. In addition, they are used in applications such as earth observation [1, 2], biomedicine [3, 4, 5] and health and safety requirements regarding exposure to electromagnetic fields [6, 7, 8] (The Electromagnetic Fields Directive 2013/35/EU). However, so far, the industrial and scientific communities have been unable to fully benefit from traceable and reliable measurement results because of limited access to suitable calibration facilities. With the global magnetic materials market continuously increasing at an annual growth rate of about 9.6 % [9], it is crucial to develop sustainable magnetic measurement capabilities that will support these end-users.

Even though the calibration of teslameters and coils, or the measurement of the magnetic properties of steel sheets for power applications (electrical motors, transformers) are already standardised, only few European NMIs are capable of providing a comprehensive set of measurement and calibration services in these areas, which require very specific instruments and techniques. In addition, new research activities and industrial products, in the fields of biomedicine [10], theragnostics [11], water remediation [12, 13], and security [14, 15] are expanding the need for traceable magnetic measurements for e.g. the characterisation of magnetic nanoparticles, rings, ribbons or bulk materials, or for sensing devices involving magnetoelectric phenomena [16, 17, 18, 19, 20].

Other fields requiring traceable and reliable magnetic measurements are all those where magnetic materials are exploited for energy conversion, harvesting and storage, such as automotive and powertrains, aerospace, and smart grids [21, 22, 23]. All these applications attract both scientific research and industry, and offer development and market opportunities especially for SMEs that wish to be dynamic and innovative, offering breakthrough technologies and solutions to new potential customers and markets. In spite of this exciting innovation and development, easy access to the measurement and calibration capabilities for magnetic field and magnetic material characterisations are still mostly lacking, leaving industry and academia with the unaddressed need to properly validate their technological solutions through traceable magnetic measurements.

To partially fill the gap between the available expertise at the European level, and the market and stakeholders needs, a new project labelled TRaMM (Traceability routes for magnetic measurements), within the Small Collaborative Projects call 2021 [24], has been funded for the September 2022 - February 2024 timeframe. The project aims at collecting as many stakeholders needs as possible in the field of magnetic calibrations and measurements, and to transfer the expertise of the Italian NMI (INRIM) in this field to two partners, CEM and NSAI, respectively the NMIs of Spain and Ireland, in order to strengthen the collaboration at the European level and to offer a set of measurement and calibration services to academia and industry that better address their current needs. Figure 1 shows the PERT diagram of the project.

II. NEED FOR THE PROJECT

Research relating to magnetic phenomena is well developed at the academic level in several European countries, with many groups and laboratories active in the charac-

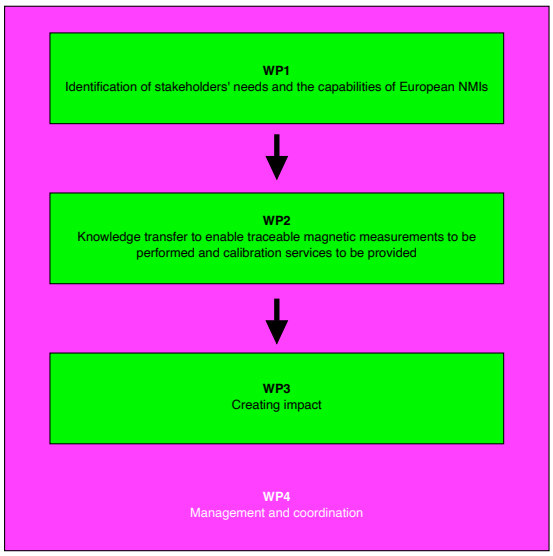

Fig. 1. PERT diagram of the TRaMM project.

terisation of magnetic materials, and a few groups particularly specialised in this subject. Scientific competence on magnetic measurements and on the characterisation of magnetic materials is therefore available in many European countries [25, 26], but most NMIs either do not offer any calibration and measurement capabilities, or just the most basic ones, leaving only very few NMIs (among which INRIM, CMI, PTB, VSL), which are able to provide a wide and complete offering on this topic [27].

The most developed measurement capability is magnetic flux density. While secondary standards which use calibrated coils or probes (Hall probes, fluxgates, etc.) are commercially available, their calibration status is often questionable. The reason for this is the lack of adequate metrological support throughout Europe. This, in turn, hinders the development of a mature industry that can exploit these technologies. A few academic laboratories and very few NMIs (e.g. INRIM, CMI, PTB) also offer competencies in the characterisation of magnetic materials. A few methods have been standardised, mostly within the framework of the IEC 60404 series of standards, especially concerning power losses in the steel sheets that are used in power technologies. Other methods have also been developed to the point that a few NMIs offer calibration and measurement capabilities approved under the CIPM Multilateral Arrangement for the measurement e.g. of magnetic permeability, power losses, (BH) product, DC polarisation, coercivity in hard magnets, etc. in some materials with specific geometries. However, specialised research laboratories have a plethora of different techniques which allow for the measurement of the magnetic properties of materials in different forms (nanoparticles, thin films, bulk samples, liquids), shapes (wires, ribbons, rings, strips, films, etc.), at different temperatures (from liquid Helium to approximately 1000 °C), and at different frequencies (from DC to GHz). Not all of these characterisations are possible in all conditions, but the academic research community and the instrumentation industry are continuously developing new methods and techniques to investigate the magnetic properties of materials in special or uncommon conditions. These techniques, although scientifically accepted, are rarely submitted to a true metrological validation, partly because, in materials research, the uncertainty deriving from the material under test, and the difficulty in measurement reproducibility, tend to hide, to a first approximation, the other uncertainty sources. In addition, ring comparisons among several laboratories have underlined the difficulty of obtaining compatible results with new measurement techniques (e.g. EU TD 1402 COST Action RADIOMAG) and even with apparently consolidated comparisons [28]. For this reason, new efforts have recently been made from a methodological point of view, to help to develop a metrological background in magnetic measurements, e.g. with new international standards (ISO/TS 198071, ISO/TS 198072) for the characterisation of magnetic nanoparticles [29, 30].

The task of extending the availability of traceable magnetic measurement and calibration services to more EU countries cannot rely only on the presence of a local scientific community that is expert in the field of magnetic measurements, because the scientific community is mostly oriented towards frontier research and rarely has the possibility, or the interest, to invest in a serious metrological infrastructure, providing traceability and calibration facilities. On the other hand, while the NMIs have the necessary experience in providing this type of infrastructure, most of them only have limited, if any, experience in magnetic measurements, which cover a very large domain requiring a wide set of competencies (magnetic measurements can broadly be divided into two groups: 1) the measurement of magnetic fields and 2) the measurement of the magnetic properties of matter; these two groups require different equipment and different approaches, and links to e.g. electrical, frequency and temperature metrology are required to guarantee a serious metrological infrastructure). In order to ensure the quickest possible means of spreading this knowledge, and to avoid duplicated efforts, a coordinated effort is envisaged, involving the NMIs wishing to develop their capabilities in magnetic measurements, and the NMIs that through a longstanding scientific activity in the field can offer high level training and a deep understanding of the required metrological background and infrastructure.

III. OVERVIEW OF THE PROJECT

Figure 2 presents schematically an overview of the project. While INRIM provides fundamental training on magnetic measurements and calibration to CEM and NSAI, the stakeholders' needs are collected and will pro-

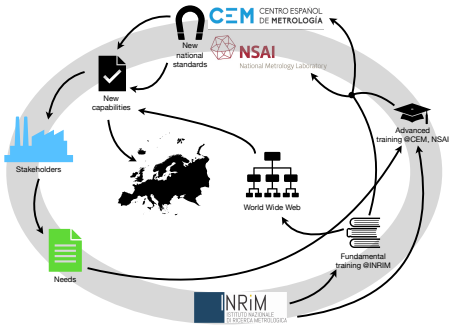

Fig. 2. Scheme of the TRaMM project.

vide the basis for the advanced training. The training materials and the stakeholders' needs will be shared online and will be available to any interested parties. Thanks to the newly developed national standards and to the newly acquired competences, the consortium of the project will be able to offer new services to the stakeholders and improve the EU capabilities in the field of magnetic measurements and calibration, thus closing the feedback loop.

IV. STAKEHOLDERS

Relevant stakeholders for the TRaMM project will therefore belong to (but are not limited to) the following categories: academia and research centres working on magnetic materials and applied magnetism (for energy transformation, actuation, sensing, biomedicine); industries belonging to electric vehicle supply chains (electric motors) and power application supply chains (electric motors and transformers); industries belonging to sensor supply chains (magnetic field probes, position, rotation, angle, speed, vibration, etc., detectors, bit detectors and systems for magnetic registration); industries belonging to the magnetic field monitoring supply chain (measurement of magnetic fields in or around industrial equipment, biomedical devices such as NMR, personal exposure meters, etc.); industries involved in medical device manufacturing; industries in the food supply chain (metal detection in food processing); industries involved in electric and electronic components (e.g. microwave components); academia and research centres working on geomagnetism; industries belonging to the steel supply chain (manufacturers and industries processing semifinished products) and to the weakly magnetic steel supply chains (aerospace, naval and military industries).

Even though not directly addressed at them, the TRaMM project is strongly focussed on stakeholders, as their needs will form the basis of the knowledge transfer that will take place among the NMIs making up the consortium. The stakeholders needs will therefore be collected to form a large set of requirements and expectations, in terms of needed magnetic calibration and measurement services (frequencies, intensities, kind of materials or samples, etc.), that will be used to analyse the alignment between the stakeholders high level needs and the metrology services provided or planned by the NMIs.

INRIM, CEM and NSAI will contact as many potential stakeholders as possible; however, any academic or industrial partner interested in magnetic calibration and measurement services is invited to contact the coordinator or one of the three NMIs to share their needs and expectations, and possibly to be part of the stakeholders committee, in order to help heading the training and knowledge transfer steps of the project.

V. TRAINING

The training process will involve expert personnel from INRIM and interested personnel from both CEM and NSAI, and will focus first on fundamental aspects of magnetic measurements and calibration, and then on more advanced topics of specific interest of the stakeholders community. Training events will be held both online and in person, and all training material will be made publicly and freely available online in order to reach as many potentially interested partners and stakeholders as possible. Additionally, interested NMIs that are not formally involved in the TRaMM project will have the possibility to attend the training events, with the aim of reaching the widest possible audience.

The training events will include several different approaches:

- classes on fundamentals of magnetism, magnetic materials and measurements;
- classes on advanced topics of magnetism, magnetic materials and measurements;
- laboratories on measurements of magnetic fields and magnetic properties of matter, calibration of measurement equipment;
- hands-on sessions and videos on specific equipments and measurement setups;
- classes and training on ensuring traceability of magnetic measurements and calibration.

The contents mentioned above will be developed according to the stakeholders' needs and the requests of the participating partners.

The following measurement and calibration techniques are among the ones that it will be possible to investigate in the framework of the TRaMM project:

- dc and ac calibration of magnetic field probes (e.g. Hall probes) under three-axial compensation of Earth magnetic field;

- calibration of a magnetic field standard through nuclear magnetic resonance;
- measurement of magnetic permeability of soft materials or ferrites;
- measurement of frequency-dependent power losses in steel sheets;
- measurement of frequency-dependent power losses of ferrites;
- measurement of static magnetic properties of nanoparticles and nanoparticles dispersions;
- measurement of magnetic properties of hard magnetic materials by vibrating sample magnetometer or B-H meter.

The specific measurement and calibration techniques that will be treated will be defined in agreement among the project partners after a thorough investigation of their and their stakeholders' needs.

VI. KNOWLEDGE TRANSFER AND IMPACT

The TRaMM project will create impact through its three objectives. With Objective 1, the involved NMIs will identify their stakeholders' needs for magnetic measurement and calibration facilities and plan the development of the services and measurement capabilities that they will offer, in order to meet these needs. With Objective 2, the involved NMIs will gain sufficient competencies to be able to offer the subset of magnetic measurement and calibration capabilities that will be relevant to their stakeholders' needs, as well as the required consultancy services that will create immediate impact for the stakeholders. Finally, with Objective 3 a smart-specialisation concept will be defined, to promote the coordination among the participating NMIs and other NMIs to pave the way for the future development of their capabilities in magnetic measurements and calibration according to the stakeholders' needs through a coordinated approach to identify priority areas and strengthened trust in capabilities. It is expected that the smart specialisation concept will create impact by widening the offering of magnetic measurement and calibration capabilities in the European Union, both through an increased number of expert NMIs in the field, and through an increased awareness, among the stakeholders, of the availability of these capabilities.

All of the aforementioned impacts will benefit existing stakeholders, which include magnetic materials properties research centres and universities, calibration laboratories, the Earth observation industry, and companies performing onsite testing of health and safety requirements regarding exposure to electromagnetic fields with respect to the Electromagnetic Fields Directive 2013/35/EU. They also include the logistics industry which is required to measure the magnetic fields of shipments sent by air freight, and the aviation industry which uses magnetic techniques for the nondestructive testing of airframes.

In the longer term, the outputs from this project will enable more NMIs to acquire capabilities in magnetic measurements and calibrations. This will even be possible after the end of this project, thanks to the availability of the training material online.

A long-term impact of the project will be the partners' ability to participate in the standardisation activities and committees relating to magnetic testing, as the project's outcomes will be shared with EURAMET Technical Committee for Electricity and Magnetism. The partners' competencies on magnetic measurements will offer the required knowledge to define the correct standardisation paths for new measurement techniques (e.g. the specific loss power for the materials that are used in biomedical applications), or for existing techniques that are currently used in non-standard conditions (e.g. magnetic fields at higher frequency values, high-intensity static magnetic fields in biological media, etc.).

To promote a wider impact, the TRaMM project will also organise a workshop, toward the end of its funding period (i.e. Fall 2023 - Winter 2024), where stakeholders, other NMIs, academia, any interested parties will be invited to join the project participants to share the experience developed during the project, and to analyse future routes for improving the collaboration at the EU level, for further extending the measurement and calibration capabilities on magnetism and magnetic properties of materials, for approaching standardisation bodies in order to drive the development of new standards and regulations at the international level toward the stakeholders requirements. All interested parties are invited to attend the workshop, and can get in touch with the project participants for further information and details.

REFERENCES

[1] M.J.S. Johnston, "Review of electric and magnetic fields accompanying seismic and volcanic activity", Surveys in Geophysics, vol. 18, 1997, pp. 441-476, doi: 10.1023/A:1006500408086.

[2] K.L. Verosub, A.P. Roberts, "Environmental magnetism: past, present, and future", J. Geophysical Research, vol. 100, 1995, pp. 2175-2192, doi: 10.1029/94JB02713.

[3] Y. Li, H. Cheng, Z. Alhalili, G. Xu, G. Gao, "The progress of magnetic sensor applied in biomedicine: a review of non-invasive techniques and sensors", J. Chinese Chem. Soc., vol. 68, 2021, pp. 216-227, doi: 10.1002/jccs.202000353.

[4] N.M. Shupak, F.S. Prato, A.W. Thomas, "Therapeutic uses of pulsed magnetic-field exposure: a review", URSI Radio Science Bulletin, vol. 2003, 2003, pp. 9-

32, doi: 10.23919/URSIRSB.2003.7909506.

[5] E.A. P'erigo, G.. Hemery, O. Sandre, D. Ortega, E. Garaio, F. Plazaola, F.J. Teran, "Fundamentals and advances in magnetic hyperthermia", Appl. Phys. Rev., vol. 2, 2015, pp. 041302, doi: 10.1063/1.4935688.

[6] A. Ahlbom, "A review of the epidemiologic literature on magnetic fields and cancer", Scand. J. Work Environ. Health, vol. 14, 1998, pp. 337-343, https://www.jstor.org/stable/40965589.

[7] P. Levallois, "Hypersensitivity of human subjects to environmental electric and magnetic field exposure: a review of the literature", Env. Heath Persp., vol. 110, 2002, pp. 613-618, doi: 10.1289/ehp.02110s4613.

[8] D.A. Savitz, "Overview of occupational exposure to electric and magnetic fields and cancer: advancements in exposure assessment", Env. Health Persp., vol. 103, 1995, pp. 69-74, doi: 10.1289/ehp.95103s269.

[9] "Magnetic Materials Market by Type (Semi-Hard Magnet, Soft Magnet, Hard/Permanent Magnet) & by Application (Automotive, Electronics, Industrial, Power Generation, and Others) - Global Forecasts to 2020", report code CH 3238, March 2016, https://www.marketsandmarkets.com/Market-Reports/magnetic-materials-397.html

[10] I. Andreu, E. Natividad, "Accuracy of available methods for quantifying the heat power generation of nanoparticles for magnetic hyperthermia", Int. J. Hyperthermia, vol. 29, 2013, pp. 739-751, doi: 10.3109/02656736.2013.826825

[11] V.I. Shubayev, T.R. Pisanic II, S. Jin, "Magnetic nanoparticles for theragnostics", Adv. Drug Delivery Rev., vol. 61, 2009, pp. 467-477, doi: 10.1016/j.addr.2009.03.007.

[12] A.G. Leone, A.A.P. Mansur, H.S. Mansur, "Advanced functional nanostructures based on magnetic iron oxide nanomaterials for water remediation: a review", Water Res., vol. 190, 2021, pp. 116693, doi: 10.1016/j.watres.2020.116693.

[13] R.D. Ambashta, M. Sillanpää, "Water purification using magnetic assistance: a review", J. Haz. Mat., vol. 180, 2010, pp. 38-49, doi: 10.1016/j.jhazmat.2010.04.105.

[14] W. Irnich, "Electronic security systems and active implantable medical devices", Pacing and clinical electrophysiology, vol. 25, 2002, pp. 1235-1258, doi: 10.1046/j.1460-9592.2002.01235.x.

[15] V. Zhukova, P. Corte-Leon, J.M. Blanco, M. Ipatov, J. Gonzalez, A. Zhukov, "Electronic surveillance and security applications of magnetic microwires", Chemosensors, vol. 9, 2021, pp. 100, doi: 10.3390/chemosensors9050100.

[16] C. Morón, C. Cabrera, A. Morón, A. García, M. González, "Magnetic sensors based on amorphous ferromagnetic materials: a review", Sensors, vol. 15, 2015, pp. 28340-28366, doi: 10.3390/s151128340.

[17] Y. Wang, J.Li, D. Viehland, "Magnetoelectrics for magnetic sensor applications: status, challenges and perspectives", Materials Today, vol. 17, 2014, pp. 269-275, doi: 10.1016/j.mattod.2014.05.004.

[18] S. Zuo, H. Heidari, D. Farina, K. Nazarpour, "Miniaturised magnetic sensors for implantable magnetomyography", Adv. Materials Tech., vol. 5, 2020, pp. 2000185, doi: 10.1002/admt.202000185.

[19] S. Wei, X. Liao, H. Zhang, J. Pang, Y. Zhou, "Recent progress of fluxgate magnetic sensors: basic research and application", Sensors, vol. 21, 2021, pp. 1500, doi: 10.3390/s21041500.

[20] B. Cao, K. Wang, H. Xu, Q. Qin, J. Yang, W. Zheng, Q. Jin, D. Cui, "Development of magnetic sensor technologies for point-of-care testing: fundamentals, methodologies and applications", Sensors and Actuators A: Physical, vol. 312, 2020, pp. 112130, doi: 10.1016/j.sna.2020.112130.

[21] C.M. Leung, J. Li, D. Viehland, X. Zhuang, "A review on applications of magnetoelectric composites: from heterostructural uncooled magnetic sensors, energy harvesters to highly efficient power converters", J. Phys. D: Appl. Phys., vol. 51, 2018, pp. 263002, doi: 10.1088/1361-6463/aac60b.

[22] F. Yang, L. Du, H. Yu, P. Huang, "Magnetic and electric energy harvesting technologies in power grids: a review", Sensors, vol. 20, 2020, pp. 1496, doi: 10.3390/s20051496.

[23] L. Sun, M. Cheng, H. Wen, L. Song, "Motion control and performance evaluation of a magnetic-geared dual-rotor motor in hybrid powertrain", IEEE Transactions on Industrial Electronics, vol. 64, 2017, pp. 1863-1872, doi: 10.1109/TIE.2016.2627018.

[24] https://msu.euramet.org/current_calls/scp_2021/

[25] https://www.magnetometry.eu

[26] https://magnetism.eu

[27] https://www.bipm.org/kcdb/cmc/quicksearch?includedFilters=&excludedFilters=cmcBranches.Density%2CcmcBranches.Fluid+flow%2CcmcRmo.APMP%2CcmcRmo.COOMET&page=0&keywords=magnetic

[28] MagNaStand Final Publishable Report: https://www.euramet.org/download/?L=0&tx_eurametfiles_download%5Bfiles%5D=41169&tx_eurametfiles_download%5Bidentifier%5D=%252Fdocs%252FEMRP%252FJRP%252FJRP_Summaries_2016%252FNormative%252F16NRM04_Final_Publishable_Report.pdf&tx_eurametfiles_download%5Baction%5D=download&tx_eurametfiles_download%5Bcontroller%5D=File&cHash=887a8ca2d84cc6137aef3d013cfc73e9

[29] ISO/TS 198071 Nanotechnologies Magnetic nanomaterials Part 1: Specification of characteristics and measurements for magnetic nanosuspensions. International Organisation for Standardisation, 2019.

[30] ISO/TS 198072 Nanotechnologies Magnetic nanomaterials Part 2: Specification of characteristics and measurements for nanostructured superparamagnetic beads for nucleic acid extraction. International Organisation for Standardisation, under development.

Index of Authors